Topics in Applied Physics 130

Yang Yang
Gang Li *Editors*

Progress in High-Efficient Solution Process Organic Photovoltaic Devices

Fundamentals, Materials, Devices and Fabrication

Springer

Topics in Applied Physics

Volume 130

Topics in Applied Physics is a well-established series of review books, each of which presents a comprehensive survey of a selected topic within the broad area of applied physics. Edited and written by leading research scientists in the field concerned, each volume contains review contributions covering the various aspects of the topic. Together these provide an overview of the state of the art in the respective field, extending from an introduction to the subject right up to the frontiers of contemporary research.

Topics in Applied Physics is addressed to all scientists at universities and in industry who wish to obtain an overview and to keep abreast of advances in applied physics. The series also provides easy but comprehensive access to the fields for newcomers starting research.

Contributions are specially commissioned. The Managing editors are open to any suggestions for topics coming from the community of applied physicists no matter what the field and encourage prospective editors to approach them with ideas.

Yang Yang · Gang Li
Editors

Progress in High-Efficient Solution Process Organic Photovoltaic Devices

Fundamentals, Materials, Devices and Fabrication

Springer

Editors
Yang Yang
Materials Science and Engineering
University of California Los Angeles
Los Angeles, CA
USA

Gang Li
Materials Science and Engineering
University of California Los Angeles
Los Angeles, CA
USA

ISSN 0303-4216 ISSN 1437-0859 (electronic)
Topics in Applied Physics
ISBN 978-3-662-45508-1 ISBN 978-3-662-45509-8 (eBook)
DOI 10.1007/978-3-662-45509-8

Library of Congress Control Number: 2014957474

Springer Heidelberg New York Dordrecht London

Printed on acid-free paper

Springer-Verlag GmbH Berlin Heidelberg is part of Springer Science+Business Media (www.springer.com)

Preface

With the world population growth and the pursuit of improvement in human life standards, energy has become one of the greatest global challenges for man. The currently dominant dependence on fossil fuels not only accelerates diminishing of the natural resource, but also leads to severe environmental and climate impact. Among all the renewable energy sources, the sun is the ultimate clean energy source for humans—an hour of solar energy from sunlight is almost the same as the world energy consumption in one year ($\sim$16 TW). The pursuit of low cost solar cell technology has always been an important scientific and industrial field. The solution process of solar cell technologies such as organic solar cells (OPV) technology has attracted growing interest due to attractive features such as synthetic variability, low-temperature processing, and the possibility of producing light-weight, flexible, roll-to-roll compatible manufacturing. Particularly in the past decade, society has achieved significant progress in this field.

This book consists of 13 chapters written by leading experts in organic solar cell field, each covering a specific area of OPV technology categorized by the following four aspects of the book—Fundamentals, Materials, Devices, Fabrication technology/Applications.

Part I—*Fundamentals* is made of four chapters. In Chap. 1, Vardeny and Sheng used optical probe techniques including broadband femtosecond transient and continuous wave (cw) photomodulation spectroscopies and electroabsorption for studying the photoexcitation dynamics in classical polymer fullerene blends, and their results show that charge transfer complex (CTC) and film morphology play a crucial role in carrier photogeneration in these systems. So and co-workers addressed charge transport aspect of OPV polymers and blends in Chap. 2, where they introduce a new transport characterization tool—admittance spectroscopy (AS), to extract charge carrier mobility. In Chap. 3, using Photoemission Spectroscopy techniques, Gao et al. provided scientific insight into the improved charge transfer at the organic semiconductors and electrode interface by insertion of metal oxide buffer layers. It is followed by Shuai and co-workers' quantitative theoretical understanding of the optical and electronic processes in organic photovoltaic materials, including optical absorption and emission spectra for conjugated

oligomers, energy transfer in polymers, charge transport in organic semiconductors, and device modeling of heterojunction solar cells based on dynamic Monte Carlo simulation and the continuum model.

In Part II—*Materials*, three chapters covered three key material types in OPV. Hsu and co-workers reviewed recent advances in p-type conjugated polymers in Chap. 5, which also presented the principle of molecular design with structure-properties relationship. Cao, Huang and co-workers' review covers progress on linear Donor-Acceptor type conjugated polymers and acceptor pended conjugated polymers as p-type photoactive material, as well as the development of water/alcohol soluble conjugated polymer interfacial materials. In Chap. 7, Brunetti reviewed in detail the features and characteristics of fullerene and its derivatives as acceptors in bulk heterojunction solar cells.

In the third part—*Devices*, we have four chapters covering morphology, interface, plasmonics, and tandem OPV devices. Wei and co-workers reviewed reciprocal-space and real-space techniques to investigate the photoactive layer morphology in Chap. 8. The effects of the relative length scales of PCBM clusters and polymer (P3HT as example) crystallites on device performance were presented. Jen's team presented an overview of the recent development of effective interfacial materials (including organic, inorganic, and hybrid materials) used for both organic/metal and organic donor/acceptor interface engineering, and the integration of these materials in different device architectures to enhance efficiency and stability are also discussed. In Chap. 10, Chen et al. reviewed recent progress related to the incorporation of plasmonic nanostructures in OPVs as a means of enhancing power conversion efficiencies. Tandem solar cell concept and the recent progress in solution process tandem OPV devices were reviewed by Yang and Li et al. in Chap. 11, which has led to close to 12 % solar cell.

In the last part—*Fabrication and Application*, Guo presented a novel processing technology—ESSENCIAL—to achieve high performance, which was followed by report on high efficiency thick OPV devices, both are roll-to-roll fabrication friendly. The Chap. 13—was contributed by Zhu, who provided a review on the progress of (semi)transparent solar cell—a very unique feature of OPV with great potential in building integrated PV and portable electronics market.

This book is organized with the intention to provide a big picture of the latest progress in the OPV field for the general audience, and at the same time give in-depth discussion on fundamentals for interested audiences. We hope the book can serve its function to draw your attention to this emerging organic solar cell field with great potential.

Los Angeles, CA, USA

Yang Yang
Gang Li

Contents

Part II Materials

Part III Devices

Contributors

Fulvio G. Brunetti Department of Chemistry and Biochemistry, University of California Santa Barbara, Santa Barbara, CA, USA

Yong Cao Institute of Polymer Optoelectronic Materials and Devices, State Key Laboratory of Luminescent Materials and Devices, South China University of Technology, Guangzhou, People's Republic of China

Kevin K.H. Chan Department of Physics and Institute for Advanced Materials, Hong Kong Baptist University, Kowloon Tong, Hong Kong, China

Fang-Chung Chen Department of Photonics and Display Institute, National Chiao Tung University, Hsinchu, Taiwan

Yen-Ju Cheng Department of Applied Chemistry, National Chiao Tung University, Hsinchu, Taiwan

Shang-Chieh Chien Department of Photonics and Institute of Electro-optical Engineering, National Chiao Tung University, Hsinchu, Taiwan

Mao-Yuan Chiu Department of Materials Science and Engineering, National Chiao Tung University, Hsin Chu, Taiwan, ROC

Ming-Kai Chuang Department of Photonics and Institute of Electro-optical Engineering, National Chiao Tung University, Hsinchu, Taiwan

Letian Dou Department of Materials Science and Engineering, University of California Los Angeles, Los Angeles, CA, USA

Chunhui Duan Institute of Polymer Optoelectronic Materials and Devices, State Key Laboratory of Luminescent Materials and Devices, South China University of Technology, Guangzhou, People's Republic of China

Yongli Gao Department of Physics and Astronomy, University of Rochester, Rochester, NY, USA

Ziruo Hong Department of Materials Science and Engineering, University of California Los Angeles, Los Angeles, CA, USA

Chain-Shu Hsu Department of Applied Chemistry, National Chiao Tung University, Hsinchu, Taiwan

Fei Huang Institute of Polymer Optoelectronic Materials and Devices, State Key Laboratory of Luminescent Materials and Devices, South China University of Technology, Guangzhou, People's Republic of China

Irfan Irfan Department of Physics and Astronomy, University of Rochester, Rochester, NY, USA

L. Jay Guo Macromolecular Science and Engineering, University of Michigan, Ann Arbor, MI, USA; Electrical Engineering and Computer Science, University of Michigan, Ann Arbor, MI, USA

Alex K.-Y. Jen Department of Materials Science and Engineering, University of Washington, Seattle, WA, USA

Yuqian Jiang MOE Key Laboratory of Organic OptoElectronics and Molecular Engineering, Department of Chemistry, Tsinghua University, Beijing, China

Harrison K.H. Lee Department of Physics and Institute for Advanced Materials, Hong Kong Baptist University, Kowloon Tong, Hong Kong, China

Chang-Zhi Li Department of Materials Science and Engineering, University of Washington, Seattle, WA, USA

Gang Li Department of Materials Science and Engineering, University of California Los Angeles, Los Angeles, CA, USA

Lingyi Meng Collaborative Innovation Center of Chemistry for Energy Materials, Xiamen University, Xiamen, China

Hui Joon Park Division of Energy Systems Research, Ajou University, Suwon, Korea

C.-X. Sheng Department of Physics and Astronomy, University of Utah, Salt Lake City, UT, USA; School of Electronic and Optical Engineering, Nanjing University of Science and Technology, Nanjing, Jiangsu, China

Zhigang Shuai MOE Key Laboratory of Organic OptoElectronics and Molecular Engineering, Department of Chemistry, Tsinghua University, Beijing, China; Collaborative Innovation Center of Chemistry for Energy Materials, Xiamen University, Xiamen, China

S.K. So Department of Physics and Institute for Advanced Materials, Hong Kong Baptist University, Kowloon Tong, Hong Kong, China

Yu-Wei Su Department of Materials Science and Engineering, National Chiao Tung University, Hsin Chu, Taiwan, ROC

Z.V. Vardeny Department of Physics and Astronomy, University of Utah, Salt Lake City, UT, USA

Chien-Lung Wang Department of Applied Chemistry, National Chiao Tung University, Hsinchu, Taiwan

Kung-Hwa Wei Department of Materials Science and Engineering, National Chiao Tung University, Hsin Chu, Taiwan, ROC

Jhong-Sian Wu Department of Applied Chemistry, National Chiao Tung University, Hsinchu, Taiwan

Jyh-Lih Wu Department of Photonics and Institute of Electro-optical Engineering, National Chiao Tung University, Hsinchu, Taiwan

Yang Yang Department of Materials Science and Engineering, University of California Los Angeles, Los Angeles, CA, USA

Hin-Lap Yip Department of Materials Science and Engineering, University of Washington, Seattle, WA, USA

Chengmei Zhong Institute of Polymer Optoelectronic Materials and Devices, State Key Laboratory of Luminescent Materials and Devices, South China University of Technology, Guangzhou, People's Republic of China

Fu Rong Zhu Department of Physics, Hong Kong Baptist University, Hong Kong, China

Part I
Fundamentals

Chapter 1
Optical Studies of Photoexcitations in Polymer/Fullerene Blends for Organic Photovoltaic Applications

C.-X. Sheng and Z.V. Vardeny

Abstract We used a variety of optical probe techniques including broadband femtosecond transient and continuous wave (cw) photomodulation spectroscopies and electroabsorption for studying the photophysics in two typical π-conjugated polymers, namely regio-regular poly (3-hexyl thiophene) (RR-P3HT) with self-organized π-stacked two-dimensional lamellae, and 2-methoxy-5-(2′-ethylhexyloxy) poly(p-para-phenylene-vinylene) (MEH-PPV) with amorphous nanomorphology; both polymers in pristine and blend with fullerene molecules. In the pristine forms we identified singlet excitons as the primary photoexcitations, having typical photoinduced absorption (PA) band that is correlated with stimulated emission. In contrast, in polymer/fullerene blends the photogenerated excitons quickly decay giving rise to a novel photoexcitation species, and the stimulated emission is absent. For the blends we provide strong evidence for the existence of charge transfer complex (CTC) manifold that is formed inside the optical gap of the polymer and fullerene constituents, which is clearly revealed in the electro-absorption spectrum. Because the lowest energy CTC lies below the optical gap then it is possible to directly generate polarons in the blends without involving intrachain excitons in the polymer phase, when using below gap pump excitation. When using excellent quality materials we present evidence that the CTC states are populated in RR-P3HT/fullerene blend within 20 ps following exciton photogeneration in the polymer chains; but no charge polarons are generated on their expense up to ~ 2 ns. Interestingly the CTC states are photogenerated much faster in D-A blends having smaller domain size such as in regio-random P3HT/PCBM and MEH-PPV/C_{60}; however the CTCs do not easily dissociate in these blends because of the large binding energy. Our findings indicate that the CTC state and film morphology play a

C.-X. Sheng · Z.V. Vardeny (✉)
Department of Physics and Astronomy, University of Utah, Salt Lake City, Utah 84112, USA
e-mail: val@physics.utah.edu

C.-X. Sheng
e-mail: cxsheng@njust.edu.cn

C.-X. Sheng
School of Electronic and Optical Engineering, Nanjing University of Science and Technology, Nanjing 210094, Jiangsu, China

Y. Yang and G. Li (eds.), *Progress in High-Efficient Solution Process Organic Photovoltaic Devices*, Topics in Applied Physics 130,
DOI 10.1007/978-3-662-45509-8_1

crucial role in carrier photogeneration in donor-acceptor blends. More thorough investigation of the CTC and its interaction with free polaron excitations may improve the power conversion efficiency of organic solar cells and drive the development of novel photoactive materials.

1.1 Introduction

In recent years, π-conjugated polymer (PCP) based organic solar cells have attracted widespread interest in academia, research institutes and commercial companies. PCPs are promising electronic materials because of their electronic properties, versatility, flexibility, easy of processing and low cost. These factors contribute to the promise that organic solar cells may be able to provide a cost effective alternative compared to inorganic solar cells. In fact the most efficient organic photovoltaic (OPV) cells to date are based on bulk heterojunctions (BHJ) comprised of a blend of a PCP and fullerene, having certified power conversion efficiency (PCE) up to 9 % [1–3]. Despite these significant advances in device performance, the intricacies of charge carrier photogeneration and evolution in donor–acceptor (D-A) blends for OPV applications are still the focus of fundamental research aiming to develop novel photoactive materials and improve the power conversion efficiency of organic solar cell devices [4, 5].

The PCP backbone chain geometry is comprised of series of overlapping σ orbitals formed via sp^2 hybridization where the π-electron is left unbonded, thereby creating a conjugated chain of delocalized π-electrons. These organic semiconductors have a highly anisotropic quasi-one-dimensional (1D) electronic structure that is fundamentally different from the structures of conventional inorganic semiconductors. As a result, the primary photoexcitations in PCPs are bound electron-hole pairs (excitons) with large binding energy, E_B, rather than free charge carriers or excitons with small E_B as in inorganic semiconductors [6]. E_B of singlet intrachain excitons has been experimentally shown to be of order of 0.5 eV [7–9], which is much higher than the room temperature energy, k_BT (where k_B is the Boltzmann factor and T is the temperature), and the most strongly coupled vibration energy of ∼0.2 eV [10–12]. Therefore achieving efficient charge photogeneration by excitons dissociation is the most crucial process in polymer-based solar cells.

The observation of ultrafast photoinduced charge transfer from a conjugated polymer molecule to a C_{60} opened up the potential of PCP based solar cells [13, 14]. This was achieved when the acceptor fullerene molecule was very close to the polymer donor. In more modern D-A blends the donors and acceptors form separate nanosize domains, and are therefore not in close proximity to each other. This poses a problem in OPV devices based on blends if the exciton diffusion length (∼10 nm) is short and thus limits the active layer thickness [15–18]. The donor-acceptor interfacial area available for exciton dissociation is substantially enhanced in PCP/fullerene blend films. However efficient exciton ionization at the D-A interface

cannot by itself guarantee efficient photocurrent generation, because charge transport in the blend needs be efficient. Optimal phase separation of polymer and fullerene domains for balancing the exciton dissociation and charge transport are essential for enhancing solar cell PCE. In order to achieve this goal the bicontinuous interpenetrating network of the electron donor (polymer) and acceptor materials (fullerene) in BHJ structure is an ideal morphology [19].

Although there are still many unanswered questions [20–23], the process of charge photogeneration in polymer/fullerene blend is usually described in a series of sequential steps as follows [4, 5, 24, 25]: (i) Absorption of an above-gap photon in the polymer domains generates intrachain exciton on the polymer chains; (ii) The exciton subsequently diffuses to the polymer/fullerene interface; (iii) where it may be quenched by electron transfer from the polymer to the fullerene. However the significant Coulomb attraction and/or wavefunction overlap between the electron-polaron in the fullerene domain and hole-polaron on the polymer domain results in the formation of charge transfer (CT) exciton state. Then (iv) free charge carrier generation requires further dissociation of these initially generated CT excitons. Importantly the CT exciton can be directly generated using below gap photoexcitation, without involving the first process of intrachain exciton generation [26, 27]. Surprisingly, in this case too the CT exciton may still dissociate into polarons in the polymer and fullerene domains. However these polarons are trapped at the interfaces with relatively long lifetime and do not substantially contribute to the photocurrent density in photovoltaic applications. It is therefore clear that the properties and dynamics of photoexcitations in PCPs and PCP/fullerene blends are of fundamental importance because they play an essential role in the device operation.

In this chapter we review our research studies of photoexcitations in blends of fullerene with two typical PCPs, namely, 2-methoxy-5-(2′-ethylhexyloxy) poly (phenylene-vinylene) (MEH-PPV) and regio-regular poly (3-hexylthiophene) (RR-P3HT), in a broad time interval from femtoseconds to milliseconds and spectral range from 0.1 to 3.5 eV [28–30]. The main experimental technique that we have used is transient photomodulation (PM), which gives information complementary to that obtained by transient photoluminescence (PL), which is limited to radiative processes, or transient photoconductivity (PC), which is sensitive to high mobility photocarriers. The PM method, in contrast, is sensitive to non-equilibrium excitations in *all* states.

1.1.1 Optical Properties of Photoexcitations in Pristine π-Conjugated Polymers and in Polymers/Fullerene Blends

One way to detect and characterize short-lived and long-lived photoexcitations in PCP and PCP/fullerene blends is to study their optical absorption using the PM technique. The photoexcitations in π-conjugated polymers give rise to gap states in the electron and phonon level spectra, respectively. The scheme of the PM experiments is the following: the polymer sample is photoexcited with a ‘pump’

beam of light, and the related change in the optical absorption of the sample is probed in a broad spectral range from the IR to visible spectral range using a variety of 'probe' light sources. The PM spectrum is essentially a difference spectrum, i.e., the difference in the optical absorption ($\Delta\alpha$) spectrum of the polymer when it contains a nonequilibrium photoexcitations concentration and that in the equilibrium ground state. Therefore the optical transitions of the various photoexcitations are of fundamental importance here. In addition, since the PM method does not change the π-electron density in the organic semiconductors, then the π-electron density is constant. Therefore there is a sum rule for $\Delta\alpha$ in the PM spectrum. Namely, there is equal 'amount' of spectral contribution with $\Delta\alpha > 0$ (photoinduced absorption-PA) and $\Delta\alpha < 0$ (photobleaching-PB) [31].

In a strictly 1D chain model, a single charge carrier added onto the polymer chain forms a spin ½ polaron [32]. However, rather than discussing the various electronic states in PCPs in terms of one-electron continuous bands (that is valence and conducting bands), the use of HOMO (highest occupied molecular orbital) and LUMO (lowest unoccupied molecular orbital) has been the preferred description. In the semiconductor description HOMO is the top of the valance band, LUMO is the bottom of the conduction band and this forms a band gap, E_g = LUMO–HOMO [33]. Once the electron-hole interaction is dominant in the model Hamiltonian that describes the electronic states in PCPs, then the excited states become an exciton which is a bound state of electron and hole [34, 35].

Most PCPs belong to the C_{2h} point group symmetry [36]. The notations of odd and even wavefunctions are therefore described in terms of the C_{2h} group irreducible representations with alternating odd (B_u) and even (A_g) parity symmetry [37, 38]. In the exciton description the ground state is $1A_g$ and the first dipole coupled state is the $1B_u$ exciton. In this case the optical gap $E_{op} = E(1B_u) - E(1A_g)$, which is smaller than the free carrier gap, E_g. In case that $E(1B_u) < E(2A_g)$, we still refer to the optical gap $E_{op} = E(1B_u) - E(1A_g)$. We note that among the various photoexcitations the subscript 'g' stands for even (gerade) parity and 'u' stands for odd (ungerade) parity. These symbols are important for possible optical transitions, since one-photon allowed transitions occur between states of *opposite* parity representations, such as $g \rightarrow u$ or $u \rightarrow g$.

In the following section we discuss and summarize the states in the gap and the associated electronic transitions of various photoexcitations in PCPs, and their blend with fullerene; the IR-active vibrations (IRAV's) related to the charged excitations are also briefly summarized here.

1.1.1.1 Optical Transitions of Photoexcitations in Pristine Polymers

It is generally accepted that the $1B_u$ exciton is the primary intrachain photoexcitation when the excitation photon energy is close to the absorption onset of the polymer. However various *interchain* photoexcitations appear to be important in thin films of many PCPs, because of the interchain interaction. The branching of

intrachain and interchain photoexcitations occurs instantaneously in many systems [39, 40]. This topic has been the focus of interest for more than two decades [41]. Here we discuss some intrachain and interchain excitations that are neutral and charged.

Singlet Excitons

The intrachain exciton that is immediately photogenerated upon photon absorption is a neutral, spinless excitation of the polymer chain. In principle optical excitation into higher excited states of the polymer is followed by sub-picosecond nonradiative hot exciton relaxation to the lowest excited state, in which vibrational energy is released [42]. The hot energy relaxation process is due to either vibrational cooling within vibronic sidebands of the same electronic state, or phonon-assisted transitions between two different electronic states, which is termed 'internal conversion' in molecular spectroscopy [43]. Usually internal conversion is the fastest relaxation channel that provides efficient nonradiative transfer from a higher excited state into the lowest excited state of the same spin multiplicity [44, 45]. Before the exciton cools down to the lowest excited state, there are two other ultrafast relaxation processes which may interfere and successfully compete with the internal conversion process. These processes include singlet exciton fission and exciton dissociation [45]. The former process creates two triplet excitons with opposite spins from one singlet exciton, in time faster than the usual intersystem crossing time from the singlet to the triplet manifold [46, 47]; whereas the latter process directly generates charge carriers on two adjacent chains [48, 49]. However in PCPs these two processes happen with much smaller probability than the internal conversion process, and although important for applications, they are not included in our present discussion.

In Fig. 1.1a we summarize the optical transitions of the singlet exciton. Two essential exciton levels ($1B_u$ and mA_g) are shown to play an important role in the exciton picture of PCPs. The mA_g level is known to have strong dipole moment coupling to $1B_u$ as deduced form various optical nonlinear spectra of PCPs analyzed via summation over states model where the "four essential states" are used [37, 38]. We therefore expect two strong optical transitions to form following the $1B_u$ photogeneration, PA_1 from $1B_u$ to mA_g and PA_2 from $1B_u$ to another A_g state, dubbed kA_g.

Following exciton cooling after the lowest exciton state is reached there are still other available processes: The 'cold' exciton may recombine radiatively by emitting light in the form of fluorescence (FL). It may also recombine non-radiatively through recombination centers by emitting phonons. Excitons may be also trapped or undergo an intersystem crossing into the triplet manifold, creating long-lived triplet (T) states. Finally, a singlet exciton may also disassociate into polaron pair (PP) or excimer onto two neighboring chains, which is a process analog to exciton dissociation in polymer/fullerene blends.

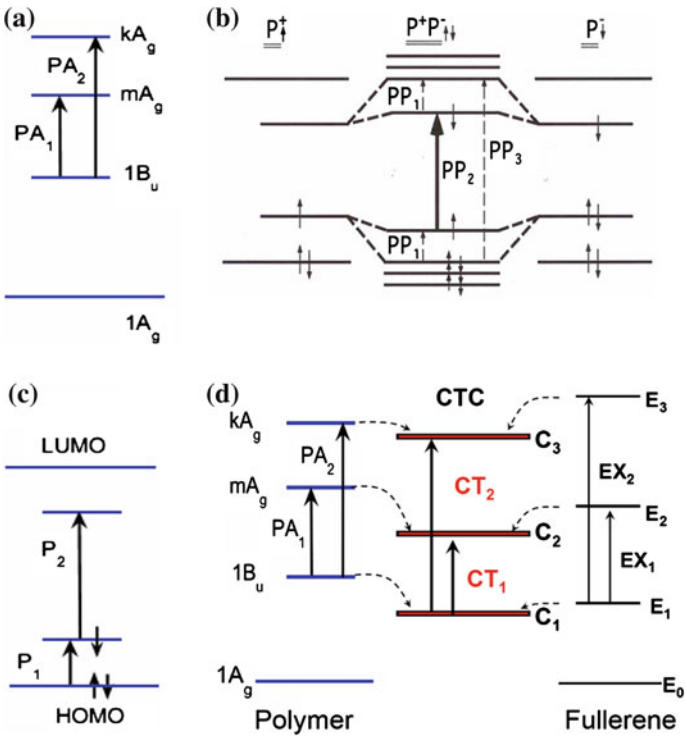

Fig. 1.1 Energy levels and associated optical transitions of exciton (**a**), polaron pair (**b**), positive polaron (**c**) and charge transfer complex (CTC) state (**d**), **a**, **c** is adapted from Sheng et al. [30]. **b** is adapted from Vardeny and Wei [31]

Polaron Pairs

It is now generally recognized that interchain interactions play a strong role in the photophysics of PCP thin films and especially in optoelectronic devices [50–65]. Since the original demonstration of interchain species in films of MEH-PPV by Rothberg et al. [50, 66], a variety of complex optical phenomena in many other PCPs have been ascribed to interchain interactions. Among the complexity of interchain photoexcitation species, a polaron pair (*PP*) [66, 67] may be the simplest and also the most important one. A polaron pair is a bound pair of two oppositely charged polarons, P^+ and P^- formed on two adjacent chains. The strong wave-function overlap leads to large splitting of the P^+ and P^- levels as shown in Fig. 1.1b. For a loosely bound *PP* its dipole allowed transitions are similar to those of the polaron, which will be introduced in the next section. However for a tightly bound *PP* excitations we expect a single transition, PP_2 to dominate the spectrum, as PP_1 is considered to be intraband transition with traditional low intensity, and PP_3 is close to the fundamental transition and therefore difficult to observe (see Fig. 1.1b). In this case there are mainly two states in the gap, and the excitation

species is also known as a neutral *BP* (BP^0) or a 'polaronic exciton'. We note, however that the PP_2 transition is close in spirit to transition PA_2 discussed above for excitons, as a second electron is also promoted to the excited level in the case of *PP*. Then from the experimental point of view, it is not easy to identify and separate the transitions of a trapped exciton from those of a tightly bound *PP* in the PM spectra. They may differ, however in their PA-detected magnetic resonance (PADMR) spectra [68].

Recently, our joint theory-experiment work provided new insight of the photophysics in pristine PCP films. We reported pressure-dependent transient picosecond and continuous-wave photomodulation studies of disordered and ordered films of MEH-PPV. Photoinduced absorption (PA) bands of intrachain excitons and polarons in the disordered film exhibited weak pressure dependence. In contrast, the ordered film exhibited two additional transient PA bands in the mid infrared that dramatically blue-shifted with pressure. Based on high-order configuration interaction calculations, we ascribed the PA bands in the ordered film to excimers [41]. The excimer is a quantum-mechanical superposition of the delocalized neutral exciton and the ionic polaron pair that is obtained in the presence of significant interchain electron hopping.

1.1.1.2 Optical Transitions of Neural and Charged Photoexcitations in Polymer/Fullerene Blends

Charged Photoexcitations: Polarons and Delocalized Polarons

In disordered polymer films a single charge carrier added onto the polymer chain forms a spin-1/2 polaron that results in two states in the gap. Figure 1.1c shows the associated optical transitions for a positively charged polaron, P^+. The polaron energy level in the gap are separated by and energy $2\omega_0$ (P) [69]. Then three optical transitions P_1, P_2 and P_3 are possible [32, 69, 70]. In both oligomers and polymers, however transition P_3 is extremely weak because of the symmetry selection rules; therefore the existence of two optical transitions upon doping or photogeneration indicates that polarons are created [70, 71]. However there might be a disorder-induced relaxation of the above-mentioned optical selection rules that may cause ambiguity as to the number of optical transitions associated with polarons in "real" polymer films, especially for photon energies $\hbar\omega > E_g$.

For highly ordered PCP such as RR-P3HT film, self-organization of the polymer chains results in formation of lamellae structure perpendicular to the film substrate; such 2D lamellae sheets have strong interchain interaction due to the short interlayer distance of the order of 3.8 Å [72]. An interaction model introduced before [73, 74] shows that the interchain interaction in RR-P3HT lamellae splits the intrachain localized polaron levels so that the delocalized polaron (DP) levels are shallower; this results in energy shift of the allowed optically transitions. We note that the transition

DP_1 is red shifted respect to P_1, whereas DP_2 is blue shifted respect to P_2. Moreover, the sum rule: $E(DP_1) + E(DP_2) = E(P_1) + E(P_2)$ approximately holds [73, 74].

Neural Photoexcitations: Charge Transfer Excitons

The charge transfer (CT) exciton or charge transfer complex (CTC) is intermediate excited state between singlet exciton and photogenerated free charge. Evidence for the existence of CTC at the interfaces between the polymer donor and PCBM acceptor domains, and its role as an intermediate state in the free charge photogeneration have been recently reported [4, 5, 21, 26, 75–86]. Several techniques such as electro-absorption, below-gap pump excitation PM, as well as photoluminescence [26, 81, 86] have been applied to study the CTC in polymer/fullerene blends.

However, the commonly used names for CT complexes are diverse, which include polaron pairs [87], geminate polaron pairs [88], interfacial charge pairs [89], charge transfer excitons [86, 90], and exciplexes [91]. The reason for this widely used nomenclature range is the existence of several different steps between the top extreme cases of excitons and free polarons. Although the full quantum mechanical description for CTC is unknown at the present time, nevertheless we may regard the CTC wave function as a linear combination of intrachain exciton ($1B_u$, mA_g, kA_g) of the polymer chain and neighboring states (E_1, E_2, E_3) of the fullerene molecule [92]. Consequently, as shown in Fig. 1.1d we expect two strong optical transitions to form following CT exciton photogeneration, namely CT_1 from C_1 to C_2, and CT_2 form C_1 to C_3 [80, 92].

1.1.1.3 Photoinduced Infrared Active Vibrational Modes (IRAV)

The neutral polymer chain has a set of Raman active A_g-type vibrations that are strongly coupled to the electronic bands via the e-p coupling [10]. These vibrations have been dubbed '*amplitude modes*' (AM) [93]. The AM model has achieved a spectacular success in explaining the resonant Raman scattering (RRS) dispersion as well as photoinduced and doping induced IRAVs in PCPs [10–12]. Because the Raman frequencies are much smaller than the optical gap, and the corresponding IRAV frequencies are much smaller than the energies of photoinduced and doping induced electronic bands, previous applications of AM model were based on the adiabatic approximation [10–12, 93]. However this approximation fails in the case of ordered PCPs such as RR-P3HT/PCBM blends, since the IR-active lines overlap with the electronic transition in this case [73, 74, 94]. Therefore both vibronic and electronic excitations as well as their quantum interference have to be taken into account.

The conductivity spectrum, $\sigma(\omega)$ in this case consists of two parts [11, 95]; one component is determined by the most strongly coupled phonons in the non-adiabatic limit; the other is related to the system response in the absence of phonons.

Within the charge-density wave approximation the sharp features in σ(ω) are given by the relation [96]:

$$\sigma(\omega) \approx \frac{1 + D_0(\omega)[1 - \alpha_p]}{1 + D_0(\omega)[1 + C - \alpha_p]} \tag{1.1}$$

where C is a constant that presents a smooth electronic response; α_p is defined as polaron-vibrational 'pinning parameter' for the trapped polaron excitation; and $D_0(\omega)$ is the 'bare' phonon propagator. The latter is given [93] by the relation: $D_0(\omega) = \Sigma_n d_{0,n}(\omega)$, and $d_{0,n}(\omega) = \lambda_n/\lambda\{(\omega_n^0)^2/[\omega^2 - (\omega_n^0)^2 - i\delta_n]\}$, where ω_n^0, δ_n and λ_n are the 'bare' phonon frequencies, their natural linewidth (inverse lifetime) and electron-phonon (e-p) coupling constant, respectively; and $\Sigma\lambda_n = \lambda$, which is the total e-p coupling.

The poles of (1.1), which can be found from the relation: $D_0(\omega) = -(1 - \alpha_p + C^{-1})$, give peaks (or IRAV's) in the conductivity (absorption) spectrum. We used the IRAV's, which appear as positive absorption lines to identify the charge state of photoexcitations in the ps PM spectra of less ordered PCPs' films [40, 97]. On the other hand the zeros in (1.1), which can be found by the relation: $D_0(\omega) = -(1 - \alpha_p)^{-1}$, give the indentations (or anti-resonances, ARs) in the conductivity (or absorption) spectrum [74, 96].

1.1.2 Experimental Set-up for Measuring Transient and CW Responses

For measuring the transient photoexcitation response in the femtosecond (*fs*) to nanosecond (*ns*) time domains we have used the *fs* two-color pump-probe correlation technique with linearly polarized light beams. Two laser systems have been traditionally used in our laboratory. A high repetition rate, low power laser for the mid-IR spectral range [30]; and a high power low repetition rate laser system for the near-IR and visible spectral range [7].

1.1.2.1 Low Intensity *Fs* Laser System

For the transient PM spectroscopy in the spectral range between 0.55 and 1.05 eV, we used a 100 fs titanium-sapphire oscillator operating at a repetition rate of about 80 MHz, which pumped an optical parametric oscillator (OPO) (Tsunami, Opal, Spectra-Physics) where both signal and idler beams were respectively used as probe beams [30]. In addition a difference frequency of the signal and idler beams set up based on a nonlinear optical crystal was used to extend the probe spectral range from ~0.15 to ~0.43 eV. The pump beam was extracted either from the fundamental at ≈1.55 eV, or from its second harmonics at 3.1 eV. To increase the signal/

noise ratio, an acousto-optical modulator operating at 40 kHz was used to modulate the pump beam intensity. For measuring the transient response at time, t with ≈150 fs time resolution, the probe pulses were mechanically delayed with respect to the pump pulses using a translation stage; the time $t = 0$ was obtained by a cross-correlation between the pump and probe pulses in a nonlinear optical crystal. Typically the laser pump intensity was kept lower than 5 μJ/cm^2 per pulse, which corresponds to ≈10^{16}/cm^3 initial photoexcitation density per pulse in the polymer films. This low density avoids the complications usually encountered with high power lasers such as bimolecular recombination and stimulated emission; both processes tend to increase the recombination rate of the photoexcited excitons.

The transient PM signal, ΔT/T(t) is the fractional changes ΔT in transmission T, which is negative for photoinduced absorption (PA) and positive for photoinduced bleaching (PB) at photon energy above the absorption onset, and stimulated emission for photon energies below the optical gap when overlap exists with the PL spectrum. The pump and probe beams were carefully adjusted to get complete spatial overlap on the film, which was kept under dynamic vacuum. In addition the pump/probe beam-walk caused by the translation stage was carefully monitored and the transient response was adjusted by the beam walk measured response.

Since some photoexcitations may live longer than the time interval between successive pulses, then a *background PA* may be formed. An advantage of this mid-IR laser system is that the background PA spectrum can be readily measured using the same pump/probe set up as for the ultrafast response. This was achieved by measuring the PA signal at $t < 0$ since the probe pulse in this situation arrives before the pump pulse, and therefore is affected by the 'left-over' photoexcitations in the film that survive in between successive pulses [98]. Recall that the background PA is modulated at frequency of 40 kHz, and thus is sensitive to long-lived photoexcitations in the film having lifetime longer than $\sim 1/f$ (= 25 μsec).

1.1.2.2 High Intensity *Fs* Laser System

For the near IR and visible range we have used the high intensity laser system [7]. This laser system is based on a Ti:sapphire regenerative amplifier that provides pulses of 100 *fs* duration at photon energies of 1.55 eV, with 400 μJ energy per pulse at a repetition rate of 1 kHz. The second harmonic of the fundamental at 3.1 eV was used as the pump beam. The probe beam was a white light supercontinuum within the spectral range from 1.1 to 2.8 eV, which was generated using a portion of the Ti-sapphire amplifier output in a 1-mm-thick sapphire plate. To improve the signal-to-noise ratio in our measurements, the pump beam was synchronously modulated by a mechanical chopper at exactly half the repetition rate of the Ti:sapphire laser system (≅500 Hz). The probe beam was mechanically delayed with respect to the pump beam using a computerized translation stage in the time interval, t up to 200 *ps*. The beam spot size on the sample was about 1 mm in diameter for the pump beam and about 0.4 mm diameter for the probe beam. The pump beam intensity was set below 300 μJ/cm^2 per pulse, which is below the signal

saturation limit. The wavelength resolution of this system was about 8 nm using a 1/8-meter monochromator having a 1.2 mm exit slit, which was placed in the probe beam after it had passed through the sample. The transient spectrum ΔT/T(t) was obtained using a phase sensitive technique with a resolution in $\Delta T/T \approx 10^{-4}$.

1.1.2.3 CW Optical Measurements

For the cw PM spectroscopy we used a standard PM setup at low temperatures [31] and references therein. The excitation beam was an Ar^+ laser with several lines in the visible spectral range and UV at 353 nm, which was modulated with a mechanical chopper at a frequency of ~300 Hz. The probe beam was extracted from a tungsten lamp in the spectral range 0.25–3 eV. A combination of various diffraction gratings, optical filters, and solid-state detectors (silicon, germanium and indium antimonite) were used to record the PM spectra. The spectral resolution was about 2 nm in the visible spectral range and 4–10 nm in the near infrared range, with ΔT/T resolution of $\approx 10^{-6}$.

In order to retrieve the mean polaron lifetime, τ, the frequency response of both in-phase and quadrature PA components were measured, and were fit to an equation

$$\Delta T(f)/T = G\tau[1 + (i2\pi f\tau)^P] \tag{1.2}$$

where G is the generation rate (proportional to the laser intensity) and p (< 1) is the dispersive parameter that describes the recombination dispersion of polarons due to disorder in the system [99].

In addition, in order to identify photogenerated polarons in the photomodulation spectrum we also measured the doping induced absorption spectrum of the polymers, where a thin polymer film was exposed to low pressure iodine gas for ~10 s. The doping induced absorption spectrum was then obtained by subtracting the optical density of the pristine polymer film from that of the doped film.

1.1.2.4 Electroabsorption

EA has provided a sensitive tool for studying the band structure of inorganic-semiconductors [100] as well as organic- semiconductors [38, 101, 102]. In general the EA spectrum emphasizes optical transitions at singularities of the joint density of states that respond sensitively to an external field, and therefore are lifted from the broad background of the absorption continuum [103]. The EA sensitivity, however diminishes for more confined electronic transitions, because the applied electric fields (of the order of 100 kV/cm) are too small of a perturbation to cause sizable changes in their associated optical transitions. Consequently EA spectroscopy has been an ideal tool to separate exciton bands from the continuum band [103]. For example in 1D semiconductors the confined excitons were shown to exhibit a quadratic Stark effect, where the EA signal scales with F^2, and its

spectrum resemble to a first derivative of the absorption edge. Whereas the EA spectrum related to the continuum band was found to scale with $F^{1/3}$, and showed Franz-Keldysh (FK) type oscillation. One of the most notable examples of the application of EA spectroscopy to organic semiconductors is polydiacetylene, in which EA spectroscopy was able to separate absorption bands of quasi-1D excitons from that of the continuum band [103]. The separation of the EA contribution of excitons and continuum band was then used to obtain the exciton binding energy in polydiacetylene, which was found to be $\sim$0.5 eV [103].

For the EA measurements we used a PCP film spin cast on a substrate with patterned metallic electrodes [104]. The EA substrate consisted of two interdigitated sets of a few hundred 30 μm wide gold electrodes, which were patterned on a sapphire substrate. The sample was placed in a cryostat for low temperature measurements. By applying a potential V to the electrodes a typical electric field, $F \sim 10^5$ V/cm was generated with $V = 300$ V and $f = 1$ kHz parallel to the film. For probing the EA spectrum we used an incandescent light source from a Xe lamp, which was dispersed through a monochromator, focused on the sample, and detected by a UV-enhanced silicon photodiode. We measured ΔT with probe light parallel and perpendicular to the direction of the applied electric field using a lock-in amplifier set to twice the frequency ($2f$) of the applied field [104], and verified that no EA signal was observed at f or $3f$. ΔT and T spectra were measured separately and the polarized EA spectrum was obtained from the ratio $\Delta T/T$. The detailed description for the EA experimental setup was presented in [7].

1.1.2.5 Solar Cell Fabrication and Testing [105]

The bulk heterojunction OPV solar cell devices were composed of a transparent indium tin oxide (ITO) anode; a spin-cast polyethylenedioxythiophene/polystyrene sulphonate (PEDOT/PSS) hole transport layer; an active material layer spin-cast from a blend of P3HT donor and PCBM acceptor; and capped with LiF/Al cathode. The ITO-coated glass substrates (Delta Technology, CB-50IN) were cleaned by ultrasonic treatment and oxygen plasma treatment. The PEDOT/PSS (Clevios, P VP AI 4083) layer was spin-cast at 5,000 RPM for 20 s at ambient conditions, and transferred to a nitrogen-filled glovebox ($O_2 < 1$ ppm) for annealing at 120 °C for 30 min. The organic blend comprised of P3HT (Plextronics, Plexcore OS 2,100) and PCBM (purity > 99.9 %) that were prepared at weight ratio of 1.2:1 in 1,2-dichlorobenzene solution that was heated at 50 °C for 30 min. and stirred overnight. The device active layer was spin-cast from the solution blend at 400 RPM for 6 min and annealed at 150 °C for 30 min; the device active area was 2 mm × 2.5 mm. The fabrication was completed by thermally evaporating a 1 nm thick film of LiF layer followed by a 100 nm thick film of Al. Finally the device was encapsulated under a cover glass using UV-curable optical adhesive (Norland, NOA 61). The device I-V characteristics under illumination were measured using a Keithley 236 Source-Measure unit. The light intensity of the solar simulator composed of a xenon lamp

and an AM 1.5G filter was calibrated at 100 mW/cm^2 using a pre-calibrated silicon photovoltaic cell. The OPV device output current was measured using phase sensitive lock-in technique.

1.2 Photoexcitation Dynamics in Pristine MEH-PPV and MEH-PPV/Fullerene Blends

1.2.1 Transient Photomodulation Spectroscopy of Pristine MEH-PPV Films

MEH-PPV is one of the most studied PCP. Due to its side group the MEH-PPV polymer is able to form an ordered phase when films are cast from 'bad' solvents such as toluene [106, 107]. In such films two or more polymer chains may be coupled together due to increased interchain interaction. Under these conditions the primary photoexcitations may contain interchain components that spread over two (or more) chains. The photoexcitations delocalization over several polymer chains may lead to several characteristic properties, including [104]: (i) reduced PL quantum efficiency; (ii) PL red-shift; (iii) relatively large generation efficiency of polaron pair and excimer excitations; (iv) substantially delayed PL due to polaron pair and excimer recombination; and (v) increased photogeneration efficiency of charge carriers in C_{60} doped polymer films.

Figure 1.2a shows the transient PM spectrum of a MEH-PPV film casted from toluene solution at "t = 0 ps". It contains excitons with PA_1 and PA_2 bands at 0.95 and 1.35 eV, as well as polarons with P_1 and P_2 bands at 0.35 and 1.6 eV, respectively. In addition, there is also a stimulated emission (SE) band as well as a photobleaching band. We showed [30] that the polarons PA bands in the PM spectrum have a slower dynamics compare to that of the exciton PA bands and the associated SE, indicating that they belong to different photoexcited species Fig. 1.2b. The band P_1 and P_2 were identified as due to polarons, since the cw polaron band P_1 also peaks at about the same value, i.e. $h\omega$(probe) = 0.4 eV. However because there are no accompanying IRAVs at room temperature, we concluded that the polarons photogenerated at t = 0 ps are Coulombically bound forming polaron pairs, or may be highly correlated forming excimers. Recently our joint theory-experiment work reported pressure-dependent transient picosecond and continuous-wave photomodulation studies of disordered and ordered films of MEH-PPV. Photoinduced absorption bands of intrachain excitons and polarons in the disordered film exhibited weak pressure dependence [41]. In contrast, the ordered film exhibited two additional transient PA bands in the mid infrared that blue-shift dramatically with pressure. Based on high-order configuration interaction calculations, we ascribed the PA bands in the ordered film to excimers [41].

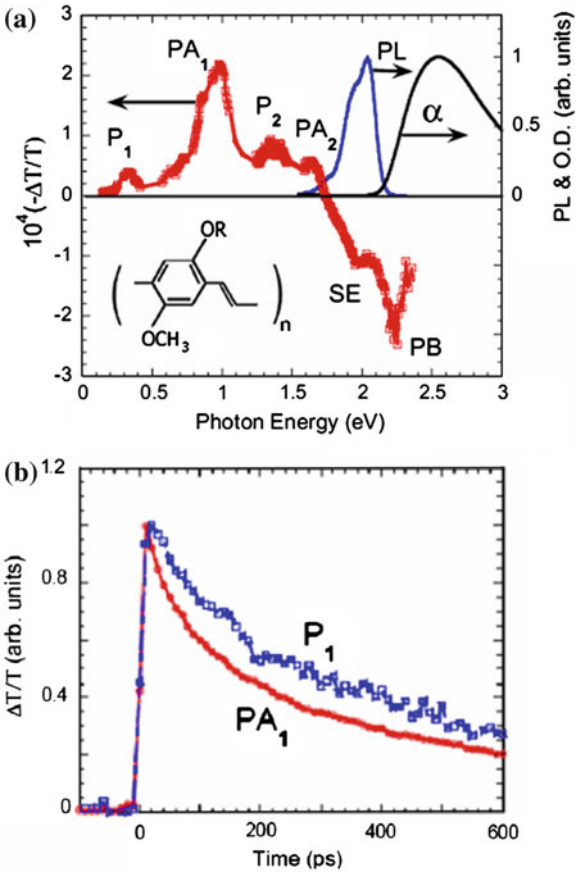

Fig. 1.2 **a** The transient PM spectrum at t = 0 of pristine MEH-PPV film cast from toluene solution in the spectral range of 0.15–2.4 eV; the *inset* shows the polymer backbone structure. Various spectral bands are assigned; P_1 and P_2 are for polarons; PA_1 and PA_2 are for excitons; and SE and PB are stimulated emission and photobleaching of the absorption, respectively. The absorption and photoluminescence spectra are also shown for comparison. **b** The decay dynamics of the exciton and polaron bands (Adapted from Sheng et al. [30])

1.2.2 Photomodulation of MEH-PPV/C_{60} Blends

1.2.2.1 Transient Photomodulation Spectroscopy with Above-Gap and Below-Gap Pump Excitations

It has been known that C_{60} doping of many π-conjugated polymers promotes a strong photoinduced charge transfer process, where the photogenerated excitons dissociate into positive polaron on the polymer chain and negative polaron on the C_{60} molecule [13]. In (1:1 by weight) MEH-PPV/C_{60} blend it was measured that the photoinduced dissociation occurs with time constant of ~50 fs [108].

Figures 1.3a and 1.4 show the transient PM spectra of a 1:1 MEH-PPV/C_{60} blend with above-gap (AG 400 nm) and below-gap (BG 800 nm) excitation, respectively. The $t = 0$ PM spectrum with AG excitation contains three PA bands peaked at 0.4 eV (P_1), 1.5 eV (P_2), and 1.0 eV (PA_1), which are respectively due to polarons and excitons on the polymer chains; and an accompanying PB band above

2.2 eV. The dissociation process of exciton in 50 % C_{60}-doped film occurs within 200 *fs* (Fig. 1.3b inset), in agreement with transient measurements done in other laboratories [109]. The inset to Fig. 1.3a shows that P_1 polaron and PB (at 2.5 eV) increase with time *on the expense* of PA_1 exciton decay; so that at $t \sim 10$ *ps* only the polaron PA bands P_1 and P_2 remain in the PM spectrum, in contrast to pristine MEH-PPV [30]. This shows that with AG excitation the intrachain excitons *separate into polarons* via an electron transfer reaction from the polymer chain (donor) onto the C_{60} molecule (acceptor); and vice versa. This is the traditional photoinduced charge transfer mechanism postulated to occur in the blend [13]. In Fig. 1.3b we show that P_1 band has a much longer lifetime compared with PA_1 of excitons, as well as with P_1 lifetime (Fig. 1.2b) in pristine MEH-PPV.

Figure 1.4 shows that with BG excitation, which is not capable of generating intrachain excitons on the polymer (i.e. PA_1 is not formed in the PM spectrum), *polarons are still photogenerated with estimated quantum efficiency (QE) of* ~ 100 *%*.

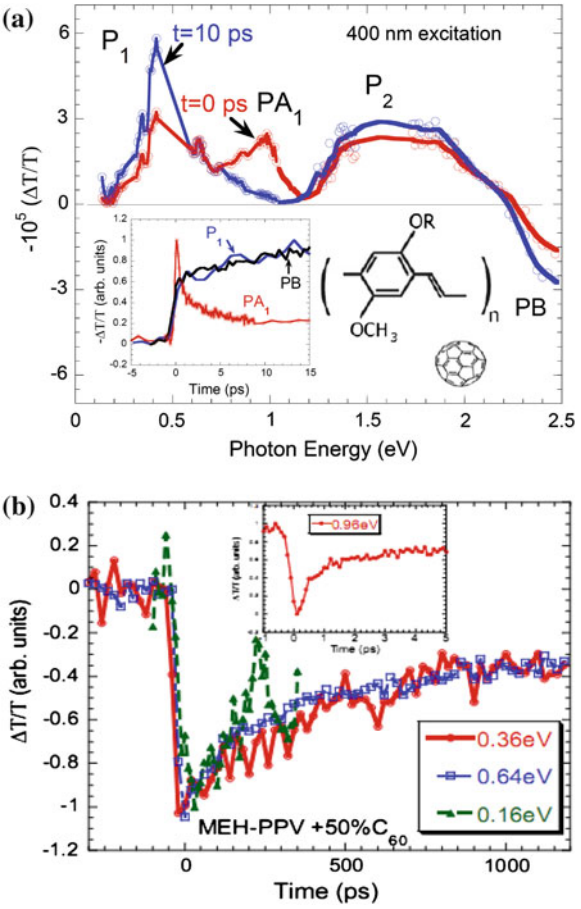

Fig. 1.3 **a** The transient PM spectrum of MEH-PPV/C_{60} (1:1) blend film with above gap at t = 0 (*red*) and 10 ps (*blue*). The polaron PA bands P_1 and P_2, exciton PA_1, and PB band are assigned. The *insets* in **a** show the ultrafast dynamics of the various bands up to 15 ps, and the polymer and fullerene backbone structures, respectively. **b** PA decay dynamics at various probe energies. The *inset* to **b** is the ultrafast PA_1 decay measured at 0.96 eV. **a** is adapted from Drori et al. [26], **b** is adapted from Sheng [110]

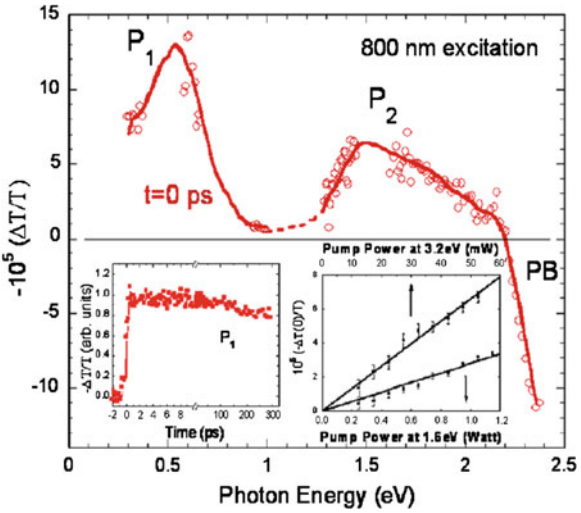

Fig. 1.4 The transient PM spectrum of MEH-PPV/C_{60} (1:1) blend film with below-gap excitation at t = 0. The polaron PA bands P_1 and P_2, exciton PA_1, and PB band are assigned. The *insets* shows the P_1 band dynamics up to 300 ps (*left*) and its excitation intensity dependence with above-gap and below-gap (*right*) (Adapted from Drori et al. [26])

This can be inferred from the two polaron bands P_1 and P_2 in the PM spectrum that are generated instantaneously (Fig. 1.4 inset). The BG excitation polarons are long-lived (Fig. 1.4 inset), and we thus conclude that they remain localized following photo-generation. This indicates that the 1.55 eV pump is a direct transition into a state that is formed below the polymer and fullerene optical gaps, which is capable of creating separated charges on the polymer and fullerene without the need of an intermediate step such as intrachain exciton. This can be readily explained if this state is a CTC lying inside the gap, *below* the donor and acceptor lowest lying excitons [75].

It is interesting to compare our results in optimum blend with blends of MEH-PPV films with less C_{60} molecules. Figure 1.5a shows the mid-IR PM spectra of 10 % C_{60} doped (by weight) MEH-PPV film at various delay times: t = 0, 2 and 100 *ps* following the pulse excitation [110]. It is seen that the PA_1 exciton band at 0.9 eV gradually disappears from the PM spectrum as the exciton dissociation occurs. In parallel with the decrease of PA_1, photoinduced IRAV at $\sim$0.18 eV gradually appears in the PM spectrum (Fig. 1.5b). This shows that photogenerated excitons decay into charge polarons indicating that exciton dissociation indeed occurs between the polymer chains and C_{60} molecules [13, 111]. However, the charge transfer reaction is not as fast as that measured in the (1:1) MEH-PPV/C_{60} blend [108]. From Fig. 1.5b we conclude that the IRAV dynamics is *delayed* respect to the exciton PA_1 instantaneous response. From the IRAV transient here we estimate that the IRAV's are photogenerated within $\sim$2 ps in the 10 % C_{60} doped film, in contrast to the time constant of about 50 fs in 50 % C_{60} doped films

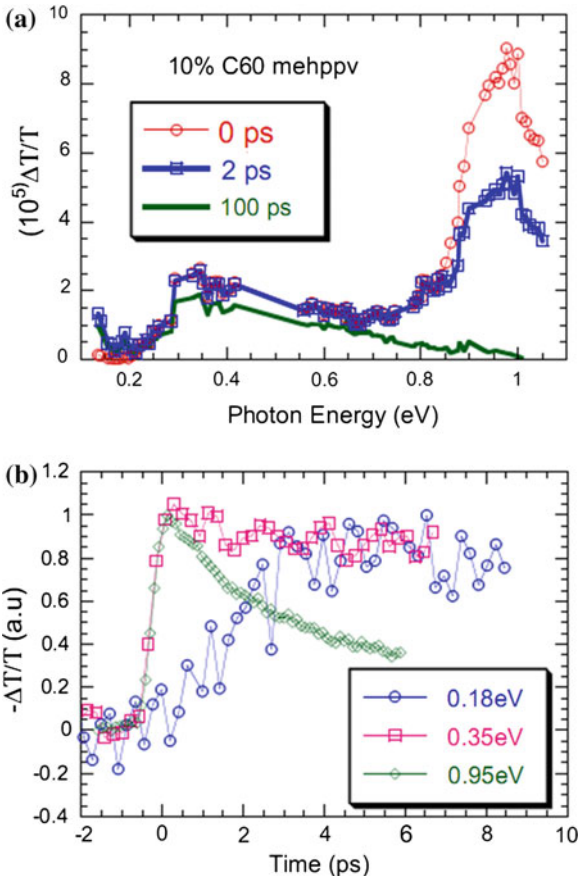

Fig. 1.5 **a** Transient PM spectra of 10 % C_{60} doped MEH-PPV film at t = 0, 2 ps, and 100 ps. **b** Transient PM responses at various probe energies (From Sheng [110] with permission)

[108]. This indicates that the photoinduced charge transfer reaction in C_{60} doped films is actually limited by the *exciton diffusion* towards C_{60} molecules close to the polymer chains. Consequently the exciton wavefunction in MEH-PPV films is not as extended as previously thought. The same conclusion was drawn for C_{60} doped DOO-PPV films, where it was estimated [112] that the exciton diffusion constant to reach the C_{60} molecules in the film is of the order of 10^{-4} cm^2/s.

1.2.2.2 CW Photomodulation Spectroscopy with Above-Gap and Below-Gap Excitations

Figure 1.6a shows that the cw PA spectrum of polarons generated with BG and AG excitation are indistinguishable from each other; both spectra contain the signature of separated polarons, namely IRAVs, and two PA bands P_1 and P_2. We thus conclude that a mechanism exists in the blend through which BG excitation is able

to generate charges on the polymer chains; in agreement with the transient spectrum in Fig. 1.4. However polarons generated with BG excitation are much longer lived (Fig. 1.6a inset), since the P_1 band frequency dependent steeply increases at low f down to $\sim$10 Hz for BG excitation, whereas the P_1 increase at low f saturates at $\sim$100 Hz for AG polarons. In fact by fitting the frequency dependence we found that the polaron lifetime with BG excitation is about *two-orders of magnitude longer* than that of polarons with AG excitation. This cannot be explained simply

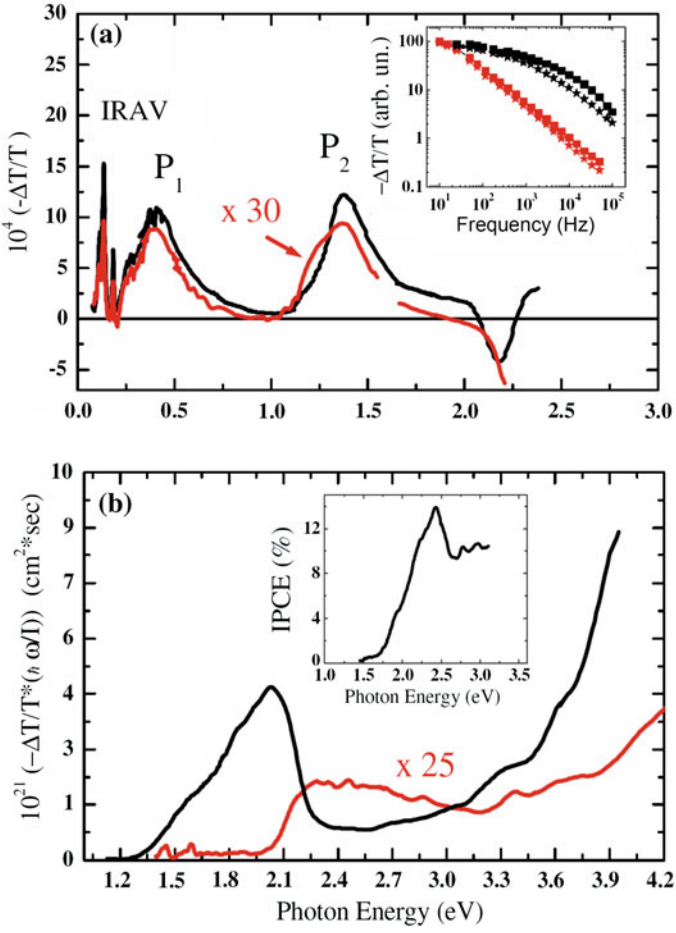

Fig. 1.6 **a** The cw PM spectrum of MEH-PPV/C_{60} (1:1) blend film at 80 K, obtained with above gap (*black*) and below-gap (*red*, X 30) excitation. The polaron PA bands P_1, P_2 and IRAV's are assigned. The *inset* shows the polaron P_1 band modulation frequency response measured with above-gap (*black*) and below-gap (*red*) excitation at two intensities that differ by a factor 5. **b** The P_1 action spectra/impinging photon of the MEH-PPV/C_{60} blend (*black*) and pristine MEH-PPV films (*red*, X 25). The *inset* shows the action spectrum of the short-circuit current in a solar cell based on the MEH-PPV/C_{60} blend (Adapted from Drori et al. [26])

by bimolecular recombination kinetics [113], where the polaron density with BG excitation is much smaller (see the decay kinetics in Fig. 1.6a for various excitation intensities). We thus conclude that polarons with BG excitation are localized, having much slower recombination kinetics.

Figure 1.6b shows the polaron P_1 action spectrum in pristine MEH-PPV and MEH-PPV/C_{60} blend. From the action spectra we conclude that polarons in pristine polymer are generated *exclusively* with AG excitation, having a clear onset at the polymer optical gap ($\sim$2.1 eV). In contrast, polarons in the blend can be photogenerated with BG excitation with high QE down to $\sim$1.3 eV. The *apparent* band in the action spectrum for $\hbar\omega < 2$ eV is caused by the immense increase in the polaron lifetime with BG excitation; and thus for calculating the effective BG polaron QE/absorbed photon, the action spectrum shown in Fig. 1.6b should be reduced by the ratio of BG and AG polaron lifetime (a factor of $\sim$120). Nevertheless the BG absorption also steeply decreases (Fig. 1.7a inset), so that these two effects somewhat compensate each other, giving a *substantial* polaron QE for BG excitation in the blend. The inset to Fig. 1.6b shows the photocurrent (PC) action spectrum in a solar cell device made with the MEH-PPV/C_{60} blend for the active layer. Although it has a BG tail down to $\sim$1.5 eV [114, 115], PC is substantially lower with BG than with AG excitation; in sharp contrast with the P_1 action spectrum shown in Fig. 1.6b. This is compelling evidence that BG excitation results in polarons that are less capable to substantially contribute to the device photovoltaic response, because they are less mobile compared to polarons generated with AG excitation. However the BG polaron generation may be detrimental to the device operation, since these localized polarons may serve as traps and recombination centers to the more mobile photocarriers generated with AG excitation.

1.2.2.3 Electroabsorption Spectroscopy

A direct proof for the existence of a CTC below the gap in the blend is provided by the EA spectroscopy. Figure 1.7a and b summarize the EA spectra of pristine polymer and C_{60}, as well as their blend, respectively. In all cases we found that near the band-edge EA $\sim F^2$, where F is the field strength [7]. This has been explained as due a second order Stark shift of the lowest lying exciton state and its phonon replicas [7]. Indeed Fig. 1.7a shows derivative like feature with zero-crossing at 2.2 eV ($\approx$E($1B_u$)) for MEH-PPV, and 2.4 eV ($\approx$continuum onset) for C_{60}. Figure 1.7b shows that the EA spectrum in the blend for $\hbar\omega$ >2 eV is a superposition of the EA spectra of the constituents, which is somewhat broader due to excess disorder in the blend. However the EA spectrum of the blend also contains a prominent derivative-like feature with zero-crossing at $\sim$1.57 eV, similar in shape as the EA of the $1B_u$ state in the polymer (Fig. 1.7a). We thus conclude that this is due to Stark shift of a *real state* that is formed in the blend below the optical gaps of both constituents. The BG absorption spectrum of the blend (Fig. 1.7a inset) indeed

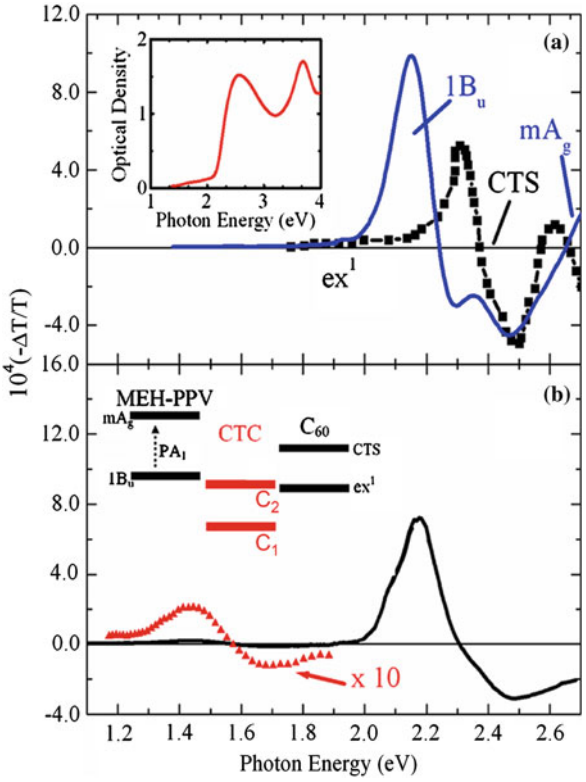

Fig. 1.7 The EA spectra of pristine MEH-PPV (*blue line*) and C_{60} (*black squares*) (**a**); and MEH-PPV/C_{60} blend (**b**), where the below-gap spectrum is also shown multiplied by a factor of 10. The various bands $1B_u$, mA_g for the polymer [113], and CTS for the C_{60} [104] [for their definition see text and *inset* **b**] are assigned. The *inset* in **a** shows the absorption spectrum of the MEH-PPV/C_{60} blend; whereas the *inset* in **b** shows schematically the respective energies of the lowest lying excitons in the MEH-PPV and C_{60}, and those of the CTC formed between the polymer and fullerene (From Drori et al. [26] with permission)

shows a long tail down to ~1.3 eV, that is too weak to produce a substantial contribution to the EA, unless the dipole moment of this BG state is very strong. Traditionally a CTC state has strong dipole moment [104], and thus is a natural candidate to explain the BG state formed in the blend. This is schematically shown in Fig. 1.7b inset, where the CTC at ~1.57 eV lies below the lowest lying singlet excitons in MEH-PPV (~2.1 eV) and C_{60} (~1.85 eV). In fact the CTC state lies even below the respective lowest triplet exciton level of the constituents; and this explains the high QE of polaron generation for this blend [75].

1.2.3 Transient Photomodulation Spectroscopy of Polymer Blends with Strong Acceptor Molecules

One current deficiency in organic solar cells however, is negligible absorption in the near-infrared (NIR) spectral range of the solar spectrum, which lies within the optical gap of most conventional organic blend systems. Several techniques have been developed to increase the near-infrared absorption including using lower-bandgap polymers [116], multiactive layer devices [117, 118], and more recently, charge-transfer complexes [4, 26, 75]. Another viable candidate may be a polymer/acceptor blend with a molecular acceptor having larger electron affinity than the traditional fullerene molecules. Below-gap optical excitation of such organic donor/acceptor blends reveals subtle features attributed to CTC, which have recently attracted much attention by their property of extending optical absorption into the NIR spectral range. One proposal is to use 2,4,7-trinitro-9-fluorenone (TNF) [molecular structure given in Fig. 1.8d inset] as the strong acceptor.

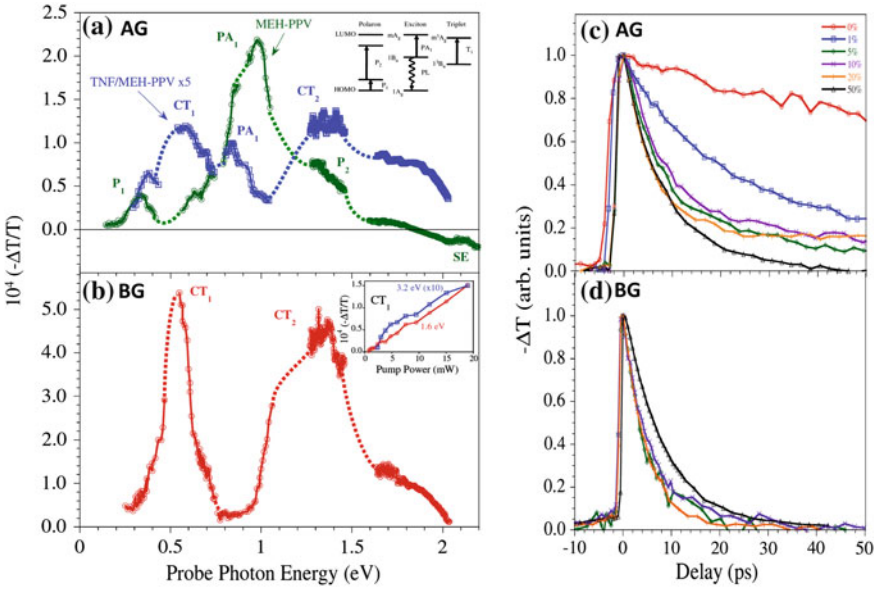

Fig. 1.8 **a** Femtosecond PM spectrum at t = 0 of (1:1) MEH-PPV/TNF pumped at 3.2 eV (*blue squares*) compared to that in pristine MEH-PPV (*green circles*). The PA bands P_1, P_2, CT_1, and CT_2 are denoted. *Inset* shows the energy levels and optical transitions of polarons, singlet excitons, and triplet excitons in MEH-PPV. **b** PM pectrum of (1:1) MEH-PPV/TNF blend pumped at 1.6 eV. *Inset* shows the PA vs pump intensity of (1:1) MEH-PPV/TNF probed at 0.69 eV (CT_1) for both BG and AG excitation. **c** and **d** Femtosecond dynamics vs TNF concentration in various MEH-PPV/TNF blends for the CT_1 PA band probed at 0.67 eV and pumped at 3.2 eV (AG) and 1.55 eV (BG), respectively (Adapted from Holt et al. [80])

When the MEH-PPV as electron donor and TNF acceptor are blended, new nonadditive optical transitions are observed [119, 120]. Bakulin et al. reported that the absorption spectrum of such blends extends into the near-infrared spectral range, along with a nonadditive photoluminescence (PL) band; new and shifted infrared-active vibrational bands and Raman-scattering spectra; and a new photo-induced absorption (PA) band. The polymer PL is strongly quenched, similar as in other polymer/fullerene blend systems [121]. In addition, TNF has a relatively high electron affinity [122] with a lowest unoccupied molecular-orbital (LUMO) energy difference from that of MEH-PPV larger than that of C_{60}; this should prevent electron back transfer after charge separation [123].

Such a body of evidence would nominate TNF as an exceptional candidate for bulk-heterojunction photovoltaic applications. In reality though, actual photocurrent in TNF devices was found to be [124] orders of magnitude lower than that in more conventional polymer/C_{60} blend devices. Yet TNF remains a model prototype for studying the influence of CTC states in organic photovoltaics. Recently a series of significant follow-up works on polymer/TNF blends has been performed [119–121], including the ultrafast dynamics measurements of an MEH-PPV doped with a low concentration of TNF molecules [125].

Figure 1.8a shows the transient PM spectra at t = 0 in a (1:1) blend of MEH-PPV/TNF compared to pristine MEH-PPV film when pumped at 3.1 eV. The transient PM spectrum of the pristine film contains two PA bands. These are P_1 peaking at 0.3 eV due to polaron excitations; and PA_1 due to excitons that peaks at (1 eV). The PA_1 band in the blend is quenched relative to that in the pristine film. The missing stimulated emission in the composite samples is due to the strongly quenched PL of MEH-PPV in the mixture but may also be due to the ground-state absorption tail in the blend. The most conspicuous contribution in the ultrafast PM spectrum of the blend is the peak around 0.5 eV that appears blue-shifted compared to the P_1 peak at 0.3 eV. The new PA band could be better resolved with BG excitation (Fig. 1.5b), where the PA_1 contribution is completely absent. This is consistent with the interpretation that the PA_1 band is due to excitons, which cannot be photogenerated with BG excitation. Together with the new PA band in the mid infrared spectral range (0.5 eV) we also found a new PA band in the near-infrared spectral range ($\sim$1.45 eV; Fig. 1.8a, b. Considering the short lifetime of these PA bands (Fig. 1.8c and d for CT_1 band), it would be consistent to consider that the PA bands at 0.5 eV and at 1.45 eV are completely new bands that are associated with the CTC itself; they are therefore labeled CT_1 and CT_2, respectively. In addition to the novel CT bands, the PA_1 exciton band in the blended system is almost quenched at t = 0 when pumped AG of the polymer. Therefore most photogenerated excitons reach the CTC state before the time resolution of the laser system (150 fs). To ensure that there was no artifact from exciton/exciton annihilation or two photon absorption in our BG experiments, we checked that the transient PA signal is linear versus pump intensity (Fig. 1.8b inset). Indeed, the pump intensities are well below the threshold for such interactions. (10^{19} cm^{-3})

We conclude that the inefficiency of the MEH-PPV/TNF blend for photovoltaic applications was exposed by the fast dynamics obtained for the CT photoexcitations, although the CTC states are formed in record time.

1.3 Photoexcitation Dynamics in Printine RR-P3HT and RR-P3HT/Fullerene Blends

One of the most studied bulk heterojunction (BHJ) organic photovoltaic materials is the blend RR-P3HT (Fig. 1.9a inset) and [6] -phenyl-C_{61}-butyric acid methyl ester (PCBM) (Fig. 1.9b inset), which is often considered as a "model BHJ system" [4, 5, 126]. The P3HT/PCBM blend films are characterized by charge photogeneration with high efficiency, and phase separated fullerene and polymer networks that

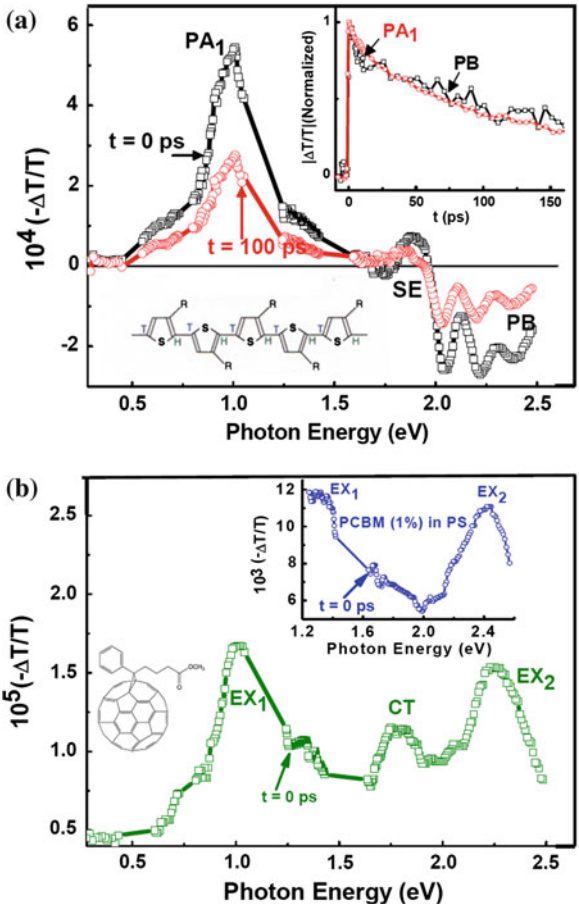

Fig. 1.9 **a** The transient photomodulation spectrum of pristine RR-P3HT film at t = 0 and t = 100 ps, respectively; the exciton bands PA_1, SE and PB are indicated. The *right inset* shows the transient decay of PA_1 and PB bands up to t = 200 ps; the *left inset* shows the polymer backbone chain. **b** The transient photomodulation spectrum of a PCBM film at t = 0; the exciton PA bands EX_1 and EX_2, and CT exciton band are indicated. The *right inset* shows *DT/T*(0) spectrum of isolated PCBM molecules in polystyrene (weight ratio of 1:100) that lacks the CT exciton band. The *left inset* shows the PCBM molecular structure (Adapted from Singh et al. [92])

facilitate charge transport. Consequently high power conversion efficiencies up to ~4.5 % can be obtained in solar cells based on RR-P3HT/PCBM BHJ photovoltaic devices [19, 127]. Numerous steady-state and time-resolved spectroscopic studies have been conducted in pristine P3HT and P3HT/PCBM blend in order to understand the properties and evolution of neutral and charged photoexcitations; but many aspects of the photophysics still remain unclear [20, 21, 30, 39, 60, 73, 74, 86, 128–137]. As a result the process of charge photogeneration in this blend is still a matter of debate. In contrast to the labyrinth photosynthesis process that has evolved in nature [138], the charge photogeneration process in organic photovoltaic cells utilizes one type of heterojunction between two organic semiconductors. The two organic semiconductors, dubbed donor (D-) and acceptor (A-) are cast from solution mixtures to form thin films having nanosize domains of relatively pristine materials and large D-A interface area [128, 139, 140]. This type of BHJ structure usually allows for light absorption in the bulk donor domains that generate excitons, followed by exciton dissociation at the D-A interfaces. However the process by which the excitons reach the D-A interfaces and dissociate to generate separate charge polarons in the D-A nano-domains is only now being the focus of attention [27, 141].

It was originally postulated that once the exciton in the bulk donor domain reaches the D-A interface, it undergoes an ultrafast electron transfer to the acceptor forming a hole-polaron (P^+) in the donor and electron-polaron (P^-) in the acceptor, which are free to participate in the subsequent charge transport process towards the device electrodes [142]. However the mutual P^+-P^- Coulomb attraction should prevent a complete charge separation even if the offset energy of the donor and acceptor active levels is taken into account [75]. On the contrary, the bound P^+-P^- pair forms a charge transfer (CT) state at the D-A interface deep below the D and A optical gaps. However in spite of ample spectroscopic evidence for the existence of such CT state at the D-A interfaces [26, 75, 77, 79, 86, 143], it has been argued that it lies too deep in the gap to have any effect on the charge photogeneration process in the blends [98]. In this part we tried to elucidate the early stages of the charge photogeneration process in the prototype D-A blend, RR-P3HT and PCBM.

The P3HT polymers and PCBM fullerene were supplied by *Plextronics Inc.* [86]. The mixing ratio of the P3HT/PCBM blends was 1.2: 1 by weight, which gives the optimal PCE-value in solar cells [141]. The films were spin cast onto CaF_2 or CsI that are transparent in the mid-IR spectral range. The RR-P3HT/PCBM blend film was thermally annealed at 150 °C for 30 min to enhance the D-A domains size [141]; whereas the region-random RRa-P3HT/PCBM film was used as deposited.

1.3.1 Transient Photomodulation Spectroscopy of Pristine RR-P3HT Films

We measured $\Delta T(t)/T$ spectra of *pristine* polymer and fullerene films (Fig. 1.9). $\Delta T(0)/T$ spectrum of pristine RR-P3HT film (Fig. 1.9a) is dominated by a single PA_1

band at 1 eV followed by photo-bleaching above 1.97 eV and a small stimulated emission band at 1.75 eV, which attests to the excellent quality of the RR-P3HT polymer used here [86]. These three spectral features originate from photogenerated excitons since they decay together (Fig. 1.1a right inset) with an exponential time constant, $\tau_0 = 70$ ps. No photogenerated polarons which peak at 0.1 and 1.8 eV [see Fig. 1.11a inset] are observed here. Figure 1.9b shows $\Delta T(0)/T$ spectrum of pristine PCBM film. It is dominated by two PA bands, namely EX_1 and EX_2 at 1.0 and 2.25 eV, respectively that are due to photogenerated excitons. A third PA band, CT at 1.75 eV originates from charge-transfer excitons in the fullerene film, since it does not exist in the photomodulation spectrum of isolated PCBM molecules in polystyrene (Fig. 1.9b right inset). No photogenerated polarons which peak at 1.15 eV [129, 144] are discerned.

1.3.2 Photomodulation of RR-P3HT/PCMB Blends

1.3.2.1 Transient Photomodulation Spectroscopy with Above-Gap and Below-Gap Pump Excitations

To better understand the transient PA spectra in the polymer/fullerene blends we measured the x-ray diffraction (XRD) pattern from the RRa- and RR-P3HT/PCBM blend films (Fig. 1.10) using the Cu$K_{\square}$ X-ray line at $\lambda = 0.154$ nm. The XRD pattern of RR-P3HT/PCBM contains a prominent Bragg band at $2\theta_{[100]} = 5.3^{o}$ and its harmonics at $2\theta = 10.7^{o}$ and 16^{o}, respectively that originate from the P3HT nanocrystalline domains in the film [72]; as well as a smaller Bragg band at $2\theta_{[311]} = 19.3^{o}$ that originates from the PCBM nanocrystalline domains in the blend

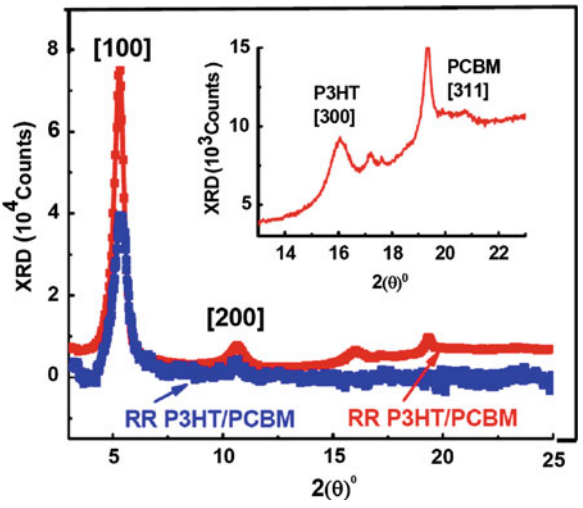

Fig. 1.10 The XRD pattern from RR-P3HT/PCBM (*red*) and RRa-P3HT/PCBM (*blue*), where the P3HT bands [100], [200] and [300] and PCBM band [311] are assigned; the inset focuses on the PCBM band (Adapted from Singh et al. [92])

[146]. We therefore conclude that the annealed RR-P3HT/PCBM blend film contains separate donor and acceptor crystalline domains. We may estimate the average nanocrystalline domain size, D from the full width at half maximum [FWHM], $\Delta_{2\theta}$ of the respective Bragg bands using the Scherrer relation: $D = 0.9\lambda/\Delta_{2\theta}\cos\theta$; we obtain $D \approx 16$ nm (20 nm) for the polymer (PCBM) nano-domains. In contrast, the XRD pattern of the RRa-P3HT/PCBM blend does not show prominent P3HT band harmonics, and in addition the PCBM band is missing (Fig. 1.10). These indicate that the PCBM molecules do not form well-separated domains here; instead, they penetrate into the P3HT lamellae and consequently are much closer on average to the polymer chains.

Figure 1.11a shows $\Delta T(t)/T$ spectra of RR-P3HT/PCBM blend. $\Delta T(0)/T$ spectrum is very similar to that of pristine RR-P3HT (Fig. 1.9a), indicating that excitons are initially photogenerated within the polymer domains. At $t > 0$ the excitons decay; however *no polarons are generated* at the expense of the exciton decay up to 300 ps since there is no PA build-up at low $\hbar\omega$(probe), where the polaron P_1 band dominates the absorption spectrum (as seen in Fig. 1.11a inset). We thus conclude that the photogenerated excitons in the polymer domains decay into a *new state* that is not separated free polarons. This new state must be related with the D-A interfaces in the films since the excitons do not form such a state in the pristine polymer, and we thus propose that is a CT exciton at the D-A interface. In contrast, the background PA spectrum in the mid-IR (Fig. 1.11a) is very similar to the P_1 band in the polaron doping induced absorption spectrum (Fig. 1.11a inset), showing that charge polarons are indeed photogenerated in this RR-P3HT/PCBM film but at later time; in agreement with the high solar cells efficiency based on this blend [86]. We thus conclude that the charge photogeneration process in the blend proceeds in two stages [27, 147]. The first stage is exciton trapping in CT states at the D-A interfaces, followed by a much slower CT state dissociation into free polarons in the D and A domains at $t \gg 2$ ns (=the time limit of our translation stage).

The exciton decay dynamics in the blend is much faster than in the pristine polymer (see PA_1 decays in Figs. 1.11a and 1.9a). The shorter lifetime in the blend is related to the exciton dynamics towards the D-A interfaces, and therefore we studied the PA_1 decay kinetics in more detail. PA_1 decay cannot be fit with a single or few exponential decay functions; nor can it be fit using a diffusion model [$\sim (1 + t/\tau)^{-1}$]. Alternatively, PA_1 decay can be fit using multiple power-law decays that originate from a Förester resonant energy transfer (FRET) into the CT exciton [148], averaged over the exciton initial distance from the D-A interface (see [92]). This model yields the following time dependent surviving exciton density N(t) in the polymer nano-grains;

$$N(t)/N(0) = \exp(-t/\tau_0)\left[m_1 + m_2\left(C_1 t^{1/2} - C_2 t^{1/3} + C_3 t^{1/6}\right)\right] \tag{1.3}$$

where $\tau_0 = 70$ ps is the natural exciton lifetime in RR-P3HT that is obtained from the PA_1 dynamics of Fig. 1.9; m_1 and m_2 are fitting parameters; and the C constants are given by the relations: $C_1 = 0.2u^{-3}$, $C_2 = 0.66u^{-2}$ and $C_3 = 0.54/u$, where

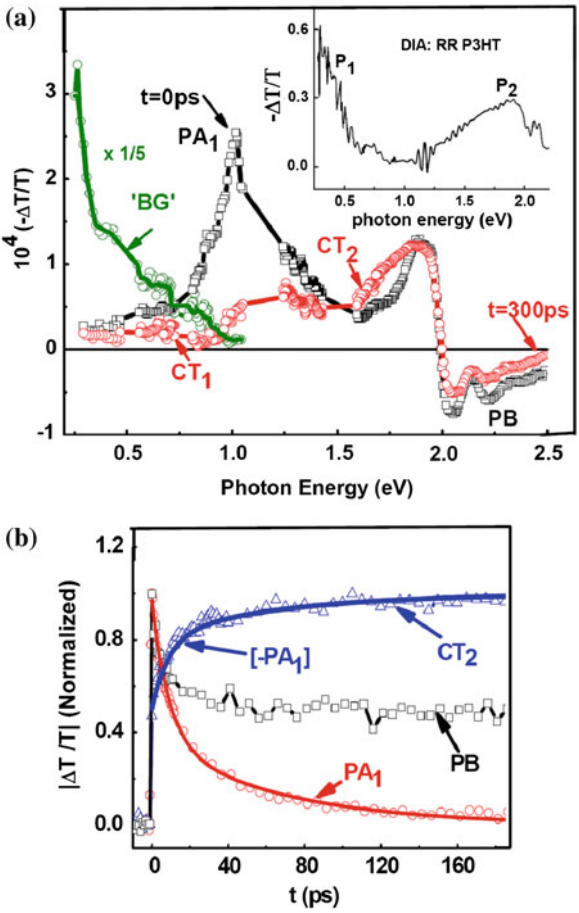

Fig. 1.11 **a** The transient photomodulation spectrum of RR-P3HT/PCBM blend film at t = 0 and t = 300 ps, respectively; the exciton band PA_1, and CT exciton bands CT_1 and CT_2 are indicated. The *green circles* and line represent the background (BG) PA spectrum measured at t = −5 ps. The *inset* shows the doping induced absorption of pristine RR-P3HT film, where the polaron bands P_1 and P_2 are assigned. **b** The transient decay of PA_1, build-up dynamics of CT_2, and the PB decay up to 180 ps. The line through the data points is a fit using the FRET mechanism (see text); the same function also fits the CT_2 build-up dynamics (Adapted from Singh et al. [92])

u = $D/2R_0$ is the parameter ratio of the grain size, D to twice the FRET radius, R_0, which was measured before to be between 3 and 9 nm [149]. Using R_0 = 6 nm and D = 16 nm from the XRD studies, we obtain u = 1.3. Subsequently the excellent fit to the PA_1 decay seen in Fig. 1.11b was obtained using $m_1 = 0.14$ and $m_2 = 7$.

In support of the CT intermediate role in the charge photogeneration process in the blend, Fig. 1.11a also shows that PA build-up indeed occurs in both mid-IR and near-IR [21] spectral ranges. In fact there are two PA bands, namely CT_1 in the mid-IR and CT_2 in the near-IR that are generated at longer time *at the expense of the exciton PA_1 decay*. Figure 1.11b shows that the CT_2 build-up dynamics in the near-IR closely matches the exciton PA_1 decay, since the same function of time fits both PA_1 decay and CT_2 build-up dynamics (measured at 1.75 eV probe). Figure 1.12a more clearly shows the two PA bands that are generated at the expense of the exciton PA_1 decay. To obtain the full photogenerated CT spectrum we subtracted the photomodulation spectrum at t = 30 ps from that at t = 0, after normalizing the two

PA bands at 1 eV and 2 eV for the CT_1 and CT_2 bands, respectively. It is seen that the CT spectrum contains two prominent PA bands that peak at 0.6 (CT_1) and 1.75 eV (CT_2), respectively, which are very different than the bands P_1 and P_2 of polarons (Fig. 1.11a inset). Consequently we propose that these two PA bands are due to optical transitions within the CT manifold at the D-A interfaces [27, 142].

To support this assumption we measured the transient photomodulation spectrum using $\hbar\omega$(pump) = 1.55 eV, which is below the optical gap of the polymer and fullerene constituents. Such low $\hbar\omega$(pump) can resonantly excite the CT state at the D-A interface since its energy was measured to be between 1.2 and 1.6 eV [86], without first photogeneration of excitons in the polymer domains. Figure 1.12b shows that under these conditions the two CT PA bands are instantaneously photogenerated; which is compelling evidence that they originate from the CT states at the interfaces. This supports our assignment for the CT bands in the transient photomodulation spectrum of this blend.

Interestingly the background PA spectrum excited with below-gap pump excitation (Fig. 1.12b) is very similar to that generated using above-gap pump excitation

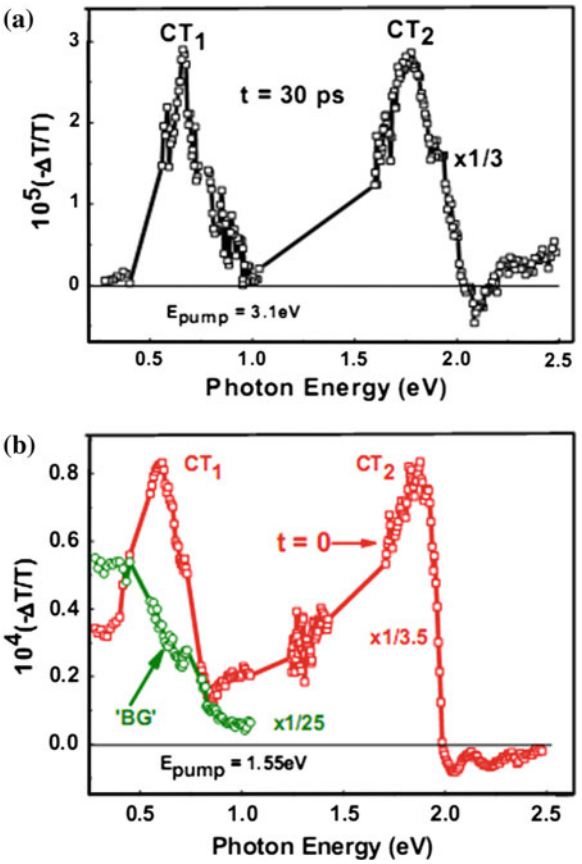

Fig. 1.12 **a** The transient photomodulation spectrum of RR-P3HT/PCBM blend film at t = 30 ps excited at 3.1 eV, normalized and subtracted from the spectrum at t = 0, that shows the two newly formed CT_1 and CT_2 bands. **b** Same as in **a** but at t = 0 and excited at 1.55 eV, which is below the gap of both polymer and fullerene constituents (Adapted from Singh et al. [92])

(Fig. 1.11a), which we identified as due to long-lived charge polarons [86]. This shows that there exists a mechanism where thermalized CT excitons at the D-A interfaces are able to separate into free polarons in the donor and acceptor domains, *regardless of the initial* $\hbar\omega$(pump) [27]. This finding is very important, since it can refute the notion that the CT state in the blend lies too deep in the gap to have any influence over the charge photogeneration process. Apparently the exciton kinetic energy when reaching the CT state plays a minor role in the charge photogeneration process; this may explain the flat spectral response of the photocurrent action spectrum in organic solar cells [86].

1.3.2.2 CW Photomodulation Spectroscopy with Above-Gap and Below-Gap Excitations

A compelling signature of photogenerated charges in π-conjugated polymers is the appearance of in-gap polaron PA bands, as seen in the PM spectrum of the blend shown in Fig. 1.13. We clearly identify the well-known polaron PA bands P_1 and P_2. In addition to the in-gap transitions, the polaron excitation also renormalizes the frequencies of the Raman active amplitude modes in the polymer chain, where the small polaron mass causes the IR active vibrations (IRAV) to possess very large oscillator strengths [96]. The below-gap pump excitation of the blend also produces the same polaron PA features as those produced with above-gap pump excitation; this confirms that polaron photogeneration is also possible with below-gap pump, in agreement with the transient PM data discussed above. We emphasize that the

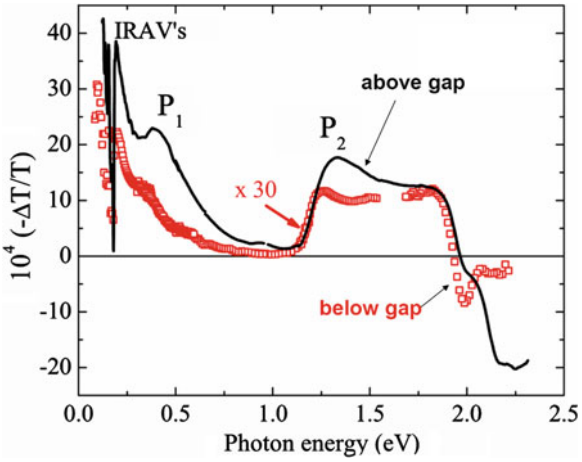

Fig. 1.13 CW PA spectra of RR-P3HT/PCBM film using above gap (*black solid line*) and below-gap (*red squares*) pump excitation. The AG (BG) pump excitation is at 2.5 (1.55) eV. Both spectra show the known PA band signature of polarons; namely, P_1, P_2 bands and IRAV, as denoted (Adapted from Drori et al. [86])

mechanism by which the polaron species are photogenerated with below-gap excitation cannot be explained by the known single-step photoinduced charge transfer reaction [21, 150]; since singlet excitons that supposedly precede charge dissociation are not photogenerated in the polymer or fullerene domains, as revealed in the picosecond transient PM spectrum (Fig. 1.11) [151].

To further investigate the process by which polarons are photogenerated with below-gap excitation we studied the polarons recombination dynamics generated with below-gap and above-gap pump excitations. The recombination dynamics was obtained from the modulation-frequency response of the P_1 band of the polarons using the bimolecular dispersive recombination model [113]. Figure 1.14 shows the PA response at temperature T = 30 K, and the fit using 1.2 from which the lifetime, τ, was obtained. We realize that τ dramatically increases with below-gap excitation.

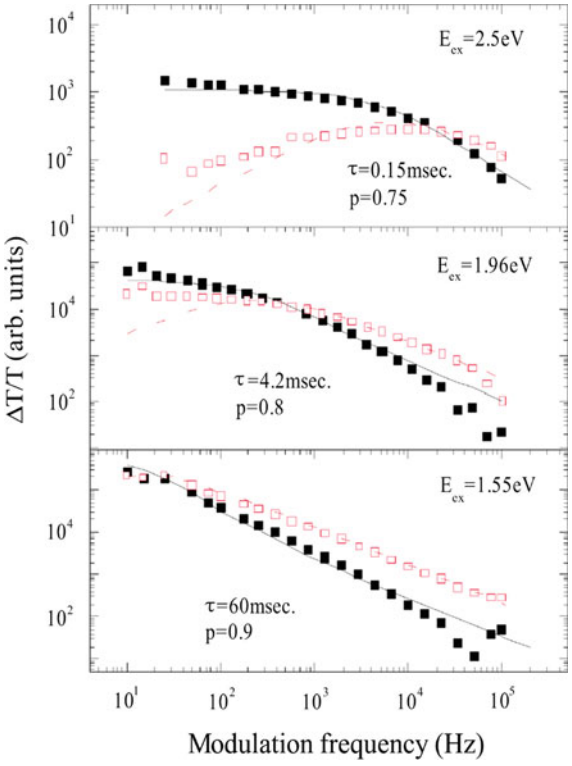

Fig. 1.14 Modulation frequency dependence of the P_1 PA polaron band in RR-P3HT/PCBM blend measured at 0.4 eV and T = 30 K; both in-phase (*full black squares*) and quadrature (*empty red squares*) PA are shown. The *lines* through the data points are fit using 1.2 where the best-fit lifetime, τ and dispersive parameter exponent, p are indicated. The various panels represent different pump excitation: *top panel* is for above-gap excitation pumped at 2.5 eV; *middle panel* is for below-gap excitation pump at 1.96 eV; *bottom panel* is for below-gap excitation at 1.55 eV (Adapted from Drori et al. [86])

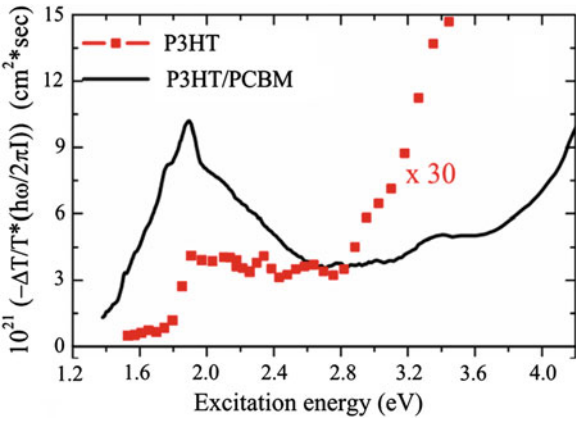

Fig. 1.15 Pump excitation dependence of polarons RR-P3HT/PCBM blend measured at T = 30 K. Polaron band P_1 action spectra for RR-P3HT (*squares*) and RR-P3HT/PCBM blend (*solid line*) measured between 0.25 and 0.4 eV, normalized to the impinging excitation photon flux (Adapted from Drori et al. [86])

The increase in τ is by about three orders of magnitude, from τ = 150 μs with above-gap pump excitation at $\hbar\omega$ = 2.5 eV to τ = 60 ms with below-gap excitation at $\hbar\omega$ = 1.55 eV. This shows that below-gap photogenerated polarons have much slower recombination kinetics. For the diffusion-limited bimolecular kinetics known to exist in polymers [113], this indicates either increased localization for the below-gap photogenerated polarons or charge separation into two different phases, namely, the polymer and fullerene domains.

We also used the polaron action spectrum for understanding the below-gap polaron photogeneration process, where we probe the strength of the polaron P_1 band between 0.25 and 0.4 eV as a function of the excitation $\hbar\omega$, normalizing by the impinging excitation photon flux, I. Figure 1.15 shows the polaron action spectra for pristine P3HT and P3HT/PCBM blend. The polaron photogeneration action spectrum of pristine P3HT has a clear onset at the polymer band edge $\hbar\omega$ = 1.85 eV; and lacks the below-gap polaron generation component. In contrast, the polaron photogeneration action spectrum in the blend extends to $\hbar\omega$ pump well into the polymer optical gap with an extrapolated onset at $\hbar\omega$ = 1.2 eV, i.e., much smaller than the polymer and fullerene absorption edges. In addition the polaron action spectrum also shows a prominent peak at ∼1.9 eV having an apparently smaller polaron generation efficiency for $\hbar\omega$ > Eg (the polymer optical gap). This (as well as Fig. 1.6b) is an illusion, however, since the polaron lifetime is longer with below-gap excitation. This so called "lifetime effect" dramatically influences the polaron action spectrum, since the measurements are done at steady-state conditions, where the polaron density is also influenced by their recombination lifetime [26, 86]. Nevertheless, this effect in the polaron action spectrum can be corrected by considering the lifetime difference measured at different pump excitations [86].

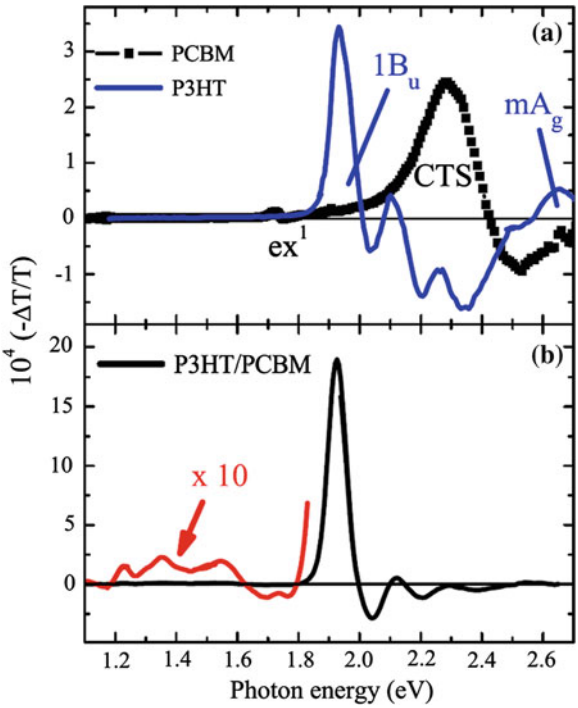

Fig. 1.16 **a** The EA spectra of pristine RR-P3HT (*blue line*) and PCBM (*black squares*). $1B_u$ and mA_g denote strongly coupled exciton states in the polymer; whereas CTS denotes the charge transfer state in the fullerene. **b** The EA spectrum of RR-P3HT/PCBM blend, where the below-gap spectrum is also shown multiplied by a factor of 10. The CTC in the blend is denoted (From Drori et al. [86] with Permission)

1.3.2.3 Electroabsorption Spectroscopy

The mechanism by which below-gap polaron photogeneration occurs without involving exciton formation may be better understood by involving a CTC state at the interface between the polymer and fullerene domains, that lies below the optical gap of the blend material constituents. One viable way to measure such a CTC state is using the EA spectroscopy; since such a state may have a large dipole moment that enhances the EA signal [83–85].

The EA spectrum of the pristine RR-P3HT (Fig. 1.16a) is dominated by the strongly coupled exciton transitions $1B_u$ and mA_g at 2.0 eV and 2.7 eV, respectively [73]. Whereas the EA spectrum of PCBM reveals the charge transfer state (denoted CTS) transition at 2.4 eV [26] in this material. We note that there are no optical EA features below the polymer and fullerene optical gaps for the pristine polymer and fullerene films. In contrast, an EA band with an onset at 1.2 eV is obtained in the blend (Fig. 1.16b). A broad derivative-like feature can be seen, followed by a broad-band that spans $\hbar\omega$(probe) range from 1.2 to 1.8 eV with several clear peaks. We assign this new EA feature to the CTC state in the gap and speculate that the various secondary peaks are due to excited states in the CTC manifold. We note that although the CTC states are mainly formed at the polymer/fullerene interfaces with relatively small cross section, it is still possible to observe its associated optical transitions using EA spectroscopy due to its strong coupled dipole moment [83, 84];

this can be barely achieved using linear absorption measurements [114]. The EA onset at 1.2 eV, which we interpret here as the onset of the CTC manifold, is the lowest $\hbar\omega$ obtained for the CTC so far in any blend. [75, 81] This may be an important contributing factor for the high PCE of ~4.2 % obtained for the OPV device based on the RR-P3HT/PCBM blend.

1.3.3 Photomodulation of Pristine RRa-P3HT and RRa-P3HT/PCMB Blends; a Comparison

For comparison, we also study the charge photogeneration mechanism in RRa-P3HT/PCBM blend where the fullerene molecules are closer to the polymer chains on average. Figure 1.17a shows $\Delta T(t)/T$ spectra of *pristine* RRa-P3HT. It also contains a single PA_1 exciton band at ~1 eV followed by stimulated emission above ~1.75 eV that shares the same dynamics (Fig. 1.17a inset). However $\Delta T(0)/T$ spectrum in RRa-P3HT/PCBM blend (Fig. 1.18a) is very different from that in RR-P3HT/PCBM blend (Fig. 1.11a). The former spectrum shows the same two CT PA bands (namely CT_1 and CT_2 discussed above) that are generated within ~500 fs (Fig. 1.18b), in concert with the ultrafast decay of the exciton PA_1 band. The fast exciton decay here is consistent with the proximity of the PCBM molecules to the P3HT polymer chains in RRa-P3HT/PCBM blend. Interestingly,

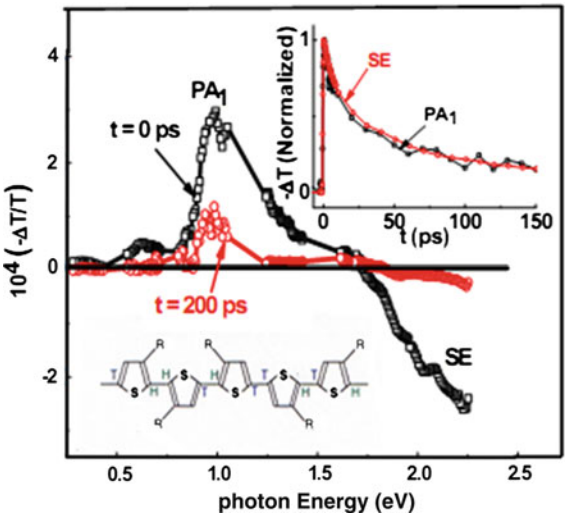

Fig. 1.17 The transient photomodulation spectrum of pristine RRa-P3HT film at t = 0 and t = 200 ps, respectively; the exciton bands PA_1 and SE are indicated. The *right inset* shows the transient decay of PA_1 and SE bands up to t = 200 ps; the *left inset* shows the polymer backbone chain (Adapted from Singh et al. [92])

the background PA spectrum here does not show long-lived polaron photogeneration; in fact the background PA spectrum is the *same* as the transient PA spectrum. This shows that the photogenerated CT excitons in this blend cannot easily dissociate into free polarons, in agreement with the poor solar cell efficiency (<0.1 %) based on this blend (Fig. 1.19). It also shows that the CT exciton dissociation is related to the D-A domain size. The larger is the D-A interface area the smaller is the CT exciton binding energy, and consequently the more efficient is the CT exciton dissociation into separate charge polarons in the D and A domains [88].

This conclusion is further supported by the I-V characteristics under solar-like illumination of photovoltaic devices based on RR-P3HT/PCBM and RRa-P3HT/PCBM blends using AM1.5 filter as shown in Fig. 1.19. It is seen that the power conversion efficiency and short circuit current of RR-P3HT/PCBM blend are more than an order of magnitude higher than that of RRa-P3HT/PCBM blend.

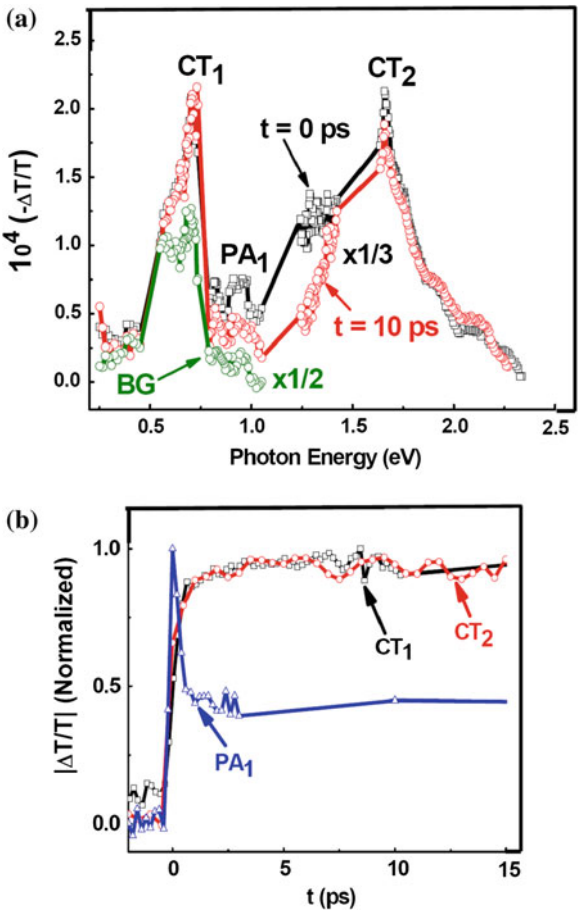

Fig. 1.18 **a** The transient photomodulation spectrum of RRa-P3HT/PCBM blend at t = 0 and t = 10 ps, respectively excited at 3.1 eV; the PA bands PA_1, CT_1 and CT_2 are assigned. **b** The transient decay of PA_1, and build-up dynamics of CT_1 and CT_2 up to 15 ps (Adapted from Singh et al. [92])

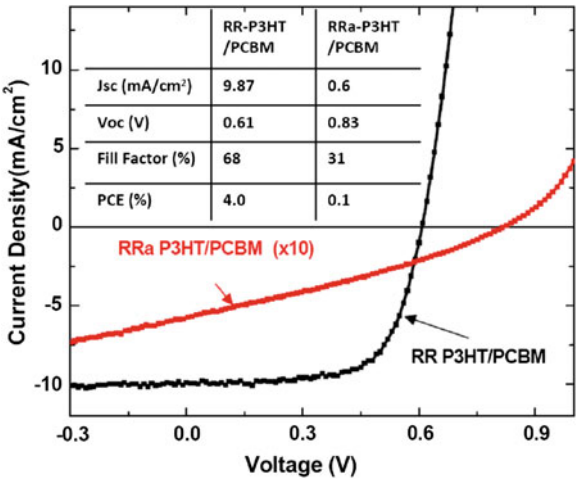

Fig. 1.19 The I-V characteristic of two solar cells based on PCBM blend with RR-P3HT (*black*) and RRa-P3HT (*red*) donor polymers under solar-like illumination of AM 1.5. The inserted Table gives the device photovoltaic characteristic parameters such as short circuit current density, J_{sc}; open-circuit voltage, V_{oc}; fill-factor, FF; and the power conversion efficiency, PCE in % (From Singh et al. [92] with permission)

1.4 Summary

In this chapter, we reviewed the studies of photophysics in two typical π-conjugated polymers, namely RR-P3HT with self-organized π-stacked two-dimensional lamellae and MEH-PPV with amorphous nanomorphology in pristine and blend with fullerene molecules, using a variety of optical probe techniques including broadband femtosecond transient and continuous wave (cw) photomodulation spectroscopies and electroabsorption. In polymer/fullerene blends the photogenerated excitons quickly decay away to give rise to a novel photoexcitation. We provide strong evidence for the existence of charge transfer complex (CTC) state (charge transfer excitons) that is formed inside the optical gap of the polymer and fullerene constituents, which is clearly revealed in the electro-absorption spectrum. Because of the below-gap CTC it is possible to directly generate polarons in the blends without involving intrachain excitons in the polymer phase, with below gap pump excitation. The CTC state lying inside the gap readily explains both the below-gap excitation and near-IR photoluminescence in the blend. Moreover, using action spectra of polaron PA we showed that the polaron generated with below-gap excitation are more localized compared with polarons with above-gap excitation.

In RR-P3HT/PCBM blend with typical D-A bulk heterojunction morphology we demonstrated that the charge photogeneration mechanism in organic solar cells occurs in two-steps. First the photogenerated excitons in the polymer domains reach the D-A interfaces within few *ps* time depending on the domain size, where they

form CT excitons. This process is followed by CT exciton dissociation into free charged polarons in the D and A domains in the *ns–μs* time scale, which remains to be observed. The CT exciton dissociation depends on the CT exciton binding energy, which is significantly lower for larger D-A interface area. Our results emphasize the importance of the D-A domain size in organic solar cells based on bulk heterojunction morphology.

In MEH-PPV/C_{60} blend (1:1 by weight) as well as in RRa-P3HT/PCBM blend, the low degree of phase separation in the blend results in the fast dissociation (<200 fs) of excitons generated in the polymer chains (as well as results in the fast populating of CTC states on the interface). However, the polarons generated from further dissociation of CTC are localized because of amorphous morphology of MEH-PPV and RRa-P3HT film.

Our findings indicate that the CTC state and film morphology play a crucial role in carrier photogeneration in donor-acceptor blends. More thorough exploration of the CT excitation their interaction with free polaron excitations may improve the power conversion efficiency of organic solar cell and drive the development of novel photoactive materials.

Acknowledgments We would like to thank our collaborators at the University of Utah Physics Department over the years 2000–2012, without whom this work would have never been completed. These are T. Basel, T. Drori, J. Holt, E. Olejnik, B. Pandit, R.C. Polson, S. Singh, M. Tong, C. Yang, and C. Wu. We also acknowledge useful collaboration with S. Mazumdar from the University of Arizona, E. Ehrenfreund from the Technion in Israel, and S. Li and D. Laird from Plextronics.

This work was supported in part over the years by the Department of Energy grant No. FG-04-ER46109. C.-X. Sheng thanks the support of NSF of China No. 61006014, NHTRDP of China, No. 2011AA050520, the Fundamental Research Funds for the Central Universities No. 3092013-0111008.

References

1. L. Dou, J. You, J. Yang, et al., Nature Photonics **6**, 180 (2012)
2. M.A. Green, K. Emery, Y. Hishikawa, W. Warta, Prog. Photovoltaics **19**, 84 (2011)
3. M.A. Green, K. Emery, Y. Hishikawa et al., Prog. Photovoltaics **20**, 12 (2012)
4. T.M. Clarke, J.R. Durrant, Chem. Rev. **110**, 6736 (2010)
5. C. Deibel, T. Strobel, V. Dyakonov, Adv. Mater. **22**, 4097 (2010)
6. Primary Photoexcitations in Conjugated Polymers: Molecular Exciton versus Semiconductor Band Model (ed.) by S. Sariciftci (World Scientific, Singapore, 1997)
7. M. Tong et al., Phys. Rev. B **75**, 125207 (2007)
8. M. Chandross, S. Mazumdar, S. Jeglinski, X. Wei, Z.V. Vardeny, E.W. Kwock, T.M. Miller, Phys. Rev. B **50**, 14702 (1994)
9. H. Zhao, S. Mazumdar, C.-X. Sheng, M. Tong, Z.V. Vardeny, Phys. Rev. B **73**, 075403 (2006)
10. Z.V. Vardeny, et al., Phys. Rev. Lett. **51**, 2326 (1983)
11. B. Horovitz, H. Gutfreund, M. Weger, Phys. Rev. B **17**, 2796 (1978)
12. E. Ehrenfreund et al., Phys. Rev. B **36**, 1535 (1987)
13. N.S. Sariciftci, L. Smilowitz, A.J. Heeger, F. Wudl, Science **258**, 1474 (1992)

14. G. Yu, J. Ga, J.C. Hummelen et al., Science **270**, 1789 (1995)
15. P. Shaw, A. Ruseckas, I. Samuel, Adv. Mater. **20**, 3516 (2008)
16. A. Huijser, T.J. Savenije, A. Shalav, L.D. Siebelles, J. Appl. Phys. **104**, 034505 (2008)
17. J.E. Kroeze, T.J. Savanije, M.J.W. Vermeulen, J.M. Warman, J. Phys. Chem. B **107**, 7696 (2003)
18. A. Haugeneder, M. Neges, C. Kallinger et al., Phys. Rev. B **59**, 15346 (1999)
19. W. Ma, C. Yang, X. Gong, K. Lee, A.J. Heeger, Adv. Funct. Mater. **15**, 1617 (2005)
20. N. Banerji, S. Cowan, E. Vauthey, A.J. Heeger, J. Phys. Chem. C **115**, 9726 (2011)
21. W. Hwang, D. Moses, A.J. Heeger, J. Phys. Chem. C **112**, 4350 (2008)
22. I.A. Howard, R. Mauer, M. Meister, F. Laquai, J. Am. Chem. Soc. **132**, 14866 (2010)
23. A.L. Ayzner, C.J. Tassone, S.H. Tolbert, B.J. Schwartz, J. Phys. Chem. C **113**, 20050 (2009)
24. J.-L. Brédas, J.E. Norton, J. Cornil, V. Coropceanu, Acc. Chem. Res. **42**, 1691 (2009)
25. T. Strobel, C. Deibel, V. Dyakonov, Phys. Rev. Lett. **105**, 266602 (2010)
26. T. Drori, C.X. Sheng, A. Ndobe et al., Phys. Rev. Lett. **101**, 037401 (2008)
27. A.A. Bakulin, A. Rao, V.G. Pavelyev et al., Science **335**, 1340 (2012)
28. X. Wei et al., Phys. Rev. Lett. **68**, 666 (1992)
29. M. Tong et al., Phys. Rev. B **75**, 125207 (2007)
30. C.-X. Sheng, M. Tong, S. Singh, Z.V. Vardeny, Phys. Rev. B **75**, 085206 (2007)
31. Z. V. Vardeny, X. Wei., in *Handbook of Conducting Polymers*, edited by T.A. Skotheim, R. L. Elsenbaumer, J. Reynolds (2nd Ed.), (Marcel Dekker Inc., New York, 1998)
32. K. Fesser et al., Phys. Rev. B **27**, 4804 (1983)
33. Z.V. Vardeny, J. Tauc, Phys. Rev. Lett. **54**, 1844 (1985)
34. Z.G. Soos, S. Ramasesha, Phys. Rev. B **29**, 5410 (1984)
35. S.V. Frolov et al., Phys. Rev. B **65**, 205209 (2002)
36. A.J. Heeger et al., Rev. Mod. Phys. **60**, 781 (1988)
37. S.N. Dixit, D. Guo, S. Mazumdar, Phys. Rev. B **43**, 6781 (1991)
38. D. Guo et al., Phys. Rev. B **48**, 1433 (1993)
39. F. Paquin, G. Latini, M. Sakowicz et al., Phys. Rev. Lett. **106**, 197401 (2011)
40. P.B. Miranda, D. Moses, A.J. Heeger, Phys. Rev. B **64**, 081201 (2001)
41. K. Aryanpour, C.-X. Sheng, E. Olejnik, B. Pandit, D. Psiachos, S. Mazumdar, Z.V. Vardeny, Phys. Rev. B **83**, 155124 (2011)
42. R. Kersting et al., Phys. Rev. Lett. **73**, 1440 (1994)
43. J.B. Birks, *Photophysics of Aromatic Molecules* (Wiley, London, 1970)
44. N.T. Harison et al., Phys. Rev. Lett. **77**, 188 (1996)
45. M. Pope, C.E. Swenberg, *Electronic Processes in Organic Crystals and Polymers*, 2nd edn. (Oxford University Press, Oxford, 1999)
46. M.W.B. Wilson, A. Rao, J. Clark, R.S.S. Kumar, D. Brida, G. Cerullo, R.H. Friend, J. Am. Chem. Soc. **133**, 11830 (2011)
47. P.M. Zimmerman, Z. Zhang, C.B. Musgrave, Nat. Chem. **2**, 648 (2010)
48. P. Miranda, D. Moses, A.J. Heeger, Phys. Rev. B **70**, 085212 (2004)
49. C. Gadermaier, G. Cerullo, G. Sansone, G. Leising, U. Scherf, G. Lanzani, Phys. Rev. Lett. **89**, 117402 (2002)
50. Rothberg, L., in *Semiconducting Polymers: Chemistry, Physics and Engineering,* vol. I, edited by G. Hadziioannou, G. G. Malliaras (Wiley, New York, 2006), pp. 179–204 (and references therein)
51. V.I. Arkhipov, H. Bässler, Phys. Status Solidi A **201**, 1152 (2004). (and references therein)
52. B.J. Schwartz, Annu. Rev. Phys. Chem. **54**, 141 (2003). and references therein
53. Conwell, E.M. in *Organic Electronic Materials: Conjugated Polymers and Low Molecular Weight Solids*, edited by R. Farchioni, G. Grosso (Springer, New York, 2001), pp. 127–180
54. I.D.W. Samuel, G. Rumbles, C.J. Collison, Phys. Rev. B **52**, R11573 (1995)
55. I.D.W. Samuel, G. Rumbles, C.J. Collison, S.C. Moratti, A.B. Holmes, Chem. Phys. **227**, 75 (1998)
56. P.K.H. Ho, J.-S. Kim, N. Tessler, R.H. Friend, J. Chem. Phys. **115**, 2709 (2001)
57. S.-H. Lim, T.G. Bjorklund, K.M. Gaab, C.J. Bardeen, J. Chem. Phys. **117**, 454 (2002)

58. P.J. Brown, D.S. Thomas, A. Köhler et al., Phys. Rev. B **67**, 064203 (2003)
59. A.B. Koren, M.D. Curtis, A.H. Francis, J.W. Kampf, J. Am. Chem. Soc. **125**, 5040 (2003)
60. J. Clark, C. Silva, R.H. Friend, F.C. Spano, Phys. Rev. Lett. **98**, 206406 (2007)
61. S. Singh, T. Drori, Z.V. Vardeny, Phys. Rev. B **77**, 195304 (2008)
62. B. Schweitzer, V.I. Arkhipov, H. Bässler, Chem. Phys. Lett. **304**, 365 (1999)
63. D. Hertel, Y.V. Romanovskii, B. Schweitzer, U. Scherf, H. Bässler, Synth. Met. **116**, 139 (2001)
64. Y. Zhang, Z. Wang, M.-K. Ng, L.J. Rothberg, J. Phys. Chem. B **111**, 13211 (2007)
65. V. Morandi, M. Galli, F. Marabelli, D. Comoretto, Phys. Rev. B **79**, 045202 (2009)
66. M. Yan et al., Phys. Rev. Lett. **72**, 1104 (1994)
67. H.A. Mizes, E.M. Conwell, Phys. Rev. B **50**, 11243 (1994)
68. P.A. Lane, X. Wei, Z.V. Vardeny, Phys. Rev. B **56**, 4626 (1997)
69. D.K. Campbell et al., Phys. Rev. B **26**, 6862 (1982)
70. M. Wohlgenannt, X.M. Jiang, Z.V. Vardeny, Phys. Rev. B **69**, 241204 (2004)
71. Z.V. Vardeny et al., Phys. Rev. Lett. **56**, 671 (1986)
72. H. Sirringhaus et al., Nature **401**, 685 (1999)
73. R. Österbacka et al., Science **287**, 839 (2000)
74. X.M. Jiang et al., Adv. Funct. Mater. **12**, 587 (2002)
75. J.J. Benson-Smith, L. Goris, K. Vandewal et al., Adv. Funct. Mater. **17**, 451 (2007)
76. M.A. Loi, S. Toffanin, M. Muccini et al., Adv. Funct. Mater. **17**, 2111 (2007)
77. M. Hallermann, S. Haneder, E. Da Como, Appl. Phys. Lett. **93**, 053307 (2008)
78. P. Parkinson, J. Lloyd-Hughes, M.B. Johnston, L.M. Herz, Phys. Rev. B **78**, 115321 (2008)
79. A.A. Bakulin, S.A. Zapunidy, Pshenichnikov, et al., Phys. Chem. Chem. Phys. **11**, 7324 (2009)
80. J. Holt, S. Singh, T. Drori, Y. Zhang, Z.V. Vardeny, Phys. Rev. B **79**, 195210 (2009)
81. M. Hallermann, I. Kriegel, E. Da Como et al., Adv. Funct. Mater. **19**, 3662 (2009)
82. J.L. Brédas, D. Beljonne, V. Coropceanu, J. Cornil, Chem. Rev. **104**, 4971 (2004)
83. Z.D. Wang, S. Mazumdar, A. Shukla, Phys. Rev. B **78**, 235109 (2008)
84. K. Aryanpour, D. Psiachos, S. Mazumdar, Phys. Rev. B **81**, 085407 (2010)
85. H. Alves, A.S. Molinari, H.X. Xie, A.F. Morpurgo, Nat. Mater. **7**, 574 (2008)
86. T. Drori, J. Holt, Z.V. Vardeny, Phys. Rev. B **82**, 075207 (2010)
87. V. Dyakonov, E. Frankevich, Chem. Rev. **227**, 203 (1998)
88. V.I. Arkhipov, P. Heremans, H. Bassler, Appl. Phys. Lett. **82**, 4605 (2003)
89. S. Westenhoff et al., J. Am. Chem. Soc. **130**, 13653 (2008)
90. D. Veldman et al., J. Am. Chem. Soc. **130**, 7721 (2008)
91. A.C. Morteani et al., Phys. Rev. Lett. **92**, 247402 (2004)
92. S. Singh, B. Pandit, T.P. Basel, S. LI, D. Laird, Z.V. Vardeny, Phys. Rev. B **85**, 205206 (2012)
93. B. Horovitz, Solid State Commun. **41**, 729 (1982)
94. C.-X. Sheng, T. Basel, B. Pandit, Z.V. Vardeny, Org. Electron. **13**, 1031 (2012)
95. M.J. Rice, Phys. Rev. Lett. **37**, 36 (1976)
96. R. Österbacka, X.M. Jiang, C.P. An, B. Horovitz, Z.V. Vardeny, Phys. Rev. Lett. **88**, 226401 (2002)
97. V. Mizrahi et al., Synth. Metals **102**, 1182, 1999; *ibid* 119, 507 (2001)
98. J. Holt., Ph.D. thesis, University of Utah, 2009
99. O. Epshtein, G. Nakhmanovich, Y. Eichen, E. Ehrenfreund, Phys. Rev. B **63**, 125206 (2001)
100. R.K. Willardson, A.C. Beer eds , *Semiconductors and Semimetals,* vol. 9 (Academic Press, New York 1972)
101. L. Sebastian, G. Weiser, H. Bassler, Chem. Phys. **61**, 125 (1981)
102. G. Weiser, Phys. Rev. B **45**, 14076 (1992)
103. L. Sebastian, G. Weiser, Phys. Rev. Lett. **46**, 1156 (1981)
104. M. Liess, S. Jeglinski, Z.V. Vardeny et al., Phys. Rev. B **56**, 15712 (1997)
105. Ye. Zhang, Ph.D. Thesis, University of Utah, 2010

106. L. Rothberg., Proc. Int. School *of Physics "Enrico Fermi" Course CXLIX,* (eds.), V.M. Agranocich, G.C. La Rocca (IOS Press, Amsterdam, 2002), p. 299
107. E. Hendry et al., Phys. Rev B **71**, 125201 (2005)
108. C. Brabec et al., Chem. Phys. Lett. **340**, 232 (2001)
109. A. Kohler, D.A.D. Santos, D. Beljonne, et al.,Nature **392**, 903 (1998)
110. C.X. Sheng, Ph.D. Thesis, University of Utah, 2005
111. K. Yoshino et al., Jpn. J. Appl. Phys. Part 2, **32**, L140 (1993)
112. S.V. Frolov et al., Chem. Phys. Lett. **286**, 2 (1998)
113. O. Epshtein et al., Phys. Rev. Lett. **90**, 046804 (2003)
114. L. Goris et al., Appl. Phys. Lett. **88**, 052113 (2006)
115. P. Panda et al., J. Phys. Chem. B **111**, 5076 (2007)
116. C. Winder, N. Sariciftci, Mater. Chem. **14**, 1077 (2004)
117. N.H. Karam, R.R. King, M. Haddad et al., Sol. Energy Mater. Sol. Cells **66**, 453 (2001)
118. J.Y. Kim, K. Lee, N.E. Coates et al., Science **317**, 222 (2007)
119. A.A. Bakulin, S.G. Elizarov, A.N. Khodarev et al., Synth. Met. **147**, 221 (2004)
120. D.Y. Paraschuk, S.G. Elizarov, A.N. Khodarev et al., JETP Lett. **81**, 467 (2005)
121. C. Im, J.M. Lupton, P. Schouwink, S. Heun, H. Becker, H. Bässler, J. Chem. Phys. **117**, 1395 (2002)
122. J.E. Kuder, J.M. Pochan, S.R. Turner, D.F. Hinman, J. Electrochem. Soc. **125**, 1750 (1978)
123. J.G. Müller, J.M. Lupton, J. Feldmann et al., Phys. Rev. B **72**, 195208 (2005)
124. W.D. Gill, J. Appl. Phys. **43**, 5033 (1972)
125. A.A. Bakulin, D.S. Martyanov, D.Y. Paraschuk et al., J. Phys. Chem. B **112**, 13730 (2008)
126. G. Dennler, M.C. Scharber, C.J. Brabec, Adv. Mater. **21**, 1223 (2009)
127. G. Li, V. Shrotriya, J. Huang et al., Nat. Mater. **4**, 864 (2005)
128. R.A. Marsh, J.M. Hodgkiss, S. Albert-Seifried, R.H. Friend, Nano Lett. **10**, 923 (2010)
129. J. Guo, H. Ohkita, H. Benten, S. Ito, J. Am. Chem. Soc. **132**, 6154 (2010)
130. I. Montanari, A.F. Nogueira, J. Nelson et al., Appl. Phys. Lett. **81**, 3001 (2002)
131. A.J. Ferguson, N. Kopidakis, S.E. Shaheen, G. Rumbles, J. Phys. Chem. C **115**, 23134 (2011)
132. K. Kanemoto, M. Yasui, T. Higuchi et al., Phys. Rev. B **83**, 205203 (2011)
133. J. Clark, J.-F. Chang, F.C. Spano et al., Appl. Phys. Lett. **94**, 163306 (2009)
134. R. Österbacka, C.P. An, X.M. Jiang, Z.V. Vardeny, Synth. Met. **116**, 317 (2001)
135. J. Piris, T.E. Dykstra, A.A. Bakulin et al., J. Phys. Chem. C **113**, 14500 (2009)
136. D. Veldman, S.C.J. Meskers, R.A.J. Janssen, Adv. Funct. Mater. **19**, 1939 (2009)
137. J. Cabanillas-Gonzalez, G. Grancini, G. Lanzani, Adv. Mater. **23**, 5468 (2011)
138. M.R. Wasielewski, Chem. Rev. **92**, 435 (1992)
139. M. Campoy-Quiles, T. Ferenczi, T. Agostinelli et al., Nat. Mater. **7**, 158 (2008)
140. R.A. Marsh, J.M. Hodgkiss, S.A. Seifried, R.H. Friend, Nano Lett. **10**, 923 (2010)
141. G. Li, R. Zhu, Y. Yang, Nature Photon. **6**, 153 (2012)
142. X.Y. Zhu, Q. Yang, M. Muntwiler, Acc. Chem. Res. **42**, 1779 (2009)
143. J.W. Kiel, A.P.R. Eberle, M.E. Mackay, Phys. Rev. Lett. **105**, 168701 (2010)
144. S. Yamamoto, J. Guo, H. Ohkita, S. Ito, Adv. Funct. Mater. **18**, 2555 (2008)
145. H. Ohkita, S. Ito, Polymer **52**, 4397 (2011)
146. P.H. Heiney, J.E. Fischer, A.R. McGhie et al., Phys. Rev. Lett. **66**, 2911 (1991)
147. J. Lee, K. Vandewal, S.R. Yost et al., J. Am. Chem. Soc. **132**, 11878 (2010)
148. T. Forster, Discuss. Faraday Soc. **27**, 7 (1959)
149. D.C. Coffey, A.J. Ferguson, N. Kopidakis, G. Rumbles, ACS Nano **4**, 5437 (2010)
150. S. Morita, A.A. Zakhidov, K. Yoshino, Solid State Commun. **82**, 249 (1992)
151. R. Mondal, S. Ko, J.E. Norton et al., J. Mater. Chem. **19**, 7195 (2009)
152. L.J.A. Koster, V.D. Mihailetchi, P.W.M. Blom, Appl. Phys. Lett. **88**, 052104 (2006)

Chapter 2
Charge Transport Study of OPV Polymers and Their Bulk Heterojunction Blends by Admittance Spectroscopy

Kevin K.H. Chan, Harrison K.H. Lee and S.K. So

Abstract The measurement and understanding the conductivity/ mobility of an organic semiconductor is one of the most critical issues in organic electronics including organic solar cells. The standard "*JV*-approach" using space-charge-limited current model has clear drawbacks in evaluating the transport properties. In this chapter, we introduce an alternative transport characterization tool—admittance spectroscopy (AS), to extract charge carrier mobility in semiconducting polymers. The complex impedance of the polymer is obtained by exciting the sample (a thin film ($\sim$200–500 nm) sandwiched by two electrodes) with an ac voltage source and the analysis of measured time dependent current of the sample allows the extraction of carrier mobility. Examples of applications of AS to OPV polymers and their bulk heterojunction blends will be provided. The reliability of AS technique in OPV polymers will be compared to time-of-flight (TOF) method.

2.1 Introduction

Organic semiconductors (OS) are now finding widespread applications in photonic devices. Prime examples are organic light-emitting diodes (OLEDs), organic photovoltaic (OPV) cells, and organic thin film transistors (OTFTs) [1–3]. Generally, at least one thin film of organic semiconductor is present in any of these devices. Under the influence of an external electric field, the loosely bound π-electrons present in the organic become delocalized. They drift along the direction of the field, constituting to the flow of electric current. Thus, the ability of quantifying the conductivity of an organic semiconductor is vital for device development and optimization. In fact, the measurement and understanding the conductivity of an

K.K.H. Chan · H.K.H. Lee · S.K. So (✉)
Department of Physics and Institute of Advanced Materials,
Hong Kong Baptist University, Kowloon Tong, Hong Kong, China
e-mail: skso@hkbu.edu.hk

Y. Yang and G. Li (eds.), *Progress in High-Efficient Solution Process Organic Photovoltaic Devices*, Topics in Applied Physics 130,
DOI 10.1007/978-3-662-45509-8_2

organic semiconductor can be viewed as one of the most critical issues in organic electronics.

Unlike inorganic semiconductors, an organic semiconductor generally has a relatively large energy gap of exceeding 1.5 eV. Its free charge carrier concentration (n) is negligible at room temperature or ill-defined. As conductivity (σ) is defined by $\sigma = nq\mu$, where q is the elementary charge, the carrier mobility (μ) becomes the prime parameter that can be used to quantify σ. Using μ, one can make some predictions about device characteristics. It is known that the drift velocity is related to the mobility. So μ can be used to predict, e.g., carrier drift length in an OPV cell, and optimize the thickness of the OPV cell. For OLEDs, independent measurements of electron/hole mobilities and drift velocities can be used to locate the carrier recombination zone. The thickness of the organic layer can then be tuned to minimize exciton quenching, and to enhance light emission. Therefore, the measurement of carrier mobility is essential for the understanding and the optimization device operation.

Perhaps, the most popular approach of measuring μ is by current-voltage (J-V) measurements. The standard sample structure is anode/organic/cathode. For the measurements of holes, the anode should possess a large work function, while the cathode should be electron-blocking. If these conditions are met and the organic is trap-free, then J and V follow space-charge-limited (SCL) condition [4]:

$$J_{SCL} = \frac{9}{8}\varepsilon_0\varepsilon_r\mu_0 \exp(0.89\beta\sqrt{F})\frac{F^2}{d} \tag{2.1}$$

where ε_0 is the permittivity in free space, ε_r is the dielectric constant ($\sim$3 for organic materials), F is the applied electric field strength, and d is the thickness of organic layer, respectively. μ_0 is the zero-field mobility, i.e., the mobility when $F = 0$. The factor β is the Poole-Frenkel slope, which indicates the sensitivity of μ with respect to applied electric field. From (2.1), we clearly see only two parameters relating to carrier transport, i.e., μ_0 and β, are required to describe the OS at a fixed temperature. The standard procedure involves fitting to (2.1) to the experimental data from which μ_0 and β are extracted.

The standard "*JV*-approach", as outlined above, is marred with problems [5]. First, the contact between the anode and the organic may not be truly Ohmic. Formation of an interfacial dipole layer may create a substantial energy barrier for carrier injection [6–8]. As pointed out by some recent studies, if the contact deviates from Ohmic, one can still force-fit the experimental data to (2.1), resulting in an "excellent fit", but obtain an erroneous result for μ_0 [5]. Second, assuming that there is an Ohmic contact at the anode, the "*JV*-approach" can remain problematic for a small gap organic semiconductor, as in the case of an OPV material. Under this scenario, the lowest unoccupied molecular orbital (LUMO) of the organic semiconductor is low enough that electrons might leak into the device from the cathode, leading to an excessive current that departs from the SCL condition [9, 10]. Force-fitting the experimental data to (2.1) will, therefore, overestimate μ_0. The considerations above clearly suggest that the "*JV*-approach" all by itself may not be

adequate for the reliable determination of transport parameters for an organic semiconductor. Additional techniques should be employed to measure μ independently.

Here, we introduce an alternative transport characterization tool, known as admittance spectroscopy (AS), to extract charge carrier mobility in semiconducting polymers. In an AS experiment, the polymer is cast in the form of a thin film ($\sim$200–500 nm) sandwiched by two electrodes. The complex impedance of the polymer is obtained by exciting the sample with an ac voltage source and the time dependent current of the sample is measured. Analysis of the frequency dependent complex admittance will allow one to extract transport data and hence carrier mobility. Examples of applications of AS to OPV polymers and their bulk heterojunction blends will be provided. The reliability of AS technique in OPV polymers will be compared to time-of-flight (TOF) method.

2.2 Description of Admittance Spectroscopy

2.2.1 Basic Principle [11, 12]

In an admittance experiment, the organic material is cast in the form of a thin film sandwiched between two electrodes. It is assumed that one of the electrodes (e.g. anode) forms an Ohmic contact with the organic while the other electrode (e.g. cathode) forms an electron-blocking contact. The sample is then subjected to the sum of a dc forward voltage (V_{dc}) and a small ac electrical excitation voltage (v_{ac}). The response function, i.e., the ac current (i_{ac}) is measured. In general, i_{ac} is not in phase with v_{ac}, and the admittance [$Y(\omega)$] is complex:

$$Y(\omega) = i_{ac}/v_{ac} = G + iB = G + i\omega C \tag{2.2}$$

where G, B, and C are the frequency dependent conductance, susceptance, and capacitance, respectively. In addition, $i = \sqrt{-1}$ and $\omega = 2\pi f$ where f is the frequency of the ac voltage. Experimentally, $Y(\omega)$ can be measured by an impedance analyzer. Details of the experimental setup are given in the next section. On the other hand, $Y(\omega)$ can be computed analytically by employing Poisson equation as given below.

To compute $Y(\omega)$, Poisson equation and total current density [$J(t)$] are employed to describe the position (x) and time (t) dependent electric field [$F(x,t)$] and charge density [$\rho(x,t)$] inside the organic material:

$$\rho(x,t) = \left(\frac{\varepsilon}{q}\right)\frac{\partial F(x,t)}{\partial x} \tag{2.3}$$

$$J(t) = q\rho(x,t)\mu(t)F(x,t) + \varepsilon\frac{\partial F(x,t)}{\partial t} \tag{2.4}$$

where ε is the permittivity of organic material and q is the electron charge. For simplicity, only the hole mobility (μ) is considered to be field independent. We assume that an Ohmic contact is formed at the anode ($x = 0$). This implies $F(0,t) = 0$ can be used as the boundary condition.

First, we consider the case when only the dc voltage (V_{dc}) is present. $F(x,t)$ is time independent and $\partial F(x,t)/\partial t = 0$ in (2.3) and (2.4). Combining (2.3) and (2.4), the dc electric field [$F_{dc}(x)$] and charge density [$\rho_{dc}(x)$] can be obtained:

$$F_{dc}(x) = \sqrt{\frac{2J}{\varepsilon\mu_{dc}}}x^{1/2} \tag{2.5}$$

$$\rho_{dc}(x) = \frac{\varepsilon}{2q}\sqrt{\frac{2J}{\varepsilon\mu_{dc}}}x^{-1/2} \tag{2.6}$$

For trap-free organic materials, the current-voltage characteristics should obey space-charge-limited current (SCLC) described in the introduction:

$$J_{dc} = \frac{9}{8}\varepsilon\mu_{dc}\frac{F_{dc}^2}{d}; \quad \mu_{dc} = \frac{d}{\tau_{dc}F_{dc}} \tag{2.7}$$

where τ_{dc} is the average carrier transit time. Then, $F_{dc}(x)$ and $\rho_{dc}(x)$ can be rewritten as

$$F_{dc}(x) = \frac{3\sqrt{d}}{2\tau_{dc}\mu_{dc}}x^{1/2} \tag{2.8}$$

$$\rho_{dc}(x) = \frac{3\varepsilon\sqrt{d}}{4qT_{dc}\mu_{dc}}x^{-1/2} \tag{2.9}$$

Next, we consider the case when both a dc and a small ac voltage (v_{ac}) are present. The solutions to (2.3) and (2.4) can be written as the sum of dc and time dependent contributions to the electric field [$f(x,t)$], charge density [$\vartheta(x,t)$] and current density [$j(t)$]:

$$\begin{aligned} F(x,t) &= F_{dc}(x) + f(x,t) \\ \rho(x,t) &= \rho_{dc}(x) + \vartheta(x,t) \\ J(t) &= J_{dc} + j(t) \end{aligned} \tag{2.10}$$

Combining (2.3), (2.4) and (2.10), the current density in frequency domain $[j(\omega)]$ can be obtained by Fourier transform to give

$$j(\omega) = q\mu(\omega)\rho_{dc}(x)f(x,\omega) + \varepsilon\mu(\omega)F_{dc}(x)\frac{\partial f(x,\omega)}{\partial x} + i\omega\varepsilon f(x,\omega) \tag{2.11}$$

Substituting (2.8) and (2.9) into (2.11), we obtain

$$j(\omega) = \frac{3\varepsilon\sqrt{d}\tilde{\mu}(\omega)}{4\tau_{dc}}x^{-1/2}f(x,\omega) + \frac{3\varepsilon\sqrt{d}\tilde{\mu}(\omega)}{2\tau_{dc}}x^{1/2}\frac{\partial f(x,\omega)}{\partial x} + i\omega\varepsilon f(x,\omega) \tag{2.12}$$

where $\tilde{\mu}(\omega) = \mu(\omega)/\mu_{dc}$ is defined as the normalized mobility. By integrating (2.12) with respect to $f(x,\omega)$, we find

$$f(x,\omega) = \frac{j(\omega)}{i\omega\varepsilon}\left(1 - \frac{3\sqrt{d}\tilde{\mu}(\omega)}{4i\omega\tau_{dc}}x^{-1/2}\left\{1 - \exp\left[\frac{-i4\omega\tau_{dc}}{3\sqrt{d}\tilde{\mu}(\omega)}x^{1/2}\right]\right\}\right) \tag{2.13}$$

Since $v_{ac}(\omega) = \int_0^d f(x,\omega)dx$, the ac modulation can be calculated

$$v_{ac}(\Omega) = \frac{j(\Omega)\tau_{dc}d}{\Omega^3\varepsilon}\left(-i\Omega^2 + 1.5\tilde{\mu}(\Omega)\Omega + 2i[0.75\tilde{\mu}(\Omega)]^2\left\{1 - \exp\left[\frac{-i4\Omega}{3\tilde{\mu}(\Omega)}\right]\right\}\right) \tag{2.14}$$

where $\Omega = 2\pi f\tau_{dc} = \omega\tau_{dc}$ is the normalized frequency. According to (2.2), (2.14) can be rearranged to

$$Y(\Omega) = \frac{\varepsilon A}{\tau_{dc}d}\left(\frac{\Omega^3}{2i[0.75\tilde{\mu}(\Omega)]^2\{1 - \exp[-i4\Omega/3\tilde{\mu}(\Omega)]\} + 1.5\tilde{\mu}(\Omega)\Omega - i\Omega^2}\right) \tag{2.15}$$

where A is the active area of the device.

Equation (2.15) formally relates the complex admittance $[Y(\omega)]$ to the carrier mobility. To take into account that the polymer can have disorder transport, the normalized mobility $[\tilde{\mu}(\Omega)]$ can be expressed in the form $\tilde{\mu}(\Omega) = \mu(\Omega)\Big/\mu_{dc} = 1 + M(i\Omega)^{1-\alpha}$ where M and α are the dispersion parameters [11, 13]. For non-dispersive transport, $M = 0$ and $\alpha = 1$. Since $Y = G + i\omega C$, one can simulate G and C versus frequency, using the three material dependent parameters μ_{dc} $(= d^2/\tau_{dc}V_{dc})$, M and α. Figure 2.1 shows the simulated C from (2.15) with $\mu_{dc} = 4 \times 10^{-4}$ cm^2/V s. Left and right panels represent the changes of line shape of C by varying M and α, respectively.

When $V_{dc} = 0$V,C should be independent of frequency and equal to the geometric capacitance $(C_{geo} = \varepsilon A/d)$. With $V_{dc} > 0$ V, C becomes frequency dependent and can be divided into three regions (Fig. 2.1). At high frequencies, the

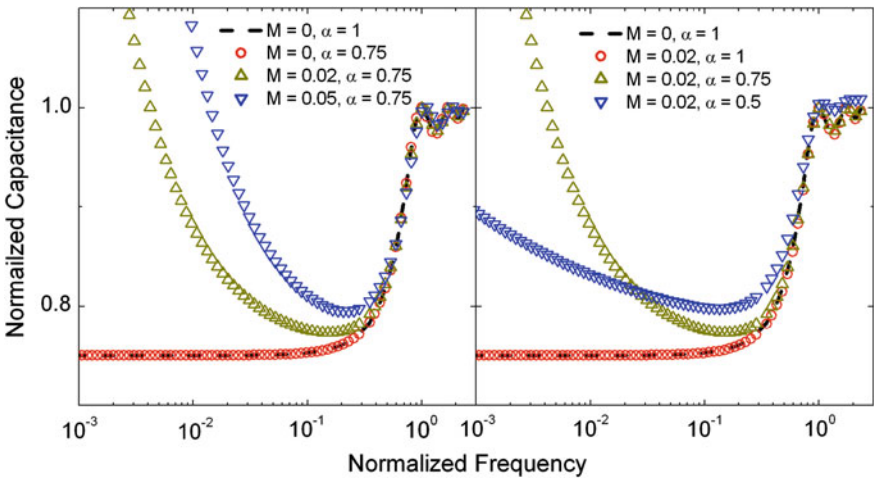

Fig. 2.1 Simulated frequency dependent capacitances of an organic material using (2.15). The *dashed line* indicates capacitance for non-dispersive transport

injected carriers remain near the anode, resulting in $C = C_{geo}$. In intermediate frequencies, C starts to decrease and reaches a minimum since the injected current lags behind v_{ac}, which leads to the phase reduction of Y. For low frequencies, C rises due to trapping effects.

2.2.2 Experimental Setup

A typical setup for AS measurement is shown in Fig. 2.2. The sample has the general structure of anode/organic/cathode. For hole mobility measurements, the anode should form an Ohmic contact with the organic material. The cathode should be electron-blocking. V_{dc} and v_{ac} are supplied by a dc power supply and an impedance analyzer, respectively. In our measurements for semiconducting polymers, the amplitude of v_{ac} is about 50 mV, with frequencies between 40 Hz and 5 MHz. V_{dc} is the range of 0–30 V. C is captured by the impedance analyzer.

From the experimental data of C versus f, one can, in principle, use (2.15) to fit the results using μ_{dc}, M and α. In practice, it is more convenient to plot the negative differential susceptance ($-\Delta B$) against f as shown in Fig. 2.3. $-\Delta B$ can be calculated from

$$-\Delta B = -2\pi f\left(C - C_{geo}\right) \tag{2.16}$$

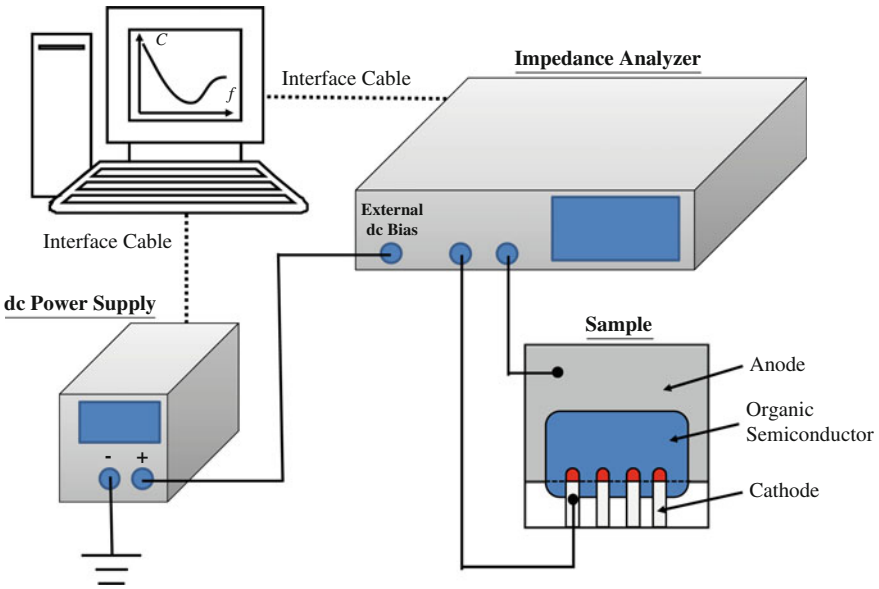

Fig. 2.2 Typical experimental setup for AS measurement

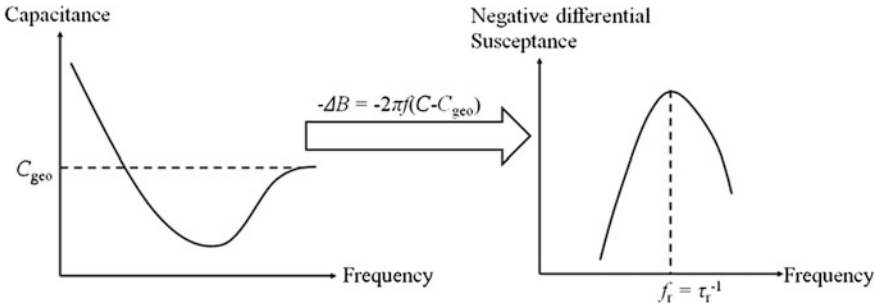

Fig. 2.3 (*Left*) a typical AS signal, and (*right*) a typical negative differential susceptance plot

From computer simulation, it was found that $-\Delta B$ appears at a distinct frequency $f_r = \tau_r^{-1}$ τ_r is the carrier relaxation time and is related to the average carrier transit time ($\tau_{average}$) by Ref [11]

$$\tau_{average} = 0.56\tau_r \tag{2.17}$$

As a result, μ_{AS} can be simply determined by

$$\mu_{AS} = \frac{d^2}{V_{dc}\,\tau_{average}} = \frac{d^2}{0.56\,V_{dc}\,\tau_r} \tag{2.18}$$

where d and V_{dc} are the thickness of polymer film and applied dc bias, respectively. The validity of (2.18) has been demonstrated in recent literatures [14–19] for molecular based organic semiconductors.

2.3 Charge Transport in OPV Polymers

In this section, the hole transports of four OPV polymers are investigated by AS. They are poly(2-methoxy-5-(3′-7′-dimethyloctyloxy)-1,4-phenylenevinylene) (MDMO-PPV), poly(3-hexylthiophene) (P3HT), poly[[4,8-bis[(2-ethylhexyl)oxy] benzo[1,2-b:4,5-b′]dithiophene-2,6-diyl][3-fluoro-2-[(2-ethylhexyl)carbonyl]thieno [3,4-b]thiophenediyl]] (PTB7), and poly[N-9″-hepta-decanyl-2,7-carbazole-alt-5,5-(4′,7′-di-2-thienyl-2′,1′,3′-benzothiadiazole)] (PCDTBT). Their chemical structures and energy level diagrams are shown in Fig. 2.4 [20–23]. For AS measurements, an Ohmic contact is essential for the contact between the anode and the polymer. Hence, a hole injection layer (HIL) is inserted to minimize the hole injection barrier. According to Fig. 2.4b, poly(3,4-ethylene dioxythioplene) doped with poly(strene-sulfonate) (PEDOT:PSS) was chosen as HIL for MDMO-PPV, P3HT and PTB7. For PCDTBT, due to its large HOMO value (−5.5 eV), molybdenum (VI) oxide (MoO_3) with a high work function (exceeding −5.6 eV) was employed. All the measurements were performed under low vacuum conditions ($\sim 10^{-3}$ Torr.) in a cryostat.

The top panels of Fig. 2.5 shows the frequency dependent capacitances of the OPV polymers. For all cases, standard features of AS signals can be observed, including (i) a clear geometric capacitance (C_{geo}) at high frequencies, (ii) a reduction of C at intermediate frequencies, and (iii) an increase of C at the low frequency region. From these observations, the conditions of unipolar injection and quasi-Ohmic contact have been achieved in all devices.

To extract the hole mobilities (μ_{AS}) of polymers, the negative differential susceptance ($-\Delta B$) needs to be calculated by (2.16) and plotted against frequency. The results are as shown in the bottom panels of Fig. 2.5. The carrier relaxation times (τ_r) can be obtained from the frequencies at which the maximum value of $-\Delta B$ occur as indicated by dashed vertical lines in Fig. 2.5e–h. As a result, μ_{AS} can be computed from (2.18). Generally, μ can be described by the Poole-Frenkel model in organic semiconductors [24]:

$$\mu = \mu_0 \exp\left(\beta\sqrt{F}\right) \tag{2.19}$$

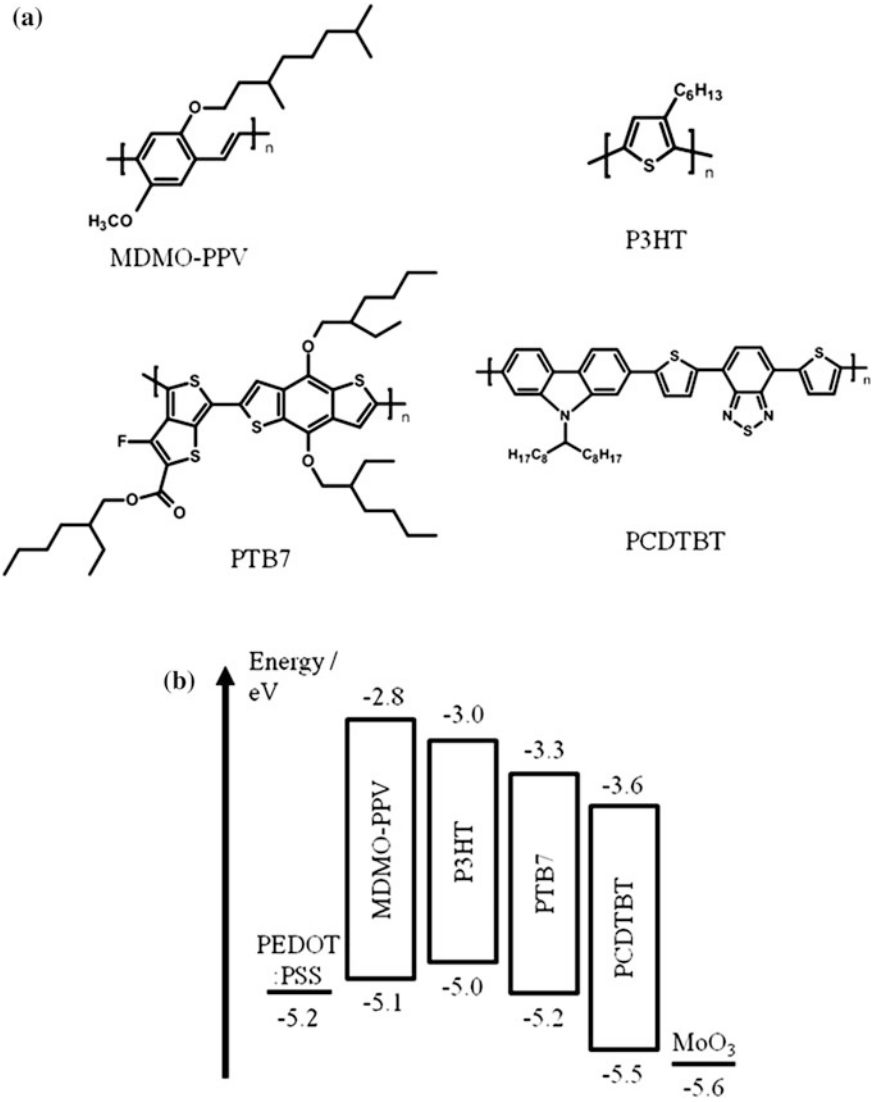

Fig. 2.4 **a** Chemical structures of MDMO-PPV, P3HT, PTB7, and PCDTBT. **b** Work functions of HILs and energy levels of polymers relative to the vacuum level [20–23]

where μ_0 and β are the zero-field mobility and the Poole-Frenkel slope, respectively. Hence, the hole mobilities of these OPV polymers were plotted against the square root of electric field (F) at room temperature (Fig. 2.6). The *solid lines* are the best fits to the data. From the y-intercepts and slopes of the fits, $\mu_{0,AS}$ and β_{AS} can be obtained and summarized in Table 2.1.

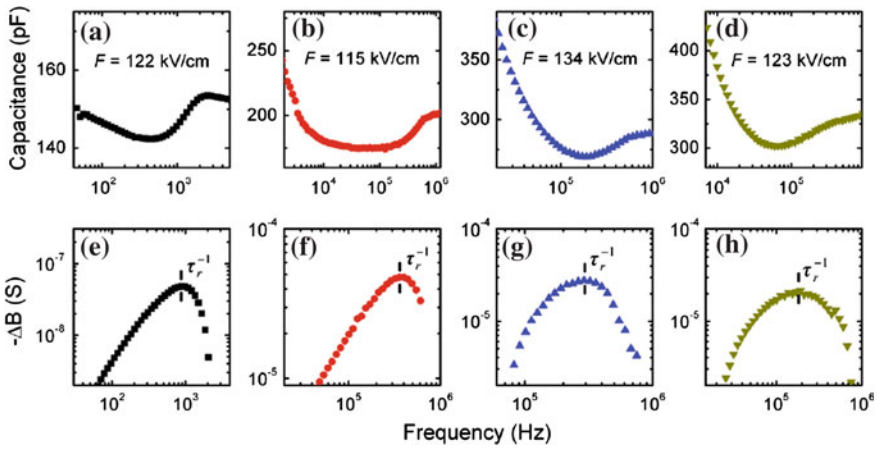

Fig. 2.5 Frequency dependent capacitances of **a** MDMO-PPV, **b** P3HT, **c** PTB7, and **d** PCDTBT at 292 K. The applied field strengths were about 120 kV/cm. From (2.16), the corresponding $-\Delta B$ are shown in the *bottom panels*: **e** MDMO-PPV, **f** P3HT, **g** PTB7, and **h** PCDTBT. The reciprocal of the carrier relaxation times, τ_r^{-1}, are marked by the *vertical dashed lines*

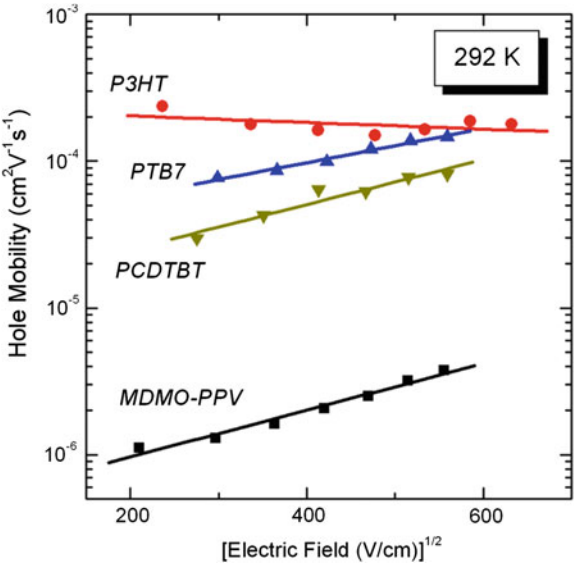

Fig. 2.6 Extracted hole mobilities of different OPV polymers from AS at 292 K. The *solid lines* are the best fits to the data

Among the four OPV polymers, $\mu_{0,AS}$ and μ_{AS} at room temperature of P3HT are the highest, which are about 2.3×10^{-4} and $1–2 \times 10^{-4}$ cm^2/V s, respectively. This can be attributed to the nano-scale ordering of P3HT thin film [25]. Hence, hole can transport through the device in shorter times via a better connection of polymer domains. For PTB7 and PCDTBT, the extracted μ_{AS} are in the range of 10^{-5} cm^2/V s. Unlike other OPV polymers, the hole mobility of MDMO-PPV is especially

Table 2.1 Zero-field mobilities and Poole-Frenkel slopes of OPV polymers at 292 K obtained independently from admittance spectroscopy (AS) and time-of-flight (TOF) experiments

	Zero-field mobilities (cm^2/V s)		Poole-Frenkel slop $(V/cm)^{-1/2}$	
Polymer	$\mu_{0,AS}$	$\mu_{0,TOF}$	β_{AS}	β_{TOF}
MDMO-PPV	4.6×10^{-7}	3.1×10^{-7}[22]	1.6×10^{-3}	1.8×10^{-3}
P3HT	2.3×10^{-4}	7.6×10^{-4}	-2.2×10^{-4}	-2.3×10^{-5}
PTB7	3.4×10^{-5}	7.4×10^{-5}	1.3×10^{-3}	3.1×10^{-4}
PCDTBT	1.2×10^{-5}	8.9×10^{-6}	1.5×10^{-3}	1.9×10^{-3}

small and about 3–9 $\times 10^{-5}$ cm^2/V s. It can be attributed to the large energetic disorder of MDMO-PPV, and will be discussed in the later section.

To check the reliability of AS, we have also performed time-of-flight (TOF) experiments, to probe the transport properties of three OPV polymers (P3HT, PTB7, and PCDTBT) in a thick film configuration (>1 μm). The basic principle and experimental setup of TOF is well-documented [1, 26]. For OPV polymers, Nd: YAG laser with wavelength of 532 nm is used for carrier excitation. The TOF transients of OPV polymers are shown in the top panels of Fig. 2.7. For PCDTBT [Fig. 2.7c], the transient is very dispersive. Hence, the carrier transit time (τ_{TOF}) can only be extracted from the log-log plot of the transient (Fig. 2.7f), as indicated in the point of intersection of the dashed lines. For P3HT and PTB7 (Fig. 2.7a, b), although the transients are less dispersive, reliable τ_{TOF} still need to be extracted from the log-log plots (Fig. 2.7d, e). The hole mobilities were computed by,

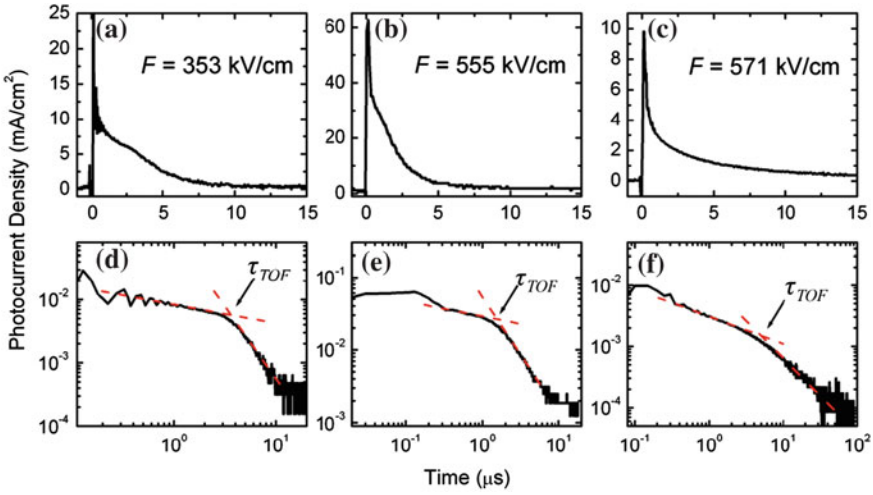

Fig. 2.7 **a–c** TOF transients of different OPV polymers **a** P3HT, **b** PTB7, **c** PCDTBT at 292 K. **d–f** The log-log plots of TOF transients, from which the hole transit time (τ_{TOF}) can be determined from the intercepts of the *dashed lines*

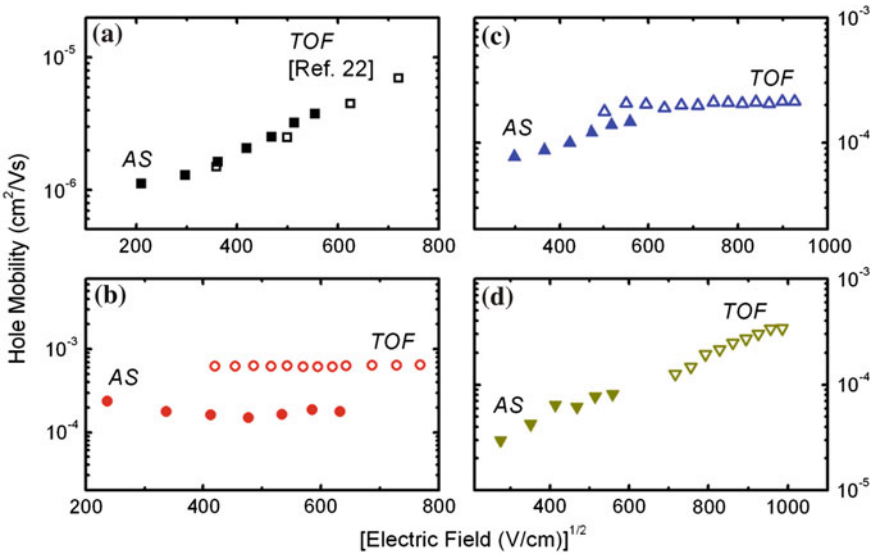

Fig. 2.8 The extracted hole mobilities of different OPV polymers from AS (*filled symbols*) and TOF (*unfilled symbols*) at 292 K. The polymers under investigation are **a** MDMO-PPV, **b** P3HT, **c** PTB7, **d** PCDTBT

$$\mu_{TOF} = \frac{d^2}{V_{dc}\,\tau_{TOF}} \tag{2.20}$$

Figure 2.8 shows the TOF data alongside with the AS data. For MDMO-PPV, μ_{TOF} is obtained from [22]. Generally, there is a good agreement between the two sets of data for each polymer. $\mu_{0,TOF}$ and β_{TOF} can also be extracted from TOF and the results are summarized in Table 2.1. The same observations are obtained: (i) μ of P3HT (polycrystalline OPV polymer) are the largest and exhibit the weakest field dependence, (ii) μ of amorphous polymers (MDMO-PPV, PTB7, and PCDTBT) increases clearly with F, and (iii) MDMO-PPV has the smallest μ.

To further understand the transport properties of OPV polymers, the temperature dependent measurements were performed. The sample temperatures were in the range of 246–336 K. The data were then analyzed with the Gaussian disorder model (GDM) [27], which is used to simulate charge hopping process within the localized hopping sites in organic semiconductors. The density-of-states (DOS) of the hopping sites is assumed to be the Gaussian distribution. The mobility is field and temperature dependent, and can be summarized as,

$$\mu(F,T) = \mu_{\infty} \exp\left[-\left(\frac{2\sigma}{3k_BT}\right)^2\right] \exp\left(\beta F^{\frac{1}{2}}\right) \tag{2.21}$$

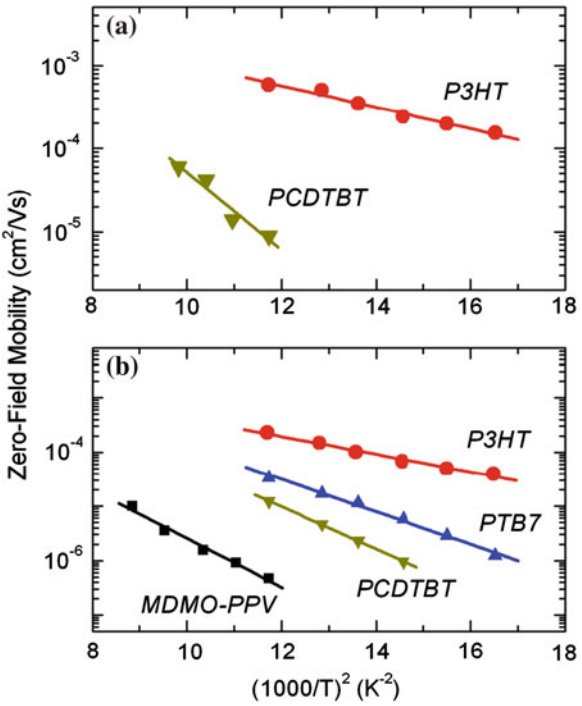

Fig. 2.9 Zero-field mobilities of OPV polymers extracted from **a** TOF, and **b** AS versus the reciprocal of the square of the temperature. The *solid lines* are the best fits to the data. σ and μ_∞ can be extracted from the slopes and y-intercepts of the fits, respectively

where μ_∞ is the high-temperature limit of mobility, k_B is the Boltzmann constant, and T is the absolute temperature. σ is defined as the energetic disorder, which is the standard deviation of the Gaussian distribution. By plotting $\mu_0 = \mu(0, T)$ versus $1/T^2$ (Fig. 2.9), σ and μ_∞ can be extracted from the slopes and y-intercepts of the fits, respectively. The transport data of the OPV polymers are summarized in Table 2.2. Due to the crystalline properties of P3HT [25], holes transport through the sample via the well-connected pathways, leading to the less dependence on temperature. As a result, σ of P3HT is found to be the smallest (70–86 meV). For amorphous polymers, including MDMO-PPV, PTB7, and PCDTBT, the values of σ are in the range of 110–130 meV.

Table 2.2 Energetic disorders (σ) and high-temperature limit of mobilities (μ_∞) of OPV polymers

	Energetic disorder (meV)		High-temperature limit of mobility (cm^2/V s)	
Polymer	σ_{AS}	σ_{TOF}	$\mu_{\infty AS}$	$\mu_{\infty TOF}$
MDMO-PPV	131	–	7.7×10^{-2}	–
P3HT	79	70	1.8×10^{-2}	2.1×10^{-2}
PTB7	107	–	1.2×10^{-1}	–
PCDTBT	123	134	4.8×10^{-1}	2.3

2.4 Charge Transport in Bulk Heterojunction (BHJ) Blends

In OPV devices, bulk heterojunction (BHJ) blends are almost always used as the active layers to achieve high performances [3, 28, 29]. Thus, the investigation of the carrier transport properties in BHJ blends is more important than pristine polymers. In the BHJ blends, OPV polymers are usually employed as electron donors. Fullerene derivatives (e.g. $PC_{61}BM$, $PC_{71}BM$, etc.) are commonly used as acceptor materials. In this section, two popular BHJ blends were studied, including P3HT:$PC_{61}BM$ (1:1 wt%), and PCDTBT:$PC_{71}BM$ (1:2 wt%). Their chemical structures and the energy level diagrams of fullerene derivatives and donor materials are shown in Fig. 2.10 [20, 23, 30, 31]. To obtain Ohmic contact, PEDOT:PSS and MoO_3 were chosen as hole injection layers (HILs) for P3HT:$PC_{61}BM$ and PCDTBT:$PC_{71}BM$,

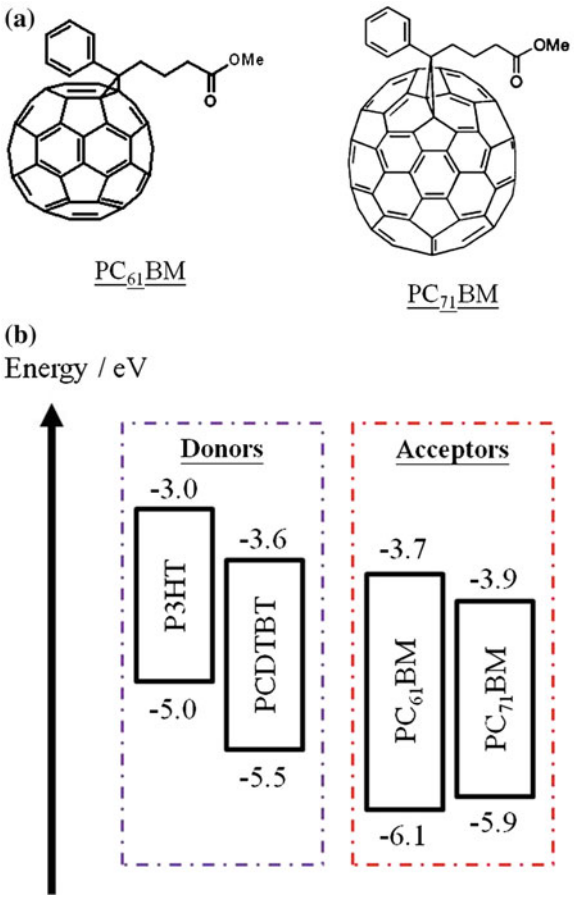

Fig. 2.10 **a** Chemical structures of $PC_{61}BM$, and $PC_{71}BM$. **b** Energy levels of donors (P3HT and PCDTBT) and acceptors ($PC_{61}BM$ and $PC_{71}BM$) [20, 23, 30, 31]

respectively, while Au was chosen as a nominally electron-blocking cathode. All the transport measurements were carried out under low vacuum ($\sim 10^{-3}$ Torr.) inside a cryostat, while the OPV measurements were performed in the ambient.

Figure 2.11 shows the frequency dependent capacitance of P3HT based (left panel), and PCDTBT based (right panel) BHJ blends (unfilled symbols). For comparison, the AS signals of pristine OPV polymers are also shown (filled symbols). The data have been normalized to their respective geometric capacitances [32]. After blending with fullerenes, the measured capacitance drops rapidly and even becomes negative at low frequencies ($C/C_{geo} < 0$). Recently, negative capacitances at low frequencies have been observed and reported [13, 14, 33]. Minority carrier injection is proposed to be the origin of this observation [14, 34–36]. In BHJ samples, although the high work function cathode (WF of Au $\sim$5.2 eV) is used, the electron injection barrier between Au and fullerenes is only about 1.3–1.5 eV. Under a sufficiently high electric field, electrons can hop across or tunnel through the energetic barrier and inject into fullerene clusters. Once injected, electrons transport through the sample via PCBM and recombine with injected holes. With the presence of electrons, the basic requirement of unipolar transport for AS measurements becomes invalid.

To avoid the minority carrier injection, a dual functional interlayer was inserted between the BHJ blend and the Au cathode. It has the functions of electron-blocking and electron-trapping (EB & ET) as illustrated in Fig. 2.12. The layer is composed of N,N′-Bis(3-methylphenyl)-N,N′-bis(phenyl)-9,9-spirobifluorene (spiro-TPD) doped with 2 % copper phthalocyanine (CuPc). As the hole mobilites of spiro-TPD and

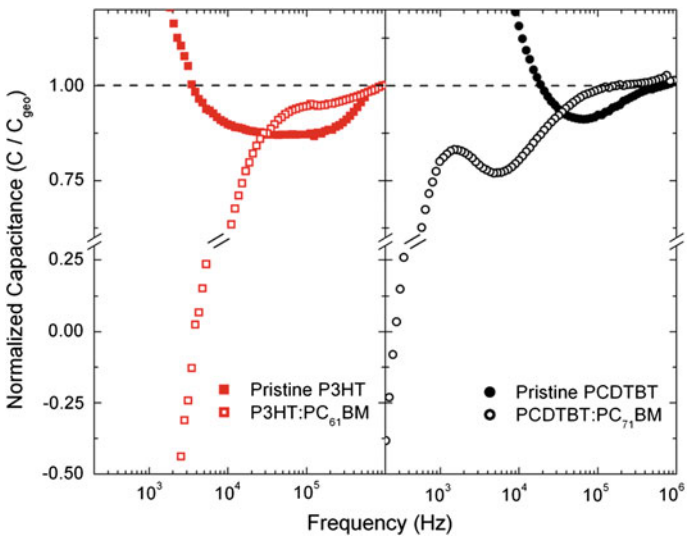

Fig. 2.11 Frequency dependent capacitances of P3HT based (*left panel*) and PCDTBT based (*right panel*) BHJ blends (*unfilled symbols*). The AS signals of pristine OPV polymers (*filled symbols*) are also shown

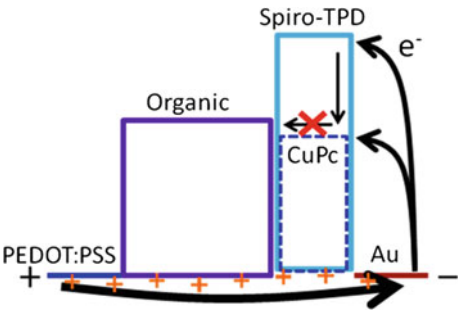

Fig. 2.12 Schematic diagram of the working mechanism of electron-blocking and electron-trapping (EB & ET) layer

CuPc are compatible to those of OPV polymers [37, 38], the hole transport in the samples is not expected to be affected by EB & ET layer. In addition, because of the high-lying LUMO of spiro-TPD (~1.9 eV), a large electron injection barrier (~1.8–2.0 eV) is formed. However, electrons still have chance to hop across the barrier under high electric field or temperature. Due to the lower LUMO value of CuPc (~3.5 eV), the injected electrons will be trapped by CuPc within EB & ET layer. Due to low doping concentration, electron conduction pathways of CuPc is expected to be discontinuous. Alternatively, detrapping of electrons to the LUMO of spiro-TPD is also not viable. As a result, the electron injection from the cathode can be suppressed by the EB & ET layer.

Figure 2.13 shows the measured AS signals of BHJ blends with the presence of EB & ET layer (filled symbols). For comparison, the signals without EB & ET layer (unfilled symbols) are also shown. For PCDTBT:$PC_{71}BM$ (Fig. 2.13b), the electron leakage can be effectively suppressed, and the standard features of typical AS signal can be observed. However, for P3HT:$PC_{61}BM$ (Fig. 2.13a), the onset of capacitance drop shifts to the lower frequency region, which indicates only some of the electrons can be blocked or trapped. In addition, current-voltage (*J-V*) measurements were performed for both BHJ blends. The data are shown in Fig. 2.14. After inserting the EB & ET layer (filled symbols), the current-densities (*J*) are reduced when compared with those without EB & ET layer (unfilled symbols). Due to incomplete suppression of electron leakage, *J* only decreases by a small fraction for P3HT:$PC_{61}BM$ (Fig. 2.14a). In contrast, for PCDTBT BHJ blend, a more significant decrease of *J* was found (Fig. 2.14b).

The insets of Fig. 2.13 shows that reliable carrier transit times (τ_r) can be determined from the $-\Delta B$ plots. Figure 2.15 shows the hole mobilities of the BHJ blends as determined from (2.18). Apart from the BHJ blends, μ_{AS} of pristine polymers are shown. For P3HT and its BHJ blends, μ_{AS} is insensitive to the ratio of donor to acceptor, and remains at 2–4 × 10^{-4} cm^2/V s (unfilled symbols in Fig. 2.15). This is consistent with the data extracted from TOF technique [39]. Figure 2.16 shows the Grazing incident x-ray diffraction (GIXRD) measurements of the BHJ films. The P3HT domains remain well-connected in the BHJ blend. Hence, holes can still transport through the film via the distinct percolation pathways. However, for PCDTBT:$PC_{71}BM$, the film is found to be amorphous (Fig. 2.16).

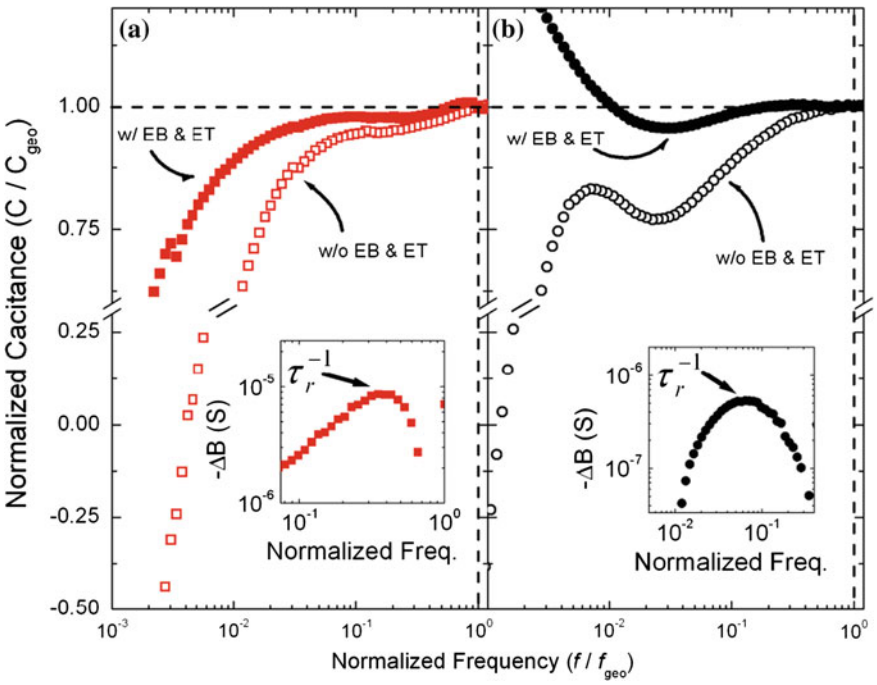

Fig. 2.13 Frequency dependent capacitances of **a** P3HT:$PC_{61}BM$ (1:1 wt%) and **b** PCDTBT:$PC_{71}BM$ (1:2 wt%) at $T = 292$ K. The *unfilled* and *filled symbols* correspond to samples without and with an EB & ET layer, respectively. The *insets* show the $-\Delta B$ plots with the presence of an EB & ET layer. The positions of transit time (τ_r^{-1}) are marked by *arrows*

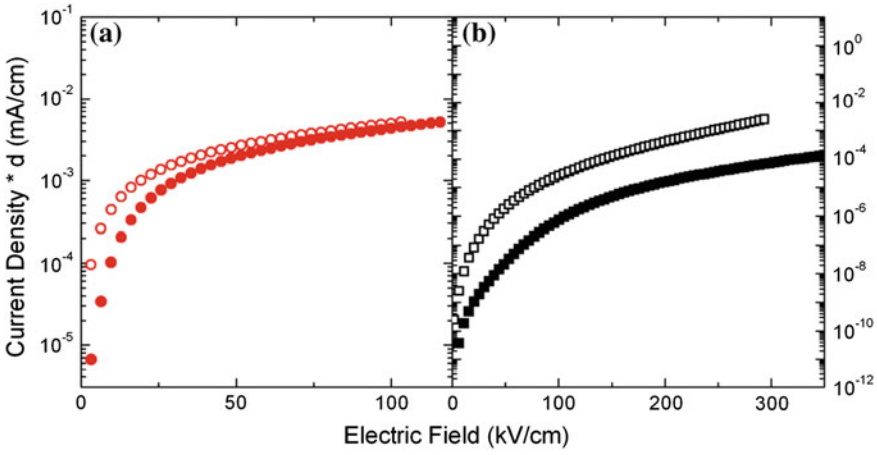

Fig. 2.14 *J-V* characteristics of **a** P3HT:$PC_{61}BM$ (1:1 wt%) and **b** PCDTBT:$PC_{71}BM$ (1:2 wt%) samples at 292 K. The *unfilled* and *filled symbols* correspond to samples without and with an EB & ET layer, respectively

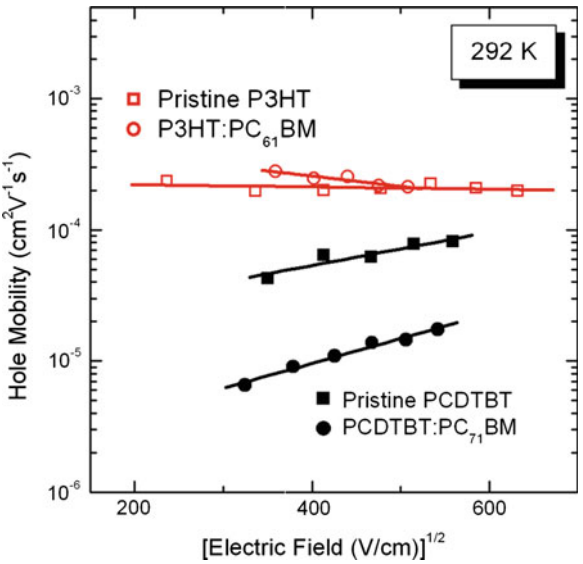

Fig. 2.15 Extracted hole mobilities of BHJ blends from AS at 292 K. Hole mobilities of pristine polymers are also shown for comparison. The solid lines are the best fits to the data

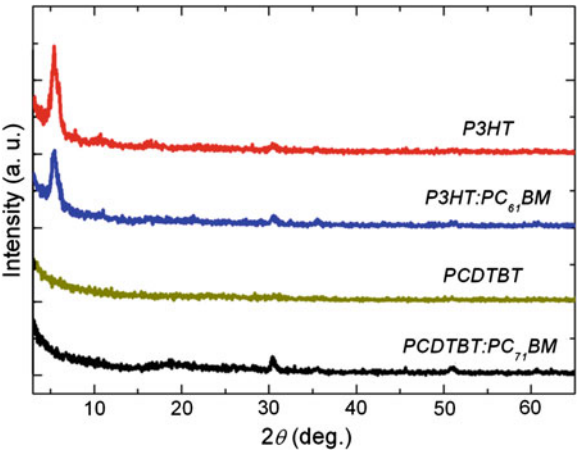

Fig. 2.16 GIXRD spectra of OPV polymers and their BHJ blends. The incident angle of the X-ray was fixed at 0.3°. Only P3HT and P3HT:$PC_{61}BM$ possess a distinct diffraction peak at about 5°

When PCDTBT is mixed with $PC_{71}BM$, the hole transporting pathways are partially blocked by $PC_{71}BM$, leading to larger hopping distances. As a result, μ_{AS} decreases by about 1 order of magnitude, from 10^{-4} to 10^{-5} cm^2/V s (filled symbols in Fig. 2.15).

Figure 2.17 shows $\mu_0 = \mu(0, T)$ versus $1/T^2$ for the BHJs and the pristine polymers. The extracted transport parameters are summarized in Table 2.3. The energetic disorders appear to be insensitive to the composition of the blends. σ remains at about 80 and 120 meV for the P3HT:$PC_{61}BM$ and PCDTBT:$PC_{71}BM$ blends, respectively. According to GIXRD spectra (Fig. 2.16), there are no distinct

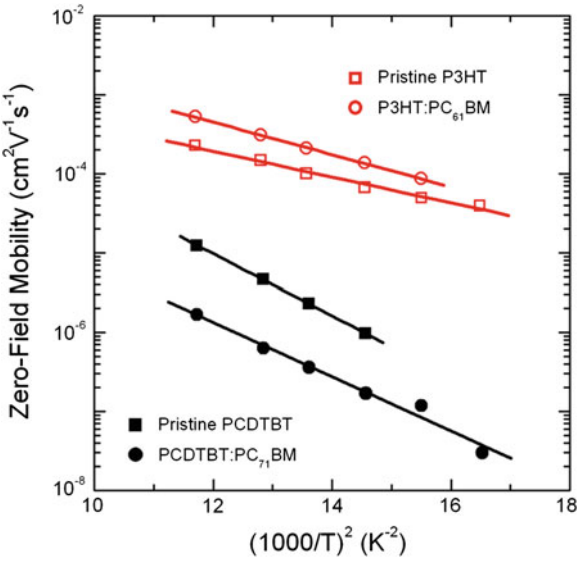

Fig. 2.17 Zero-field mobilities of OPV polymers and their BHJ blends extracted from AS versus the reciprocal of the square of temperature. The *solid lines* are the best fits to the data

Table 2.3 Energetic disorders (σ) of OPV polymers and their BHJ blends

Polymer and BHJ blends	Blend ratio (donor:acceptor)	σ (meV)
P3HT:PC_{61}BM	1:0	79
	1:0.5	80
	1:1	88
PCDTBT:PC_{71}BM	1:0	123
	1:2	115
	1:4	122

changes in the structural properties of the films are observed after blending with the acceptors. In the range of compositions used in our work, hole transport pathways remain well-connected.

Below, we highlight some possible connections between transport parameters and OPV device performances. Two OPV cells, namely, P3HT:PC_{61}BM (1:1 wt%) and PCDTBT:PC_{71}BM (1:2 wt%) OPV cells were fabricated with optimized thicknesses of about 150 and 70 nm, respectively [40]. The *J-V* characteristics of these OPV cells under illumination are shown in Fig. 2.18a, and their performances are summarized in Table 2.4. It is well-documented that the OPV performance depends on various factors, such as photon absorption, charge generation/recombination rates, donor/acceptor energy levels, and carrier mobilities…etc [28]. Here, we point out that OPV performances can be correlated to the energetic disorder (σ) of the BHJ.

Figure 2.18b shows *J-V* characteristics of the OPV cells, which have been normalized with open-circuit voltage (V_{OC}) and short-circuit current density (J_{SC}).

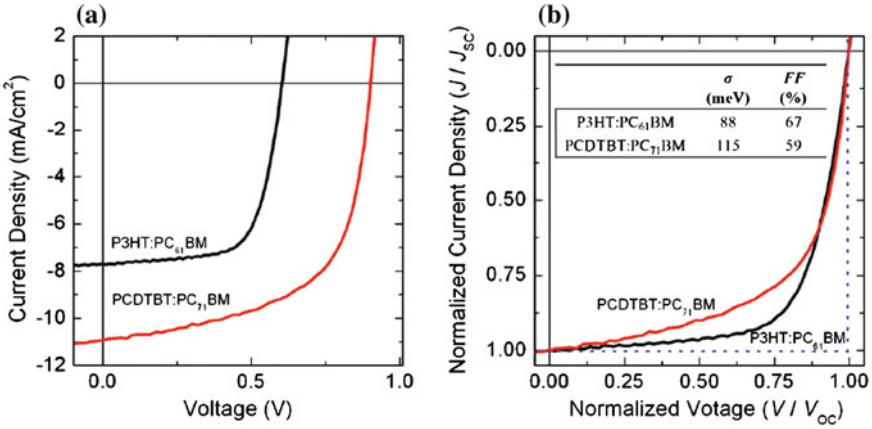

Fig. 2.18 **a** *J-V* characteristics of two OPV cells under illumination. **b** Normalized *J-V* characteristics with J_{SC} and V_{OC}

Table 2.4 OPV performances and energetic disorders of two BHJ blends

BHJ blend	σ (meV)	V_{OC} (V)	J_{SC} (mA/cm^2)	*FF* (%)	*PCE* (%)
P3HT:PC_{61}BM	88	0.61	7.5	67	3.0
PCDTBT:PC_{71}BM	115	0.90	10.2	59	5.5

With this normalization, *J-V* characteristics are only affected by the fill-factor (*FF*), but not other factors (such as photons absorption and donor/acceptor energy levels). For the BHJ blend with a larger σ, such as PCDTBT:PC_{71}BM (σ = 115 meV), a smaller value of *FF* (59 % for PCDTBT:PC_{71}BM) can be observed. As σ describes the spread of hopping sites for charge carriers, a larger σ implies the presence of more trapped states at the tail of the density-of-states (DOS). Thus, carriers can be easily trapped at these tailed states, resulting in recombination centers [41–43]. As a result, the photo-generated current will be lost within the OPV cells, leading to the poor *FF*.

Besides *FF*, recent researches showed that there is a relationship between V_{OC} and σ [43, 44]. It has been widely accepted that V_{OC} mainly depends on the energy difference between the HOMO of donor and the LUMO of acceptor (ΔE_{DA}). It can be expressed as [45]

$$qV_{OC} = \Delta E_{DA} + k_B T \ln\left(\frac{G}{\gamma N_h N_e}\right) \tag{2.22}$$

where G is the charge pair generation rate, γ is the recombination rate coefficient, N_h and N_e are the DOS for holes and electrons, respectively. The second term in (2.22) is generally found to be between −0.3 and −0.5 eV. Thus, V_{OC} can be calculated, and shown in Table 2.5 alongside with ΔE_{DA} for the two BHJ blends used here.

Table 2.5 V_{OC} of OPV cells with two BHJ blends obtained from both calculations and experiments

BHJ Blend	ΔE_{DA} (eV)	σ^2/k_BT (eV)	V_{OC}/(2.22) (V)	V_{OC}/Expt. (V)	V_{OC}/(2.23) (V)
P3HT:$PC_{61}BM$ (σ = 88 meV)	1.3	0.3	0.8–1.0	0.61	0.5–0.7
PCDTBT:$PC_{71}BM$ (σ = 115 meV)	1.6	0.5	1.1–1.3	0.90	0.6–0.8

However, the computed V_{OC} differs markedly from the experimentally determined V_{OC}. To explain this deviation, Blakesley et al. [43] suggested that the Gaussian distribution of hopping sites for carriers should also be considered in the calculation. Thus, (2.22) can be modified as

$$qV_{OC} = \Delta E_{DA} + k_BT \ln\left(\frac{G}{\gamma N_h N_e}\right) - \frac{\sigma^2}{k_BT} \tag{2.23}$$

A new term, which is related to σ, appears. σ^2/k_BT for each BHJ blend is calculated and shown in Table 2.5. With the consideration of σ, the measured and calculated V_{OC} become more consistent for both BHJ blends. Although the origin of correlation between V_{OC} and σ is still under debate, it is believed that performance of OPV cells can be enhanced by minimizing σ of BHJ blends.

2.5 Conclusion

The charge transport properties of OPV polymers (MDMO-PPV, P3HT, PTB7 and PCDTBT) and their BHJ blends (P3HT:$PC_{61}BM$ and PCDTBT:$PC_{71}BM$) were studied by AS technique and the Gaussian disorder model. To check the reliability of AS measurement, the hole mobilities (μ) and energetic disorders (σ) of pristine OPV polymers were cross-compared by both AS and TOF measurements. We found that, for all OPV polymers, there is a good agreement between both sets of data. Furthermore, we observed that the crystalline properties of polymers can affect the transport properties. For polycrystalline OPV polymer (such as P3HT), due to the well-connected pathways, μ is found to be the largest, while the value of σ is the smallest.

For the investigations of BHJ blends, owing to the electron leakage, a negative capacitance is observed in AS measurements. To avoid this, an electron-blocking and electron-trapping (EB & ET) layer, which is composed of spiro-TPD doped with 2 % CuPc, was inserted between the cathode and the BHJ blend. With this interlayer, we found that μ is composition dependent for the amorphous films (PCDTBT:$PC_{71}BM$), but not for the polycrystalline films (P3HT:$PC_{61}BM$). We suggest that the hole transport pathways within amorphous films can be partially

blocked by the presence of PCBM, resulting in larger hopping distances. However, σ is found to be insensitive to the composition of the BHJ blends as there is no distinct change in the structural properties of the films.

Apart from the charge transport studies, we suggest that OPV performance can be correlated to the energetic disorder (σ). Both the fill factor (*FF*) and the open-circuit voltage (V_{OC}) can be affected by σ. For a BHJ blend with a large σ, it implies that more trapped states are present in the tail of DOS. As a result, photo-generated free carriers can recombine at these states, leading to the poor *FF*. For V_{OC}, although the origin of its correlation with σ is still unclear, it is found that a large σ has a negative effect on V_{OC}.

Acknowledgment Supports of this work by the Research Grant Council of Hong Kong, and the Research Committee under Grant # HKBU211412 and FRG/10-11/090 are gratefully acknowledged. In addition, K.K.H. Chan acknowledges the support of the Research Grants Council of the Hong Kong Special Administrative Region, China (Project No. [T23-713/11]). The GIXRD used in this work was supported by the Centre for Surface Analysis and Research (CSAR) with funding from the Special Equipment Grant SEG-HKBU06. Finally, we want to acknowledge Dr. Stephen Tsang and Prof. Franky So (U. Florida) for many helpful discussions and fabrication of some of the OPV cells.

References

1. F. So (ed.), *Organic Electronics: Materials, Processing, Devices and Applications* (CRC Press, Francis and Taylor, Florida, 2010)
2. H. Sasabe, J. Kido, J. Mater. Chem. C **1**, 1699 (2013)
3. W. Cai, X. Gong, Y. Cao, Sol. Energy Mater. Sol. Cells **94**, 114 (2010)
4. P.W.M. Blom, C. Tanase, D.M. de Leeuw, R. Coehoorn, Appl. Phys. Lett. **86**, 092105 (2005)
5. Z.B. Wang, M.G. Helander, M.T. Greiner, J. Qiu, Z.H. Lu, J. Appl. Phys. **107**, 034506 (2010)
6. Y. Gao, Mater. Mater. Sci. Eng. R **69**, 39 (2010)
7. J. Hwang, A. Wan, A. Kahn, Sci. Eng. R **64**, 1 (2009)
8. H. Ishii, K. Sugiyama, E. Ito, K. Seki, Adv. Mater. **11**, 605 (1999)
9. F.L. Bloom, W. Wagemans, M. Kemerink, B. Koopmans, Phys. Rev. Lett. **99**, 257201 (2007)
10. J. Bisquert, Phys. Chem. Chem. Phys. **13**, 4679 (2011)
11. S.W. Tsang, S.K. So, J.B. Xu, J. Appl. Phys. **99**, 1 (2006)
12. H.C.F. Martens, H.B. Brom, P.W.M. Blom, Phys. Rev. B **60**, R8489 (1999)
13. H.C.F. Martens, H.N. Huiberts, P.W.M. Blom, Appl. Phys. Lett. **77**, 1852 (2000)
14. K.H. Chan and S.K. So, J. Photon. for Energy **1**, 011112 (2011)
15. K.K. Tsung, S.K. So, J. Appl. Phys. **106**, 083710 (2009)
16. K.L. Tong, S.W. Tsang, K.K. Tsung, S.C. Tse, S.K. So, J. Appl. Phys. **102**, 093705 (2007)
17. J. Chen, C. Shi, Q. Fu, F. Zhao, Y. Hu, Y. Feng, and D. Ma, J. Mater. Chem. **22**, 5164 (2012)
18. M.G. Helander, Z.B. Wang, Z.H. Lu, Org. Electron. **12**, 1576 (2011)
19. B. Li, J. Chen, Y. Zhao, D. Yang, D. Ma, Org. Electron. **12**, 974 (2011)
20. G. Dennler, M.C. Scharber, C.J. Brabec, Adv. Mater. **21**, 1323 (2009)
21. Y. Liang, Z. Xu, J. Xia, S.T. Tsai, Y. Wu, G. Li, C. Ray, L. Yu, Adv. Mater. **22**, E135 (2010)
22. S.M. Tuladhar, D. Poplavskyy, S.A. Choulis, J.R. Durrant, D.D.C. Bradley, J. Nelson, Adv. Funct. Mater. **15**, 1171 (2005)
23. N. Blouin, A. Michaud, D. Gendron, S. Wakim, E. Blair, R. Neagu-Plesu, M. Belletête, G. Durocher, Y. Tao, M. Leclerc, J. Am. Chem. Soc. **130**, 732 (2008)

24. J. Frenkel, Phys. Rev. **54**, 647 (1938)
25. L.H. Jimison, M.F. Toney, I. McCulloch, M. Heeney, A. Salleo, Adv. Mater. **21**, 1568 (2009)
26. K.K. Tsung, S.K. So, Appl. Phys. Lett. **92**, 103315 (2008)
27. H. Bässler, Phys. Stat. Sol. B **175**, 15 (1993)
28. H. Hoppe, N.S. Sariciftci, J. Mater. Res. **19**, 1924 (2004)
29. A.J. Heeger, Chem. Soc. Rev. **39**, 2354 (2010)
30. Y. Lian, D. Feng, Y. Wu, S.T. Tsai, G. Li, C. Ray, L. Yu, J. Am. Chem. Soc. **131**, 7792 (2009)
31. C.Y. Yu, C.P. Chen, S.H. Chan, G.W. Hwang, C. Ting, Chem. Mater. **21**, 3262 (2009)
32. S.W. Tsang, N. Drolet, S.C. Tse, Y. Tao, Z.H. Lu, Appl. Phys. Lett. **97**, 153306 (2010)
33. E. Ehrenfreund, C. Lungenschmied, G. Dennler, H. Neugebauer, N.S. Sariciftci, Appl. Phys. Lett. **91**, 012112 (2007)
34. H.K.H. Lee, K.K.H. Chan, S.K. So, Org. Electron. **13**, 541 (2012)
35. H.H.P. Gommans, M. Kemerink, R.A. Janssen, J. Phys. Rev. B **72**, 235204 (2005)
36. J. Bisquert, G.G. Belmonte, Á. Pitarch, H.J. Bolink, J. Chem. Phys. Lett. **422**, 184 (2006)
37. W.H. Choi, S.K. So, Proc. of SPIE **7415**, 74151L (2009)
38. T. Yasuda, T. Tsutsui, Chem. Phys. Lett. **402**, 395 (2005)
39. J. Huang, G. Li, Y. Yang, Appl. Phys. Lett. **87**, 112105 (2005)
40. K.K.H. Chan, S.W. Tsang, H.K.H. Lee, F. So, S.K. So, Org. Electron. **13**, 850 (2012)
41. J. Nelson, Phys. Rev. B **67**, 155209 (2003)
42. M. Tachiya, K. Seki, Phys. Rev. B **82**, 085201 (2010)
43. J.C. Blakesley, D. Neher, Phys. Rev. B **84**, 075210 (2011)
44. B. Qi, J. Wang, J. Mater. Chem. **22**, 24315 (2012)
45. L.J.A. Koster, V.D. Mihailetchi, R. Ramaker, P.W.M. Blom, Appl. Phys. Lett. **86**, 123509 (2005)

Chapter 3
Improvement of Charge Transfer Between Electrode and Semiconductor by Thin Metal Oxide Insertion

Irfan Irfan and Yongli Gao

Abstract Efficient charge transfer at semiconductor and electrode interface is one of the most crucial issues for the performance of any electronic device. A counter intuitive phenomenon of transfer improvement by insertion of a thin metal oxide film at the semiconductor and electrode interface has gained much attention recently. In this chapter, we will describe our understanding of the mechanism of performance improvement with such insertions based on our surface analytical investigations. We will start by introducing the measurement techniques utilized in our investigations. We will discuss results on the insertion of a thin layer of MoO_x between indium tin oxide (ITO) and two well studied organic semiconductors, and demonstrate that the optimum insertion layer thickness is just a few nanometers. We will also illustrate the importance of high vacuum during the deposition of such insertion layers and the impact of exposure on device performance.

3.1 Introduction

Semiconductors are materials with important electronic properties. The importance of semiconductors was not completely realized until the invention of transistors at the Bell Lab in 1947 [1]. W. Shockley, J. Bardeen, and W.H. Brattain were awarded the Nobel prize within a decade of the invention. Since then, semiconducting materials are leading the saga of technological advancement. The transistors provided an exponential impetus to an already growing electronics industry against fragile and bulky thermionic triode valves [2, 3]. In the last few decades the field of electronics has completely redesigned the landscape of day to day human life. With an explosive increase in demands of convenient electronic gadgets like laptops and cell phones, demands for higher performance, and cost reduction are chorused. It becomes more challenging when these demands are blended with the demand of

I. Irfan · Y. Gao (✉)
Department of Physics and Astronomy, University of Rochester, Rochester, NY 14627, USA
e-mail: ygao@pas.rochester.edu

Y. Yang and G. Li (eds.), *Progress in High-Efficient Solution Process Organic Photovoltaic Devices*, Topics in Applied Physics 130,
DOI 10.1007/978-3-662-45509-8_3

environmental compatibility. Researchers are at the crossroads to meet the current demands. Most of the researchers are pursuing the conventional path with strong arguments of already existing large scale manufacturing facilities and advanced understanding of conventional semiconductors. A significant section of researchers believes in exploring new frontiers, because of limited number of existing conventional semiconductor materials, restrictions in engineering their properties like band gap, and demanding manufacturing parameters like high temperature. It is thus a challenge and an opportunity at the same time for scientists to explore new frontiers which can stand the test of current demands.

Organic semiconductors and polymers are promising candidates with high potential to meet some of the current challenges. High environment compatibility and less demanding manufacturing parameters are extremely attractive to begin with [4–6]. The ease of tailoring basic material parameters such as ionization potential (IP), electron affinity (EA) and band gap further advocates their candidature. A great deal of effort in the past three decades has been directed towards studying organic semiconductors. While many fruits of these researches have started to take shape, a few of them are leading the feast. Spectacular success of organic light emitting diodes (OLED) is being considered as a landmark in the field of organic semiconductor research [7–10]. While electroluminescence in organic material was first observed in the early 1960s by Pope [11], impetus in OLED research came with the successful demonstration of two-layer OLED by Tang [12]. Credited with several milestones in OLED research [13–16], OLEDs are now being extensively commercialized [4, 7–9, 17]. Research in the field of organic photovoltaic cells (OPV) is also being viewed with strong optimism. The first two-layer OPV cell was successfully demonstrated by C.W. Tang [18] with 1 % power conversion efficiency (PCE). With many progressively successful steps [6, 19–21], OPV has recently overcome the psychological barrier of 10 % PCE [5, 22]. Research efforts in organic thin film transistors (OTFT) are also very successful with reports of high carrier mobilities in organic semiconductors [23–26].

Based upon our past research experience in conventional semiconductor materials that a metal/semiconductor interface is vital for the performance of an inorganic device [27–29], The injection (extraction) of charges at electrode/organic interfaces in OLED (OPV) research is considered to be one of the most critical issues in enhancing device performance. Several attempts have been made to address the issue effectively. The counter intuitive phenomenon of inserting a transition metal oxide between the hole transport layer and the anode to improve hole injection was another milestone step in OLED research, which was first successfully demonstrated by Tokito et al. [30]. Shrotriya et al. [31] were the first to apply this idea in OPV research and they demonstrated encouraging performance enhancement in polymeric OPV cells. Irwin et al. [32] also presented improved OPV performance with NiO_x. These reports raised the question that how an oxide layer with an ordinarily insulating nature could result in improved charge injection or collection in an electronic device. This question lays the foundation of our investigations compiled in this chapter.

Investigation of the evolution of electronic energy level alignment during the interface formation is a key to understand the underlying mechanism. Ultraviolet photoemission spectroscopy (UPS), X-ray photoemission spectroscopy (XPS), and inverse photoemission spectroscopy (IPES) measurements have been widely applied in the past to understand the performance of conventional [33–35] as well as organic semiconductor based devices [36–38]. The spectroscopic technique are used in interface studies with a layer-by-layer approach: a thin film is deposited on to another one with systematically increasing thickness steps, and at each step the spectra are measured to provide a detailed understanding of the evolution of electronic structure during the interface formation [39–46].

This chapter is aimed at exploring the fundamental physics and mechanism of counter intuitive phenomenon of performance enhancement by insertion of oxide layers. Based on results of several experiments, we will explain underlying fundamental mechanisms of performance improvement with such insertions. We will discuss the mechanism with reference to experimental observation of other groups and their interpretations to present a complete overview. In Sect. 3.2, we will discuss the measurement techniques. In Sect. 3.3, we will demonstrate the phenomena of insertion of a thin layer of molybdenum oxide between ITO and copper phthalocyanine (CuPc) as well as with chloro-aluminum phthalocyanine (AlPc-Cl). We will also explain the thickness dependence of the insertion layer and based on electronic energy level alignment. In Sect. 3.4, we will highlight the importance of high vacuum during the deposition of insertion layer and will demonstrate that air and oxygen exposure will hamper the device performance. At the end the chapter will be summarized.

3.2 Measurement Techniques

In this section we will be discussing basic principles of experimental techniques we have utilized in the present work. The aim is to provide a reasonable introductory level description to readers about the important tools employed in the research. The main focus will be on photoemission spectroscopy (PES), which we have used for most of the research work presented in the chapter.

3.2.1 Photoemission Spectroscopy

In order to investigate a system, a probe that can directly interact and stimulate the system is considered the most useful. To study the electronic structure of a material, photons are the most suited and widely used, as in the case of photoemission spectroscopy (PES). Electrons ejected from an atom, after the absorption of high energy photons, contain considerable information about the electronic states of the atom. The basic principle of PES is presented in Fig. 3.1, where incident photons on

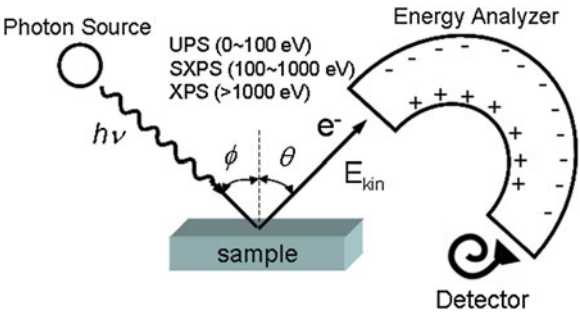

Fig. 3.1 Schematics of a photemission experiment

the sample excite electrons. The excited electrons escape into vacuum and are detected by an energy analyzer.

The basic principle of the photoelectric effect was explained by Einstein in 1905 [47]. In the photoelectric effect a negative current flow (electrons) is observed from a surface irradiated with photons. According to Fan's model [48], photoemission is a three step process. In the first step, an electron gets excited by absorbing a photon. In the second step, the excited electron travels outward through the solid, with possible electron scattering by collisions. In the final step, the electron escapes into the vacuum where it can be detected by the energy analyzer. This separation of stages is somewhat artificial and, in principle, the whole photoemission process can be treated as one step.

In a simplified model, the emitted electron comes from a one-electron orbital within the sample and escapes into vacuum without suffering energy loss. In this case, the energy of the emitted electron equals the photon energy minus the initial binding energy of the corresponding bound electronic states. Therefore, the analysis of the energy distribution of the photo emitted electrons provides unambiguous information about the occupied electronic states. The kinetic energy of a photemitted electron can be expressed as,

$$\mathrm{KE} = \mathrm{h}\nu - \mathrm{E_B} - \Phi \tag{3.1}$$

where $h\upsilon$ is the photon energy, E_B the binding energy of the electron in the initial state with respective to the Fermi level, and Φ is the work function of the sample surface. In a PES experiment, photons with a known energy are used to excite electrons out of the sample surface, whose kinetic energy and momentum can be measured in an electrostatic analyzer placed at a convenient place close to the sample surface.

The schematic of this relation is presented in Fig. 3.2 [49], where the ejected electrons are from all the occupied energy levels, within the reach of probing photon energy, including the valence band (VB) in inorganic or highest occupied molecular orbital (HOMO) in organic semiconductors.

It is important at this point to mention the requirement of ultra high vacuum (UHV). The requirement of UHV is crucial because of two reasons. The first reason

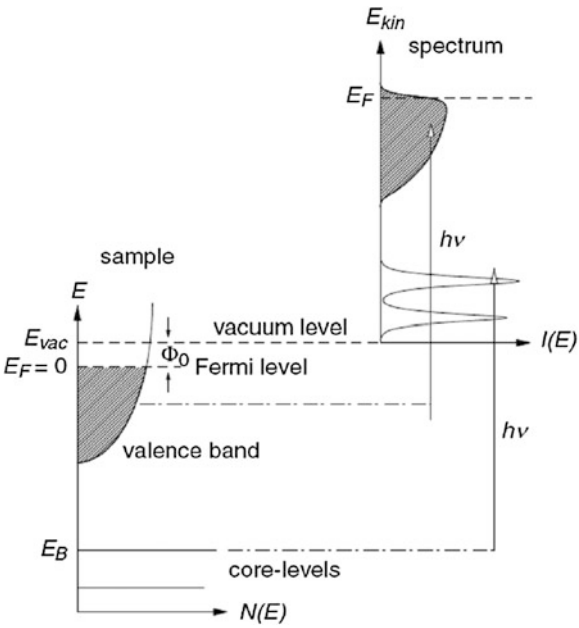

Fig. 3.2 A schematic representation of photoemission spectroscopy and reconstruction of energy levels measured with it (from [49])

is to maintain the integrity of surface under investigation and minimize accumulation of impurities present in the ambiance. The second reason is to measure correct KE of photo emitted electrons. In higher ambient pressure the possibility of photo emitted electron interacting with other molecules and thus possibly changing KE before reaching the energy analyzer is high. The UHV ambiance insures that both the conditions are fulfilled.

3.2.1.1 Surface Sensitivity

The photo emitted electrons from the sample surface have varying capacity of escape from the surface, which in turn depends on the kinetic energy of the electrons. In a surface study, one should recognize the fact that the number of surface atoms at a probing surface scales as $1/6\ N_A^{2/3}$, where N_A is the number of atoms in the bulk. As such, the signal from the bulk atoms will quickly dominate that originating from the surface if the probing depth of the experimental technique exceeds several atomic layers. The PES turns out to be one of the most trustworthy analytical tools, as it capitalizes on the detection of photo emitted electrons. Electrons strongly interact with the rest of the system, leading to a relatively short escape depth, or a small mean free path (MFP). The MFP λ is the average distance an electron can travel before suffering an inelastic scattering. The MFP is mostly dependent on the kinetic energy of the emitted electron and is almost independent of the material. The universal curve for MFP in number of monolayers as a function

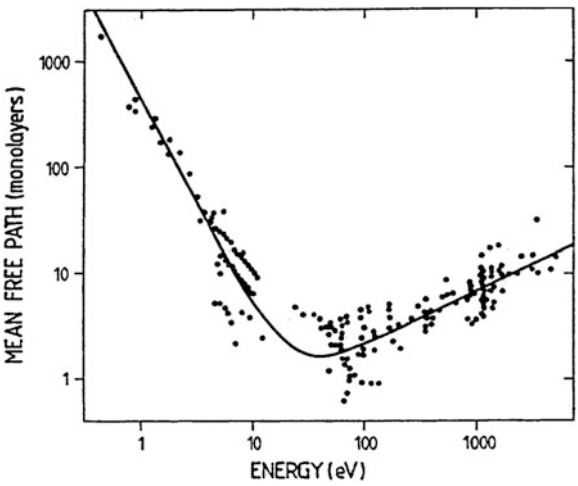

Fig. 3.3 Universal curve of electron mean free path in solids (from [50])

of the kinetic energy of the emitted electrons is presented in Fig. 3.3 [50], where one notices that within the energy range of interest, typically between 10 and 2,000 eV, the MFP is only of the order of a few monolayers.

PES can be categorized into several classes depending on the region of interest and appropriate photon energy to probe the system. The most common regions of interest in electronic structure measurements are deep core levels and shallow occupied regions. In the next two sections we will discuss the X-ray and ultraviolet photoemission spectroscopy used to study the core and the shallow occupied regions, respectively.

3.2.1.2 X-Ray Photoemission Spectroscopy

In XPS, photons with energy $\sim$1 keV and a small energy dispersion is utilized to study core levels of a system. The most commonly utilized X-ray sources are the unmonochromatized $K\alpha$ radiation resulting from collisions of high energy electrons onto Mg or Al anode. These collisions produce a large amount of heat at the anode and thus it is a strict requirement to continuously cool the anode by circulating water or other suitable methods. In order to improve the energy and spatial resolution, the X-ray source can be further monochromatized through a specially-designed quartz crystal. The typical photon energies for Mg Kα and Al Kα lines are 1,254.6 and 1,486.6 eV, respectively. XPS is also widely known as electron spectroscopy for chemical analysis (ESCA), since it is extensively used as a means to identify elements on a given sample surface. In this most basic application, a survey spectrum of the sample is obtained by scanning over the full energy range. The elements present at the sample surface can then be recognized by comparing the binding energy of the obtained peaks with a set of reference data from an XPS hand book, since each and every element has its own set of characteristic peaks.

Further, the more detailed XPS analysis involves studies of small chemical shifts. The binding energies of the core-level electrons are very sensitive to any changes in the chemical environment. Such changes can be revealed by a small chemical shift of the core-level peaks.

3.2.1.3 Ultraviolet Photoemission Spectroscopy

An X-ray source in principal can be used to investigate the electronic structure of the valence region of a solid, but the photo-ionization cross section for the valence electrons is much smaller than that of the core electrons. To overcome this problem and study the electronic structure of the valence region with a higher cross section the ultraviolet light generated by a He discharge lamp as the photon source is employed. This technique is known as UPS, based on the fact that the photon energy used in the measurements is in the ultraviolet region. Another advantage of using He discharge as the photon source is the better spectrum resolution due to the small line width of only about 20 meV for the most used He I line at 21.22 eV. However there is a small 23.1 eV line which is about 4 % of the He I line intensity [44, 51]. The peak through 23.1 eV line is usually buried as a small back ground toward the lower binding energy side of the corresponding peak generated through 21.22 eV photons. The UPS measurements are usually far less damaging to samples than XPS, a very valuable feature in the investigation of organic semiconductors that are usually vulnerable to photo-induced damages. The probing depth of UPS is typically around 15 Å.

In Fig. 3.4, a typical UPS spectrum of a clean Au surface is presented. In the sequence from lower to higher binding energy, the spectrum illustrates the Fermi edge of Au, occupied 5d states and a sharp cut off, respectively. The Fermi edge is derived from the occupied states just below the Fermi level. The Fermi edge is used as a reference point to calculate the binding energies of other energy levels. It is important to note here that the Fermi level position obtained from the metallic

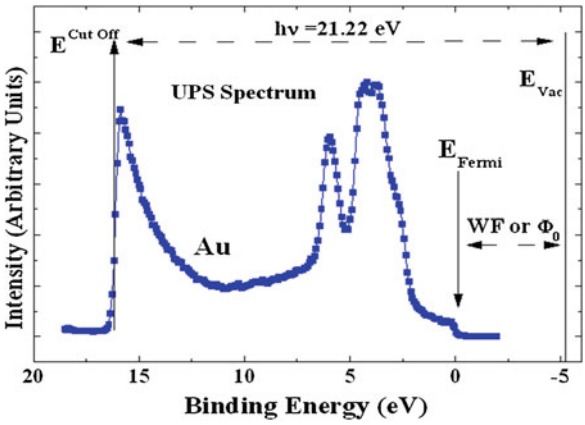

Fig. 3.4 The UPS spectrum of a clean Au surface

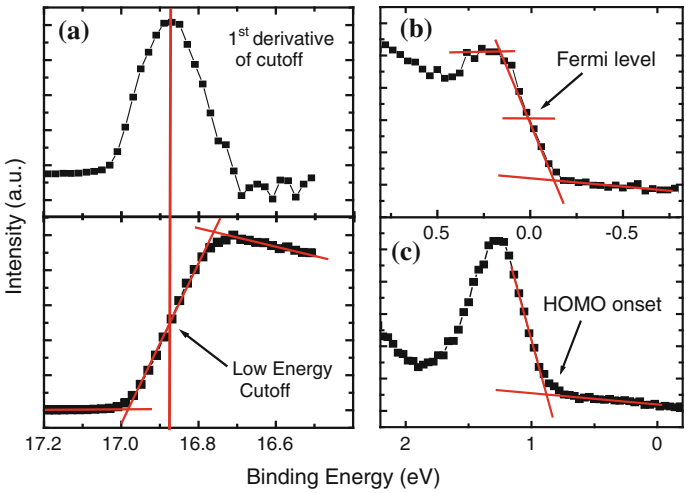

Fig. 3.5 Analysis of UPS data **a** the cut-off position, **b** the Fermi edge and **c** the HOMO onset position

surface remains fixed because of being in thermal equilibrium with a big stainless steel chamber, and hence in general cases can also be used as a reference for semiconducting samples. At the left side of the spectrum, a sharp cutoff can be identified, which is called the secondary electron cutoff. Usually a few volt negative bias is applied at the sample to clearly observe the cut off or the vacuum level energy. The vacuum level of a surface after the photoexcitation can be conveniently calculated by adding 21.22 eV to the cutoff energy, as depicted in the figure.

The determination of the cut-off and HOMO onset position is crucial in UPS data analysis. In this section, we will only discuss the most commonly used method to determine the positions of the UPS features. We will be using the same analysis method for UPS data in this chapter. A simple illustration is presented in Fig. 3.5. The cutoff energy is defined as the position of the maximum of the first derivative of the measured curve in the cutoff region. This point is usually at the midpoint of the sharp cutoff. The measured Fermi level of a metal is expected to obey Fermi-Dirac statistics and therefore the Fermi level is defined at the midpoint of the leading edge of the spectrum, as shown in Fig. 3.5b. The binding energy of the HOMO onset of an organic semiconductor is determined by the intersect of the linear extrapolation of the leading edge of the HOMO peak and the straight background line, as shown in Fig. 3.5c. The Fermi level in most of the presented spectra is fixed at zero binding energy and all the measured positions are referenced with respect to the Fermi level.

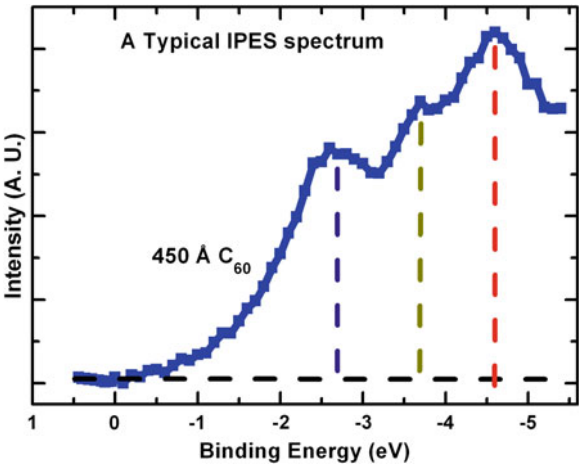

Fig. 3.6 An IPES spectrum of C_{60} with four major unoccupied peaks. The LUMO peak is at the binding energy of −2.7 eV

3.2.2 Inverse Photoemission Spectroscopy

In a simple description inverse photoemission is a time-reversed process of photoemission. In IPES a sample under investigation is bombarded with electrons of monochromatic kinetic energies, usually less than 20 eV. The relaxation of the incident electrons into the unoccupied energy levels generates photons through radiative decay. The emitted photons are collected, which provide a direct measure of the unoccupied energy levels of the sample [52–56]. There are two working methods of IPES. The first one fixes the kinetic energy of the incident electrons and directly measure the unoccupied spectrum of emitted photons using a photon detector. The second approach measures at single photon energy, and obtain the information of the unoccupied states by varying the kinetic energy of the electrons arriving at the sample surface. Due to the fixed photon energy in the second approach it is also called isochromat mode. Given the energies of the incident electrons this technique has approximately the same surface sensitivity as UPS. Typical energy resolution ranges from 0.3–0.8 eV depending on the energy dispersion in the incident electron beam and the resolution of the photon detector [54–56].

In Fig. 3.6, an IPES spectrum is presented. The IPES data were obtained from a 450 Å thick C_{60} film. The LUMO edge can be obtained by the intersection of the linear extrapolation of the leading edge of the LUMO peak with the linear background.

3.3 MoO_x Inter-layer Between ITO and Organic Semiconductors

A lot of efforts have been made in order to improve the charge transport and collection at the electrodes. Introduction of a high work function transition metal oxide insertion layer between conducting indium tin oxide and organic semiconductors was an attempt first made by Tokito et al. [30] As shown in Fig. 3.7a [30], they reported that an OLED device with 30 nm of VO_x insertion on 120 nm ITO started light emission (luminance of 1 cadmium/cm^2) at bias of 3 V, and another with a MoO_x layer at 3.7 V. In comparison, a control device with 150 nm ITO began light emission at 4.7 V. 1,000 cd/cm^2 luminance level was achieved at about 10, 8 and 7 V for ITO only, MoO_x/ITO, and VO_x/ITO electrodes, respectively. More recently, improved hole injection and stable device performance are reported by insertion of transition metal oxides inter-layer in OLED [57, 58]. In OPV researches, using metal oxide as an inter-layer between the ITO anode and the hole transport layer was successfully demonstrated by Shrotriya et al. [31]. For devices with an optimized 5 nm MoO_x insertion layer, they observed about 14, 22, and 21 % improvements in Jsc, Voc, and fill factor, respectively, in comparison with those without. Irwin et al. [32] also demonstrated an efficiency enhancement by a thin nickel oxide insertion layer. The observations raised questions on how an insulating layer may reduce the resistivity, what is the optimum thickness of such insertion layer, and what is the mechanism of this improvement.

In this section, we present a systematic investigation of MoO_x inter-layer between ITO and organic semiconductors using UPS, IPES, and XPS. We will

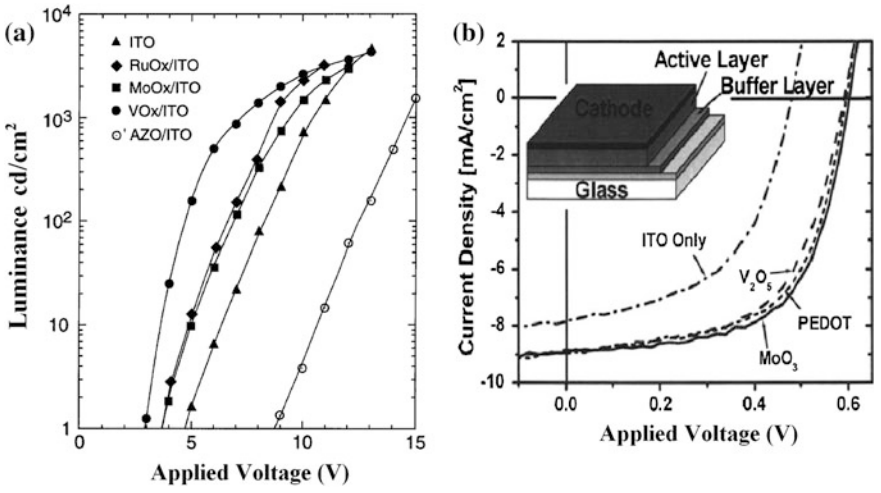

Fig. 3.7 Devices with TMO inter-layers, **a** luminance versus voltage [30], and b Current density versus voltage [31]

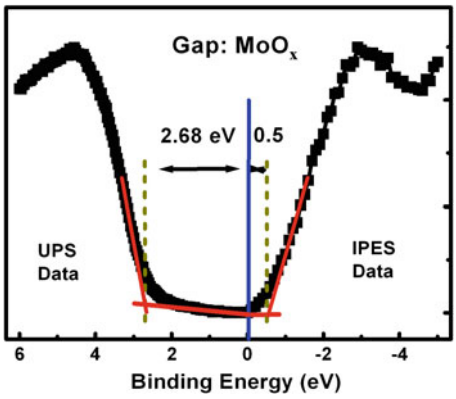

Fig. 3.8 Band gap of MoO_x

show the electronic energy level evolutions of AlPc-Cl/ITO and CuPc/ITO interfaces with and without a MoO_x insertion layer. Based on the electronic structure evolutions the beneficial nature of the insertion layer will be discussed. We will also discuss the mechanism responsible for this counter intuitive phenomenon of device performance enhancement and the optimum thickness of such insertion layers.

In Fig. 3.8, combined UPS and IPES data are presented for MoO_x. The VB onset and conduction band (CB) edge of 30 Å MoO_x film on ITO were measured to be 2.68, and 0.5 eV, respectively. Thus a band gap of 3.2 eV was measured for the MoO_x film. Measured band gap values are consistent with earlier reported values [59].

3.3.1 Interface Formation with CuPc

Copper phthalocyanine has been utilized in some of the high efficiency small molecule OPV cells. In a recent work, the effect of MoO_x insertion layer on CuPc/C_{60} photovoltaic cell was studied. The results demonstrated that with the MoO_x insertion layer, the power conversion efficiency was enhanced by 26 % mostly due to a significant enhancement in the fill factor [46, 60]. In this section, we will discuss the electronic energy level evolution at the CuPc/ITO interface with and without a 10 nm MoO_x insertion layer.

In Fig. 3.9, the UPS spectra of CuPc on ITO are presented as a function of the thickness of the CuPc films. In Fig. 3.9a, b the cut-off and the HOMO regions are presented, respectively. The cut-off BE of the ITO substrate was measured to be 16.57 eV, which corresponds to a surface work function of 4.65 eV, obtained by subtracting the cut-off BE from the photon energy of the excitation source (21.22 eV). With increasing thickness of the CuPc film, cut-off values were observed to shift towards lower WF (or higher BE) values. The shift saturated around 32 Å CuPc thickness. From Fig. 3.9b, the HOMO onset for 8 Å CuPc film

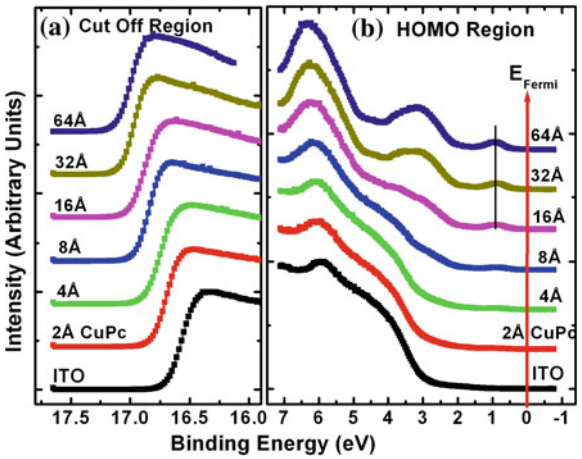

Fig. 3.9 The UPS spectra of CuPc on ITO as a function of CuPc thickness (from [45])

was measured at 0.31 eV. With further increase in the CuPc thickness the occupied level peaks remained more or less unchanged, as illustrated by the dashed line in the figure, on the HOMO peaks.

The UPS data for the cut-off and the HOMO regions with a 100 Å MoO_x film are plotted in Fig. 3.10a, b, respectively. The ITO WF was measured to be 4.59 eV and with the deposition of a 100 Å MoO_x film the WF was measured to be 6.82 eV. With the deposition of CuPc on MoO_x/ITO, the WF first decreased rapidly, then the shift in WF became more gradual. In Fig. 3.10b, the valence band peak of MoO_x was observed at $\sim$3.8 eV. The MoO_x peak gradually shifted towards the higher BE with increasing thickness of CuPc. This shift was measured to be $\sim$0.2 eV up to 8 Å of CuPc deposition. With further CuPc deposition all the occupied level peaks were observed to be continuously shifting towards the higher BE. The HOMO

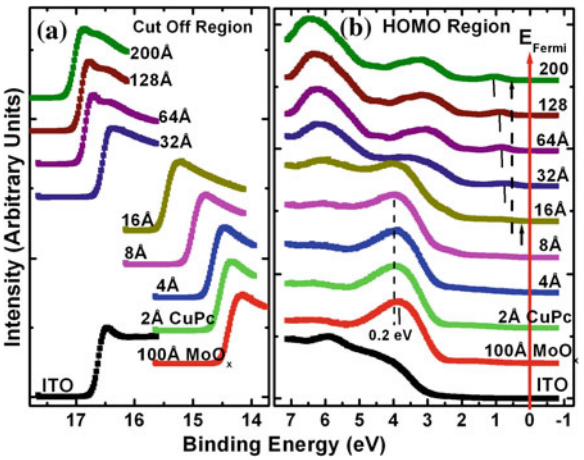

Fig. 3.10 The UPS spectra of CuPc on MoO_x/ITO as a function of CuPc thickness (from [45])

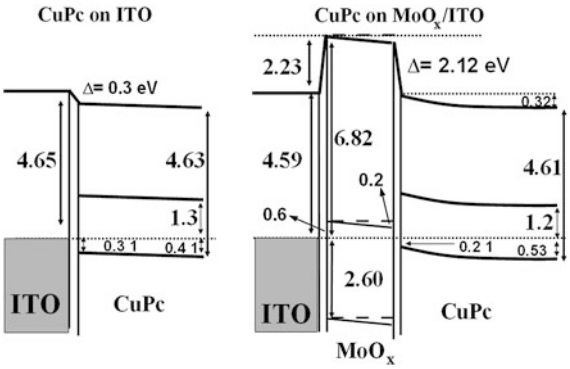

Fig. 3.11 The energy level alignment diagrams for, **a** CuPc on ITO, and **b** CuPc on MoO_x/ITO interfaces (from [45])

onset BE for 8, 64, and 200 Å thick CuPc films were measured to be 0.21, 0.36, and 0.53 eV, respectively.

The energy level alignment diagrams for the CuPc/ITO and the CuPc/MoO_x interfaces are presented in Fig. 3.11a, b, respectively. In Fig. 3.11a, the ITO WF was measured to be 4.65 eV. At the CuPc/ITO interface we observed an interface dipole of 0.33 eV, due to transfer of holes from ITO to the CuPc side. After the formation of the interface dipole a near flat band situation was observed. The initial hole injection barrier was measured to be 0.31 eV, with the ionization potential (IP) of 4.65 eV. In Fig. 3.11b, the ITO WF was measured to be 4.59 eV, which became 6.82 eV, with the deposition of 100 Å MoO_x. With the deposition of CuPc on MoO_x/ITO the VB peak of MoO_x was observed to shift towards higher BE. A large dipole moment at the interface was observed, due to the rapid transfer of holes from MoO_x side to the organic side. The conservative estimate of the shift is 0.2 eV, in the MoO_x energy levels towards the higher BE. The estimate is made from the shift of MoO_x valence band peak towards the higher BE with the deposition of CuPc, as depicted in Fig. 3.11b. A large interface dipole of 2.97 eV is observed at the CuPc/MoO_x interface. The initial hole injection barrier was observed to be 0.21 eV. With further deposition of CuPc the energy levels gradually relaxed back to their normal values and thus creating a band bending like region in the organic side. At the thickness of 200 Å CuPc the HOMO onset value was measured to be 0.53 eV.

Kim et al. [46, 60] have reported 30 % improvement in the fill factor (FF) and 37 % improvement in the overall power conversion efficiency, with a 100 Å MoO_x inter-layer between ITO anode and a CuPc layer. We assign the improvement to the lower hole injection barrier at the CuPc/MoO_x interface and the presence of a drift electric field. There are two possible improvement mechanisms in the presence of the drift electric field, which will be discussed in detail in the next section. The first is that the drift field is a steering field which is helpful for easier extraction of holes at the anode. The second is that the field facilitates the absorption of photons incident on the material through transparent anode side, which is supported by the reported improved absorption with MoO_x inter-layer [60].

3.3.2 Thickness Dependence of MoO_x Insertion Layer

After establishing the advantageous nature of the transition metal oxide insertion layer between ITO and CuPc, it is crucial to further conduct a detailed investigation of anode/organic interfaces with different thicknesses of the insertion layer and find out the optimum thickness. It is important to point out at this point that with the transition metal oxide insertion layer there are two competing mechanisms of the opposite effect. The first is that the high WF of the insertion layer causes the energy levels of the organic material to shift towards the lower binding energy, thus reducing the hole-injection barrier. The other is that the resistance of the oxide layer will increase with the thickness. In this section, we will discuss this issue and explore the optimum thickness of the insertion-layer on the basis of energy level alignment.

In order to avoid variations originating from different sample preparation conditions, we designed a sample with a gradually changing thickness of MoO_x. The ITO substrate used in this experiment was oxygen plasma (OP) treated in situ. The surface WF uniformity of OP treated ITO was measured with UPS, and the uniform region with WF of 5.22 ± 0.1 eV was selected for further measurements. We deposited 1.25 × 6 mm strips of MoO_x with thicknesses ranging from 0 to 300 Å in 7 steps onto the OP treated ITO substrate. A thin metal shutter parallel to the substrate surface with a sharp edge was attached to a micrometer, about 1 mm below the substrate to expose the specific area of substrate for MoO_x deposition. The shutter was adjusted to fabricate MoO_x films of stepped thicknesses. Subsequently AlPc-Cl was deposited layer-by-layer on the stepped MoO_x substrate.

In Fig. 3.12, the UPS spectra of the MoO_x on ITO are presented as function of the thickness of the MoO_3 layer. Figure 3.12a, b show the cut off and HOMO regions of the UPS data, respectively. The schematics of MoO_3 with stepped thicknesses of 0, 10, 20, 50, 100, 200, and 300 Å is shown in the inset of Fig. 3.12b.

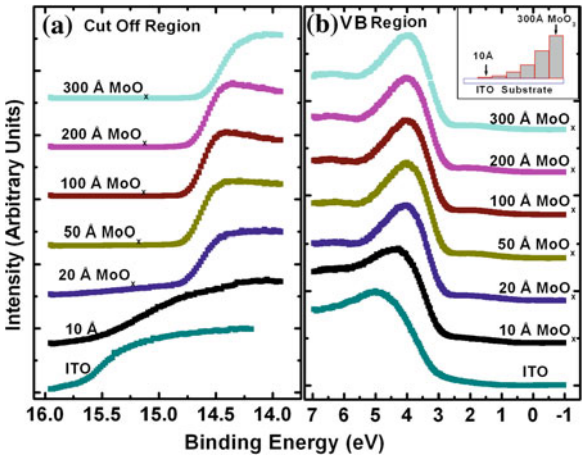

Fig. 3.12 UPS data for 300–10 Å MoO_x and ITO for **a** the cut-off region, and **b** the VB region. Inset: the schematics of gradual thickness of MoO_x (from [42])

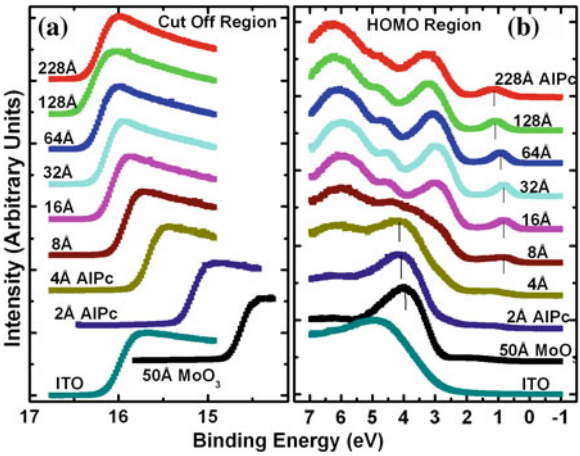

Fig. 3.13 UPS data for 0–228 Å AlPc-Cl/50 Å MoO_3/ITO **a** the cut-off region and **b** the HOMO region (from [42])

The WF increase for the 10 and 20 Å MoO_x on ITO was measured to be 0.66 and 1.42 eV, respectively, and it remained almost the same for further MoO_x deposition, indicating saturation at around 20 Å. From Fig. 3.12b, a characteristic peak of MoO_x was observed to develop and saturate at 4.0 eV. In the HOMO region, the MoO_x features became prominent after 20 Å, and after 50 Å all spectra remained almost the same. It further supports the notion of the electronic energy level saturation between 20 and 50 Å. It is not surprising that the WF saturation occurs sooner than the HOMO, as the former is related only to the surface properties of the material.

AlPc-Cl was subsequently deposited layer-by-layer on the 0–300 Å stepped MoO_3 substrates and UPS data were recorded for each coverage of AlPc-Cl from all the stepped strips. We present a set of representative spectra of 50 Å MoO_x interlayer thickness in Fig. 3.13. The UPS data for the cut-off and the HOMO regions are plotted in Fig. 3.13a, b, respectively. The ITO WF was measured to be 5.22 eV and the deposition of MoO_x moved the WF towards lower BE by 1.36 eV. With the deposition of AlPc-Cl on MoO_x/ITO the WF at first decreased rapidly till 16 Å and then the reduction became slower and more gradual. At 128 Å AlPc-Cl deposition the WF was measured to be 4.93, 0.3 eV lower than the ITO WF of this strip. The MoO_x peak at 4.0 eV also shifted about 0.2 eV upon 4 Å AlPc-Cl deposition. The HOMO BE for 16, 64 and 128 Å coverages were measured to be 0.32, 0.45 and 0.55 eV respectively.

Energy level alignment diagrams for AlPc-Cl/ITO, 50 Å MoO_3/ITO and AlPc-Cl/50 Å MoO_x/ITO, interfaces are depicted in Fig. 3.14a–c, respectively. The ITO WF was measured to be 5.22 eV. At the AlPc-Cl/ITO interface a downward vacuum level shift was observed with an interface dipole of 0.33 eV and a flat band situation there onwards. The HOMO onset for AlPc-Cl was observed to be 0.7 eV below the Fermi level. The interface between ITO and MoO_x had an interface dipole of 1.36 eV and the VB onset of MoO_x was measured to be 2.8 eV. The energy levels of MoO_x were flat after 20 Å deposition. The high WF of MoO_x lifted

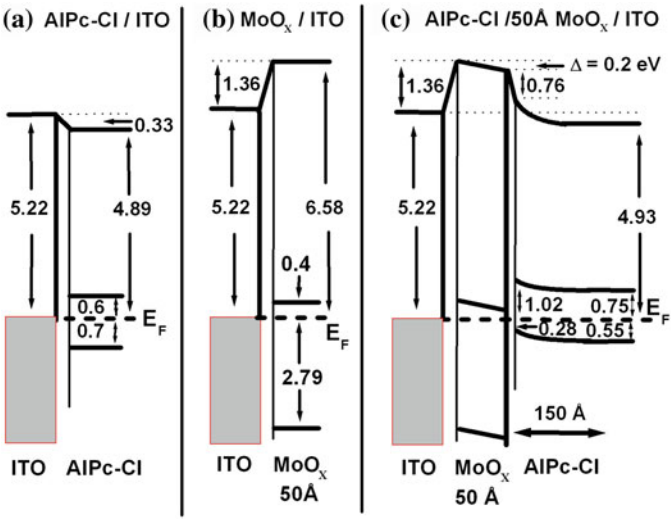

Fig. 3.14 Energy level alignment at **a** AlPc-Cl/ITO, **b** 50 Å MoO_3/ITO, and **c** AlPc-Cl/50 Å MoO_3/ITO (from [42])

up the AlPc-Cl energy levels, resulting in a hole accumulation and band-bending-like region at the AlPc-Cl interface. The thickness of this bending region is estimated to be ~150 Å, as the shift in energy levels was saturated between 128 and 228 Å of AlPc-Cl. At 128 Å of AlPc-Cl deposition, the AlPc-Cl HOMO onset was measured to be 0.55 eV. In addition to the reduced barrier, the band-bending-like situation in AlPc-Cl creates a drift electric field for holes towards the AlPc-Cl/MoO_x interface.

In Fig. 3.15, the WF versus MoO_x inter-layer thickness (square) is plotted for 4 Å (circle), 8 Å (triangle up), 32 Å (triangle down), and 128 Å (trapezoid) AlPc-Cl coverages. It is simple to deduce the saturation of the WF of MoO_3 inter-layer at the thickness (square data points) of 20 Å. At 128 Å AlPc-Cl coverages (trapezoid) the WF of AlPc-Cl saturates around 4.9 eV irrespective of MoO_x inter-layer thickness, representing the saturation of band-bending-like situation in AlPc-Cl. The 32 Å AlPc-Cl coverages have a similar trend, with WF values less than 0.2 eV higher than that of the 128 Å coverages. The 4 and 8 Å AlPc-Cl data demonstrate a clear MoO_x inter-layer thickness dependence. In the absence of MoO_3 inter-layer the variation in WF values is less than 0.2 eV for all the four AlPc-Cl coverages. With increasing inter-layer thickness the WF saturation requires more AlPc-Cl to be deposited. The potential drop observed across MoO_x inter-layer is about 0.2 eV by AlPc-Cl, regardless of the thickness of the MoO_x. The data in Fig. 3.15, indicate that for the final 128 Å thickness of AlPc-Cl about the same WF difference from MoO_x for inter-layer ≥20 Å, but clearly undergoes a slower relaxation in WF as AlPc-Cl thickness increases for thicker MoO_x inter-layer. Since the drift field is the gradient of built-in potential, swifter relaxation would result in a larger drift field at

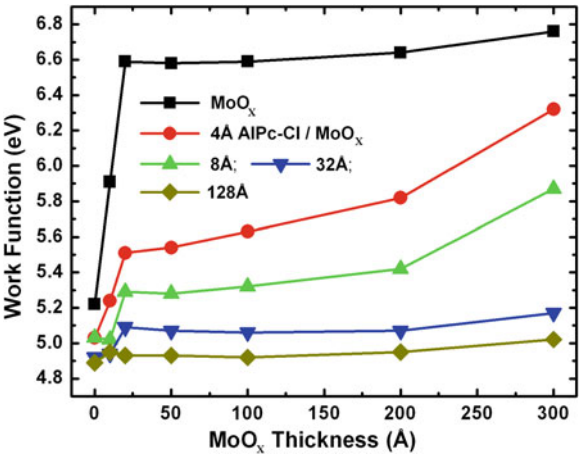

Fig. 3.15 Work function versus MoO_x inter-layer thickness for 4 Å (*circle*), 8 Å (*triangle up*), 32 Å (*triangle down*) and 128 Å (*trapezoid*) AlPc-Cl coverages (from [42])

the interface. This in turn would result in a higher hole current. It should be mentioned that there is trade-off between the drift enhancement and increased resistivity by MoO_x, so it is more likely that 20 Å is the optimum choice. The prediction of optimum thickness solely on the device performance basis was recently reported by Cattin et al. [61] which is quite consistent with our UPS results.

As MoO_x is expected to be mostly insulating and neutral, there has to be induced electron accumulation at the ITO/MoO_x interface to counter the hole accumulation at the AlPc-Cl/MoO_x interface. Thus MoO_x behaves like a dielectric slab inside a charged parallel plate capacitor. Due to the presence of opposite charges across the MoO_x inter-layer, there would be about a linear downward shift in all the energy levels of MoO_x. A conservative estimate of this downward shift can be made from the shift of the MoO_x HOMO peak as indicated by the short bars in Fig. 3.13b, which is about 0.2 eV. Interestingly, this shift in MoO_x peak by AlPc-Cl was found to be about the same for all the MoO_x inter-layers. It should be noted that the strictly insulating nature of MoO_x assumed here may require some qualification. In Fig. 3.8, a long tail of defect states can be observed, which extends into the gap of MoO_3, which may be originating from the oxygen deficiency. These defect states may accommodate hole hopping conductivity across MoO_x. The MoO_x CB edge was observed 0.5 eV above the Fermi level, so extraction of electrons directly from the LUMO of the organic side is less likely as in the case reported by M. Kroger et al. [7] Another indirect evidence of a higher CB position in our sample is the shift of the MoO_x VB level for ≥0.2 eV towards higher binding energy. The data however, do not contradict with the possibility of electron extraction from the CB defect states in MoO_x.

3.4 Discussions

After presenting our MoO_x insertion layer results, it is prudent to present a broader view before concluding the effects of the inter-layers. In this section, we will present a quick survey of OPV device results from different groups on this issue. We will also list mechanisms proposed by different groups based on device and electronic energy-level alignment results. We will then discuss our results with a broader view.

Presented in Fig. 3.16a are the current density versus applied voltage characteristics of OPV devices of FTO/MoOx/CuPc/P3HT:PCBM/Al with varying MoO_x thickness [62]. It is straightforward to deduce that with increasing thickness of the inter-layer the current increases linearly while Voc remains largely unaffected. Increasing the inter-layer thickness to $\sim$20 nm significantly hampers the device performance. The current is the worst affected while the Voc is almost intact. In Fig. 3.16b, the J-V characteristics of inverted BHJ OPV devices of ITO/P3HT:

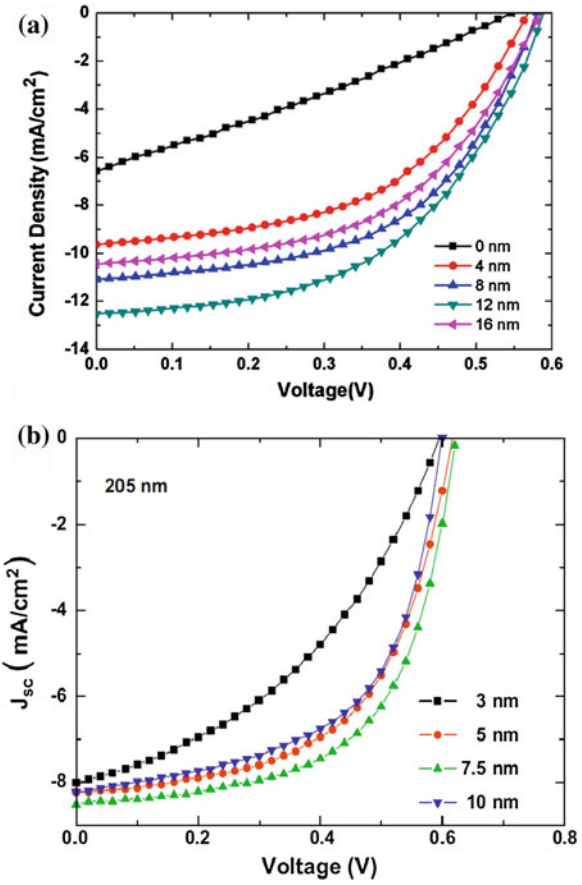

Fig. 3.16 OPV results with varying MoOx inter-layer thicknesses, **a** from [62] and **b** from [63]

PC71BM/MoO_x/Ag with varying MoOx inter-layer thickness are presented [63]. The results demonstrate almost pure fill factor improvement, while leaving both the Jsc and the Voc largely unaffected. Thicker inter-layer interestingly again illustrates a deleterious effect. Zeng et al. [64] have reported the effect of 10 nm MoO_x inter-layer on ZnPc/C_{60} OPV cell in comparison to ITO only anode. They demonstrated 6.7, 11.3 and 6.3 % improvements in Voc, Jsc and FF, respectively. In their results also thicker MoO_x inter-layer is found to be deleterious, with the Jsc being the worst affected. Hori et al. [65] have also demonstrated 28, 36, and 32 % improvements in Voc, Jsc, and FF, respectively, in poly 3-hexylthiphene (PAT6)/C_{60} inverted solar cell with 2 nm MoO_x.

At present there is no consensus on the exact mechanism of performance improvement. Here we will list a few possible mechanisms reported by several groups. The first mechanism of improvement is that the TMO mostly affects the growth of the donor layer and enhances light absorption, which in turn increases the efficiency. Zuo et al. [60] have demonstrated higher light extraction with a RuO_x inter-layer due to ordered growth of CuPc on top of RuO_x. Kim et al. have also demonstrated a higher light absorption with a MoO_x inter-layer. While ordered growth may play a role in the enhancement, it should not be the leading one. Furthermore similar device enhancement results are also reported with inverted OPV structure, where the TMO inter-layer is deposited after the deposition of an active layer and hence incapable of affecting the growth of the active layer [66, 67]. Hori et al. [65] have also demonstrated a higher light absorption with an MoO_x inter-layer, in an inverted OPV cell

There are a number of groups which based on energy level alignment argue defect state assisted improvement, including Ishii's group [68]. They have assigned the improvement to the band-bending in the organic side and a gap state at about 1 eV below the Fermi level, assisting charge transfer. Vashilapov et al. have also demonstrated that a MoO_x inter-layer (with $x < 3$) performs better than a MoO_3 inter-layer, on account of gap (or defect) states at about 1 eV and 2.3 eV below the Fermi level and thus assisting the charge transfer. We will discuss this possibility in detail in the next section.

Kahn's group at Princeton University proposed a mechanism in which improved charge transfer originates from the conduction band edge of MoO_x [69]. They observed CB edge of MoO_x to be almost pinned, and the HOMO of the organic side to be very close to the Fermi level [59]. Thus they assigned the hole injection improvement, originating from electron extraction from the HOMO of the organic semiconductor to the ITO anode through CB of MoO_x. It is interesting to note that most of the groups working on electronic structure measurements have predicted higher current to be the major cause of improvement based on the energy-level alignment.

Let us start establishing a sound mechanism of performance improvement in a gradual manner with simple points. The first is that all the groups have observed harmful effect of thicker inter-layers (>15 nm). This is not surprising since MoO_x is an oxide and is not expected to be a good conductor itself. The higher performance is therefore mostly a result of a modified interface in a thin region and is not in any

way associated with the bulk properties of MoO_x. The trend of performance reduction with thicker inter-layers also exclude the possibility of performance enhancement with the tunneling mechanism, since with larger distances (higher thicknesses) the tunneling mechanism should suffer much faster performance reduction than the observed thickness dependence trend. The second is that the high work function of a MoO_x layer must be playing an important role. The MoO_x WF must be a little bit higher than the IP of organic side in order to pull the HOMO of the organic side very close to the Fermi level. This point will also be discussed in detail in the next section and the higher WF requirement will be further underscored. Another point we would like to emphasize is the higher drift field with thin inter-layers, as presented in Fig. 3.15. The higher drift field is creating a steering field which would help easier extraction of holes from the organic side. It does not contradict the hole extraction mechanism of the Princeton group, through the CB edge of MoO_x, particularly with defect states on conduction band side extending close to the Fermi level, as observed in the IPES data of Fig. 3.8. Another possibility is that the high electric field at the organic/MoO_x interface due to the accumulation of electrons at the MoO_x side and the accumulation of holes at the organic side, may provide a suitable site for photon absorption, which in turn improves the OPV performance.

In conclusion, we have presented an electronic structure of interface formation with and without a 100 Å MoO_x inter-layer with CuPc. We have also demonstrated the electronic structure evolution of interfaces with 0–300 Å stepped MoO_x inter-layers between ITO and AlPc-Cl. It was observed that the high work function of the metal oxide inter-layer pulls up the energy levels of organic side towards lower binding energy at the interface, resulting in band-bending-like situation in the organic material. Thus the band-bending-like phenomenon in AlPc-Cl introduces a drift electric field inside the organic hole transport layer. This built in drift field enhances hole extraction to the ITO and thus enhancing the performance of devices with a thin MoO_x inter-layer. The optimum thickness of MoO_x inter-layer was found to be between 20 and 50 Å. In the next section, we will describe mostly the effect of air and oxygen exposure on electronic properties of MoO_x thin films. We will also discuss the issue of gap states and would make an attempt to link the device performance with these states.

3.5 Effect Oxygen and Air Exposure on MoO_x Films

In the last section, we explained the beneficial mechanisms of MoO_x inter-layer. However, there still exist many fundamental questions to be addressed for comprehensive understanding and controlled utilization of MoO_x insertion layer with reproducible device performance. In this section, we will discuss a few issues which would be crucial in the application of insertion layers.

The growing interest in transition metal oxides, MoO_x in particular creates an urgent need to conduct detailed study of its electronic properties and changes it can

undergo in normal handling and fabrication processes. A recent report discussed the importance of the high MoO_x WF as a crucial factor in the performance enhancement of OPV devices [43]. However, the surface work function of MoO_x has been reported as 5.3, 5.68 and 6.86 eV by Shrotriya et al. [31], Kinoshita et al. [70] and Kroger et al. [57] respectively, in spite of the fact that all the groups used the same technique, the UPS to determine the WF. It is imperative to resolve the discrepancy in order to understand how to control the device fabrication and to obtain consistent device performance.

In this section, we will report the study of electronic structure evolution of MoO_x films exposed to air and oxygen using UPS, IPES and XPS. The changes in the valence electronic structure, WF, and ionization potential were monitored as a function of air and oxygen exposure. It was found that the vacuum deposited MoO_x films started with high initial WF values, but with air and oxygen exposure the surface WF gradually reduced to much lower values. The reduction is attributed to adsorptions of oxygen and moisture on the MoO_x surface. Gap states were observed in the energy gap with increasing exposure both in the air and oxygen. The correlation of the gap states with the exposures and device performance is presented.

UPS, IPES and XPS studies were performed using a modified VG ESCA Lab system. The UHV system consists of three interconnecting chambers, a spectrometer chamber, an in situ oxygen plasma treatment chamber, and an evaporation chamber with a precision air leak valve. Two ITO substrates were treated in situ in oxygen ambiance of 600 m Torr at bias voltage of −500 V for 30 s. 50 Å thermally evaporated MoO_x films were deposited on both the substrates. The first MoO_x film was exposed to oxygen in controlled steps from 1 to 5×10^{14} L. One Langmuir (L) exposure is equal to the 10^{-6} Torr s exposure, and it will result in one monolayer of gas adsorbates if the sticking coefficient is unity. The exposures up to 10^4 L were performed inside the spectrometer chamber, and the rest exposures were performed in the evaporation chamber. The oxygen exposures were performed by using ultra pure carrier grade oxygen (UN 1072) from Airgas Inc. The relative humidity in the laboratory was about 63 % during the air exposure. The second MoO_x film was exposed to air in controlled steps from 10^2 to 2×10^{14} L. Dry air has $\sim$20.95 % oxygen by volume and thus the oxygen exposure of 2×10^{14} L is similar to a dry air exposure of $\sim 10^{15}$ L in terms of the effect of oxygen on the surface. All the measurements were performed at room temperature.

3.5.1 Oxygen Exposure to MoO_x Thin Films

In this part, we will address the crucial issue, which has been a cause of concern and much debate among the experts. The beneficial effect of MoO_x insertion layer is well established but there were two completely different explanations for this enhancement. The pivotal point in resolving the discrepancy is the WF of MoO_x insertion layer. The reported values of WF are in a range between 5.3 and 6.9 eV. It is imperative to resolve the discrepancy in order to understand how to control the

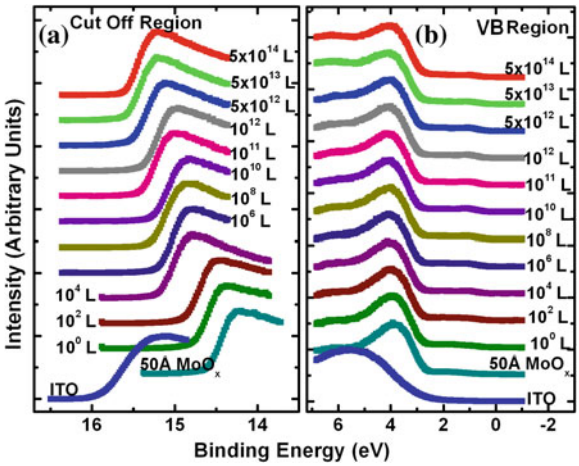

Fig. 3.17 Energy level evolution of oxygen exposed MoO_x film. The presented UPS data are for ITO, 50 Å MoO_x, from 1L, to 5×10^{14} L oxygen exposure (from [44])

device fabrication and to obtain consistent device performance. Our contribution is to find that the vacuum deposited MoO_x film starts with high initial WF values, but with oxygen exposure the surface WF is gradually reduced to substantially lower values.

In Fig. 3.17, the energy level evolution of 50 Å MoO_x film on ITO are presented as increasing amount of oxygen exposure. The cut off and the valence band regions of the UPS data are presented in Fig. 3.17a, b, respectively. Short bars are placed at the centroid of MoO_x VB peaks to track the shift in the peak BE values. The in situ OP treated ITO WF was found to be 5.58 eV. The deposition of 50 Å MoO_x led to a high increment of 1.16 eV in the surface WF. From Fig. 3.17b, a characteristic peak of MoO_x can be observed at $\sim$3.9 eV and VB onset was measured to be 2.66 eV. With oxygen exposure a continuous surface WF reduction was observed which saturated around $\geq 10^{13}$ L oxygen exposure. At the final step of 5×10^{14} L exposure the WF was measured to be 5.75 eV, which is 1 eV lower than the initial MoO_x WF. The VB peak as well had a smaller but continuous shift towards the higher BE and at the 5×10^{14} L oxygen exposure the VB peak was measured to be 4.04 eV.

In Fig. 3.18, the core energy level evolution of Mo $3d_{5/2}$ and $3d_{3/2}$ (a), and O1 s (b) are exhibited as a growing amount of oxygen exposure. Once again there was no appreciable shift in the peak binding position of both Mo 3d and O 1 s core levels. No significant peak broadening was observed in oxygen 1 s core levels from the initial thermally evaporated value of 1.78 eV. However, some peak broadening was again observed in Mo $3d_{5/2}$ peak. The initial full width at half maximum (FWHM) for Mo $3d_{5/2}$ peak was 1.63 eV, which became 2.00 eV for 5×10^{12} L oxygen exposure. The separation between the spin orbit splitting levels Mo $3d_{5/2}$ and $3d_{3/2}$ was 3.10 eV, which is consistent with reported values in the literature [71].

In Fig. 3.19, the growth of a gap state close to the Fermi energy level is shown as a function of oxygen exposure. A broad satellite feature peaked at $\sim$2.0 eV in the

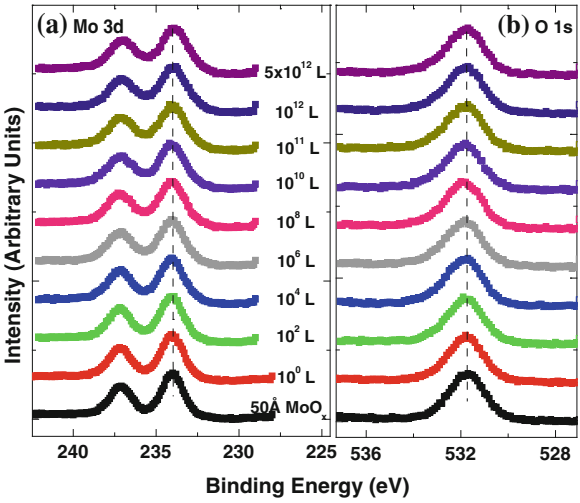

Fig. 3.18 XPS data for core level evolution of MoO_x film, **a** the Mo 3d and **b** the O 1 s core levels for, ITO, 50 Å MoO_x, 1L, to 5×10^{14} L oxygen exposure (from [44])

MoO_x spectrum is an artifact caused by the He β line that is at 23.09 eV and about 1/50 in intensity of the main He I line [51]. The growth of a gap state at ∼1.1 eV is observed with the oxygen exposure. The gap state peak is clearly visible from 10^4 L onwards which becomes more prominent with further air exposure. Nakayama et al. [68] have reported a similar interface electronic state at ∼1 eV upon initial deposition of MoO_x on F8BT which attenuated after 23 Å of MoO_x. The data in Fig. 3.19 suggest that the gap state observed by Nakayama et al. is from electron transfer from F8BT to MoO_x. At present it is not clear what effects this gap state has on the device performance. It is also interesting to note that Kroger et al. meticulously ruled out the existence of a gap state in MoO_x [57, 59]. The results indicate that the gap state indeed is not intrinsic to MoO_x. Instead, it is by charge transfer to MoO_x at the interface from interactions with other materials.

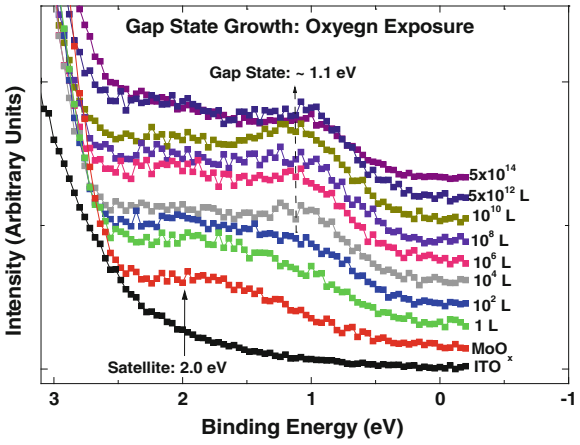

Fig. 3.19 The near HOMO region UPS data in situ oxygen plasma treated ITO, 50 Å MoO_x, from 1L to 5×10^{14} L oxygen exposure (from [44])

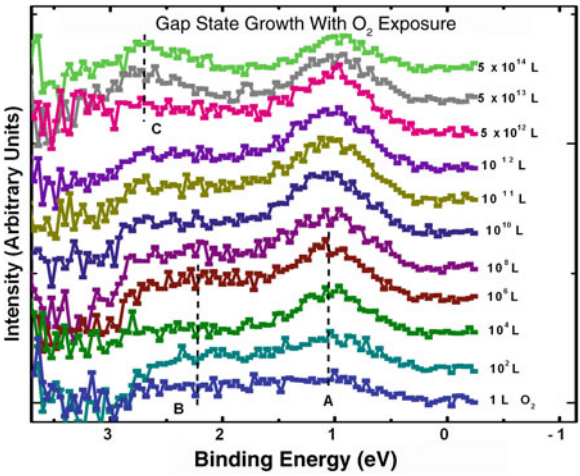

Fig. 3.20 The evolution of gap states with oxygen exposure (from [45])

In Fig. 3.20, the growth of gap states is presented with increasing oxygen exposure. The spectra of gap states are obtained by subtracting the valence region spectrum of as evaporated MoO_x film, as a background from the VB region of individual exposed spectrum. Before background subtraction the dominant oxygen 2p peak intensities were normalized and peak position of as evaporated spectrum was shifted to match the peak positions of each of the exposed spectrum. The gap state "A" at around $\sim$1.1 eV, is dominant throughout the measurements. Initially the intensity of the gap state "A" increases rapidly with the exposures and then it saturates around 10^{10} Langmuir (L) exposure. Beyond 10^{10} L exposures the intensity starts to decrease. A low intensity gap state around 2.3 eV is also observed at an early stage of exposure. The intensity of gap state "B" is observed to be maximum at 10^6 L exposure, and thereafter it starts to diminish. The third gap state marked as "C" develops at a mature exposure stage around $\sim$2.8 eV. At 5×10^{14} L exposure, the intensity of the gap state "C" is comparable to the gap state "A".

3.5.2 Air Exposure to MoO_x Films

After establishing the WF reduction of MoO_x film upon exposure to oxygen, in this part the effect of air exposure on MoO_x films will be discussed. Air exposure experiment along with the previous oxygen exposure experiment would allow the decoupling of the effect of oxygen molecules and humidity on the surface of MoO_x film. It was found that the vacuum deposited MoO_x films also started with high initial WF values, but with air exposure the surface WF gradually reduced to substantial lower values.

In Fig. 3.21, the UPS spectra of the MoO_x on ITO are presented as a function of the air exposure. Figure 3.21a, b show the cut off and the valence band regions of

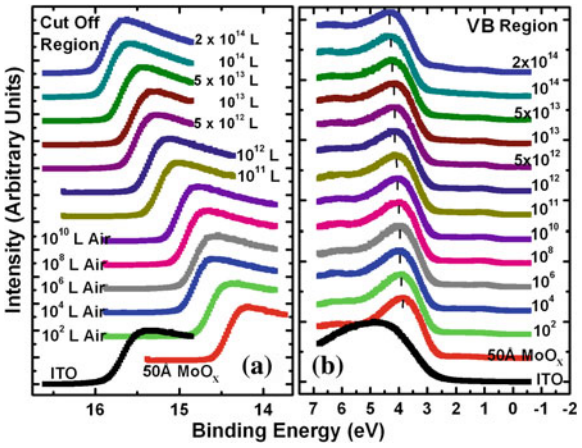

Fig. 3.21 UPS data for ITO, 50 Å MoO_x, from 10^2 L to 2×10^{14} L air exposure **a** the cut-off region and **b** the VB region (from [43])

the UPS data, respectively. Short bars are placed at the centroid of MoO_x VB peaks to track the shift in the peak BE values. The in situ OP treated ITO WF was measured to be 5.50 eV which increased to 6.75 eV upon the deposition of 50 Å MoO_x. From Fig. 3.21b, a characteristic peak of MoO_x can be observed at ~3.91 eV and VB onset is measured to be 2.69 eV. With air exposure the surface WF kept continuously decreasing and at the final step of 2×10^{14} L exposure the surface WF was measured to be 5.32 eV, which is 1.44 eV lower than the initial surface WF. The VB peak has a smaller but continuous shift towards higher BE and at the 2×10^{14} L exposure the VB peak is measured to be 4.33 eV, about 0.42 eV higher than the initial unexposed value.

In Fig. 3.22, the binding energy evolution of the core levels of Mo $3d_{5/2}$ and $3d_{3/2}$ (a), and O 1 s (b) are presented as the air exposure increases. It is straight forward to conclude that no significant core level peak shift has occurred due to the

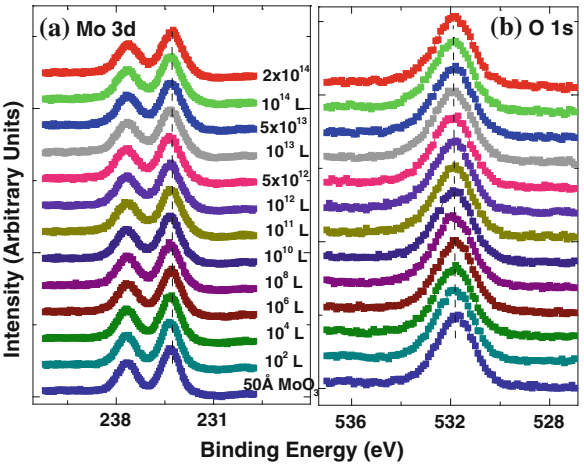

Fig. 3.22 XPS data for, **a** the Mo 3d and **b** the O 1 s core level for, ITO, 50 Å MoO_x, 10^2 L, 2×10^{14} L air exposure (from [44])

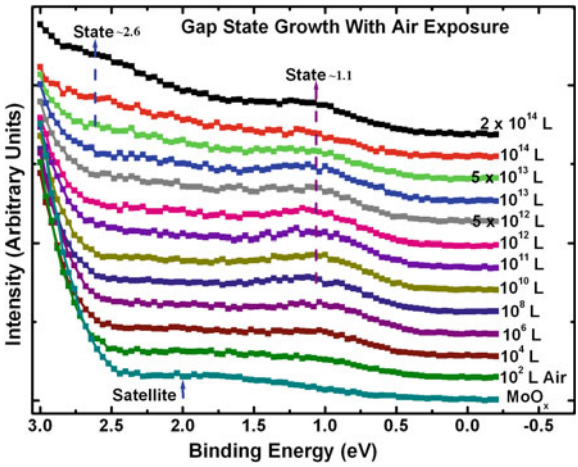

Fig. 3.23 Near VB region of 50 Å MoO_x, for 10^2 L to 2×10^{14} L air exposure (from [43])

air exposure. The FWHM of O 1s peak is 1.8 eV. Not only the peak BE but also the FWHM remained the same for O 1s core level. The FWHM for Mo $3d_{5/2}$ peak in the beginning is found to be 1.6 eV. With air exposure however, FWHM for the Mo $3d_{5/2}$ peak keeps increasing. At the final 2×10^{14} L air exposure it is calculated to be 1.9 eV. The separation between spin orbit splitting levels Mo $3d_{5/2}$ and $3d_{3/2}$ is 3.10 eV which is consistent with reported values in the literature [32]. It is interesting to note that the core level positions remain unchanged during the exposure, in contrast to the valence peak shift of 0.42 eV toward higher binding energy. This indicates that the shift is confined to the valence states due to the adsorption of the gas molecules.

In Fig. 3.23, the growth of a gap state near the Fermi energy level is shown as a function of air exposure. The broad peak at ~2.0 eV is a satellite of the VB peak from the He β line at 23.09 eV from unfiltered He I (21.22 eV) ultraviolet photon source [33]. With the air exposure the gap state at ~1.1 eV grows. The gap state peak is clearly visible from 10^4 L onwards which becomes more prominent with further air exposure. It can be understood that the electron transfer from the adsorbates to MoO_x dopes the latter at the surface, and as a result the VB peak of MoO_x shifts downward by 0.43 eV as shown in Fig. 3.21. From this figure it is clear that the gap state is not intrinsic to the MoO_x but originates from electron transfer from adsorbates sticking to the MoO_x film at the surface.

In Fig. 3.24, the evolution of gap states in the VB region is presented with increasing air exposure on a 50 Å MoO_x film. In the figure the growth of a gap state is observed at <1.0 eV, marked as "D" in the figure, which is similar to the gap state in the previous subsection. Initially the intensity of the state "D" increases sharply with air exposures and then it saturates around 10^8 L exposure. The gap state "D" is dominant until 10^{12} L exposure. Another gap state at ~2.3 eV is also observed, which is similar to the state 'B' of the previous subsection. Initially the intensity of the state is low. The gap state marked as 'F' develops at a mature exposure stage

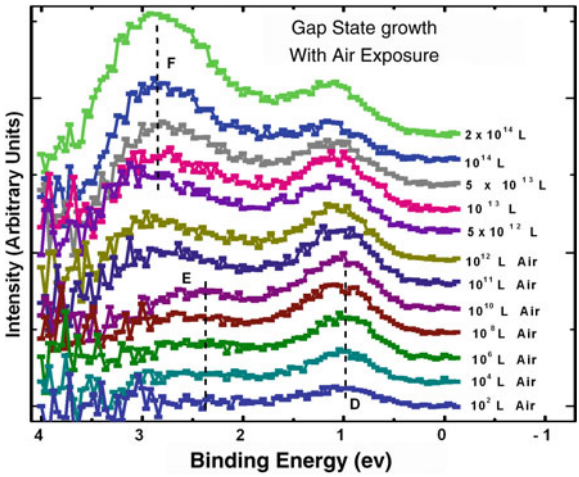

Fig. 3.24 The evolution of gap states with air exposure (from [45])

around ~2.9 eV. At the final air exposure, the intensity of the 'F' state is dominant in the spectrum.

3.5.3 Comparison of Air Versus Oxygen Exposure

In Fig. 3.25, the work function is plotted as a function of exposure in a logarithmic scale. The square data points are for the air exposed film and open circles for the oxygen exposed film. The inset in Fig. 3.25 shows WF versus exposure in a linear scale. The WF for OP treated ITO substrates were 5.50 and 5.58 eV for the air and oxygen exposed films, respectively. The air exposure resulted in lower surface WF values. At the final 2×10^{14} L air exposure the surface WF was measured to be 5.32 eV. The oxygen exposure also results in a faster, but otherwise similar surface WF decrement trend up to 10^{13} L exposure. The similarity of the WF evolution indicates that oxygen adsorption is the main cause for the WF decrease in both air and oxygen exposure at this stage, and the contribution from nitrogen is insignificant in comparison. At the final oxygen exposure of 5×10^{14} L, the surface WF was measured to be 5.75 eV. The inset clearly shows that the surface work functions of both the films have reached a near saturation region. In the inset it is observed that the near saturation region is in early 10^{14} L exposure for both air and oxygen exposed MoO_x films. However, the WF reduction is about 40 % more for air-exposed film than that of oxygen exposed film. This additional reduction in WF is attributed to the absorption of moisture in air exposed film for exposure $>10^{13}$ L. The study suggests that lower values of the WF reported previously are most likely due to exposure of the samples to the ambient prior to the UPS measurements. It is important to notice here that thermally evaporated molybdenum tri-oxide in vacuum

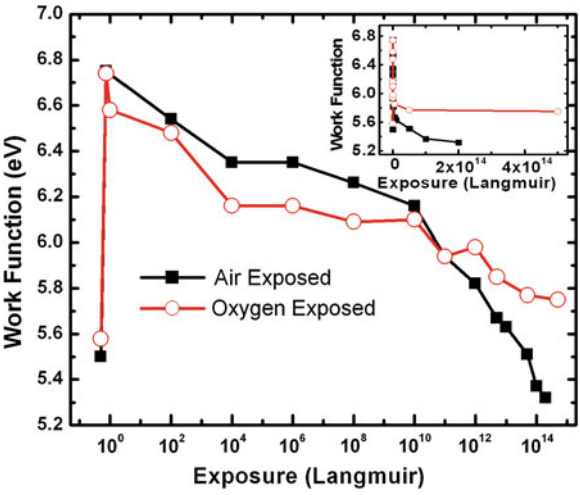

Fig. 3.25 Work function versus exposure (from [43])

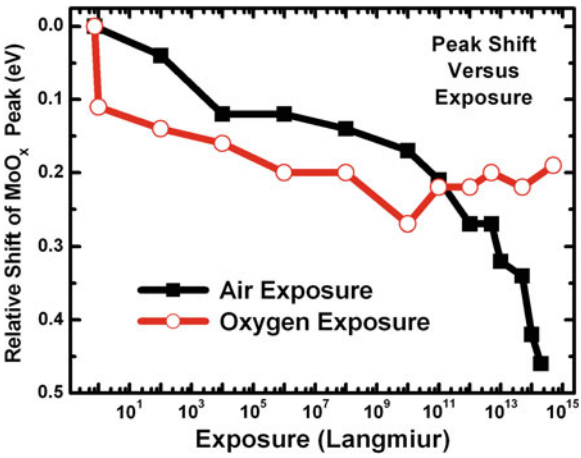

Fig. 3.26 Relative shifts of MoO_x VB peak with air and oxygen exposures

is likely to form oxygen deficient film. Our XPS analysis indicates that oxygen exposure is not an efficient way to compensate this deficiency.

In Fig. 3.26, the shift of VB peak of MoOx film is illustrated with increasing air and oxygen exposure. The observed trend of shift of VB peak is quite similar to the trend of WF reduction, but the amount is about a quarter of WF reduction. The VB peak also manifests saturation with oxygen exposures beyond 10^{11} L, while shift in the air exposed film continues much beyond 10^{11} L air exposures.

The reduction in the WF and growth of the gap state are consistent to a physical model of electron transfer from adsorbed oxygen to MoO_x, forming an interface dipole layer pointing toward the MoO_x surface. As the oxygen ionization potential is high (12.06 eV), the dielectric screening by the MoO_x has to be included to

facilitate such a charge transfer [72]. Below $\leq 10^{13}$ L exposure charge transfer from oxygen molecule seems to be the dominant mechanism. Beyond 10^{13} L of air exposure, the reduction of the work function is most likely from the polarization of the adsorbed water molecule, as the gap state intensity no longer increases at this stage as shown in Fig. 3.24.

The UPS and XPS studies illustrated the evolution of the electronic structure of the MoO_x during the interface formation with organic materials and with exposure to oxygen or air. It can be concluded that the high WF of MoO_x is the dominant factor that brings the HOMO level of the organic toward the Fermi level of the anode and creates a band-bending-like region that encourages holes to drift toward the anode. The reduction of WF by gas exposure can be clearly correlated to deteriorating device performance [43], The low CB edge of MoO_x should also be an important factor contributing to the carrier transport [69]. However, its significance is secondary in comparison to the WF as the gas exposure brings the frontier orbitals even lower by $\sim$0.4 eV while the device performance is deteriorated. It can also be concluded that the gap state is associated with the electron doping of MoO_x by organic materials or other adsorbates. It grows and saturates at high gas exposures, opposite to the trend of the device performance.

In Fig. 3.27, relative intensities of the gap states are presented as a function of the exposures. The intensities of the gap states with the oxygen exposures are presented in Fig. 3.27a, and with the air exposures are presented in Fig. 3.27b. Comparing the evolution of states "A" and "D", both the gap states can be assign to the effect of oxygen on the MoO_x films. While comparing the evolution of states

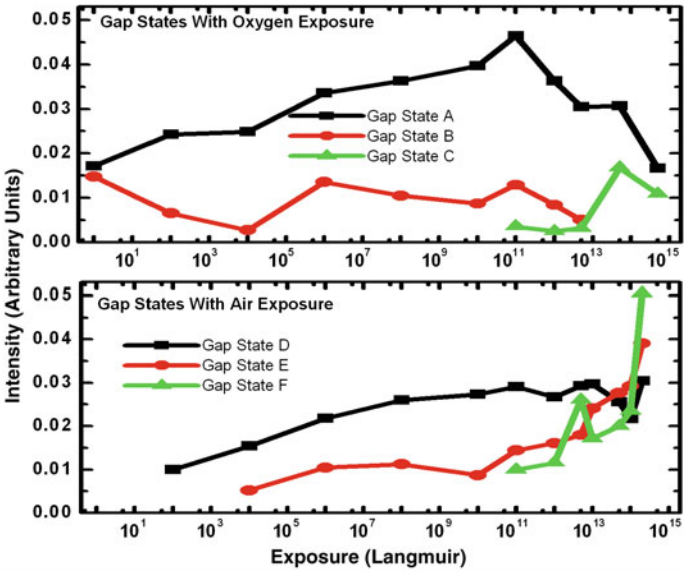

Fig. 3.27 Comparison of gap states with air and oxygen exposures (from [45])

"C" and "F", the origin of these states can be attributed to the effect of moisture on the MoO_x films. Earlier it was discussed that the WF reduction in exposed MoO_x films is a two stage process. The first stage of reduction is caused by adsorption of oxygen on the MoO_x films (25). This stage reduces the WF from 6.8 to ~5.8 eV. The second stage of WF drop is caused by the adsorption of moisture on the MoO_x films. It is interesting to note that a gap state similar to the "A" and the "D" states, also around 1 eV has been reported earlier by Nakayama et al. [73] Therefore, it can be concluded that the first stage WF drop, caused by oxygen exposure, must be related to the charge transfer between adsorbed oxygen and the surface of MoO_x film.

A number of studies have reported deleterious effects of exposure and low vacuum processing of TMO films, as demonstrated in Fig. 3.28. In one report, a substantial degradation in a hole only device performance has been demonstrated with a 15 min (~7×10^{11} L) air exposure of the MoO_x film (Fig. 3.28a) [43]. The exposures over 10^{11} L also mark the appearance of the gap state "F" in Fig. 3.24. Since the growth of the gap state is caused by moisture, as discussed earlier, the major degradation in the device is attributed to the gap state. In another report, a

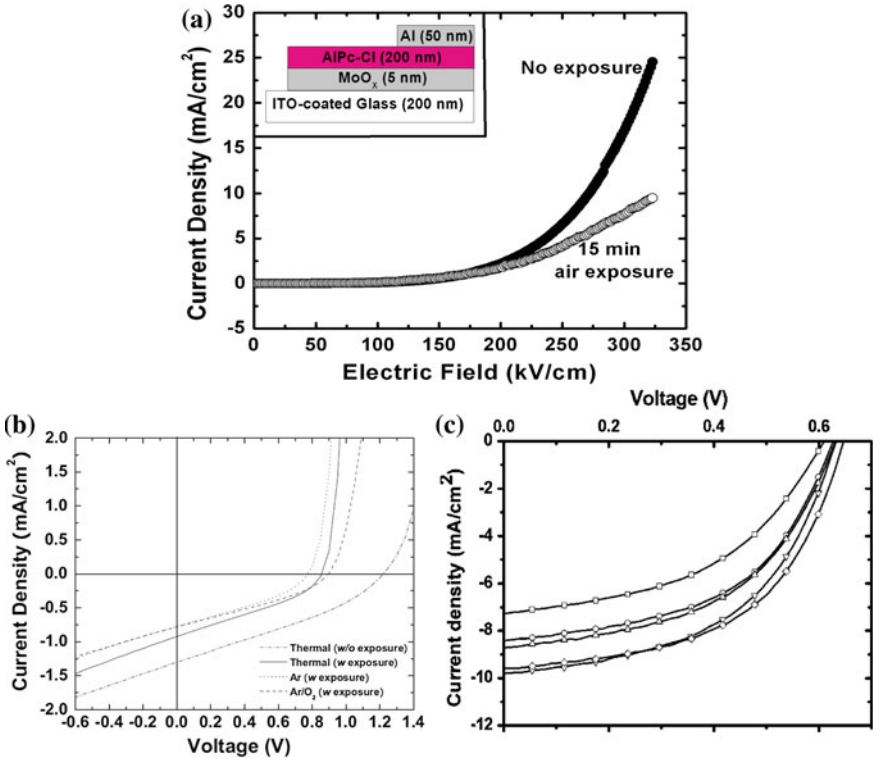

Fig. 3.28 Devices with and without the exposure of MoO_x films **a** from [43], **b** from [74], and **c** from [75]

similar degradation was observed in the OPV performance by a 30 min ($\sim 1.4 \times 10^{12}$ L) air exposure (Fig. 3.28b) [74]. In Fig. 3.28c degradation in the OPV performance is demonstrated with low vacuum processing of TiO_x inter-layer [75]. Symbols in the figure represent the pressure during the fabrication of TiO_x layer (□: 6.5×10^{-5} Torr; ○: 1.5×10^{-5} Torr; ▲: 6.5×10^{-6} Torr;▼: 1.5×10^{-6} Torr; ◇: 6.5×10^{-7} Torr). It should be noted that both Nakayama et al. [68] and Maria et al. [76] have attributed the improvement of device performance to the presence of the gap state similar to the "D" state around 1 eV. Our understanding is that the WF reduction from high (6.8 eV) to moderate ($\sim$5.8 eV) is coupled with the growth of the gap state for O_2 exposure and may not be significantly deleterious to devices, since the reduced WF is still higher than the ionization potential of most of the organic semiconductors. The appearance of the gap state "F" which further reduces the WF from $\sim$5.8 to 5.4 eV is probably the most harmful to devices Meyer et al. [77]. have also reported no significant effect on the device performance with an air exposure of 3 min (10^{11} L), probably just before the appearance of the gap state "F". However, at present an exact correlation of gap states is not well established and further investigations are required to ascertain that.

3.6 Summary

The metal/organic interface plays a critical role in an organic device. Efficient charge transport across the metal/organic interface is pivotal to enhance efficiency of devices. Therefore, it is crucial to understanding the electronic structure and the interface formation. In this chapter, we have compiled our investigations on the metal/organic interface formation with and without thin metal oxide inter-layer films.

We have presented the effect of a 100 Å MoO_x inter-layer at the CuPc/ITO. We have also demonstrated the electronic structure evolution of interfaces with 0–300 Å stepped MoO_x inter-layers between ITO and AlPc-Cl. We found out that the high work function of the metal oxide inter-layer pulls up the energy levels of organic side towards lower binding energy at the interface, resulting in reduced hole injection barrier and band-bending-like situation in the organic material. The band-bending-like phenomenon introduces a drift electric field inside the organic layer. This built in drift field enhances hole extraction to the ITO and thus enhancing the performance of devices with a thin MoO_x inter-layer. The optimum thickness of MoO_x inter-layer was established to be a few nm.

We have illustrated the effect of air and oxygen exposure on MoOx films. We have conclusively resolved the controversy for MoOx work function values. We found out that the vacuum evaporated MoOx films started with high work functions ($\sim$6.8 eV), which gradually reduced up to 5.8 eV with increasing oxygen exposures and up to 5.4 eV with increasing air exposure. Three gap states were also identified with the exposures.

Acknowledgments The authors would like to acknowledge the support of the National Science Foundation Grant no. DMR-1006098.

References

1. J. Bardeen, W.H. Brattain, Phys. Rev. **74**, 230 (1948)
2. S. M. Sze, Curr. Contents Eng. Technol. Appl. Sci **28** (1982)
3. J. Millman, *Integrated Electronics* (McGraw Hill, New Delhi, 1991)
4. Z. Kafafi, *Organic Electroluminescence* (CRC Taylor & Francis, Boca Raton, 2005)
5. G. Li, R. Zhu, Y. Yang, Nat. Photonics **6**, 153 (2012)
6. S.R. Forrest, MRS Bull. **30**, 28 (2005)
7. G.P. Crawford, *Flexible Flat Panel Displays* (Wiley, Hoboken, 2005)
8. Sony Website, www.sony.com/oledmonitors
9. Samsung Website, www.oled-info.com/samsung-oled
10. DOE Website, in solid state lighting
11. M. Pope, C.E. Swenberg, Annu. Rev. Phys. Chem. **35**, 613 (1984)
12. C.W. Tang, S.A. Vanslyke, Appl. Phys. Lett. **51**, 913 (1987)
13. C.W. Tang, S.A. Vanslyke, C.H. Chen, J. Appl. Phys. **65**, 3610 (1989)
14. R.H. Friend et al., Nature **397**, 121 (1999)
15. M.G. Helander, Z.B. Wang, J. Qiu, M.T. Greiner, D.P. Puzzo, Z.W. Liu, Z.H. Lu, Science **332**, 944 (2011)
16. Z.B. Wang, M.G. Helander, J. Qiu, D.P. Puzzo, M.T. Greiner, Z.M. Hudson, S. Wang, Z.W. Liu, Z.H. Lu, Nat. Photonics **5**, 753 (2011)
17. F. So, J. Kido, P. Burrows, MRS Bull. **33**, 663 (2008)
18. C.W. Tang, Appl. Phys. Lett. **48**, 183 (1986)
19. J.G. Xue, S. Uchida, B.P. Rand, S.R. Forrest, Appl. Phys. Lett. **84**, 3013 (2004)
20. Y. Sun, G.C. Welch, W.L. Leong, C.J. Takacs, G.C. Bazan, A.J. Heeger, Nat. Mater. **11**, 44 (2012)
21. G. Yu, J. Gao, J.C. Hummelen, F. Wudl, A.J. Heeger, Science **270**, 1789 (1995)
22. N. Website, (2012) http://www.nrel.gov/ncpv/images/efficiency_chart.jpg
23. V.C. Sundar, J. Zaumseil, V. Podzorov, E. Menard, R.L. Willett, T. Someya, M.E. Gershenson, J.A. Rogers, Science **303**, 1644 (2004)
24. G. Horowitz, J. Mater. Res. **19**, 1946 (2004)
25. V. Podzorov, S.E. Sysoev, E. Loginova, V.M. Pudalov, M.E. Gershenson, Appl. Phys. Lett. **83**, 3504 (2003)
26. V. Podzorov, V.M. Pudalov, M.E. Gershenson, Appl. Phys. Lett. **82**, 1739 (2003)
27. C.R. Crowell, Surf. Sci. **13**, 13 (1969)
28. E.M. Liston, L. Martinu, M.R. Wertheimer, J. Adhes. Sci. Technol. **7**, 1091 (1993)
29. C. Sequin, E. Baldinge, Solid-State Electronics **13**, 1527 (1970)
30. S. Tokito, K. Noda, Y. Taga, J. Phys. D-Appl. Phys. **29**, 2750 (1996)
31. V. Shrotriya, G. Li, Y. Yao, C.W. Chu, Y. Yang, Applied Physics Letters **88**, 073508 (2006)
32. M.D. Irwin, B. Buchholz, A.W. Hains, R.P.H. Chang, T.J. Marks, Proc. Natl. Acad. Sci. USA **105**, 2783 (2008)
33. I. Irfan, W. Xia, H. Lin, H.J. Ding, C.W. Tang, Y.L. Gao, Thin Solid Films. **520**:1988 (2012)
34. X.N. Li, D.W. Niles, F.S. Hasoon, R.J. Matson, P. Sheldon, J. Vac. Sci. Technol.a-Vac. Surf. Films **17**, 805 (1999)
35. H. Lin, W. Irfan, HNWu Xia, Y. Gao, C.W. Tang, Sol. Energy Mater. Sol. Cells **99**, 349 (2012)
36. W. Chen, S. Chen, H. Huang, D. C. Qi, X. Y. Gao, A. T. S. Wee, Appl. Phys. Lett. **92** (2008)
37. W. Chen, H. Huang, S. Chen, Y.L. Huang, X.Y. Gao, A.T.S. Wee, Chem. Mater. **20**, 7017 (2008)

38. W. Chen, D.-C. Qi, H. Huang, X. Gao, A.T.S. Wee, Adv. Funct. Mater. **21**, 410 (2011)
39. W. Chen, D. Qi, X. Gao, A.T.S. Wee, Prog. Surf. Sci. **84**, 279 (2009)
40. Y.L. Gao, Mater. Sci. Eng. R-Rep. **68**, 39 (2010)
41. H. Ishii, K. Sugiyama, E. Ito, K. Seki, Adv. Mater. **11**, 605 (1999)
42. I. Irfan, H. Ding, Y. Gao, D. Y. Kim, J. Subbiah, F. So, Appl. Phys. Lett. **96** (2010)
43. Irfan, H. Ding, Y. Gao, C. Small, D. Y. Kim, J. Subbiah, and F. So, App. Phys. Lett. **96** (2010)
44. I. Irfan, H. Ding, F. So, Y. Gao, J. Photonics Energy **1**, 011105 (2011)
45. I. Irfan, Y. Gao, J. Photonics Energy Accepted **2**, 021213 (2012)
46. D. Y. Kim, J. Subbiah, G. Sarasqueta, F. So, H. Ding, Irfan, Y. Gao, Appl. Phys. Lett. **95** (2009)
47. A. Einstein, Ann. Phys. **17**, 132 (1905)
48. H.Y. Fan, Phys. Rev. **68**, 43 (1945)
49. F. Reinert, S. Hufner, New J. Phys. **7** (2005)
50. M.P. Seah, W.A. Dench, Surf. Interface Anal. **1**, 2 (1979)
51. J.B. Peel, E.I. Vonnagyfelsobuki, J. Chem. Educ. **64**, 463 (1987)
52. P.T. Andrews, I.R. Collins, Phys. Scr. **T29**, 116 (1989)
53. D.X. Dai, J.H. Hu, Z.J. Yang, Vacuum **41**, 525 (1990)
54. F.J. Himpsel, Surf. Sci. Rep. **12**, 1 (1990)
55. P.D. Johnson, S.L. Hulbert, Rev. Sci. Instrum. **61**, 2277 (1990)
56. N.V. Smith, Rep. Prog. Phys. **51**, 1227 (1988)
57. M. Kroeger, S. Hamwi, J. Meyer, T. Riedl, W. Kowalsky, A. Kahn, Appl. Phys. Lett. **95**, 123301 (2009)
58. F. Wang, X. Qiao, T. Xiong, D. Ma, Org. Electron. **9**, 985 (2008)
59. M. Kroger, S. Hamwi, J. Meyer, T. Riedl, W. Kowalsky, A. Kahn, Org. Electron. **10**, 932 (2009)
60. D.Y. Kim, G. Sarasqueta, F. So, Sol. Energy Mater. Sol. Cells **93**, 1452 (2009)
61. L. Cattin, et al., J. Appl. Phys. **105**, 034507 (2009)
62. F. Cheng, G. Fang, X. Fan, N. Liu, N. Sun, P. Qin, Q. Zheng, J. Wan, X. Zhao, Sol. Energy Mater. Sol. Cells **95**, 2914 (2011)
63. D.W. Zhao, S.T. Tan, L. Ke, P. Liu, A.K.K. Kyaw, X.W. Sun, G.Q. Lo, D.L. Kwong, Sol. Energy Mater. Sol. Cells **94**, 985 (2010)
64. W. Zeng, K.S. Yong, Z.M. Kam, Z.-K. Chen, Y. Li, Synth. Met. **161**, 2748 (2012)
65. T. Hori, T. Shibata, V. Kittichungchit, H. Moritou, J. Sakai, H. Kubo, A. Fujii, M. Ozaki, Thin Solid Films **518**, 522 (2009)
66. J. Subbiah, C.M. Amb, I. Irfan, Y. Gao, J.R. Reynolds, F. So, ACS Appl Mater Interfaces **4**, 866 (2012)
67. J. Subbiah, D. Y. Kim, M. Hartel, F. So, Applied Physics Letters **96**, 063303 (2010)
68. Y. Nakayama, K. Morii, Y. Suzuki, H. Machida, S. Kera, N. Ueno, H. Kitagawa, Y. Noguchi, H. Ishii, Adv. Funct. Mater. **19**, 3746 (2009)
69. M. Kroeger, S. Hamwi, J. Meyer, T. Riedl, W. Kowalsky, A. Kahn, Appl. Phys. Lett. **95**, 123301 (2009)
70. Y. Kinoshita, R. Takenaka, and H. Murata, Applied Physics Letters **92**, 123301 (2008)
71. F. Werfel, E. Minni, J. Phys. C-Solid State Phys. **16**, 6091 (1983)
72. M. Sayer, A. Mansingh, J.B. Webb, J. Noad, J. Phys. C-Solid State Phys. **11**, 315 (1978)
73. Y. Nakayama, K. Morii, Y. Suzuki, H. Machida, S. Kera, N. Ueno, H. Kitagawa, Y. Noguchi, H. Ishii, Adv. Funct. Mater. **19**, 3746 (2009)
74. M. Zhang, Irfan, H. Ding, Y. Gao, and C. W. Tang, Appl. Phys. Lett. **96** (2010)
75. S. Yoon, Appl. Phys. Lett. **92**, 143504 (2008)
76. V. Maria, Appl. Phys. Lett. **98**, 123301 (2010)
77. J. Meyer, A. Shu, M. Kroeger, A. Kahn, Appl. Phys. Lett. **96** (2010)

Chapter 4
Theoretical Modeling of the Optical and Electrical Processes in Polymeric Solar Cells

Zhigang Shuai, Lingyi Meng and Yuqian Jiang

Abstract The elementary processes occurred in organic solar cell include optical absorption, excitation energy transfer, photoinduced charge transfer, charge transport, and charge collection at the electrodes. Even though modern quantum chemistry has achieved great success in electronic structure calculations, it is still not enough to describe these elementary processes at first-principles. We describe in this chapter our recent progresses toward quantitative theoretical understanding of the optical and electronic processes in organic photovoltaic materials, including optical absorption and emission spectra for conjugated oligomers, energy transfer in polymers, charge transport in organic semiconductors, and device modeling of heterojunction solar cells based on dynamic Monte Carlo simulation and the continuum model.

4.1 Introduction

Elementary electronic processes in organic and polymeric solids have been intensively investigated over the past decades [1, 2]. Carbon atom is the basic element in these materials, where 4 valence electrons form chemical bonds, sigma (σ) or pi (π) bonds, the former forms the skeleton for the conjugated polymer and the latter contributes mostly to the electronic valence and conduction bands. The electronic function comes from the unsaturated π-electron. The prototypical conjugated polymer is polyacetylene with a repeat unit of (CH) group connected alternatively by single and double bond, denoted as $(CH)_N$. Since Heeger, MacDiarmid and

Z. Shuai (✉) · Y. Jiang
MOE Key Laboratory of Organic OptoElectronics and Molecular Engineering, Department of Chemistry, Tsinghua University, 100084 Beijing, China
e-mail: zgshuai@tsinghua.edu.cn

Z. Shuai · L. Meng
Collaborative Innovation Center of Chemistry for Energy Materials, Xiamen University, 361005 Xiamen, China

Y. Yang and G. Li (eds.), *Progress in High-Efficient Solution Process Organic Photovoltaic Devices*, Topics in Applied Physics 130,
DOI 10.1007/978-3-662-45509-8_4

Shirakawa discovered that polyacetylene can be doped to become conducting polymer [3, 4], tremendous efforts have been focused in this field, which led to the discoveries of organic and polymeric nonlinear optical phenomena [5], polymer light-emitting diodes [6] and flexible display [7], polymer lasing [8–10], organic and polymeric field effect transistor [11, 12], chemico- and biosensors [13], and most impressively, polymer solar cells [14] as exclusively discussed in this book. We have gained fundamental understandings of the electronic processes from pi-electron conjugation to Peierls instability in one-dimensional system [15], electron-phonon coupled nonlinear excitations like soliton and polaron [16], structure property relationship for the nonlinear optical response [17]. However, we are still at a stage in debating the nature of the photoexcitation [18] and in improving our understandings of the charge and energy excitation transfer processes [19] as well as electronic structures at various interfaces [20].

Polymer bulk heterojunction structure for solar cells has been proposed for a while [21] which drove the field to a much higher level and the power conversion efficiency has been increased ten-fold during the past decade. However, the more and more complex materials structures have only obscured our fundamental understanding in terms of the elementary processes. Our knowledge on the photoinduced charge generation [22], charge transport mechanism [23], and influences of the various interfaces is quite limited and often quite controversial. This in turn hinders the further improvements of the performances for electronic devices. In this chapter, we do not intend to discuss the controversial issues in this field, even though some progresses have been achieved but without definite answers. Instead, we focus on two subjects which are both important and practical for OPV materials design and device improvement, namely, the first-principles optical absorption and emission spectra calculation and the device modeling.

The optical absorption spectra for conjugated polymer or oligomer have strong impact on the portion of photons absorbed from solar emission. Optical emission after photoexcitation consists of an important factor for excitation energy transfer: in a localized exciton picture, the energy transfer can be simply viewed as emission reabsorption so that the spectra overlap between absorption and emission becomes the Franck-Condon factor for the Förster energy transfer rate. Such rate along with the exciton life time determines the exciton diffusion length, which is general short in conjugated polymers, limiting the power conversion efficiency. We will discuss the theoretical aspects on how to compute the optical absorption and emission spectra as well as excited state life time from first-principles. The next process after exciton migration is the charge generation or charge separation at the micro-interface between donor and acceptor. In general, the photoexcitation forms a bound electron-hole pair, or exciton, useless for electrical current. When such species reach the donor/acceptor interface, hole stays in donor (polymer) and the electron moves to acceptor. This process is extremely fast [24] and very much morphology dependent [25]. Such bound pair, sometimes termed as interchain polaron pair, can contribute to current only after further dissociation, subject to charge recombination for energy loss at the same time. The further charge dissociation process is driven by the internal electric field [26]. There have been

tremendous investigations on the charge transport processes in organic and polymeric materials. Often, phenomenological disorder models, most notably proposed by Bassler [27] and more recently developed by Blom and coworkers [28, 29], have been extensively applied. The fundamental assumptions are that there are considerable amounts of disorders with a Gaussian distributed energy levels and the charge hops through these disordered sites following the Miller-Abraham formalism by the phonon-assisted mechanism. Indeed, through multi-scale first-principles calculation on disordered polymers, Vukmirovic and Wang found that the typical charge mobility ranges 10^{-6} to 10^{-4} cm^2/Vs [30] and both the temperature and field-strength dependence from such disordered model agree with experiments on polymer electronic device. On another hand, if one views polymer with rigid and regular skeleton, the charge mobility along the conjugation chain direction is usually around a few hundred cm^2/Vs [31]. And if there forms ordered interchain stacking structure at microscale, for instance, for regioregular polythiophene, the charge mobility along the π–π stacking direction has been estimated to be around a few cm^2/Vs from deformation potential theory calculation [32]: earlier experimental results demonstrated that the microscale ordering in polymer can increase the charge mobility from 10^{-6} to around 10^{-2} to 10^{-1} cm^2/Vs, opening the door to plastic electronics [33]. However, recent progresses are such fascinating that the charge mobility reaches 1–10 cm^2/Vs [34, 35], challenging our present understanding based on disorders. On another hand, the charge transport in molecular crystals or films field-effect-transistor has become a central issue recent years [23]. Our theoretical understanding has been greatly promoted through first-principles calculation coupled with charge transfer theory or charge diffusion dynamics: now, quantitative prediction of charge mobility for organic materials becomes possible [36, 37]. Since there have been extensive reviews on the charge transport phenomena, [23, 36–39], we will not discuss such issue here, even though, the charge transport within donor-acceptor heterojunction materials is still far from clear.

In this chapter, we discuss two theoretical aspects on organic photovoltaics, one on the optical spectra, absorption and emission, and the excited state lifetime, which are closely correlated with exciton diffusion length, and another on the device modeling either from dynamic Monte Carlo simulation and continuum device model.

4.2 Optical Properties of Conjugated Polymers: Parameters for Determining the Exciton Diffusion

Optical property of conjugated polymers consists of optical absorption and emission, optical excitation and decay lifetime, as well as excitation energy transfer, each of which is essential to photovoltaic process. The exciton diffusion length is expressed as $L_{ex} = \sqrt{ZD\tau}$, where Z is a constant related to spatial dimension of random walk and τ is the exciton lifetime $\tau = 1/(k_r + k_{nr})$, k_r and k_{nr} are radiative and non-radiative decay rates. Under the hopping picture, the diffusion coefficient D can

be approximated as $D = a^2 k_{et}$, where a is the intersite spacing. In Förster energy transfer model, k_{et} is determined by the overlap between the emission and the absorption spectrum times the intermolecular electronic coupling term for exciton. Long exciton diffusion length means efficient charge dissociation. Thus, polymer emission and absorption spectra as well as exciton decay rates are essential for determining the solar cell performance.

4.2.1 First-Principles Calculations of Optical Absorption and Emission Spectra

The optical absorption is described by the absorption cross section, defined as the rate of photon energy absorbed per molecule per unit radiant energy flux,

$$\sigma_{\text{abs}}(\omega) = \frac{4\pi^2\omega}{3c}\sum_{v_i,v_f} P_{iv_i}(T)\left|\left\langle \Theta_{fv_f}\left|\vec{\mu}_{fi}\right|\Theta_{iv_i}\right\rangle\right|^2 \delta\left(\hbar\omega - E_{fi} - E_{fv_f} + E_{iv_i}\right) \tag{4.1}$$

and inversely, the emission spectrum is defined as the differential spontaneous photon emission rate per molecule per unit frequency at ω

$$\sigma_{\text{em}}(\omega) = \frac{4\omega^3}{3c^3}\sum_{v_i,v_f} P_{iv_i}(T)\left|\left\langle \Theta_{fv_f}\left|\vec{\mu}_{fi}\right|\Theta_{iv_i}\right\rangle\right|^2 \delta\left(E_{if} + E_{iv_i} - E_{fv_f} - \hbar\omega\right) \tag{4.2}$$

Here we apply the Born–Oppenheimer approximation, vibronic states $|\Psi_{iv_i}\rangle$ and $|\Psi_{fv_f}\rangle$ are described by the products of the electronic states $|\Phi_i\rangle$, $|\Phi_f\rangle$ and the vibrational states $|\Theta_{iv_i}\rangle$, $|\Theta_{fv_f}\rangle$; i and f are labels of the initial and the final electronic states, respectively, and the corresponding vibrational quantum numbers are denoted by v_i and v_f. $P_{iv_i}(T)$ is the Boltzmann distribution function for the initial vibronic manifold. $\vec{\mu}_{fi} = \langle \Phi_f|\vec{\mu}|\Phi_i\rangle$ is the electric transition dipole moment: the interaction between light and molecule is described by the electric dipole approximation and the weak field limit (first-order perturbation). Around the equilibrium geometry, the vibrational states are given by the harmonic oscillator in the normal mode coordinate space. In general, the molecular ground state and the electronically excited state possess different potential energy surfaces. Namely, the vibrational frequency can be different even for the same mode. Since the transition moments in (4.1) and (4.2) should be evaluated in the same space, it is convenient to relate the two coordinate spaces through the Duschinsky rotation matrix:

$$Q_{ik} = \sum_{l}^{N} S_{i\leftarrow f,kl} Q_{fl} + \underline{D}_{i\leftarrow f,k} \tag{4.3}$$

where Q_{ik} is the vibrational coordinate for kth mode of the initial state, S is the Duschinsky rotation matrix and D is a the displacement vector connecting the minima of the two parabolas. That is, any one vibrational state vector in the initial (final) parabola can be regarded as a linear combination of all the vectors in the final (initial) parabola plus a rigid shift in origin, see Scheme 4.1. In addition, the electric dipole transition moment depends on the vibrational coordinate:

$$\vec{\mu}_{fi} = \vec{\mu}_0 + \sum_k \vec{\mu}_k Q_k + \sum_{k,l} \vec{\mu}_{kl} Q_k Q_l + \cdots \tag{4.4}$$

where the first term is coordinate independent, which is enough for strongly dipole allowed transition (Franck-Condon approximation, FC), the second term is the first-order expansion in the Taylor series (Herzberg-Teller term, HT). Substituting (4.4) into (4.1) and (4.2), and then Fourier transforming the delta-function, the optical spectrum function can be recast into the following forms (taking emission as example):

$$\sigma_{\mathrm{em}}(\omega) = \sigma_{\mathrm{em}}^{\mathrm{FC}}(\omega) + \sigma_{\mathrm{em}}^{\mathrm{FC/HT}}(\omega) + \sigma_{\mathrm{em}}^{\mathrm{HT}}(\omega) \tag{4.5}$$

$$\sigma_{\mathrm{em}}^{\mathrm{FC}}(\omega) = \frac{2\omega^3}{3\pi\hbar c^3} |\vec{\mu}_0|^2 \int_{-\infty}^{\infty} \mathrm{e}^{-i(\omega-\omega_{if})t} Z_{iv}^{-1} \rho_{\mathrm{em},0}^{\mathrm{FC}}(t,T)\mathrm{d}t \tag{4.6}$$

$$\sigma_{\mathrm{em}}^{\mathrm{FC/HT}}(\omega) = \frac{2\omega^3}{3\pi\hbar c^3} \sum_k \vec{\mu}_0 \cdot \vec{\mu}_k \int_{-\infty}^{\infty} \mathrm{e}^{-i(\omega-\omega_{if})t} Z_{iv}^{-1} \rho_{\mathrm{em},k}^{\mathrm{FC/HT}}(t,T)\mathrm{d}t \tag{4.7}$$

$$\sigma_{\mathrm{em}}^{\mathrm{HT}}(\omega) = \frac{2\omega^3}{3\pi\hbar c^3} \sum_{k,l} \vec{\mu}_k \cdot \vec{\mu}_l \int_{-\infty}^{\infty} \mathrm{e}^{-i(\omega-\omega_{if})t} Z_{iv}^{-1} \rho_{\mathrm{em},kl}^{\mathrm{HT}}(t,T)\mathrm{d}t \tag{4.8}$$

where Z_{iv} is the partition function, and

$$\rho_{\mathrm{em},0}^{\mathrm{FC}}(t,T) = \mathrm{Tr}\left[\mathrm{e}^{-i\tau_f \hat{H}_f} \mathrm{e}^{-i\tau_i \hat{H}_i}\right] \tag{4.9}$$

$$\rho_{\mathrm{em},k}^{\mathrm{FC/HT}}(t,T) = \mathrm{Tr}\left[Q_{fk} \mathrm{e}^{-i\tau_f \hat{H}_f} \mathrm{e}^{-i\tau_i \hat{H}_i}\right] \tag{4.10}$$

$$\rho_{\mathrm{em},kl}^{\mathrm{HT}}(t,T) = \mathrm{Tr}\left[Q_{fk} \mathrm{e}^{-i\tau_f \hat{H}_f} Q_{fl} \mathrm{e}^{-i\tau_i \hat{H}_i}\right] \tag{4.11}$$

are the three kinds of thermal vibration correlation functions. $\tau_f = t/\hbar$, $\tau_i = -i\beta - \tau_f$, and $\beta = (k_{\mathrm{B}}T)^{-1}$. Within the multi-dimensional harmonic oscillator model, (4.9–4.11) can be evaluated analytically with consideration of Duschinsky rotation effect [40, 41] and Herzberg-Teller [42]. All the quantities appeared in the

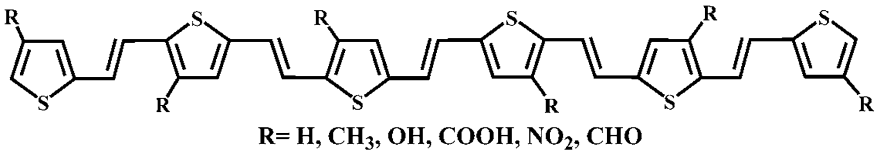

Scheme 4.1 Molecular structure of pristine and substituted PTV oligomers

formalisms can be obtained by modern quantum chemistry, such as vertical and adiabatic electronic excitation energies, vibrational frequency and normal modes at both ground state and excited state, transition electrical dipole moment and its first-order derivative with respect to normal mode. Duschinsky rotation matrix and the displacement vector appeared in (4.3) can be obtained by putting the ground state and the excited state molecular geometries in one common reference frame according to translational and rotational Eckart conditions [43].

4.2.2 Excited State Decay Rate: Radiative and Non-radiative

According to the Jablonski diagram, there are three main decay pathways from the lowest photoexcited state S_1 to the ground state: (i) the radiative decay from S_1 to S_0; (ii) the non-radiative internal conversion (IC) from S_1 to S_0 with a rate k_{IC}; (iii) the intersystem crossing (ISC) process from S_1 to the first triplet excited state (T_1) with a rate k_{ISC}.

The radiative decay rate can be simply expressed as the integration over the wavelength of the light emission spectrum:

$$k_r(T) = \int_0^\infty \sigma_{emi}(\omega, T) d\omega \tag{4.12}$$

The IC rate can be evaluated through Fermi's golden rule presented as:

$$k_{IC} = \frac{2\pi}{\hbar} \left| H'_{fi} \right|^2 \delta\left(E_{fi} + E_{fv_f} - E_{iv_i}\right) \tag{4.13}$$

Here the perturbation is the non-Born-Oppenheimer coupling:

$$H'_{fi} = -\hbar^2 \sum_l \left\langle \Phi_f \Theta_{fv_f} \left| \frac{\partial \Phi_i}{\partial Q_{fl}} \frac{\partial \Theta_{iv_i}}{\partial Q_{fl}} \right\rangle \right. \tag{4.14}$$

Under Condon approximation, (4.14) is evaluated as

$$H'_{fi} = \sum_{l} \langle \Phi_f | \hat{P}_{fl} | \Phi_i \rangle \langle \Theta_{fv_f} | \hat{P}_{fl} | \Theta_{iv_i} \rangle \tag{4.15}$$

Here, $\hat{P}_{fl} = -i\hbar \frac{\partial}{\partial Q_{fl}}$ is the normal mode momentum. Inserting (4.15) into (4.13), the IC rate becomes

$$k_{IC} = \sum_{kl} k_{ic,kl} \tag{4.16}$$

$$k_{ic,kl} = \frac{2\pi}{\hbar} R_{kl} Z_{iv}^{-1} \sum_{v_i, v_f} \mathrm{e}^{-\beta E_{iv_i}} P_{kl} \delta\left(E_{fi} + E_{fv_f} - E_{iv_i}\right) \tag{4.17}$$

Here electronic coupling term

$$R_{kl} = \langle \Phi_f | \hat{P}_{fk} | \Phi_i \rangle \langle \Phi_i | \hat{P}_{fl} | \Phi_f \rangle \tag{4.18}$$

and vibrational coupling term

$$P_{kl} = \langle \Theta_{fv_f} | \hat{P}_{kl} | \Theta_{iv_i} \rangle \langle \Theta_{iv_i} | \hat{P}_{fl} | \Theta_{fv_f} \rangle \tag{4.19}$$

The delta function in (4.17) is again Fourier transformed which gives rise to:

$$k_{ic,kl} = \frac{1}{\hbar^2} R_{kl} \int_{-\infty}^{\infty} dt \left[\mathrm{e}^{i\omega_{if} t} Z_{iv}^{-1} \rho_{ic,kl}(t, T) \right] \tag{4.20}$$

where $\rho_{ic,kl}(t, T) = \mathrm{Tr}\left(\hat{P}_{fk} \mathrm{e}^{-i\tau_f \hat{H}_f} \hat{P}_{fk} \mathrm{e}^{-i\tau_i \hat{H}_i} \right)$ is the IC correlation function, for which, Peng et al. [44] derived the analytical expression for diagonal case ($k = l$) and Niu et al. [45] obtained more general expression for both diagonal and non-diagonal couplings, thus completely abandoning the "promoting mode" approximation. Namely, any vibrational mode could serve as a promoting mode for the internal conversion process. It can be applied to complex molecules. The electronic coupling appeared in (4.18) is also termed as non-adiabatic coupling, which can be obtained through first-order perturbation [46]:

$$\langle \Phi_f | \frac{\partial}{\partial Q_{fl}} | \Phi_i \rangle = \frac{\left\langle \Phi_f^0 \middle| \partial V / \partial Q_{fl} \middle| \Phi_i^0 \right\rangle}{E_i^0 - E_f^0} \tag{4.21}$$

where V is the electron-nuclear interaction term in Hamiltonian, and the numerator can be expressed as a sum over transition electric field from nucleus:

$$\left\langle \Phi_f^0 \middle| \partial V/\partial Q_{fl} \middle| \Phi_i^0 \right\rangle = -\sum_{\sigma} \frac{Z_\sigma e^2}{\sqrt{M_\sigma}} \sum_{\tau=x,y,z} E_{f\leftarrow i,\sigma\tau} L_{\sigma\tau} \tag{4.22}$$

where

$$E_{f\leftarrow i,\sigma\tau} = \int \mathrm{d}\mathbf{r} \rho_{fi}(\mathbf{r}) \frac{e(r_\tau - R_{\sigma\tau})}{|\mathbf{r} - \mathbf{R}_\sigma|^3}$$

is the electric field at $\mathbf{r}$ from the a nucleus at $\mathbf{R}_\sigma$ and ρ_{fi} is the electron transition density between initial and final states. All can be computed from quantum chemistry program.

4.2.3 Application to Polythienylenevinylene Derivatives

As an example to apply the above formalisms to design polymeric photovoltaic materials, we consider polythienylenevinylene (PTV) derivatives. In fact, the most prominent polymer for photovoltaic application has been poly(3-hexyl thiophene) (P3HT), which when processed with P3HT to form bulk heterojunction structure can give rise up to 6 % power conversion efficiency [47]. The band gap of P3HT is 2 eV, much higher than the silicon band gap 1.1 eV. One of the recent developments towards reaching higher efficiency is to synthesize low band gap polymer to absorb as much as possible solar emissions, for instance, the intra-chain donor-acceptor backbone polymers or copolymers [48]. One strategy to lower the band gap of polythiophene is to consider polythienylvinylene, see Scheme 4.1. The band gaps of PTV and its derivatives are around 1.55–1.8 eV. However, the pristine PTV was shown to possess very low power conversion efficiency, $\sim$0.2 % [49], regardless of the improved absorption spectrum and large charge mobility. It has been observed that the photo-induced transfer from PTV to PCBM is very low and the excited state decay is very fast (0.6 ps) [50], instead of nanoseconds. Such fast non-radiative decay prohibits any appreciable fluorescence. In fact, there is a concomitant relationship between fluorescence and photovoltaic process: the former is necessary for excitation energy transfer prior to charge separation.

Further experiments have been devoted to make substituted PTV in order to increase the power conversion efficiency. One strategy is to increase optical emission efficiency, which is much easier to characterize without fabricating device. It has been known that the absence of photoluminescence is due the lowest-excited state ordering, commonly occurred in conjugated polymer, like polyacetyelene, or polydiacetylene [51]. Namely, the lowest excited state is of even parity, dipole-forbidden, often $2A_g$ state, while for the luminescent polymer like polyparaphenylenevinylene (PPV), it is of odd parity, dipole-allowed $1B_u$ state [52]. It has been demonstrated that upon side-chain substitutions, the luminescence can be recovered through $1B_u/2A_g$ crossover [53, 54]. The side-chain substitution can cause the

main-chain charge redistribution at the frontier molecular orbital and stabilize the charge-type excitation ($1B_u$ state). Theoretically, the substitution effect on the lowest-lying excited state ordering is very difficult to predict, since quantum chemistry so far does not allow accurate calculation of the excited state for large molecules. Complete active space self-consistent field plus its second order perturbation (CASPT2) can provide a rather reliable description for low-lying excited states [55]. However, the computational costs usually prohibit any computational efforts for complex conjugated oligomers or polymers. We have earlier improved semiempirical ZINDO coupled with multireference configuration interaction (MRCI/ZINDO) approach to calculate the excited state and nonlinear optical properties for conjugated molecules, which has been shown to give reliable low-lying excited state structure [56, 57]. Furthermore, Chen et al. [56] proposed a simple rule to judge the substitution effect on the crossover of the excited state ordering based on frontier molecular orbitals, which is practical for luminescent polymer design. The following quantity $\rho_{H/L}$ is defined:

$$\rho_{\frac{H}{L}} = \frac{\sum_{\mu \in sub} \left| C_{H_\mu} \right|^2}{\sum_{\mu \in sub} \left| C_{L_\mu} \right|^2}$$

$C_{H(L)}$ is the molecular orbital coefficient of the HOMO(LUMO) at the substitution site of the main chain, and the summations only cover the orbitals of the carbon atoms in the backbone linking the side groups. Therefore, $\rho_{H/L}$ can mark charge redistribution between the HOMO and LUMO induced by substituent groups. Since $1B_u$ usually consists of single excitation from HOMO to LUMO, charge transfer occurring from HOMO to LUMO should be significant to stabilize the $1B_u$ state. If $\rho_{H/L}$ deviates from 1 remarkably, charge transfer from substituent group to the main chain will occur upon excitation from HOMO to LUMO, so that the $1B_u$ can be stabilized to become the lowest-lying excited state. Otherwise, if $\rho_{H/L}$ is close to 1, then the excited state ordering is not expected to be altered upon substitution.

The regioregular PTVs at solid state possess planar conformation, leading to highly conjugated backbones. Therefore, the model systems are kept planar with C_{2h} symmetry in this work. Based on the S_0 geometries optimized by B3LYP/def2-SV(P), the vertical excitation energies of the three low-lying excited states for the six PTV derivatives (Scheme 4.1) are calculated with TDDFT/B3LYP and MRCI/ZINDO methods, and the results are presented in Table 4.1 [58].

It is noted that (i) for the pristine and CH_3-, OH- substituted PTV, the lowest excited state is of A_g symmetry, prohibiting any appreciable fluorescence according to Kasha's rule; (ii) both NO_2- and CHO substitution can alter the excited state ordering thus to recover the fluorescence; (iii) TDDFT/B3LYP method always stabilizes the $1B_u$ state to be the lowest one. This is due to the artefact of the charge self-interaction contained in the functional. Several recent efforts have tried to correct such mistakes, including spin-flip approach [59], non-adiabatic effect [60], double-excitation [61], etc. These are in active progress. The MRCI/ZINDO calculated excited state structure correlated well with $\rho_{H/L}$ value from the simple rule

Table 4.1 Vertical excitation energies (E_{ver}) of the three low-lying excited states at the ground state geometry for PTV derivatives and their corresponding oscillator strengths (f)

	MRCI/ZINDO		TDDFT/B3LYP	
R	E_{vert} (eV)	f	E_{vert} (eV)	f
H	A_g: 2.50	0.0000	B_u: 1.94	3.9113
	B_u: 2.76	3.1055	A_g: 2.28	0.0000
	A_g: 3.18	0.0000	A_g: 2.66	0.0000
CH_3	A_g: 2.51	0.0000	B_u: 1.93	3.9387
	B_u: 2.73	2.9759	A_g: 2.28	0.0000
	A_g: 3.12	0.0000	A_g: 2.64	0.0000
OH	A_g: 2.38	0.0000	B_u: 1.75	3.5981
	B_u: 2.41	2.2482	A_g: 2.03	0.0000
	A_g: 2.89	0.0000	A_g: 2.55	0.0000
CO-OH	B_u: 2.41	3.3457	B_u: 2.03	3.3678
	A_g: 2.58	0.0000	A_g: 2.32	0.0000
	A_g: 2.83	0.0000	A_g: 2.58	0.0000
NO_2	B_u: 2.45	3.0844	B_u: 2.03	2.9424
	A_g: 2.55	0.0000	A_g: 2.24	0.0000
	A_g: 2.84	0.0000	A_g: 2.51	0.0000
CH-O	B_u: 2.38	3.2248	B_u: 1.96	3.1874
	A_g: 2.51	0.0000	A_g: 2.21	0.0000
	A_g: 2.77	0.0000	A_g: 2.49	0.0000

based on the molecular orbital analysis, as well as the available experiments, see Table 4.2.

If we look at the frontier orbitals of these compounds, see Fig. 4.1, we can see that for CH_3-substitution does not alter the charge distribution when compared with pristine one, while OH-substitution can indeed redistribute orbital, but it does so both to HOMO and LUMO in a very similar way. COOH, NO_2 and CHO substituents are strongly electron-withdrawing groups, and they all caused remarkable charge redistributions, especially in LUMO. That explains that CH_3 and OH substitutions cannot give rise to fluorescence but COOH, NO_2 and CHO can. Indeed, experiment indicated COOH-PTV is light-emissive and its photovoltaic efficiency has been increased 10 times from pristine polymer [63].

Now we look at the optical spectra for the three compounds predicted to be emissive. TDDFT/B3LYP is employed to calculate all the vibrational modes for

Table 4.2 Calculated $\rho_{H/L}$ from the optimized geometry for different substituted OTVs, in comparison with the MRCI/ZINDO results and experimental luminescent properties: strong luminescent molecules possess a $\rho_{H/L}$ value well deviated from 1

R	H	CH_3	OH	COOH	NO_2	CHO
$\rho_{H/L}$	1.29	1.20	0.91	1.51	1.40	1.85
S_1 from MRCI/ZINDO	$2A_g$	$2A_g$	$2A_g$	$1B_u$	$1B_u$	$1B_u$
Luminescence from exp.	No [62]	No [63]	No [50]	*Yes* [63]	NA	NA

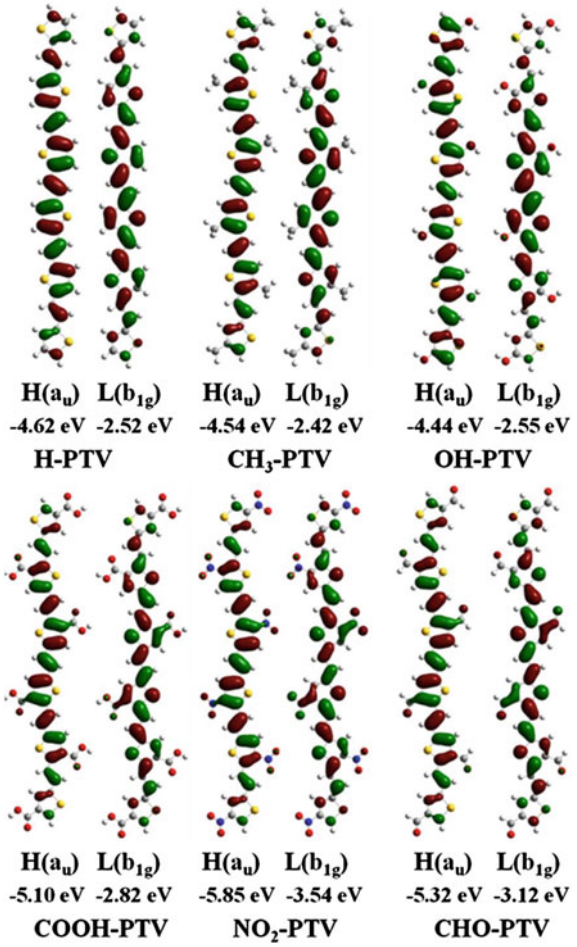

Fig. 4.1 Frontier orbitals of PTV: H for HOMO and L for LUMO

excited state and the ground state as well as the vibronic coupling. Keeping in C_{2h} symmetry, no imaginary frequency is found from the optimized ground state structure for all three PTVs, indicating local minimums are located. While there is a very small imaginary frequency existed in optimized excited state structure for COOH-PTV and NO_2-PTV, no matter by keeping C_{2h} symmetry or C_1 symmetry. Such mode corresponds to the slight out-of plane motion with vanishing vibronic coupling strength. Thus, it is safe to replace such mode by the corresponding one in the ground state, ignoring the distortion effect for this particular mode.

We first present the absorption and emission spectra for the experimentally available COOH-PTV at 300 K including Duschinsky effect in order to rationalize our methodology. The theoretical spectra compared with the experimental results [63] are presented in Fig. 4.2, which is quite satisfactory. Note that the broadening in spectrum is naturally temperature dependent, originated from the coupling

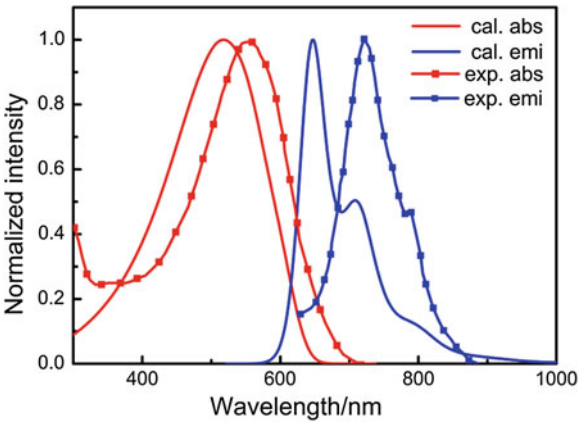

Fig. 4.2 Comparison of optical absorption and emission spectra between theory (T = 300 K) and experiment (in dilute $CHCl_3$ solution) for COOH-PTV

between electronic excited state and all the vibration modes, without any arbitrary broadening. We find the line shapes in theoretical spectra are in good agreement with the experiment. Such agreement validates our vibration correlation function theory and the electronic structure calculation.

Under the displaced harmonic oscillator model, there should exist mirror symmetry between the absorption and emission spectra. But such symmetry is absent both in experiment and in theory, see Fig. 4.2. To understand the origin of such asymmetry, we calculate the spectra without considering the mode mixing effect, while keeping the difference in normal mode frequency between excited state and ground state as obtained from TDDFT (Fig. 4.3). And we find that the structures of spectra are nearly the same as the spectra with Duschinsky rotation effect (DRE) and the asymmetry still exists. This means the mixing of normal modes in the initial and final electronic states is not the cause of asymmetry. Therefore, the asymmetry of spectra can be ascribed to the distortion effect. Such asymmetry also existed in

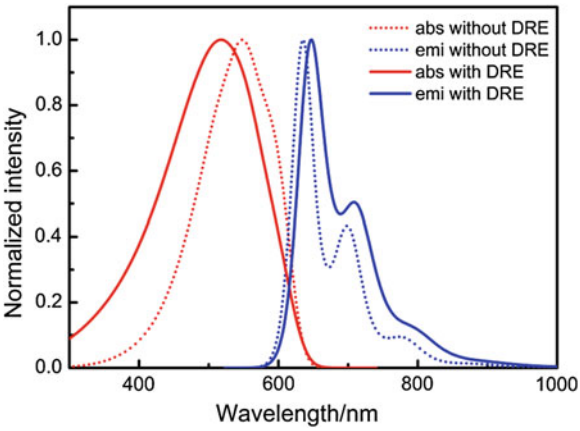

Fig. 4.3 The optical absorption (abs) and emission (emi) spectra of COOH-PTV with DRE compared to the spectra without DRE but with different normal mode frequency at 300 K

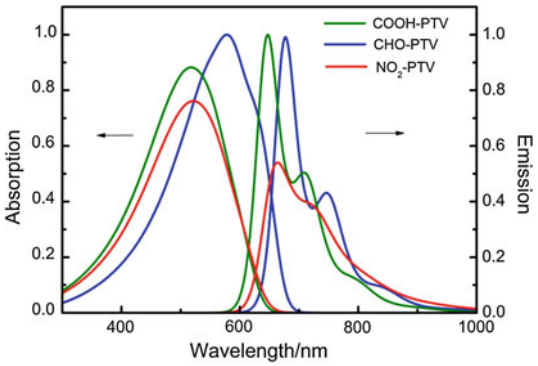

Fig. 4.4 Theoretical absorption and emission spectra for COOH-PTV, NO_2-PTV, and CHO-PTV

polythiophene and polyparaphenylenevinylene [64], because in the excited state, C–C single bond is shortened so that the frequency of torsional motion increases.

We next calculate the optical spectra of NO_2-PTV and CHO-PTV, shown in Fig. 4.4. The absorptions peak at 518, 522, 578 nm for COOH-PTV, NO_2-PTV, and CHO-PTV respectively, while for emission, the peak positions are at 648, 663, and 678 nm correspondingly. The bandgap of CHO-PTV is indeed much lower than other compounds. The theoretical spectra illustrate that CHO-PTV possesses a large overlap between absorption and emission spectra, helpful for faster energy transfer. Thus, we conclude that CHO-PTV possesses the smallest bandgap as well as the largest spectra overlap.

Now we look at the excited state decay rates calculated according to formalisms (4.12) and (4.20), see Table 4.3. The exciton life time is simply calculated as $\tau = \frac{1}{k_r + k_{nr}}$. It is seen that all of the three compounds possess efficient fluorescence ($k_r \gg k_{nr}$) as well as long exciton lifetime to facilitate charge dissociation.

It should be noted that in our vibration correlation function formalism, harmonic potential energy surface approximation is adopted, which could be a strong approximation, especially for small molecule with very few degrees of freedom and a large electronic transition gap. For radiative decay process, the transition energy is largely mediated by the photon energy, leaving the vibrational quanta very small. In nonradiative decay, the electronic energy of excited state is transformed through vibration relaxation into final state. If the number of modes is too few and/or the transition energy is too large, the number of vibration quanta for each mode is required to be big in order to accept the electronic energy. As a result, the anharmonicity can be important in the nonradiative decay process. However, if the number of normal modes is large enough, for instance in conjugated polymers, then

Table 4.3 Radiative, nonradiative decay rates and exciton life time for the emissive substituted PTVs

R	COOH	NO_2	CHO
k_r/s^{-1}	5.25×10^8	3.94×10^8	4.50×10^8
k_{nr}/s^{-1}	1.19×10^6	2.24×10^8	2.51×10^6
τ/ns	1.90	1.62	2.21

many modes can take part in sharing the electronic transition energy. Thus for any one of the mode, only small number of vibrational quanta is required. So, for each mode, the deviation from the potential energy surface equilibrium is small and the harmonic model is expected to be a reasonable approximation. Hence, we expect that the harmonic model is more applicable for polymer than for molecule. Detailed verification can be found in [58].

4.2.4 Synopsis

In this section, we present a general formalism for calculating the optical absorption and emission spectra as well as the excited state decay rates. The material design strategy has been proposed on increasing fluorescence quantum efficiency, due to the concomitant relationship between light-emitting and photovoltaics. Taking polythienylenevinylene as example, which is non-emissive and of low power conversion efficiency, we applied a combined quantum chemistry approach to propose theoretical design strategy to improve the optoelectronic property of PTV. We showed that COOH group substitution in PTV can lead to invert the excited state ordering, allowing light-emitting, but CH_3 and OH groups do not cause any appreciable effect. We predict that the electron-withdrawing groups NO_2 and CHO can make PTV light-emitting, much as COOH group. These results are further confirmed by molecular orbital calculations based on a simple rule for substitution effect on the excited state ordering, namely, substitution should cause charge redistribution amongst HOMO and LUMO in order stabilize the light-emitting state $1B_u$ to be the lowest one.

Starting from the lowest excited state and the ground state potential energy parabola, optical absorption and emission spectra are computed for COOH-, NO_2- and CHO-PTV through our correlation function formalism. The broken mirror symmetry for COOH-PTV found both in experiment and computation is attributed to distortion effect, namely, the vibrational mode frequencies, especially the low frequency parts are different for the ground state and the excited state. The theoretical spectra of COOH-PTV are consistent with the experimental measurements. From the radiative and non-radiative decay rates for COOH-, CHO- and NO_2-PTVs as computed by the same correlation function formalism, we find that CHO-PTV possesses not only a long excited state lifetime (2.21 ns), but also large overlap between absorption and emission spectra. These facts indicate that CHO-PTV is not only a good light-emitting polymer, but also a good photovoltaic donor material possessing long intrinsic exciton diffusion length. Although NO_2 is a stronger electron-withdrawing group than COOH or CHO, the calculations show that the spectrum overlap between absorption and emission in NO_2-PTV is relatively small. Therefore, even though the excited state ordering of NO_2-PTV meets the basic requirement for molecular design, both the light emitting and photovoltaic performances are predicted to be poorer than COOH-PTV, while CHO-PTV is predicted to present better light emitting and photovoltaic performances than

COOH-PTV. Such theoretical information should be useful for materials design and the methodology presented in this section is ready to be employed by any graduate students.

Following the photo-absorption and exciton diffusion/dissociation, the next important step is the charge transfer and charge transport. We refer to a monograph for describing such process [65, 66].

4.3 Molecular Parameters for Exciton Transfer in Organic Semiconductors

As long as the exciton diffusion length is concerned, apart from the spectra overlap extensively discussed in previous section, intermolecular excitonic/electronic coupling is the central parameter. The microscopic origin comes from the long range Coulomb interaction. Namely, excitation in one molecule, or a chromophore, or a conjugated segment travels to other place through transition electrical dipole coupling.

For the singlet-singlet energy transfer (ET) process in a dimer,

$$^1D^* + {}^1A \rightarrow {}^1D + {}^1A^* \tag{4.23}$$

The electronic coupling of ET can be simply expressed by a first-order perturbation from the product state of donor and acceptor wave functions:

$$V_{DA} = \langle \psi_{D^*}\psi_A | H_{DA} | \psi_D \psi_{A^*} \rangle \tag{4.24}$$

where H_{DA} is the perturbation describing the donor-acceptor interaction. Considering $|\psi_D\rangle$, $|\psi_A\rangle$ as the Hartree-Fock self-consistent-field ground-state determinant, the singlet excited state wave functions can be written approximately as a spin-adapted configuration interaction (CI) form:

$$|\psi_{D^*}\rangle = \frac{1}{\sqrt{2}} \sum_{i_D a_D} Z_{i_D a_D}^{D^*} (a_{D\uparrow}^+ i_{D\uparrow} + a_{D\downarrow}^+ i_{D\downarrow}) |\psi_D\rangle \tag{4.25}$$

$$|\psi_{A^*}\rangle = \frac{1}{\sqrt{2}} \sum_{i_A a_A} Z_{i_A a_A}^{A^*} (a_{A\uparrow}^+ i_{A\uparrow} + a_{A\downarrow}^+ i_{A\downarrow}) |\psi_A\rangle \tag{4.26}$$

$a_{D\uparrow}^+ [i_{D\uparrow}]$ creates an electron with spin up on unoccupied molecular orbital (MO) a (annihilates an electron with spin up on occupied MO i), and $Z_{i_D a_D}^{D^*}$, $Z_{i_A a_A}^{A^*}$ are the CI expansion coefficients associated with the $i \rightarrow a$ single excitation. So (4.24) can be rewritten as

$$V_{DA} = \frac{1}{2}\sum_{i_D a_D} Z^{D^*}_{i_D a_D} \sum_{i_A a_A} Z^{A^*}_{i_A a_A} \langle \psi_D \psi_A | (i^+_{D\uparrow} a_{D\uparrow} + i^+_{D\downarrow} a_{D\downarrow}) H_{DA} (a^+_{A\uparrow} i_{A\uparrow} + a^+_{A\downarrow} i_{A\downarrow}) | \psi_D \psi_A \rangle \tag{4.27}$$

The general intermolecular interaction can be written in the second quantization form:

$$H_{DA} = \sum_{pq} h_{pq} p^+ q + \frac{1}{2}\sum_{pqrs} \langle pq|rs\rangle p^+ q^+ sr \tag{4.28}$$

where

$$\begin{aligned} h_{pq} &= \int \phi^*_p(1)(T + V^{ele-nuc})\phi_q(1)\mathrm{d}\vec{r}_1 \\ \langle pq|rs\rangle &= \int \phi^*_p(1)\phi^*_q(2)\frac{1}{r_{12}}\phi_r(1)\phi_s(2)\mathrm{d}\vec{r}_1 d\vec{r}_2 \end{aligned} \tag{4.29}$$

where spin-orbital indices p, q, r, s in each term should contain mixed D and A. Equation (4.27) can finally be expressed as

$$V_{DA} = \sum_{i_D a_D} Z^{D^*}_{i_D a_D} \sum_{i_A a_A} Z^{A^*}_{i_A a_A} [2(a_D i_D | i_A a_A) - (a_D a_A | i_A i_D)] \tag{4.30}$$

$(a_D i_D | i_A a_A) = \int \phi^*_{a_D}(1)\phi_{i_D}(1)\frac{1}{r_{12}}\phi^*_{i_A}(2)\phi_{a_A}(2)dr_1 dr_2$ is the two-electron Coulombic interaction, while $(a_D a_A | i_A i_D)$ is exchange interaction. The former can be two-center integral, which is of long range character, namely, one electron in D and another in A. The latter is a four-center integral, namely, intermolecular bond-bond correlation term, which decays exponentially with the intermolecular distance, thus negligible for long range energy transfer.

For the triplet-triplet energy transfer,

$$^3D^* + {}^1A \rightarrow {}^1D + {}^3A^* \tag{4.31}$$

We have:

$$V_{DA} = \frac{1}{2}\sum_{i_D a_D} Z^{D^*}_{i_D a_D} \sum_{i_A a_A} Z^{A^*}_{i_A a_A} \langle \psi_D \psi_A | (i^+_{D\uparrow} a_{D\uparrow} - i^+_{D\downarrow} a_{D\downarrow}) H_{DA} (a^+_{A\uparrow} i_{A\uparrow} - a^+_{A\downarrow} i_{A\downarrow}) | \psi_D \psi_A \rangle \tag{4.32}$$

It can be shown that the Coulombic terms cancel, leaving only the exchange term:

$$V_{DA} = -\sum_{i_D a_D} Z^{D^*}_{i_D a_D} \sum_{i_A a_A} Z^{A^*}_{i_A a_A} (a_D a_A | i_A i_D) \tag{4.33}$$

It demonstrates that only the short-range exchange interaction determines the triplet-triplet energy transfer, which was referred to Dexter mechanism. Here we will not consider this. Only Förster model will be discussed in this chapter.

The intermolecular coupling term can be cast into a practical form by expanding the $1/r_{12}$ in the Coulomb term:

$$\frac{1}{r_{12}} = \frac{1}{|\vec{R}_{DA} + \vec{r}_{A2} - \vec{r}_{D1}|} = \frac{1}{\sqrt{R^2_{DA} + 2\vec{R}_{DA} \cdot (\vec{r}_{A2} - \vec{r}_{D1}) + (\vec{r}_{A2} - \vec{r}_{D1})^2}} \tag{4.34}$$

where R_{DA} is the donor—accepter intercenter distance, r_{D1} the coordinate of electron 1 with respect to the center of donor. Since the latter is much less than the former, $1/r_{12}$ can be expanded:

$$\frac{1}{r_{12}} = \frac{1}{R_{DA}}\left[1 - \frac{\vec{R}_{DA} \cdot (\vec{r}_{A2} - \vec{r}_{D1})}{R^2_{DA}} - \frac{1}{2}\frac{(\vec{r}_{A2} - \vec{r}_{D1})^2}{R^2_{DA}} + \frac{3}{2}\left(\frac{\vec{R}_{DA} \cdot (\vec{r}_{A2} - \vec{r}_{D1})}{R^2_{DA}}\right)^2 + \cdots\right] \tag{4.35}$$

It is easily remarked that only the cross terms of r_{A2} and r_{D1} contribute to the V_{DA}, because of the orthogonality for quantum state. Note that the transition electrical dipoles for donor and acceptor are:

$$\vec{\mu}_D = \sqrt{2}\langle \psi_{D^*} | e\vec{r}_{D1} | \psi_D \rangle$$
$$\vec{\mu}_A = \sqrt{2}\langle \psi_{A^*} | e\vec{r}_{A2} | \psi_A \rangle$$

Then V_{DA} can be simplified as:

$$V_{DA} = \frac{\vec{\mu}_A \cdot \vec{\mu}_D}{R^3_{DA}} - \frac{3(\vec{R}_{DA} \cdot \vec{\mu}_A)(\vec{R}_{DA} \cdot \vec{\mu}_D)}{R^5_{DA}} \tag{4.36}$$

That is, the coupling arises from the coupling between donor and acceptor through transition electrical dipole interaction: an electronic excited state is viewed as fluctuating electrical dipole, or electron-hole pair formed by promoting electron from occupied MOs to unoccupied MOs. This approach averages away the shapes of the donor and acceptor molecules and should be applied when the size of the interacting molecules is small with respect to the intermolecular separation [67].

A more general expression can be obtained through transition density distribution. In fact, the transition dipole can be rewritten as:

$$\vec{\mu}_D = \int d\vec{r}\rho_D^{ge}(\vec{r})e\vec{r} \tag{4.37}$$

Here:

$$\rho_D^{ge}(\vec{r}) = N \int \cdots \int \mathrm{d}\vec{\mathbf{r}}_2 \ldots \mathrm{d}\vec{\mathbf{r}}_N \Psi_g(\vec{\mathbf{r}}, \vec{\mathbf{r}}_2, \ldots, \vec{\mathbf{r}}_N)\Psi_e^*(\vec{\mathbf{r}}, \vec{\mathbf{r}}_2, \ldots, \vec{\mathbf{r}}_N)$$

The intermolecular excitation coupling can be now rewritten as:

$$V_{DA} = \mathrm{e}^2 \sum_{\sigma}^{D} \sum_{\tau}^{A} \frac{\rho_D(\sigma)\rho_A(\tau)}{r_{\sigma\tau}} \tag{4.38}$$

Here $r_{\sigma\tau}$ represents the distance between atomic centers σ and τ, and $\rho_D(\sigma)[\rho_A(\tau)]$ is the atomic transition density on site σ [τ]. This expansion for the Coulombic interaction is beyond the dipole-dipole level and has been applied for several conjugated systems [68–71]. When the separation of D and A is comparable to their physical sizes, the topology of the transition densities cannot be ignored [72].

The transition density cube (TDC) method has been developed to calculate the coupling according to (4.38), of which the donor and acceptor transition densities are each represented in a 3D grid [68, 73]. Nevertheless, this approach requires a large amount of computer time and the numerical quality is rather limited due to the steep cusp in the Coulomb kernel $1/r_{12}$. Hsu et al. [73, 74] have embedded the Coulomb coupling calculation by analytically solving (4.30). Moreover, they developed the fragment excitation difference (FED) method to calculate the excitation energy transfer coupling which includes the Coulomb interaction, exchange interaction as well as a term arising from the overlap of donor-acceptor electronic densities. Their results showed that, for a pair of stacked naphthalenes, the Coulombic interaction dominates the electronic coupling after 5 Å face-to-face separation [74].

We tested the Coulomb coupling calculation for such a pair of stacked naphthalenes. Only the Coulombic interaction between the ground state and lowest excited state (L_a or 1^1B_{2u}) is presented here based on CIS/3-21G. According to Förster mechanism, the acceptor molecule is optimized in its ground state, while the donor molecule is optimized in its lowest excited state, both at the B3LYP/6-31 g* level. From Fig. 4.5, our calculation is in nice agreement with [73]. It is found that the Coulomb coupling decays as d^{-3} for the stacked naphthalenes.

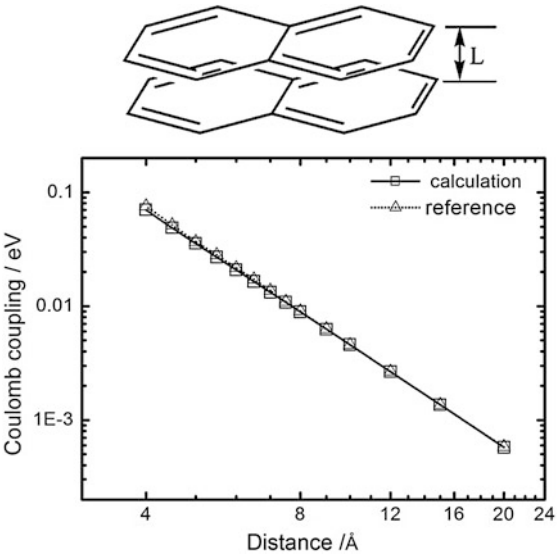

Fig. 4.5 Coulomb coupling as a function of intermolecular separation for a pair of naphthalene for the L_a (1^1B_{2u}) state between a pair of stacked naphthalenes

4.4 Dynamic Monte Carlo Simulation of Bulk Heterojunction Device

Theoretical progresses have been made towards quantitative predictions of opto-electronic properties for organic electronics, such charge mobility in organic field-effective transistors [36–39] and light-emitting efficiency and optical spectrum [42]. However, for the photovoltaic performance, theoretical treatments at present stage are quite fragmented, namely, we have good knowledge for the donor-acceptor interfaces [24–26], or optical absorption and emission as demonstrated in Sect. 4.2 of this chapter, or the exciton diffusion processes. However, we still do not get a unified approach to predict the power conversion efficiency starting from first-principles. We describe here a continuum device model which assumed uniformly distributed p-n junction in the bulk materials [75] and the dynamic Monte Carlo (DMC) approach developed to simulate complicated chemical processes, proposed first by Watkins et al. [76]. The basic algorithm of DMC is based on first-reaction method (FRM) [77] to describe the key processes, the exciton generation, diffusion, the dissociation at the interface, the charge drift and diffusion and the injection from the electrodes, and the collection by the electrodes [78]. Previous simulations have always assumed balanced electron and hole transports, namely, equal charge mobility, in order to avoid space charge accumulation. Such simplification has been removed recently by Yang and Forrest [79] and Meng et al. [80], by combining DMC with a Poisson equation solver, which can present the electrostatic potential according to the charge density, and in turn, the potential influence both the charge and exciton transport.

The first step is to generate morphology for the polymer donor and fullerene acceptor blends. The easiest way for describing the two-phase structure is to use Ising model. In the Ising model, the spin up and down correspond to the donor and acceptor phases, respectively [76], and the Hamiltonian for the energy contributed to site i is:

$$\varepsilon_i = -\frac{J}{2}\sum_j (\delta_{s_i,s_j} - 1) \tag{4.39}$$

where $\delta_{si,sj}$ is the Dirac delta function, and s_i, s_j are the spin indices at site i and j. The summation over j includes all first and second nearest neighbors, and the energetic interaction is inversely proportional to the distance between neighboring sites i and j (the energy is scaled by a factor of $1/\sqrt{2}$ for the second nearest neighbors). To obtain a series of morphologies with different phase interpenetration, we need to decide the appropriate initial configuration and the corresponding interaction energy J. In our simulation, the initial morphology with minimal phase separation is chosen and the interaction energy J is set as +1.0 $k_B T$. To relax the system to an energetically stable state, the neighboring pairs of sites are chosen randomly in system, and then the acceptance probability for an attempt to swap the site spins is calculated as:

$$P(\Delta\varepsilon) = \frac{\exp(-\Delta\varepsilon/(k_B T))}{1 + \exp(-\Delta\varepsilon/(k_B T))} \tag{4.40}$$

where Δε is the total energy change caused by swapping the site spins. After a large number of attempted spin swapping, a desired morphology series with varying scale of phase separation can be generated and stored for later use.

Two special cases: the bilayer morphology (M1 in Fig. 4.6) and an optimal checkered structure (M4 in Fig. 4.7) are also chosen in the simulation for comparison, in addition to the well dispersed morphology M3 and the less separated M2.

In the model system, the lattice is of the 60 × 60 × 30 sites in the x, y, and z directions, respectively, and a lattice constant of 3 nm is used. A single occupancy of lattices for any particle (exciton, electron or hole) is imposed, and the system temperature T is fixed at 298 K. The electrodes are in the x-y plane located at $z = 0$ and $z = 90$ nm. Periodic boundary conditions are applied in both x and y directions. We note that the thickness of solar cell active layer is around 100 nm.

Three types of mobile particles (electrons, holes and excitons) are considered in our simulation. In the first reaction method (FRM), [77, 81, 82, 83], the description for each of the particle is associated with an event, and each event has a waiting time τ_q. An event is associated with a configurational change in system, e.g., inserting or removing a particle, updating the coordinates of particles. All the possible events in the system are stored in an ascending order for waiting time and form a temporal sequence. This queue of events will constantly be updated to reflect the time evolution

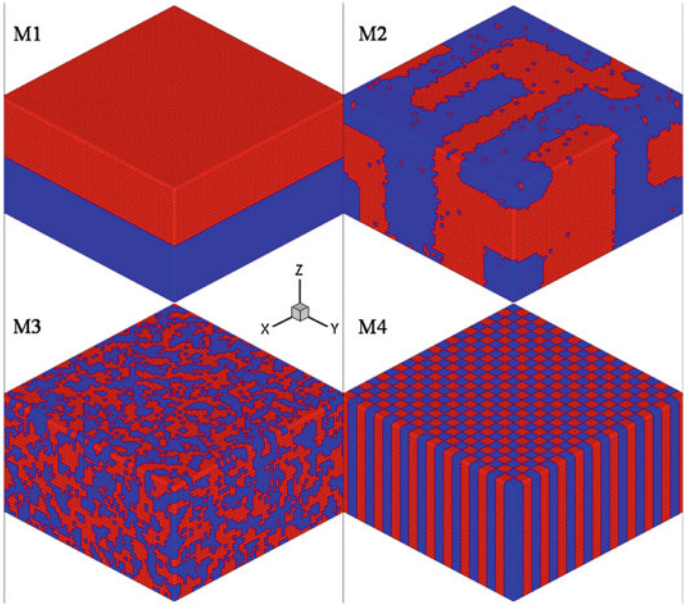

Fig. 4.6 Typical morphologies with different scale of phase separation, *M1* for the bilayer, *M2* and *M3* for the blend generated by using the Ising Model, and *M4* for the checkered structure. The electron and hole conductors are colored with *red* and *blue*, respectively

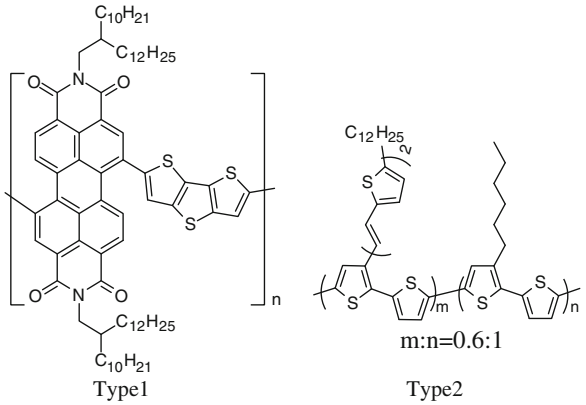

Fig. 4.7 The chemical structures of poly(perylene diimide-*alt*-dithienothiophene) (PPDI, *Type 1*) and bis (thienylenevinylene)-substituted polythiophene (PBTT, *Type 2*)

of the system. At each time step, the event at the start of the queue is selected to execute and then removed from the queue. Later on, the simulation time is incremented by the time expired and all of the waiting times in queue are reduced by this time expired. The execution of a current event will probably preclude the occurrence of subsequent events in conformance with certain rules, e.g., the single occupancy of lattices, and in turn it requires that the newly enabled event be created and then

inserted in the queue. Marsh et al. [83] have demonstrated that the dynamic properties of carriers can be indistinguishably described by both the FRM and the full dynamical Monte Carlo algorithm (in which the whole event queue must be updated for every configuration change).

The waiting time τ_q is calculated as:

$$\tau_q = -\frac{1}{W}\ln(X) \tag{4.41}$$

where X is a random number uniformly distributed in (0, 1), and W is the occurring rate of an event. Only the event occurring first is inserted in the queue. As a result, we need to calculate the waiting time for all the events and select the event with the shortest waiting time. Then this time increment is counted in the simulation.

The model system we choose is a polymer blend of PPDI [84] and PBTT [85], see Fig. 4.7. The fabricated all-polymer solar cell exhibited strong absorption throughout the visible and extending into the near infrared range. The charge mobilities are also relatively high with electron mobility for PPDI about 1.3×10^{-2} and hole mobility for PBTT $\sim 10^{-3}$ cm^2/Vs. The power conversion efficiency is found to be greater than 1 % at the beginning, and later, was increased to 1.5 %. The purpose of this study is to find out the essential processes determining the photovoltaic effect, in order to achieve the optimal performance.

The donor and acceptor polymers are simplified in a lattice model, distributed in the morphology generated in Fig. 4.6. Excitons are created at randomly chosen sites in either the hole or electron polymer at constant rate. From the experimental absorption spectrum, the exciton generation rate is calculated to be 900 s^{-1} nm^{-2} at AM1.5 with illumination of 90 mW/cm^2 by integrating of the spectrum up to 800 nm. Note that one can convert the solar emission spectrum to obtain a photon irradiation rate at 4,000 s^{-1} nm^{-2}. Namely, the quantum efficiency upper limit is 900/4,000 = 22.5 % for such blend. Right after the exciton creation, there are three events followed: hopping, recombination and dissociation at the interface, before charge collection at the electrodes. The excitons generated in these polymers are assumed to be singlet prior to dissociation at the donor and acceptor interface. Therefore, the exciton dissociation rate W_{ed} must be set sufficiently high, namely, in the simulation, once we find the exciton reaches interface, the dissociation event is put on the top priority.

In organic semiconductors, the exciton lifetime ranges from a few hundreds picoseconds to a few nanoseconds. The diffusion length of exciton is estimated to be around 10–20 nm in these polymers. The exciton hopping follows a Förster process, namely, the hopping rate from site i to a nearby site j is given by

$$W_{ij} = W_e\left(\frac{R_0}{R_{ij}}\right)^6 \tag{4.42}$$

where R_{ij} is the distance between sites i and j, R_0 is the exciton localization radius, and W_e is the hopping attempt frequency. Hopping rates for excitons are evaluated

by including lattice neighbors out to a radius of 15 nm. The parameters $W_e R_0^6 = 2\ \mathrm{nm}^6\ \mathrm{ps}^{-1}$ and exciton recombination rate $W_{er} = 1/500\ \mathrm{ps}^{-1}$ are set, so that the exciton diffusion length is around 10 nm. In our model, the exciton hopping is only allowed between the same type of site.

Charge carriers (electrons and holes) are generated either from the exciton dissociation or injection from the electrodes, and the electron (hole) can only occupy the acceptor (donor) site. All electrostatic interactions in the device are included in the model, and the Coulombic interaction between sites i and j is calculated as:

$$V_{ij} = \frac{q_i q_j}{4\pi\varepsilon_0 \varepsilon} \frac{1}{R_{ij}} \tag{4.43}$$

where q_i and q_j are the site charges respectively, ε is the dielectric constant and R_{ij} is the distance between sites i and j.

The created charge carrier moves following Marcus theory [86] to hop in the bulk:

$$W_{ij} = V_{hop} \exp\left(-\frac{(E_j - E_i + E_r)^2}{4E_r k_B T}\right) \tag{4.44}$$

E_i and E_j are the energies of hopping sites i and j, containing the internal electric field effect solved from Poisson equation, and E_r corresponds to charge reorganization energy. For the charge carriers, all the Coulomb interactions between neighboring charges (within a distance less than R_c) and modifications from the effect of the internal electric field (Poisson equation solution) are included in calculating the site energy. Hopping is restricted to the adjacent sites (the nearest neighboring sites, thus there are 6 adjacent sites in a cubic lattice), whose energy is calculated by taking into account of the Gaussian standard deviation σ to the density of states. The prefactor V_{hop} is derived from the Einstein relationship under isoenergetic site condition as:

$$V_{hop} = \frac{6 k_B T \mu_{e/h}}{q a_0^2} \exp\left(\frac{E_r}{4 k_B T}\right) \tag{4.45}$$

where $\mu_{e/h}$ is the electron/hole mobility. If the electron and hole are located on the adjacent sites, they may recombine with a rate W_{cr}. A charge carrier adjacent to the electrode is extracted from the device with a rate W_{ce}, which is calculated by using the Marcus formula. The energy difference (driving force) between the Fermi level of an Al electrode and the LUMO of PPDI is taken as $-E_{IB} = -0.4$ eV. We will treat this extraction as an inverse process of charge injection and then W_{ce} is calculated. To simulate the effect of "charge leak", the electron (hole) can be extracted from the device at both the cathode and anode. The image charge effects are also included in calculating the Coulombic interactions for charges near the electrodes (up to the cutoff radius) [87–89]. The charge attraction barrier U actually depends as well on

the external electric field and the Coulomb field binding the carrier with its image twin in the electrode [88, 89]:

$$U = E_{IB} - \frac{q^2}{16\pi\varepsilon_0\varepsilon a_0} - qFa_0 \tag{4.46}$$

where a_0 is the lattice constant, E_{IB} the barrier height in the absence of both electric field and image charge effect, F the electric field solved from Poisson equation, q the elementary charge, ε the medium dielectric constant, and ε_0 the electric permittivity.

The charge injection is restricted to the lattice sites in contact with an electrode, that is, the electron conductor lattice near the cathode and the hole conductor lattice near the anode; thus, the distance of the injection contact is fixed to the lattice constant in (4.45). The subsequent charge carrier motions in the device will take fully account of the local electric field. Near the electrodes, the image charge effects are included up to a cutoff distance of 15 nm.

The conventional Miller-Abrahams expression has been used to calculate the rate of a charge jumping from the Fermi level of the electrode to a site in the dielectric [87]; by considering the restriction on the injection sites, the Miller-Abrahams expression is simplified as:

$$W_{ij} = W_0 \begin{cases} \exp\left(-\frac{E_j - E_i}{k_B T}\right) & : \quad E_i < E_j \\ 1 & : \quad E_i \geq E_j \end{cases} \tag{4.47}$$

where the prefactor W_0 is derived from the Einstein relation under isoenergetic site condition as:

$$W_0 = \frac{6k_B T\,\mu_{e/h}}{qa_0^2} \tag{4.48}$$

The Gaussian standard deviation σ to the density of states is taken into account in the calculation of the site energies for charge injection. Therefore, the site energies are taken as $E_j = U + \sigma R$ and $E_i = \sigma R$, where R is a normally distributed random number and U is calculated by using (4.46).

The freshly generated charge carriers are not allowed to be extracted instantly. To be specific, any charge carrier created adjacent to the electrodes must hop at least one step in the polymer blend before it can be extracted. These different treatments for charge injection and charge extraction can lead to appropriate charge densities adjacent to the electrodes, which enable us to numerically solve the Poisson equation.

For a conventional inorganic solar cell, thermally-activated charges represent another source of dark current in addition to charge injection. Therefore, exciton thermal activation is also incorporated into our FRM algorithm to simulate the dark saturation current density J_{S} under reverse bias voltage. Thermally activated

excitons undergo exciton diffusion and charge separation at the interface in the same way as photo-generated excitons. The generation rate for the thermally activated excitons is evaluated based on the dark saturation current density J_S under reverse bias voltage. In practice, the thermal generation rate $W_{egt} = 32\ s^{-1}\ nm^{-2}$ is set for thermally activated excitons, which leads to a dark current density $J_S \approx 0.36\ mA/cm^2$ under the external applied voltage of −1.5 V. This simulation result is consistent with the experimental dark saturation current density of $0.37\ mA/cm^2$ [84].

The coupled Poisson equation in the dynamic Monte-Carlo is:

$$\frac{\partial^2}{\partial z^2}\psi(z) = \frac{q}{\varepsilon_0 \varepsilon}[n(z) - p(z)] \tag{4.49}$$

This equation relates the potential ψ(z) to the electron and hole densities n(z) and p(z) in the system. The Gummel iteration method is utilized to solve the discretized Poisson equation [90]. To simulate the device performance under dark condition for the polymer blend, the boundary condition for the potential in solving the Poisson equation can be set as:

$$\psi(L_z) - \psi(0) = V_a \tag{4.50}$$

where V_a is the external applied voltage and L_z is the device dimension in the z direction. This is based on the assumption that an organic photovoltaic device in the dark is in equilibrium in the case of zero external field ($V_a = 0$), which is similar to the situation in a traditional inorganic device.

Under illumination, the open-circuit voltage V_{OC} is determined by a number of possible factors: the light-induced splitting of the quasi-Fermi levels, which is related to the difference between the electron affinity (or crudely speaking the LUMO level) of the acceptor material and the ionization potential (HOMO level) of the donor material in the active layer. Therefore, the boundary condition for the potential in solving the Poisson equation under illumination is set as [91]:

$$\psi(L_z) - \psi(0) = V_a - \frac{1}{q}E_{gap} \tag{4.51}$$

where E_{gap} is the energy difference between the electron affinity of the acceptor material and the ionization potential of the donor material.

The solution to the Poisson equation with the boundary condition gives the total electrostatic potential due to space charge and a linearly distributed driving potential. It can be derived that the driving electric field is simply the average of the total electric field at the boundaries. In the DMC simulation, the charge drift is governed by the Coulombic interactions and the driving electric field obtained by solving the Poisson equation. The driving force due to the difference in the work functions between the electrodes is no longer considered. Thus all electrostatic or Coulombic interactions in the device have been included in the DMC-PE model.

By considering charge injection and thermal activation, the charge accumulation process in the device is enhanced. The charge recombination rate is thus set at 10^{-5} ps^{-1} to balance the excess charge density. These values lead to a typical charge density of $\sim 10^{22}$ m^{-3} when the charge mobilities are set either to the same equal values as in the previous DMC simulations (e.g., $\mu_n = \mu_p = 10^{-3}$ cm^2 V^{-1} s^{-1}) [78] or to different values as measured experimentally (e.g., $\mu_n = 10^{-2}$ cm^2 V^{-1} s^{-1} and $\mu_p = 10^{-4}$ cm^2 V^{-1} s^{-1}) for the polymer blend [84].

Thus, we now sketch the combined dynamic Monte Carlo simulation and Poisson equation method in Fig. 4.8, while all the parameters are listed in Table 4.4.

The simulation is required to reach a steady state, and the internal quantum efficiency (IQE) and the current density for different conditions are saved and calculated over a time interval long enough to average out the fluctuations (typically >0.1 s). Under the current assumption, the parameters will not change with the scale of phase separation. The charge extracted from the electrodes per area and unit time is taken as the current density. Then, the outside circle current is calculated as the average of the net current density at the cathode and anode respectively.

Under the short-circuit conditions, the IQE and its two constituent components, exciton dissociation efficiency (the ratio of the number of excitons dissociated to the number of excitons generated) and charge collection efficiency (the ratio of the net number of charges that exit the device to twice of the number of excitons dissociated), are calculated for various blends and checkered morphologies, and are plotted as shown in Fig. 4.9. Generally, the exciton dissociation tends to increase, while the charge collection efficiency will decrease as the interfacial area increases.

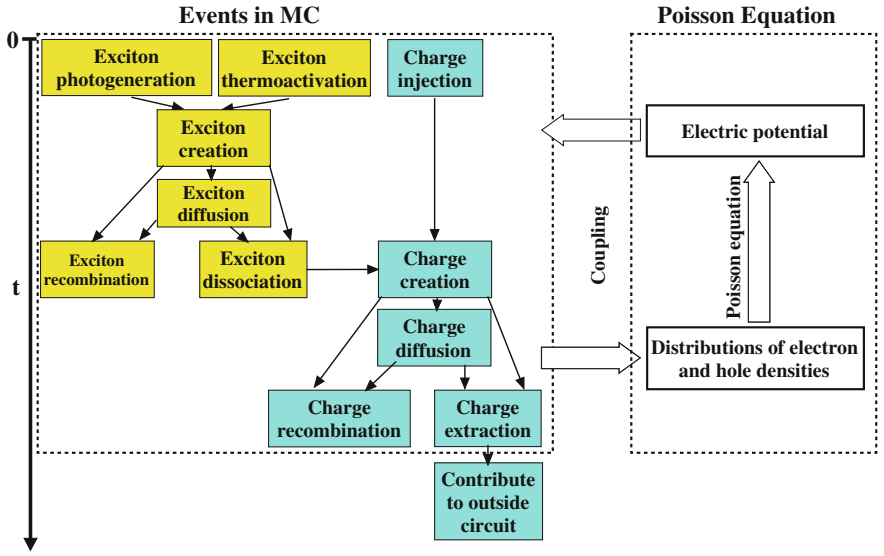

Fig. 4.8 Schematic representation of the dynamic Monte Carlo coupled to the Poisson equation (DMC-PE) simulation processes

Table 4.4 Parameters used in the DMC-PE modeling

T	298.0 K	Temperature
ε	3.5	Dielectric constant
a_0	3 nm	Lattice constant
R_c	15 nm	Cutoff distance
W_{eg}	900 s^{-1} nm^{-2}	Exciton creation rate for photo-generated excitons
W_{egt}	32 s^{-1} nm^{-2}	Exciton creation rate for thermo-activated excitons
$W_eR_0^6$	2 nm^6 ps^{-1}	Exciton hopping rate
W_{er}	2×10^{-3} ps^{-1}	Exciton recombination rate
E_r^*	0.187 eV	polaron binding energy
V_{hop} (p)	1.06×10^{-3} ps^{-1}	Charge hopping rate prefactor for holes
V_{hop} (n)	1.06×10^{-1} ps^{-1}	Charge hopping rate prefactor for electrons
σ^*	0.062 eV	Gaussian standard deviation
W_{cr}	1×10^{-5} ps^{-1}	Charge recombination rate
E_{IB}	0.4 eV	Difference between LUMO (A) and Fermi level of aluminum cathode
E_{gap}	1.1 eV	Difference between LUMO (A) and HOMO (D)
J_S	0.36 mA/cm^2	Dark saturation current density

The parameters marked with an asterisk are taken from [83]

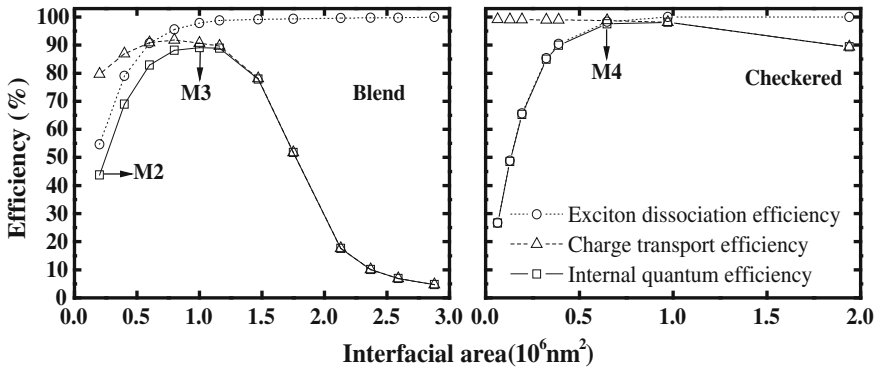

Fig. 4.9 For the blend and checkered morphologies, the exciton dissociation efficiency, the charge collection efficiency, and the internal quantum efficiency vary with interfacial area between the electron and the hole conductors

These lead to the peak of IQE, corresponding to the characteristic feature size of around 10 nm, while for the checked series, the maximum IQE occurs when the width of the square rods is around 9 nm. For the blend morphologies with low interfacial area, e.g., the M2, the pure phases are not perfectly separated due to the thermal effect in the Ising model, and thus many small isolated islands remain in

those majority phases. These islands tend to act as traps for the free charges which can only be got rid of by waiting for the opposite charges to recombine at the interface between the islands and the majority phases. As a result, the charge collection efficiency for the M2 cannot reach the 100 % level as expected, while a peak can occur at a large-scale phase separation.

The calculated *I–V* curves under both dark and illumination conditions are shown in Fig. 4.10. It can be seen that our simulation results provide a consistent picture of the device performance under dark condition. Similar to the photo-generated current, the dark current is also sensitive to the morphology of the polymer blend. Note that an optimized morphology structure (peak in Fig. 4.9) is used in the calculation. That explains both the photo- and dark currents are larger than the experimentally measured values. The experimental mobilities ($\mu_n = 10^{-2}$ cm^2 V^{-1} s^{-1}, $\mu_p = 10^{-4}$ cm^2 V^{-1} s^{-1}) are used in the simulation.

For an ideal solar cell, it is assumed that the photogenerated current density J_{ph} is voltage independent, which means that J_{ph} is equal to the short-circuit current density J_{SC} at any applied voltage [92, 93]. The simulated open-circuit voltage, 0.64 V, is in excellent agreement with the experimental data (0.63 V) [84], as shown in Fig. 4.10. Under the open-circuit condition, the dark current from injection has strongly increased and eventually cancels the photogenerated current. More precisely, two types of current present, driven by different effective voltages that cancel each other: one from injection with the open-circuit voltage as the effective voltage, while the other from exciton dissociation for which the effective drive voltage is the open-circuit voltage shifted by the energy difference between the acceptor and donor materials E_{gap} (4.51).

Such agreement convinces us that the DMC-PE model can provide reasonable description for the performance of organic solar cells. Since the open-circuit voltage is due to the cancellation of the photo-generated current and the dark current, it requires that any approach increasing the photo-generated current with respect to the injected current can enhance the open-circuit voltage. For example, it has been

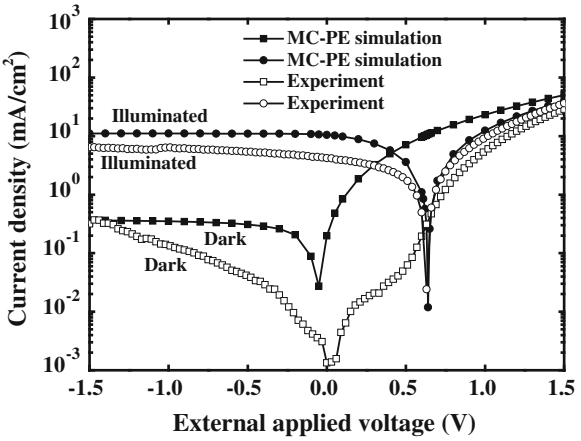

Fig. 4.10 Comparison of the *I–V* curves from the DMC-PE simulations and experiments

found that increasing the exciton dissociation rate [94], which increase the photo-generated current, becoming beneficial to the enhancement of the open-circuit voltage.

By incorporating the Poisson equation into the DMC model with FRM, the constraint of having to consider balanced mobilities for electrons and holes in the polymer blend is removed. Some of the key physical properties we are interested in, e.g., the potential and charge density distributions, can now be studied more appropriately. As shown in Fig. 4.11, when electrons and holes have equal mobilities, the potential distribution in the OPV device is nearly linear; this confirms our previous assumption that, in a polymer blend with balanced carrier mobilities [78, 95] the charge drift is determined by a linear electric field. When mobilities for electrons and holes are different, which is usually the case and here $\mu_n > \mu_p$ for the polymer blend, the potential distribution becomes more complicated and space charges begin to accumulate in the device. As a consequence, the electric field increases in the region near the anode to enhance the extraction of holes, as shown in Fig. 4.12, while in the region near the cathode the electric field decreases to suppress the extraction of electrons. As the difference in the mobilities of hole and electron increases, deviation from linearity for the potential distribution in the polymer blend is remarkable.

We also investigate the effects of exciton creation rate, charge mobility, and charge recombination rate on the short-circuit current and the IQE. As shown in Fig. 4.12, the short-circuit current increases sublinearly with increasing light intensity or exciton creation rate. However, when the charge mobility is over 10^{-3} cm^2 V^{-1} s^{-1}, the short-circuit current and the internal quantum efficiency become less sensitive to the mobility. As a result, further increase in mobility does not significantly improve the device performance. This means that as a way to

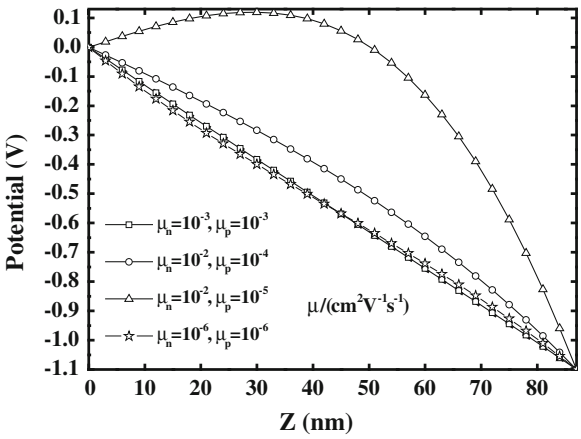

Fig. 4.11 The electrostatic potential distribution in the device under short-circuit condition. As the difference in hole and electron mobilities increases, the space charge accumulation effects are enhanced, which cause the potential to gradually deviate from the linear distribution

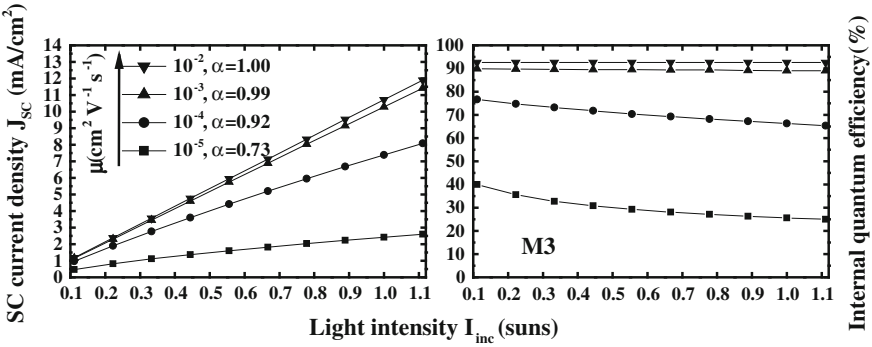

Fig. 4.12 The dependency of short-circuit current and internal quantum efficiency on the mobility and the light intensity for the morphology M3. J_{SC} is related to I_{inc} as $J_{SC} \propto I_{inc}^{\alpha}$, and α varies with mobility

improve the PCE, the strong absorption is more effective than the high mobility, especially as the particular mobility is high enough to extract almost all the charges diffusing in the system.

A typical feature of organic solar cells is that the short-circuit current density J_{SC} does not scale linearly with the exciton generation rate W_{eg} or light intensity I_{inc} [87]. Instead, a power law relationship is found and given by $J_{SC} \propto I_{inc}^{\alpha}$, where $\alpha \leq 1$ [88, 91]. Such deviation from linearity has been ascribed to nongeminate charge recombination [76, 91]. When the charge mobility decreases, the average time for free charges exiting from the device tends to increase, and the occurrence probability of nongeminate charge recombination would increase. This results in a bigger deviation from unity for α, and more rapid decrease in IQE with increasing light intensity, as shown in Fig. 4.12.

Recent theoretical calculations based on analysis of energy levels of frontier orbits have predicted that 15 % power conversion efficiency for polymer/fullerene system is possible [96]. For the fill factor 0.65, we simulate PCE contour curves as a function of the blend morphologies and the charge mobility as plotted in Fig. 4.13. It should be noted that the optimal 5 % PCE is limited by many factors listed in Table 4.4. Figure 4.13 shows that by improving the polymer morphology and increasing the charge mobility, the PCE can be increased from the experimental value of 1.3 % to about 5 %.

4.5 Continuum Device Model

The continuum device model, or drift-diffusion model, captures the drift of carriers under an electric field and diffusion due to the gradient in concentrations [97]. In modeling the electronic process in organic light emitting diodes (OLEDs), such approach has been widely employed [98, 99], and recently, it has been extensively

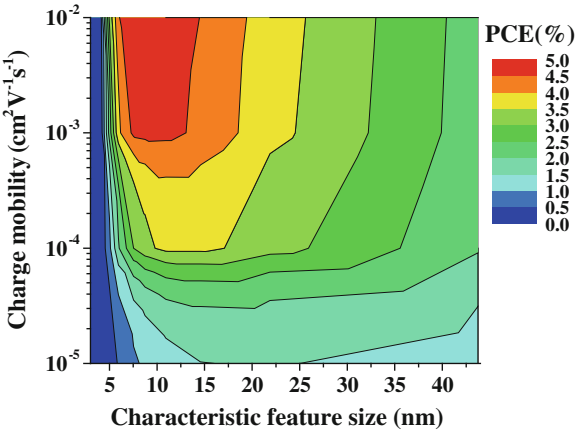

Fig. 4.13 Contour plots showing the calculated power conversion efficiency (PCE) for the blend morphologies versus the charge mobility and the characteristic feature size in the blend

applied in modeling photovoltaic devices [75, 100–108]. Barker et al. [100] developed a one-dimensional device model for a bilayer organic device. The experimental data can be well reproduced. In their approach, electrons and holes are assumed to be only generated directly by absorbing a fraction of incident light leading to charge separation at interface. Koster et al. [75] has demonstrated an equilibrium one-dimensional device model for the BHJ solar cells. The model includes drift and diffusion of charge carriers, the influence of space charge on the electric field, field- and temperature-dependent generation of free charge carriers, and bimolecular recombination. The current density-voltage (J-V) characteristics are solved self-consistently which are shown to be in excellent agreement with the experimental curves. Here, we are reviewing some of the recent progresses in drift-diffusion model and will apply it to model the low band gap polymer solar cell.

The solar emission generates exciton in polymer and the exciton migrates to the donor acceptor interface to generate bound electron and hole pair. The bound e-h pair may dissociate into free carriers with a rate k_d or geminately decay to the ground state with a rate k_f. The separation of e-h pair is a competition between dissociation and decay. According to Braun's model [109], the probability of e-h pair dissociation is given by

$$P = k_d / (k_d + k_f) \tag{4.52}$$

Once the e-h pair is dissociated, the free charge carriers have to move toward the respective electrodes, generating steady current in the device. The electron (hole) current density $J_{n(p)}$ has two contributions: the drift current due to the electrostatic potential gradient and the diffusion current due to the charge density gradient as determined by the following equations:

$$J_n = -qn\mu_n \frac{\partial}{\partial x}\psi + qD_n \frac{\partial}{\partial x}n \quad \text{and} \quad J_p = -qp\mu_p \frac{\partial}{\partial x}\psi - qD_p \frac{\partial}{\partial x}p, \tag{4.53}$$

where q is the elementary charge, $D_{n(p)} = \mu_{n(p)} k_B T/q$ is the carrier diffusion coefficient [97] and $\mu_{n(p)}$ is the carrier mobility. The electrostatic potential ψ and the electron (hole) density $n(p)$ satisfy the Poisson equation

$$\frac{\partial^2}{\partial x^2}\psi(x) = \frac{q}{\varepsilon}[n(x) - p(x)], \tag{4.54}$$

where ε is the dielectric constant. When electrons and holes meet during transport, there occurs charge recombination. The bimolecular recombination is one of the most important charge-carrier loss mechanisms. And for some system, the loss is mainly through charge traps. The bimolecular recombination rate is

$$R = k_r(np - n_{int}^2) \tag{4.55}$$

where the bimolecular recombination constant is $k_r = \frac{q}{\varepsilon}\min(\mu_n, \mu_p)$, and $n_{\text{int}} = N_c \exp(-qE_{gap}/k_B T)$ is the intrinsic carrier density of electrons/holes, where N_c is the effective density of states of either conduction or valence band edge.

The net generation of free charge carriers depends on e-h pair generation and its subsequent dissociation as well as recombination. In steady-state, the number of bound e-h pairs per unit volume (X) follows:

$$\frac{dX}{dt} = G - k_f X - k_d X + R = 0 \tag{4.56}$$

where G is the generation rate of e-h bound pair. The net generation rate of free charge carriers U is then written as

$$U = k_d X - R = PG - (1 - P)R \tag{4.57}$$

Here, U is related to the gradient of current density $J_{n(p)}$ through the continuity equations

$$\frac{\partial}{\partial x}J_n(x) = qU(x) \quad \text{and} \quad \frac{\partial}{\partial x}J_p(x) = -qU(x) \tag{4.58}$$

To obtain a solution of the equations, boundary conditions of charge densities and electrostatic potential are essential. The effective electron and hole densities at respective electrode equal to N_c gives the boundary condition for carrier densities. And (4.50) serves as the boundary condition for the electrostatic potential. Poisson equation and the continuity equations could be solved iteratively by a numerical scheme developed by Gummel [90]. Finally, the J-V curve and carrier densities can be obtained.

The separation of bound e-h pairs into free charges is an important process in BHJ solar cells. The photocurrent is governed by the field and temperature dependent dissociation of e-h pairs according to Onsager's theory [110]. Braun has made an important refinement to this theory by pointing out that the bound e-h pair has a finite lifetime [109]. Therefore, the exciton dissociate rate k_d can be calculated according to

$$k_d = \frac{3R}{4\pi a^3} e^{-E_b/kT}(1 + b + \frac{b^2}{3} + \cdots) \tag{4.59}$$

where R is the Langevin bimolecular recombination rate, E_b is the e-h pair binding energy $\sim q^2/(4\pi\varepsilon a)$, and $b = q^3F/(8\pi\varepsilon k_B^2T^2)$, F is the electric field strength. Recently, an extended Onsager theory has been proposed based on finite recombination rate at nonzero reaction radius [111]. It was found that the exponential kinetics for both recombination and separation processes assumed in Braun's model might not be true.

Several models have been proposed to describe the charge recombination mechanism. These include: (i) the original and classical Langevin model [112] with the recombination rate constant $k_r = \frac{q}{\varepsilon}(\mu_n + \mu_p)$; (ii) the minimum mobility model [113] where the recombination rate constant is given by $k_r = \frac{q}{\varepsilon}\min(\mu_n, \mu_p)$; (iii) the potential fluctuation model [114] where a potential barrier was imposed, $k_r = \frac{q}{\varepsilon}\exp(-\frac{\Delta E}{k_BT})(\mu_n + \mu_p)$; (iv) carrier concentration gradient model [115] in which the recombination rate is proportional to the local product of electron and hole concentrations; (v) two-dimensional Langevin recombination theory [116] where the recombination rate depends on the square root of density of charge carriers; and (vi) unified theory of geminate and bulk electron-hole recombination [117] where the recombination occurring at a nonzero separation with a finite intrinsic rate is taken into account to explain the observed much smaller recombination rate constant than those predicted from Langevin theory.

Since the one-dimensional drift-diffusion model can only be applied to BHJ or bilayer system can only describe motion in one-dimension across the active layer, ignoring the 3-D morphology effect. A natural extension of the current model to higher dimension is expected to be able to account for the effect of morphology. Buxton and Clarke [101] developed a two-dimensional device model to simulate the morphological effects such as domain size, order and percolation on J-V curve and other device performance. However, the dissociation probability of e-h pairs is not properly taken into account. Williams and Walker [118] presented a two-dimensional model in which the effects of optical interference and the competition between dissociation and decay of e-h pairs were considered. Maturova et al. [103, 104, 106] also developed a two-dimensional morphological model, where the active layer is divided into two regions, called donor–acceptor mix and acceptor pure phases. Since the precise location of charge separation could not be specified, to establish the quantitative relationship between the performance of solar cells and the degrees of phase separation remains a challenging issue.

On the other hand, such equilibrium device model can only give a description of the steady-state behavior. Hwang and Greenham [102] utilized a time-dependent device model to deal with the transient photocurrent of organic BHJ solar cells. The simulated transient photocurrent reproduced the experimental results. They further improved the time-dependent device model by incorporating electron trapping [105].

Now, we are ready to apply the above mentioned methods to model the BHJ solar cell, namely, to simulate J-V curve. The primary objective is to establish quantitative relationship between the device performance and the microscopic processes such as charge dissociation and recombination rates, and charge mobility.

Recently, highly efficient BHJ photovoltaic cells with poly [N-9″-hepta-decanyl-2,7-carbazole-alt-5,5-(4′,7′-di-2-thienyl-2′,1′,3′-benzothiadiazole)] (PCDTBT) as the donor and [6]-phenyl C_{70}-butyric acid methyl ester ($PC_{70}BM$) as the acceptor (see Fig. 4.14) have been reported [119]. The PCDTBT/$PC_{70}BM$ solar cells exhibit one of the best performance of polymer solar cells studied to date, with PCE is 6.1 % and V_{OC} is as high as 0.88 V. We performed simulations on the solar cells using the one-dimensional continuum device model.

It is essential to understand the fundamental processes of excitons and carriers governing photovoltaic conversion. Here we are interested in revealing the effect of e-h bound pair dissociation rate k_d and recombination rate k_f on V_{OC}. The PCDTBT/$PC_{70}BM$ solar cells exhibit one of the best performance of polymer solar cells studied to date, with $J_{SC} = 10.6$ mA cm^{-2}, $V_{OC} = 0.88$ V, $FF = 0.66$ and $\eta_e = 6.1$ %. The thickness of the active layer is 80 nm. The device is irradiated under both

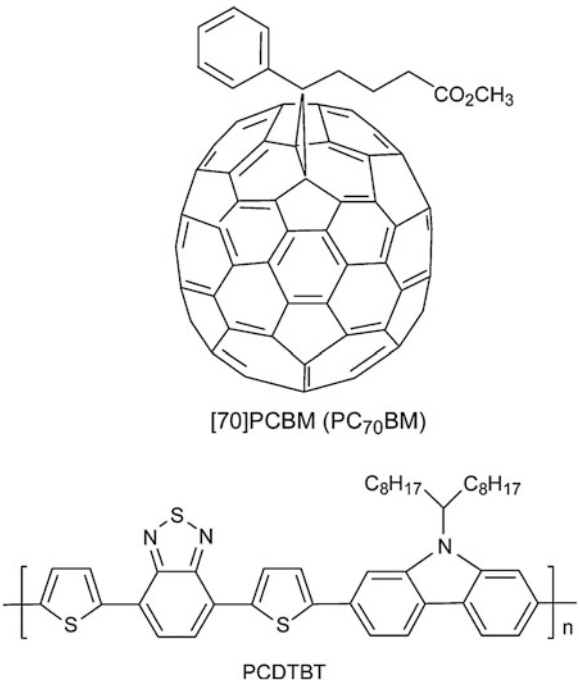

Fig. 4.14 The chemical structures of $PC_{70}BM$ and PCDTBT

monochromatic green light (532 nm) with an intensity of 19.67 mW cm^{-2} and AM 1.5 G with 100 mW cm^{-2}.

Firstly, the exciton generation rate G is determined by the experimental optical absorption spectrum for the blend and the AM 1.5 G solar spectrum through the following equation:

$$G = \int_0^{800\text{nm}} (N_i(\lambda) - N_o(\lambda))d\lambda \Big/ L = \int_0^{800\text{nm}} (N_i(\lambda) \times (1 - 10^{-A(\lambda)\times L}))d\lambda \Big/ L \tag{4.60}$$

where A is the normalized absorption coefficient, λ is the photon wavelength, N_i is the incident photon number per unit area, N_o is transmitted photon number, L is the thickness of the active layer of the solar cell.

For the BHJ structure, it is assumed that exciton generation is uniform, namely, the exciton generation is not space-dependent. Through (4.59), we obtain the rate as $G = 1 \times 10^{28}$ m^{-3} s^{-1} under AM 1.5 G radiations. The charge carrier mobilities are taken from the experimental measurements as $\mu_n = 3.5 \times 10^{-3}$ cm^2 V^{-1} s^{-19} and $\mu_p = 1.0 \times 10^{-3}$ cm^2 V^{-1} s^{-1} [120]. The dielectric constant ε for conjugated polymers is typically between 3 and 4, here we set it to be 3.5. The effective density of states N_c for electrons and holes at the electrodes is chosen to be 2.5×10^{25} m^{-3} [75]. The energy gap E_{gap} between the LUMO of the acceptor and the HOMO of the donor is 1.3 eV, which sets the boundary condition for solving the Poisson equation.

It has been shown that k_d depends on the electron-hole pair separation distance a as well as on the built-in field and temperature [75, 109]. Here, we vary the electron-hole pair distance a from 1 to 2.2 nm, which results in a range of k_d from 10^5 to 10^7 s^{-1}. The decay rate k_f is correspondingly varied from 10^5 to 10^7 s^{-1}. These values cover the practically accessible organic materials useful in photovoltaic cell applications. The simulated V_{OC} versus k_d and k_f is shown in Fig. 4.15.

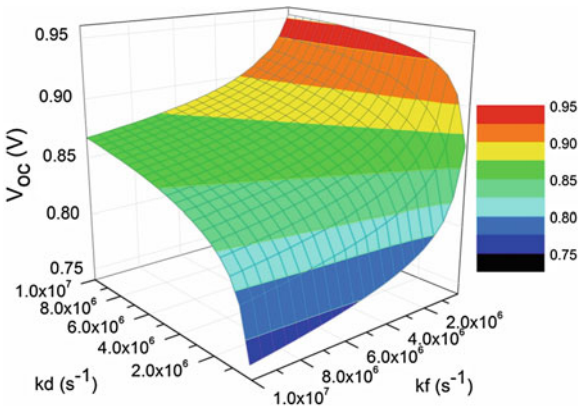

Fig. 4.15 Influence of the dissociate rate k_d and the decay rate k_f on the open-circuit voltage V_{OC} of the PCDTBT/$PC_{70}BM$ solar cells

For large open-circuit voltage $V_{OC} > 0.9$ V, which corresponds to a regime of $k_d > 4k_f$, as high as 79.1 % of the bound electron-hole pairs dissociate into free charge carriers without significant carrier decay to the ground state. In this case, a large number of free charge carriers could participate in the transport and reach the electrodes. In order to optimize the performance of organic solar cells, V_{OC} as functions of several parameters are analyzed here. V_{OC} is limited primarily by the effective band gap E_{gap}, namely, the gap between LUMO of acceptor and the HOMO of donor, and can be defined from the quasi-Fermi level splitting as [121]

$$eV_{OC} = E_{gap} - \underbrace{k_B T \ln\left(\frac{N_L N_H}{np}\right)}_{>0} \tag{4.61}$$

where N_L and N_H are the densities of states in the LUMO of the acceptor and HOMO of the donor respectively that cannot be exceeded by n and p. Brabec et al. [121] presented experimental measurements showing an almost linear correlation of V_{OC} with E_{gap} for solar cells based on blends from polyphenylenevinylene with different fullerene derivatives.

For comparison, the experimental and simulated J-V curves under the illumination of both monochromatic green light (532 nm) and AM 1.5 G irradiation are simulated by device model in Fig. 4.16. The good agreement between the experiment and the simulation justifies the model adopted in our investigation and underlying mechanisms incorporated.

In Fig. 4.17, we present the result of light intensity effect on V_{OC}. V_{OC} exhibits a straight line when plotted as a function of logarithm of light intensity. The fitted slope, 0.026 V is approximately equal to the experiment data $\sim$0.03 V conducted by Tromholt et al. [122] and consistent with the theoretical prediction based on the notion that the quasi-Fermi levels are constant throughout the device, as pointed out by Koster et al. [75].

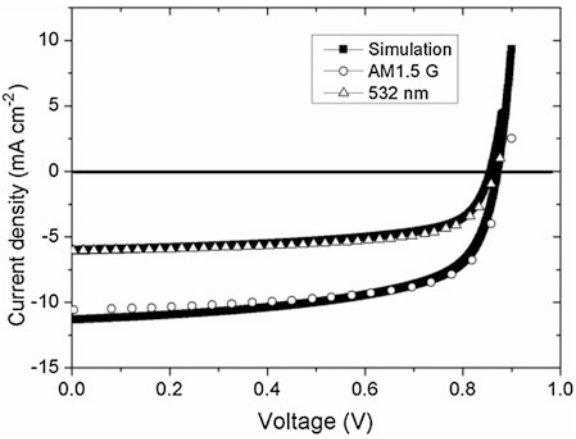

Fig. 4.16 Comparison of the theoretical simulation of J-V curve with the experimental measurements for PCDTBT/$PC_{70}BM$ device. Two types of illumination condition are considered, AM 1.5 G and monochrome at 532 nm

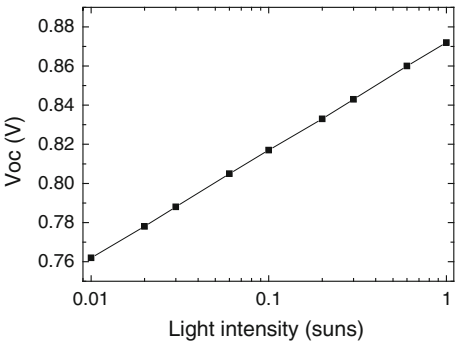

Fig. 4.17 Light intensity dependence of V_{OC} simulated by device model for the PCDTBT/$PC_{70}BM$ device

$$V_{oc} = \frac{E_{gap}}{q} - \frac{kT}{q}\ln\frac{(1-p)k_r N_c^2}{PG} \tag{4.62}$$

Namely, V_{OC} is proportional to the logarithm of light intensity.

We further look at the effect of the charge carrier mobility on V_{OC} as shown in Fig. 4.18. The increase in mobility leads to reduction of V_{OC}. Since the bimolecular recombination constant $k_r = \frac{\varepsilon}{q}\mu$, is proportional to the mobilities, and considering that recombination is a key loss mechanism, it is thus natural that high mobility results in high recombination rate. Hence the electron and hole density are reduced when large number of free charge carriers recombine throughout transport.

Last, we look at the charge mobility effects on short circuit current and the power conversion efficiency (Fig. 4.19). For the sake of comparison, we choose the all polymer device of the last section. It is seen that as the mobility increases, the short circuit current increases and then levels off, due to the steady current limit plus the

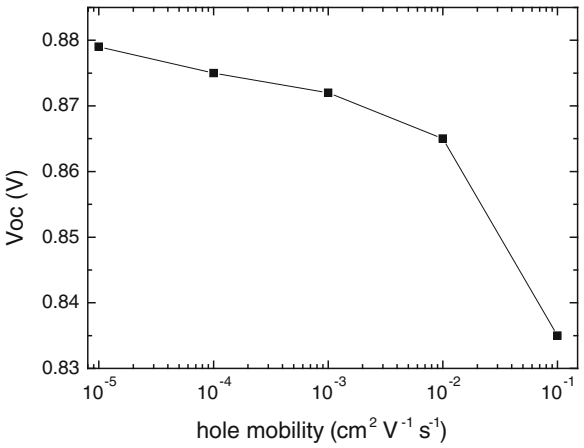

Fig. 4.18 V_{OC} as a function of hole mobility μ_p (the electron mobility μ_n is taken as 3.5 × μ_p) simulated by device model for the PCDTBT/$PC_{70}BM$ device

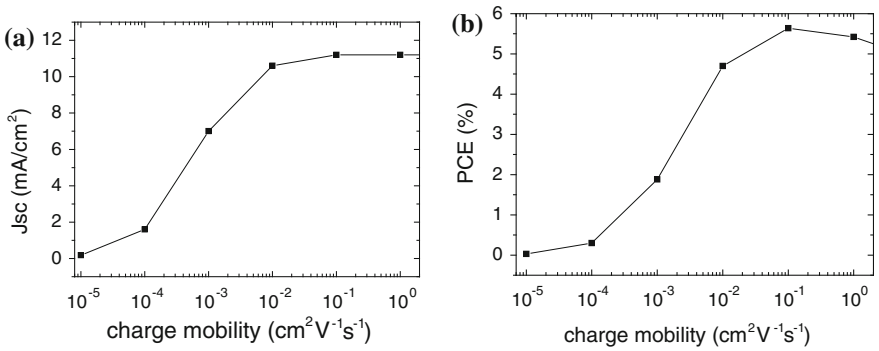

Fig. 4.19 J_{SC} (**a**) and PCE (**b**) as a function of charge mobility calculated for the all-polymer device

limited photo-generation of carriers. Similarly, the power conversion efficiency first increases, then levels off, and finally decreases, because the V_{oc} decreases with charge mobility. This is in good agreement with previous studies [123, 124].

4.6 Conclusion and Outlook

In summary, we have presented progresses in theoretical modeling of the photovoltaic processes in polymer through computational studies, covering the optical absorption and emission spectra, as well as exciton decay processes associated with exciton migration, and the device performance. The performance is essentially determined by the corresponding chemical (or electronic) structures and physical morphologies. On one hand, some basic performance parameters depend critically on chemical compositions (or electronic structures) of organic solar cells, for instance, the short-circuit current I_{SC} is actually constrained by the spectral light-harvesting ability of the constituent molecular semiconducting materials and their charge mobility; the open-circuit voltage V_{OC} is linked directly to the quasi-Fermi level difference between the LUMO of acceptor and the HOMO of donor. Theoretical analyses are important in screening chemical structures to achieve better performance. Furthermore, electron dynamic based on electronic structures for describing elementary steps in photovoltaic process can now be quantum mechanically calculated, for instance, some theoretical advances in understanding exciton-related processes in organic photovoltaic materials have been illustrated in this chapter. So far, our understanding of exciton dynamics is limited to hopping picture. Quantum coherence effect should be considered for better understanding.

On the other hand, the physical morphology has also been demonstrated to be a key factor in determining the optoelectronic properties in organic devices. One can significantly improve the device performance by optimizing the nanoscale phase-

separation morphology: a large interfacial area is beneficial to both efficient exciton dissociation and charge transport channels all the way to the electrode for efficient charge collection. Numerical simulation tools, e.g., the dynamic Monte Carlo method and the continuum device model presented in this Chapter, indeed help to quantitatively analyze these morphology dependencies for photovoltaic performance.

As discussed above, the overall photovoltaic process modeling is a typical multiscale issue, thus the device performance is controlled by a series of complicated phenomena that span a wide range of length and time scales. As a consequence, only those theoretical simulation methods with multiscale characteristics can effectively describe the photovoltaic mechanism in organic solar cells.

Theoretical models at different scales (e.g., from first-principles methods to classical continuum medium calculations) could be integrated in "decoupled" or "coupled" schemes. The former usually refers that one can quantum mechanically calculate the electronic structures and some key dynamic processes of the concerned photovoltaic systems, and then these properties or parameters, classically numerical simulation methods could be well established. The latter mainly relies on effective information exchange between different models to realize a coupled simulation scheme. Commonly well-defined physical quantities by the involved theoretical models are usually exchanged as a bridge between different simulation models. These multiscale/multiphysics simulation methods are indispensable tools to optimize the design of functional organic optoelectronic materials in the future.

Acknowledgments The authors are indebted to Dr. Qian Peng and Dr. Yingli Niu for their contributions in the study of optical absorption/emission spectra and the excited state decays, and to Dr. Yuan Shang for his contribution to the continuum device model. The research in Shuai's group has been funded the National Natural Science Foundation of China, the Ministry of Science and Technology of China, and the Chinese Academy of Sciences.

References

1. M. Pope, C.E. Swenberg, *Electronic Processes in Organic Crystals and Polymers*, 2nd edn. (Oxford University Press, New York, 1999)
2. E. Silinsh, V. Capek, *Organic Molecular Crystals: Interaction, Localization, and Transport Phenomena* (American Institute of Physics, New York, 1994)
3. H. Shirakawa, E.J. Louis, A.G. MacDiarmid, C.K. Chiang, A.J. Heeger, Chem. Commun. **578**, (1977)
4. W.P. Su, J.R. Schrieffer, A.J. Heeger, Phys. Rev. Lett. **42**, 1698 (1979)
5. J.L. Bredas, C. Adant, P. Tackx, A. Persoons, Chem. Rev. **94**, 243 (1994)
6. J.H. Burroughes, D.D.C. Bradley, A.R. Brown, R.N. Marks, K. Mackay, R.H. Friend, P.L. Burns, A.B. Holmes, Nature **347**, 539 (1990)
7. G. Gustafsson, Y. Cao, G.M. Treacy, F. Klavetter, N. Colaneri, A.J. Heeger, Nature **357**, 477 (1992)
8. F. Hide, M.A. Diaz-Garcia, B.J. Schwartz, M.R. Andersson, Q.B. Pei, A.J. Heeger, Science **273**, 1833 (1996)
9. N. Tessler, G.J. Denton, R.H. Friend, Nature **382**, 695 (1996)

10. S.V. Frolov, W. Gellemann, M. Ozaki, K. Yoshino, Z.V. Vardeny, Phys. Rev. Lett. **78**, 729 (1997)
11. G. Horowitz, Adv. Mater. **10**, 365 (1998)
12. H. Sirringhaus, P.J. Brown, R.H. Friend, M.M. Nielsen, K. Bechgaard, B.M.W. Langeveld-Voss, A.J.H. Spiering, R.A.J. Janssen, E.W. Meijer, P. Herwig, D.M. de Leeuw, Nature **401**, 685 (1999)
13. L. Kergoat, B. Piro, M. Berggren, G. Horowitz, M.C. Pham, Anal. Bioanal. Chem. **402**, 1813 (2012)
14. C. Brabec, V. Dyakonov, J. Parisi, N.S. Sariciftci (eds.), *Organic Photovoltaics* (Springer, Berlin, 2003)
15. R.E. Peierls, *Quantum Theory of Solids* (Oxford University Press, London, 1955)
16. A.J. Heeger, S. Kivelson, J.R. Schrieffer, W.P. Su, Rev. Mod. Phys. **60**, 781 (1988)
17. S.R. Marder, C.B. Gorman, F. Meyers, J.W. Perry, G. Bourhill, J.L. Bredas, B.M. Pierce, Science **265**, 632 (1994)
18. D. Moses, J. Wang, A.J. Heeger, N. Kirova, S. Brazovskii, Proc. Natl. Acad. Sci. U.S.A. **98**, 13496 (2001)
19. I. Hwang, G.D. Scholes, Chem. Mater. **23**, 610 (2011)
20. H. Ishii, K. Sugiyama, E. Ito, K. Seki, Adv. Mater. **11**, 605 (1999)
21. G. Yu, J. Gao, J.C. Hummelen, F. Wudl, A.J. Heeger, Science **270**, 1789 (1995)
22. N. Banerji, S. Cowan, M. Leclerc, E. Vauthey, A.J. Heeger, J. Am. Chem. Soc. **132**, 17459 (2010)
23. V. Coropceanu, J. Cornil, D.A. da Silva Filho, Y. Olivier, R. Silbey, J.L. Bredas, Chem. Rev. **107**, 926 (2007)
24. V. Lemaur, M. Steel, D. Beljonne, J.L. Bredas, J. Cornil, J. Am. Chem. Soc. **127**, 6077 (2005)
25. Y.P. Yi, V. Coropceanu, J.L. Bredas, J. Am. Chem. Soc. **131**, 15777 (2009)
26. J.L. Bredas, J.E. Norton, J. Cornil, V. Coropceanu, Acc. Chem. Res. **42**, 1691 (2009)
27. H. Bassler, Phys. Status Solidi B. **175**, 15 (1993)
28. P.W.M. Blom, M.J.M. de Jong, J.J.M. Vleggaar, Appl. Phys. Lett. **68**, 3308 (1996)
29. C. Tanase, E.J. Meijer, P.W.M. Blom, D.M. de Leeuw, Phys. Rev. Lett. **91**, 216601 (2003)
30. N. Vukmirovic, L.W. Wang, Nanolett. **9**, 3996 (2010)
31. P. Prins, F.C. Grozema, J.M. Schins, S. Patil, U. Scherf, L.D.A. Siebeles, Phys. Rev. Lett. **96**, 146601 (2006)
32. R.A. Street, J.E. Northrup, A. Salleo, Phys. Rev. B. **71**, 165202 (2005)
33. H. Sirringhaus, Adv. Mater. **17**, 2411 (2005)
34. H. Yan, Z. Chen, Y. Zheng, C. Newman, J. Quinn, F. Dotz, M. Kastler, A. Facchetti, Nature **457**, 679 (2009)
35. H.N. Tsao, D.M. Cho, I. Park, M.R. Hansen, A. Mavrinskiy, D.Y. Yoon, R. Graf, W. Pisula, H.W. Spiess, K. Muellen, J. Am. Chem. Soc. **133**, 2605 (2011)
36. L.J. Wang, G.J. Nan, X.D. Yang, Q. Peng, Q.K. Li, Z.G. Shuai, Chem. Soc. Rev. **39**, 423 (2010)
37. Z.G. Shuai, L.J. Wang, Q.K. Li, Adv. Mater. **23**, 1145 (2011)
38. A. Troisi, Chem. Soc. Rev. **40**, 2347 (2011)
39. S. Staftstrom, Chem. Soc. Rev. **39**, 2484 (2010)
40. R. Ianconescu, E. Pollak, J. Phys. Chem. **108**, 7778 (2004)
41. A.M. Mebel, M. Hayashi, K.K. Liang, S.H. Lin, J. Phys. Chem. A **103**, 10674 (1999)
42. Y.L. Niu, Q. Peng, C.M. Deng, X. Gao, Z.G. Shuai, J. Phys. Chem. A **114**, 7817 (2010)
43. C. Eckart, Phys. Rev. **47**, 552 (1935)
44. Q. Peng, Y.P. Yi, Z.G. Shuai, J.S. Shao, J. Chem. Phys. **126**, 114302 (2007)
45. Y.L. Niu, Q. Peng, Z.G. Shuai, Sci. China Ser. B- Chem. **51**, 1153 (2008)
46. M. Hayashi, A.M. Mebel, K.K. Liang, S.H. Lin, J. Chem. Phys. **108**, 2044 (1998)
47. J.Y. Kim, K. Lee, N.E. Coates, D. Moses, T.Q. Nguyen, M. Dante, A.J. Heeger, Science **2007**(317), 222 (2007)

48. N. Blouin, A. Michaud, M. Leclerc, Adv. Mater. **19**, 2295 (2007)
49. J. Hou, L.J. Huo, C. He, C.H. Yang, Y.F. Li, Macromolecule **39**, 4657 (2006)
50. I.W. Hwang, Q.H. Xu, C. Soci, B. Chen, A.K.Y. Jen, D. Moses, A.J. Heeger, Adv. Funct. Mater. **17**, 563 (2007)
51. B.S. Hudson, B.E. Kohler, E.C. Lim (eds.), *Excited States* (Academic, New York, 1973)
52. Z. Shuai, J.L. Bredas, S.K. Pati, S. Ramasesha, Phys. Rev. B **56**, 9298 (1997)
53. J.W.Y. Lam, B.Z. Tang, J. Polym. Sci. Part A Polym. Chem. **41**, 2607 (2003)
54. I. Gontia, S.V. Frolov, M. Liess, E. Ehrenfreund, Z.V. Vardeny, Phys. Rev. Lett. **82**, 4058 (1999)
55. D. Beljonne, Z.G. Shuai, L. Serrano-Andres, J.L. Bredas, Chem. Phys. Lett. **279**, 1 (1997)
56. L.P. Chen, X.J. Hou, L.Y. Zhu, S.W. Yin, Z.G. Shuai, J. Theo, Comput. Chem. **5**, 391 (2006)
57. Q. Peng, Y.L. Niu, Y.Q. Jiang, Y. Li, Z.H. Wang, Z.G. Shuai, J. Chem. Phys. **134**, 074510 (2011)
58. Y.Q. Jiang, Q. Peng, X. Gao, Z.G. Shuai, Y.L. Niu, S.H. Lin, J. Mater. Chem. **22**, 4491 (2012)
59. A.I. Krylov, Chem. Phys. Lett. **338**, 375 (2001)
60. O.V. Greitsenko, E.J. Baerends, Phys. Chem. Chem. Phys. **11**, 4640 (2009)
61. S. Grimme, M. Waletzke, J. Chem. Phys. **111**, 5645 (1999)
62. M. Liess, S. Jeglinski, P.A. Lane, Z.V. Vardeny, Synth. Met. **84**, 891 (1997)
63. L. Huo, T.L. Chen, Y. Zhou, J. Hou, H.-Y. Chen, Y. Yang, Y. Li, Macromolecules **42**, 4377 (2009)
64. J. Gierschner, H.-G. Mack, L. Luer, D. Oelkrug, J. Chem. Phys. **116**, 8596 (2002)
65. Z.G. Shuai, L.J. Wang, C.C. Song, *Theory of Charge Transport in Carbon Electronic Materials* (Springer, Heidelberg, 2012)
66. H. Wiesenhofer, D. Beljonne, G.D. Scholes, E. Hennebicq, J.L. Brédas, E. Zojer, Adv. Funct. Mater. **15**, 155 (2005)
67. B.P. Krueger, G.D. Scholes, G.R. Fleming, J. Phys. Chem. B. **102**, 5378 (1998)
68. D. Beljonne, J. Cornil, R.J. Silbey, P. Millié, J.L. Brédas, J. Chem. Phys. **112**, 4749 (2000)
69. S. Athanasopoulos, E. Hennebicq, D. Beljonne, A.B. Walker, J. Phys. Chem. C **112**, 11532 (2008)
70. E. Hennebicq, G. Pourtois, G.D. Scholes, L.M. Herz, D.M. Russell, C. Silva, S. Setayesh, A. C. Grimsdale, K. Müllen, J.L. Brédas, D. Beljonne, J. Am. Chem. Soc. **127**, 4744 (2005)
71. G.D. Scholes, Ann. Rev. Phys. Chem. **54**, 57 (2003)
72. C.P. Hsu, P.J. Walla, M. Head-Gordon, G.R. Fleming, J. Phys. Chem. B **105**, 11016 (2001)
73. C.P. Hsu, Z.Q. You, H.C. Chen, J. Phys. Chem. C **112**, 1204 (2008)
74. C.P. Hsu, Acc. Chem. Res. **42**, 509 (2009)
75. L.J.A. Koster, E.C.P. Smits, V.D. Mihailetchi, P.W.M. Blom, Phys. Rev. B **72**, 085205 (2005)
76. P.K. Watkins, A.B. Walker, G.L.B. Verschoor, Nano Lett. **5**, 1814 (2005)
77. D.T. Gillespie, J. Comput. Phys. **22**, 403 (1976)
78. L.Y. Meng, Y. Shang, Q.K. Li, Y.F. Li, X.W. Zhan, Z.G. Shuai, R.G.E. Kimber, A.B. Walker, J. Phys. Chem. B **114**, 36 (2010)
79. F. Yang, S.R. Forrest, ACS Nano **2**, 1022 (2008)
80. L.Y. Meng, D. Wang, Q.K. Li, Y.P. Yi, J.L. Bredas, Z.G. Shuai, J. Chem. Phys. **134**, 124102 (2011)
81. A.P.J. Jansen, Comput. Phys. Commun. **86**, 1 (1996)
82. J.J. Lukkien, J.P.L. Segers, P.A.J. Hilbers, R.J. Gelten, A.P.J. Jansen, Phys. Rev. E **58**, 2598 (1998)
83. R.A. Marsh, C. Groves, N.C. Greenham, J. Appl. Phys. **101**, 083509 (2007)
84. X. Zhan, Z.A. Tan, B. Domercq, Z. An, X. Zhang, S. Barlow, Y. Li, D. Zhu, B. Kippelen, S. R. Marder, J. Am. Chem. Soc. **129**, 7246 (2007)
85. J. Hou, Z.A. Tan, Y. Yan, C. He, C.H. Yang, Y. Li, J. Am. Chem. Soc. **128**, 4911 (2006)
86. R.A. Marcus, Rev. Mod. Phys. **65**, 599 (1990)
87. U. Wolf, V.I. Arkhipov, H. Baessler, Phys. Rev. B **59**, 7507 (1999)

88. V.I. Arkhipov, U. Wolf, H. Bässler, Phys. Rev. B **59**, 7514 (1999)
89. S. Barth, U. Wolf, H. Bässler, Phys. Rev. B **60**, 8791 (1999)
90. H.K. Gummel, IEEE Trans. Electron Devices **11**, 455 (1964)
91. M. Riede, T. Mueller, W. Tress, R. Schueppel, K. Leo, Nanotechnology **19**, 424001 (2008)
92. L.J.A. Koster, V.D. Mihailetchi, R. Ramaker, P.W.M. Blom, Appl. Phys. Lett. **86**, 123509 (2005)
93. S.M. Sze, *Physics of Semiconductor Devices* (Wiley, New York, 1981)
94. Y. Shang, Q. Li, L. Meng, D. Wang, Z. Shuai, Appl. Phys. Lett. **97**, 143511 (2010)
95. M. Casalegno, G. Raos, R. Po, J. Chem. Phys. **132**, 094705 (2010)
96. M.C. Scharber, D. Mühlbacher, M. Koppe, P. Denk, C. Waldauf, A.J. Heeger, C.J. Brabec, Adv. Mater. **18**, 789 (2006)
97. S. Selberherr, *Analysis and Simulation of Semiconductor Devices* (Spinger, New York, 1984)
98. B.K. Crone, P.S. Davids, I.H. Campbell, D.L. Smith, J. Appl. Phys. **87**, 1974 (2000)
99. B. Ruhstaller, S.A. Carter, S. Barth, H. Riel, W. Riess, J.C. Scott, J. Appl. Phys. **89**, 4575 (2001)
100. J.A. Barker, C.M. Ramsdale, N.C. Greenham, Phys. Rev. B **67**, 075205 (2003)
101. G.A. Buxton, N. Clarke, Phys. Rev. B **74**, 085207 (2006)
102. I. Hwang, N.C. Greenham, Nanotechnology **19**, 424012 (2008)
103. K. Maturova, M. Kemerink, M.M. Wienk, D.S.H. Charrier, R.A.J. Janssen, Adv. Funct. Mater. **19**, 1379 (2009)
104. K. Maturova, S.S. van Bavel, M.M. Wienk, R.A.J. Janssen, M. Kemerink, Nano Lett. **9**, 3032 (2009)
105. I. Hwang, C.R. McNeil, N.C. Greenham, J. Appl. Phys. **106**, 094506 (2009)
106. K. Maturova, R.A.J. Janssen, M. Kemerink, ACS Nano **4**, 1385 (2010)
107. J.T. Shieh, C.H. Liu, H.F. Meng, S.R. Tseng, Y.C. Chao, S.F. Horng, J. Appl. Phys. **107**, 084503 (2010)
108. Y.M. Nam, J. Huh, W.J. Jo, Sol. Energy Mater. Sol. Cells. **94**, 1118 (2010)
109. C.L. Braun, J. Chem. Phys. **80**, 4157 (1984)
110. L. Onsager, J. Chem. Phys. **2**, 599 (1934)
111. M. Wojcik, M. Tachiya, J. Chem. Phys. **130**, 104107 (2009)
112. P. Langevin, Ann. Chim. Phys. **28**, 433 (1903)
113. L.J.A. Koster, V.D. Mihailetchi, P.W.M. Blom, Appl. Phys. Lett. **88**, 052104 (2006)
114. G.J. Adriaenssens, V.I. Arkhipov, Solid State Commun. **103**, 541 (1997)
115. C. Deibel, A. Wagenpfahl, V. Dyakonov, Phys. Rev. B **80**, 075203 (2009)
116. G. Juska, K. Genevicius, N. Nekrasas, G. Sliauzys, R. Osterbacka, Appl. Phys. Lett. **95**, 013303 (2009)
117. M. Hilczer, M. Tachiya, J. Phys. Chem. C **114**, 6808 (2010)
118. J. Williams, A.B. Walker, Nanotechnology **19**, 424011 (2008)
119. S.H. Park, A. Roy, S. Beaupre, S. Cho, N. Coates, J.S. Moon, D. Moses, M. Leclerc, K. Lee, A.J. Heeger, Nat. Photonics **3**, 297 (2009)
120. S. Wakim, S. Beaupre, N. Blouin, B.R. Aich, S. Rodman, R. Gaudiana, Y. Tao, M. Leclerc, J. Mater. Chem. **19**, 5351 (2009)
121. C.J. Brabec, A. Cravino, D. Meissner, N.S. Sariciftci, T. Fromherz, M.T. Rispens, L. Sanchez, J.C. Hummelen, Adv. Funct. Mater. **11**, 374 (2001)
122. T. Tromholt, E.A. Katz, B. Hirsch, A. Vossier, F.C. Krebs, Appl. Phys. Lett. **96**, 073501 (2010)
123. M.M. Mandoc, L.J.A. Koster, P.W.M. Blom, Appl. Phys. Lett. **90**, 133504 (2007)
124. C. Deibel, A. Wagenpfahl, V. Dyakonov, Phys. Status Solidi-Rapid. Res. Lett. **2**, 175 (2008)

Part II
Materials

Chapter 5
Recent Advances in P-Type Conjugated Polymers for High-Performance Solar Cells

Yen-Ju Cheng, Chien-Lung Wang, Jhong-Sian Wu and Chain-Shu Hsu

Abstract Bulk-heterojunction (BHJ) polymer solar cells have achieved significant progress in the recent years, with the efficiency now over 10 %. The p-type polymer in the BHJ blend played a key role in the amazing technology advance. In this chapter, we will timely update over 80 conjugated polymers leading to high-performance solar cells. The principle of molecular design with structure-properties relationship with respect to device characteristics will also be discussed, as the materials and morphology are tightly interconnected.

5.1 Introduction

Bulk-heterojunction (BHJ) solar cells based on a fullerene/polymer composite have been developed over 15 years [1]. The efficiency of polymer-based solar cells grew slowly from 3 to 5 % for many years. However, this type of solar cell has made remarkable improvement in efficiency since 2009. Such a rapid progress is very significant compared to any other types of current solar cells, showing promise and brightness for future communization. In addition to advanced device engineering and controlled active layer morphology, the major breakthrough in this active area comes from development of new conjugated polymers for efficient light-harvesting and charge transport. Theoretical calculation predicts that the PCE of BHJ solar cell over 10 % is achievable if a p-type material equipped with all required properties is fulfilled [2]. Through tremendous research effort to create numerous novel conjugated polymers, encouraging device performances with PCEs up to 8–9 % have been accomplished recently [3–7].

Several important reviews have examined the development of conjugated polymers for solar cells applications [8–22]. In view of rapid growth of this active

Y.-J. Cheng · C.-L. Wang · J.-S. Wu · C.-S. Hsu (✉)
Department of Applied Chemistry, National Chiao Tung University,
1001 University Road, Hsinchu, Taiwan
e-mail: cshsu@mail.nctu.edu.tw

Y. Yang and G. Li (eds.), *Progress in High-Efficient Solution Process Organic Photovoltaic Devices*, Topics in Applied Physics 130,
DOI 10.1007/978-3-662-45509-8_5

field and increasing number of publications in the past five years, this chapter will timely update over 80 conjugated polymers leading to high-performance solar cells. The principle of molecular design with structure-properties relationship with respect to device characteristics will be discussed.

5.2 Polythiopene-Based Conjugated Polymer Incorporating Electron-Deficient Acceptor Units

Among conjugated polymers, regioregular poly(3-alkylthiophene)s (P3ATs) are the most representative and well-studied ones because of their unique optoelectrical properties, chemical stability, and solution processability [23, 24]. The molecular properties of P3AT are strongly affected by the chemical identity of the repeating unit, while the device performances of P3AT-based optoelectronics depend not only on P3ATs' intrinsic molecular properties, but also their solid-state structures. The conjugated backbone of polythiophene is considered to be relatively "flexible". Theoretical study indicates that twisting an unsubstituted sex ithiophene from total end-to-end dihedral angles of 0^{o}–180^{o} requires only 2.5 kcal $mole^{-1}$ [25]. Thermodynamic analysis of poly(3-alkylthiophenes) also reveals a low twist-glass transition at −23 °C for P3HT and 67 °C for poly(3-butylthiophene) (P3BT), which represent the temperatures at which relaxation via twisting motion of the thiophene rings is activated [26]. Thus, for head-to-tail regioregular P3ATs, the flexibility of the conjugated backbones makes small barriers for the polymer chains to adjust into the *trans*-coplanar conformation and facilitates P3ATs to reach high crystallinity. When applied into optoelectronic applications, crystalline nature of P3ATs plays an important role in the device performances. Crystallization of P3ATs not only enhances the charge carrier mobilities, but also extends light harvesting region of the P3AT thin films [27, 28]. Adapting the *trans*-coplanar conformation in P3AT chains minimizes the inter-ring dihedral angles, and eases inter-chain packing. Combining with the low aromaticity of thiophene rings and high quinoid character of polythiophene, P3ATs possess average E_g around 2.0 eV and provides a broad absorption from 350 to 650 nm [12]. Because of the advantages of easy processability, adequate absorption range and high charge carrier mobilities, P3ATs are one of the most useful materials in the applications of organic field effect transistors (OFETs) and polymer solar cells (PSCs). Averaged power conversion efficient (PCE) of P3HT:PC_{61}BM-based PSCs achieved over 4 %, when the optimized morphology of the active layer is reached through various treatments [12, 29–37]. A high PCE of 6.5 % was achieved by applying P3HT/indene-C_{60} bisadduct (ICBA) as an active material [38].

The molecular properties of P3ATs and the performances of P3HT-based PSCs make P3AT a representative conjugated polymer. However, the further enhancement in the performances of P3HT based PSCs is majorly hindered by the relatively large E_g ($\sim$2.0 eV) and the high-lying highest occupied molecular orbital (HOMO)

of P3HT, which limits the light-harvesting range of the active materials and the V_{oc} ($\sim$0.6 V) of the devices. Tremendous efforts have been put into modulating the energy levels of frontier orbitals of polythiophene-based or -incorporated polymers. Since alternating an electron-rich donor (D) unit and an electron-deficient acceptor (A) unit in a conjugated polymer backbone has been recognized as an effective method in tuning the position of the frontier molecular orbitals, in this section, we emphasize on the strategies for the HOMO energy level (E_{HOMO}), LUMO energy level (E_{LUMO}) and band gap (E_g) engineering via introducing various A units into the conjugated backbone of polythiophenes. Representative alternating copolymers with oligo(thiophene) (Fig. 5.1; Th_x, x = 1–8) and electron-deficient aromatic units (A in Fig. 5.1), such as: 2,1,3-benzothiadiazole (BT), naphtho[1,2-c:5,6-c′]bis[1,2,5]thiadiazole (NT), 1,4-diketo-pyrolo[3,4-*c*]pyrrole (DPP), thieno[3,4-*c*]pyrrole-4,6-dione(TPD), 2,3-diarylquinoxaline (QX), and isoindigo (iI) will be summarized. The concepts of molecular design, strategies for the E_{HOMO}, E_{LUMO} and E_g engineering and the resulting solar cell performances will be discussed. Due to different preparation methods and measurement conditions, the numerical values of E_{HOMO}, E_{LUMO}, E_g and the device performances of the materials developed by different research groups may not be comparable on the quantitative bases. However, the comparison remains useful for establishing trends in similar systems. In addition, it has been widely known that the alkyl side chains of P3ATs have pronounced influence not only on the solubility, phase behavior and phase structure of the pristine polymers, but also on the morphology of P3AT/PCBM blends [39–41]. Adequate length and density of the alkyl side chains on the conjugated backbones allow good balance between the solubility and optimal phase-separation morphology of the blends, and thus the resulting device performances [36, 41, 42]. Prudent choices of the alkyl side chains demonstrated in several researches will also

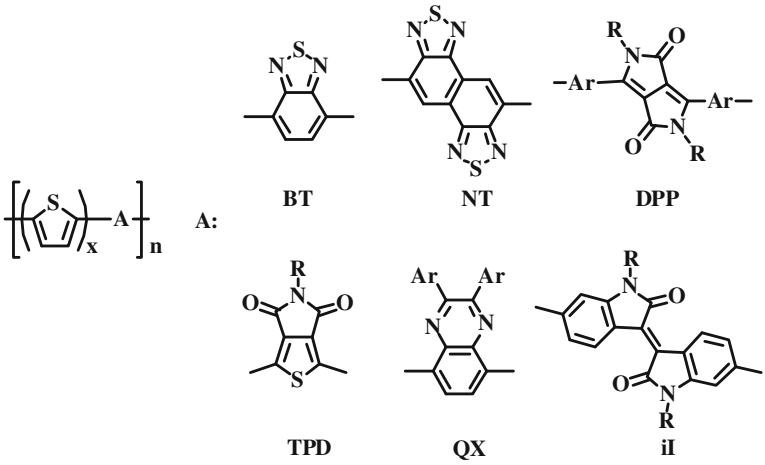

Fig. 5.1 Representative alternating conjugated copolymers with oligothiophene (Th_x) and electron-deficient aromatic units (A)

be discussed. Recently, instead of modifying alkyl side chains for the purposes of solubility or morphological control, Thompson's group demonstrated the E_{HOMO} engineering of P3AT via adjusting the bulkiness of the alkyl side chains [43]. The resulting copolymer poly(3-hexylthiophene-*co*-3-(2-ethylhexyl)thiophene) (P3HT-*co*-EHT) shows E_{HOMO} ranging from 5.30–5.48 eV depending on the molar ratio of 3-(2-ethylhexyl)thiophene comonomer. Optimized PCE of 3.58 % with a higher V_{oc} of 0.69 V was reported when $P3HT_{75}$-*co*-EHT_{25}:$PC_{61}BM$ was applied as the active material. Further increase in the molar ratio of EHT resulted in increased V_{OC}, but led to significant decreases in J_{sc}, FF and thus PCE.

5.2.1 Polythiophene-Based Polymers Containing 2,1,3-Benzothiadiazole Moieties

Incorporation of BT as A units in the π-conjugated polymer chain for the purpose of E_g engineering can be traced back to 1996 when the Meijer's group prepared alternating copolymer of pyrrole and BT [44]. The target at that time was aiming for preparing metallic conductive polymers approaching zero E_g and achieving a fundamental understanding of the relationship between the chemical structure of the polymer and its electronic properties [45–47]. Copolymer of BT and bithiopheneunits (**P1**) was first synthesized via electrochemical polymerization of 4,7-di(2-thienyl)-2,1,3-benzothiadiazole (Th_2BT) [48]. **P1** shows a much lower E_g (1.1 eV) than that of P3HT (1.9 eV), which demonstrated the effectiveness in decreasing E_g through the incorporation of BT units into the polythiophene backbone. However, due to its insolubility in common solvents, **P1** cannot be further processed after the polymerization reaction. To make the alternating Th_2/BT copolymer soluble, Jayakannan et al. [49] introduced octyl side chains to the 3- or 4-position at the 2-thienyl units of Th_2BT to prepare **P2** and **P3** through iron(III) chloride-mediated oxidative polymerization. The number-average molecular weight (M_n) and polydispersity (PDI) are 15.5 kDa and 2.7 for **P2**, and 23.4 kDa and 2.9 for **P3**. The steric hindrance caused by the octyl chains decreased the π-conjugation along the polymer backbone and resulted in a larger E_g for **P2** (1.96 eV). The effect of the relative positions of the octyl chains on E_g can be seen when **P2** and **P3** are compared. Placing the octyl chains closer to the BT unit further decreased the coplanarity of the conjugated backbone, which resulted in an even larger E_g of **P3** (2.01 eV). Thus, although forming the alternating arrangement of D (Th_2) and A (BT) along the conjugated backbone, the bulkiness of alkyl side chains disrupted the coplanarity of poly(Th_2-*alt*-BT), and resulted in copolymers with E_g similar or even larger to that of P3HT. To obtain Th_x/BT-based copolymers with both good solubility and lower E_g, researchers applied the synthetic strategy of copolymerizing the Th_2BT with thiophene and bithophene to afford **P4** and **P5** [50, 51]. Both **P4** and **P5** are soluble in common solvents. The M_n of **P4** is 7.4 kDa (PDI = 3.4), and M_n of **P5** is 36.1 kDa (PDI = 3.2). The increase of the thiophene

ring in each repeat unit effectively restored the coplanarity of the backbone, and resulted in smaller E_gs. The optical E_g is 1.38 eV for **P4** and 1.65 eV for **P5**. The E_{HOMO}s of **P4** and **P5** are −4.88 and −5.07 eV and the E_{LUMO}s of **P4** and **P5** are −3.42 and −3.53 eV, respectively. Liang et al. further increased number of thiophene units per repeat unit (**x** in Fig. 5.1) to 6 (**P6**) and 8 (**P7**) [52]. The optical E_g is 1.78 eV for **P6** and 1.82 eV for **P7**. The E_{HOMO}s of **P6** and **P7** are −5.26 and −5.23 eV and the E_{LUMO}s of **P6** and **P7** are −3.37 and −3.30 eV. Thus, as the number of **x** increases, the E_gs of the resulting copolymers approach the E_g of P3HT (1.9 eV), implying that the effect of the BT units in decreasing E_g is gradually fading due to the dilution of the BTs along the conjugated backbone. E_{LUMO}s of **P4**–**P7** also showed a general tendency to approach the E_{LUMO} of P3HT. However, no general tendency was observed in the E_{HOMO}s of these polymers. It may be due to the variations of the number, identity and distribution of the alkyl side chains, affecting the conjugation of the polymers at the ground state. The molecular weights, physical properties, as well as the PSC performances of the copolymers are summarized in Table 5.1.

The PCEs of PSCs using **P4**–**P7**:$PC_{61}BM$ as active materials ranging from 0.13–2.6 %. Except **P6**:$PC_{61}BM$, all devices demonstrated higher V_{oc} than the P3HT:$PC_{61}BM$-based devices ($\sim$0.60 V). The unexpected low V_{oc} of **P6**-based PSCs was speculated to result from the low solubility and poor film quality. The J_{sc}s and FFs of **P4**–**P7**-based devices are lower than those of P3HT:$PC_{61}BM$-based devices (J_{sc}: 9.5 mA cm^{-2}; FF: 68 %) [53], which resulted in the lower overall PCEs. Surpassing the PCE of P3HT-based PSCs was achieved by Chen and co-workers [54], who developed a Th_4/BT-based alternating copolymer, **P8**. Long and branched 2-octyldodecyl groups were used as side chains to ensure good solubility and to reach high molecular weight. The 2-octyldodecyl groups were placed on the bithiophene comonomer unit, instead of the Th_2BT unit. The M_n of **P8** is 35 kDa (PDI = 1.63). Its E_g and E_{HOMO} are 1.59 and −5.18 eV. The E_g value is smaller and the E_{HOMO} value is lower than those of the other Th_4/BT copolymer analogue (**P5**).

Table 5.1 Molecular weights, physical properties and PSC performances of Th_x-BT and Th_x-NT based LBG copolymers

	HOMO (eV)	LUMO (eV)	Optical E_g (eV)	V_{oc} (V)	J_{sc} (mA cm^{-2})	FF (%)	PCE (%)	References
P3HT	−4.9	−3.0	1.9	0.63	9.5	68	5.0	[53, 36]
P1			1.1					[48]
P2			1.96					[49]
P3			2.01					[49]
P4	−4.88	−3.42	1.38	0.65	0.6	33	0.13	[50]
P5	−5.07	−3.53	1.65	0.74	5.60	63	2.6	[51]
P6	−5.26	−3.37	1.78	0.51	5.34	51	1.39	[52]
P7	−5.23	−3.30	1.82	0.68	5.20	49	1.73	[52]
P8	−5.18		1.59	0.72	12.3	70.5	6.26	[54]
P9	−5.16	−3.77	1.54	0.76	12.0	69	6.3	[51]

Therefore, placing the alkyl side chains further away from the BT unit leads to a better π-conjugation along the copolymer backbone. The best device based on **P8**: $PC_{71}BM$ provided a V_{oc} of 0.72 V, J_{sc} of 12.3 mA cm^{-2}, FF of 71 %, leading to a high PCE of 6.26 %.

Another successful example using the similar concept of the alternating Th_4/acceptor copolymers was reported by Osaka et al. [51]. By replacing the BT units with the naphtho[1,2-*c*:5,6-*c*′]bis[1,2,5]thiadiazole (NT) units, **P9** has even lower E_{HOMO} and smaller E_g than **P5** (Table 5.1). **P9** has high molecular weight (M_n of 52.6 kDa with PDI of 2.4) and is soluble in warm chlorinated benzenes. PSCs used **P9**:$PC_{61}BM$ as active material showed higher V_{oc}, and slightly lower J_{sc} and FF than the devices based on **P8**:$PC_{71}BM$, which also resulted in a high PCE of 6.3 % (Fig. 5.2).

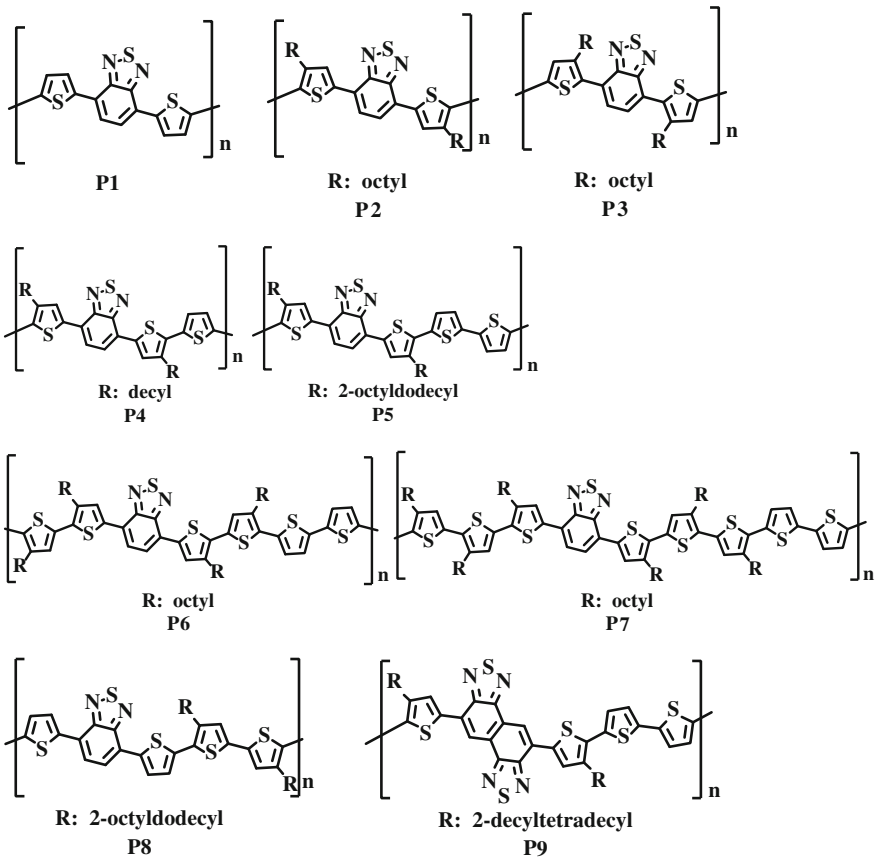

Fig. 5.2 Chemical structures of the Th_x-BT and Th_x-NT based LBG copolymers

5.2.2 Polythiophene-Based Polymers Containing 1, 4-Diketo-3,6-diarylpyrrolo[3,4-c]pyrrole (DPP-Ar_2) Moieties

The 1,4-diketo-pyrolo[3,4-*c*] pyrrole (DPP) derivatives were first used as red pigments. They can be made in various preparative routes from readily available chemicals, benzonitrile and dialkyl succinate [55]. Due to its rigid planar structure, and strong intermolecular interaction, DPP unit without proper aliphatic side chains as solubilizing groups is highly crystalline, and thus insoluble in common solvents incorporation of *N*-alkylated 1,4-diketo-3,6-diphenylpyrrolo[3,4-*c*]pyrrole (DPP-Ph_2) unit into conjugated polymer backbones was first reported for the materials used in the nonlinear optical (NLO) and polymer light emitting diode (PLED) applications. The electron-deficient nature of the DPP unit bathochromically shifts the absorption and emission spectra of the resulting conjugated molecules to allow efficient sensitizing at wavelengths around 400–550 nm or to achieve a deep red emitter [56–59]. However, the homopolymer of DPP-Ph_2 (**P10**, Fig. 5.3) was not suitable for PSC application due to its too large E_g of 2.12 eV. The emergence of 1,4-diketo-3,6-diarylpyrrolo[3,4-c]pyrrole(DPP-Ar_2)-containing LBG polymers occurred recently when the flanking groups (Ar_1, Fig. 5.3) of DPP were replaced from the phenelyene groups to thienyl (Th) groups. Since then, high-performance PSCs based on the 1,4-diketo-3,6-dithienylpyrrolo[3,4-*c*]pyrrole (DPP-Th_2)-containing polymers have been vigorously developed. In this section, the molecular engineering of the Th_x/DPP-containing LBG polymers and their analogues will be introduced. Compared to the Th_x/BT copolymers, the strategies in modifying Th_x/DPP copolymers are more diverse. As shown in Fig. 5.3, the focus here is the influence of the flanking groups (Ar_1), the comonomer unit (Ar_2), and the lateral alkyl side chains (R) on the photophysical properties and photovoltaic performances of the materials. The chemical structures of the DPP-incorporated copolymers are shown in Fig. 5.4. Their molecular weights, physical properties, and PSC performances are summarized in Table 5.2.

The first advantage of DPP-Th_2-based LBG polymers in PSC application comes from their absorption coverage. The absorption spectrum of DPP-Th_2 homopolymer

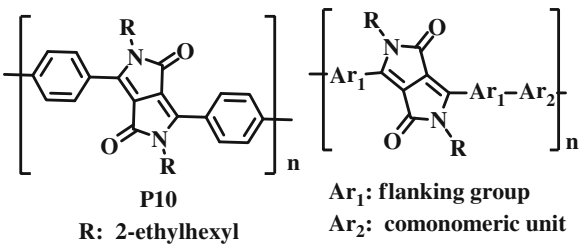

Fig. 5.3 Chemical structure of poly(*N*-alkylated 1,4-diketo-3,6-diphenylpyrrolo [3,4-*c*]pyrrole) **P10** and the representative structure of the 1,4-diketo-3,6-diarylpyrolo[3,4-*c*]pyrrole containing LBG polymers

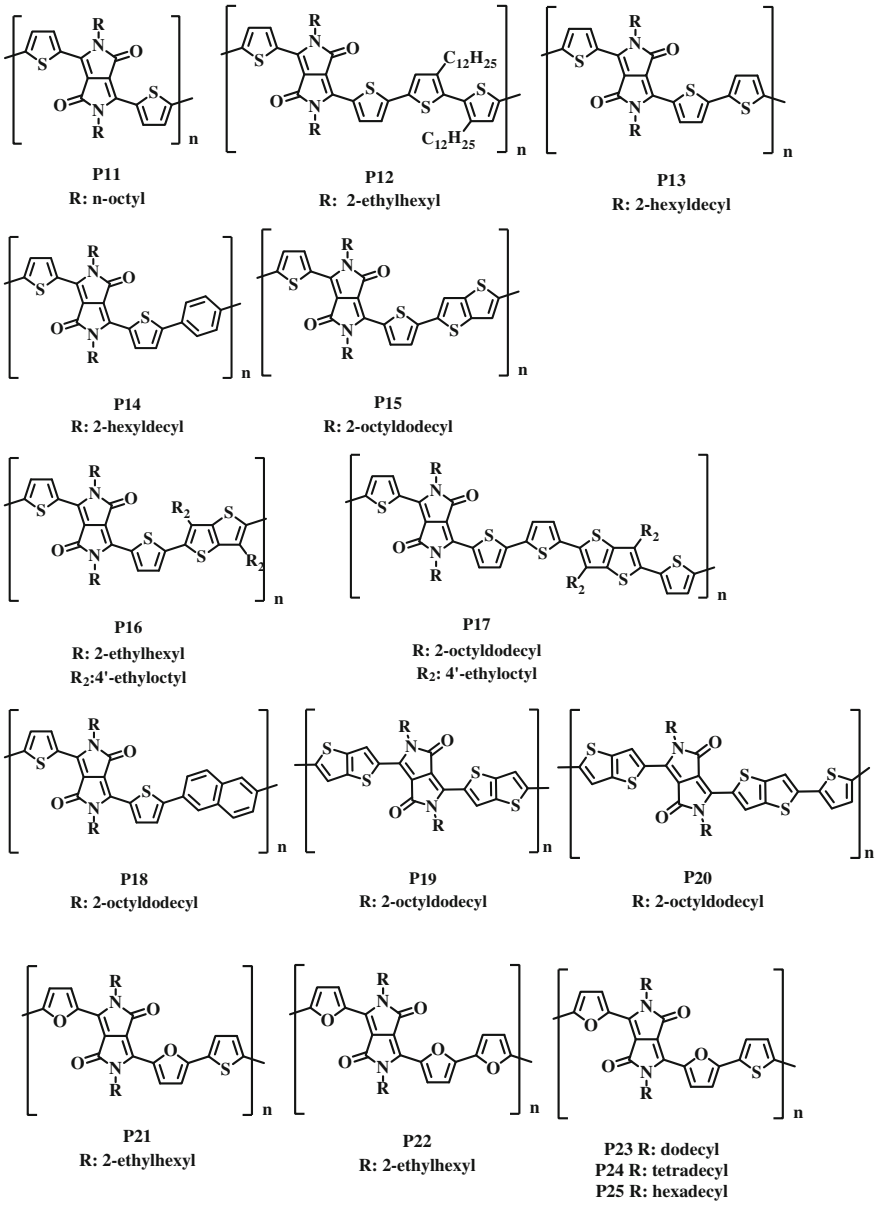

Fig. 5.4 Chemical structures of the Th_x/DPP based and related copolymers

(**P11**) covers from 600–1,000 nm, which is favorable in solar radiation harvesting. However, the electron-deficient nature of the DPP unit also brings disadvantages for **P11**, as it leads to a too low E_{LUMO} (−3.85 eV). The small LUMO-LUMO offset between **P11** and $PC_{61}BM$ inhibits the photoinduced electron transfer and resulted

Table 5.2 Physical properties and PSC performances of Th_x/DPP based copolymers and their analogues

	HOMO (eV)	LUMO (eV)	Optical E_g (eV)	V_{oc} (V)	J_{sc} (mA cm^{-2})	FF (%)	PCE (%)	References
P10	−5.47	−3.70	2.12					[59]
P11	−5.15	−3.85	1.25	0.64	0.76	58	0.3	[60]
P12	−5.53	−3.83	1.40	0.61	11.3	58	4.0	[61]
P13	−5.30	−3.74	1.30	0.65	11.8	60	4.7	[62, 63]
P14	−5.35	−3.53	1.53	0.80	10.3	65	5.5	[63, 64]
	−5.48	−3.66						
P15	−5.33	−3.92	1.31	0.63	2.8	61	1.2	[63]
P16	−5.31	−3.84	1.33	0.68	6.0	59	2.3	[63]
P17	−5.33	−3.69	1.52	0.65	8.2	63	3.4	[63]
P18	−5.29	−3.79	1.50	0.76	11.8	52	4.7	[65]
P19	−5.04	−3.76	1.28	0.57	8.9	59	3.0	[66]
P20	−5.06	−3.68	1.38	0.58	15.0	61	5.4	[66]
P21	−5.4	−3.8	1.41	0.74	11.2	60	5.0	[67]
P22	−5.5	−3.8	1.35	0.73	9.1	58	3.8	[67]
P23	−5.2	−3.8	1.4	0.65	12.2	60	5.2	[68]
P24	−5.2	−3.8	1.4	0.65	14.8	64	6.5	[68]
P25	−5.3	−3.9	1.4	0.65	12.3	69	6.2	[68]

in a low PCE of 0.3 % [60]. The device performance of PDPP-based PSCs were further improved through copolymerizing DPP-Th_2 with comonomer units such as phenylene, thienyl, bithiophene, thienylthiophene, furan, and naphthalene.

Janssen et al. first reported a LBG conjugated polymer, **P12** consisting of alternating DPP-Th_2 and 3,3′-didodecyl-2,2′-bithiophene-5,5′-diyl units with a M_n of 20 kDa [61]. Although **P12** possesses slightly higher E_g (1.4 eV) than **P11**, its higher-lying LUMO (−3.83 eV) allows more efficient photo-induced electron transfer. When an active layer of **P12**:$PC_{71}BM$ blend was used, an optimized PCE of 4.0 % with a V_{oc} of 0.61 V, J_{as} and FF of 0.58 was achieved, as shown in Table 5.2.

Solubility of the DPP-Th_2-incorporated copolymers can be adjusted by the R groups on the DPP core (Fig. 5.3). Copolymerizing DPP-Th_2 with aromatic units containing no alkyl side chains requires better solubilizing groups on the DPP core. Adapting longer branching alkyl chain, the 2-hexyldecyl groups, on the DPP core increased the solubility of the resulting DPP incorporated copolymers, and allowed for the preparation of **P13–P15**. **P13** contains alternating DPP-Th_2/thiophene-2,5-diyl (Th) units and **P14** consists of alternating DPP-Th_2/phenylene (Ph) units [62, 64]. The M_n of **P13** is 54 kDa, and **P14** possesses a bimodal molecular weight distribution with two M_ns, 10 and 65 kDa. The unsubstituted Th units induces better planarity along the conjugated backbone and results in a smaller E_g (1.30 eV) and higher charge carrier mobility of **P13** when compared to **P12**. Optimized cells using **P13**:$PC_{71}BM$

in a 1:2 weight ratio provided a PCE of 4.7 % with V_{oc} of 0.65 V, J_{sc} of 11.8 mA/cm^2, and FF of 0.60. As for **P14**, introducing the Ph groups between the DPP-Th_2 units in the main chain increases the E_g and lowers the HOMO level. **P14** possesses E_g of 1.53 eV and E_{HOMO} of −5.35 eV. The lower-lying HOMO of **P14** results a higher V_{oc}. In combination with $PC_{71}BM$, optimized cells based on **P14** provided a PCE of 5.5 % with V_{oc} of 0.80 V, J_{sc} of 10.3 mA/cm^2, and FF of 0.65.

In attempts to enhance the π–π stacking of the conjugated backbones and take advantage of the high charge carrier mobility of the polymers consisting of fused aromatic rings [69, 70], larger π-conjugated segments, thieno[3,2-*b*]thiophene (TT) and naphthalene (N) units were utilized as comonomer units with DPP-Th_2 units [63, 65]. Janssen et al. reported three DPP- and TT-incorporated alternating copolymers (**P15**–**P17**). Longer branched 2-octyldodecyl group on the DPP core was used when unsubstituted TT and 2,5-dithienyl-3,6-di(4′-ethyloctyl) thieno[3,2-*b*]thiophene (TT-Th_2) were adopted as comonomer units (**P15** and **P17**), while shorter branched 2-ethylhexyl group on the DPP core was chosen when 3,6-di(4′-ethyloctyl) thieno[3,2-*b*]thiophene was used as comonomer unit (**P16**). The M_ns of **P15**–**P17** are in the range of 9–15 kDa. **P15** and **P16** have similar E_g (1.31 and 1.33 eV) with **P13**, while the E_g of **P17** is much larger (1.53 eV). In terms of widening the E_g, replacing the Th units with TT units or placing alkyl substituents on the TT units are less significant than extending the number of Th units between the DPP units. The differences in the commoner units of **P15**–**P17** showed little effect on the E_{HOMO}s of the copolymers, but large effect on the E_{LUMO}s. The introduction of the alkyl chains on the TT units and extending the number of Th units between the DPP units varied the E_{LUMO}s of **P15**–**P17**, which are −3.92, −3.84 and −3.69 eV, respectively. PSCs based on $PC_{61}BM$ and **P15**–**P17** exhibited similar FFs (0.59–0.61) and V_{oc}s (0.63–0.68 V). However, the significant difference among the J_{sc}s of **P15** (2.8 mA/cm^2), **P16** (6.0 mA/cm^2), and **P17** (8.0 mA/cm^2) results in the differences in PCE of **P15** (1.2 %), **P16** (2.3 %), and **P17** (3.4 %). Since the charge carrier mobilities of the polymers are in the order of **P15** (μ_h: 3×10^{-2} cm^2/Vs) > **P16** (μ_h: 1×10^{-2} cm^2/Vs) > **P17**(μ_h: 5×10^{-3} cm^2/Vs), the lowest J_{sc} and PCE of **P15** were attributed to its smallest LUMO-LUMO offset to $PC_{61}BM$. The increase of the offset from **P15**–**P17** allows more efficient exciton dissociation, which was also supported by the increase of external quantum efficiency (EQE) from **P15** to **P17**. Nevertheless, **P13**, which has a LUMO-LUMO offset to $PC_{61}BM$ in between those of **P16** and **P17**, demonstrates a higher PCE. Thus, in addition to the LUMO-LUMO offset, other parameters, such as solid-state morphology, are also needed to be considered in reaching high PCE.

Sonar et al. reported an alternating copolymer of DPP-Th_2 and naphthalene-1,4-diyl (**P18**). 2-Octyldodecyl groups were also used on the DPP core as no alkyl substituents are on the naphthalene unit. M_n of **P18** is 64 kDa. The E_g of **P18** is 1.50 eV, which is larger than those of the DPP-Th_2/TT alternating copolymers (**P15** and **P16**), but is close to that of the DPP-Th_2/Ph alternating copolymer **P14**. Thus, replacing the Ph units with naphthalene units in the DPP based copolymers also shows insignificant effect on the E_g, as it is the case in the E_gs of **P13** (DPP-Th_2/Th; 1.30 eV) and **P15** (DPP-Th_2/TT; 1.31 eV). The E_{HOMO} (−5.29 eV) and E_{LUMO}

(−3.79 eV) of **P18** are also close to those of **P14**. Optimized cells using **P18**:$PC_{71}BM$ in a 1:2 weight ratio provided a PCE of 4.7 % with V_{oc} of 0.76 V, J_{sc} of 11.8 mA/cm^2, and FF of 0.52. The high J_{sc} was attributed to the low band gap nature, good inter-chain π–π interactions and the high charge carrier mobility of **P18** (μ_h: 0.98 cm^2/Vs).

The TT units were also used as the flanking groups (Ar_1) of DPP by Bronstein et al. [66]. **P19** is the homopolymer polymerized from 3,6-bis(2-bromothieno-[3,2-b]thiophen-5-yl)-2,5-bis(2-octyldodecyl)pyrrolo[3,4-c]-pyrrole-1,4-(2H,5H)-dione (diBr-DPP-TT_2), and **P20** is the alternating copolymer copolymerized from diBr-DPP-TT_2 and 2,5-di(trimethyltin)thiophene. The introduction of 2-octyldodecyl groups on the DPP core only provides moderate solubility to the polymers. The M_ns of **P19** and **P20** are 14 and 16 kDa, respectively. The high polydispersity indexes (PDIs) of **P19** (4.9) and **P20** (5.4) are due to the low solubility of the polymers in acetone and hexane, which made the removal of lower-molecular-weight oligomers difficult. Replacing the flanking groups from Th to TT pushed up the HOMO levels, but kept the E_{LUMO} and E_g values. The E_{HOMO}s of **P19** and **P20** are −5.04 and −5.06 eV, which are at less 0.09 eV higher lying than the DPP-Th_2-based copolymers. The E_gs of **P19** and **P20** are 1.28 and 1.38 eV. The E_{LUMO}s of **P19** and **P20** are −3.76 and −3.68 eV, which provide sufficient LUMO-LUMO offset relative to PCBM and allow efficient exciton dissociation. The TT flanking units enhance the coplanarity of the polymers and facilitate efficient charge-carrier transport. A record high μ_h of 1.95 cm^2/Vs was observed in a polymer-based OFET using **P20**. μ_h of 0.037 cm^2/Vs and μ_e of 0.30 cm^2/Vs were reported for **P19**. PSCs based on 1:2 mixtures of **P19**:$PC_{71}BM$ and **P20**:$PC_{71}BM$ showed relatively low V_{oc}s, which are 0.57 V for **P19** and 0.58 V for **P20**, due to the relatively high-lying HOMO of the polymers. Yet, satisfactory J_{sc} of 8.9 mA/cm^2 and FF of 0.59 resulted in a PCE of 3.0 % for **P19**; and a high J_{sc} of 15.0 mA/cm^2 and FF of 0.61 with a PCE of 5.4 % for **P20**.

Although long and branched solubilizing alkyl groups improve solubility, they are normally considered to hinder intermolecular ordering, and thus hamper the transport of charge carriers across the polymer chains [71, 72]. To reduce the length and bulkiness of the solubilizing side chains along the conjugated backbones, and enhance the ordered packing of polymer chains, Fréchet et al. used furan units as either flanking groups or as comonomer unit of the DPP unit and synthesized a series of DPP-furan-incorporated copolymers (**P21**–**P25**). 2-Hexyldecyl groups on DPP are required to guarantee solubility of the DPP-Th_2 or DPP-TT_2 copolymers, especially when there is no alkyl substituent on their comonomer units, such as the case of **P13**. Replacing the 2-hexyldecyl groups of **P13** with the shorter 2-ethylhexyl groups leads to a copolymer with a significantly lower M_n of 2 kDa [67]. On the contrary, **P21** and **P22**, which also use 2-ethylhexyl groups as solubilizing groups, possess better solubility and reach higher M_ns of 66 and 29 kDa, respectively. **P23**–**P25** adopting furan as flanking units and linear dodecyl, tetradecyl and hexadecyl as solubilizing groups also afford high M_ns of 46, 58, and 55 kDa, respectively.

The furan-incorporated copolymers, **P21**–**P25**, have larger E_gs, ranging between 1.35 and 1.41 eV, than their all-thiophene counterpart (**P13**). **P21** and **P22**, which have branched solubilizing groups, also have deeper HOMO levels than that of **P13**, while the HOMO levels of those with linear solubilizing groups (**P23**–**P25**) are similar to that of **P13**. Reducing the bulkiness of the solubilizing groups does improve the processibility, structural ordering and charge transport properties of the materials. The PSCs made of **P21**:$PC_{71}BM$ and **P22**:$PC_{71}BM$ blends afforded PCEs of 5.0 and 3.8 %, which are comparable with those produced with **P13**:$PC_{71}BM$. PSCs made with **P23**–**P25**:$PC_{71}BM$ demonstrated even higher PCEs ranging from 5.2 to 6.5 %. This improvement in PCE was attributed to the replacement from the branched to linear solubilizing groups, which leads to the shortening of π–π stacking distances between backbones and the increases of the correlation lengths along both the π–π stacking direction and the direction along the lamellar normal.

5.2.3 *Polythiophene-Based Polymers Containing Isoidigo (iI) Moieties*

Encouraged by the good performances of Th_x/DPP-based copolymers, Reynold et al. took advantage of the electron-withdrawing nature of another pigment, isoindigo (iI), and prepared iI-based oligothiophenes. The BHJ photovoltaics based on the blend of this oligomer and $PC_{61}BM$ exhibited a PCE of 1.76 % with a V_{oc} of 0.74 V, J_{sc} of 6.3 mA/cm^2 and FF of 0.38 [73]. As shown in Fig. 5.5, the alternating Th/iI copolymers were developed at the same time by Zhang et al. (**P26**) [74], Wang et al. (**P27**) [75]. **P26** has M_n of 17.2 kDa (PDI of 2.1) and **P27** has M_n of 86 kDa (PDI of 2.2). As shown in Table 5.3, the Th_x/iI alternating copolymers have low-lying HOMO levels (−5.49 eV for **P26** and −5.85 eV for **P27**), and narrow E_g around 1.6 eV. PSCs based on **P26**:$PC_{71}BM$ and **P27**:$PC_{71}BM$ demonstrated high V_{oc} around 0.9 V due to the low-lying HOMO levels of the copolymers. With J_{sc} of 5.4 mA cm^{-2} and FF of 0.63, a PCE of 3.0 % was reported (Table 5.3). Wang et al. [76] further prepared a Th_3/iI alternating copolymer (**P28**, Fig. 5.5) through copolymerization of 2,5-bis(trimethylstannyl)thiophene and (*E*)-6,6′-bis(5-bromo-4-octylthiophen-2-yl)-1,1′-bis(2-hexyldecyl)-[3,3′-biindolinylidene]-2,2′-dione.

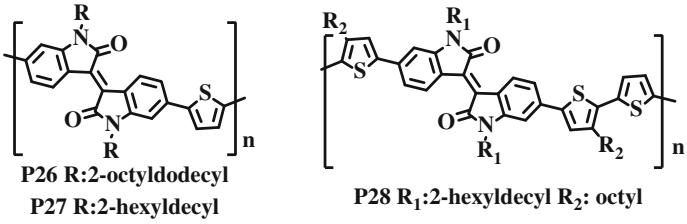

Fig. 5.5 Chemical structures of the Th_x/iI based LBG copolymers

Table 5.3 Physical properties and PSC performances of Th_x/iI based copolymers and their analogues

	HOMO (eV)	LUMO (eV)	Optical E_g (eV)	V_{oc} (V)	J_{sc} (mA cm^{-2})	FF (%)	PCE (%)	References
P26	−5.49	−3.91	1.58	0.87	1.76	60	0.92	[74]
P27	−5.85	−3.88	1.6	0.89	5.4	63	3.0	[75]
P28	−5.82	−3.83	1.5	0.70	13.1	69	6.3	[76]

P28 has M_n of 43 kDa with PDI of 3.1. The E_{HOMO} and E_{LUMO} of **P28** are similar to those of **P27**. PSCs based on **P28**:$PC_{71}BM$ showed a lower V_{oc} of 0.7 V, but a much higher J_{sc} of 13.1 mA/cm^2 when compared to the **P27**:$PC_{71}BM$ based PSCs. With a FF of 0.69, a high PCE of 6.3 % was reached (Table 5.3).

5.2.4 *Polythiophene-Based Polymers Containing 2,3-Diarylquinoxaline (QX) Moieties*

Th_x/QX type copolymers were first synthesized because of the strong interests in investigating the chemical and physical properties of polymers showing strong intramolecular charge transfer properties [77]. Narrower E_g and lower-lying HOMO have been demonstrated by the first few Th_x/QX alternating copolymers reported by Yamamoto et al. However, the copolymers are only soluble in CF_3COOH, but not in common solvents such as chloroform and toluene. Good solubility in the Th_x/QX alternating copolymer was achieved when two 3-(octyoxy)phenyl substituents are placed at the 2- and 3-positions of the QX units [78]. The resulting copolymer **P29** (Fig. 5.6) gave M_n of 41–42 kDa [78, 79], and is soluble in common solvents, such as chloroform, THF, toluene. **P29** has low-lying HOMO (E_{HOMO} = −5.7 eV) and E_g of 1.7 eV. **P29**:$PC_{71}BM$-based PSCs, reported by Wang et al. [79], showed a high V_{oc} around 0.9 V due to the very low-lying HOMO of **P29**. An optimized PCE of

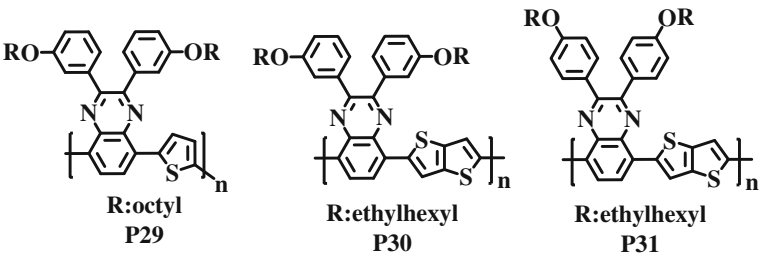

Fig. 5.6 Chemical structures of the Th/QX and TT/QX based LBG copolymers

Table 5.4 Physical properties and PSC performances of Th/QX and TT/QX copolymers

	HOMO (eV)	LUMO (eV)	Optical E_g (eV)	V_{oc} (V)	J_{sc} (mA cm^{-2})	FF (%)	PCE (%)	References
P29	−5.7	−3.3	1.70	0.89	10.5	64	6.0	[79]
P30	−5.15	−3.68	1.54	0.73	9.87	55.1	3.97	[80]
P31	−5.01	−3.54	1.56	0.60	8.22	59.4	2.93	[80]

6.0 % with V_{oc} of 0.89 V, J_{sc} of 10.5 mA cm^{-2} and a FF of 0.64 was achieved (Table 5.4). To study how the position of electron-donating side groups affects the positions of the frontier orbitals, Han et al. [80] copolymerized 5,8-dibromo-2,3-bis (3-(2-ethylhexyloxy)phenyl)quinoxaline and 5,8-dibromo-2,3-bis(4-(2-ethylhexyloxy)phenyl)quinoxaline with 2,5-bis(trimethylstannyl)thieno[3,2-*b*]thiophene and obtained **P30** and **P31** (Fig. 5.6). It is worthwhile to discuss the comparison of **P29** and **P30**, as it provides information about the property differences between the Th/QX and TT/QX copolymers. Similar to the tendency observed in the Th/DPP-based copolymers, replacing the Th units with TT units decreases solubility and M_n of the copolymers, but promotes conjugation in the conjugated backbone, which leads to a higher-lying E_{HOMO} and a decrease in E_g. Although branched alkyl chain (-EH) is used, **P30** and **P31** have lower M_n of 5.7 and 7.0 kDa than that of **P29** with linear octyl groups. The E_{HOMO} raises from −5.7 eV of **P29** to −5.15 eV of **P30** and the E_g narrows from 1.7 eV of **P29** to 1.54 eV of **P30**. 2-Ethylhexyloxy groups on the phenyl ring *para* to the QX unit in **P31** exert more pronounced electron-donating ability than those with the meta-substitution in **P30**. The electron-donating effect further elevated the E_{HOMO} from −5.15 eV of **P30** to −5.01 eV of **P31**. The performances of **P30**:$PC_{71}BM$ and **P31**:$PC_{71}BM$-based PSCs are summarized in Table 5.4. A clear trend of decrease in V_{oc} from 0.89 to 0.60 V can be seen due to the elevation of the E_{HOMO} from −5.7 eV of **P29** to −5.01 eV of **P31**. **P30**:$PC_{71}BM$ and **P31**:$PC_{71}BM$-based PSCs showed PCE of 3.97 and 2.93 %, respectively.

5.2.5 Polythiophene-Based Polymers Containing Thieno [3,4-c]pyrrole-4,6-dione (TPD) Moieties

TPD is another useful comonomer unit in preparing alternating Th/A copolymers with low-lying HOMO and high V_{oc}. Wei et al. copolymerized 4,4′-didodecyl-5,5′-bis(trimethylstannyl)-2,2′-bithiophene with 1,3-dibromo-5-ethylhexylthieno[3,4-*c*]pyrrole-4,6-dione to afford **P32** (Fig. 5.7) [81]. To promote solubility, the branched -EH chain of the TPD unit was used. M_n of **P32** was 9.7 kDa with a PDI of 1.4 (Table 5.5). **P32** has low-lying HOMO (E_{HOMO} = −5.56 eV) and an E_g of 1.82 eV. The optimized **P32**:$PC_{71}BM$ based PSCs possessed a remarkably high V_{oc} around 0.92 V, and J_{sc} of 13.1 mA cm^{-2}. With FF of 0.64, a high PCE of 7.3 % was

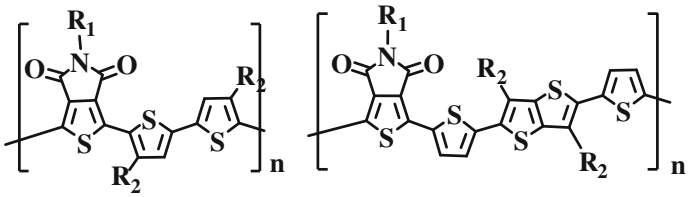

Fig. 5.7 Chemical structures of the Th_2/TPD based LBG copolymers

Table 5.5 Physical properties and PSC performances of Th_2/TPD based copolymers

	HOMO (eV)	LUMO (eV)	Optical E_g (eV)	V_{oc} (V)	J_{sc} (mA cm^{-2})	FF (%)	PCE (%)	References
P32	−5.56	−3.10	1.82	0.92	13.1	61	7.3	[81, 82]
P33	−5.54	−3.00	1.84	0.85	8.99	67	5.1	[83]

reported [82]. To increase the coplanarity of the conjugated backbone and enhance crystalline, Wei et al. further incorporated the TT unit into the Th/TPD based copolymer. They copolymerized 2,5-bis [5-(trimethylstannyl)thiophen-2-yl]-3,6-dioctylthieno[3,2-*b*]thiophene with 1,3-dibromo-5-(2-hexyldecyl)-5*H*-thieno[3,4-*c*] pyrrole-4,6-dione to afford **P33** (Fig. 5.7) [83]. To maintain good solubility, the branched 2-hexyldecyl instead of -EH chain on the TPD unit was used. M_n of **P33** was 9.2 kDa with a PDI of 1.2 (Table 5.5). Replacing the 4,4′-didodecyl-2,2′-bithiophene units in the conjugated backbones with the 2,5-di(thiophen-2-yl)thieno [3,2-b]thiophene units does not change the position of the frontier orbitals and E_g significantly. The E_{HOMO}, E_{LUMO} and E_g of **P33** were −5.54, −3.0 and 1.84 eV, respectively, which are close to those of **P32**. The **P33**:$PC_{71}BM$ based PSCs also possessed a high V_{oc} of 0.85 V. With J_{sc} of 8.99 mA cm^{-2} and FF of 0.67, a PCE of 5.1 % was reported [83] (Table 5.5).

5.3 Benzo[1,2-*b*:4,5-*b′*]dithiophene (BDT)-Based Donor–Acceptor Conjugated Polymers

The electron-rich benzo[1,2-*b*:4,5-*b*′]dithiophene (BDT) unit, a central benzene ring fused with two thiophenes, emerges as an attractive building block for conjugated polymers due to its symmetric, rigid and coplanar structure. These structural features are beneficial to induce intermolecular π–π interaction for efficient charge transport. Therefore, research efforts have been focused on the synthesis of

Table 5.6 Physical properties and PSC performances of BDT-based copolymers

	HOMO (eV)	LUMO (eV)	Optical E_g (eV)	V_{oc} (V)	J_{sc} (mA cm^{-2})	FF (%)	PCE (%)	References
P35	−5.12	−3.35	1.61	0.70	14.7	64.1	6.58	[86]
P36	−5.01	−3.24	1.62	0.62	13.2	63	5.15	[86]
P37	−5.22	−3.45	1.60	0.76	15.2	66.9	7.73	[86]
P38	−4.94	−3.22	1.59	0.58	14.1	62.4	5.1	[87]
P39	−5.15	−3.31	1.68	0.74	14.1	68.9	7.2	[87]
P40	−5.41	−3.60	1.75	0.68	11.0	43.4	3.2	[87]
P41	−5.48	−359	1.73	0.75	9.1	39.4	2.7	[87]
P42	−5.12	−3.49	1.65	0.76	14.1	58	6.22	[88]
P43	−5.56	−3.75	1.8	0.85	9.81	66	5.5	[89]
P43	−5.43	−3.40	1.82	0.87	9.1	53.8	4.2	[90]
P43	−5.4	–	1.7	0.85	11.5	68	6.6	[91]
P44	−5.48	–	1.7	0.87	8.1	56	3.9	[91]
P45	−5.57	–	1.7	0.81	9.7	67	5.4	[91]
P46	−5.47	−3.44	1.51	0.85	12.78	58.2	6.32	[92]
P47	−5.54	−3.33	–	0.91	12.91	61.2	7.2	[93]
P48	−5.4	−3.13	–	0.87	10.03	57.3	5.0	[93]
P49	−5.29	−2.87	1.98	0.70	11.14	55.2	4.36	[94]
P50	−5.36	−3.05	2.0	0.79	12.45	72.2	7.1	[94]
P51	−5.4	−3.6	1.77	0.69	11.6	66	5.3	[95]
P52	−5.12	−2.94	1.96	0.82	9.01	60.3	4.46	[96]

BDT-based polymers for the applications of organic field-effect transistors (OFETs). The BDT-based polymer **P34** has achieved a high hole mobility of 0.25 cm^2 V^{-1} s^{-1} [84]. In 2008, Yang and co-workers reported a series of BDT-based donor-acceptor conjugated polymers used for the applications of organic photovoltaics (OPVs) [85]. Thieno[3,4-*b*]-thiophene (TT) unit is an unique thiophene-based building block for the construction of p-type conjugated polymers, because TT moiety tends to adapt more quinoidal resonance structure along the conjugated backbone, resulting in smaller E_g [12, 15, 22]. Alternating poly(benzodithiophene-*alt*-thieno[3,4-*b*]thiophene (**PBDTTT**) derivatives prepared by polymerization of BDT unit with thieno[3,4-*b*]thiophene moiety represent the most successful polymers for OPV applications. The functional groups substituted on the 2-position of thieno[3,4-*b*]thiophene unit play an important role in determining the molecular properties. Hou et al. [86] reported that **P35**, having stronger electron-withdrawing alkyl carbonyl group on the thieno[3,4-*b*]thiophene unit, showed lower E_{HOMO} and E_{LUMO} (−5.12 and −3.35 eV, respectively) than **P36** (−5.01 and −3.24 eV) with ester group as the side chain; however, the E_g of **P35** is approximately the same as that of **P36**. Furthermore, when thieno[3,4-*b*]thiophene unit was substituted with a fluorine atom with high electron affinity, the resulting polymer **P37** exhibited a lower E_{HOMO} accordingly. The absorption spectra of these

polymers in solid state showed similar absorption onset (~770 nm) and thus similar E_g. The device based on **P36**:$PC_{71}BM$ blend exhibited a PCE of 5.15 %, whereas the device based on **P35**:$PC_{71}BM$ blend exhibited a higher PCE of 6.58 % because of larger V_{oc} and J_{sc}. Furthermore, because **P37** possesses a relatively lower-lying E_{HOMO}, the device based on **P37**:$PC_{71}BM$ blend showed the highest PCE of 7.73 % with a V_{oc} of 0.76 V, a J_{sc} of 15.2 mA/cm^2, and a FF of 0.67.

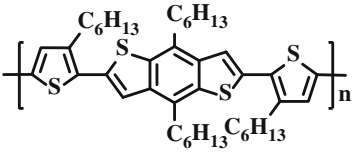

P34

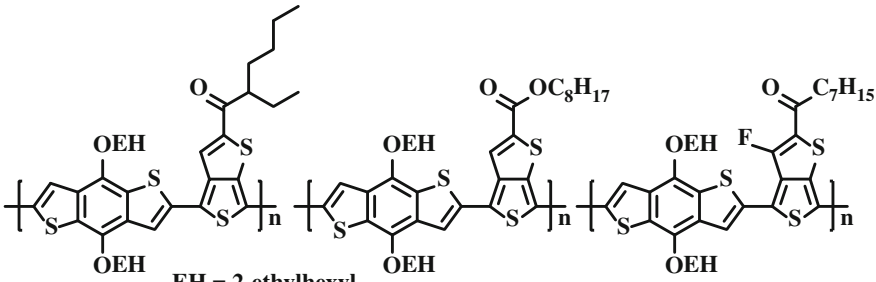

P35 EH = 2-ethylhexyl **P36** **P37**

A series of fluorinated BDT-based polymers **P38**–**P41** were also reported by Yu et al. [87]. Compared to the absorption of **P38** and **P39** in solid state, **P40** and **P41** showed sharper peaks and more blue-shifted absorption onset due to the electron-withdrawing effect of the fluorine atoms. The blue-shifted absorption onset of **P39** compared to **P38** is attributed to the change of the alkyl side chain from *n*-octyl for **P38** to 2-ethylhexyl for **P39**. The bulkier side chain causes longer polymer interchain distances, thus reducing interchain interaction. The absorption spectra of **P40** and **P41** in solid state are very similar, suggesting that further substitution of fluorine to the thieno[3,4-*b*]thiophene unit in **P41** does not change its optical properties. The cyclic voltammetry results indicate that both E_{HOMO}s and E_{LUMO}s can be lowered by the introduction of fluorine to the thieno[3,4-*b*]thiophene or the benzodithiophene units in the polymer backbone. Under the optimal device conditions, the devices based on **P38**, **P39**, **P40** or **P41**:$PC_{71}BM$ blend exhibited PCEs of 5.1, 7.2, 3.2 and 2.7 %, respectively. Although **P38** and **P40** have similar molecular weight and backbone structure, the FF of **P38** is around 50 % higher than that of **P40**. Besides, the J_{sc} values of **P38** and **P39** are also higher than those of **P40** and **P41** by ca. 3–4 mA/cm^2. The dramatic decreased FF values observed in **P40**:$PC_{71}BM$ and **P41**:$PC_{71}BM$ blends devices are mostly due to the small mobilities and poor miscibility of the polymers with $PC_{71}BM$. Very recently, Cao

and coworkers introduced poly [(9,9-bis(3′-(*N*, *N*-dimethylamino) propyl)-2,7-fluorene)-*alt*-2,7-(9,9–dioctylfluorene)] (**PFN**) as a cathode interlayer, the device using **P39**:$PC_{71}BM$ as the active layer exhibited a V_{oc} of 0.76 V, a J_{sc} of 15.75 mA/cm^2, a FF of 0.7, leading to a very impressive PCE of 8.37 % [6].

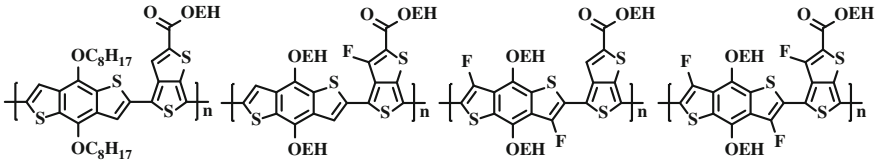

Considering that introducing electron-withdrawing groups on thieno[3,4-*b*]thiophene unit can lower the E_{HOMO}s of the corresponding polymers to obtain greater V_{oc} in OPV devices, BDT-based **P42** having a strong electron-withdrawing sulfonyl group on the thieno[3,4-*b*]thiophene unit was reported by Li et al. [88]. The absorption spectra of **P42** were essentially unchanged in solution and solid states, and the E_g deduced from the absorption onset of polymer thin film spectrum is 1.65 eV. The E_{HOMO} and E_{LUMO} of **P42** were estimated to be at −5.12 and −3.49 eV, respectively. The device based on **P42**:$PC_{71}BM$ blend exhibited a J_{sc} of 14.1 mA/cm^2, a V_{oc} of 0.76 V, and a FF of 0.58, leading to a high PCE of 6.22 %, indicating that sulfonyl group is also an effective substituent for BDT/thieno[3,4-*b*]thiophene-based polymers.

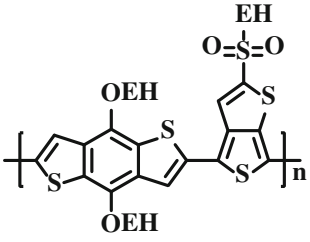

P42

Thieno[3,4-*c*]pyrrole-4,6-dione (TPD) unit is a simple compact and planar structure, which can facilitate electron delocalization and strengthen interchain interactions in conjugated polymers. Furthermore, TPD unit with electron-withdrawing ability can efficiently lower the E_{HOMO}s of the TPD-containing polymers to increase V_{oc} in BHJ solar cells. Leclerc and coworkers [89] first prepared **P43** containing BDT and TPD units in an alternating manner. The E_g of **P43** obtained from the absorption onset is 1.8 eV. Interestingly, the absorption spectrum of **P43** in solution is very similar to that in thin film. The E_{HOMO} and E_{LUMO} of **P43** were

estimated to be at −5.56 and −3.75 eV, respectively. The device based on **P43**: $PC_{71}BM$ blend exhibited a J_{sc} of 9.81 mA/cm^2, a V_{oc} of 0.85 V, and a FF of 0.66, leading to a promising PCE of 5.5 %. At the same time, Jen et al. [90] also reported an identical polymer **P43** which resulted in a PCE of 4.2 %.

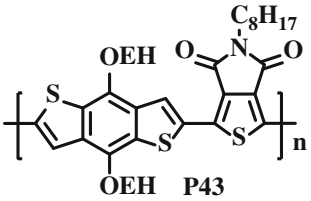

P43

Later on, Fréchet et al. [91] also reported BDT/TPD-based alternating copolymers (**P43**, **P44** and **P45**) with different alkyl groups on the TPD units. By replacing the ethylhexyl chains in **P44** with the less bulky alkyl chains, **P43** and **P45** showed broader and red-shifted absorption spectra. The E_gs obtained from the absorption onset of polymer films are around 1.7 eV for the three polymers. The similar E_{HOMO}s of these polymers were found (−5.4 eV for **P43**; −5.48 eV for **P44**, and −5.57 eV for **P45**). The device based on **P44**:$PC_{71}BM$ blend exhibited a PCE of 3.9 %. Compared to **P44**, the device based on **P45**:$PC_{71}BM$ blend exhibited a higher PCE of 5.4 % because of larger FF and J_{sc}. Furthermore, the device based on **P43**:$PC_{71}BM$ blend showed the highest PCE of 6.6 % with higher J_{sc} than the devices using **P44** and **P45**. Notably, 1,8-diiodooctane (DIO) with higher boiling point was used as an additive to optimize the morphology of active layer. On the other hand, the Grazing Incidence X-ray Scattering (GIXS) analysis showed that TPD-based polymers are able to maintain the face-on orientation of the polymer backbone and preserve a small π-stacking distance in the blend containing $PC_{71}BM$.

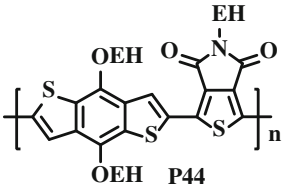

P44

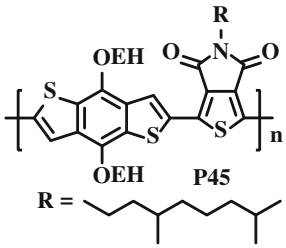

P45

BDT-based polymer **P46** incorporating thiadiazolo[3,4-c]pyridine (PyT) as the acceptor was reported by You et al. [92]. **P46** showed significant red-shifted absorption in the solid state than in solution state due to strong π-π stacking in the solid state. The E_{HOMO}, E_{LUMO} and E_g of **P46** were estimated to be at −5.47/−3.44 eV and 1.51 eV, respectively. The device based on **P46**:$PC_{61}BM$ blend

exhibited a J_{sc} of 12.78 mA/cm^2, a V_{oc} of 0.85 V, and a FF of 0.582, leading to a PCE of 6.32 %.

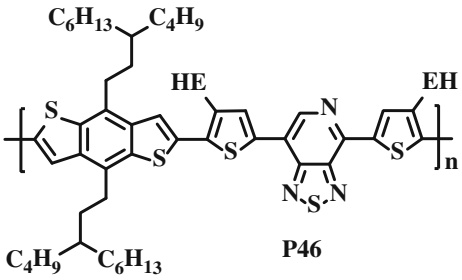

P46

Based on many examples in the literatures, introduction of small and electronegative fluorine atoms is an effective way to lower the E_{HOMO}s of the conjugated polymers, leading to large V_{oc} values of OPV devices. By using similar strategy, **P47** with two fluorine atoms on benzothiadiazole acceptor units was designed and synthesized by You et al. [93]. The corresponding nonfluorinated polymer **P48** was also prepared for comparison. The absorption maximum of **P47** in a chlorobenzene (CB) solution is red-shifted by 80 nm at room temperature relative to that at 100 °C, indicating that strong aggregation occurs at room temperature. Moreover, **P47** exhibits an additional absorption shoulder in solid state, implying more ordered interchain stacking in thin film. The optical E_g of **P47** deduced from the absorption onset of the thin film spectrum is 1.7 eV. The E_{HOMO} and E_{LUMO} of **P47** were estimated to be at −5.54 and −3.33 eV, respectively. The device based on **P47**:$PC_{61}BM$ blend exhibited a J_{sc} of 12.9 mA/cm^2, a V_{oc} of 0.91 V, and an FF of 0.61, leading to a high PCE of 7.2 %. The **P47**:$PC_{61}BM$ blend has a higher absorption coefficient than that of the **P48** blend, which likely accounts for the higher J_{sc} value observed in **P47**-based device.

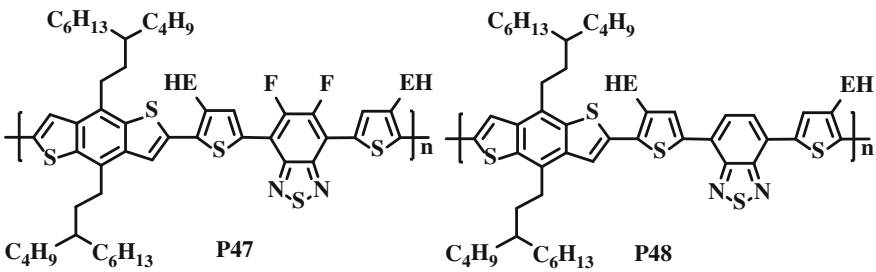

P47 P48

Structurally similar to benzothiadiazole, benzo[*d*][1,2,3]triazole unit is another attractive acceptor units for D-A polymer. The central nitrogen atom in triazole unit is available to attach an additional solubilizing alkyl chain. You et al. reported

BDT-based polymers **P49** and **P50** introducing 2-(2-butyloctyl)-2*H*-benzo[*d*][1,2,3] triazole (HTAZ) and 2-(2-butyloctyl)-5,6-difluoro-2*H*-benzo[*d*] [1,2,3]triazole (FTAZ) as the acceptors [94]. Compared to the widely used benzothiadiazole, HTAZ acceptor has weaker electron-withdrawing ability. Therefore, HTAZ-based polymers usually have wider E_gs. Again, **P50** showed lower E_{HOMO} and E_{LUMO} (−5.36 and −3.05 eV) than **P49** (−5.29 and −2.87 eV) due to the additional electron-withdrawing fluorine atoms on the FTAZ acceptors. By using 1,2,4-trichlorobenzene (TCB) as a solvent to spin cast the active layer followed by solvent annealing, the device based on **P49**:$PC_{61}BM$ blend exhibited a PCE of 4.36 %. Furthermore, the device based on **P50**:$PC_{61}BM$ blend exhibited a J_{sc} of 12.45 mA/cm^2, a V_{oc} of 0.79 V, and a FF of 0.72, leading to a PCE of 7.1 %. The effect of fluorine atoms resulted in an increased V_{oc} in the device based on **P50**:$PC_{61}BM$ blend.

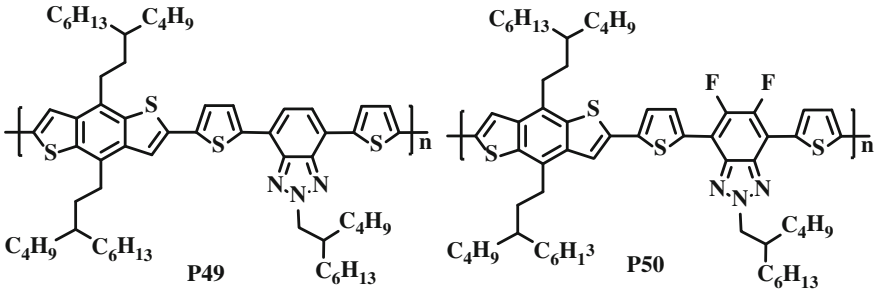

P51 containing thiazolothiazole units was reported by Jenekhe et al. [95]. The E_{HOMO} and E_g of **P51** were estimated to be at −5.4 and 1.77 eV. The device based on **P51**:$PC_{71}BM$ blend exhibited a J_{sc} of 11.6 mA/cm^2, a V_{oc} of 0.69 V, and a FF of 0.66, leading to an average PCE of 5.3 %.

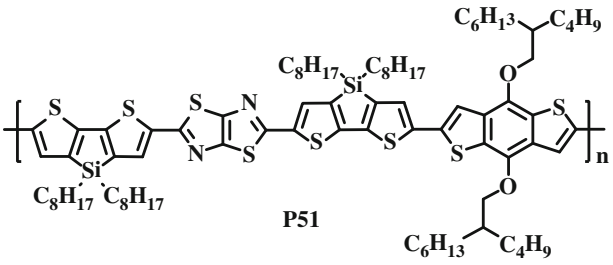

BDT-based polymer incorporating bi-thiazole units was developed by Li et al. [96]. The absorption maxima of **P52** is red-shifted by 45 nm from solution to solid state, which indicates strong interchain interaction in solid state. The E_g deduced from the absorption onset of polymer thin film spectrum is 1.96 eV. The E_{HOMO}

Table 5.7 Physical properties and PSC performances of BT-BDT-based copolymers

	HOMO (eV)	LUMO (eV)	Optical E_g (eV)	V_{oc} (V)	J_{sc} (mA cm^{-2})	FF (%)	PCE (%)	References
P53	−5.09	−3.22	1.58	0.68	14.59	62.6	6.21	[97]
P54	−5.11	−3.25	1.58	0.74	17.48	58.7	7.59	[97]
P55	−5.04	−3.19	1.63	0.66	11.53	54.7	4.16	[97]
P35	−5.07	−3.21	1.60	0.70	15.51	59.2	6.43	[86]
P56	−5.31	−3.44	1.75	0.92	10.70	57.5	5.66	[98]
P57	−5.19	−3.26	1.58	0.80	11.71	61	6.0	[99]
P58	−5.26	−3.10	1.73	1.0	5.8	34.6	2.11	[99]
P59	−5.32	−3.58	1.67	0.82	12.53	54.9	5.64	[100]
P60	−5.41	−3.72	1.63	0.86	12.05	59.9	6.21	[100]
P61	−5.3	−3.2	2.0	0.85	10.4	59	5.22	[101]

and E_{LUMO} of **P52** were estimated to be at −5.12 and −2.94 eV, respectively. The optimal PCE of the device based on **P52**:$PC_{71}BM$ blend reached 4.46 % with a V_{oc} of 0.82 V, a J_{sc} of 9.01 mA/cm^2, and a FF of 0.60 (Table 5.6).

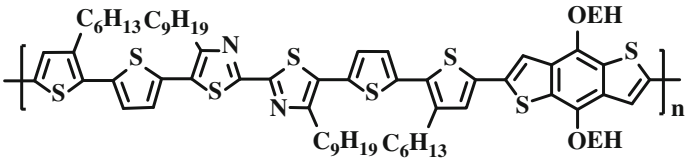

P52

Since the BDT derivatives have been proved to be a superior donor component for making donor-acceptor copolymers, chemical modification on the BDT unit is a practical and efficient strategy to further improve its molecular properties. Introduction of two thienyl rings at 4, 8 positions of the BDT unit to extend the conjugation in the vertical direction is a rational design, considering that the absorption ability can be thus improved and thiophene moiety is an essential ingredient for efficient charge transportation. On the basis of 4,8-bis(2-thienyl)-BDT (BT-BDT) structure, one or two aliphatic side chains can be substituted on the 3- or 4- or 5-positions of the two vertically extended thiophene rings to guarantee sufficient solubility.

Similarly, BT-BDT unit was also used to copolymerize with alkoxycarbonyl-substituted thieno[3,4-*b*]thiophene monomer or alkylcarbonyl-substituted thieno-[3,4-*b*]thiophene monomer to give **P53** and **P54**, respectively [97]. The branched alkyl side chains(2-ethylhexyl) on the extended thiophene moieties were employed for sufficient solubility of the corresponding polymers. **P53** and **P54** showed more red-shifted and broader absorption bands compared to that of their alkoxy-substituted analogues (**P35** and **P55**) due to the enhancement of intermolecular

interactions resulting from the extended conjugation of the alkyl thienyl side chains of the 2-D conjugated polymers. The E_g values are 1.58 eV for **P53** and **P54**, which are slightly smaller than that of **P55** (1.63 eV) and **P35** (1.60 eV). By replacing the alkoxy side chain with the alkyl thienyl conjugated side chain, the E_{HOMO}s and E_{LUMO}s levels of the corresponding polymers are shifted to slightly lower energy levels, which is beneficial for a higher V_{oc} for the PSCs. The devices based on **P53** or **P54**:$PC_{71}BM$ blend exhibited high PCEs of 6.21 and 7.59 %, respectively. These results might be due to the improved hole mobility and the broader absorption of the 2-D conjugated structure.

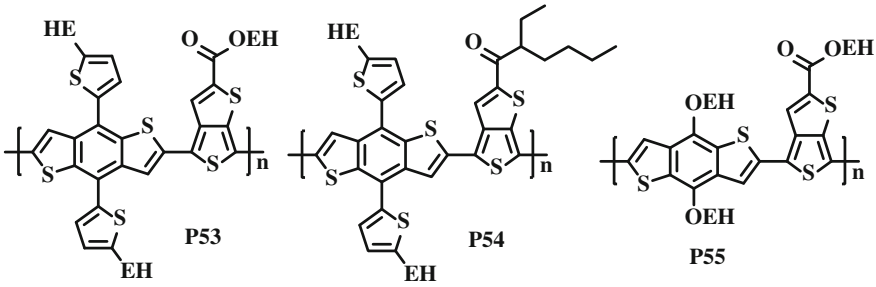

P56 using benzothiadiazole as the acceptor was reported by Hou et al. [98]. Compared to solution state, **P56** exhibited more red-shifted absorption spectrum in solid state as a result of the stronger aggregation. The E_{HOMO} and E_g of **P56** were estimated to be at −5.31 and 1.75 eV, respectively. The device based on **P56**: $PC_{71}BM$ blend exhibited a J_{sc} of 10.7 mA/cm^2, a V_{oc} of 0.92 V, and a FF of 0.58, leading to a PCE of 5.66 %. The high V_{oc} agrees well with the low-lying E_{HOMO} calculated from CV.

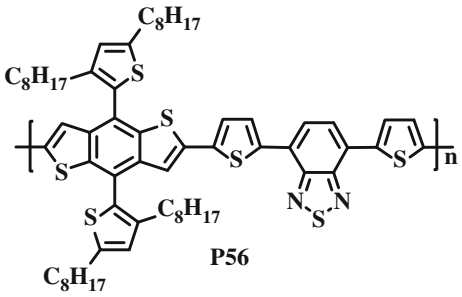

BT-BDT-based polymer **P57** using a new acceptor unit, naphtho[1,2-*c*:5,6-*c*]bis [1,2,5]-thiadiazole (NT), was reported by Huang et al. [99]. The corresponding **P58** using benzothiadiazole (BT) as the acceptor was also synthesized for comparison. Compared to BT, NT consisting two fused 1,2,5-thiadiazole rings has a larger

coplanar structure, which can enhance the interchain packing and carrier mobilities of the corresponding polymer. Besides, the electron-withdrawing ability of NT is slightly stronger than that of BT, which will reduce the E_g of **P57**. In comparison to **P58**, **P57** showed red-shifted absorbance spectra both in o-dichlorobenzne (ODCB) solution and in thin film, which was a result of the more electron-deficient NT acceptor. The E_gs deduced from the absorption onset of polymer thin film spectra are 1.73 eV for **P58** and 1.58 eV for **P57**. The best device based on **P57**:$PC_{71}BM$ blend exhibited a J_{sc} of 11.71 mA/cm^2, a V_{oc} of 0.80 V, and a FF of 0.61, leading to a PCE of 6.0 %. However, the device using **P58**:$PC_{71}BM$ blend only exhibited a lower PCE of 2.11 % due to the strong steric hindrance of the substituted hexyl chains.

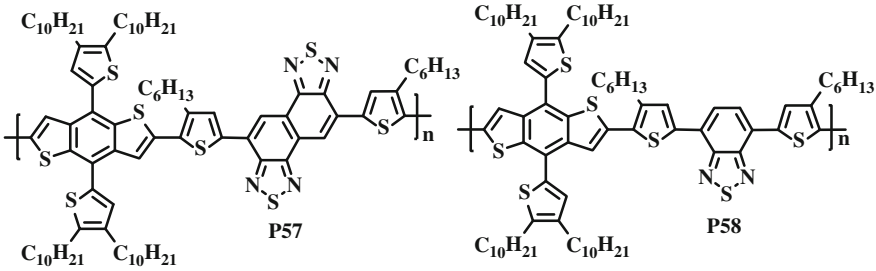

In addition, BT-BDT-based polymers **P59** and **P60** incorporating the modified BT units as the acceptors were also reported by Peng et al. [100]. The BT units in **P59** and **P60** were subsitituated with an electron-donating alkoxy and an electron-deficient fluorine moieties, respectively. **P59** and **P60** showed similar absorption spectra, and the E_gs deduced from the absorption onset of polymer thin film spectrum are 1.67 eV for **P59** and 1.63 eV for **P60**. The E_{HOMO}s/E_{LUMO}s of **P59** and **P60** were estimated to be at −5.32/−3.58 and −5.41/−3.72 eV, respectively. The devices based on **P59** or **P60**:$PC_{71}BM$ blend exhibited high PCEs of 5.64 and 6.21 %, respectively.

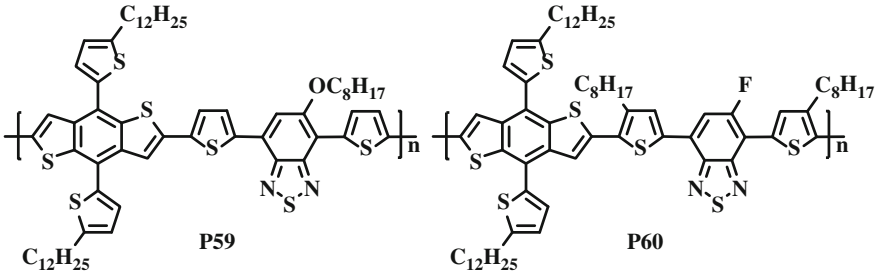

Table 5.8 Physical properties and PSC performances of **IDT**-based copolymers

	HOMO (eV)	LUMO (eV)	Optical E_g (eV)	V_{oc} (V)	J_{sc} (mA cm^{-2})	FF (%)	PCE (%)	References
P62	−5.36	−3.52	1.75	0.85	11.2	67.2	6.41	[103]
P63	−5.33	−3.52	1.81	0.87	10.9	60	5.69	[104]
P64	−5.28	−3.61	1.67	0.87	11.2	64	6.24	[104]
P64	−5.3	−3.6	1.7	0.88	11.50	61	6.2	[105]
P65	−5.23	−3.53	1.61	0.83	11.6	63	6.06	[106]
P66	−5.26	−3.69	1.48	0.74	10.1	43	3.21	[106]
P62	−5.23	−3.52	1.72	0.81	11.23	55	5.02	[107]
P67	−5.38	−3.64	1.72	0.86	11.23	56	5.4	[107]
P68	−5.48	−3.67	1.78	0.92	10.87	51	5.10	[107]
P69	−5.21	−2.94	1.83	0.89	13.3	48.9	5.79	[108]
P70	−5.24	−3.10	1.68	0.82	13.27	56.7	6.17	[108]

Li et al. [101] also reported a BT-BDT–based polymer **P61** using thiazolo[5,4-*d*] thiazole as the acceptor unit. In spite of a branched 2-hexyldecyl group, polymer **P61** showed limited solubility in chloroform or dichlorobenzene solution. The E_g deduced from the absorption onset of **P61** thin film spectrum is 2.0 eV. The E_{HOMO} and E_{LUMO} of **P61** were estimated to be at −5.3 and −3.2 eV, respectively. By adding the processing additive DIO, the device based on **P61**:$PC_{71}BM$ blend exhibited a J_{sc} of 10.4 mA/cm^2, a V_{oc} of 0.85 V, and an FF of 0.59, leading to a PCE of 5.22 % (Table 5.7).

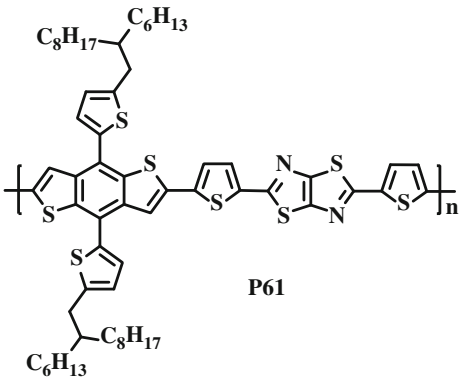

P61

5.4 Ladder-Type Conjugated Copolymers

5.4.1 *Indacenodithiophene(IDT)–Based Donor-Acceptor Conjugated Polymers*

The synthesis of indacenoditihophene (IDT) small molecule was first reported by Wong et al. in 2006 [102]. Two outer thiophenes in IDT are covalently fastened to the central phenyl ring by two carbon bridges, forming a pentacyclic multifused conjugated structure. The extended conjugation and coplanarity make IDT a superb building block for preparing photoactive polymers. Ting et al. [103] first reported IDT-based alternating copolymer (**P62**) using benzothiadiazole as the acceptor. Alternating polymer **P62** possesses a E_g of 1.75 eV with a high absorption coefficient of 1.60×10^5 cm^{-1} in solid state. Blending **P62** with $PC_{71}BM$ in the active layer delivered an average PCE of ca. 5.4 %. By solvent vapor annealing (SA) to optimize the active layer morphology, the device exhibited the highest PCE of 6.4 % with a V_{oc} of 0.85 V, a J_{sc} of 11.2 mA/cm^2, and a FF of 0.67. The FF of SA-fabricated device is increased by ca. 12 %, which is associated with the improved morphology.

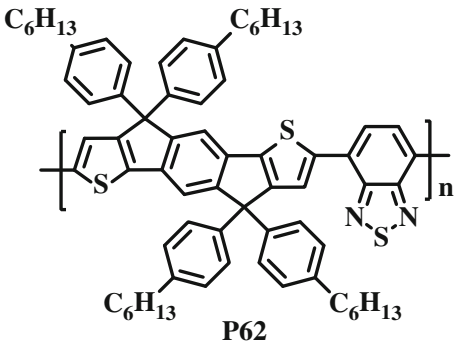

P62

Jen and co-workers [104] reported IDT-based polymers **P63** and **P64** introducing 2,3-diphenylquinoxaline and phenanthrenequnioxaline units as the electron-deficient acceptors, respectively. Compared to the nonfused 2,3-diphenylquinoxaline, fused phenanthrenequnioxaline significantly increases the coplanarity and facilitates the intermolecular packing and charge transport. Moreover, the extended π-conjugation led to reduced E_g in the corresponding polymer. **P64** showed a narrower E_g of 1.67 eV than **P63** (1.81 eV) in the polymer film. The device based on **P63**:$PC_{71}BM$ blend exhibited a PCE of 5.69 %. Furthermore, due to **P64** possessing a lower E_g and preferred energy levels that are well matched with $PC_{71}BM$, the device based on **P64**:$PC_{71}BM$ blend showed an increased PCE of 6.24 % with a V_{oc} of 0.87 V, a J_{sc} of 11.2 mA/cm^2, and a FF of 0.64. Notably, by using a C60 bis-adduct surfactant to modify the energy level alignment at the organic/cathode interface in conventional BHJ devices, **P64**:$PC_{71}BM$ blend device

still exhibited a high PCE of 6.22 % with a V_{oc} of 0.88 V, a J_{sc} of 11.5 mA/cm^2, and a FF of 0.61 [105].

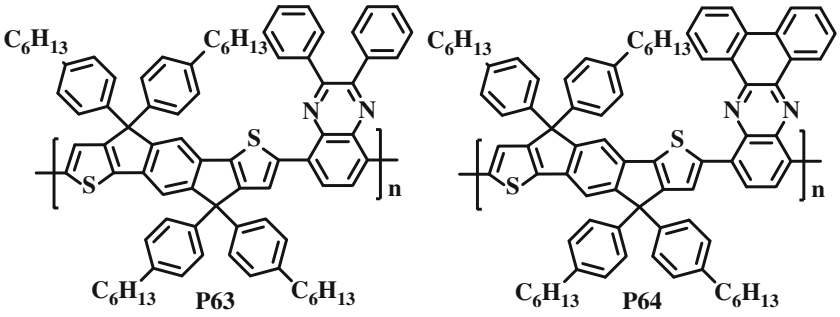

The electron-deficient phenanthrenequnioxaline structure was further modified by replacing the fused phenyl rings with thienyl units, leading to a new coplanar dithienobenzoquinoxaline unit. Moreover, the qunoxaline unit in dithienobenzoquinoxaline can be also changed to pyridopyrazine moiety, forming another electron-deficient dithienobenzopyridopyrazine unit. Therefore, two IDT-based polymers **P65** and **P66** using dithienobenzoquinoxaline and dithienobenzopyridopyrazine as the electron-deficient acceptors, respectively, were reported by Jen and co-workers [106]. **P66** having a more electron-deficient pyridine moiety exhibited a smaller E_g of 1.48 eV compared to **P65** with a benzene ring counterpart (1.61 eV). The **P65**-based device showed a V_{oc} of 0.83 V, a J_{sc} of 11.6 mA/cm^2, and a FF of 0.63, resulting a high PCE of 6.06 %. Under the same conditions, the **P66** device only showed a PCE to 3.21 % with a V_{oc} of 0.74 V, a J_{sc} of 10.1 mA/cm^2, and a FF of 0.43. The lower performance of **P66** is most likely due to excition nonradiative recombination at the interface since the pyridine unit may serve as an electron trap compared with benzene unit in **P65**.

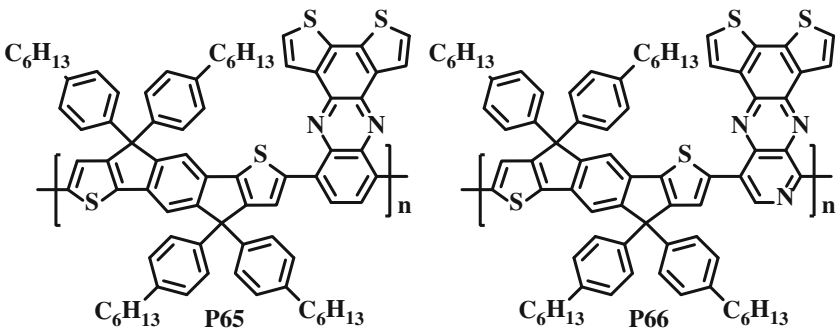

Fluorine atoms are introduced into the benzothiadiazole (BT) to synthesize the monofluoro- and difluoro-substituted BT units, which were then copolymerized with the indacenodithiophene unit to furnish two D-A polymers, **P67** and **P68** [107]. It should be noted that **P67** is a regiorandom polymer because of the asymmetrical difluoro-substituted BT acceptor. Both **P67** and **P68** showed E_g of 1.72 eV, implying that the introduction of monofluoro-substituent onto **P67** showed a little effect on the optical properties of polymers. Compared to **P67**, the absorption spectra of **P68** in solution and thin film showed blue-shifted peaks due to the stronger F atoms effect on the E_{HOMO}. Therefore, **P68** has a lower E_{HOMO} and a similar E_{LUMO} compared to that of **P67**. Under the same device conditions, the devices based on **P62** or **P67**:$PC_{71}BM$ blend exhibited PCE of 5.02 and 5.4 % with V_{oc} of 0.81 and 0.86 V, respectively. The higher PCE of the **P67**-based device than the **P62**-based device was attributed to the larger V_{oc}, benefiting from the deeper E_{HOMO} of **P67**. The V_{oc} of the **P68**:$PC_{71}BM$ blend device reached 0.92 V due to the deepest E_{HOMO} of **P68**, leading to the high PCE of 5.1 %.

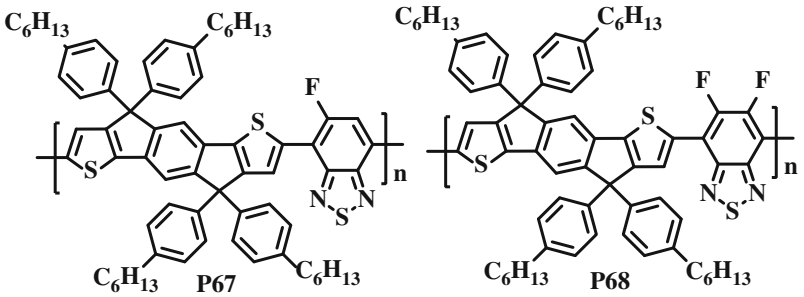

The early reported IDT structures used two 4-hexylphenyl groups substituted on the sp^3 carbons of the cyclopentadiene rings. These aryl-based side chains close to the conjugated backbones are rather bulky and rigid, which suppress the intermolecular interaction between the polymers. Introducing more flexible aliphatic side chains to the carbon bridges is a better design to circumvent this deficiency. Therefore, IDT derivatives having aliphatic substituents were synthesized and copolymerized with electron-deficiency units for application in OPVs. Two IDT-based copolymers **P69** and **P70** with bis(thiophen-2-yl)-thiazolothiazole (TTz) and bis(thiophen-2-yl)-benzothiadiazole (DTBT) have been synthesized by Li and co-workers [108]. The device based on **P69**:$PC_{71}BM$ blend exhibited a high PCE of 5.79 % with a large J_{sc} of 13.3 mA/cm^2 and a high V_{oc} of 0.89 V, while the device based on **P70**:$PC_{71}BM$ blend exhibited an even higher PCE of 6.17 % with a J_{sc} of 13.27 mA/cm^2, a V_{oc} of 0.82 V, and a FF of 56.9 %. These results indicate that the copolymers based on the IDT as electron-rich donor with aliphatic side chains are promising p-type materials for high efficiency PSCs (Table 5.8).

Table 5.9 Physical properties and PSC performances of Si-IDT- and Ge-IDT-and tetrathienoanthracene-based copolymers

	HOMO (eV)	LUMO (eV)	Optical E_g (eV)	V_{oc} (V)	J_{sc} (mA cm^{-2})	FF (%)	PCE (%)	References
P71	−5.32	−3.25	1.8	0.81	8.86	48.8	3.47	[109]
P72	−5.25	−3.55	1.7	0.80	8.80	51.6	3.64	[109]
P71	−5.5	−3.6	1.8	0.88	9.39	52	4.3	[110]
P75	−5.1	−3.7	1.4	0.63	3.53	65	1.4	[110]
P73	−5.3	−3.1	1.8	0.94	3.44	54	1.7	[111]
P74	−5.2	−3.2	1.7	0.80	8.36	64	4.3	[111]
P76	–	–	1.74	0.86	10.1	58	5.02	[113]
P77	−5.04	−3.28	1.69	0.66	15.0	58	5.62	[114]

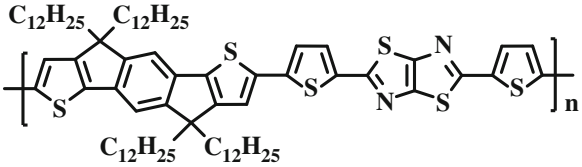

P69

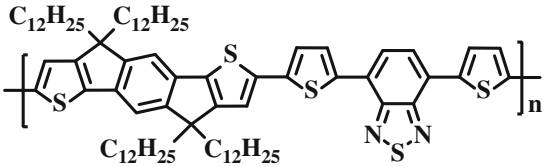

P70

5.4.2 *Sila-indacenodithiophene(IDT)–Based Donor-Acceptor Conjugated Polymers*

Silicon possesses different steric and electronic nature compared with carbon atom, which provides a useful tool to tailor electronic and optical properties of the conjugated system. The synthesis of silaindacenodithiophene (Si-IDT), where the silicon atoms are used to bridge and fasten two neighboring aryl rings, has been reported by Jen's group [109] and McCulloch's group [110, 111]. A silicon atom embedded into two aryl rings forms a five-membered silole unit. In fact, compared with thiophene, furan, and pyrrole, silole always exhibits extraordinary molecular properties as a result of its unique σ*–π* conjugation [112]. Therefore, silole unit is

very appealing building block to construct conjugated systems for optoelectronic applications. Si-IDT-based copolymers **P71** and **P72** using benzothiadiazole and dithienobenzothiadiazole as the comonomer units were reported, respectively [109]. The optical band gaps were estimated to be 1.80 and 1.70 eV for **P71** and **P72**. The silicon-bridged polymer **P72** exhibited a high hole mobility up to 0.012 $cm^2\ V^{-1}\ s^{-1}$. The devices based on **P71** or **P72**:$PC_{71}BM$ blend exhibited PCE of ca. 3.5 %. Similarly, McCulloch reported **P71** with a slightly higher device performance of 4.3 % [110].

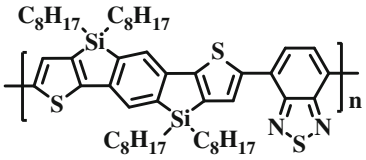

P71

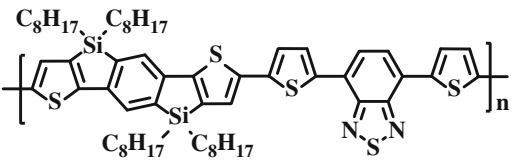

P72

Furthermore, similar to **P71** and **P72**, the corresponding fluorinated **P73** and **P74** with 5,6-difluorobenzothiadiazole and 5,6-difluoro-dithienobenzothiadiazole units were also prepared by McCulloch and Ashraf [111]. The incorporation of fluorine atoms to the polymer backbone has shown to influence both the polymer electronic energy levels and thin film morphology. **P74-**based device exhibited the highest PCE of 4.3 %, whereas the device based on **P73** exhibited a low PCE of 1.7 %.

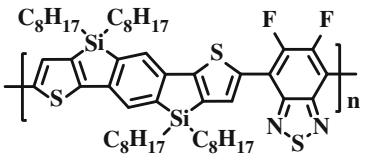

P73

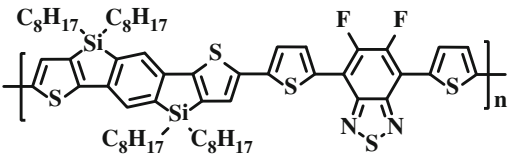

P74

McCulloch and co-workers [110] also synthesized a Si-IDT-based polymer, **P75**, using 1,4-diketopyrrolo[3,4-c]-pyrrole (DPP) unit as electron-deficiency acceptor, showing a greater mobility than 0.1 $cm^2\ V^{-1}\ s^{-1}$.

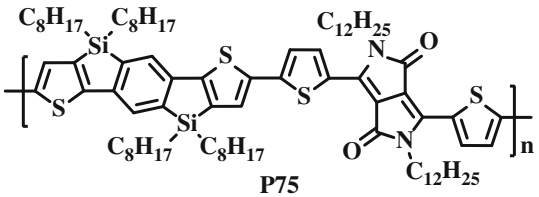

P75

5.4.3 Germa-Indacenodithiophene(Ge-IDT)–Based Donor-Acceptor Conjugated Polymers

It has been found that silaindacenodithiophene was unstable under basic conditions required for Suzuki cross-coupling. Therefore, the use of Stille polymerization with stannylated SiIDT is the best synthetic approach. However, it has been known that dithienogermoles were stable to the basic conditions of Suzuki coupling due to reducing polarisation of the C–Ge bond over the C–Si bond. It is of interest to synthesize Ge-bridged IDT analogue to investigate electronic and steric effects of Ge. The germaindacenodithiophene (GeIDT) monomer was polymerized with 2,1,3-benzothiadiazole-4,7-bis (boronic acid pinacol ester) by Suzuki polycondensation reaction to afford **P76** [113]. In contrast to the carbon analogue **P62** lacking obvious crystallinity, the X-ray results indicated that **P76** forms semi-crystalline thin films, despite the inclusion of the four bulky 2-ethylhexyl groups. In solution state, the absorption of **P76** gave an absorption maximum at 630 nm, whereas it shown a main absorption peak at 644 nm with a shoulder at 596 nm in the solid state due to aggregation in thin film. The device based on **P76**:$PC_{71}BM$ blend showed an increased PCE of 5.02 % with a V_{oc} of 0.86 V, a J_{sc} of 10.1 mA/cm^2, and a FF of 0.58.

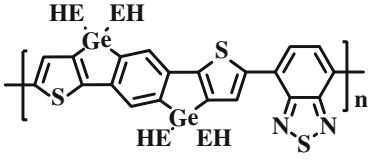

P76

5.4.4 Tetrathienoanthracene-Based Donor-Acceptor Conjugated Polymer

The tetrathienoanthracene unit was a promising building block for D-A type conjugated copolymers. The two-dimensional (2D) extended π-conjugated length will favor stronger intermolecular π–π stacking. Tetrathienoanthracene monomer was copolymerizes with thieno[3,4-*b*]thiophene unit to furnish a series of polymers [114]. Absorption spectra of **P77** showed the absorption peak at 664 nm, which corresponds to a E_g around 1.69 eV. **P77** possesses a low band gap with the E_{HOMO} of −5.04 eV and the E_{LUMO} of −3.28 eV. By using chloroform/DIO as co-solvent system, the device based on **P77**:$PC_{61}BM$ with 2-butyloctyl alkyl side chains exhibited a PCE of 5.62 % (Table 5.9).

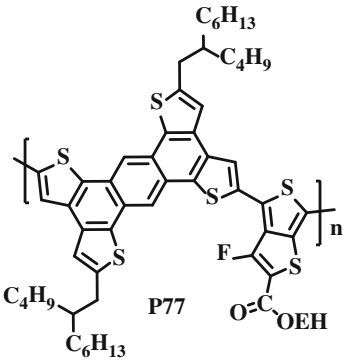

5.4.5 *Conjugated Polymers Containing Multifused Alternate Benzene/Thiophene Arenes*

Diindeno[1,2-*b*:2′,1′-*d*]thiophene (DIDT), another type of pentacyclic structure where the central thiophene is connected with two outer phenyl rings through two embedded CP rings, emerges as an appealing synthetic target due to its highly planar structure. The ability of functionalization at bridging carbon allows for introducing four highly solubilizing aliphatic side chains without affecting its coplanarity, making DIDT derivatives highly soluble. Accordingly, a donor-acceptor conjugated polymer **P78** consisting of DIDT unit as an electron-rich donor and benzothiadiazole as the acceptor was developed by Cheng et al. [115]. **P78** exhibited the HOMO levels of −5.36 eV. **P78**:$PC_{71}BM$ (1:2, w/w) based device showed a V_{oc} of 0.7 V, a J_{sc} of 5.3 mA/cm^2 and a FF of 44 %, and a of PCE to 1.65 %.

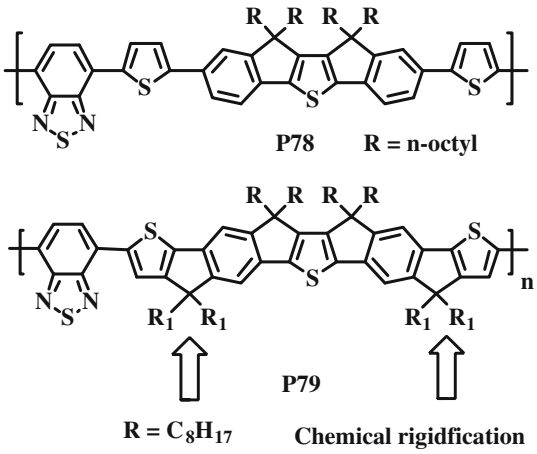

If the 3,7-positions of the DIDT units in **P78** are covalently rigidified with the 3-positions of two adjacent thiophene rings by a carbon bridge, an alternate thienyl-phenylene-thienylene-phenylene-thienyl (TPTPT) nonacylic arene building block with forced coplanarity will be emerged. Compared to DIDT, TPTPT unit may exhibit improved optical and electronic properties due to the higher thiophene content and extended coplanarity of the conjugated backbone. Cheng et al. [116] reported the synthesis of the distannyl-TPTPT monomer which was copolymerized with 4,7-dibromo-2,1,3-benzothiadiazole BT acceptor monomer to afford an alternating D-A copolymers **P79**. **P79** exhibited an absorption maximum at 452 nm and an ICT band at 639 nm. In addition, the optical band gaps (E_g^{opt}) of **P79** deduced from the absorption edges of thin film spectra are determined to be 1.73 eV. It should be emphasized that **P79** showed significantly red-shifted absorption maximum in comparison with its corresponding non-fused **P78** analogue (444 nm vs. 415 nm for the localized transition and 628 nm vs. 544 nm for the ICT transition in chloroform solution), demonstrating that the effective conjugated length of the coplanar donor is increased and electron coupling between the rigidified donor and the acceptor units is substantially enhanced. Note that the intensities of the shorter wavelength bands of the polymer in the solid state are apparently stronger than those in the solution state, which also suggests that the rigid and coplanar nonacyclic units can enhance their light absorption ability in the solid state. The HOMO energy levels being estimated to be −5.24 eV for **P79** is in an ideal range to assure better air-stability and greater attainable V_{oc} in the final device. Despite the amorphous nature in thin films, **P79** showed good hole transporting properties due to their rigid and coplanar structures. **P79** exhibited a higher hole mobility of 5.1×10^{-4} cm^2/Vs by SCLC theory, compared to **P78** with 1×10^{-4} cm^2/Vs. The device using **P79**:$PC_{71}BM$ (1:4, w/w) blend delivered superior performance with a J_{sc} of 11.4 mA/cm^2, a V_{oc} of 0.76 V, a FF of 61 %, and an exceptional PCE of 5.3 %, which dramatically outperforms the device based on the non-fused **P78**:$PC_{71}BM$ (1:2, w/w) blend by 3-fold. The inverted device incorporating **P79**:$PC_{71}BM$ (1:4, w/w) blend further achieved a high PCE of 5.9 % with J_{sc} = 12.10 mA/cm^2, V_{oc} = 0.76 V and FF = 64 %.

Thieno[3,2-*b*]thiophene (TT) unit has been an appealing building block for high mobility p-type semiconductors. This fused structure possesses higher aromatic stabilization energy than a thiophene, which can potentially lower the HOMO level for higher V_{oc} [117]. Moreover, the C_{2h} symmetry and coplanar geometry allow more ordered packing and stronger interchain interactions to achieve exceptional hole mobility, which is beneficial for J_{sc}. Cheng et al. [118] have reported a multifused hexacyclic diindenothieno[2,3-*d*]thiophene (DITT) unit, where the central TT ring is connected with two outer phenyl rings through two embedded cyclopentadienyl (CP) rings. This monomer was polymerized by Suzuki coupling with 4,7-bis(5-bromo-2-thienyl)-2,1,3-benzothiadiazole (DTBT) acceptor to afford a new class of alternating D-A conjugated polymers **P80**. The optical band gap (E_g^{opt}) deduced from the onset of absorption in the solid state is determined to be 1.87 eV for **P80**. Note that the E_g^{opt} of **P78** is 1.85 eV which is lower than that of **P80**, suggesting that the TT unit in DITT may have higher aromaticity than the

thiophene unit in DIDT. It should be emphasized that the HOMO level of TT-based **P80** is lower than that of corresponding thiophene-based **P78** (−5.40 eV vs. −5.36 eV), again suggesting that TT unit embedded in the structure is indeed capable of increasing the oxidation potential. The device using **P80**:$PC_{71}BM$ (1:4, w/w) blend delivered superior performance with a V_{oc} of 0.92 V, a J_{sc} of 10.71 mA/cm^2, a FF of 58.4 % with an exceptional PCE of 5.8 % which greatly outperformed the **P78**-based device. The hole mobility of the **P80**:$PC_{71}BM$ blend is 1.41×10^{-4} cm^2/Vs which might be responsible for its better J_{sc}, FF and photovoltaic performance. Hybridization of benzene and thieno[2,3-*d*]thiophene units into a coplanar ladder-type DITT structure indeed successfully achieves a superior V_{oc} while maintaining a high J_{sc} value, overcoming the trade-off between V_{oc} and J_{sc}.

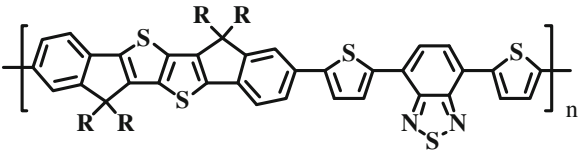

P80

5.4.6 *Conjugated Polymers Using Dithienofluorene- and Dithienocarbazole-Based Arenes with Carbon, Silicon and Nitrogen Atoms as Bridges*

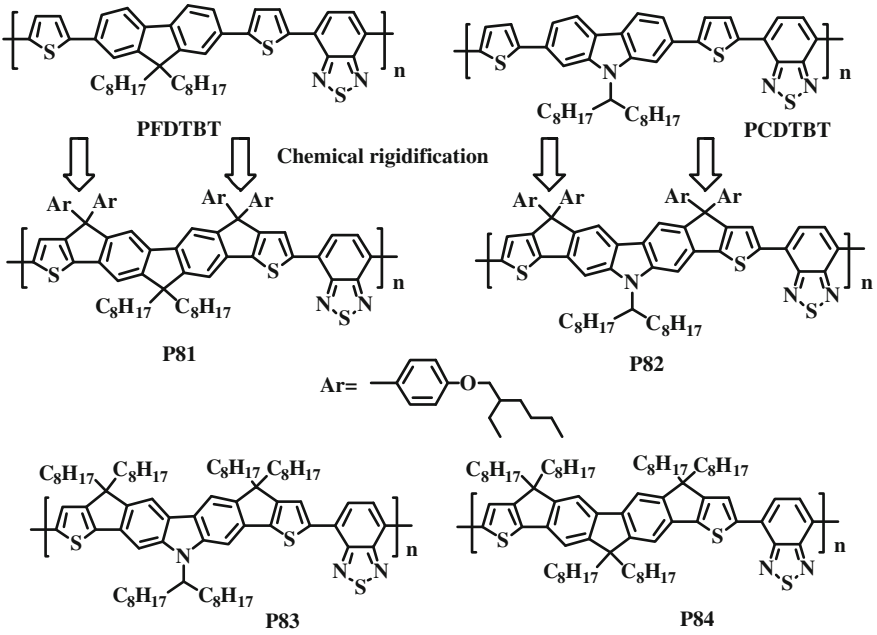

Alternating copolymers poly(2,7-fluorene-*alt*-dithienylbenzothiadiazole) (**PFDTBT**) [119] and poly(2,7-carbazole-*alt*-dithienylbenzothiadiazole) (**PCDTBT**) [120] have been a promising class of p-type photoactive materials for the application in PSCs. Cheng et al. [121] reported two D-A copolymers poly(fluorene-dicyclopentathiophene-*alt*-benzothiadiazole) **P81** and poly(carbazole-dicyclopentathiophene-*alt*-benzothiadiazole) **P82**. Both polymers were designed based on the skeletons of the well-known **PFDTBT** and **PCDTBT** polymers. The structural uniqueness of **P81** and **P82** is that the 3-position of two outer thiophenes are covalently tied with the 3,6-positions of central fluorene or carbazole cores by a carbon bridge, forming two cyclopentadienyl (CP) rings embedded in a multi-fused heptacyclic structure. The optical band gaps (E_g^{opt}) deduced from the onset of absorption in the solid state are determined to be 1.76 eV for **P81** and 1.66 eV for **P82**. These results suggest that donating strength of carbazole is stronger than that of fluorene moiety, shifting the ICT band of **P82** to the lower energy. It should be emphasized that **PFDCTBT** and **PCDCTBT** have more red-shifted absorption spectra and smaller band-gaps in comparison with their corresponding non-fused **PFDTBT** (E_g^{opt} = 1.87 eV) and **PCDTBT** (E_g^{opt} = 1.88 eV) analogues, pointing out that the electron coupling between the rigidified donor and the acceptor units is enhanced. The HOMO levels were estimated to be −5.32 eV for **P81** and −5.38 eV for **P82**. Without extensive optimization, the preliminary photovoltaic performance based on **P81** already showed a J_{sc} of 9.5 mA/cm^2, a V_{oc} of 0.77 V, a fill factor (FF) of 0.38, leading to a decent PCE of 2.8 % while the device using **P82** as the p-type material delivered superior performance with a J_{sc} of 10.7 mA/cm^2, a V_{oc} of 0.80 V, a FF of 0.43, improving the PCE to 3.7 %. Because two 4-(2-ethylhexyloxy)phenyl moieties substituted at the carbon of CP rings may dilute strong intermolecular interactions, the profiles of absorption spectra of **P81** and **P82** are essentially unchanged with slight broadening of the bands from solution state to solid state. To tailor the intermolecular interaction for optimizing bulk properties, it is promising to modify the molecular structure of CDCT by replacing the branch ethylhexoxyphenyl groups on the CP rings with more flexible octyl groups. On the basis of the modified CDCT-C8 as the core structure, a D-A copolymer, poly (carbazole-dicyclopentathiophene-*alt*-benzothiadiazole), **P83**, was reported [122]. Furthermore, compared to **PCDCTBT** showing the absorption maxima at 412 and 607 nm in the thin film, **P83** exhibited bathochromic shifts of the absorption maxima at 425 and 645 nm. These phenomena clearly indicate that the aliphatic side chains indeed are capable of enhancing inter-chain π–π stacking interactions effectively in the solid state. The device based on the **P83**:$PC_{71}BM$ (1:3 in wt%) blend exhibited a V_{oc} of 0.74 V, a J_{sc} of 10.3 mA/cm^2, a FF of 60 %, delivering an impressive PCE of 4.6 %. This value represents not only a ca. 24 % enhancement in efficiency compared to the devices based on the **P82** (PCE = 3.7 %) but also one of the best performances among carbazole-based conjugated polymers in the literatures. The **P83**:$PC_{71}BM$ (1:3 in wt%) composite also showed very high hole mobility of 1.2×10^{-3} cm^2 V^{-1} s^{-1}, which is in good agreement with its high current density and fill factor. This improvement is highly associated with the modification of the side chains on the CDCT structure to optimize the inter-chain interactions for enhanced charge transporting.

In a similar manner, FDCT structure in **P81** was also modified by replacing the branch ethylhexoxyphenyl groups with more flexible octyl groups to afford **P84** in

order to tune the intermolecular interaction for enhanced absorption intensity, reduced optical band gap, and improved charge mobility [123]. The absorption maxima of **P84**, substituted with flexible octyl side chains, red-shifted by ca. 20 nm from the toluene solution to the solid state. Furthermore, the optical band gap of **P84** deduced from its absorption edge in solid state was determined to be 1.71 eV, which is narrower than that of **P81** (1.76 eV). These optical behaviors confirm that the side chain modification of **P84** effectively promotes stronger intermolecular interaction in solid state.

The field-effect hole mobilities of **P81** and **P84** were extracted from the transfer characteristics of the field-effect transistor (FET) devices fabricated with top-contact geometry using Au electrodes. **P84** exhibited a high field-effect hole mobility of 3.3×10^{-2} cm^2 V^{-1} s^{-1}, which is higher than that of **P81** (1.4×10^{-3} cm^2 V^{-1} s^{-1}) by an order of magnitude, due to the extended coplanarity and rigidity of FDCT structure. This result indicates that flexible aliphatic side chains in **P84** strengthens the intermolecular π–π interaction to the enhance hole-mobility compared to the ethylhexoxyphenyl side chains in **P81**. The solar cells with inverted architecture were fabricated based on the configuration of ITO/ZnO/C-PCBSD/**P84**:$PC_{71}BM$ (1:3, w/w)/poly(3,4-ethylenedioxythiophene) poly(styrenesulfonate) (PEDOT:PSS)/Ag, where C-PCBSD is a cross-linked fullerene interlayer [124]. By adding 2.5 vol.% 1-chloronathaphlene (CN) into ODCB as the processing additive, the PCE was dramatically improved to 6.7 % as a result of the simultaneously increased J_{sc} and FF values. By inserting a solution-processed vanadium oxide (VO_x) film on top of the PEDOT:PSS layer, an exceptionally high PCE of 7 % was achieved, which represents the highest value ever reported for the fluorine-based BHJ solar cells at its time. Based on the sp^3-hybridized carbon-bridged dithienocyclopentacarbazole (DTCC) system to tailor and control the optical and electronic properties, it is highly desirable to further elaborate this system by incorporating sp^3-hybridized silicon or nitrogen elements to replace the carbon bridges. As such, two new heptacyclic dithienosilolo-carbazole (DTSC) and dithienopyrrolo-carbazole (DTPC) structures were developed by Cheng et al. [125] with silole and pyrrole units fused between the thiophene and carbazole units, respectively. On the basis of the modified DTSC and DTPC units as electron-rich donors to polymerize with the benzothiadiazole acceptor, two novel alternating D-A copolymers poly(dithienosilolo-carbazole-*alt*-benzothiadiazole) (**P85**) and poly(dithienopyrrolo-carbazole-*alt*-benzothiadiazole) (**P86**) have been synthesized. These ladder-type heptacyclic systems have exhibited very intriguing properties. The HOMO/LUMO energy levels of **P86** and **P85** were determined to be −4.76/−3.29 eV and −5.35/−3.58 eV with the corresponding band gaps of 1.47 and 1.77 eV respectively. This result indicated that the HOMO/LUMO energy levels are highly dependent on the bridging elements in the heptacyclic backbone. It has been known that silole unit possesses certain extent of electron-accepting ability which in turn lowers the HOMO/LUMO energy levels of **P85** [112]. In contrast, the stronger electron-donating ability of the pyrrole moiety will increase the HOMO/LUMO energy levels of **P86**. The lowest-lying HOMO level observed for *Si*-bridged **P85** may ensure better air-stability and greater attainable V_{oc} in the final device.

N-bridged **P86** exhibited the most bathochromic shift of the absorption ICT maximum at 742 nm in the toluene solution, whereas *Si*-bridged **P85** exhibited the most hypsochromic shift absorption maximum at 590 nm. Furthermore, the optical band-gaps (E_g^{opt}) deduced from the absorption edges of thin film spectra are in the following order: **P85** (1.83 eV) > **P83** (1.64 eV) > **P86** (1.50 eV). These values are in good agreement with the band gaps (E_g^{EC}) estimated by electrochemical measurement (**P85** = 1.77 eV, **P83** = 1.64 eV, and **P86** = 1.47 eV). The transition energy of the photo-induced charge transfer band is highly dependent on the donating strength of the donor and accepting strength of the acceptor in the conjugated backbone. Because all of the polymers have the same acceptor, the difference of their λ_{max} as well as E_g^{opt} indicates that the donor strength of the heptacyclic arene is in the order: DTPC > DTCC > DTSC. Compared to DTCC, the weaker electron-donating ability of DTSC is again associated with the electron-accepting effect of silole units.

The hole mobilities of solution-processed **P85**, **P86** and **P83** thin film were measured using a bottom-gate, top-contact device configuration with evaporated gold source/drain electrodes and octadecyltrichlorosilane-modified SiO_2 gate dielectric on n-doped silicon wafer surface. The hole mobilities were obtained from the transfer characteristics of the devices in saturation regime. The thin film of **P86** was annealed at 200 °C for 10 min under nitrogen, annealed **P86** device showed the hole mobility of 8.5×10^{-4} cm^2 V^{-1} s^{-1} with an on-off ratio of $4.0 \times 10^{2.}$ Encouragingly, the devices of **P85** and **P83** exhibited higher hole mobilities of 0.073 and 0.110 cm^2 V^{-1} s^{-1} with good on-off ratios of 1.1×10^6 and 1.7×10^4 in the optimal condition respectively. The hole mobilities of **P85** and **P83** are among the best performances in the amorphous benzothiadiazole-based donor-acceptor type copolymers.

The device based on the **P86**:$PC_{71}BM$ (1:2 in wt%) blend exhibited a V_{oc} of 0.50 V, a J_{sc} of 10.5 mA/cm^2, a FF of 49.9 %, delivering a PCE of 2.6 %. Encouragingly, the device using **PDTSCBT**:$PC_{71}BM$ (1:3 in wt%) as the p-type material delivered a superior performance with a V_{oc} of 0.82 V, a J_{sc} of 11.1 mA/cm^2, a FF of 56.7 %, improving the PCE to 5.2 %. Compared to **P86** and **P83**, the largest V_{oc} of the **P85**-based device is associated with the lowest-lying HOMO (Table 5.10).

Table 5.10 Physical properties and PSC performances of the ladder-type copolymers

	HOMO (eV)	LUMO (eV)	Optical E_g (eV)	V_{oc} (V)	J_{sc} (mA cm^{-2})	FF (%)	PCE (%)	References
P78	−5.36	−3.23	1.85	0.7	5.3	44	1.65	[115]
P79	−5.24	−3.36	1.73	0.76	11.4	61	5.3	[116]
P80	−5.40	−3.61	1.87	0.92	10.71	58.4	5.8	[118]
P81	−5.32	−3.55	1.76	0.77	9.5	38	2.8	[121]
P82	−5.38	−3.61	1.66	0.80	10.7	43	3.7	[121]
P83	−5.31	−3.67	1.64	0.74	10.3	60	4.6	[122]
P84	−5.30	−3.55	1.71	0.83	12.57	66.8	7.0	[123]
P85	−5.35	−3.58	1.83	0.82	11.1	56.7	5.2	[125]
P86	−4.76	−3.29	1.50	0.50	10.5	49.9	2.6	[125]

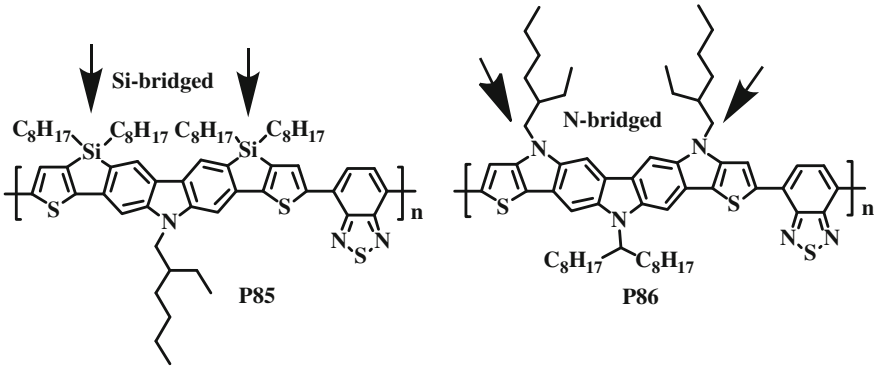

5.5 Conclusions

With extensive research on material development as well as device engineering, bulk heterojunction-based solar cells have made a dramatic progress in improving performance and stability. Power conversion efficiencies exceeding 8 % have been reported from both academia and industry. In this chapter, we have updated and summarized the recent development of the most important p-type conjugated polymers mostly reported after 2009. In combination of synthetic endeavors, molecular designs such as chemical planarization, quinoidiation, donor-acceptor approach, and side-chain engineering have led to a variety of superior p-type conjugated polymers. These advances have paved an important way towards a better understanding of structure-property relationships.

To produce BHJ photovoltaic devices with PCEs exceeding 10 % will certainly require efforts from interdisciplinary cooperation. By integrating new advanced device concepts and the nanostructure engineering of the morphology, the future development of novel conjugated polymers will ensure their key role in bringing high efficiency and low cost plastic solar cells one step closer to successful commercialization.

References

1. G. Yu, J. Gao, J.C. Hummelen et al., Polymer photovoltaic cells—enhanced efficiencies via a network of internal donor-acceptor heterojunctions. Science **270**(5243), 1789–1791 (1995)
2. M.C. Scharber, D. Wuhlbacher, M. Koppe et al., Design rules for donors in bulk-heterojunction solar cells—towards 10 % energy-conversion efficiency. Adv. Mater. **18**(6), 789–794 (2006)

3. T. Yang, M. Wang, C. Duan et al., Inverted polymer solar cells with 8.4 % efficiency by conjugated polyelectrolyte. Energy Environ. Sci. **5**(8), 8208–8214 (2012)
4. L.T. Dou, J.B. You, J. Yang et al., Tandem polymer solar cells featuring a spectrally matched low-bandgap polymer. Nat. Photonics **6**(3), 180–185 (2012)
5. C.E. Small, S. Chen, J. Subbiah et al., High-efficiency inverted dithienogermole-thienopyrrolodione-based polymer solar cells. Nat. Photonics **6**(2), 115–120 (2012)
6. Z.C. He, C.M. Zhong, X. Huang et al., Simultaneous enhancement of open-circuit voltage, short-circuit current density, and fill factor in polymer solar cells. Adv. Mater. **23**(40), 4636–4643 (2011)
7. R.F. Service, Outlook brightens for plastic solar cells. Science **332**(6027), 293 (2011)
8. E. Bundgaard, F.C. Krebs, Low band gap polymers for organic photovoltaics. Solar Energy Mater. Solar Cells **91**(11), 954–985 (2007)
9. R. Kroon, M. Lenes, J.C. Hummelen et al., Small bandgap polymers for organic solar cells (polymer material development in the last 5 years). Polym. Rev. **48**(3), 531–582 (2008)
10. B.C. Thompson, J.M.J. Frechet, Organic photovoltaics—polymer-fullerene composite solar cells. Angew. Chem. Int. Edit. **47**(1), 58–77 (2008)
11. S. Gunes, H. Neugebauer, N.S. Sariciftci, Conjugated polymer-based organic solar cells. Chem. Rev. **107**(4), 1324–1338 (2007)
12. Y.J. Cheng, S.H. Yang, C.S. Hsu, Synthesis of conjugated polymers for organic solar cell applications. Chem. Rev. **109**(11), 5868–5923 (2009)
13. J.W. Chen, Y. Cao, Development of novel conjugated donor polymers for high-efficiency bulk-heterojunction photovoltaic devices. Acc. Chem. Res. **42**(11), 1709–1718 (2009)
14. Y.F. Li, Y.P. Zou, Conjugated polymer photovoltaic materials with broad absorption band and high charge carrier mobility. Adv. Mater. **20**(15), 2952–2958 (2008)
15. Y.F. Li, Molecular Design of photovoltaic materials for polymer solar cells: toward suitable electronic energy levels and broad absorption. Acc. Chem. Res. **45**(5), 723–733 (2012)
16. H.J. Son, B. Carsten, I.H. Jung et al., Overcoming efficiency challenges in organic solar cells: rational development of conjugated polymers. Energy Environ. Sci. **5**(8), 8158–8170 (2012)
17. C.H. Duan, F. Huang, Y. Cao, Recent development of push-pull conjugated polymers for bulk-heterojunction photovoltaics: rational design and fine tailoring of molecular structures. J. Mater. Chem. **22**(21), 10416–10434 (2012)
18. G. Li, R. Zhu, Y. Yang, Polymer solar cells. Nat. Photonics **6**(3), 153–161 (2012)
19. Z.-G. Zhang, J. Wang, Structures and properties of conjugated donor-acceptor copolymers for solar cell applications. J. Mater. Chem. **22**(10), 4178–4187 (2012)
20. H. Zhou, L. Yang, W. You, Rational design of high performance conjugated polymers for organic solar cells. Macromolecules **45**(2), 607–632 (2012)
21. F. He, L. Yu, How far can polymer solar cells go? In need of a synergistic approach. J. Phys. Chem. Lett. **2**(24), 3102–3113 (2011)
22. L. Huo, J. Hou, Benzo[1,2-b:4,5-b [prime or minute]]dithiophene-based conjugated polymers: band gap and energy level control and their application in polymer solar cells. Polym. Chem.Uk **2**(11), 2453–2461 (2011)
23. R.D. McCullough, The chemistry of conducting polythiophenes. Adv. Mater. **10**(2), 93–116 (1998)
24. H. Sirringhaus, P.J. Brown, R.H. Friend et al., Two-dimensional charge transport in self-organized, high-mobility conjugated polymers. Nature **401**(6754), 685–688 (1999)
25. S.S. Zade, M. Bendikov, Twisting of conjugated oligomers and polymers: case study of oligo- and polythiophene. Chem.-Eur. J. **13**(13), 3688–3700 (2007)
26. K. Yazawa, Y. Inoue, T. Yamamoto et al., Twist glass transition in regioregulated poly(3-alkylthiophene). Phys. Rev. B **74**(9), 094204-1–094204-12 (2006)

27. O. Inganäs, G. Gustafsson, W.R. Salaneck et al., Thermochromism in thin films of poly(3-alkylthiophenes). Synth. Met. **28**(1–2), 377–384 (1989)
28. C. Yang, F.P. Orfino, S. Holdcroft, A phenomenological model for predicting thermochromism of regioregular and nonregioregular poly(3-alkylthiophenes). Macromolecules **29**(20), 6510–6517 (1996)
29. A.J. Moule, K. Meerholz, Controlling morphology in polymer-fullerene mixtures. Adv. Mater. **20**(2), 240–245 (2008)
30. Y.M. Chang, L. Wang, Efficient poly(3-hexylthiophene)-based bulk heterojunction solar cells fabricated by an annealing-free approach. J. Phys. Chem. C **112**(45), 17716–17720 (2008)
31. Y. Zhao, Z.Y. Xie, Y. Qu et al., Solvent-vapor treatment induced performance enhancement of poly(3-hexylthiophene): methanofullerene bulk-heterojunction photovoltaic cells. Appl. Phys. Lett. **90**(4), 043504 (2007)
32. Y. Yao, J.H. Hou, Z. Xu et al., Effect of solvent mixture on the nanoscale phase separation in polymer solar cells. Adv. Funct. Mater. **18**(12), 1783–1789 (2008)
33. W.L. Wang, H.B. Wu, C.Y. Yang et al., High-efficiency polymer photovoltaic devices from regioregular-poly(3-hexylthiophene-2,5-diyl) and [6]-phenyl-C-61-butyric acid methyl ester processed with oleic acid surfactant. Appl. Phys. Lett. **90**(18), 183512 (2007)
34. A.C. Arsenault, T.J. Clark, G. Von Freymann et al., From colour fingerprinting to the control of photoluminescence in elastic photonic crystals. Nat. Mater. **5**(3), 179–184 (2006)
35. G. Li, V. Shrotriya, J.S. Huang et al., High-efficiency solution processable polymer photovoltaic cells by self-organization of polymer blends. Nat. Mater. **4**(11), 864–868 (2005)
36. W.L. Ma, C.Y. Yang, X. Gong et al., Thermally stable, efficient polymer solar cells with nanoscale control of the interpenetrating network morphology. Adv. Funct. Mater. **15**(10), 1617–1622 (2005)
37. L. Li, G. Lu, X. Yang, Improving performance of polymer photovoltaic devices using an annealing-free approach via construction of ordered aggregates in solution. J. Mater. Chem. **18**(17), 1984–1990 (2008)
38. G. Zhao, Y. He, Y. Li, 6.5 % Efficiency of polymer solar cells based on poly(3-hexylthiophene) and indene-C60 bisadduct by device optimization. Adv. Mater. **22**(39), 4355–4358 (2010)
39. J.M. Szarko, J.C. Guo, Y.Y. Liang et al., When function follows form: effects of donor copolymer side chains on film morphology and BHJ solar cell performance. Adv. Mater. **22** (48), 5468–5472 (2010)
40. P.T. Wu, G.Q. Ren, S.A. Jenekhe, Crystalline random conjugated copolymers with multiple side chains: tunable intermolecular interactions and enhanced charge transport and photovoltaic properties. Macromolecules **43**(7), 3306–3313 (2010)
41. B.C. Thompson, B.J. Kim, D.F. Kavulak et al., Influence of alkyl substitution pattern in thiophene copolymers on composite fullerene solar cell performance. Macromolecules **40** (21), 7425–7428 (2007)
42. L.H. Nguyen, H. Hoppe, T. Erb et al., Effects of annealing on the nanomorphology and performance of poly(alkylthiophene): fullerene bulk-heterojunction solar cells. Adv. Funct. Mater. **17**(7), 1071–1078 (2007)
43. B. Burkhart, P.P. Khlyabich, B.C. Thompson, Influence of the ethylhexyl side-chain content on the open-circuit voltage in rr-poly(3-hexylthiophene-co-3-(2-ethylhexyl)thiophene) copolymers. Macromolecules **45**(9), 3740–3748 (2012)
44. H.A.M. van Mullekom, J.A.J.M. Venkemans, E.W. Meijer, Alternating copolymer of pyrrole and 2,1,3-benzothiadiazole. Chem. Commun. **18**, 2163–2164 (1996)
45. J.L. Bredas, A.J. Heeger, F. Wudl, Towards organic polymers with very small intrinsic band gaps. I. Electronic structure of polyisothianaphthene and derivatives. J. Chem. Phys. **85**(8), 4673–4678 (1986)

46. J.S. Panek, M. Yang, Diastereoselective additions of chiral (E)-crotylsilanes to.alpha.-alkoxy and.beta.-alkoxy aldehydes. A one-step, silicon-directed tetrahydrofuran synthesis. J. Am. Chem. Soc. **113**(26), 9868–9870 (1991)
47. J. Roncali, Synthetic principles for bandgap control in linear π-conjugated systems. Chem. Rev. **97**(1), 173–206 (1997)
48. M. Karikomi, C. Kitamura, S. Tanaka et al., New narrow-bandgap polymer composed of benzobis(1,2,5-thiadiazole) and thiophenes. J. Am. Chem. Soc. **117**(25), 6791–6792 (1995)
49. M. Jayakannan, P.A. van Hal, R.A.J. Janssen, Synthesis and structure-property relationship of new donor–acceptor-type conjugated monomers and polymers on the basis of thiophene and benzothiadiazole. J. Polym. Sci. Part A Polym. Chem. **40**(2), 251–261 (2002)
50. Y. Xia, X. Deng, L. Wang et al., An extremely narrow-band-gap conjugated polymer with heterocyclic backbone and its use in optoelectronic devices. Macromol. Rapid Comm. **27** (15), 1260–1264 (2006)
51. I. Osaka, M. Shimawaki, H. Mori et al., Synthesis, characterization, and transistor and solar cell applications of a naphthobisthiadiazole-based semiconducting polymer. J. Am. Chem. Soc. **134**(7), 3498–3507 (2012)
52. F. Liang, J. Lu, J. Ding et al., Design and synthesis of alternating regioregular oligothiophenes/benzothiadiazole copolymers for organic solar cells. Macromolecules **42** (16), 6107–6114 (2009)
53. X. Gong, M. Tong, F.G. Brunetti et al., Bulk heterojunction solar cells with large open-circuit voltage: electron transfer with small donor-acceptor energy offset. Adv. Mater. **23**(20), 2272–2277 (2011)
54. K.H. Ong, S.L. Lim, H.S. Tan et al., A versatile low bandgap polymer for air-stable, high-mobility field-effect transistors and efficient polymer solar cells. Adv. Mater. **23**(11), 1409–1413 (2011)
55. Z. Hao, A. Iqbal, Some aspects of organic pigments. Chem. Soc. Rev. **26**(3), 203–213 (1997)
56. W.K. Chan, Y. Chen, Z. Peng et al., Rational designs of multifunctional polymers. J. Am. Chem. Soc. **115**(25), 11735–11743 (1993)
57. T. Beyerlein, B. Tieke, New photoluminescent conjugated polymers with 1,4-dioxo-3,6-diphenylpyrrolo[3,4-c]pyrrole (DPP) and 1,4-phenylene units in the main chain. Macromol. Rapid Comm. **21**(4), 182–189 (2000)
58. D. Cao, Q. Liu, W. Zeng et al., Synthesis and characterization of novel red-emitting alternating copolymers based on fluorene and diketopyrrolopyrrole derivatives. J. Polym. Sci. Part A Polym. Chem. **44**(8), 2395–2405 (2006)
59. A.R. Rabindranath, Y. Zhu, I. Heim et al., Red Emitting N-Functionalized Poly(1,4-diketo-3,6-diphenylpyrrolo[3,4-c]pyrrole) (Poly-DPP): a deeply colored polymer with unusually large stokes shift. Macromolecules **39**(24), 8250–8256 (2006)
60. A.P. Zoombelt, S.G.J. Mathijssen, M.G.R. Turbiez et al., Small band gap polymers based on diketopyrrolopyrrole. J. Mater. Chem. **20**(11), 2240–2246 (2010)
61. M.M. Wienk, M. Turbiez, J. Gilot et al., Narrow-bandgap diketo-pyrrolo-pyrrole polymer solar cells: the effect of processing on the performance. Adv. Mater. **20**(13), 2556–2560 (2008)
62. J.C. Bijleveld, A.P. Zoombelt, S.G.J. Mathijssen et al., Poly(diketopyrrolopyrrole–terthiophene) for ambipolar logic and photovoltaics. J. Am. Chem. Soc. **131**(46), 16616–16617 (2009)
63. J.C. Bijleveld, R.A.M. Verstrijden, M.M. Wienk et al., Copolymers of diketopyrrolopyrrole and thienothiophene for photovoltaic cells. J. Mater. Chem. **21**(25), 9224–9231 (2011)
64. J.C. Bijleveld, V.S. Gevaerts, D. Di Nuzzo et al., Efficient solar cells based on an easily accessible diketopyrrolopyrrole polymer. Adv. Mater. **22**(35), E242–E246 (2010)

65. P. Sonar, S.P. Singh, Y. Li et al., High mobility organic thin film transistor and efficient photovoltaic devices using versatile donor-acceptor polymer semiconductor by molecular design. Energy Environ. Sci. **4**(6), 2288–2296 (2011)
66. H. Bronstein, Z.Y. Chen, R.S. Ashraf et al., Thieno[3,2-b]thiophene-diketopyrrolopyrrole-containing polymers for high-performance organic field-effect transistors and organic photovoltaic devices. J. Am. Chem. Soc. **133**(10), 3272–3275 (2011)
67. C.H. Woo, P.M. Beaujuge, T.W. Holcombe et al., Incorporation of furan into low band-gap polymers for efficient solar cells. J. Am. Chem. Soc. **132**(44), 15547–15549 (2010)
68. A.T. Yiu, P.M. Beaujuge, O.P. Lee et al., Side-chain tunability of furan-containing low-band-gap polymers provides control of structural order in efficient solar cells. J. Am. Chem. Soc. **134**(4), 2180–2185 (2012)
69. I. McCulloch, M. Heeney, C. Bailey et al., Liquid-crystalline semiconducting polymers with high charge-carrier mobility. Nat. Mater. **5**(4), 328–333 (2006)
70. I. McCulloch, M. Heeney, M.L. Chabinyc et al., Semiconducting thienothiophene copolymers: design, synthesis, morphology, and performance in thin-film organic transistors. Adv. Mater. **21**(10–11), 1091–1109 (2009)
71. C. Piliego, T.W. Holcombe, J.D. Douglas et al., Synthetic control of structural order in N-Alkylthieno[3,4-c]pyrrole-4,6-dione-based polymers for efficient solar cells. J. Am. Chem. Soc. **132**(22), 7595–7597 (2010)
72. M.-H. Chen, J. Hou, Z. Hong et al., Efficient polymer solar cells with thin active layers based on alternating polyfluorene copolymer/fullerene bulk heterojunctions. Adv. Mater. **21**(42), 4238–4242 (2009)
73. J. Mei, K.R. Graham, R. Stalder et al., Synthesis of isoindigo-based oligothiophenes for molecular bulk heterojunction solar cells. Org. Lett. **12**(4), 660–663 (2010)
74. G. Zhang, Y. Fu, Z. Xie et al., Synthesis and photovoltaic properties of new low bandgap isoindigo-based conjugated polymers. Macromolecules **44**(6), 1414–1420 (2011)
75. E. Wang, Z. Ma, Z. Zhang et al., An isoindigo-based low band gap polymer for efficient polymer solar cells with high photo-voltage. Chem. Commun. **47**(17), 4908–4910 (2011)
76. E. Wang, Z. Ma, Z. Zhang et al., An easily accessible isoindigo-based polymer for high-performance polymer solar cells. J. Am. Chem. Soc. **133**(36), 14244–14247 (2011)
77. T. Yamamoto, Z.-H. Zhou, T. Kanbara et al., π-conjugated donor—acceptor copolymers constituted of π-excessive and π-deficient arylene units. Optical and electrochemical properties in relation to CT structure of the polymer. J. Am. Chem. Soc. **118**(43), 10389–10399 (1996)
78. T. Yamamoto, B.-L. Lee, H. Kokubo et al., Synthesis of a new thiophene/quinoxaline CT-type copolymer with high solubility and its basic optical properties. Macromol. Rapid Commun. **24**(7), 440–443 (2003)
79. E. Wang, L. Hou, Z. Wang et al., An easily synthesized blue polymer for high-performance polymer solar cells. Adv. Mater. **22**(46), 5240–5244 (2010)
80. Y. Huang, M. Zhang, L. Ye et al., Molecular energy level modulation by changing the position of electron-donating side groups. J. Mater. Chem. **22**(12), 5700–5705 (2012)
81. M.-C. Yuan, M.-Y. Chiu, S.-P. Liu et al., A thieno[3,4-c]pyrrole-4,6-dione-based donor—acceptor polymer exhibiting high crystallinity for photovoltaic applications. Macromolecules **43**(17), 6936–6938 (2010)
82. M.-S. Su, C.-Y. Kuo, M.-C. Yuan et al., Improving device efficiency of polymer/fullerene bulk heterojunction solar cells through enhanced crystallinity and reduced grain boundaries induced by solvent additives. Adv. Mater. **23**(29), 3315–3319 (2011)
83. G.-Y. Chen, Y.-H. Cheng, Y.-J. Chou et al., Crystalline conjugated polymer containing fused 2,5-di(thiophen-2-yl)thieno[2,3-b]thiophene and thieno[3,4-c]pyrrole-4,6-dione units for bulk heterojunction solar cells. Chem. Commun. **47**(17), 5064–5066 (2011)

84. H.L. Pan, Y.N. Li, Y.L. Wu et al., Low-temperature, solution-processed, high-mobility polymer semiconductors for thin-film transistors. J. Am. Chem. Soc. **129**(14), 4112–4113 (2007)
85. J. Hou, M.-H. Park, S. Zhang et al., Bandgap and molecular energy level control of conjugated polymer photovoltaic materials based on benzo[1,2-b:4,5-b′]dithiophene. Macromolecules **41**(16), 6012–6018 (2008)
86. H.Y. Chen, J.H. Hou, S.Q. Zhang et al., Polymer solar cells with enhanced open-circuit voltage and efficiency. Nat. Photonics **3**(11), 649–653 (2009)
87. H.J. Son, W. Wang, T. Xu et al., Synthesis of fluorinated polythienothiophene-co-benzodithiophenes and effect of fluorination on the photovoltaic properties. J. Am. Chem. Soc. **133**(6), 1885–1894 (2011)
88. Y. Huang, L. Huo, S. Zhang et al., Sulfonyl: a new application of electron-withdrawing substituent in highly efficient photovoltaic polymer. Chem. Commun. **47**(31), 8904–8906 (2011)
89. Y.P. Zou, A. Najari, P. Berrouard et al., A thieno[3,4-c]pyrrole-4,6-dione-based copolymer for efficient solar cells. J. Am. Chem. Soc. **132**(15), 5330–5331 (2010)
90. Y. Zhang, S.K. Hau, H.L. Yip et al., Efficient polymer solar cells based on the copolymers of benzodithiophene and thienopyrroledione. Chem. Mater. **22**(9), 2696–2698 (2010)
91. C. Piliego, T.W. Holcombe, J.D. Douglas et al., Synthetic control of structural order in N-alkylthieno[3,4-c]pyrrole-4,6-dione-based polymers for efficient solar cells. J. Am. Chem. Soc. **132**(22), 7595–7597 (2010)
92. H.X. Zhou, L.Q. Yang, S.C. Price et al., Enhanced photovoltaic performance of low-bandgap polymers with deep LUMO levels. Angew. Chem. Int. Edit. **49**(43), 7992–7995 (2010)
93. H.X. Zhou, L.Q. Yang, A.C. Stuart et al., Development of fluorinated benzothiadiazole as a structural unit for a polymer solar cell of 7 % efficiency. Angew. Chem. Int. Edit. **50**(13), 2995–2998 (2011)
94. S.C. Price, A.C. Stuart, L. Yang et al., Fluorine substituted conjugated polymer of medium band gap yields 7 % efficiency in polymer—fullerene solar cells. J. Am. Chem. Soc. **133**(12), 4625–4631 (2011)
95. S. Subramaniyan, H. Xin, F.S. Kim et al., New thiazolothiazole copolymer semiconductors for highly efficient solar cells. Macromolecules **44**(16), 6245–6248 (2011)
96. M.J. Zhang, X. Guo, Y.F. Li, Photovoltaic performance improvement of D–A copolymers containing bithiazole acceptor unit by using bithiophene bridges. Macromolecules **44**(22), 8798–8804 (2011)
97. L.J. Huo, S.Q. Zhang, X. Guo et al., Replacing alkoxy groups with alkylthienyl groups: a feasible approach to improve the properties of photovoltaic polymers. Angew. Chem. Int. Edit. **50**(41), 9697–9702 (2011)
98. L.J. Huo, J.H. Hou, S.Q. Zhang et al., A polybenzo[1,2-b:4,5-b′]dithiophene derivative with deep HOMO level and its application in high-performance polymer solar cells. Angew. Chem. Int. Edit. **49**(8), 1500–1503 (2010)
99. M. Wang, X.W. Hu, P. Liu et al., Donor acceptor conjugated polymer based on naphtho[1,2-c:5,6-c]bis[1, 2, 5]thiadiazole for high-performance polymer solar cells. J. Am. Chem. Soc. **133**(25), 9638–9641 (2011)
100. Q. Peng, X.J. Liu, D. Su et al., Novel benzo[1,2-b:4,5-b′]dithiophene-benzothiadiazole derivatives with variable side chains for high-performance solar cells. Adv. Mater. **23**(39), 4554–4558 (2011)
101. L.J. Huo, X. Guo, S.Q. Zhang et al., PBDTTTZ: a broad band gap conjugated polymer with high photovoltaic performance in polymer solar cells. Macromolecules **44**(11), 4035–4037 (2011)

102. K.-T. Wong, T.-C. Chao, L.-C. Chi et al., Syntheses and structures of novel heteroarene-fused coplanar π-conjugated chromophores. Org. Lett. **8**(22), 5033–5036 (2006)
103. Y.C. Chen, C.Y. Yu, Y.L. Fan et al., Low-bandgap conjugated polymer for high efficient photovoltaic applications. Chem. Commun. **46**(35), 6503–6505 (2010)
104. Y. Zhang, J.Y. Zou, H.L. Yip et al., Indacenodithiophene and quinoxaline-based conjugated polymers for highly efficient polymer solar cells. Chem. Mater. **23**(9), 2289–2291 (2011)
105. K.M. O'Malley, C.Z. Li, H.L. Yip et al., Enhanced open-circuit voltage in high performance polymer/fullerene bulk-heterojunction solar cells by cathode modification with a C60 surfactant. Adv. Energy Mater. **2**(1), 82–86 (2012)
106. Y. Zhang, J.Y. Zou, H.L. Yip et al., Synthesis, characterization, charge transport, and photovoltaic properties of dithienobenzoquinoxaline- and dithienobenzopyridopyrazine-based conjugated polymers. Macromolecules **44**(12), 4752–4758 (2011)
107. Y. Zhang, S.C. Chien, K.S. Chen et al., Increased open circuit voltage in fluorinated benzothiadiazole-based alternating conjugated polymers. Chem. Commun. **47**(39), 11026–11028 (2011)
108. M.J. Zhang, X. Guo, X.C. Wang et al., Synthesis and photovoltaic properties of D–A copolymers based on alkyl-substituted indacenodithiophene donor unit. Chem. Mater. **23**(18), 4264–4270 (2011)
109. J.Y. Wang, S.K. Hau, H.L. Yip et al., Benzobis(silolothiophene)-based low bandgap polymers for efficient polymer solar cells. Chem. Mater. **23**(3), 765–767 (2011)
110. R.S. Ashraf, Z.Y. Chen, D.S. Leem et al., Silaindacenodithiophene semiconducting polymers for efficient solar cells and high-mobility ambipolar transistors. Chem. Mater. **23**(3), 768–770 (2011)
111. B.C. Schroeder, Z.G. Huang, R.S. Ashraf et al., Silaindacenodithiophene-based low band gap polymers—the effect of fluorine substitution on device performances and film morphologies. Adv. Funct. Mater. **22**(8), 1663–1670 (2012)
112. K. Tamao, M. Uchida, T. Izumizawa et al., Silole derivatives as efficient electron transporting materials. J. Am. Chem. Soc. **118**(47), 11974–11975 (1996)
113. Z.P. Fei, R.S. Ashraf, Z.G. Huang et al., Germaindacenodithiophene based low band gap polymers for organic solar cells. Chem. Commun. **48**(24), 2955–2957 (2012)
114. F. He, W. Wang, W. Chen et al., Tetrathienoanthracene-based copolymers for efficient solar cells. J. Am. Chem. Soc. **133**(10), 3284–3287 (2011)
115. C.H. Chen, Y.J. Cheng, M. Dubosc et al., Alternating and diblock donor-acceptor conjugated polymers based on diindeno[1,2-b:2′,1′-d]thiophene Structure: synthesis, characterization, and photovoltaic applications. Chem-Asian J **5**(12), 2483–2492 (2010)
116. Y.J. Cheng, C.H. Chen, Y.S. Lin et al., Ladder-type nonacyclic structure consisting of alternate thiophene and benzene units for efficient conventional and inverted organic photovoltaics. Chem. Mater. **23**(22), 5068–5075 (2011)
117. G. Subramanian, P.V. Schleyer, H. Jiao, Are the most stable fused heterobicycles the most aromatic? Angew. Chem. Int. Ed. Engl. **35**(22), 2638–2641 (1996)
118. Y.J. Cheng, S.W. Cheng, C.Y. Chang et al., Diindenothieno[2,3-b]thiophene arene for efficient organic photovoltaics with an extra high open-circuit voltage of 1.14 ev. Chem. Commun. **48**(26), 3203–3205 (2012)
119. M. Svensson, F. Zhang, S.C. Veenstra et al., High-performance polymer solar cells of an alternating polyfluorene copolymer and a fullerene derivative. Adv. Mater. **15**(12), 988–991 (2003)
120. N. Blouin, A. Michaud, D. Gendron et al., Toward a rational design of poly(2,7-Carbazole) derivatives for solar cells. J. Am. Chem. Soc. **130**(2), 732–742 (2007)
121. J.S. Wu, Y.J. Cheng, M. Dubosc et al., Donor-acceptor polymers based on multi-fused heptacyclic structures: synthesis, characterization and photovoltaic applications. Chem. Commun. **46**(19), 3259–3261 (2010)

122. Y.J. Cheng, J.S. Wu, P.I. Shih et al., Carbazole-based ladder-type heptacylic arene with aliphatic side chains leading to enhanced efficiency of organic photovoltaics. Chem. Mater. **23**(9), 2361–2369 (2011)
123. C.Y. Chang, Y.J. Cheng, S.H. Hung et al., Combination of molecular, morphological, and interfacial engineering to achieve highly efficient and stable plastic solar cells. Adv. Mater. **24**(4), 549–553 (2012)
124. Y.-J. Cheng, C.-H. Hsieh, Y. He et al., Combination of indene-C60 bis-adduct and cross-linked fullerene interlayer leading to highly efficient inverted polymer solar cells. J. Am. Chem. Soc. **132**(49), 17381–17383 (2010)
125. J.S. Wu, Y.J. Cheng, T.Y. Lin et al., Dithienocarbazole-based ladder-type heptacyclic arenes with silicon, carbon, and nitrogen bridges: synthesis, molecular properties, field-effect transistors, and photovoltaic applications. Adv. Funct. Mater. **22**(8), 1711–1722 (2012)

Chapter 6
Development of Active Materials and Interface Materials for High Performance Bulk-Heterojunction Polymer Solar Cells

Chunhui Duan, Chengmei Zhong, Fei Huang and Yong Cao

Abstract Bulk-heterojunction polymer solar cell (BHJ-PSC) is one of the most promising emerging solar cell technologies, due to its compatibility with low-cost, large scale fabrication by solution processing etc. In this book chapter, we review our efforts on two of the most important research areas in the field—(1). The development of conjugated polymer-based photo-active materials for BHJ polymer solar cell, focusing on linear Donor-Acceptor type conjugated polymers and acceptor pended conjugated polymers; and (2). Water/alcohol soluble conjugated polymer interfacial materials.

6.1 Introduction

Photovoltaic technologies, which are well known as straightforward means of converting solar irradiation into electricity, have been considered as practical and effective approaches to solve global energy crises and environmental pollution issues in the future. Among all kinds of photovoltaic technologies, bulk-heterojunction polymer solar cell (BHJ-PSC) is one of the most promising ones, due to its compatibility with low-cost, large scale fabrication by solution processing [1–6]. In recent years, appreciable achievements have been realized in the field of BHJ-PSCs due to the synergistic progresses of novel photovoltaic materials and device technologies [7–16]. Encouragingly, power conversion efficiencies (PCEs) over 8 % have already been reported by several independent scientific groups [17–20]. Moreover, some companies have even achieved higher PCE of above 9 % [21–24].

C. Duan · C. Zhong · F. Huang · Y. Cao (✉)
Institute of Polymer Optoelectronic Materials and Devices, State Key Laboratory of Luminescent Materials and Devices, South China University of Technology, Guangzhou 510640, People's Republic of China
e-mail: yongcao@scut.edu.cn

Y. Yang and G. Li (eds.), *Progress in High-Efficient Solution Process Organic Photovoltaic Devices*, Topics in Applied Physics 130,
DOI 10.1007/978-3-662-45509-8_6

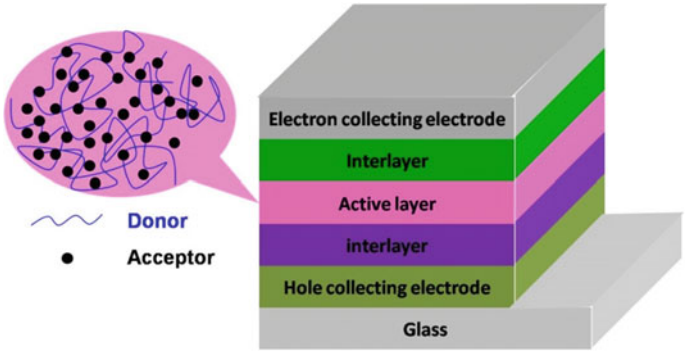

Scheme 6.1 Sandwich architecture of BHJ-PSC devices

Typically, BHJ-PSCs adopt the so-called sandwich structure, where the blend of conjugated polymer electron donor material and fullerene derivative electron acceptor material was sandwiched between hole collecting electrode and electron collecting electrode (see Scheme 6.1) [25]. Undoubtedly, donor material is the most important component to achieve highly efficient BHJ-PSC, specifically considering the limited choice of electron acceptors [10, 26]. Moreover, it is clear that the electrical properties of the interfaces between organic active layer and the electrodes are also not to be neglected in order to achieve high PCEs in BHJ-PSCs [16, 27–30]. As a consequence, extensive efforts concerning the developments of photo-active donor polymers and interfacial modification between active layer and electrode have been put by scientists all around the community to push forward the practical application of BHJ-PSCs [2]. In this chapter, we review our efforts on the development of conjugated polymer-based photo-active materials and interfacial materials, as well as their applications in BHJ-PSCs.

6.2 Donor Polymers for BHJ-PSCs

Generally, an ideal donor polymer should have the following properties simultaneously, (1) broad absorption spectra coupled with high extinction coefficient to harvest as many incident photons as possible, (2) optimal energy levels to match acceptor materials that can provide sufficient driving force for efficient charge dissociation while preserving a high open-circuit voltage (V_{oc}), (3) high hole mobility to guarantee efficient charge transporting, and (4) appropriate solubility and miscibility with acceptors to form desired bi-continuous penetrating network in active layers [3, 26]. In the early stage of BHJ-PSCs development, homopolymers such as poly[2-methoxyl-5-((2′-ethylhexyl)oxy)-1,4-phenylenevinylene] (MEH-PPV) [25], poly[2-methoxyl-5-((3′,7′-dimethyloctyl)oxyl)-1,4-phenylenevinylene] (MDMO- PPV) [31], and poly(3-hexylthiophene) (P3HT) [13] were usually used as

donor materials. Nevertheless, the poor light-harvesting ability of these homopolymers limited their practical applications [3, 26]. Soon later, Donor-Acceptor (D-A) conjugated polymers or the so-called push-pull conjugated polymers became the main stream of donor materials in BHJ-PSCs, because their absorption spectra and energy levels could be easily manipulated by controlling the intramolecular charge transfer (ICT) interaction between donor units and acceptor units on the conjugated main chains [8, 10]. Towards highly efficient BHJ-PSCs, a large amount of donor materials, including linear D-A type narrow-band-gap (NBG) copolymers, and acceptor pended NBG copolymers have been developed in our group [8, 10]. Significant advances in PCEs have thus been achieved owing to the successful development of these donor polymers [32–35].

6.2.1 Linear D-A Type Conjugated Polymers

Regarding to linear D-A type NBG conjugated polymers, various aromatic heterocycles are their fundamental constructing subunits, which determine the intrinsic optical and electronic properties, as well as charge transporting abilities of the resulting polymers. Benzothiadiazole (BT) is a star acceptor unit for push-pull NBG conjugated polymers in BHJ-PSCs applications, because of its suitable electron affinity. Relative to other acceptor units, one of the advantages of BT is that its resulting copolymers usually possess deep-positioning highest occupied molecular orbital (HOMO) energy levels, providing good chemical stability for the polymers and high open-circuit voltage (V_{oc}) for the resulting solar cell devices [26, 36, 37]. As early as 2002, Hou et al. [38] had synthesized a series of narrow-band-gap random conjugated copolymers from 9,9-dioctylfluorene (DOF) and 4,7-di-2-thienyl-2,1,3-benzothiadiazole (DBT) by Suzuki coupling, in which the content of DBT varied from 5 to 35 %. Compared with the alternating copolymer of DOF and DBT developed in Andersson's group [39], the random copolymers prepared by Hou et al. had much higher number-average molecular weights (M_n) (>10 kg mol^{-1} vs. 4.8 kg mol^{-1}) and better solubility. P1a with a DBT content of 35 % exhibited efficient absorption in the range from 300 to 650 nm and deep-positioning HOMO energy level of −5.47 eV. BHJ-PSCs fabricated with P1a:$PC_{61}BM$ (methano-fullerene [6] -phenyl-C_{61}-butyric acid methyl ester) blends with a device configuration of ITO/PEDOT:PSS/P1a:$PC_{61}BM$ (1:2)/Ba/Al exhibited a PCE up to 2.24 %, along with a short-circuit current density (J_{sc}) of 5.18 mA cm^{-2}, and an appreciable high V_{oc} of 0.95 V [40]. Besides thiophene, pyrrole and furan were also utilized as flanked π-bridge for BT to construct NBG conjugated copolymers [41, 42]. Compared with thiophene bridged analogues, polymers bridged by pyrrole and furan usually exhibited similar absorption features, but higher-positioning HOMO energy levels, thus leading to lower V_{oc} in the resulting BHJ-PSCs. For examples, BHJ-PSCs fabricated from P1b:PCBM (1:4) exhibited a V_{oc} of 0.6 V, and a low PCE of 0.15 % [41], while solar cell of P1c:PCBM (1:2) showed a V_{oc} of 0.85 V, a J_{sc} of 3.39 mA cm^{-2}, a FF of 0.39 and a PCE of 1.13 % [42]. Notably, P1a

possessed a relative large optical band gap (E_g) of 2.01 eV, which is one of the main limitations for its PCE. Extending the absorption spectra of the resulting polymers is therefore critical to further exploit the potential of copolymer from fluorene and BT. Wang et al. [43] had successfully developed a series of D-A type copolymers (P2a, P2b and P2c) based on fluorene and BT with much red-shifted absorption spectra by increasing the number of bridging thiophene rings between donor units and acceptor units. Compared with their two thiophene rings-containing analogue, P2a–c exhibited significantly red-shifted absorption spectra at both short wavelength region and long wavelength region, which may be caused by the increase of conjugation length of the NBG units in the resulting polymers [43]. Besides, there is little influence on the HOMO levels of the resulting polymers by increasing the number of thiophene rings in their repeating units, which are beneficial for keeping a high V_{oc} in the resulted BHJ-PSCs. P2a exhibited the best photovoltaic performance with a PCE of 2.63 %, a V_{oc} of 0.86 V, a J_{sc} of 5.86 mA cm^{-2}, and a FF of 0.52, which is better than that of PFO-DBT [43]. Moreover, Wang's work showed that the polymers with alkyl side chains on the 3- (see P2a) or 3′-position (see P2c) of the thiophene rings exhibited better performance than those polymers with alkyl side chains on 4′-position (see P2b) of the thiophene rings, due to the 4′-position alkyl on the thiophene rings induced a large steric hindrance effect [43]. These results indicated that the incorporation of alkyl side chains on the six-membered rings or the five-membered rings with neighboring six-membered rings of conjugated polymers would generate large steric hindrance and result in poor solar cell performance [43]. Similar notion was also observed by Zhou et al. soon after [44]. An another effective approach to extend the absorption spectra of BT-based D-A type conjugated copolymers is replacing fluorene unit with stronger donor units, such as thiophene [45], cyclopenta[2,1-*b*:3,4-*b*′]dithiophene (CPDT) [46], dithieno [2,1-*b*:2′,3′-*d*]-silole (DTS) [47], and benzo[1,2-*b*:4,5-*b*]-dithiophene (BDT) [37], etc. Xia et al. [45] developed a NBG conjugated copolymer P3, which possessed extremely narrow E_g of 1.38 eV, from thiophene and alkyl-substituted DBT by a Pd-catalyzed Stille coupling reaction. The polymer P3 had good solution processability in common organic solvents and showed a wide absorption range from 330 to 895 nm in its solid state. Nevertheless, cyclic voltammetry (CV) experiments indicated that P3 exhibited a relative high-positioning HOMO energy level of −4.88 eV. The BHJ-PSC with device architecture of ITO/PEDOT:PSS/P3:$PC_{61}BM$ (1:3)/Ba/Al delivered a low PCE of 0.13 %, which was mainly caused by the extremely small J_{sc} of 0.6 mA cm^{-2} [45]. The chemical structures of conjugated polymers P1-P3 were presented in Scheme 6.2, and the HOMO energy levels, band gaps and photovoltaic performances of P1-P3 were summarized in Table 6.1.

Besides changing flanked thiophene π-bridge with other five-member heterocycles or increasing the numbers of flanked thiophene rings, the replacement of the 2-position sulfur atom of BT with other heteroatoms, such as selenium atom and nitrogen atom is another effective method to develop efficient donor polymers for BHJ-PSCs applications [48–51]. Replacing the 2-position sulfur atom of BT with selenium atom would lead to a new acceptor unit of 2,1,3-benzoselenadiazole. Considering the larger atom radius and smaller electronegativity of selenium

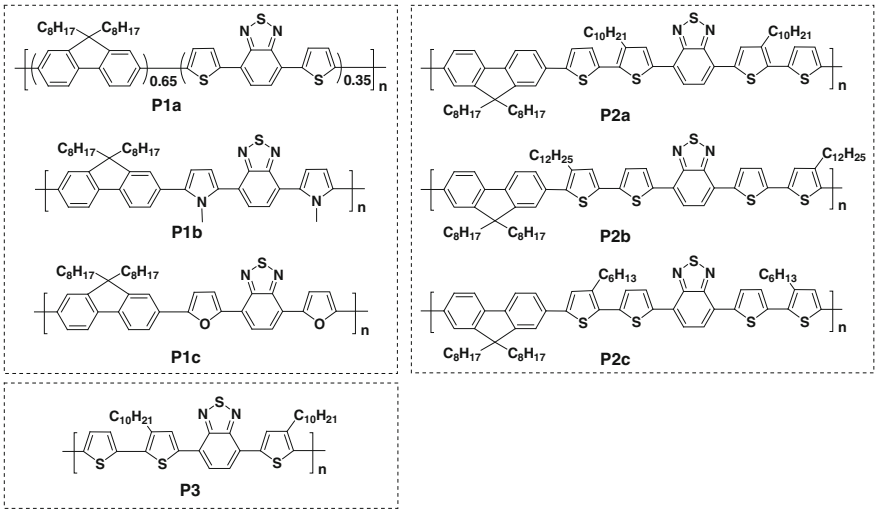

Scheme 6.2 Chemical structures of donor polymers P1-P3

Table 6.1 HOMO energy levels, optical band gaps and device performances of P1-P3

Polymers	HOMO (eV)	E_g (eV)	V_{oc} (V)	J_{sc} (mA cm^{-2})	FF	PCE (%)	References
P1a	−5.47	2.01	0.95	5.18	0.35	2.24	[38, 40]
P1b	−5.53	1.98	0.60	0.73	0.345	0.15	[41]
P1c	–	–	0.85	3.39	0.391	1.13	[42]
P2a	−5.40	1.79	0.90	3.97	0.41	1.82	[43]
P2b	−5.37	1.81	0.70	2.80	0.38	0.74	[43]
P2c	−5.34	1.77	0.86	5.86	0.52	2.63	[43]
P3	−4.88	1.38	0.60	0.65	0.33	0.13	[45]

compared with sulfur atom, replacing sulfur atom with selenium would certainly lead to significant changes on the optical and electronic properties of the resulting polymers. Yang et al. [48] have shown that benzoselenadiazole-derived conjugated copolymers exhibited red-shifted absorption spectra with respective to their BT-based analogues. For example, E_g as small as 1.77 eV can be achieved for the random copolymer from DOF and diselenophenyl benzoselenadiazole [48], However, the resulting polymer delivered a limited PCE of 0.1 %, which was possibly caused by the low content of selenadiazole-based NBG units and thereby weak absorbance of the polymers in the long wavelength region [48]. By increasing the content of NBG units of dithienylbenzoselenadiazole to 35 %, the resulting polymer P4a exhibited an enhanced PCE of 0.91 %, with an appreciable high V_{oc} of 0.85 V [49]. To further increase the absorption intensity of benzoselenadiazole-based conjugated polymers in long wavelength region, Zhao et al. [50] developed an

alternating copolymer (P4b) from branched alkyl-substituted carbazole and thiophene-flanked benzoselenadiazole by Pd-catalyzed Suzuki coupling reaction. P4b had a relative high M_n of 14 kg mol^{-1} and a narrow polydispersity index (PDI) of 1.21, as well as good solubility in common organic solvents, such as chloroform, tetrahydrofuran (THF) and chlorobenzene [50]. The E_g of P4b is 1.73 eV, which is much smaller than that of its BT-based analogue [52]. The HOMO energy level of P4b was measured to be −5.28 eV, which is much higher than that of its BT-based analogue. BHJ-PSC based on P4b:$PC_{71}BM$ (methano-fullerene [6,6] -phenyl-C_{71}-butyric acid methyl ester) exhibited a moderate PCE value of 2.58 %, along with a moderate V_{oc} of 0.75 V, a J_{sc} of 7.23 mA cm^{-2} and a FF of 0.45 [50]. If the sulfur atom on the BT unit is replaced by a nitrogen atom, a new acceptor unit benzotriazole (TAZ) emerged. With respect to BT, the electron withdrawing ability of TAZ is somewhat weaker due to that the lone pair electron on the nitrogen atom is more basic than the lone pair electron on the sulfur atom and is hence more easily donated into the TAZ ring. As a result, the absorbance of TAZ-based polymers would be blue-shifted compared with those of their BT-derived analogues. On the other hand, the nitrogen atom in TAZ ring affords a position for introducing an additional solubilizing alkyl chain on each repeating units, which is beneficial for improving the solubility and processability of the resulting polymers [51, 53–55]. Zhang et al. [51] have developed a series of TAZ-based D-A type alternating copolymers (P5a, P5b and P5c) for usage as donor materials in BHJ-PSCs. All polymers (P5a, P5b and P5c) have good solubility in common organic solvents, but relative large band gaps (2.24 eV for P5a, 2.18 eV for P5b, and 1.87 eV for P5c, respectively). The HOMO energy levels of P5a, P5b and P5c were determined to be −5.67, −5.54 and −5.20 eV. When utilized as donors in BHJ-PSCs, the PCEs of P5a–c were approximate 1 %, After inserting an alcohol soluble conjugated polymer as electron collecting layer, the V_{oc} of the resulting BHJ-PSCs were drastically enhanced, thus leading to improved performance [51]. One of the successful breakthrough concerning the development of BT- or BT analogues-based photovoltaic materials is the use of naphtho[1,2-*c*:5,6-*c*]bis[1,2,5]-thiadiazole (NT) [34]. With respect to BT, NT possesses an enlarged planar aromatic structure containing two fused BT ring, which is beneficial for the interchain packing of the resulting polymer and thereby facilitates the charge carrier transporting. Besides, the electron-withdrawing ability of NT is somewhat stronger than that of BT, which will reduce the E_g of the resulting polymers, leading to more efficient light harvesting while ensuring enough driving force for exciton dissociation. Wang et al. [34] firstly developed a highly efficient NBG photovoltaic material by using NT as the acceptor unit. The polymer P6b exhibited good solubility in common organic solvents even though it has a high M_n of 40.5 kg mol^{-1} with a PDI of 3.2. Compared with the BT-based polymer P6a, the NT-based polymer P6b demonstrated red-shifted absorbance, enhanced hole mobility and slightly elevated HOMO energy level. The BHJ-PSC device with the configuration of ITO/PEDOT:PSS/P6b:$PC_{71}BM$/Ca/Al delivered an impressive PCE of 6.0 %, coupled with a V_{oc} of 0.80 V, a J_{sc} of 11.71 mA cm^{-2}, and a FF of 0.61. P6b exhibited a substantial better performance than that of the BT-based polymer P6a, which exhibited a PCE

of 2.11 % (a V_{oc} of 1.00 V, a J_{sc} of 5.80 V, and a FF of 0.35) under the same conditions [34].

Besides BT and BT analogues, other aromatic heterocycles such as thienopyrazine and thienothiadiazole are as well promising acceptor for constructing NBG conjugated polymers in BHJ-PSCs applications [56, 57]. For example, Xia et al. [56] reported a random copolymer (P7) from DOF and dithienylthienopyrazine for BHJ-PSCs applications. The E_g and HOMO energy level of P7 were estimated to be 1.77 and −5.22 eV, respectively. BHJ-PSC device based on a blend of P7:$PC_{61}BM$ (1:1) displayed a PCE of 0.83 %, with a J_{sc} of 4.1 mA cm^{-2}, a V_{oc} of 0.70 V and a FF of 0.29 [56]. To further extend the spectral response of solar cell devices, Xia et al. [57] synthesized a new alternating NBG conjugated copolymer (P8) by Pd-catalyzed Stille coupling reaction. P8 exhibited excellent solution processibility and an extremely small E_g of 1.01 eV, but a relative high-positioning HOMO energy level of −4.71 eV. P8 was successfully used as active material in high detectivity near-infrared photodetector [58]. To take the advantages of BT and TAZ units, Dong et al. [59] prepared a new building block [1,2,5]thiadiazole[3,4-*f*]benzotriazole (TZBTTT), which had very strong electron-withdrawing ability and integrated both the merits of BT and TAZ, as the acceptor unit to construct D-A type NBG polymers for BHJ-PSCs applications. Two new alternating D-A type conjugated copolymers (P9a and P9b) using TZBTTT as the acceptor unit and DOF or *N*-9′-heptadecanyl-carbazole as donor units, respectively, were prepared by Pd-catalyzed Suzuki coupling reaction. Benefiting from the linked branched alkyl side chains on triazole rings, P9a and P9b with moderate M_n of 10.3 and 12.8 kg mol^{-1}, respectively, have excellent solubility in common organic solvents such as chlorobenzene and *o*-dichlorobenzene. Moreover, P9a and P9b possessed ideal band gaps of 1.33 and 1.35 eV, respectively, and exhibited intense absorption in near infrared region. The HOMO energy levels of P9a and P9b were evaluated to be −5.16 and −5.18 eV, respectively. The LUMO energy levels of both polymers were −3.83 eV, which was very close to that of an ideal donor polymer [3]. When utilized as donor phase in BHJ-PSCs, P9a and P9b exhibited attractive photovoltaic performances after inserting an alcohol soluble conjugated polymer as cathode interlayer. The best device of P9b:$PC_{71}BM$ (1:4) demonstrated a PCE of 3.17 %, a V_{oc} of 0.70 V, a J_{sc} of 8.5 mA cm^{-2} and an FF of 0.41 [59]. The chemical structures of P4-P9 were demonstrated in Scheme 6.3, and the HOMO energy levels, band gaps and photovoltaic performances of P4-P9 were summarized in Table 6.2.

Quinoxaline is also a promising acceptor unit for constructing D-A type conjugated copolymer as donor polymers in BHJ-PSCs. Compared with BT, the electron withdrawing ability of quinoxaline is somewhat weaker, resulting in slight larger band gaps for the resulting polymers. Nevertheless, one of the advantages of quinoxaline is that it can preserve relative deep-positioning HOMO energy levels for the resulting polymers, which is favorable for both the polymers' chemical stability and obtaining a high V_{oc} in the resulted BHJ-PSC devices. He and coworkers [33] reported a new D-A type conjugated copolymer (P10) based on quinoxaline and 4,5-ethylene-2,7-carbazole (ECz). Notably, ECz in P10 is a novel member of the carbazole family, where the 4,5-ethylene linkage enlarged the

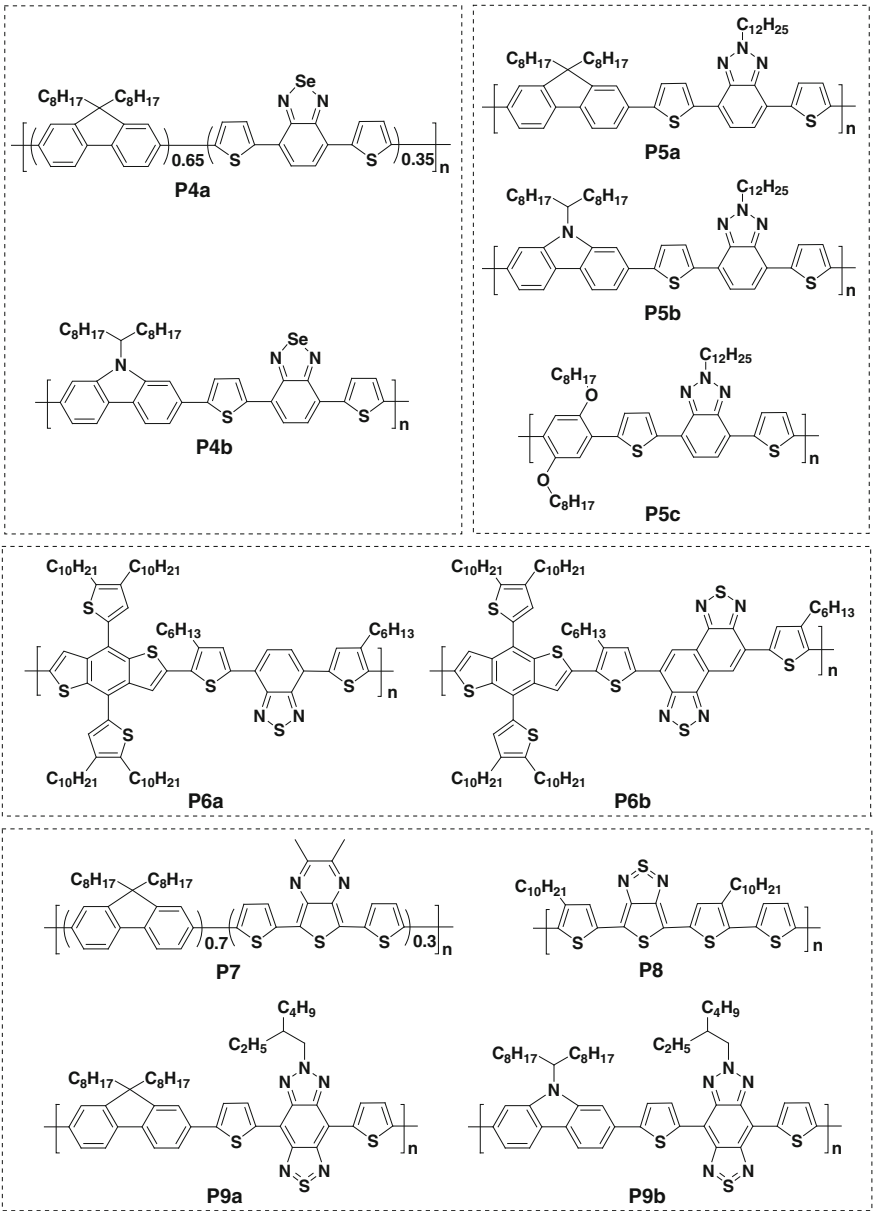

Scheme 6.3 Chemical structure of photovoltaic materials P4-P9

skeleton of carbazole. In addition, the 4,5-ethylene linkage has the possibility of being converted to a double band, leading to a new carbazole with enhanced aromaticity and larger conjugation extent. The polymer P10 possessed a high

Table 6.2 HOMO energy levels, optical band gaps and device performances of P4-P9

Polymers	HOMO (eV)	E_g (eV)	V_{oc} (V)	J_{sc} (mA cm^{-2})	FF	PCE (%)	References
P4a	–	–	0.85	2.53	0.327	0.91	[49]
P4b	−5.28	1.73	0.75	7.23	0.45	2.58	[50]
P5a	−5.67	2.24	1.00	2.64	0.515	1.30	[51]
P5b	−5.54	2.18	0.90	4.68	0.653	2.75	[51]
P5c	−5.20	1.87	0.55	4.50	0.561	1.39	[51]
P6a	−5.26	1.73	1.00	5.80	0.346	2.11	[34]
P6b	−5.19	1.58	0.80	11.71	0.610	6.00	[34]
P7	−5.22	1.77	0.70	4.10	0.289	0.83	[56]
P8	−4.71	1.01	0.35	0.83	0.386	0.11	[57]
P9a	−5.16	1.33	0.65	6.90	0.44	2.56	[59]
P9b	−5.18	1.35	0.70	8.50	0.41	3.17	[59]

weight-average molecular weight (M_w) of 50.7 kg mol^{-1} with a PDI of 2.09. The solubility of the polymer P10 in common organic solvents at room temperature was very good, due to the high content of solubilizing alkyl side chains on each repeat unit. The polymer P10 exhibited a medium band gap, with an absorption peak at 557 nm in its solid state. CV experiments indicated that the HOMO and LUMO levels of P10 were −5.15 and −3.45 eV, respectively. With P10:$PC_{71}BM$ (1:4) composite as the active layer, and an alcohol soluble conjugated polymer modified Al electrode as cathode, BHJ-PSCs displayed a highest PCE of 6.07 %, with a V_{oc} of 0.81 V, a J_{sc} of 11.4 mA cm^{-2} and a FF of 0.658 [33]. Zhang et al. [60] developed a series of new D-A type conjugated copolymers (P11a, P11b, P12a and P12b) based on thiophene-substituted quinoxaline or its cyclized phenazine derivative (see Scheme 6.4) by common Suzuki coupling reaction. It was revealed that the copolymer P11a and P12a using thiophene-substituted quinoxaline as acceptor unit demonstrated significantly red-shifted absorption with respect to the similar copolymers based on phenyl-substituted quinoxaline. Moreover, it was found that converting the freely rotating thiophene rings on P11a and P12a into polycyclic aromatic units could effectively decrease the steric hindrance and increase the coplanarity of the resulting polymers (P11b and P12b), thereby leading to substantially red-shifted absorbance, reduced band gaps, as well as enhanced hole mobilities. Unfortunately, the increased coplanarity exerted great negative influence on the solubility of the resulting polymers, in which case P11a and P12a had excellent solubility in common organic solvents, while P11b and P12b showed poor solubility [60]. The poor solubility of P11b and P12b hence led to poor morphology when blended with $PC_{71}BM$. Atomic force microscopy (AFM) images indicated pronounced phase separation along with large domain size in P11b:$PC_{71}BM$ and P12b:$PC_{71}BM$ blend films. Consequently, BHJ-PSCs of coplanarity-enhanced polymers (P11b and P12b) exhibited poorer performances than those of P11a and P12a. Among all the four quinoxaline-based copolymers developed by

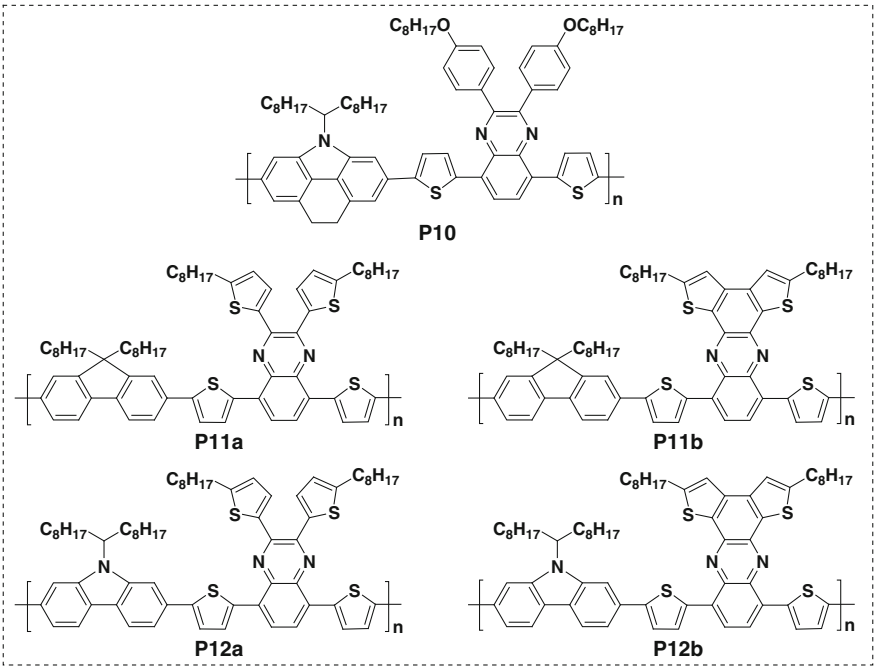

Scheme 6.4 Chemical structure of photovoltaic materials P10-P12

Zhang et al., P11a displayed the best performance with a PCE of 4.4 %, a V_{oc} of 0.90 V, a J_{sc} of 7.4 mA cm^{-2}, and a FF of 0.59 [60]. Yet anyhow, Zhang's work provided an approach to improve the coplanarity of conjugated photovoltaic polymers and indicated that a synergistic optimization of the polymers' structure is critical for obtain promising materials for BHJ-PSC applications. The chemical structures of quinoxaline-based photovoltaic polymers P10-P12 were presented in Scheme 6.4, and the HOMO energy levels, band gaps and photovoltaic performances of P10-P12 were summarized in Table 6.3.

Table 6.3 HOMO energy levels, optical band gaps and device performances of P10-P14

Polymers	HOMO (eV)	E_g (eV)	V_{oc} (V)	J_{sc} (mA cm^{-2})	FF	PCE (%)	References
P10	−5.15	1.70	0.81	11.4	0.658	6.07	[33]
P11a	−5.26	1.86	0.90	7.4	0.59	4.4	[60]
P11b	−5.21	1.68	0.85	4.7	0.51	2.1	[60]
P12a	−5.23	1.90	0.88	6.6	0.53	3.5	[60]
P12b	−5.17	1.66	0.75	6.4	0.54	3.0	[60]
P13	−5.39	1.82	0.90	9.5	0.507	5.4	[32]
P14	−5.35	1.72	0.85	5.86	0.60	3.02	[65]

In addition to acceptor units, as equally importantly, donor units also play key roles on the optoelectronic properties including absorption spectra, energy levels and charge transporting ability of the resulting D-A type conjugated copolymers, which in turn dominated the final photovoltaic performances of the related BHJ-PSCs. Up to now, a large amount of electron-rich aromatic heterocycles (such as fluorene, carbazole, silafluorene, cyclopenta[2,1-*b*:3,4-*b*′]dithiophene, dithieno[3,2-*b*:2′,3′-*d*] silole, and benzo[1,2-*b*:4,5-*b*]dithiophene, etc.) were successfully explored as donor units to construct high efficient D-A type NBG conjugated copolymers for BHJ-PSCs applications. Among all of the donor units, silafluorene is a promising one for NBG photovoltaic materials. As early as 2008, Wang et al. [32] reported an alternating copolymer (P13) of alkyl substituted silafluorene and DBT. The E_g of P13 was estimated to be 1.82 eV, which is 0.1 eV smaller than that of its fluorene-derived analogue PFDTBT [32, 39]. It was found that the absorption peak (565 nm) of P13 red-shifted approximately 20 nm relative to that of its fluorene-derived analogue PFDTBT [32, 39]. The HOMO energy level of P13 was estimated to be −5.39 eV by CV experiments. Moreover, it was found that the hole mobility of P13 measured from field-effect transistors (FETs) was almost one order of magnitude higher than that of its fluorene-based analogue under the same conditions. The optimal absorption spectrum, deep-positioning HOMO energy level, as well as enhanced charge transporting ability thereby contributed to the impressive PCE of 5.4 % for the resulting BHJ-PSC of P13:$PC_{61}BM$, with a high V_{oc} of 0.90 V, a J_{sc} of 9.5 mA cm^{-2}, and a FF of 0.507 [32]. It is worth pointing out that the high molecular weight (M_n = 79 kg mol^{-1}) may also play an important role on the outstanding photovoltaic property of P13. [10, 32, 61] Noticeably, P13 with lower molecular weight and poorer photovoltaic property was also reported by Leclerc's group independently almost at the same time [62]. These results indicated that changing the bridging atoms of donor units is an effective strategy to develop high performing photovoltaic donor polymers. Afterwards, a lot of highly efficient D-A type photovoltaic materials using different heteroatom-bridged aromatic polycyclic compound as donor units were successfully developed [10, 18, 47, 63–70]. For example, an unprecedented high PCE of 8.5 % was achieved for the inverted BHJ-PSCs from a germanium-bridged NBG conjugated polymer and $PC_{71}BM$ [18]. Moreover, Chen et al. [71] and Scharber et al. [72] further revealed that the enhanced photovoltaic properties of silicon atom bridged polymers compared with their carbon atom bridged analogues were mainly caused by the improvements in crystallinity and charge transporting ability, as well as the slightly extended absorption spectra. These improvements can essentially be attributed to the larger atom radius of silicon atom than that of carbon atom, which in turn can displace the solubilizing side chains far away from the conjugated main chains, leading to better coplanarity of polymer main chains and better interchain packing. Cai et al. [73] reported another D-A type alternating copolymer (P14) based on silafluorene donor and BT-derived acceptor unit. The polymer P14 exhibited an optimal E_g of 1.72 eV, and a deep-positioning HOMO energy level of −5.35 eV. Gel permeation chromatography (GPC) measurement indicated that P14 possessed

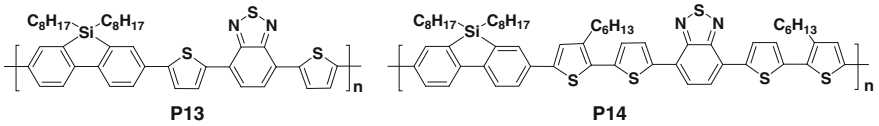

Scheme 6.5 Chemical structures of linear D-A type conjugated copolymers P13 and P14

a high M_n of 122 kg mol^{-1}. Moreover, the solubility of P14 in common solvents such as chlorobenzene and chloroform was still excellent, possibly endowed by its bulky side chains. Interestingly, it was found that the J_{sc} and PCE of related solar cells can be significantly enhanced by over 50 % when the P14:$PC_{61}BM$ blend were processed from chloroform solution rather than from chlorobenzene solution. These enhancements were attributed to the increased absorption coefficient of polymer thin film and the formation of polymer-rich fibrillar domains in active layer [73]. The chemical structures of silafluorene-based D-A type conjugated polymers P13 and P14 were demonstrated in Scheme 6.5, and the HOMO energy levels, band gaps and photovoltaic performances of P13 and P14 were summarized in Table 6.3.

6.2.2 Acceptor-Pended D-A Type Conjugated Polymers

In addition to explore new building units for the well-known linear D-A type NBG copolymers, new molecular design strategies are also desired to develop highly efficient conjugated donor polymers for BHJ-PSCs applications. Huang et al. [74] proposed a novel molecular design strategy, i.e. acceptor-pended D-A conjugated polymers, to construct new donor polymers for BHJ-PSCs. As shown in Scheme 6.6a, b, the conjugated main chains of this kind of conjugated polymer were composed of electron-rich units (donor units), while the electron-withdrawing groups (acceptor groups) were pended at the end of the conjugated side chains through π-bridges to generate donor-π-acceptor chromophores. Compared with the traditional linear D-A type conjugated copolymers, the acceptor-pended conjugated copolymers have some unique advantages. Firstly, the absorption spectra and band gaps of the acceptor-pended conjugated copolymers could be effectively tuned, due to that ICT interaction from main chains to side chains could be well controlled by simply changing the donor/acceptor groups or the π-bridges. Secondly, the HOMO energy levels of the resulting polymers can be kept at a deep-position by choosing suitable donor units to construct main chains, because the HOMO levels were usually considered to be controlled by the donors, while the LUMO levels were controlled by acceptors [36]. It is now well known that a deep-positioning HOMO energy level is beneficial for not only improving the chemical stability of the resulting conjugated polymers, but also gaining a high V_{oc} in solar cells [26, 36]. Thirdly, the acceptor-pended D-A polymers may have better isotropic charge transporting ability with respect to traditional linear D-A type conjugated polymers,

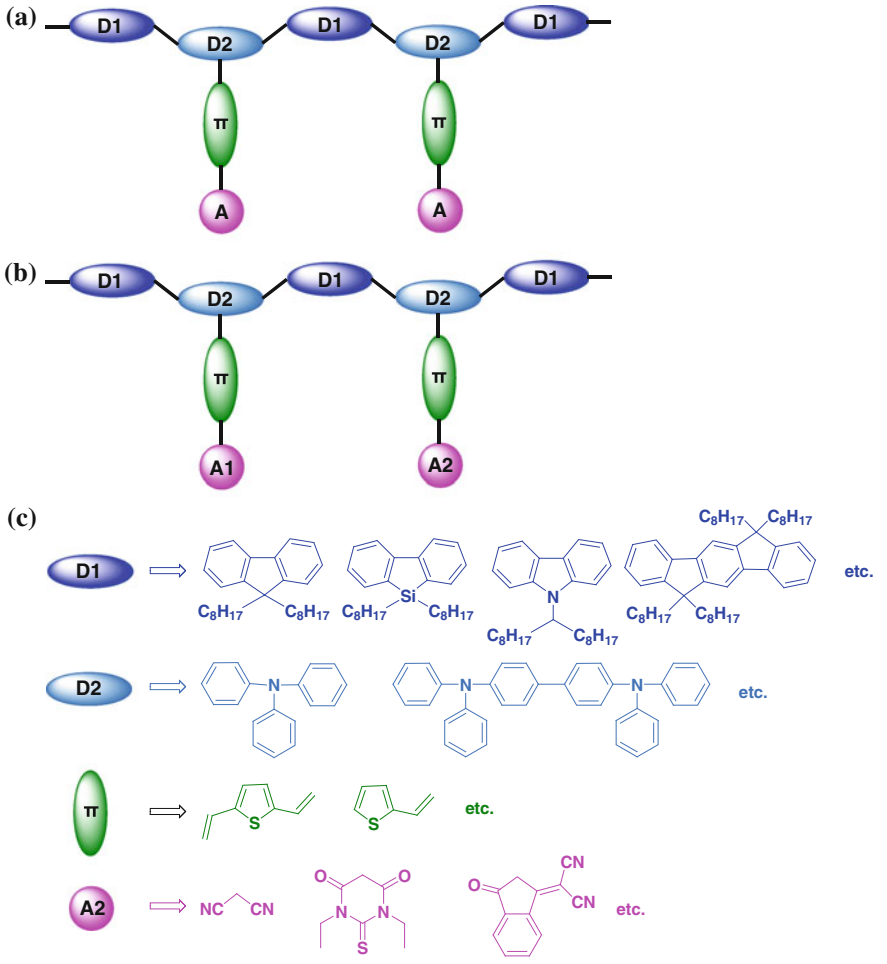

Scheme 6.6 **a** The structure of acceptor-pended conjugated copolymers with one kind of acceptor unit. **b** The structure of acceptor-pended conjugated copolymers with two different kinds of acceptor units. **c** The components used to construct acceptor-pended conjugated copolymers

taking into account their two-dimensional-like conjugated structures. Fourthly, the bulky conjugated side chains would endow the resulting polymers good solubility and processibility in common organic solvents. Finally, the same conjugated precursor polymers can give rise to a series of resulting polymers by simple chemical modification, which possess close degrees of polymerization and molecular weight distributions, but different optoelectronic and photovoltaic properties. As a result, the acceptor-pended molecular design can provide ideal prototypes to establish the relationships between polymers' structure and properties.

Based on this new molecular design, Huang et al. [74] developed two new NBG conjugated polymers for photovoltaic applications. Fluorene and triphenyl amine were used as D1 and D2, respectively, to construct the conjugated main chains, while acceptor groups of malononitrile and diethylthiobarbituric acid were connected with triphenyl amine on conjugated backbone via styrylthiophene π-bridges. Along with the increase of electron affinity of acceptor groups, the absorption spectra of the resulting polymers were effectively red-shifted. Meanwhile, the relative deep-positioning HOMO energy levels (∼−5.3 eV) were almost unchanged. Moreover, the hole mobility of the resulting polymers measured by space charge limited current (SCLC) method were even slightly higher than that of P3HT under the same conditions, despite the fact that the two polymers were amorphous because of their two-dimensional-like conjugated structures. And encouragingly, BHJ-PSCs using the two polymers as donor phase exhibited promising PCEs of 4.74 and 4.37 %, respectively, along with appreciable high V_{oc} around 1.0 V [74]. Later, several research groups also involved in this field and many other donor units, acceptor groups and π-bridges (see Scheme 6.6c) were extensively explored to construct new photovoltaic donor polymers based on this novel molecular design [75–88]. For examples, Duan et al. [77] had developed a series of new donor polymers (P15a, P15b and P15c, see Scheme 6.7) where DOF and triphenyl amine were used as D1 and D2, respectively, while thiophene instead of styrylthiophene was π-bridge to improve the photo-oxidation stability of the resulting polymers. The absorption spectra and energy levels of P15a, P15b and P15c were shown in Fig. 6.1a, b, respectively. Along with the increase of electron-withdrawing strength of the pendant acceptors, the ICT absorption bands of the polymers were significantly red-shifted. Meanwhile, the intensity of ICT absorption bands was also enhanced. More interestingly, the HOMO energy levels of the three polymers P15a, P15b and P15c were extremely close, while the LUMO energy levels were decreased in sequence along with the reduction of band gaps [77]. Besides, the acceptor-pended design provided an ideal platform to develop photovoltaic polymers which can harvest photons in different wavelength region simultaneously.

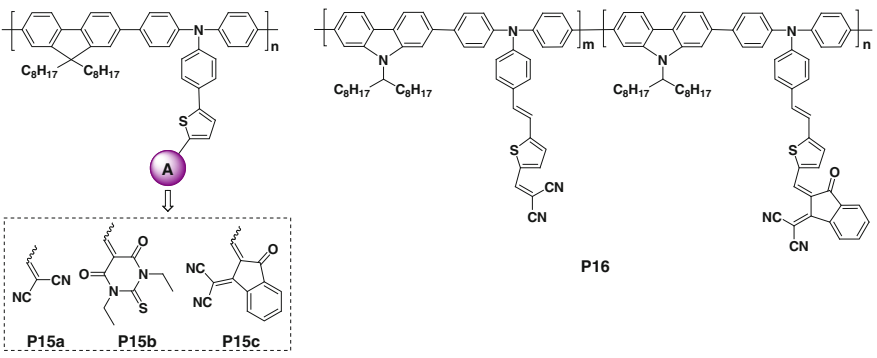

Scheme 6.7 Chemical structures of acceptor-pended conjugated copolymers P15–P16

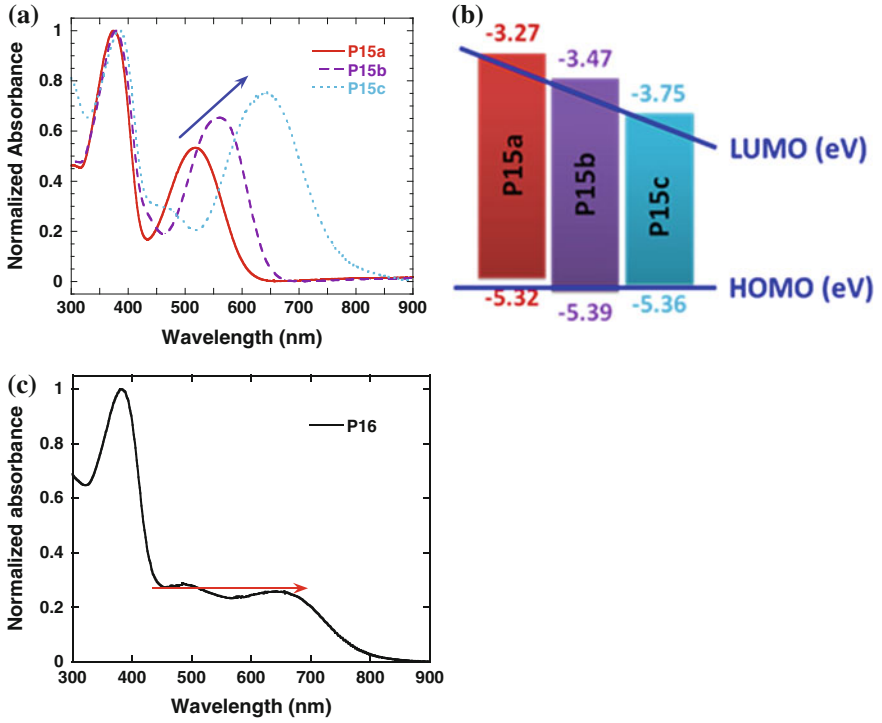

Fig. 6.1 **a** Absorption spectra of P15a, P15b and P15c. **b** Energy diagram of P15a, P15b and P15c. **c** Absorption spectrum of P16

As the schematic diagram shown in Scheme 6.6b, introducing acceptor units with different electron affinity onto the same precursor polymer would lead to the formation of several kinds of different donor-π-acceptor chromophores, which can absorb solar irradiation in different wavelength regions. For instance, Duan et al. [79] had attached two different acceptor groups in sequence onto the same precursor polymer to afford P16 (see Scheme 6.7), which showed effective light-harvesting in the whole visible light region (see Fig. 6.1c). The HOMO energy levels, band gaps and photovoltaic performances of P15-P16 were summarized in Table 6.4.

Table 6.4 HOMO energy levels, optical band gaps and device performances of P15-P16

Polymers	HOMO (eV)	E_g (eV)	V_{oc}(V)	J_{sc}(mA cm^{-2})	FF	PCE (%)	References
P15a	−5.32	2.05	0.99	5.42	0.396	2.12	[69]
P15b	−5.39	1.92	0.97	7.56	0.392	2.87	[69]
P15c	−5.36	1.61	0.97	4.54	0.372	1.65	[69]
P16	−5.27	1.57	0.90	6.09	0.37	2.30	[71]

6.3 Water/Alcohol Soluble Conjugated Polymers-Based Interfacial Materials for BHJ-PSCs

A lot of researches have shown that charge transporting in organic semiconductor devices is critically affected by the interfaces between different functional layers. Generally an ideal Ohmic contact in the organic layer/electrode interface with minimum energy barrier is desired for efficient photo-generated charge carrier extraction and transporting [89]. For example, in a typical BHJ-PSC device, an electron energy barrier height of several tens of mV at the electron collecting electrode interface can result in severe electron build-up inside the active layer, leading to poor device performance [16]. However, there is a lack of choice in proper electrode materials, especially electron collecting electrode materials, whose work function can exactly match the energy level of the organic semiconductors. Therefore, the modification of organic active layer/electrode interface is a critical step towards achieving high performance in BHJ-PSCs [16, 27–30]. Interface engineering through the addition of interlayer is one of the simplest and most effective ways to improve the efficiency of BHJ-PSC devices [16, 27–30]. A hole collecting/transporting layer (HCL) between BHJ layer and hole collecting electrode was used to increase the hole collection, while an electron collecting/transporting layer (ECL) between BHJ layer and electron collecting electrode was used to increase the electron collection [16, 27–30].

There are several criteria for selecting good ECL materials for BHJ-PSCs applications. First, it should definitely have excellent electron extraction and transporting ability. It should be able to minimize the electron energy barrier in organic active layer/electron collecting electrode interface, which could transform the Schottky contact into Ohmic contact and ultimately lead to enhanced performance in BHJ-PSC devices [90]. Secondly, the ECL should also function as a blocking layer to selectively transport only electrons and block holes or excitons from entering the electron collecting electrode (e.g. very high hole injection/extraction energy barrier) [91]. Thirdly, the ECL should function as buffer layer to prevent the chemical reaction between organic active layer and metal electrode, and to stop the diffusion of metal ions into organic layer, which will degrade the active layer materials [92]. Lastly, the ECL should have good optical transparency, especially when it is applied in inverted solar cells where light absorption in the ECL layer should be minimized.

Water/alcohol soluble conjugated polymers (WASCPs) thus attracted the attentions of researchers due to they can meet most of the criteria mentioned above very well. WASCPs usually consist of two parts: the conjugated main chains and highly polar side chains. The conjugated main chains endow them good semiconducting properties, and the highly polar side chains ensure them good solubilities in high polarity solvents such as water, alcohol, *N,N*-dimethylformamide etc. (Scheme 6.8) The unique molecular structures of WASCPs thus endow them two main advantages for usage as ECLs in BHJ-PSCs. Firstly, WASCPs can be processed from high polarity solvents and thus can overcome the interface erosion

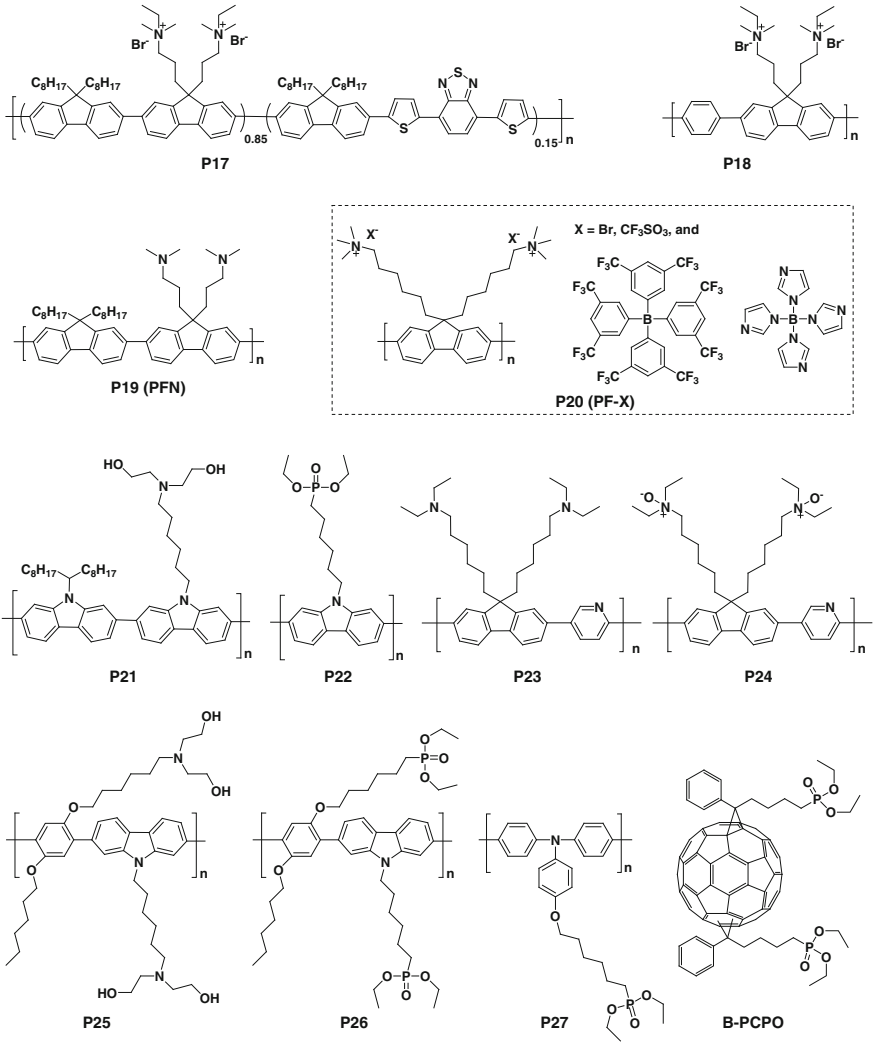

Scheme 6.8 Chemical structures of some WASCPs used as ECLs in BHJ-PCSs

problem when fabricating multilayer devices. Secondly, WASCPs can effectively enhance the electron injection or extraction from almost all the high work-function metals, which is an unique advantage of WASCPs compared with previously developed interlayer materials and interface modification methods [29]. WASCPs have the additional advantages of better charge transporting and greater room in structure design compared with other successful organic ECL materials such as PEO [93]. Thereby, many efforts were put on the using of WASCPs as ECLs to improve the performance of BHJ-PSCs [94–96]. This section presents our recent

developments on WASCPs and their application as ECL in BHJ-PSCs. Scheme 6.8 shows the chemical structures of some WASCPs which have been demonstrated as effective ECLs for BHJ-PSCs.

6.3.1 *Interface Modification for Metal Electrodes in Conventional BHJ-PSC Devices*

Electron collecting electrodes with suitable work function are required for efficient extraction of photo-generated electrons in BHJ-PSC devices. In principle, high work function metals, such as Au, Cu or Pd, could efficiently serve as electron-extracting electrodes. However, the mismatching work function of the cathode greatly affects the photovoltaic parameters of BHJ-PSCs, especially the V_{oc}, and the maximum performance can only be achieved when the work function of the cathode is the same or lower than the LUMO level of the acceptor to form Ohmic contact. Such energy level alignment can be done by shifting the work function of metals to lower values through the incorporation of WASCP interlayers as was already demonstrated in polymer light-emitting diodes (PLEDs) [29, 97, 98]. Following this idea, Luo et al. reported the use of WASCP-based ECL for BHJ-PSCs using Al as cathode. The insertion of a thin layer WASCP of P17 or P18 (see Scheme 6.8) between the active layer (Donor polymer: $PC_{61}BM$ blend) and Al cathode led to a staggering 0.3 V increase in the V_{oc} [94]. The donor materials used in the study were P1a and PFO-TST50 (see Scheme 6.9). Besides showing the potential of WASCPs in BHJ-PSC applications, Luo et al. also briefly investigated

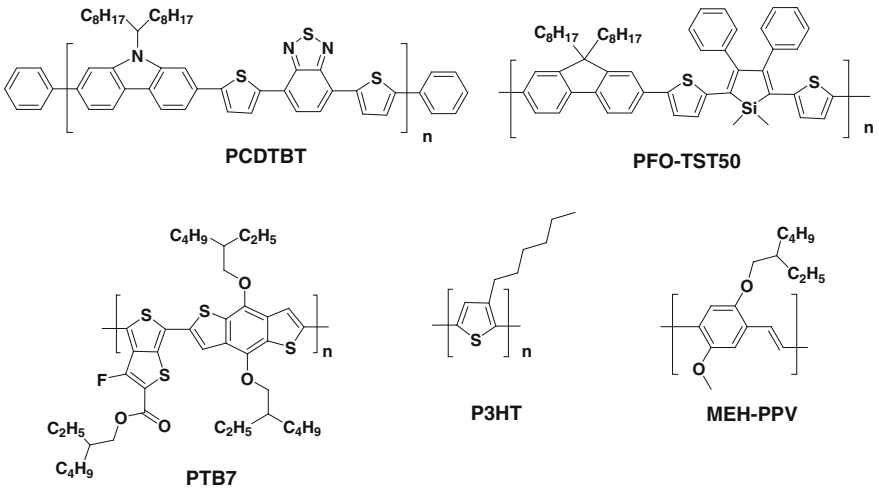

Scheme 6.9 Chemical structures of some polymer donor materials whose photovoltaic properties can be improved by WASCPs interlayers

the possible mechanisms and it was demonstrated that the inserted ECL layer behaves like a thin dielectric layer by impedance spectroscopy, which is indirect proof of the existence of interfacial dipole. He et al. [99] further investigated the effect of four ionic type WASCPs (PF-X, X for different counterions: Br^-, trifluoromethanesulfonate, tetrakis(1-imidazolyl)borate and tetrakis[3,5-bis(trifluoromethyl)phenyl]borate) and one neutral WASCP PFN as ECL for BHJ-PSC devices based on different donor materials. It was found that significant V_{oc} enhancement was only presented in P1a-based devices, while not in devices using P3HT or MEH-PPV as the donor materials (Scheme 6.9). In addition, the choice of the counter cations was found to have little influence on the performance of WSETMs in BHJ-PSCs, as the five different materials resulted in similar photovoltaic performance. On the other hand, a crude correlation between reduced dark current and the enhancement of V_{oc} was established, which led to a deeper understanding of the origin of the enhancement of V_{oc} in specific materials systems [99].

Similar works using polyfluorene-based WASCPs with different polar groups were reported by other research groups around the same time as Luo's report. Na et al. [95] studied WASCPs with hybrid quaternary ammonium end-capped alkyl/alkoxyl side chains, while Zhao et al. [96] studied WASCPs with phosphonate end-capped alkyl side chains as interfacial materials for Al electrode modification. It should be noted that these WASCPs were reported to be effective in P3HT:$PC_{61}BM$ system, which was different from those WASCPs in He's report, suggesting that the enhancement effect may be confined to certain combinations of WASCP polar groups and donor materials. The reason for this is still unclear. Nevertheless, further studies in our lab revealed that WASCP/Al electrode design can greatly extend the potential in newly developed donor materials [33, 51]. Using a newly developed low band gap donor P10, a PCE of 6.07 % could be achieved by PFN/Al cathode device compared with 3.99 % for Al cathode reference device [33], which is an improvement of over 50 %. In another report by Zhang et al. [51] PFN/Al cathode devices can improve the performance of P5b:$PC_{61}BM$ system by 80 % compared with bare Al cathode devices. Later, conjugated alternating copolymers based on carbazole developed by Xu et al. [100, 101] were also used as ECL materials (such as P21 and P22) with Al electrodes, and small improvements in V_{oc} and PCE were observed in P1a:$PC_{61}BM$ system. The frequently used WASCP PFN was later shown to be also very effective for low work function metal electrode, as PFN/Ca/Al electrode devices using poly[[4,8-bis[(2-ethylhexyl)oxy]benzo[1,2-*b*:4,5-*b*′]dithiophene-2,6-diyl][3-fluoro-2-[(2-ethylhexyl)carbonyl]thieno[3,4-*b*]thiophene-diyl]] (PTB7):$PC_{71}BM$ system reached record efficiency in a recent report by He et al. [17] The PCE of such devices reached a staggering value of 8.22 % (8.37 % certified by National Center of Supervision and Inspection on Solar Photovoltaic Products Quality of China), which is a record efficiency at the time, and is significantly higher than 5.00 % for the bare Al electrode devices and 7.13 % for Ca/Al electrode devices.

Most recently, Guan et al. used amine *N*-oxides instead of commonly used amines as polar groups for WASCPs molecular design [102]. This novel design increased the solubility of WASCPs in alcohol and other polar solvents and further

improved the electron injection/extraction ability compared with amine-based WASCPs. The best amine *N*-oxides functionalized WASCP P24 can improve the BHJ-PSC device performance of PCDTBT:$PC_{71}BM$ system from 4.0 to 6.9 %, while the amine functionalized counterpart P23 can only improve the PCE to 5.7 %.

The donor materials whose photovoltaic properties can be improved by WASCP according to our current published results are listed in Scheme 6.9 and the BHJ-PSC device performances are summarized in Table 6.5. It can be seen from Table 6.5 that the utilization of WASCP/metal electron collecting electrode could lead to obvious improvement in BHJ-PSC performance for a variety of donor materials. These encouraging results indicated that WASCPs would be good candidates of electron collecting electrode interfacial materials for the future development of printable large-scale solar cells.

6.3.2 *Interface Modification for ITO in Inverted BHJ-PSC Devices*

The conventional device structure of BHJ-PSCs has some inherent device stability problems due to the use of acidic PEDOT:PSS as hole transporting/collecting layer (HTL) [103] and the use of low work function metals as electron collecting electrode. Therefore, device architectures that can remove PEDOT:PSS (or at least separate it from ITO) and use non-vacuum deposited air-stable high work function metal electrodes at the top interface are desired. Because of this, the inverted device structure became popular in BHJ-PSC device research in recent years. In a typical inverted solar cell, the ITO is still used as the transparent electrode where sunlight enters the device, however in the inverted structure ITO serves as electron collecting electrode rather than hole collecting electrode, therefore an ECL instead of HTL is needed between ITO and the active layer in order to achieve efficient electron extraction. N-type metal oxides (n-MOs) such as ZnO and TiO_x are the most commonly utilized ECL materials for inverted solar cells due to the high optical transparency in the visible and near infrared region, high carrier mobility, and its solution processibility [104, 105]. Even though reasonable efficiencies have been reached with n-MOs as the ECL in inverted PSCs, it still has great room for improvement, as the surface of n-MOs contains hydroxyl groups that can cause charge trapping at the metal oxide/active layer interface [106].

WASCP thin films can also be implemented as independent ECL for inverted PSCs to replace the n-MO layer. This design is advantageous to n-MO ETL in terms of compatibility with large scale fabrication technologies, since WASCPs can be processed at room temperature, while high temperature annealing is usually required for the solution processed n-MO thin films. Zhu et al. [107] reported the use of carbazole-containing WASCPs P25 and P26 as single layer ECL for PCDTBT:$PC_{71}BM$ inverted BHJ-PSC devices, and the PCE can be improved from 1.63 % without interlayer to 5.48 %, owing to the significant improvement in FF and V_{oc}. Kelvin probe measurement was conducted on the ITO electrode with or

Table 6.5 Device performance of polymer solar cells on various bulk-heterojunction systems with WASCP-based ECLs and different metal electrode (ITO/PEDOT:PSS/Active Layer/ECL/metal)

Donor: acceptor	Cathode	J_{sc} (mA cm^{-2})	*FF* (%)	V_{oc} (V)	PCE (%)	References
P1a:$PC_{61}BM$	Al	3.9	38.0	0.65	1.0	[86]
	P17/Al	3.9	39.4	0.95	1.9	
	P18/Al	4.7	45.0	1.00	2.1	
PFO-TST50: $PC_{61}BM$	Al	7.9	32.2	0.65	1.7	
	P17/Al	8.9	36.6	0.80	2.6	
	P18/Al	8.0	39.3	0.80	2.5	
P1a:$PC_{61}BM$	Al	3.41	47.5	0.92	1.46	[91]
	PF-Br/Al	3.41	48.8	1.07	1.75	
	PF-OTf/Al	3.50	47.9	1.07	1.76	
	PF-BIm4/Al	3.36	50.5	1.06	1.78	
	PF-BArF4/ Al	3.35	48.2	1.06	1.70	
	PFN/Al	4.41	42.8	1.05	1.99	
P10:$PC_{71}BM$	Al	9.10	56.3	0.78	3.99	[33]
	Ca/Al	9.84	57.4	0.80	4.52	
	PFN/Al	11.4	65.8	0.81	6.07	
PTB7:$PC_{71}BM$	Ca/Al	15.5	66.0	0.70	7.13	[17]
	PFN/Ca/Al	16.1	69.0	0.76	8.22	
	PFN/Al	8.10	55.0	0.85	4.52	
PCDTBT:$PC_{71}BM$	Al	11.30	49.0	0.70	3.95	
	PFN/Al	12.10	62.0	0.90	6.73	
PCDTBT:$PC_{71}BM$	Al	11.4	53.8	0.65	4.0	[94]
	P23/Al	11.3	56.0	0.90	5.7	
	P24/Al	11.6	66.2	0.91	6.9	
P1a:$PC_{61}BM$	Al	3.58	40	0.95	1.36	[93]
	P21/Al	4.00	41	1.02	1.67	
	P22/Al	3.80	40	1.01	1.53	
P5a:$PC_{61}BM$	Al	2.03	51.2	0.80	0.90	[51]
	PFN/Al	2.64	51.5	1.00	1.30	
P5b:$PC_{61}BM$	Al	3.91	48.4	0.80	1.51	
	PFN/Al	4.68	65.3	0.90	2.75	

without the WASCP layers and it was found that the work function of ITO could be shifted from 4.7 to 4.2 eV by P25 and 4.3 eV by P26. Thus the improvement in device performance was attributed to this effect. Later Xu et al. [108] applied triphenylamine-based WASCP P27 as ECL for inverted devices using PCDTBT:$PC_{71}BM$ system. The PCE was improved from 2.57 % for bare ITO devices (ITO/PCDTBT:$PC_{71}BM$/MoO_3/Al) to 4.59 % for ITO/P27 devices. Similar work function lowering effect was observed in ITO/P27 electrodes.

Most recently, Duan et al. [109] developed a new fullerene-based alcohol soluble material B-PCPO as ECL for inverted BHJ-PSC applications. Compared with previous WASCPs, B-PCPO inherited the n-type nature and good electron transporting ability from fullerene (most WASCPs on the other hand, are inherently p-type). Inverted BHJ-PSC devices using B-PCPO as ECL and PCDTBT:$PC_{71}BM$ as active layer exhibited PCE as high as 6.2 % compared with 4.8 % for bare ITO devices. X-ray photoelectron spectroscopy (XPS) revealed that the work function of ITO was lowered from 4.3 to 3.9 eV after adding the B-PCPO layer on top.

6.4 Summary and Outlook

This chapter provides an overview of the recent development of donor polymers and WASCP-based interfacial materials for BHJ-PSC applications in South China University of Technology. Although great progresses in PCEs of BHJ-PSCs have been achieved in recent years benefiting from various efforts devoted by scientists all around the world, there is still a long way ahead of the wide spread commercialization of BHJ-PSCs. It is a consensus that promising active materials are most important for the realization of highly efficient BHJ-PSCs. Although some donor materials developed in recent years have already exhibited promising photovoltaic properties, the development of novel design and better-performing donor materials is still urgent. In the future development of new donor polymers for BHJ-PSCs, several criteria should be considered simultaneously: (1) enough solubility should be ensured for solution processing; (2) broad absorption spectra and high extinction coefficient to harvest incident photons as much as possible; (3) optimal energy levels to concurrently ensure efficient charge dissociation and minimal V_{oc} loss; (4) high charge transporting ability to reduce charge carrier recombination as much as possible; (5) good photochemical stabilities and the ability of stabilizing the bi-continuous penetrating network of active layer.

The electrical contact of interfaces between different layers is also critical for high performance BHJ-PSCs, besides the high efficiency donor/acceptor materials and the optimization of active layer morphology. WASCPs can be processed from water or other polar solvents, which can avoid interfacial mixing problem upon fabrication of multilayer devices by solution processing, and can dramatically improve charge injection/collection at the electrode to greatly improve the device performance. Due to their successful application in PLEDs, WASCPs were applied as the ECLs in BHJ-PSCs and the state-of-the-art BHJ-PSCs with record PCE of 8.37 % have been realized. Moreover, WASCPs showed a wide range of adaptability to all kinds of donor materials and electrodes. It should be noted that most of WASCPs used in BHJ-PSCs were directly borrowed from those that previously designed primarily for PLEDs. With better understanding on the requirements of BHJ-PSCs, the WASCPs developed in future specifically for BHJ-PSC applications should have higher electron mobility and greater dipole strength, so that they may

further improve the BHJ-PSC device performances and thereby fully exploit the potential of solution-processed PSCs.

Acknowledgments The authors thank the financial support from the Ministry of Science and Technology, China (MOST) National Research Project (No. 2009CB623601) and the Natural Science Foundation of China (No. 21125419, 50990065, 51010003, 51073058 and 20904011).

References

1. S. Günes, H. Neugebauer, N.S. Sariciftci, Conjugated polymer-based organic solar cells. Chem. Rev. **107**(4), 1324–1338 (2007)
2. G. Li, R. Zhu, Y. Yang, Polymer solar cells. Nat. Photonics **6**(3), 153–161 (2012)
3. B.C. Thompson, J.M.J. Fréchet, Polymer-fullerene composite solar cells. Angew. Chem. Int. Ed. **47**(1), 58–77 (2008)
4. F.C. Krebs, J. Fyenbo, M. Jorgensen, Product integration of compact roll-to-roll processed polymer solar cell modules: methods and manufacture using flexographic printing, slot-die coating and rotary screen printing. J. Mater. Chem. **20**(41), 8994–9001 (2010)
5. C.J. Brabec, S. Gowrisanker, J.J.M. Halls, D. Laird, S.J. Jia, S.P. Williams, Polymer-fullerene bulk-heterojunction solar cells. Adv. Mater. **22**(34), 3839–3856 (2010)
6. G. Dennler, M.C. Scharber, C.J. Brabec, Polymer-fullerene bulk-heterojunction solar cells. Adv. Mater. **21**(13), 1323–1338 (2009)
7. Service RF. Outlook brightens for plastic solar cells. Science **332**(6027), 293 (2011)
8. J. Chen, Y. Cao, Development of novel conjugated donor polymers for high-efficiency bulk-heterojunction photovoltaic devices. Acc. Chem. Res. **42**(11), 1709–1718 (2009)
9. Y.Y. Liang, L.P. Yu, A new class of semiconducting polymers for bulk heterojunction solar cells with exceptionally high performance. Acc. Chem. Res. **43**(9), 1227–1236 (2010)
10. C.H. Duan, F. Huang, Y. Cao, Recent development of push-pull conjugated polymers for bulk-heterojunction photovoltaics: rational design and fine tailoring of molecular structures. J. Mater. Chem. **22**(21), 10416–10434 (2012)
11. Y. Liang, Z. Xu, J. Xia, S.-T. Tsai, Y. Wu, G. Li, C. Ray, L. Yu, For the bright future—bulk heterojunction polymer solar cells with power conversion efficiency of 7.4 %. Adv. Mater. **22** (20), E135–E138 (2010)
12. H.-Y. Chen, J. Hou, S. Zhang, Y. Liang, G. Yang, Y. Yang, L. Yu, Y. Wu, G. Li, Polymer solar cells with enhanced open-circuit voltage and efficiency. Nat. Photonics **3**(11), 649–653 (2009)
13. W. Ma, C. Yang, X. Gong, K. Lee, A.J. Heeger, Thermally stable, efficient polymer solar cells with nanoscale control of the interpenetrating network morphology. Adv. Funct. Mater. **15**(10), 1617–1622 (2005)
14. J. Peet, J.Y. Kim, N.E. Coates, W.L. Ma, D. Moses, A.J. Heeger, G.C. Bazan, Efficiency enhancement in low-bandgap polymer solar cells by processing with alkane dithiols. Nat. Mater. **6**(7), 497–500 (2007)
15. J.Y. Kim, K. Lee, N.E. Coates, D. Moses, T.Q. Nguyen, M. Dante, A.J. Heeger, Efficient tandem polymer solar cells fabricated by all-solution processing. Science **317**(5835), 222–225 (2007)
16. L.-M. Chen, Z. Xu, Z. Hong, Y. Yang, Interface investigation and engineering—achieving high performance polymer photovoltaic devices. J. Mater. Chem. **20**(13), 2575–2598 (2010)
17. Z. He, C. Zhong, X. Huang, W.-Y. Wong, H. Wu, L. Chen, S. Su, Y. Cao, Simultaneous enhancement of open-circuit voltage, short-circuit current density, and fill factor in polymer solar cells. Adv. Mater. **23**(40), 4636–4643 (2011)

18. C.E. Small, S. Chen, J. Subbiah, C.M. Amb, S.-W. Tsang, T.-H. Lai, J.R. Reynolds, F. So, High-efficiency inverted dithienogermole-thienopyrrolodione-based polymer solar cells. Nat. Photonics **6**(2), 115–120 (2012)
19. L. Dou, J. You, J. Yang, C.-C. Chen, Y. He, S. Murase, T. Moriarty, K. Emery, G. Li, Y. Yang, Tandem polymer solar cells featuring a spectrally matched low-bandgap polymer. Nat. Photonics **6**(3), 180–185 (2012)
20. X. Li, WCH. Choy, L. Huo, F. Xie, WEI. Sha, B. Ding, X. Guo, Y. Li, J. Hou, J. You, Y. Yang, Dual plasmonic nanostructures for high performance inverted organic solar cells. Adv. Mater. (2012). doi:10.1002/adma.201200120
21. http://www.polyera.com/newsflash/world-record-inverted-opv-efficiency-acheived
22. http://www.polyera.com/newsflash/polyera-achieves-world-record-organic-solar-cell-performance
23. http://www.engineer.ucla.edu/newsroom/featured-news/archive/2012/ucla-engineers-create-tandem-polymer-solar-cells-that-set-record-for-energy-conversion
24. http://www.sumitomo-chem.co.jp/
25. G. Yu, J. Gao, J.C. Hummelen, F. Wudl, A.J. Heeger, Polymer photovoltaic cells: enhanced efficiencies via a network of internal donor-acceptor heterojunctions. Science **270**, 1789–1791 (1995)
26. M.C. Scharber, D. Mühlbacher, M. Koppe, P. Denk, C. Waldauf, A.J. Heeger, C.J. Brabec, Design rules for donors in bulk-heterojunction solar cells—towards 10 % energy-conversion efficiency. Adv. Mater. **18**(6), 789–794 (2006)
27. H. Ma, H.-L. Yip, F. Huang, A.K.Y. Jen, Interface engineering for organic electronics. Adv. Funct. Mater. **20**(9), 1371–1388 (2010)
28. R. Po, C. Carbonera, A. Bernardi, N. Camaioni, The role of buffer layers in polymer solar cells. Energy Environ. Sci. **4**(2), 285–310 (2011)
29. F. Huang, H.B. Wu, Y. Cao, Water/alcohol soluble conjugated polymers as highly efficient electron transporting/injection layer in optoelectronic devices. Chem. Soc. Rev. **39**(7), 2500–2521 (2010)
30. H.-L. Yip, A.K.Y. Jen, Recent advances in solution-processed interfacial materials for efficient and stable polymer solar cells. Energy Environ. Sci. **5**(3), 5994–6011 (2012)
31. S.E. Shaheen, C.J. Brabec, N.S. Sariciftci, F. Padinger, T. Fromherz, J.C. Hummelen, 2.5 % efficient organic plastic solar cells. Appl. Phys. Lett. **78**(6), 841–843 (2001)
32. E.G. Wang, L. Wang, L.F. Lan, C. Luo, W.L. Zhuang, J.B. Peng, Y. Cao, High-performance polymer heterojunction solar cells of a polysilafluorene derivative. Appl. Phys. Lett. **92**(3), 033307 (2008)
33. Z. He, C. Zhang, X. Xu, L. Zhang, L. Huang, J. Chen, H. Wu, Y. Cao, Largely enhanced efficiency with a PFN/Al bilayer cathode in high efficiency bulk heterojunction photovoltaic cells with a low bandgap polycarbazole donor. Adv. Mater. **23**(27), 3086–3089 (2011)
34. M. Wang, X.W. Hu, P. Liu, W. Li, X. Gong, F. Huang, Y. Cao, Donor acceptor conjugated polymer based on naphtho[1,2-c:5,6-c]bis[1,2,5]thiadiazole for high-performance polymer solar cells. J. Am. Chem. Soc. **133**(25), 9638–9641 (2011)
35. T. Yang, M. Wang, Y. Cao, F. Huang, L. Huang, J. Peng, X. Gong, S.Z.D. Cheng, Y. Cao, Polymer solar cells with a low-temperature-annealed sol–gel-derived moox film as a hole extraction layer. Adv. Energy Mater. **2**(5), 523–527 (2012)
36. N. Blouin, A. Michaud, D. Gendron, S. Wakim, E. Blair, R. Neagu-Plesu, M. Belletete, G. Durocher, Y. Tao, M. Leclerc, Toward a rational design of poly(2,7-carbazole) derivatives for solar cells. J. Am. Chem. Soc. **130**(2), 732–742 (2008)
37. J.H. Hou, M.H. Park, S.Q. Zhang, Y. Yao, L.M. Chen, J.H. Li, Y. Yang, Bandgap and molecular energy level control. of conjugated polymer photovoltaic materials based on benzo [1,2-b : 4,5-b′] dithiophene. Macromolecules **41**(16), 6012–6018 (2008)
38. Q. Hou, Y.S. Xu, W. Yang, M. Yuan, J.B. Peng, Y. Cao, Novel red-emitting fluorene-based copolymers. J. Mater. Chem. **12**, 2887–2892 (2002)

39. M. Svensson, F. Zhang, S.C. Veenstra, W.J.H. Verhees, J.C. Hummelen, J.M. Kroon, O. Inganäs, M.R. Andersson, High-performance polymer solar cells of an alternating polyfluorene copolymer and a fullerene derivative. Adv. Mater. **15**(12), 988–991 (2003)
40. Q.M. Zhou, Q. Hou, L.P. Zheng, X.Y. Deng, G. Yu, Y. Cao, Fluorene-based low band-gap copolymers for high performance photovoltaic devices. Appl. Phys. Lett. **84**, 1653–1655 (2004)
41. M.L. Sun, L. Wang, W. Yang, Pyrrole-based narrow-band-gap copolymers for red light-emitting diodes and bulk heterojunction photovoltaic cells. J. Appl. Polym. Sci. **118**(3), 1462–1468 (2010)
42. J. Luo, R.Q. Yang, W. Yang, Y. Cao, Optoelectronic properties of fluorene-co-4,7-difuran-2,1,3-benzothiadiazole copolymers. Sci. China Chem. **53**(3), 576–580 (2010)
43. E.G. Wang, M. Wang, L. Wang, C.H. Duan, J. Zhang, W.Z. Cai, C. He, H.B. Wu, Y. Cao, Donor polymers containing benzothiadiazole and four thiophene rings in their repeating units with improved photovoltaic performance. Macromolecules **42**, 4410–4415 (2009)
44. H.X. Zhou, L.Q. Yang, S.Q. Xiao, S.B. Liu, W. You, Donor-acceptor polymers incorporating alkylated dithienylbenzothiadiazole for bulk heterojunction solar cells: pronounced effect of positioning alkyl chains. Macromolecules **43**(2), 811–820 (2010)
45. Y.J. Xia, X.Y. Deng, L. Wang, X.Z. Li, X.H. Zhu, Y. Cao, An extremely narrow-band-gap conjugated polymer with heterocyclic backbone and its use in optoelectronic devices. Macromol. Rapid Commun. **27**(15), 1260–1264 (2006)
46. Z. Zhu, D. Waller, R. Gaudiana, M. Morana, D. Muhlbacher, M. Scharber, C. Brabec, Panchromatic conjugated polymers containing alternating donor/acceptor units for photovoltaic applications. Macromolecules **40**(6), 1981–1986 (2007)
47. J.H. Hou, H.Y. Chen, S.Q. Zhang, G. Li, Y. Yang, Synthesis, characterization, and photovoltaic properties of a low band gap polymer based on silole-containing polythiophenes and 2,1,3-benzothiadiazole. J. Am. Chem. Soc. **130**(48), 16144–16145 (2008)
48. R. Yang, R. Tian, J. Yan, Y. Zhang, J. Yang, Q. Hou, W. Yang, C. Zhang, Y. Cao, Deep-red electroluminescent polymers:synthesis and characterization of new low-band-gap conjugated copolymers for light-emitting diodes and photovoltaic devices. Macromolecules **38**(2), 244–253 (2005)
49. J. Luo, Q. Hou, J.W. Chen, Y. Cao, Luminescence and photovoltaic cells of benzoselenadiazole-containing polyfluorenes. Synth. Met. **156**(5–6), 470–475 (2006)
50. W. Zhao, W. Cai, R. Xu, W. Yang, X. Gong, H. Wu, Y. Cao, Novel conjugated alternating copolymer based on 2,7-carbazole and 2,1,3-benzoselenadiazole. Polymer **51**(14), 3196–3202 (2010)
51. L.J. Zhang, C. He, J.W. Chen, P. Yuan, L.A. Huang, C. Zhang, W.Z. Cai, Z.T. Liu, Y. Cao, Bulk-heterojunction solar cells with benzotriazole-based copolymers as electron donors: largely improved photovoltaic parameters by using PFN/A1 bilayer cathode. Macromolecules **43**(23), 9771–9778 (2010)
52. N. Blouin, A. Michaud, M. Leclerc, A low-bandgap poly(2,7-Carbazole) derivative for use in high-performance solar cells. Adv. Mater. **19**(17), 2295–2300 (2007)
53. S.C. Price, A.C. Stuart, L.Q. Yang, H.X. Zhou, W. You, Fluorine substituted conjugated polymer of medium band gap yields 7% efficiency in polymer-fullerene solar cells. J. Am. Chem. Soc. **133**(12), 4625–4631 (2011)
54. B. Peng, A. Najari, B. Liu, P. Berrouard, D. Gendron, Y. He, K. Zhou, Y. Zou, M. Leclerc, A new dithienylbenzotriazole-based poly(2,7-carbazole) for efficient photovoltaics. Macromol. Chem. Phys. **211**(18), 2026–2033 (2010)
55. Z. Zhang, B. Peng, B. Liu, C. Pan, Y. Li, Y. He, K. Zhou, Y. Zou, Copolymers from benzodithiophene and benzotriazole: synthesis and photovoltaic applications. Polym. Chem. **1**(9), 1441–1447 (2010)
56. Y.J. Xia, J. Luo, X.Y. Deng, X.Z. Li, D.Y. Li, X.H. Zhu, W. Yang, Y. Cao, Novel random low-band-gap fluorene-based copolymers for deep red/near infrared light-emitting diodes and bulk heterojunction photovoltaic cells. Macromol. Chem. Phys. **207**(5), 511–520 (2006)

57. Y.J. Xia, L. Wang, X.Y. Deng, D.Y. Li, X.H. Zhu, Y. Cao, Photocurrent response wavelength up to 1.1 mu m from photovoltaic cells based on narrow-band-gap conjugated polymer and fullerene derivative. Appl. Phys. Lett. **89**(8), 081106 (2006)
58. X. Gong, M. Tong, Y. Xia, W. Cai, J.S. Moon, Y. Cao, G. Yu, C.-L. Shieh, B. Nilsson, A. J. Heeger, High-detectivity polymer photodetectors with spectral response from 300 nm to 1450 nm. Science **325**(5948), 1665–1667 (2009)
59. Y. Dong, W.Z. Cai, X.W. Hu, C.M. Zhong, F. Huang, Y. Cao, Synthesis of novel narrow-band-gap copolymers based on [1,2,5] thiadiazolo [3,4-f] benzotriazole and their application in bulk-heterojunction photovoltaic devices. Polymer **53**(7), 1465–1472 (2012)
60. J. Zhang, W.Z. Cai, F. Huang, E.G. Wang, C.M. Zhong, S.J. Liu, M. Wang, C.H. Duan, T.B. Yang, Y. Cao, Synthesis of quinoxaline-based donor-acceptor narrow-band-gap polymers and their cyclized derivatives for bulk-heterojunction polymer solar cell applications. Macromolecules **44**, 894–901 (2011)
61. R.C. Coffin, J. Peet, J. Rogers, G.C. Bazan, Streamlined microwave-assisted preparation of narrow-bandgap conjugated polymers for highperformance bulk heterojunction solar cells. Nat. Chem. **1**, 657–661 (2009)
62. P.-L.T. Boudreault, A. Michaud, M. Leclerc, A new poly (2,7-Dibenzosilole) derivative in polymer solar cells. Macromol. Rapid Commun. **28**(22), 2176–2179 (2007)
63. N. Allard, R.B. Aich, D. Gendron, P.-L.T. Boudreault, C. Tessier, S. Alem, S.-C. Tse, Y. Tao, M. Leclerc, Germafluorenes: new heterocycles for plastic electronics. Macromolecules **43**(5), 2328–2333 (2010)
64. W. Yue, Y. Zhao, S.Y. Shao, H.K. Tian, Z.Y. Xie, Y.H. Geng, F.S. Wang, Novel NIR-absorbing conjugated polymers for efficient polymer solar cells: effect of alkyl chain length on device performance. J. Mater. Chem. **19**(15), 2199–2206 (2009)
65. T.-Y. Chu, J. Lu, S. Beaupre, Y. Zhang, J.-R. Pouliot, S. Wakim, J. Zhou, M. Leclerc, Z. Li, J. Ding, Y. Tao, Bulk heterojunction solar cells using thieno [3,4-c] pyrrole-4,6-dione and Dithieno [3,2-b:2′,3′, d] silole copolymer with a power conversion efficiency of 7.3 %. J. Am. Chem. Soc. **133**(12), 4250–4253 (2011)
66. C.M. Amb, S. Chen, K.R. Graham, J. Subbiah, C.E. Small, F. So, J.R. Reynolds, Dithienogermole as a fused electron donor in bulk heterojunction solar cells. J. Am. Chem. Soc. **133**(26), 10062–10065 (2011)
67. Y. Zhang, J.Y. Zou, H.L. Yip, Y. Sun, J.A. Davies, K.S. Chen, O. Acton, A.K.Y. Jen, Conjugated polymers based on C, Si and N-bridged dithiophene and thienopyrroledione units: synthesis, field-effect transistors and bulk heterojunction polymer solar cells. J. Mater. Chem. **21**(11), 3895–3902 (2011)
68. J.-Y. Wang, S.K. Hau, H.-L. Yip, J.A. Davies, K.-S. Chen, Y. Zhang, Y. Sun, A.K.Y. Jen, Benzobis (silolothiophene)-based low bandgap polymers for efficient polymer solar cells. Chem. Mater. **23**(3), 765–767 (2011)
69. R.S. Ashraf, Z. Chen, D.S. Leem, H. Bronstein, W. Zhang, B. Schroeder, Y. Geerts, J. Smith, S. Watkins, T.D. Anthopoulos, H. Sirringhaus, J.C. de Mello, M. Heeney, I. McCulloch, Silaindacenodithiophene semiconducting polymers for efficient solar cells and high-mobility ambipolar transistors. Chem. Mater. **23**(3), 768–770 (2011)
70. J.E. Donaghey, R.S. Ashraf, Y. Kim, Z.G. Huang, C.B. Nielsen, W. Zhang, B. Schroeder, C. R.G. Grenier, C.T. Brown, P. D'Angelo, J. Smith, S. Watkins, K. Song, T.D. Anthopoulos, J. R. Durrant, C.K. Williams, I. McCulloch, Pyrroloindacenodithiophene containing polymers for organic field effect transistors and organic photovoltaics. J. Mater. Chem. **21**(46), 18744–18752 (2011)
71. H.-Y. Chen, J. Hou, A.E. Hayden, H. Yang, K.N. Houk, Y. Yang, Silicon atom substitution enhances interchain packing in a thiophene-based polymer system. Adv. Mater. **22**(3), 371–375 (2010)
72. M.C. Scharber, M. Koppe, J. Gao, F. Cordella, M.A. Loi, P. Denk, M. Morana, H.-J. Egelhaaf, K. Forberich, G. Dennler, R. Gaudiana, D. Waller, Z. Zhu, X. Shi, C.J. Brabec, Influence of the bridging atom on the performance of a low-bandgap bulk heterojunction solar cell. Adv. Mater. **22**(3), 367–370 (2010)

73. W. Cai, M. Wang, J. Zhang, E. Wang, T. Yang, C. He, J.S. Moon, H. Wu, X. Gong, Y. Cao, Solvent effect leading to high performance of bulk heterojunction polymer solar cells by novel polysilafluorene derivatives. J. Phys. Chem. C **115**(5), 2314–2319 (2011)
74. F. Huang, K.S. Chen, H.L. Yip, S.K. Hau, O. Acton, Y. Zhang, J. Luo, A.K.Y. Jen, Development of new conjugated polymers with donor-π-bridge-acceptor side chains for high performance solar cells. J. Am. Chem. Soc. **131**, 13886–13887 (2009)
75. C.H. Duan, W.Z. Cai, F. Huang, J. Zhang, M. Wang, T.B. Yang, C.M. Zhong, X. Gong, Y. Cao, Novel silafluorene-based conjugated polymers with pendant acceptor groups for high performance solar cells. Macromolecules **43**(12), 5262–5268 (2010)
76. C.H. Duan, K.S. Chen, F. Huang, H.L. Yip, S.J. Liu, J. Zhang, A.K.Y. Jen, Y. Cao, Synthesis, characterization, and photovoltaic properties of carbazole-based two-dimensional conjugated polymers with donor-π-bridge-acceptor side chains. Chem. Mater. **22**(23), 6444–6452 (2010)
77. C.H. Duan, C.D. Wang, S.J. Liu, F. Huang, C.H.W. Choy, Y. Cao, Two-dimensional like conjugated copolymers for high efficiency bulk-heterojunction solar cell application: Band gap and energy level engineering. Sci. China. Chem. **54**, 685–694 (2011)
78. C.H. Duan, W.Z. Cai, C.M. Zhong, Y.H. Li, X.H. Wang, F. Huang, Y. Cao, Bandgap engineering of indenofluorene-based conjugated copolymers with pendant donor-π-acceptor chromophores for photovoltaic applications. J. Polym. Sci., Part A: Polym. Chem. **49**(20), 4406–4415 (2011)
79. C.H. Duan, X.W. Hu, K.S. Chen, H.L. Yip, W. Li, F. Huang, A.K.Y. Jen, Y. Cao, Fully visible-light-harvesting conjugated polymers with pendant donor-π-acceptor chromophores for photovoltaic applications. Sol. Energy Mater. Sol. Cells **97**, 50–58 (2012)
80. Z.G. Zhang, Y.L. Liu, Y. Yang, K.Y. Hou, B. Peng, G.J. Zhao, M.J. Zhang, X. Guo, E.T. Kang, Y.F. Li, Alternating copolymers of carbazole and triphenylamine with conjugated side chain attaching acceptor groups: synthesis and photovoltaic application. Macromolecules **43**, 9376–9383 (2010)
81. S.L. Hsu, C.M. Chen, K.H. Wei, Carbazole-based conjugated polymers incorporating push/pull organic dyes: synthesis, characterization, and photovoltaic applications. J. Polym. Sci. Part A: Polym. Chem. **48**(22), 5126–5134 (2010)
82. D. Sahu, H. Padhy, D. Patra, J.H. Huang, C.W. Chu, H.C. Lin, Synthesis and characterization of novel low-bandgap triphenylamine-based conjugated polymers with main-chain donors and pendent acceptors for organic photovoltaics. J. Polym. Sci. Part A: Polym. Chem. **48**(24), 5812–5823 (2010)
83. H.J. Fan, Z.G. Zhang, Y.F. Li, X.W. Zhan, Copolymers of fluorene and thiophene with conjugated side chain for polymer solar cells: effect of pendant acceptors. J. Polym. Sci. Part A: Polym. Chem. **49**, 1462–1470 (2011)
84. Y.J. Cheng, L.C. Hung, F.Y. Cao, W.S. Kao, C.Y. Chang, C.S. Hsu, Alternating copolymers incorporating cyclopenta [2,1-b:3,4-b0] dithiophene unit and organic dyes for photovoltaic applications. J. Polym. Sci. Part A: Polym. Chem. **49**, 1791–1801 (2011)
85. Z.G. Zhang, H.J. Fan, J. Min, J. Zhang, M.J. Zhang, X. Guo, X.W. Zhan, Y.F. Li, Synthesis and photovoltaic properties of copolymers of carbazole and thiophene with conjugated side chain containing acceptor end groups. Polym. Chem. **2**, 1678–1687 (2011)
86. D.G. Chen, Y. Yang, C. Zhong, Z.R. Yi, F. Wu, L. Qu, Y. Li, Y.F. Li, J.G. Qin, Synthesis and photovoltaic properties of two-dimensional D-A copolymers with conjugated side chains. J. Polym. Sci. Part A: Polym. Chem. **49**(17), 3852–3862 (2011)
87. Z.G. Zhang, Y. Yang, S. Zhang, J. Min, J. Zhang, M.J. Zhang, X. Guo, Y.F. Li, Effect of acceptor substituents on photophysical and photovoltaic properties of triphenylamine–carbazole alternating copolymers. Synth. Met. **161**, 1383–1389 (2011)
88. Z. Gu, P. Tang, B. Zhao, H. Luo, X. Guo, H. Chen, G. Yu, X. Liu, P. Shen, S. Tan, Synthesis and photovoltaic properties of copolymers based on benzo [1,2-b:4,5-b′] dithiophene and thiophene with different conjugated side groups. Macromolecules **45**(5), 2359–2366 (2012)

89. C.J. Brabec, A. Cravino, D. Meissner, N.S. Sariciftci, T. Fromherz, M.T. Rispens, L. Sanchez, J.C. Hummelen, Origin of the open circuit voltage of plastic solar cells. Adv. Funct. Mater. **11**(5), 374–380 (2001)
90. I.H. Campbell, S. Rubin, T.A. Zawodzinski, J.D. Kress, R.L. Martin, D.L. Smith, N.N. Barashkov, J.P. Ferraris, Controlling Schottky energy barriers in organic electronic devices using self-assembled monolayers. Phys Rev B **54**(20), R14321–R14324 (1996)
91. P. Peumans, V. Bulovic, S.R. Forrest, Efficient photon harvesting at high optical intensities in ultrathin organic double-heterostructure photovoltaic diodes. Appl. Phys. Lett. **76**(19), 2650–2652 (2000)
92. M. Boman, S. Stafström, J.L. Brédas, Theoretical investigations of the aluminum/polythiophene interface. J. Chem. Phys. **97**, 9144–9153 (1992)
93. F. Zhang, M. Ceder, O. Inganäs, Enhancing the photovoltage of polymer solar cells by using a modified cathode. Adv. Mater. **19**(14), 1835–1838 (2007)
94. J. Luo, H.B. Wu, C. He, A.Y. Li, W. Yang, Y. Cao, Enhanced open-circuit voltage in polymer solar cells. Appl. Phys. Lett. **95**(4), 043301 (2009)
95. S.-I. Na, S.-H. Oh, S.-S. Kim, D.-Y. Kim, Efficient organic solar cells with polyfluorene derivatives as a cathode interfacial layer. Org. Electron. **10**(3), 496–500 (2009)
96. Y. Zhao, Z. Xie, C. Qin, Y. Qu, Y. Geng, L. Wang, Enhanced charge collection in polymer photovoltaic cells by using an ethanol-soluble conjugated polyfluorene as cathode buffer layer. Sol. Energy Mater. Sol. Cells **93**(5), 604–608 (2009)
97. C.M. Zhong, C.H. Duan, F. Huang, H.B. Wu, Y. Cao, Materials and devices toward fully solution processable organic light-emitting diodes. Chem. Mater. **23**(3), 326–340 (2011)
98. C.V. Hoven, A. Garcia, G.C. Bazan, T.-Q. Nguyen, Recent applications of conjugated polyelectrolytes in optoelectronic devices. Adv. Mater. **20**(20), 3793–3810 (2008)
99. C. He, C.M. Zhong, H.B. Wu, R.Q. Yang, W. Yang, F. Huang, G.C. Bazan, Y. Cao, Origin of the enhanced open-circuit voltage in polymer solar cells via interfacial modification using conjugated polyelectrolytes. J. Mater. Chem. **20**(13), 2617–2622 (2010)
100. X.F. Xu, B. Han, J.W. Chen, J.B. Peng, H.B. Wu, Y. Cao, 2,7-carbazole-1,4-phenylene copolymers with polar side chains for cathode modifications in polymer light-emitting diodes. Macromolecules **44**(11), 4204–4212 (2011)
101. X.F. Xu, W.Z. Cai, J.W. Chen, Y. Cao, Conjugated polyelectrolytes and neutral polymers with Poly(2,7-carbazole) backbone: synthesis, characterization, and photovoltaic application. J. Polym. Sci. Part A: Polym. Chem. **49**(5), 1263–1272 (2011)
102. X. Guan, K. Zhang, F. Huang, G.C. Bazan, Y. Cao, Amino N-oxide functionalized conjugated polymers and their amino-functionalized precursors: new cathode interlayers for high-performance optoelectronic devices. Adv. Funct. Mater. **22**, 2846−2854 (2012)
103. M.P. de Jong, van van IJzendoorn, L.J. de Voigt, Stability of the interface between indium-tin oxide and poly (3,4-ethylenedioxythiophene)/poly(styrenesulphonate) in polymer light-emitting diodes. Appl. Phys. Lett. **77**, 2255−2257 (2000)
104. M.S. White, D.C. Olson, S.E. Shaheen, N. Kopidakis, D.S. Ginley, Inverted bulk-heterojunction organic photovoltaic device using a solution-derived ZnO underlayer. Appl. Phys. Lett. **89**(14), 143517 (2006)
105. C. Waldauf, M. Morana, P. Denk, P. Schilinsky, K. Coakley, S.A. Choulis, C.J. Brabec, Highly efficient inverted organic photovoltaics using solution based titanium oxide as electron selective contact. Appl. Phys. Lett. **89**(23), 233517 (2006)
106. L.-L. Chua, J. Zaumseil, J.-F. Chang, E.C.W. Ou, P.K.H. Ho, H. Sirringhaus, R.H. Friend, General observation of n-type field-effect behaviour in organic semiconductors. Nature **434** (7030), 194–199 (2005)
107. Y. Zhu, X. Xu, L. Zhang, J. Chen, Y. Cao, High efficiency inverted polymeric bulk-heterojunction solar cells with hydrophilic conjugated polymers as cathode interlayer on ITO. Sol. Energy Mater. Sol. Cells **97**, 83–88 (2012)

108. X.F. Xu, Y.X. Zhu, L.J. Zhang, J.M. Sun, J. Huang, J.W. Chen, Y. Cao, Hydrophilic poly (triphenylamines) with phosphonate groups on the side chains: synthesis and photovoltaic applications. J. Mater. Chem. **22**(10), 4329–4336 (2012)
109. C.H. Duan, C.M. Zhong, C.C. Liu, F. Huang, Y. Cao, Highly efficient inverted polymer solar cells based on an alcohol soluble fullerene derivative interfacial modification material. Chem. Mater. **24**(9), 1682–1689 (2012)

Chapter 7
Fullerene and Its Derivatives for Organic Solar Cells

Fulvio G. Brunetti

Abstract We describe in detail the features and characteristics of fullerene and its derivatives, specifically as acceptors in the field of bulk heterojunction solar cells. Examples of alterations on the PCBM structure are schematically presented, examining the effects of these modifications on device performance. Additionally, we discuss alternatively functionalized fullerenes, including the emerging bis-adduct derivatives.

7.1 Introduction

7.1.1 A Historical Background

Up to the second half of the last century, "Plastics" were synonymous with insulators, commonly employed to wrap metal cables in order to avoid short-circuits. This was due to the common belief in the scientific community which considered inorganic metals the only possible conductive material. In 1954, the concept of organic semiconductors was introduced for the first time when a perylene-bromine complex with an electrical conductivity of *ca.* 1×10^{-3} ohm^{-1} cm^{-1} was described [1]. Earlier in 1862, Letheby [2] produced a "blue substance" by anodic oxidation of aniline hydrogen sulfate that, depending on its oxidation state [3] and degree of protonation [4], has demonstrated to be a conductive material. Organic compounds with semiconducting properties were subsequently obtained starting from melanins [5], pyrroles [6], and acetylene [7]. It turned out that all these "unusual" molecules with high molecular weight were polymers with π-conjugated systems. These polymers attracted the attention of Shirakawa, MacDiarmid, and Heeger, leading to the 2,000 Nobel Prize in chemistry. Particularly, the redox treatment of polyacet-

F.G. Brunetti (✉)
Department of Chemistry and Biochemistry, University of California Santa Barbara, Santa Barbara, CA 93106, USA
e-mail: fulvio.giacomobrunettti@gmail.com

Y. Yang and G. Li (eds.), *Progress in High-Efficient Solution Process Organic Photovoltaic Devices*, Topics in Applied Physics 130,
DOI 10.1007/978-3-662-45509-8_7

ylene with halogens generated a conductivity of 10^5 Sm^{-1} [8, 9], very similar to that of metals, such as lead and titanium (10^6 Sm^{-1}). This process was called "doping" due to the analogy in conductivity changes of the doping of inorganic semiconductors.

As a consequence of these discoveries, conductive organic systems stimulated physicists to adopted these materials for solar energy conversion in an effort to mimic the natural photosynthetic process [10]. In these pioneering studies, devices based on pure semi-conducting molecules and polymers demonstrated a very inefficient photocurrent generation [11, 12].

In fact, photovoltage and photocurrent was detected exclusively by adopting a unique composition of the active layer which is based on a donor and accepting material, fine-mixed together and sandwiched in between two electrodes. This specific two-component architecture is commonly denoted as donor-acceptor bulk heterojunction (BHJ) solar cell [13].

7.1.2 BHJ: A General Overview

BHJ cells have been demonstrated to be a successful architecture for the conversion of absorbed light into current, representing a landmark for the development of this growing technology. Remarkably, in less than two decades, the performance of BHJs has been constantly increasing and the latest outlook marks a world record efficiency of 10.1 % from Mitsubishi Chemical [14]. Moreover, predictions in this field have announced a possible 15 % sunlight conversion in the near future [15]. In addition, the inexpensive cost of production and the possibility of using low-temperature printing technology, similar to that employed for newsprint, render plastic solar cells a promising solution for the increasing energy demand [16].

Since pure organic semiconducting materials are not sufficient for sunlight conversion, an additional component is required for exciton dissociation. Specifically, BHJ, schematically represented in Fig. 7.1, consists in a fine interpenetrating phase-separated network of a donor, usually a semiconducting polymer, though small molecule donors have made important inroads with 7 % efficiency [17], together with an acceptor, a fullerene derivative.

Due to the light-harvesting capability of the semiconducting polymer, an excited donor is generated upon sunlight absorption (D*). The exciton (D*) diffuses at the hetorinterface, interacts with the accepting component and forms a donor acceptor complex (D-A)*, minimizing its energy. The formed complex (D-A)* can (i) relax back to the original ground state or (ii) dissociate with formation of free charges. In case of the photoexcitation decay to the ground state (i), a thermal, non-radiative or radiative process may occur. On the other hand, the dissociation of the exciton (ii) generates an ion radical pair that eventually leaves a whole (radical cation) in the donor and an electron (radical anion) in the acceptor. Finally, charges migrate to and are collected at the corresponding electrodes, resulting in a flow of current [18].

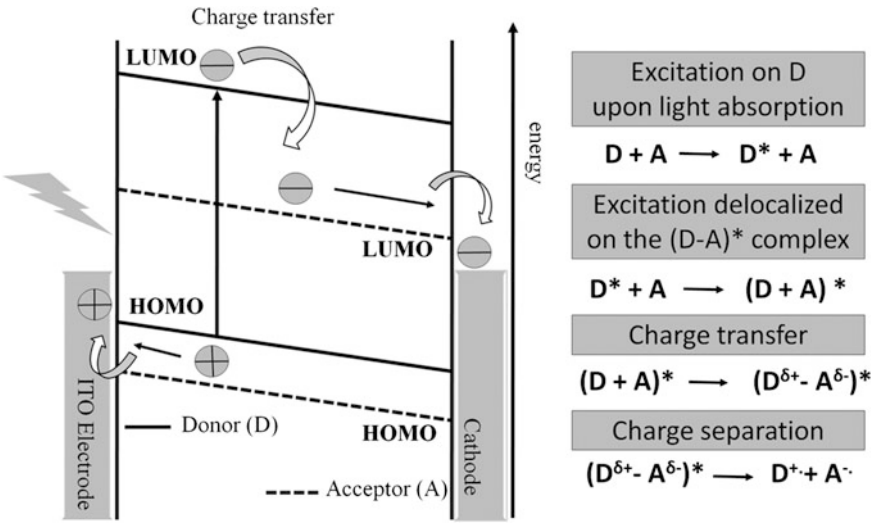

Fig. 7.1 Schematic of the charge transfer process in a bulk heterojunction solar cell

As mentioned in the description of the BHJ active layer, the combined effect of a donor with an accepting component is the cornerstone requirement for exciton dissociation during the charge transfer process. Hence, in this chapter, an exhaustive description of acceptors and their performances in OPVs is presented, emphasizing the efforts to improve the device efficiencies for large-scale solar cell production [19].

7.1.3 Electron Accepting Components in BHJ

To date, the most widely used accepting component in plastic solar cells is buckminsterfullerene and its functionalized derivatives [20]. Since the 1985 discovery [21] with a 1996 Nobel prize, fullerenes are considered the third allotrope form of carbon and have acquired interest in many fields of science that range from bio applications to molecular electronics [13, 22, 23].

Surprisingly, the discovery of fullerenes was accidental. In an effort to clarify the mechanism of formation of long-chain carbon molecules in interstellar space, a stable cluster of carbon atoms was produced and detected by evaporating graphite into a high-density helium flow under laser irradiation [24]. Optimization of experimental conditions led to a selective cluster distribution of C_{60} accompanied by a small percentage of a higher species, C_{70}.

Several authors attributed to buckminsterfullerene C_{60} the "unusually beautiful" structure of a soccer ball where the 60 vertices are replaced by carbon atoms and the symmetry belongs to the truncated icosahedral group [25]. More specifically, this

"soccerball" presents a diameter of *ca.* 7 nm (*ca.* 1 Å including van der Waals diameter) and is composed of 32 faces arranged in 12 pentagons and 20 hexagons of sp^2 hybridized carbons. Initially, fullerene was described as aromatic with inner and outer surfaces covered with a sea of π electrons, resulting in a stable spherical-shaped molecule. It would appear that, this carbonaceous cluster should be inert and difficult to functionalize, resembling the reactivity of graphite. However, experimental evidence revealed that fullerenes have a considerable propensity to react with radicals, halogens, dipoles, and nucleophiles [26, 27]. The "facile" reactivity of fullerenes is rationalized when considering their unique spherical shape. In general, sp^2 orbitals are trigonal planar and they minimize their energy when lying in a plane with an angle of 120°. Nevertheless, fullerene sp^2 orbitals are forced to be curved in order to confer the spherical shape, generating an angle strain [28]. Due to these angle tensions, fullerenes are electrophiles and dienophiles and, consequently, they can be "easily" functionalized by addition reactions [29]. On top of that, the "strained" sp^2 orbitals confer not only a certain grade of reactivity but, more importantly, unique physical and optoelectronic properties [28, 30, 31] Remarkably, fullerene and its derivatives are species that can generate stable radical anions, taking on as many as 6 electrons, reversibly [32]. In fact, the addition of an electron in the buckminsterfullerene cage relieves the angle strain of the sp^2 hybridized orbitals, conferring a higher sp^3 character. Therefore, orbitals rearrange in a 3D tetrahedral orientation that reduces their energy and stabilizes the radical anion. Moreover, its stability allows the charge transfer to take place with a quantum efficiency close to unit, and reduces the back electron transfer or recombination processes [13]. Additionally, the spherical 3D shape facilitates the migration of the charges through the fullerene layer and their collection at the proper electrode.

Thanks to these peculiar features, fullerenes promptly demonstrated a promising electron accepting behavior in the field of plastic solar cells. Because of their success, they are considered a milestone in OPV and have been continuously contributing to the improvement of power conversion efficiency (PCE) [33, 34].

7.2 The Advent of PCBM

Just after the discovery of the photoinduced electron transfer from a semiconducting polymer to fullerene, pure C_{60} was replaced by a more soluble phenyl-C_{61}–, denoted as [6] $PC_{60}BM$ [35]. In fact, in the pioneering work of F. Wudl and A. J. Heeger poly(2-methoxy-5-(2'-ethyl-hexyloxy)-1,4-phenylene vinylene (MEH-PPV) and pristine C_{60} were initially employed to detect the electron transfer from the exited state of MEH-PPV onto buckminsterfullerene [13]. Afterwards, in 1995, the methano PCBM fullerene derivative has been widely employed as the accepting component for the so-called BHJs. The main reason behind the choice of a functionalized derivative is not only the enhanced solubility that allows the casting of a blend containing up to 80 % of fullerene but, more importantly, the possibility of

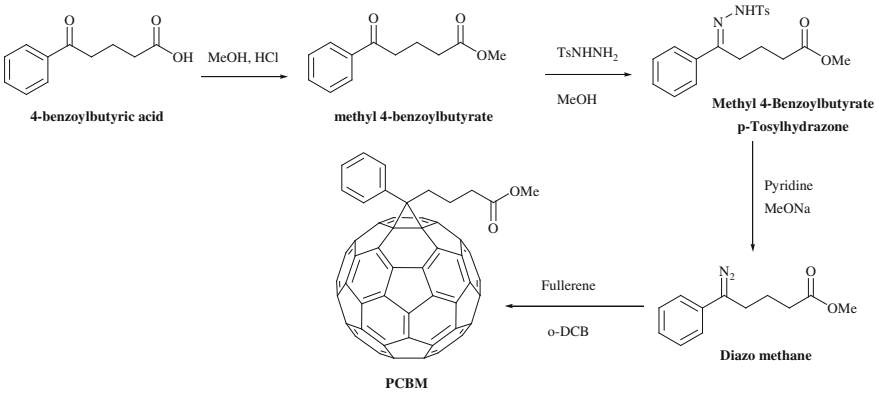

Scheme 7.1 Synthesis of PCBM

inserting functional groups that can tune the photophysical properties. Obviously, functionalized fullerenes lose their pristine electronic shell since addition reactions employ an electron pair for the formation of the new bonds. However, the functionalization opens the possibility of inserting a plethora of different electron withdrawing and donor groups with direct influence on the location of the HOMO-LUMO levels and the optical absorption. These groups can also increase the solubility or induce an ordered morphology [36, 37]. Additionally, considering the donor counterpart, a tunable acceptor can easily fit the energy requirements of numerous polymers [38].

The use of PCBM instead of pristine fullerene can be considered the first example of improvement of photocurrent efficiency. Due to its outstanding performance, numerous attempts have been made to tune and modulate the electronic properties of this acceptor by modifying the phenyl butyric acid methyl ester PCBM functionality. Even though the discovery of a more efficient derivative, ICBA [39], synthesized only at beginning of 2010, PCBM has been demonstrated to be a versatile acceptor, capable of making efficient devices with countless polymeric materials. To date, due to its success and commercial availability, PCBM is still considered "the standard" to evaluate the performance of new acceptors, donor polymers and, more importantly, in fundamental devices studies including morphology, physical treatments and in general wherever a control device is required. The synthesis of PCBM, described by Hummelen et al. [35] is depicted in Scheme 7.1.

Commercial 4-benzoylbutyric acid was esterified in methanol in the presence of a catalytic amount of inorganic acid and the resulting methyl ester was treated with tosylhydrazine in refluxing toluene to yield methyl 4-benzoylbutyrate tosylhydrazone. The diazo derivative was finally added onto the fullerene cage by oxidation of the corresponding tosylhydrazone in pyridine and MeONa.

Analogously, the corresponding donor material that is usually employed to test a device is the poly(3-hexyl-thiophene) P3HT. It is a valid reference for the numerous low band-gap polymers that are continuously synthesized in an effort to harvest more photons from sunlight. Similar to PCBM, P3HT is the common semiconducting polymer when testing new acceptors [40, 41]. Indeed, P3HT was the donor counterpart employed with ICBA, an experiment described in detail below [39].

7.2.1 PCBM: Structural Changes

Due to the success of PCBM that has persisted for almost two decades, its structure has been carefully engineered in an effort to improve device efficiency. In fact, PCBM offers several moieties to be modified in order to vary either its chemical or optoelectronic properties, such as solubility, self-assembling, absorption, LUMO HOMO levels, etc. Hence, when examining the PCBM structure (Fig. 7.2), different sites of the molecule can be modified and functionalized for the insertion or substitution of a variety of functional groups. Its phenyl group is open to substitution reactions in *orto*, *meta* and *para* positions. Moreover, the aromatic ring itself can be replaced by a thiophene, furan or fluorene rings. The phenyl butyric methyl ester functionality is inserted onto the fullerene cage by a cyclopropane methano bridge. Therefore, the methano carbon atom of the cyclopropane bridge is another possible site of modification. Additionally, PCBM has an ester group that has been modified with numerous alcohol derivatives. Even the alkyl chain in between the ester and the methano bridge has been varied in length. Due to the numerous examples, the following paragraphs provide a description of the most representative modifications on the PCBM structure and their influence on photovoltaic performance.

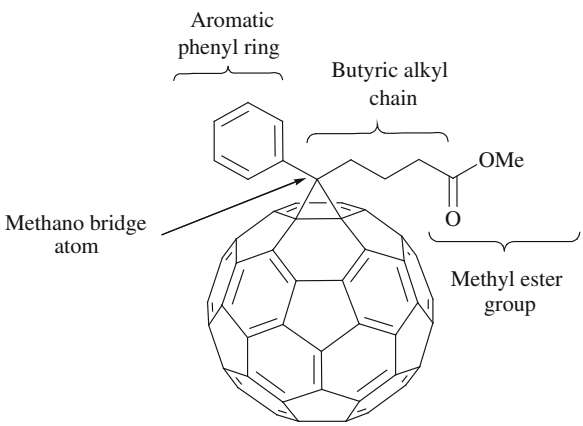

Fig. 7.2 Alterations on the PCBM structure

7.2.2 PCBM: Substitutions on the Aromatic Phenyl Ring

Protons of the phenyl ring have been mono and multi substituted, at different positions, by alkoxy, methylenedioxy, thiomethyl groups, and fluoro atoms. Structures of this compilation of PCBM derivatives, reported by Hummelen and co-workers [42], are represented in Chart 7.1 (left). The aim of this work was to demonstrate the effect of the substituent in *orto* and *para* positions on the LUMO energy levels. The substituent in *orto* should facilitate the electronic overlap through the space of the oxygen or sulfur lone pair with the fullerene π-system, whereas the functionality in *para* should interact by resonance through the phenyl ring. The presence of two resonance peaks around 80 ppm in the carbon NMR corroborates a hindered rotation of the phenyl ring which results in the horizontal orientation of the phenyl ring with respect to the fullerene surface. However, the only effect on the LUMO was observed in the case of a combined effect of three methoxy groups, interacting though resonance. Particularly, derivative 2,4,6-OMe-PCBM presented a LUMO 86 mV higher than the unsubstituted PCBM due to the joined effect of the three methoxy groups though the benzene ring. A single substituent reduced the potential of only a few mV (*ca.* 7–8 mV) regardless of its position.

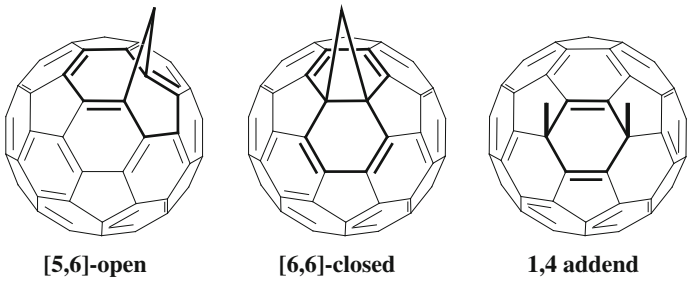

Fig. 7.3 Open [5,6], closed [6,6] fullerene structures and 1,4 addends

Fig. 7.4 Bis-adduct isomers

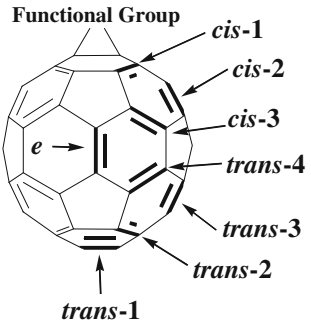

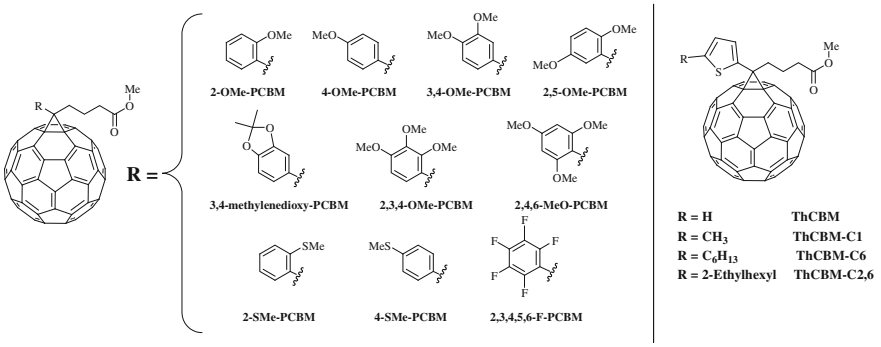

Chart 7.1 Phenyl modified PCBMs (*left*) and ThCBM (*right*) derivatives

Contrary to methoxy, a methyl thioether group did not raise the LUMO energy, demonstrating no effects either through space or resonance, while the pentafluoro derivative rendered 2,3,4,5,6-F-PCBM a better acceptor which resulted in a lowered LUMO. Solar cells were fabricated adopting the following architecture ITO/PEDOT/(MDMO-PPV:PCBMs)/LiF/Al and *o*-dichlorobenzene as the casting solvent. As expected, the V_{oc} (open circuit voltage) of these polymer-fullerene solar cells increased when a PCBM derivative with raised LUMO was employed, demonstrating the possibility of fabricating solar cells with an enhanced open circuit voltage. A *quasi*-linear correlation between LUMO energy levels and open circuit voltages has been reported but, to the best of our knowledge, the authors did not discuss the PCE of the entire compilation of PCBM derivatives.

With the aim of facilitating the interaction of the acceptor with P3HT, thienyl and alkyl substituted [6,6] -thienyl-C_{61}-butyric acid methyl esters, ThCBM, were synthesized as PCBM analogs by replacing the phenyl ring with a thienyl unit (Chart 7.1 right) [43, 44]. Charge transportation and electrochemistry properties were not affected by the substitution of the benzene ring with a thienyl moiety. In fact, a charge carrier mobility of 1.8 (± 0.8) 10^{-3} cm^2 V^{-1} s^{-1} was measured which is comparable to that of PCBM [45]. A solution of 1:1 w/w of ThCBM and P3HT in *o*-dichlorobenezene was employed for the active layer deposition. The as-cast solar cell performed poorly in terms of efficiency (η = 0.3 %, J_{sc} = 14.35 A/m^2, V_{oc} = 0.59 V). However, after a thermal annealing treatment at 140 °C for 4 min, efficiency improved to ca. 3 %, due to an impressive enhancement of the fill factor from 36.5 to 61.4 %. AFM photographs revealed a higher degree of de-mixing of the two components together with an enhancement of the P3HT crystallinity upon thermal treatment.

In 2010, 4 years after the first description of the ThCBM, *alpha* alkyl substituted analogues, referred to as ThCBM-C*n*, have been considered for their use in OPV. For comparison, PCBM and unsubstituted ThCBM were also tested again to guarantee the same experimental conditions. The only difference with the previous work on ThCBM is the casting solvent and the thermal treatment. In this more

Table 7.1 Examining the data

Compound	[a]Solubility (mg ml^{-1})	[b]LUMO (eV)	[c]J_{sc} (mA cm^{-2})	[c]V_{oc} (V)	[c]FF (%)	[c]PCE (%)
PCBM	80	−3.75	10.40	0.62	0.61	3.90
ThCBM	50	−3.76	10.33	0.62	0.62	4.00
ThCBM-C1	50	−3.77	10.51	0.60	0.63	3.95
ThCBM-C6	180	−3.77	10.61	0.63	0.64	4.26
ThCBM-C2,6	180	−3.77	10.53	0.64	0.57	3.84

[a] In chlorobenzene

[b] Bu_4NPF_6, DCM, 100 mV s^{-1}

[c] device schematization: ITO/PEDOT:PSS/P3HT:PCBM or ThCBM-Cn in (1: 0,8, w/w) LiF/Al, annealed at 160 °C for 10 min in the glove box

recent work, chlorobenzene was utilized for the active layer casting instead of o-dichlorobenzene. However, similar values of PCE for both PCBM and ThCBM were achieved analogously to the previous work of Hummelen end co-workers that differ only in absolute value [43].

When examining the data in Table 7.1, ThCBM-C6 bearing hexyl chain clearly outperformed the efficiency of PCBM- and unsubstituted ThCBM- based devices. It is probably an intrinsic feature of the hexyl chain that positively maximizes the interactions between the ThCBM-C6 and the P3HT in the active layer. ThCBM-C6 also gave the best values in terms of short circuit current and fill factor, and, consequently, PCE. The authors attributed its success to the high solubility, however, a non-covalent interaction of the hexyl thiophene units in the active layer, may be responsible and may have oriented the two photoactive components, inducing a particular beneficial morphology.

Similar to the case of the ThCBM analogues, other parameters must be considered when designing new acceptors [46]. An induced assembling or a controlled morphology among two active components can result in better charge transport and improved fill factor. Phase separation upon annealing represents an additional issue that can dramatically affect the surface topology, and ensuing charge migration. In order to suppress this destructive segregation due to increased crystallinity, disorder was intentionally induced in the active layer by adding additives [47] or block copolymers [48]. Alternatively, an amorphous functional group can be inserted directly in the acceptor structure. A compelling example is the synthesis of a triphenyl (TPA-PCBM) and a methyl fluorene (MF-PCBM) derivative that reduced the crystallinity of the PCBM structure (Chart 7.2) [49].

Contrary to the PCBM, which exhibits a crystallization peak at 295 °C, differential scanning calorimetry analysis of TPA-PCBM and MF-PCBM derivatives did not show crystallization transitions around 300 °C. On the other hand, due to the insertion of bulkier triphenyl amine group and the fluorene unit, a glass transition at 170 and 180 °C were observed for TPA-PCBM and MF-PCBM, respectively. Electron-transport properties were investigated by fabricating n-channel field-effect transistor, revealing field effect mobilities of 1.6×10^{-2}, 1.1×10^{-2} and 5.4×10^{-3} cm^2 V^{-1} s^{-1} in the case of PCBM, TPA-PCBM, and MF-PCBM,

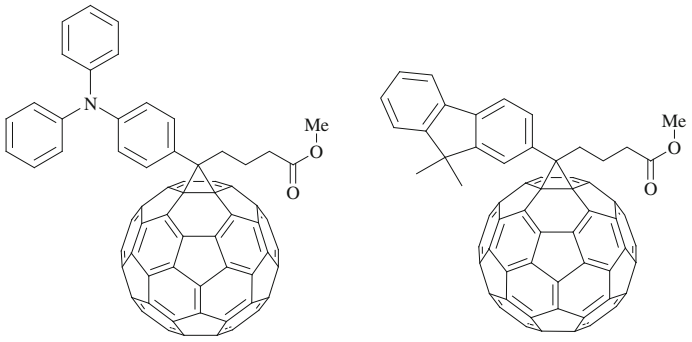

TPA-PCBM **MF-PCBM**

Chart 7.2 TPA-PCBM and MF-PCBM derivatives

Table 7.2 PCBM-control device dropped its efficiency

Compound	[a]J_{sc} (mA cm^{-2})	[a]V_{oc} (V)	[a]FF (%)	[a]PCE (%)	[b]PCE (%)	[c]Mobilities (cm^2 V^{-1} s^{-1})
PCBM	10.4	0.63	64	4.2	1.8	1.6 10^{-2}
TPA-PCBM	9.9	0.65	62	4.0	4.0	1.1 10^{-2}
MF-PCBM	9.8	0.65	59	3.8	3.8	5.4 10^{-3}

[a] Inverted device schematization: ITO/ZnO/C60-SAM/P3HT:PCBMs derivatives/PEDOT:PSS/Ag in (1:0,7, w/w), annealed at 150 °C for 10–30 min in the glove box
[b] After annealing 150 °C, 10 h
[c] *n*-channel OFET

respectively. Although TPA-PCBM and MF-PCBM derivatives exhibit higher LUMO energies than PCBM, the open circuit voltage was only slightly higher than the control device while the efficiencies remained comparable. Interestingly, the performances of TPA-PCBM- and MF-PCBM- based devices remained constant even after 10 h of heating at 150 °C. On the contrary, the PCBM-control device dropped its efficiency from 4.2 to 1.8 % as listed in Table 7.2.

A destructive phase segregation was observed employing optical microscopy. An evident crystallization was accompanied by a more pronounced absorption of P3HT at 510, 550 and 600 nm and a decreased intensity of PCBM's absorption peak at 355 nm. These changes in absorption are in agreement with a π-π stacking of P3HT chains and an enhanced segregation of PCBM [50].

7.2.3 Modifications on the PCBM Alkyl Chain

Li and co-workers [51] have investigated the effect on the device performance by varying the length of the butyl alkyl chain of the PCBM. The alkyl chain ranges from the smallest propionic derivative, to the largest enanthic ester. In other words,

Table 7.3 Optoelectronic properties, together with device efficiencies

blend	[a]V_{oc} (V)	[a]J_{sc} (mA cm^{-2})	[a]FF (%)	[a]PCE (%)	[b]Mobilities (cm^2 V^{-1} s$^{-1)}$	[c]AFM film roughness	[d]Intensity absorption (a.u.)
P3HT/F1	0.564	10.8	60.3	3.7	2.2 10^{-3}	9.2	1
P3HT/F2	0.571	9.6	64.6	3.5	1.3 10^{-3}	15.8	3
P3HT/F3	0.535	8.1	53.2	2.3	8.4 10^{-5}	23.3	5
P3HT/F4	0.596	9.9	61.5	3.6	3.9 10^{-4}	14.2	2
P3HT/F5	0.540	9.3	56.4	2.8	2.8 10^{-4}	13.6	4

[a] Device schematization: ITO/PEDOT:PSS/P3HT:F1-F5 (1:1, w/w) Ca/Al, *o*-DCB
[b] Electron mobilities of P3HT/F1-F5 blends
[c] Surface root-mean-square of P3HT/F1-F5 blends (1:1 w/w) d) 1 is the most absorbing blend and 5 the less

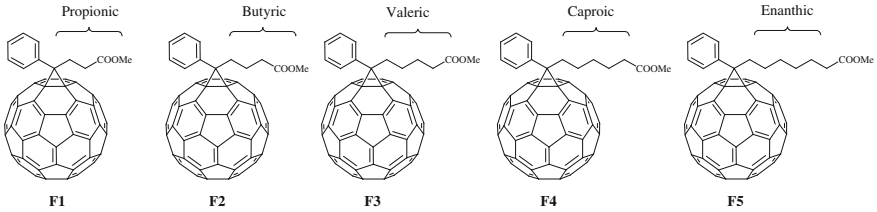

Chart 7.3 Structure of F1-F5 PCBM derivatives

the chain length varied from 3 to 7 carbon atoms, including the butyric acid methyl ester PCBM parent compound. Optoelectronic properties, together with device efficiencies, are summarized in Table 7.3 (Chart 7.3).

It appears from the Table above that efficiency can substantially drop by inserting or removing a methylene group in the butyl chain. The blend of the propionic PCBM-like derivative F1 demonstrated a better mobility and the highest short circuit current that also resulted in the more intense UV-Vis absorption. The morphology studies revealed that the P3HT/F1 blend gave the smoothest active film that is probably somehow correlated with the nanostructure of the active layer. On the contrary, F3 showed the lowest absorption intensity, the roughest film, and the lowest conductivity with only a 2.3 % efficiency. Interestingly, the authors demonstrated how a small variation in the chain length of just a methylene unit can dramatically affect the performance of the OPV devices and its related parameters. These variations were correlated to the film nanostructure that clearly influenced the active layer performance.

7.2.4 Modifications on the Ester Functional Group

From a synthetic point of view, ester groups are one of the most versatile functionalities that can be easily hydrolyzed, transesterified, amidated or used in Friedel Craft reactions upon the conversion to an acyl chloride. Therefore, it is expected

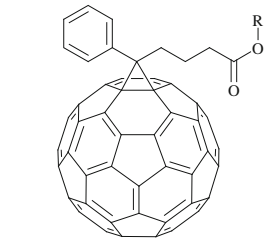

R = Methyl PCBM
R = Butyl PCBB
R = 1-(methyl)-heptyl PCBMH
R = octyl PCBO
R = dodecyl PCBD
R = cetyl PCBC

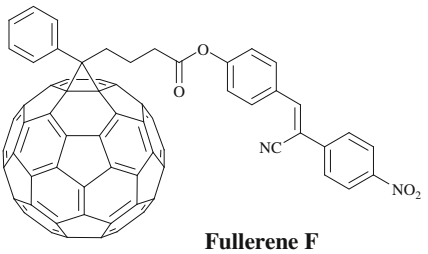

Fullerene F

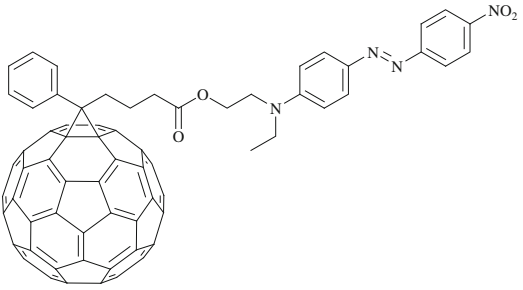

PCBDR

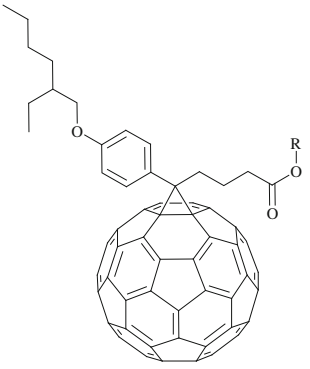

R = Me *p*-EHO-PCBM
R = H *p*-EHO-PCBA

Chart 7.4 PCBM ester analogues

that the methyl ester of the PCBM would be converted to several PCBM ester analogues. In this paragraph, some examples of altered PCBM esters are presented and the effects on the performance are correlated to the modifications of the ester group.

Cao and co-workers [52] have synthesized a family of corresponding alkyl PCBM esters, butyl (PCBB), 1-(methyl)-heptyl (PCBMH), octyl (PCBO), dodecyl (PCBD) and cetyl (PCBC), aimed to the possibility of facilitating interfacial contacts at the interface and, consequently, improving device characteristics.

Among these different alkyl esters (Chart 7.4, top left), [6,6]-phenyl C61-butyric acid butyl ester, PCBC, slightly outperformed the PCBM control device with a power conversion efficiency of 2.45 and 2.00 %, respectively. The structure of the devices is schematically represented as follows: ITO/PEDOT:PSS/MEH-PPV : PCBM esters/Ba/Al in the ratio of 1 : 4 w/w. PCBB based device was optimized by varying the polymer-acceptor weight ratio. The highest conversion was obtained when a high content of fullerene (32 to 1) was utilized, pushing the PCE to 2.84 %. With regard to the other ester analogues, a longer ester alkyl chain lowered the photosensitivity although a uniform blend was observed by AFM analysis. In fact, a

longer chain is responsible for a reduced conductivity since it tends to isolate fullerene units and, therefore, prevents the charge migration process.

Solubility, blend morphology, and microstructures represent just a few factors to be considered when designing new materials for OPV. However, since our source of photons comes from sunlight, which posses a wide range of wavelengths, absorption capability of the blend should match as much as possible solar radiation.

A wide and intense absorption at longer wavelength allows the device to harvest a larger number of photons that can be potentially converted into electricity. In terms of optical absorption, fullerenes have a weak absorption in the visible due to their high degree of symmetry. In fact, longer wavelength transitions are formally forbidden, however, this limitation can be overcome by inserting a visible light sensitizer in the functional group. Following this strategy, the intensity absorption of PCBM has been remarkably and easily increased by modifying the methyl ester with chromophores. Two recent and compelling examples of PCBM with enhanced visible absorption have been described by Sharma [53] and Wudl [54] (Chart 7.4, Fullerene F and PCBDR). Sharma and co-workers linked 4-nitro-4′-hydroxy-α-cyanostilbene (NHCS) to PCBM, increasing the absorption coefficient in the range of wavelengths of 380–500 nm to 5.3×10^{-4} M^{-1} cm^{-1} and 2.5×10^{-4} M^{-1} cm^{-1}, respectively, against 2.4×10^{-4} M^{-1} cm^{-1} and 1.2×10^{-4} M^{-1} cm^{-1} in the case of PCBM.

Surprisingly, a 0.20 eV higher LUMO (LUMO of fullerene F is -3.75 eV) was electrochemically obtained which is inconsistent with the addition of an electron withdrawing group that usually lowers the LUMO energy level. Additionally, the cyclic voltammograms of either PCBM or fullerene F, revealed uncommonly broad reduction waves. The authors did not discuss the electrochemical behavior or provide any explanation for the raised LUMO.

Despite these fundamental contradictions, a significantly high power conversion efficiency of 5.25 % was claimed after a thermal treatment at 120 °C. Chloroform and chloroform/acetone were used for the blend solution (Table 7.4). Clearly, in view of the mentioned contradictions, this work needs to be reproduced in a different laboratory.

Table 7.4 Chloroform and chloroform/acetone were used for the blend solution

Material	[a]V_{oc} (V)	[a]J_{sc} (mA cm^{-2})	[a]FF (%)	[a]PCE (%)	[b]Mobilities (cm^2 V^{-1} s^{-1})	[c]Mobilities (cm^2 V^{-1} s^{-1})
P3HT/PCBM	0.68	8.0	54	2.93	–	–
P3HT/F[d]	0.86	8.5	58	4.23	3.5×10^{-5}	9.6×10^{-6}
P3HT/F[e]	0.82	9.4	60	4.62	7.4×10^{-4}	6.4×10^{-4}
P3HT/F[f]	0.81	10.3	63	5.25	1.13×10^{-3}	1.2×10^{-3}

[a] Device schematization: ITO/PEDOT:PSS/P3HT:PCBM or F (1:1, w/w) Al
[b] Electron mobilities of P3HT/Fullerene F blends
[c] Hole mobilities of P3HT/Fullerene F blends
[d] Chloroform as cast solvent
[e] Chloroform/acetone as cast solvent
[f] Chloroform/acetone as cast solvent and thermal annealed at 120 °C

A conceptually similar example concerns PCBDR, a PCBM dyad that absorbs in the range of 400-660 nm. PCBDR was obtained by inserting disperse-red (DR) as the sensitizer ester unit. Disperse-red 1 is a commercially available dye containing an aminoazobenzene push-pull system that confers to PCBM a higher intensity absorption in the visible. Aminoazobenzene molecules have been extensively studied due to their photochemical and thermal trans-cis isomerization. Particularly, in these molecules, n–π* and π–π* bands overlap and the Z state isomerizes back quickly, with lifetimes on the order of milliseconds in solution that can last a few seconds in polymer blend [55].

The performance of this dyad in solar cells was tested, employing the following device architecture ITO/PEDOT:PSS/P3HT:PCBDR (1:1, w/w)/TiO_x/Al. A moderate PCE of 0.9 % upon thermal annealing was measured against 2.1 % of the standard P3HT:PCBM device. Despite a similar electron mobility of 3.9×10^{-3} cm^{-2} V^{-1} s^{-1} comparable to that of PCBM (4×10^{-3} cm^{-2} V^{-1} s^{-1}), the short circuit current was only 4.3 mA cm^{-2}, roughly half that of the control device (7.4 mA cm^{-2}). It should be noted that recombination processes in these systems are generally the main drawback that reduces the efficiency, however, the aforementioned Z-E isomerization could also be responsible for destabilizing the donor-acceptor complex at the interfaces or trapping the charges during their migration; this is a complicated phenomenon that requires additional research to be confirmed.

Regarding the modifications of the ester functional group of PCBM, its hydrolysis yields an insoluble PCBM acid that has probably discouraged its use in BHJs. However, Yang et al. [56] by-passed this solubility issue, studying the behavior of a (6,6)-phenyl C_{61}-butyric acid derivative (*p*-EHO-PCBA) with a branched alkyl chain (Chart 7.4, bottom right). The 2-ethyl-hexyloxy chain renders soluble the fullerene acid and, consequently, facilitates its manipulation and purification process. The authors were directed by the fact that photoactive derivatives bearing a carboxylic acid have enhanced interactions at the interfaces with a TiOx optical spacer [57]. In addition, the presence of this optical spacer is beneficial to the overall device PCE [58]. Therefore, the performance of this modified PCBM acid was tested by adopting the following device: ITO/PEDOT:PSS/P3HT : fullerene derivatives (1:1, w/w)/TiO_x/Al device that includes the TiO_x layer. Either *p*-EHO-PCBA, the analogue methyl ester of *p*-EHO-PCBM, or PCBM were spin-coated as the control devices.

Indeed, solar cells with a TiO_x optical spacer were more efficient than those without the optical spacer and, particularly, *p*-EHO-PCBA (PCE = 2.64 %) outperformed both the analogue ester derivative *p*-EHO-PCBM (PCE = 2.34 %) and PCBM (PCE = 2.29 %, the same within experimental error) that were utilized in the same device architecture and experimental conditions. The electron mobility was also investigated, revealing values of 1.59×10^{-3} cm^{-2} V^{-1} s^{-1}, 1.04×10^{-2} cm^{-2} V^{-1} s^{-1} and 2.85×10^{-2} cm^{-2} V^{-1} s^{-1} for *p*-EHO-PCBA, *p*-EHO-PCBM and PCBM, respectively. The authors attributed the main cause of the deteriorated mobilities to the bulky solubilizing groups, when compared with pristine PCBM.

Interestingly, this example of *p*-EHO-PCBA, *p*-EHO-PCBM reported by C. Yang demonstrated the synergy between device design and synthesis in order to adapt the active layer structure to the requirements of an improved device performance.

7.2.5 *Modification on the Cyclopropane Ring: N-Bridge Imino-PCBMs (APCBM): [5,6] Open Fulleroid and [6,6] Closed Methano Fullerene*

Methano fullerene derivatives exist as the stable closed [6,6] isomer, in which an electron pair is involved in the formation of the methan bridge [59]. In theory, the open [5,6] is another possible isomer for methano fullerene derivatives but this kinetic-controlled product is promptly converted in the more stable closed [6,6] structure. On the contrary, iminofullerenes present both stable isomers, the open [5,6] and the closed [6,6] architecture and their structure is showed in Chart 7.5. In the case of the open [5,6] isomer, the imino-bridge is located on the pentagon-hexagon junction while the closed [6,6] isomer is a 58 π−electron species, more symmetric than the open [5,6], and the bridge is placed along the hexagon-hexagon junction (Fig. 7.3). The open isomer should have an electronic behavior similar to C_{60} while the closed [6,6] behaves like a methano fullerene derivative. Interestingly, it turned out that the properties of these two isomers are almost comparable in terms of LUMO energies and Voc in solar cell devices [60]. The first reduction potentials of both isomers differ by 40 meV from that of PCBM. This difference is probably due to the enhanced electronegativity of the nitrogen bridge atom, when compared to the corresponding carbon atom of the cyclopropane ring.

The only noticeable difference is in the optical absorption of the open structure due to the lower symmetry that allows lowest-energy transitions, formally dipole forbidden. The lower symmetry is also confirmed by NMR experiments. The ^{13}C

Chart 7.5 Imino PCBM derivatives

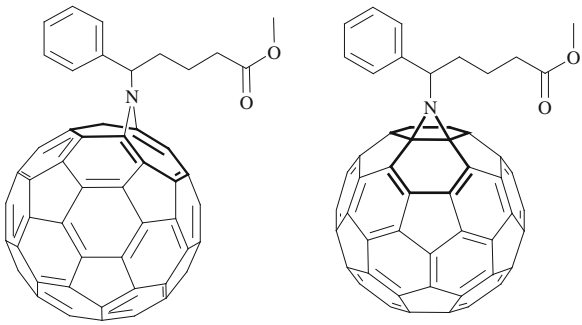

[5,6]-open APCBM **[6,6]-closed APCBM**

Table 7.5 The open structure possesses a higher electron mobility than that of PCBM and the closed isomer

Material	[a]V_{oc} (V)	[a]J_{sc} (mA cm^{-2})	[a]FF (%)	[a]PCE (%)	[b]Mobilities (cm^2 V^{-1} s^{-1})	[c]E^1_{red}(eV)
PCBM[d]	N/A	N/A	N/A	N/A	2.8×10^{-2}	-1.158
Open [5,6] APCBM	0.58	8.10	60	2.8	4.1×10^{-2}	-1.114
Closed [6,6] APCBM	0.58	7.14	56	2.3	2.3×10^{-2}	-1.110

[a] Device schematization: ITO/PEDOT:PSS/P3HT:APCBM isomers (1:1, w/w) Al

[b] Electron mobilities of APCBM isomers casted from chloroform

[c] Electrochemically determined in *o*-DCB, by employing tetrabutylammonium perchlorate as the electrolyte and a scan rate of 50 mVsec^{-1}

[d] No data available for PCBM-based solar cell in the same experimental conditions

spectrum revealed the presence of 42 signals, attributed to the fullerene carbon atoms against only 12 for the closed isomer.

The open structure possesses a higher electron mobility than that of PCBM and the closed isomer [61] (Table 7.5).

Besides the higher electron mobility and higher intensity absorption of the open [5,6] APCB, solar cells based on the open isomer demonstrated a better thermal stability without loss of photocurrent variations even at 160 °C. Photographs of the AFM of P3HT:APCBM blends revealed a pronounced phase separation in the case of the closed APCBM that is probably responsible for the lower PCE.

Based on these data, a higher degree of symmetry in the acceptor component negatively influenced the device performance. Destructive interface segregations are predominant in the case of the more symmetric closed [6,6] isomer. Intuitively, based on the notion "like dissolves like", the miscibility of the imino-bridge isomers with a polymeric structure, which has a "wide" distribution of molecular weight and a random assembling in the bulk, appeared to be more favorable when the acceptor component is less symmetric.

7.3 Other Methanofullerene Derivatives: Diphenyl Methanofullerene: DPM-12 and DPM 6

The 4,4′-dialkyloxydiphenylmethano C_{60} fullerenes were named DPM-12 [62] and DPM-6 [63] by varying the length of the alkoxy chains and they are illustrated in Chart 7.6. They represent another family of methano fullerene derivatives and differ from the typical PCBM structure. However, the functional group is added by adopting the general procedure for the synthesis of methanofullerenes [64]. Due to the presence of two alkoxy phenyl moieties, DPMs are a highly symmetric molecule (C_{2v}) and the presence of a hexyl and dodecyl alkoxy chains, renders these molecules soluble in common organic solvents and, therefore, suitable for OPV acceptors. The characteristics of DPM-based devices [63] are schematically reported in Table 7.6.

Chart 7.6 Structure of DPMs

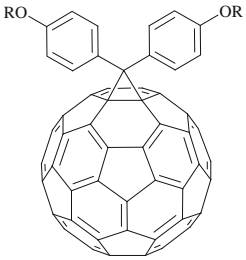

R = $C_{12}H_{25}$ DMP-12

R = C_6H_{13} DMP-6

Table 7.6 The characteristics of DPM-based devices

Blend	Weight Ratio	[a]V_{oc} (V)	[a]J_{sc} (mA cm^{-2})	[a]FF (%)	[a]PCE (%)
P3HT:PCBM	1:1	0.64	9.72	59	3.1
P3HT:DPM-6[65]	1:1	0.73	7.52	51	2.6
P3HT:DPM-6	1:2	0.64	3.04	58	1.0
P3HT:DPM-12	1:2	0.65	4.70	58	2.3

[a] Device schematization: ITO/PEDOT:PSS/P3HT:DPMs/Al, casted from chlorobenzene

When considering the acceptor-donor weight ratio, DPM-6 with a shorter alkyloxy chain requires half the amount of DPM-12 for the blend formation. Additionally, the reduced amount of alkane chains in DPM-6 improved the electron mobility that is an order of magnitude higher than that of DPM-12 (2×10^{-4} m^2 V^{-1} s^{-1}) and the overall photocurrent efficiency from 2.3 to 2.6 % for DPM-12 and DPM-6, respectively. Compared to PCBM, the electron mobility of DPM-6 is still 3–4 times lower than the PCBM that showed a PCE above 3 %. The different performance can be only attributed to the J*sc*, since the FF is almost comparable and the Voc is considerably higher than that of the control device (more than 100 mV) [62]. Interestingly, even though PCBM and DPMs present the same LUMO energy levels, the open circuit voltage differs significantly. Authors attributed this difference to the distinct occupancy of the electron density of states (DOS) of donor and acceptor when forming the active layer. In fact, in the case of the DMP:P3HT blend, a full occupancy of the DOS was observed for DPM that implies a higher rise of the Fermi level. On the other hand, PCBM showed a lower density of states which are confined only to the tail of the DOS. A general understanding of the distribution of the electronic state in the BHJ seems to be a pure theoretical rationalization of the formation of the BHJ active layer. A possible correlation with the inner morphology of the photoactive film is also provided by studying the modification of the blend before and after thermal annealing. TEM analysis revealed a higher crystallinity degree in the case of PCBM that resulted in the formation of large separate domains and needle-like structures that are not visible in the case of the DPMs. In conclusion, interfacial contacts between the

donor and the acceptor currently remain a hot topic in OPVs. Very often, notions on the electrochemical properties and fundamental charge transfer mechanism cannot be directly applied to BHJs that involve processes in the solid state. The properties of the material in different states can vary significantly and DPMs represent just an example.

7.4 Alternatively Functionalized Fullerenes

Despite a large number of methano fullerene derivatives described so far, resembling the PCBM structure, photoactive fullerenes with different functionalities have also been employed in OPVs. In fact, the 30 electron pairs behave as non-conjugated double bonds and they are open to the insertion of a variety of functional groups [26, 66]. For example, cycloaddition reactions such as, 4 + 2 or 1,3 dipolar addition, represent a solid protocol for the synthesis of ortho-quinodimethane adducts [67] and fulleropyrrolidines [68]. In both cases, the active species are generated in situ by heating of the corresponding precursors. Treatment of fullerenes with a mixture of dibromo ortho-xylenes and an iodine salt yield quinodimethano derivatives while an *alpha*−amino acid and an aldehyde generate an azomethine ylide intermediate that leads to the formation of fulleropyrrolidines. With regards to radical reactions, fullerene is easily halogenated or oxidized [69]. More interestingly, radical intermediates can functionalize fullerene at position [1, 4] instead of the common [6] in cycloaddition reactions. Herein, a few examples of alternatively functionalized fullerenes are presented and their applications in OPV are also discussed in an effort to synthesize photoactive fullerenes whose functional group differs from the methano cyclopropane bridge.

7.4.1 Di-Hydronaphthyl Bridged Ester Fullerene and 1,4 Addends Derivatives

A family of dihydronaphthyl derivatives has been synthesized and tested as an alternative to PCBM (Chart 7.7, left). As mentioned above, the active species, an ortho-quinodimethane, was generated by heating methyl-(3,4-dibromomethyl)-benzoate in the presence of potassium iodide. A diene was formed in situ that reacted with one of the 30 double bonds of C_{60}, yielding the corresponding cycloaddition product. In this work described by Frechet and co-workers [40, 41], the ester functional group was modified to fine tune the fullerene properties. Aryl moieties bearing electron withdrawing and donor groups were inserted as ester functionalities, such as mono and trimethoxy benzene as well as fluoro and penta fluoro benzene. Contrary to the aryl functionalized PCBM derivatives [42], previously described in paragraph 2.2, only small variations on LUMO energies were

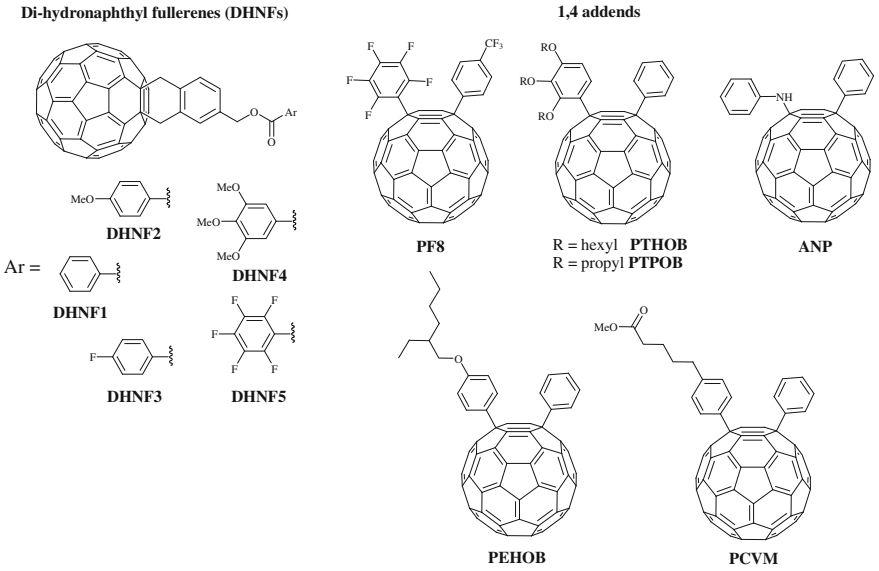

Chart 7.7 Structures of Di-hydronaphthyl bridged ester fullerene and 1,4 addend derivatives

observed (<0.1 V). This demonstrated that modifications on the ester functionality have very little influence on the electron density of the fullerenoid cage. The accepting behavior of these fullerenoids was studied employing a standard device architecture while the weight percentage of the accepting component was varied from 30 to 55 %. The PCE of the phenyl ester DHNF1 was somewhat higher than the control device when 55 % of acceptor content was employed for the active layer. Within experimental error, the efficiencies of the control device and the phenyl ester DHNF1 are equivalent, with values of 4.4 and 4.5 %, respectively. These data encourage the use of alternative photoactive fullerenes with a functional group that differs from the PCBM methano bridge.

In Chart 7.7 (right) a more recent example of 1,4 addends as alternative photoactive fullerenes is presented [70]. They were obtained via a fullerenol intermediate that involves a phenyl hydrazine derivative in the presence of an oxidizing species, $NaNO_2$, in a biphasic system of toluene water [71]. The proposed mechanism for these fullerene adducts is based on a radical process described elsewhere [72].

The beauty of these derivatives is their light-harvesting capability due to the loss of symmetry upon the 1,4 functionalization. Thanks to their unique properties, a family of 1,4 addends were specifically designed for their use in BHJ. In fact, a less symmetric fullerene allows transition at longer wavelengths that are forbidden in the case of C_{60} PCBM. Moreover, the direct insertion of differently substituted phenyl moieties leads to a facile tunability of the electronic energy levels.

Due to solubility issues, only two derivatives, PTPOB and PHOB, were tested in photovoltaic devices. A P3HT:PTPOB active layer with a weight ratio of 1–1 achieved a PCE of 2.3 % after thermal annealing at 165 °C for 10 min. The control device with PCBM with a weight ratio of 1–0.8 gave a similar efficiency of 2.8 %. On the other hand, the P3HT:PHOB-based solar cell performed poorer, with an efficiency of only 1.2 %, probably due to the presence of a high content of alkane branched alkyl chains.

In terms of device characteristics 1,4 adducts allowed the fabrication of solar cells with an open circuit voltage 70 mV higher than PCBM. In addition, 1,4 addends showed a higher absorption intensity comparable to that of C_{60} bis-adducts [73] or $PC_{70}BM$ [74] or $PC_{84}BM$ [75] but with the advantage of being a single defined molecule instead of a mixture of several isomers.

In conclusion, we believe that this class of compounds remains unexplored since only a few examples have been reported in the literature [72]. For instance, the 1,4 multi-adducts may possess combined features of 1,4 mono-addends and multi-adducts. Additionally, the multi-addition could also overcome the low solubility of derivatives depicted in Chart 7.7, making possible their use as BHJ active layers.

7.5 Bis-Adducts and Emerging Fullerene Derivatives

After more than 25 years, an indene C60 bis-adduct, referred to as ICBA (Chart 7.8) [39], outperformed the power conversion efficiency of a control device based on PCBM/P3HT. It took more than two decades to discover a valid replacement for PCBM that, until then, had dominated the scene of BHJ devices.

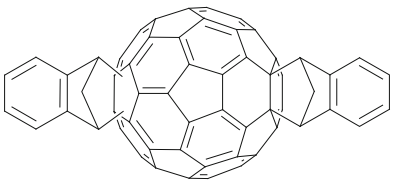

ICBA

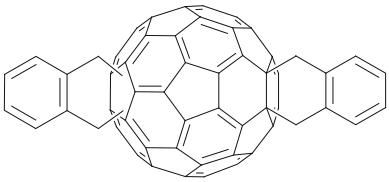

bis-oQDMC$_{60}$

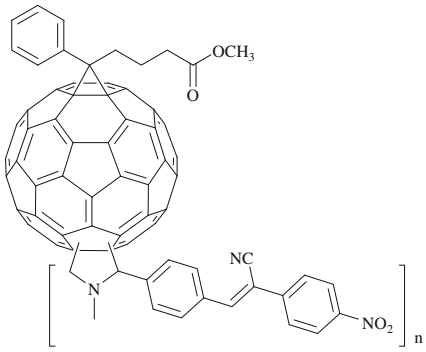

Fullerene A

Chart 7.8 Most representative bis-adduct derivatives

Table 7.7 The thermal treatment

Acceptor	[a]V_{oc} (V)	[a]J_{sc} (mA cm^{-2})	[a]FF (%)	[a]PCE (%)	[b]Solubility (mg ml^{-1})	[c]LUMO (eV)
PCBM	0.58	10.5	63	3.84	80	−3.91
PCBM[d]	0.59	9.9	64	3.73		
ICBA	0.80	9.3	65	4.84	90	−3.74
ICBA[d]	0.84	10.61	73	6.48		

[a] Device schematization: ITO/PEDOT: PSS/P3HT:Acceptor (1:1, w/w) Ca/Al, as casted from *o*-DCB
[b] Chloroform
[c] *o*-DCB/acetonitrile and tetrabutylammonium hexafluorophosphate as the electrolyte
[d] Thermal annealing at 120 °C for 10 min [76]

Initially, solar cells fabricated with ICBA gave an efficiency of 5.44 % against 3.88 % of the control device [39]. Subsequently, PCE of 5.44 % was improved to 6.5 % due to an annealing process at150 °C for 10 min and an optimum donor: acceptor weight ratio of 1:1, while no significant changes were observed for PCBM under the same modified conditions [76]. In fact, the annealing process positively influenced the morphological nanostructure of the film achieving a surface root-mean-square of 7.9 nm that is close to that reported for the best P3HT:PCBM solar cell (9.5 nm) [77]. Moreover, the thermal treatment at 150 °C for 10 min pushed the fill factor to 73 % and the short circuit current from 9.30 to 10.6 mA/cm^2 (see Table 7.7). In addition, the main advantage of using these bis-adducts is the higher open circuit voltage when compared to mono-adducts. Cyclic voltammetry measurements usually revealed increased LUMO energies for multi-adducts that result in higher *V*oc devices (LUMO of ICBA is 0.17 eV higher than PCBM).

The dramatic contribution of ICBA in the solar cell performance, has granted larger interest in the development of new fullerene multi-adducts. Bis-thienyl substituted fullerenes [78], tris-adducts of PCBM [79], di(4-methylphenyl)methano C_{60} bis-adduct [80] are just a few recent examples.

However, before ICBA was described, the features of multi-adducts were already known. Blom and co-workers [73] have utilized bis-PCBM in organic solar cells. A LUMO 100 meV higher than the monoadduct contributed to slightly improve the solar cell efficiency from 3.8 % in the case of PCBM mono-adduct to 4.5 % for the bis-adducts. Once again, the increased LUMO level was the major contribution to the higher efficiency.

More recently, Voroshazi et al. [81] have reported mono and bis o-quinodimethane C_{60} adducts (oQDMC$_{60}$) which demonstrated an enhanced open circuit voltage of 0.82 mV. Authors were probably inspired by the performance of the novel photoactive naphthodihydro fullerenes reported by Frechet and co-workers, removing the ester functionality.

The LUMO energy level of oQDMC$_{60}$ is −4.12 eV, slightly lower than ICBA but comparable with that of bis-PCBM. However, lower values of FF and J*sc* reduced the efficiency to 4.6 %.

Experimental data summarized in Table 7.8 are in agreement with those reported in the literature and ICBA values are relative to the non-optimized device [39].

Table 7.8 Experimental data

Acceptor	[a]V_{oc} (V)	[a]J_{sc} (mA cm^{-2})	[a]FF (%)	[a]PCE (%)	[b]Solubility (mg mL^{-1})	[c]LUMO (eV)	[d]Mobilities (cm^2 V^{-1} s^{-1})
PCBM	0.57	9.6	70	3.8	14.1	−4.30	1.0×10^{-3}
Mono-o-QDMC$_{60}$	0.64	9.5	67	4.1	2.8	−4.25	2.0×10^{-3}
Bis-o-QDMC$_{60}$	0.82	9.4	66	5.2	61.1	−4.12	7.1×10^{-4}
Bis-PCBM	0.69	9.4	65	4.2	147.0	−4.18	6.0×10^{-4}
ICBA[e]	0.83	9.7	69	5.6	140.5	−4.04	

[a] Device schematization: ITO/PEDOT: PSS/P3HT:Acceptor (1: 0.8, w/w for mono-adducts and 1:1.2 for bis-adducts) Ca/Al, annealed at 170 °C for 10 min, *o*-DCB and chlorobenzene as cast solvent mixture, octanedithiole was used as additive

[b] *o*-DCB

[c] *o*-DCB and tetrabutylammonium hexafluorophosphate as the electrolyte

[d] Electron mobility of P3HT/acceptor blends

[e] In the experimental conditions reported by Voroshazi et al. [81]

Bis-o-QDMC$_{60}$-based devices were annealed at 170 °C, 20 °C higher than in the case of ICBA. Interestingly, when considering the chemical structure of ICBA and bis-o-QDMC$_{60}$, they appear very similar and both derivatives were obtained by a 4 + 2 cycloaddition reaction. However, ICBA demonstrated a higher solubility in the casting solvent, similar to bis-PCBM that is probably the key factor of its higher performance. As suggested by Troshin et al. [82] the optimum values of V*oc*, J*sc*, FF and PCE are confined in a specific range of solubilities. The authors, based on more than 27 different mono-adduct derivatives, demonstrated that a fullerene derivative too soluble or insoluble is not suitable for solar cells. However, these correlations are based on mono-adducts, therefore a similar systematic study for multi-adducts is required to confirm possible analogies in terms of solubility for ICBA, bis-o-QDMC$_{60}$ and bis-PCBM.

In general, ICBA, bis-o-QDMC$_{60}$ and bis-PCBM can be defined as "symmetric" bis-adduct derivatives where the same functional group has been added twice on the same fullerene unit. Recently, an "asymmetric" photoactive bis-adduct bearing two different functional groups was described by Sharma and co-workers (Chart 7.8) [83]. A pyrrolidine was subsequently inserted to a PCBM mono-adduct by a 1,3 dipolar cycloaddition reaction. The 1,3 dipole was generated by heating terephthaldehyde and sarcosine yielding the PCBM pyrrolidine bis-adducts. Then, a Knoevenagel condensation reaction with 4-nitrobenzyl cyanide afforded a methano fulleropyrrolidine multi-adduct, referred to as fullerene A. A characteristic of fullerene A, common to the other multi-functionalized fullerenes described in this paragraph, is the increased LUMO energy (0.15 eV higher than PCBM) together with a more intense absorption in the visible region. The solubility also increased when compared with PCBM. Fullerene A was tested utilizing the following solar cell architecture ITO/PEDOT:PSS/P3HT:fullerene/Al, achieving a power conversion efficiency of 5.32 %. The best performance was obtained employing a weight ratio of P3HT and fullerene A of 1:1, an unusual solvent mixture of THF and *o*-DCB and a thermal annealing treatment.

The absorption intensity and active layer morphology improved utilizing this particular solvent mixture and the thermal treatment as well. In fact, an enhanced P3HT inter-chain interaction was monitored by XRD diffraction. The $2\theta = 5.56°$ peak shifted to a lower angle after thermal treatment which is consistent with a larger *d* spacing of P3HT [84] and a better film crystallinity. The PCE increased from 3.88 to 4.50 % when THF/o-DCB mixture, instead of pure THF, was employed to spin-coat the active layer and a PCE = 5.3 % was finally achieved after the annealing process. Interestingly, Fullerene A, demonstrated a good solubility in an uncommon solvent, such as THF, that contributed to improve the device performance, opening new alternatives for the blend deposition.

Despite their success, multi adducts present some drawbacks. In fact, C_{60} can be derivatized only by addition reactions that involve a double bond of the pristine fullerene, altering the original properties of the pure fullerene. Two pairs of electrons are employed for the introduction of the two functional groups which are responsible for the lowered electron mobility when compared with analogue mono-adducts. In addition, 8 different isomers are formed with very little control on the position of the second added functionalities, as illustrated in Fig. 7.4.

The mixture of isomers required time-consuming and costly purification techniques, such as HPLC. Due to the costs and the lengthy purifications, the whole mixture is generally employed for the fabrication of OPVs. However, when operating with a mixture, there is no discrimination of the actual contribution of each single isomer in the efficiency of the device. On top of that, the trans 1 derivative (see Fig. 7.4) presents two functional groups on the extreme of the fullerene that probably affect the charge migration or, more generally, the nanostructured domains of the film.

7.6 Endohedral Fullerenes: Trimetallic Nitride Derivative

Endohedral fullerenes represent an emerging class of fullerenes characterized by the presence of a metal, atoms or molecule inside the fullerene. The formation of the buckyball into a cage is probably due to its capability of incorporating certain species inside it. Unfortunately, due to a milligram scale-production, endohedral fullerenes have been mainly studied for academic purposes, due to the difficulties of a bulk synthesis. Trimetallic nitride endohedral fullerenes, $M_3N@C_{80}$, are a subgroup of endohedral fullerenes where M can be a rare-earth metal such as Sc, Y, Gd, Tb, Dy, Ho, Er, Tm, Lu. Among them, trimetallic nitride endohedral fullerenes $Lu_3N@C_{80}$ posses the closest LUMO to that of P3HT, offering the possibility of fabricating high V_{oc} devices. They were synthesized for the first time by Stevenson et al. [85] and thanks to their "larger production", they have been recently functionalized and employed in OPV [86, 87]. Table 7.9 summarizes the performances of ITO/PEDOTT:PSS/P3HT:acceptor/LiF/Al devices. Specifically, the blend of 1-(3-hexoxycarbonyl)propyl-[6,6]-$Lu_3N@C_{81}$ ($Lu_3N@C_{80}$PCBH) with P3HT resulted in a V_{oc} of 260 mV higher than that of PCBM control device and a PCE of 4 % against only 3.4 % of PCBM.

Table 7.9 Performances of ITO/PEDOTT:PSS/P3HT:acceptor/LiF/Al devices

Acceptor	[a]V_{oc} (V)	[a]J_{sc} (mA cm^{-2})	[a]FF (%)	[a]PCE (%)	$E_{p,\ red(1)}$ (eV)
$PC_{60}BM$	630	8.9	61	3.4	−1.220
$Lu_3N@C_{80}PCBH$	810	8.85	59	4.24	−1.500

[a] Device schematization: ITO/PEDOTT:PSS/P3HT:fullerene acceptor/LiF/Al, annealed at 130 °C for 1 min, *o*-DCB as the cast solvent
[b] Calculated from reduction potential in o-DCB and *n*-Bu_4NPF_6 as the electrolyte

Due to the increased volume of the endohedral fullerenes, a reduced amount in weight is necessary to obtain an efficient film microstructure (P3HT: $Lu_3N@C_{80}PCBH$, 1:0.5) which differs significantly from the one to one weight ratio usually employed with PCBM. Based on these data, a finer network promotes exciton dissociation, reducing energy losses of the photo-excited electrons. $Lu_3N@C_{80}PCBH$ represents a rare example of the application of endohedral fullerenes in OPVs. Despite their potential features and outstanding performance, the scarcity of these fullerenes renders these materials impossible to be utilized in a massive production of solar cells. However, the growing technology and the market demand could eventually lead to a wider production.

7.7 Conclusion and Outlook

In conclusion, ICBA represents a new generation of accepting materials, demonstrating the possibility to further improve the performance of fullerenes in BHJs. Other non-fullerene small molecules have also been recently discovered as promising acceptors in BHJ [88–91] which even further enlarge our perspective on photoactive components. From the synthetic point of view, numerous derivatives and methodologies are on their way to be released soon. We believe that it is only a matter of time to control and limit the number of isomers for a better understanding of the properties of each single isomers in C_{60} bis and multi adducts as well as C_{70}. Emerging new synthetic procedures may employ (i) template reactions to yield only a few cis adduct derivatives, (ii) retro cycloadditions in order to block some specific positions on the fullerene cage, allowing the functionalization on other sites and, finally, the initial cycloadduct can be thermally removed [92, 93], (iii) bi-dentate reactive units to ensure the addition on spatially close positions [94].

Finally, less efforts have been directed to the design of new accepting materials when compared to the polymer counterpart, leaving unexplored a large area of interest. Materials whose structures differ from PCBM have probably been underestimated, if considering the numerous examples to modify the PCBM structure or optimize the P3HT-PCBM control devices [77]. Additionally,

improvements for PCBM are sometimes not appropriate for other acceptors. Therefore, considering progress in all these directions, there are still plenty of possibilities that are waiting to be discovered.

Acknowledgment The author thanks Fred Wudl for helpful discussions.

References

1. H. Akamatu, H. Inokuchi, Y. Matsunaga, Nature **173**, 168 (1954)
2. H. Letheby, J. Chem. Soc. **15**, 161 (1862)
3. A.G. Green, A.G. Woodhead, J. Chem. Soc. Trans. **97**, 2388 (1910)
4. J.C. Chiang, A.G. Macdiarmid, Synth. Met. **13**, 193 (1986)
5. J. Mcginnes, P. Corry, P. Proctor, Science **183**, 853 (1974)
6. R. Mcneill, R. Siudak, J.H. Wardlaw, D.E. Weiss, Aust. J. Chem. **16**, 1056 (1963)
7. T. Ito, H. Shirakaw, S.J. Ikeda, Polym. Sci. A Polym. Chem. **12**, 11 (1974)
8. H. Shirakawa, E.J. Louis, A.G. Macdiarmid, C.K. Chiang, A.J. Heeger, J. Chem. Soc., Chem. Commun. 578 (1977)
9. C.K. Chiang, M.A. Druy, S.C. Gau, A.J. Heeger, E.J. Louis, A.G. Macdiarmid, Y.W. Park, H. Shirakawa, J. Am. Chem. Soc. **100**, 1013 (1978)
10. C.W. Tang, Appl. Phys. Lett. **48**, 183 (1986)
11. G. Yu, C. Zhang, A.J. Heeger, Appl. Phys. Lett. **64**, 1540 (1994)
12. D. Braun, D. Moses, C. Zhang, A.J. Heeger, Appl. Phys. Lett. **61**, 3092 (1992)
13. N.S. Sariciftci, L. Smilowitz, A.J. Heeger, F. Wudl, Science **258**, 1474 (1992)
14. R.F. Service, Science **332**, 293 (2011)
15. G. Dennler, M.C. Scharber, T. Ameri, P. Denk, K. Forberich, C. Waldauf, C. Brabec, J. Adv. Mater. **20**, 579 (2008)
16. H. Sirringhaus, T. Kawase, R.H. Friend, T. Shimoda, M. Inbasekaran, W. Wu, E.P. Woo, Science **290**, 2123 (2000)
17. Y.M. Sun, G.C. Welch, W.L. Leong, C.J. Takacs, G.C. Bazan, A.J. Heeger, Nat. Mater. **11**, 44 (2012)
18. C. Deibel, T. Strobel, V. Dyakonov, Adv. Mater. **22**, 4097 (2010)
19. A.C. Arias, J.D. MacKenzie, I. McCulloch, J. Rivnay, A. Salleo, Chem. Rev. **110**, 3 (2010)
20. G. Yu, J. Gao, J.C. Hummelen, F. Wudl, A.J. Heeger, Science **270**, 1789 (1995)
21. H.W. Kroto, J.R. Heath, S.C. Obrien, R.F. Curl, R.E. Smalley, Nature **318**, 162 (1985)
22. R.E. Smalley, Acc. Chem. Res. **25**, 98 (1992)
23. H.W. Kroto, A.W. Allaf, S.P. Balm, Chem. Rev. **91**, 1213 (1991)
24. J.R. Heath, Q. Zhang, S.C. Obrien, R.F. Curl, H.W. Kroto, R.E. Smalley, J. Am. Chem. Soc. **109**, 359 (1987)
25. H.W. Kroto, Nature **329**, 529 (1987)
26. F. Diederich, C. Thilgen, Science **271**, 317 (1996)
27. J.H. Holloway, E.G. Hope, R. Taylor, G.J. Langley, A.G. Avent, T.J. Dennis, J.P. Hare, H.W. Kroto, D.R.M. Walton, J. Chem. Soc., Chem. Commun. 966 (1991)
28. R.C. Haddon, Science **261**, 1545 (1993)
29. F. Wudl, Acc. Chem. Res. **25**, 157 (1992)
30. L. Echegoyen, L.E. Echegoyen, Acc. Chem. Res. **31**, 593 (1998)
31. P.M. Allemand, A. Koch, F. Wudl, Y. Rubin, F. Diederich, M.M. Alvarez, S.J. Anz, R.L. Whetten, J. Am. Chem. Soc. **113**, 1050 (1991)
32. Q.S. Xie, E. Perezcordero, L. Echegoyen, J. Am. Chem. Soc. **114**, 3978 (1992)
33. B.C. Thompson, J.M.J. Frechet, Angew. Chem. Int. Ed. **47**, 58 (2008)
34. F.G. Brunetti, R. Kumar, F. Wudl, J. Mater. Chem. **20**, 2934 (2010)

35. J.C. Hummelen, B.W. Knight, F. Lepeq, F. Wudl, J. Yao, C.L. Wilkins, J. Org. Chem. **60**, 532 (1995)
36. H. Hoppe, N.S. Sariciftci, J. Mater. Chem. **16**, 45 (2006)
37. C.J. Brabec, M. Heeney, I. McCulloch, J. Nelson, Chem. Soc. Rev. **40**, 1185 (2011)
38. J.W. Chen, Y. Cao, Acc. Chem. Res. **42**, 1709 (2009)
39. Y.J. He, H.Y. Chen, J.H. Hou, Y.F. Li, J. Am. Chem. Soc. **132**, 1377 (2010)
40. S.A. Backer, K. Sivula, D.F. Kavulak, J.M.J. Frechet, Chem. Mater. **19**, 2927 (2007)
41. A. Varotto, N.D. Treat, J. Jo, C.G. Shuttle, N.A. Batara, F.G. Brunetti, J.H. Seo, M.L. Chabinyc, C.J. Hawker, A.J. Heeger, F. Wudl, Angew. Chem. Int. Ed. **50**, 5166 (2011)
42. F.B. Kooistra, J. Knol, F. Kastenberg, L.M. Popescu, W.J.H. Verhees, J.M. Kroon, J.C. Hummelen, Org. Lett. **9**, 551 (2007)
43. L.M. Popescu, P. van't Hof, A.B. Sieval, H.T. Jonkman, J.C. Hummelen, Appl. Phys. Lett. *89*, 213507 (2006)
44. H.Y. Zhao, X.Y. Guo, H.K. Tian, C.Y. Li, Z.Y. Xie, Y.H. Geng, F.S. Wang, J. Mater. Chem. *20*, 3092 (2006)
45. V.D. Mihailetchi, J.K.J. van Duren, P.W.M. Blom, J.C. Hummelen, R.A.J. Janssen, J.M. Kroon, M.T. Rispens, W.J.H. Verhees, M.M. Wienk, Adv. Funct. Mater. **13**, 43 (2003)
46. P.M. Beaujuge, J.M.J. Frechet, J. Am. Chem. Soc. **133**, 20009 (2011)
47. J. Peet, J.Y. Kim, N.E. Coates, W.L. Ma, D. Moses, A.J. Heeger, G.C. Bazan, Nat. Mater. **6**, 497 (2007)
48. K. Sivula, Z.T. Ball, N. Watanabe, J.M. Frechet, J. Adv. Mater. **18**, 206 (2006)
49. Y. Zhang, H.L. Yip, O. Acton, S.K. Hau, F. Huang, A.K.Y. Jen, Chem. Mater. **21**, 2598 (2009)
50. C.H. Woo, B.C. Thompson, B.J. Kim, M.F. Toney, J.M.J. Frechet, J. Am. Chem. Soc. **130**, 16324 (2008)
51. G.J. Zhao, Y.J. He, Z. Xu, J.H. Hou, M.J. Zhang, J. Min, H.Y. Chen, M.F. Ye, Z.R. Hong, Y. Yang, Y.F. Li, Adv. Funct. Mater. **20**, 1480 (2010)
52. L.P. Zheng, Q.M. Zhou, X.Y. Deng, M. Yuan, G. Yu, Y. Cao, J. Phys. Chem. B **108**, 11921 (2004)
53. J.A. Mikroyannidis, A.N. Kabanakis, S.S. Sharma, G.D. Sharma, Adv. Funct. Mater. **21**, 746 (2011)
54. M.F. Wang, E. Chesnut, Y.M. Sun, M.H. Tong, M. Guide, Y. Zhang, N.D. Treat, A. Varotto, A. Mayer, M.L. Chabinyc, T.Q. Nguyen, F. Wudl, J. Phys. Chem. C **116**, 1313 (2012)
55. J.A. Delaire, K. Nakatani, Chem. Rev. **2000**, 100 (1817)
56. C. Yang, J.Y. Kim, S. Cho, J.K. Lee, A.J. Heeger, F. Wudl, J. Am. Chem. Soc. **130**, 6444 (2008)
57. J.S. Liu, E.N. Kadnikova, Y.X. Liu, M.D. McGehee, J.M.J. Frechet, J. Am. Chem. Soc. **126**, 9486 (2004)
58. J.Y. Kim, S.H. Kim, H.H. Lee, K. Lee, W.L. Ma, X. Gong, A. Heeger, J. Adv. Mater. **18**, 572 (2006)
59. D.M. Guldi, H. Hungerbuhler, I. Carmichael, K.D. Asmus, M. Maggini, J. Phys. Chem. A **104**, 8601 (2000)
60. S.H. Park, C.D. Yang, S. Cowan, J.K. Lee, F. Wudl, K. Lee, A.J. Heeger, J. Mater. Chem. **19**, 5624 (2009)
61. C. Yang, S. Cho, A.J. Heeger, F. Wudl, Angew. Chem. Int. Ed. **48**, 1592 (2009)
62. I. Riedel, E. von Hauff, H. Parisi, N. Martin, F. Giacalone, V. Dyakonov, Adv. Funct. Mater. **2005**, 15 (1979)
63. H.J. Bolink, E. Coronado, A. Forment-Aliaga, M. Lenes, A. La Rosa, S. Filippone, N. Martin, J. Mater. Chem. **21**, 1382 (2011)
64. S. Shi, K.C. Khemani, Q.C. Li, F. Wudl, J. Am. Chem. Soc. **114**, 10656 (1992)
65. G. Garcia-Belmonte, P.P. Boix, J. Bisquert, M. Lenes, H.J. Bolink, A. La Rosa, S. Filippone, N. Martin, J. Phys. Chem. Lett. **1**, 2566 (2010)
66. R. Taylor, D.R.M. Walton, Nature **363**, 685 (1993)
67. P. Belik, A. Gugel, J. Spickermann, K. Mullen, Angew. Chem. Int. Ed. **32**, 78 (1993)

68. M. Maggini, G. Scorrano, M. Prato, J. Am. Chem. Soc. **115**, 9798 (1993)
69. G.A. Olah, I. Bucsi, C. Lambert, R. Aniszfeld, N.J. Trivedi, D.K. Sensharma, G.K.S. Prakash, J. Am. Chem. Soc. **113**, 9385 (1991)
70. A. Varotto, N.D. Treat, J. Jo, C.G. Shuttle, N.A. Batara, F.G. Brunetti, J.H. Seo, M.L. Chabinyc, C.J. Hawker, A.J. Heeger, F. Wudl, Angew. Chem. Int. Ed. **50**, 5166 (2011)
71. G.W. Wang, Y.M. Lu, Z.X. Chen, Org. Lett. **11**, 1507 (2009)
72. Y. Matsuo, Y. Sato, T. Niinomi, I. Soga, H. Tanaka, E. Nakamura, J. Am. Chem. Soc. **131**, 16048 (2009)
73. M. Lenes, G.J.A.H. Wetzelaer, F.B. Kooistra, S.C. Veenstra, J.C. Hummelen, P.W.M. Blom, Adv. Mater. **20**, 2116 (2008)
74. M.M. Wienk, J.M. Kroon, W.J.H. Verhees, J. Knol, J.C. Hummelen, P.A. van Hal, R.A. J. Janssen, Angew. Chem. Int. Ed. **42**, 3371 (2003)
75. F.B. Kooistra, V.D. Mihailetchi, L.M. Popescu, D. Kronholm, P.W.M. Blom, J.C. Hummelen, Chem. Mater. **18**, 3068 (2006)
76. G.J. Zhao, Y.J. He, Y.F. Li, Adv. Mater. **22**, 4355 (2010)
77. G. Li, V. Shrotriya, J.S. Huang, Y. Yao, T. Moriarty, K. Emery, Y. Yang, Nat. Mater. **4**, 864 (2005)
78. J.H. Choi, K.I. Son, T. Kim, K. Kim, K. Ohkubo, S. Fukuzumi, J. Mater. Chem. **20**, 475 (2010)
79. M. Lenes, S.W. Shelton, A.B. Sieval, D.F. Kronholm, J.C. Hummelen, P.W.M. Blom, Adv. Funct. Mater. **19**, 3002 (2009)
80. Y.J. Cheng, M.H. Liao, C.Y. Chang, W.S. Kao, C.E. Wu, C.S. Hsu, Chem. Mater. **23**, 4056 (2011)
81. E. Voroshazi, K. Vasseur, T. Aernouts, P. Heremans, A. Baumann, C. Deibel, X. Xue, A. J. Herring, A.J. Athans, T.A. Lada, H. Richter, B.P. Rand, J. Mater. Chem. **21**, 17345 (2011)
82. P.A. Troshin, H. Hoppe, J. Renz, M. Egginger, J.Y. Mayorova, A.E. Goryochev, A.S. Peregudov, R.N. Lyubovskaya, G. Gobsch, N.S. Sariciftci, V.F. Razumov, Adv. Funct. Mater. **19**, 779 (2009)
83. J.A. Mikroyannidis, D.V. Tsagkournos, S.S. Sharma, G.D. Sharma, J. Phys. Chem. C **115**, 7806 (2011)
84. H.Y. Chen, H.C. Yang, G.W. Yang, S. Sista, R.B. Zadoyan, G. Li, Y. Yang, J. Phys. Chem. C **113**, 7946 (2009)
85. S. Stevenson, G. Rice, T. Glass, K. Harich, F. Cromer, M.R. Jordan, J. Craft, E. Hadju, R. Bible, M.M. Olmstead, K. Maitra, A.J. Fisher, A.L. Balch, H.C. Dorn, Nature **401**, 55 (1999)
86. R.B. Ross, C.M. Cardona, F.B. Swain, D.M. Guldi, S.G. Sankaranarayanan, E. Van Keuren, B.C. Holloway, M. Drees, Adv. Funct. Mater. **19**, 2332 (2009)
87. R.B. Ross, C.M. Cardona, D.M. Guldi, S.G. Sankaranarayanan, M.O. Reese, N. Kopidakis, J. Peet, B. Walker, G.C. Bazan, E. Van Keuren, B.C. Holloway, M. Drees, Nat. Mater. **8**, 208 (2009)
88. X. Gong, M.H. Tong, F.G. Brunetti, J. Seo, Y.M. Sun, D. Moses, F. Wudl, A. Heeger, J. Adv. Mater. **23**, 2272 (2011)
89. F.G. Brunetti, X. Gong, M. Tong, A.J. Heeger, F. Wudl, Angew. Chem. Int. Ed. **49**, 532 (2010)
90. J.T. Bloking, X. Han, A.T. Higgs, J.P. Kastrop, L. Pandey, J.E. Norton, C. Risko, C.E. Chen, J.L. Bredas, M.D. McGehee, A. Sellinger, Chem. Mater. **23**, 5484 (2011)
91. P.E. Schwenn, K. Gui, A.M. Nardes, K.B. Krueger, K.H. Lee, K. Mutkins, H. Rubinstein-Dunlop, P.E. Shaw, N. Kopidakis, P.L. Burn, P. Meredith, Adv. Energy Mater. **1**, 73 (2011)
92. N. Martin, M. Altable, S. Filippone, A. Martin-Domenech, L. Echegoyen, C.M. Cardona, Angew. Chem. Int. Ed. **45**, 110 (2006)
93. F.G. Brunetti, M.A. Herrero, J.D.M. Munoz, S. Giordani, A. Diaz-Ortiz, S. Filippone, G. Ruaro, M. Meneghetti, M. Prato, E. Vazquez, J. Am. Chem. Soc. **129**, 14580 (2007)
94. R.K.M. Bouwer, J.C. Hummelen, Chem. Eur. J. **16**, 11250 (2010)

Part III
Devices

Chapter 8
Nano-scale Morphology for Bulk Heterojunction Polymer Solar Cells

Yu-Wei Su, Mao-Yuan Chiu and Kung-Hwa Wei

Abstract In any high performance polymer solar cell, the morphology is always an important aspect. The bulk-heterojunction morphology is a challenging research area, which is the focus of this chapter. Many characterization techniques have been used to investigate the BHJ morphologies of active layers in OPVs; which can be classified into reciprocal-space and real-space techniques. We will discuss both the reciprocal-space techniques generally used to obtain spatially averaged information (X-ray or neutron scattering), as well as real-space techniques for analyzing the phase separation and aggregation of BHJ morphology. Our focus will be on how X-ray scattering and transmission electron microscopy based characterization techniques can be used to analyze the effects of the relative length scales of PCBM clusters and polymer (P3HT as example) crystallites on device performance.

8.1 Introduction

For polymer solar cells (PSCs), the most prevalent active layer morphology is based on a bulk heterojunction (BHJ) architecture in which conjugated polymers and fullerenes, serving as electron donors and acceptors, respectively, are blended together [1]. Active layers with BHJ structures comprising conjugated polymers and nanometer-sized fullerenes often form complicated morphologies that typically arise from the limited polymer:fullerene miscibility, resulting in phase-separated polymer- and fullerene-rich domains that coexist with an molecularly-mixed amorphous polymer:fullerene domains The presence phase-separated domains in the active layer of a BHJ solar cell can affect the device performance because these domains provide not only interfaces for charge separation for photogenerated excitons but also percolation pathways for charge carrier transport to the respective

Y.-W. Su · M.-Y. Chiu · K.-H. Wei (✉)
Department of Materials Science and Engineering, National Chiao Tung University, Hsin Chu, Taiwan, ROC
e-mail: khwei@mail.nctu.edu.tw

Y. Yang and G. Li (eds.), *Progress in High-Efficient Solution Process Organic Photovoltaic Devices*, Topics in Applied Physics 130,
DOI 10.1007/978-3-662-45509-8_8

electrodes; the former require a fine dispersion of fullerene units in the polymer, due to the short exciton diffusion length in the polymer (≤10 nm), while the latter necessitates a decent fullerene domain size to form complementary interpenetrating networks for charge transport to the respective electrodes while avoiding charge recombination.

The morphology of the active layer can be controlled indirectly, but only to a limited extent, by varying such parameters as the chemical composition [2–6] (ratio of polymer and fullerene), the solvent used [2, 3, 7] (with and without additives), and the postproduction treatment conditions [4, 5, 8–16] (thermal annealing), but often the effects of these variables are not understood a priori. Moreover, the self-organization of conjugated polymers is an attractive area of research because the resulting device performance can vary greatly depending on the orientation of polymer crystallites. Indeed, extensive studies have revealed that the active layer morphology influences nearly every aspect of the performance of OPVs, especially their charge separation, charge carrier mobility, series resistance, and rates of electron/hole recombination. Because of the high crystallinity of regio-regular poly (3-hexylthiophene) (RR-P3HT), the morphologies of P3HT:PCBM systems have been the ones studied most intensively. Many characterization techniques have been used to investigate the morphologies of active layers in OPVs; they can be classified into reciprocal-space and real-space techniques. Reciprocal-space techniques generally obtain spatially averaged information—for example, through the use of X-ray or neutron scattering. The packing of RR-P3HT molecules in BHJ solar cells has been probed extensively by X-ray scattering [4, 17–21]. In contrast, techniques for analyzing the phase separation and aggregation of P3HT:PCBM systems require real-space techniques, which typically result in spatially localized data. Common real-space techniques include optical, scanning probe, and electron microscopy [10, 22–25]. In this chapter, due to the limit of space, we focus more on how X-ray scattering and transmission electron microscopy based characterization techniques can be used to analyze the effects of the relative length scales of PCBM clusters and P3HT crystallites on device performance. The improved performance of P3HT:PCBM systems presumably results from (i) self-organization of the P3HT units into oriented crystallites that enhances hole mobility and (ii) matched PCBM aggregation phase domains that provide superior percolation networks for electron transport [26].

8.2 X-Ray Based Techniques

To improve the device performance of OPVs, it is important to have the capability to describe a broad range of physical microstructures. X-rays have been used widely to study the microstructures within organic electronic materials because this region of the electromagnetic spectrum has wavelengths on the order of the physical features being investigated. Many small-scale features (e.g., covalent bond lengths, polymer packing, nanoscale phase segregation) can also be understood by selecting

a specific wavelength (λ) and tuning the incident and collection angles. Through reciprocal space (Fourier space) analysis, X-ray scattering can provide information regarding the structural arrangements in a film, based on elastic scattering of the incident X-rays from the atoms in the system. Scattering measurements can be performed in three geometric modes: transmission, gracing incidence, and reflection [27]. In the transmission scattering geometry (Fig. 8.1a), the sample is placed between the X-ray source and the area detector. The scattering intensity $I(q)$, is measured as a function of the scattering angle (2θ) measured between the incoming beam and the scattered beam. The scattering vector (q) is defined as

$$q = \frac{4\pi}{\lambda} \sin\theta \tag{8.1}$$

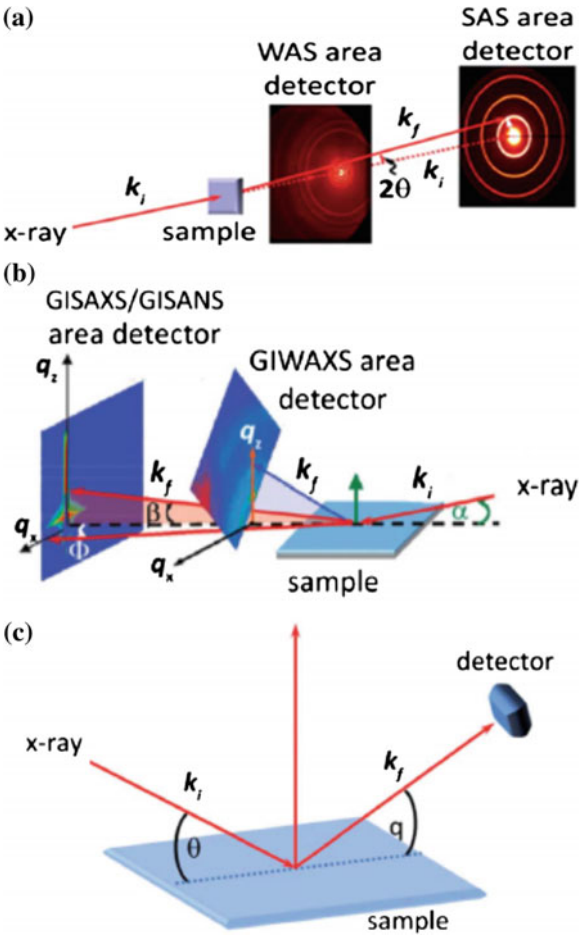

Fig. 8.1 X-ray scattering measurements in **a** transmission; **b** grazing incidence; and **c** reflection geometries (reprinted with permission from [36]. Copyright © 2011 American Chemical Society) (reprinted with permission from [27]. Copyright © 2012 The Royal Society of Chemistry)

In the grazing-incidence scattering geometry (Fig. 8.1b), the incident wavevector, k_i, is kept at a grazing angle (α) with respect to the sample surface to minimize unwanted background signals. The scattered beam of the wavevector k_f, makes an angle β with respect to the sample surface and an in-plane scattering angle Φ with respect to the transmitted beam. The defined scattering vector (q) and components can be expressed as

$$q = k_f - k_i \tag{8.2}$$

$$q_x = k_0[\cos(\Phi)\cos(\beta) - \cos(\alpha)] \tag{8.3a}$$

$$q_y = k_0 \sin(\Phi)\cos(\beta) \tag{8.3b}$$

$$q_z = k_0[\sin(\beta) + \sin(\alpha)] \tag{8.3c}$$

$$k_0 = |k_i| = |k_f| = \frac{2\pi}{\lambda} \tag{8.4}$$

where k_0 is the elastically conserved wave vector modulus. Wide-angle scattering (WAS) is the collective name given to techniques including wide-angle X-ray scattering (WAXS), grazing-incidence wide-angle X-ray scattering (GIWAXS), and X-ray diffraction (XRD). Both scattering and diffraction involve light being re-directed as a result of interacting with atoms. A more precise definition in optics distinguishes scattering, generally implying interaction of electromagnetic waves (or photons) with spatially unordered atoms, from diffraction, the interaction of electromagnetic waves with neatly arranged atoms. Small-angle scattering (SAS) is also the collective name given to techniques including small-angle X-ray scattering (SAXS) and grazing-incidence neutron (GISANS) and X-ray (GISAXS) scattering. In the reflection geometry (Fig. 8.1c), the incident beam impinges onto the surface at an angle θ, with the intensity $I(q)$ detected with respect to 2θ. Relative to the grazing-incidence scattering geometry, its in-plane scattering angle Φ is null and the incident angle and exit angles are both equal to θ. Therefore, both q_x and q_y are equal to zero. The perpendicular scattering vector q_z is given by

$$q_z = 2k_0 \sin(\theta) \tag{8.5}$$

In this section, we focus on the history of the development of WAXS and SAXS for the analysis of microcrystalline of polymer and aggregated domains of fullerenes, respectively, in photoactive layers.

8.2.1 Wide Angle X-Ray Scattering

Organic crystalline materials are well-known examples with orientation order of molecules and the interplay between crystalline and amorphous regions, which

determines their optical and mechanical properties, respectively. This phenomenon is due to the manner in which electrons of highly directional molecular orbitals in soft matter interacting with light. For example, the self-organization of conjugated polymers for use in thin film organic optoelectronic devices is an active area of investigation because the in-plane charge mobility can vary greatly depending on the orientation of the polymer crystallites [28–30]. WAXS and XRD are most commonly employed as auxiliary tools to qualitatively describe the lattice spacing and corresponding grain sizes in organic semiconductor films. Figure 8.2a reveals that the wide-angle X-ray diffraction patterns of non-regioregular P3HT cast films feature a strong peak at 5.25° (16.82 Å), corresponding to the interchain spacing in P3HT associated with the interdigitated alkyl chains, and another weak peak at 23.25° (3.82 Å), corresponding to the interchain spacing in P3HT associated with face-to-face packing of the thiophene rings [31]. In contrast, the patterns of spin-coated films feature a very weak peak at this first-order reflection (5.25°), implying that the degrees of conjugation of spin-coated films are less than those of cast films.

The same peak positions (5.25° and 23.25°) in pristine P3HT:$PC_{61}BM$ blend films casted onto PEDOT:PSS-coated ITO substrates have been observed. [32]. The intensity at 5.25° increased after thermal annealing (Fig. 8.2b-I). Additional strong peaks arose from the crystalline ITO layer beneath the structure. The inset to Fig. 8.2b-I reveals an interchain spacing of 1.64 nm (16.4 Å) for P3HT associated with the interdigitated alkyl chains, slightly shorter than that in pure non-regio-regular P3HT cast films. In contrast, this peak for the spin-coated P3HT:$PC_{61}BM$ blend film in a completed device (Fig. 8.2b-II) was almost invisible. Again, only a very slight increase in intensity at 5.25° was observed after thermal annealing. These XRD data for the pristine spin-coated blend film were the same as those for the pure P3HT spin-coated film (Fig. 8.2a). Accordingly, wide-angle XRD has limitations when analyzing the crystalline structures of polymer:fullerene blend films, due to large quantity of light elements (C, H, O) in organic materials.

To solve the issue of weak signals from wide-angle XRD/WAXS, the incident synchrotron X-ray beam can be fixed at a grazing angle above the critical angle for total reflection of the film material. Because of its longer X-ray traveling distance in the material, the resulting GIWAXS system can then be used to obtain higher intensities and to determine crystalline structures on the atomic length scale. The two-dimensional (2-D) area detector of GIWAXS generates averaged information regarding the morphology through rapid collection of signals over a large range of scattering angles. Unlike the long measurement time required for a point or line detector, the short measurement time when using an area detector can minimize beam damage to the OPV materials and enable in situ time-resolved measurements. GIWAXS can be used to determine molecular packing structures and the orientations of crystalline domains in conjugated P3HT thin films. Figure 8.2c-I shows the self-organization of P3HT results in 2-D conjugated sheets formed through interchain stacking, leading to (100) reflections, due to the lamellar layer structure, and (010) reflections, due to π–π interchain stacking. The inset to Fig. 8.2c-I reveals that high region-regularity (RR = 96 %) P3HT features a preferential “edge-on” orientation of ordered domains, with the (100)-axis normal to the film and the

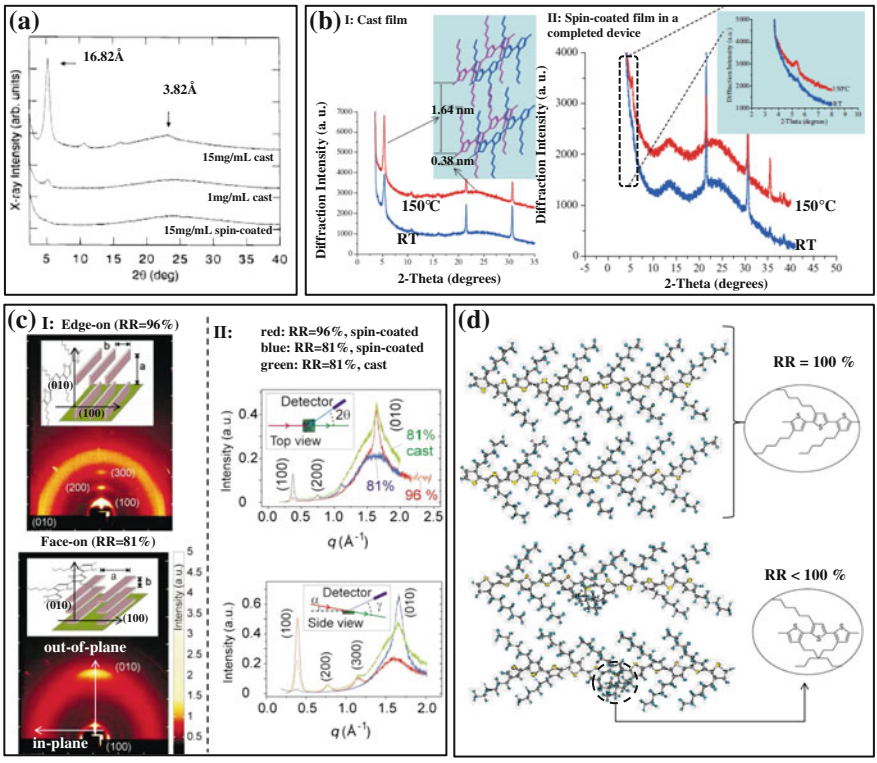

Fig. 8.2 **a** XRD patterns of 15 mg/mL spin-coated, 1 mg/mL cast, and 15 mg/mL cast P3HT films (reprinted permission from [31]. Copyright © 1998 American Chemical Society). **b** *I* XRD patterns of a P3HT:$PC_{61}BM$ film on a ITO/PEDOT:PSS substrate before and after annealing at 150 °C. *II* XRD patterns of a P3HT:PC61BM film from a completed solar cell device before and after annealing at 150 °C (reprinted permission from [32]. Copyright © 2005 Wiley-VCH Verlag GmbH & Co). **c** *I* 2-D GIWAXS diffraction patterns of P3HT films with high RR (96 %) and low RR (81 %) stacked in edge-on and face-on structures, respectively. *II* 1-D GIWAXS intensity profiles from in-plane and out-of-plane scattering geometries (reprinted permission from [28]. Copyright © 1999 Nature Publishing Group). **d** Energy-minimized molecular structures of P3HT; RR = 100 % and < 100 % (reprinted permission from [18]. Copyright © 2006 Nature Publishing Group)

(010)-axis in the plane of the film. In contrast, low region-regularity (RR = 81 %) P3HT features a preferential "face-on" orientation with the (100)-axis in the plane and the (010)-axis normal to the film. The chain packing of high- and low- RR is shown in Fig. 8.2d, which illustrates an energy-minimized molecular structure of P3HT with RR of 100 % and lower than 100 %. The intensity profiles in Fig. 8.2c-II were obtained through line-integration of the semi-circle 2-D diffraction patterns, which were collected in in-plane and out-of-plane scattering geometries. The spin-coated low region-regularity (RR = 81 %, blue line) film provided a stronger peak for the (010) reflection from the out-of plane scattering geometry; in contrast, the

spin-coated high region-regularity (RR = 96 %, red line) film featured stronger peaks for the (010) reflection from in-plane scattering geometry and (100) reflection from the out-of-plane geometry. The solution-cast low region-regularity (RR = 81 %, green line) film presented a (010) reflection from both of these two scattering geometries.

The 2-D diffraction pattern of the pristine low RR-P3HT film (Fig. 8.3a-I, first from the left) exhibits out-of-plane diffraction patterns for the (100), (200), (300), and (010) peaks, corresponding to diffraction angles (2θ) of 5.3, 10.7, 15.9, and 23.3°, respectively [18]. It indicates that this film possessed a face-on lamellar structure with its (010)-axis oriented normal to the substrate (see Fig. 8.2c). In the corresponding 1-D diffraction pattern (Fig. 8.3a-II, the first from the left), the peak intensity at a value of 2θ of 5.3° from the out-of-plane and in-plane patterns decreased and increased, respectively, upon increasing the RR. After annealing at 140 °C (second from the left), the second and third rings were darker in color, revealing that the intensities of the (200) and (300) peaks had increased. For the pristine blend film (third from the left), the intensity of the (100) peak for the low RR-P3HT (RR = 90.7 %) decreased dramatically from both the in-plane and out-of-plane patterns, indicating that blending with $PC_{61}BM$ molecules transformed the original face-on stacking structure. Upon increasing the RR, the intensity of the (100) peak was enhanced; the same phenomena were observed after thermal annealing. These grazing-incidence X-ray diffraction (GIXRD) data support the conclusion that thermal annealing of blend films can improve their intraplane chain stacking [26]. In addition, the low RR-P3HT stimulated the segregation of crystalline P3HT domains out of the disordered blend. Some researchers have reported that adding a low amount of an additive to a polymer:fullerene blend solution can improve the resulting power conversion efficiency (PCE). Figure 8.3b-I presents the 2-D GIWAXS patterns of as-spun P3HT:$PC_{61}BM$ films obtained after various amounts of 1,8-octanedithiol (OT) had been added to 250 μL of the blend solution [21]. The patterns of all of these polymer blend films featured high intensity in the out-of-plane direction; therefore, the packing of P3HT was an edge-on structure. As revealed from the 1-D out-of-plane profiles (Fig. 8.3b-II), the crystallinity of the (100) peak for P3HT increased significantly in the presence of OT, reaching a steady state after 5 μL had been added. The inset to Fig. 8.3b-II reveals average interlayer spacings [d(100)] in P3HT crystals ranging from 16.5 Å (when on OT had been used) to 15.6–15.7 Å (when 2–7.5 μL of OT had been added). The diffraction intensity plotted with respect to the azimuthal angle reveals that the size distribution of the P3HT crystals became broader upon increasing the amount of OT (Fig. 8.3b). Figure 8.3c shows 2-D GIWAXS patterns of PTB7 (a thieno[3,4-b] thiophene and benzodithiophene alternating copolymer):$PC_{61}BM$ blend films prepared by pure chlorobenzene (CB), mixtures of CB and diiodooctane (DIO) (98:2 v/v%), pure dichlorobenzene (DCB), and mixtures of DCB and DIO (98:2 v/v%). The (100) scattering of PTB7 copolymer exhibits similar ring-like patterns at q = 0.3–0.4 $Å^{-1}$ and the (010) scattering is only observed out of plane, suggesting that PTB7 copolymer chains mainly remain in the face-on conformation [33].

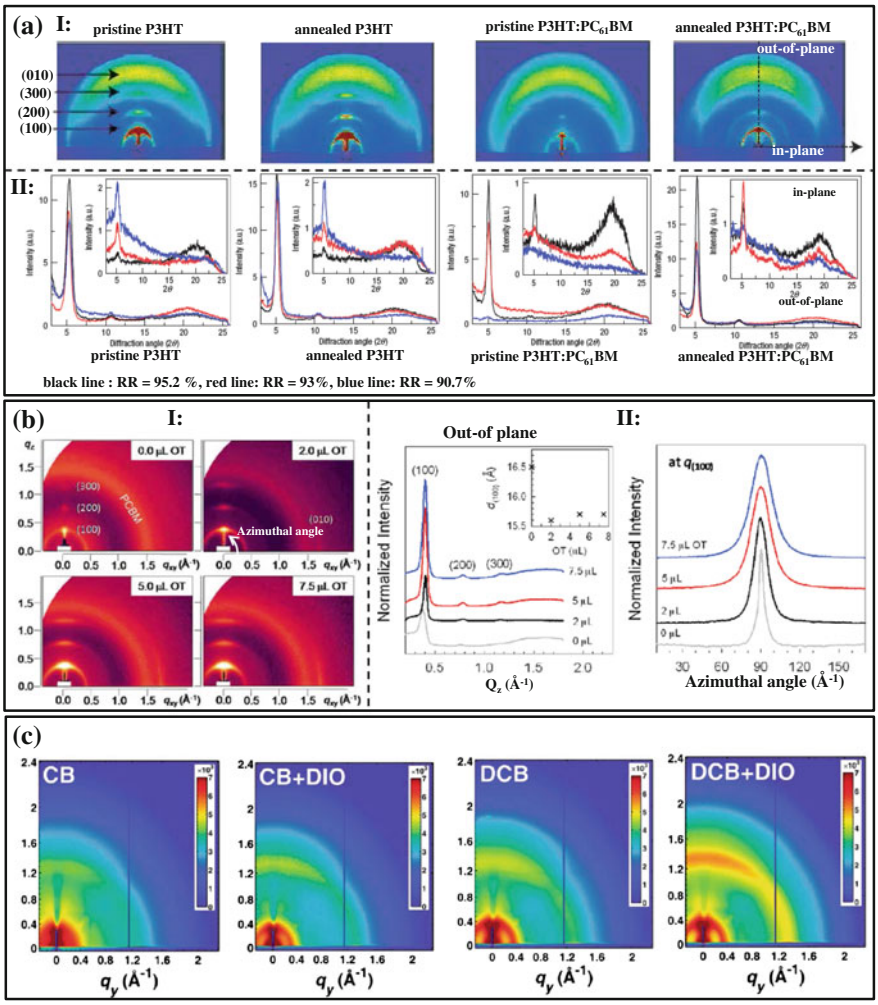

Fig. 8.3 **a** *I* 2-D GIWAXS diffraction patterns of P3HT films and P3HT:$PC_{61}BM$ (1:1) blend films under pristine and annealed conditions. *II* 1-D GIWAXS diffraction patterns of P3HT films and P3HT:$PC_{61}BM$ (1:1) blend films under pristine and annealed conditions, recorded in out-of-plane and in-plane directions (reprinted permission from [18]. Copyright © 2006 Nature Publishing Group). **b** *I* 2-D GIWAXS patterns of P3HT:$PC_{61}BM$ (1:1) blend films incorporating various amounts of OT *II* the 1-D out-of-plane patterns, and azimuthal scan patterns. Inset to 1-D out-of-plane patterns: interlayer spacing in the (100) direction calculated with respect to the amount of OT (reprinted permission from [21]. Copyright © 2009 American Chemical Society). **c** 2-D GIWAXS patterns of PTB7:$PC_{61}BM$ blend films prepared by pure CB, mixtures of CB and DIO (98:2 v/v%), pure DCB, and mixtures of DCB and DIO (98:2 v/v%) (reprinted permission from [33]. Copyright © 2011 American Chemical Society)

8.2.2 Simultaneous GISAXS/GIWAXS

In contrast to the ability of WAXS to characterize structures in sub-nanometer, SAXS provides a powerful means of investigating the domain shapes and sizes, size distributions, and spatial correlations. In addition, another advantage is to capture the rapid formation of PCBM nano aggregates in P3HT matrices upon annealing [6, 26, 34]. It is essential to extract structural parameters of the morphology from SAXS intensities and then perform fitting to a model.

Phase-separated domains in the active layers of BHJ solar cells provide interfaces for charge separation of photo-generated excitons and pathways for separated charge carrier transport to the respective electrodes; therefore, they critically affect a device's PCE.

It is reported that simultaneous GISAXS/GIWAXS techniques [26] were used for studying the mutual interactions between the donor and acceptor units—phenomena that actually govern the final phase separation or morphology [6, 26]. Figure 8.4a displays the GISAXS/GIWAXS profiles of as-cast and thermal annealed P3HT:$PC_{61}BM$ films. The sizes of the P3HT crystallites at the (100) reflection (D_{100}) can be obtained using Scherrer's relation: [17]

$$D_{hkl} = \frac{0.9\lambda}{\beta_{hkl}\cos\theta} \tag{8.6}$$

where D_{hkl} is the apparent crystallite size along the [*hkl*] direction and β_{hkl} is the full width at half maximum of an (*hkl*) diffraction (in radians). The P3HT crystallites dramatically increased in size—from 9.6 nm in the as-cast film to 16.0 nm—after annealing at 150 °C for 15 min. In Fig. 8.4a, a small scattering peak in the low-Q range (ca. 0.006 $Å^{-1}$) of the GISAXS curves for the as-cast film is possibly

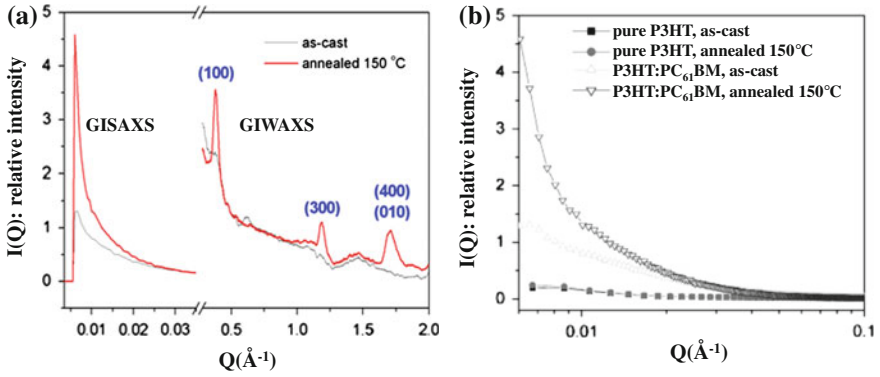

Fig. 8.4 **a** GISAXS/GIWAXS curves of as-cast and annealed P3HT:$PC_{61}BM$ films (not to scale). **b** GISAXS curves of P3HT and P3HT:$PC_{61}BM$ thin films after casting and annealing process (reprinted permission from [26]. Copyright © 2008 Wiley-VCH Verlag GmbH & Co)

attributable to the presence of $PC_{61}BM$ in P3HT. For confirming this scattering peak, pure P3HT thin films was also characterized by GISAXS for identifying the phase separation inside the P3HT:$PC_{61}BM$ thin films. Figure 8.4b shows that the annealing at 150 °C for 15 min does not affect the low-Q intensity of the GISAXS profile of the P3HT film, indicating that even if there is local phase separation inside the P3HT film, it does not contribute much to the intensity change in the low-Q region. Moreover, the GISAXS intensity of the as-cast or annealed P3HT/PCBM thin film is much larger than that of the as-cast or annealed pure P3HT thin film, probably due to the large electron density difference between PCBM and P3HT (0.7 vs. 0.4 electrons $Å^{-3}$). Therefore, the GISAXS features in the low-Q region of P3HT/PCBM thin film are clearly dominated by PCBM, and we attribute the large GISAXS intensity change in the P3HT/PCBM thin film after annealing at 150 °C for 15 min to a significant growth of the PCBM aggregates. The PCBM scattering intensity increased dramatically as a result of the PCBM molecules diffusing out of the P3HT matrix and forming larger PCBM clusters [35]. The radius of gyration (Rg) of a PCBM cluster can be determined from the scattering peak intensity using the Guinier approximation:

$$I(Q) = I(0)\exp\left(-\frac{Q^2R_g^2}{3}\right) \tag{8.7}$$

where $I(Q)$ is the scattering intensity, $I(0)$ is the zero-angle scattering intensity, and Q is defined as $4\pi\sin(\theta/2)/\lambda$ in terms of the scattering angle θ and the wavelength λ. After annealing at 150 °C for 15 min, the value of Rg increased dramatically to 23 ± 3 from 15 ± 2 nm for the as-cast film. Thus, it appears that large-scale diffusion of PCBM molecules into the P3HT matrix to form aggregates occurred only at temperatures at or above 150 °C. Hence, different mechanisms dominate the development of the P3HT/PCBM blend morphology at different temperatures. At the glass transition temperature (100 °C), increased planar stacking of P3HT chains occurred, thereby increasing the P3HT/PCBM crystallite size without affecting the cluster size of the PCBM molecules. At 150 °C, the PCBM molecules diffused to form large clusters; therefore, phase separation of P3HT and PCBM occurred to provide improved continuous pathways for the holes and electrons.

The dimensions and orientations of P3HT crystallites and the sizes of $PC_{61}BM$ aggregates in BHJ thin films have been determined [6]. The $PC_{61}BM$ aggregate size and density required for optimal performance of a film in a photovoltaic device resulted in deteriorated ordering in the out-of-plane direction, but it improved the in-plane packing of the P3HT lamellae. When the P3HT crystallites and $PC_{61}BM$ aggregates had comparable domain sizes and number densities, the inter-percolated networks for electron- and hole-transport were optimized in the film. This new understanding of the underlying mechanism of carrier mobility in BHJ thin films might be critical if we are to improve the efficiency of future solar cells.

The competition between fullerene aggregation and P3HT crystallization upon annealing of BHJ solar cells has been revealed using time-resolved GISAXS/

GIWAXS [36]. With its enhanced time and spatial resolution (5 s/frame; minimum q = ca. 0.004 $Å^{-1}$), GISAXS can be used to capture in detail the rapid growth of PCBM aggregates, from 7 to 18 nm, within 100 s of annealing at 150 °C. Simultaneously, the enhanced crystallization of P3HT into lamellae oriented mainly perpendicular, but also parallel to, the substrate is also observed. The kinetics of both $PC_{61}BM$ aggregation and P3HT crystallization could be characterized using similar Avrami exponents close to unity. Other crystalline conjugated polymers blended with fullerenes and exhibiting an "additive effect" have also been investigated using GISAXS/GIWAXS to determine the relationship between the morphology and the device performance [37]. When the active layer was processed with a diiodoalkane additive, which effectively induced higher polymer crystallinity and removed the grain boundary of the large $PC_{71}BM$-rich grains, a more-uniform film morphology resulted on the mesoscale. The morphologies and device performances of a low-bandgap conjugated polymer and its blend with PCBM have been characterized using GIWAXD and small-angle neutron scattering [38]. The results revealed that crystallization of PSBTBT and segregation of PCBM occurred during spin coating, with thermal annealing increasing the ordering of PSBTBT and enhancing the segregation of PCBM, forming domains that were approximately 10 nm in size, leading to improved photovoltaic performance.

8.2.3 X-Ray Reflectivity

Recently, morphological studies using complementary techniques to determine the phase separation behavior of P3HT and $PC_{61}BM$ in the in-depth (vertical) direction of films have become very active, in an attempt to correlate and utilize the vertical phase separation features of the two components to further improve device performance [39]. Among such studies, X-ray photoelectron spectroscopy has revealed that PCBM is enriched near the film–substrate interface in P3HT:$PC_{61}BM$ blends [40]; with its greater in-depth spatial resolution, neutron reflectivity has revealed a stratified morphology comprising a main layer of uniform P3HT:$PC_{61}BM$ and a $PC_{61}BM$-enriched interfacial layer(s) [40, 41]. Results from variable-angle spectroscopic ellipsometry (VASE) have suggested, however, a linear decrease in the $PC_{61}BM$ concentration, starting from the film–substrate interface, in P3HT/PCBM blend films [42]. In contrast, electron tomography revealed that P3HT was substantially depleted from the film surface, suggesting that the film surface might be PCBM-enriched [10]. Concentration fluctuations of P3HT initiated from the surface of pure P3HT toward the bulk of the P3HT/PCBM blend have, however, been reported based on secondary ion mass spectrometry (SIMS) [43]; consequently, surface-directed spinodal decomposition during solvent evaporation has been proposed as a possible mechanism for the vertical and the subsequent lateral (or local) phase separations of bicontinuous P3HT and PCBM nanodomains. Spinodal decomposition could not account, however, for the phase separation behavior of the blend on several other occasions [14, 15, 36]. In most of these cases, enrichment of

PCBM adjacent to the film–substrate interface was observed for the P3HT:PCBM films similarly processed; nevertheless, the surface compositions of the films were inconsistent. Therefore, the precise vertical phase separation behavior of this intensively studied system awaits further scrutiny [39]. Notably, in all of the studies we have mentioned, a two-phase model—namely, the film space is filled with either P3HT or $PC_{61}BM$—was postulated to deduce or interpret the vertical phase separation of the two components in the films. A vertical composition profile deduced based on selective sensitivity of the employed tool toward either P3HT or PCBM alone, however, would not be appropriate when the two-phase assumption is likely to fail near the asymmetric film's interface with either the air or the substrate.

A neutron and X-ray reflectivity study [44] has aimed to resolve quantitatively and systematically the vertical composition profiles of P3HT:$PC_{61}BM$ thin films spun-cast onto Si wafers, using the variation in contrast of the X-ray and neutron reflectivity (XR/NR) with high spatial resolution in the in-depth direction and excellent film penetration power [45]. The results revealed that a three-phase model, with porosity included as the third phase, was indispensable when attempting to resolve the absolute vertical volume fraction profiles of PCBM and P3HT in the film, especially near the surface and interface. Figure 8.5 provides a cartoon representation of an optimized morphology for P3HT:$PC_{61}BM$ thin-film solar cells. This optimized morphology of the annealed P3HT/PCBM film was determined on the basis of the vertical phase separation features observed using NR/XR and the

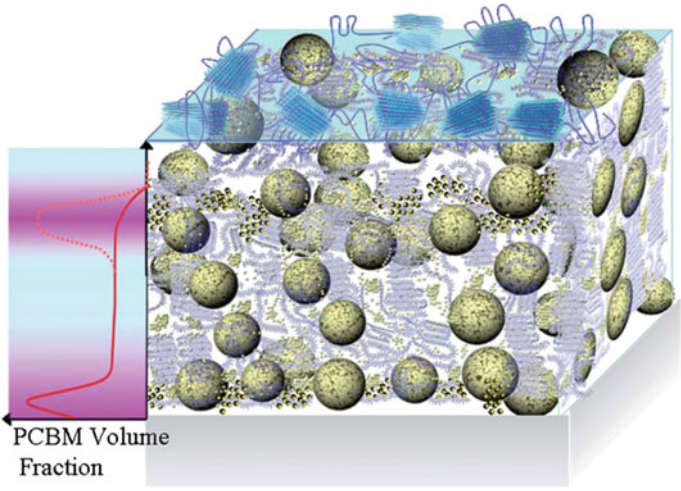

Fig. 8.5 Cartoon representation of an optimized morphology for P3HT:$PC_{61}BM$ thin-film solar cells. Intercalated $PC_{61}BM$ aggregates (*large spheres*) and P3HT lamellar domains (worm-like stacks) are dispersed in the matrix of amorphous chains of P3HT with dissolved PCBM (*small spheres*). To the *left* Vertical P3HT- and $PC_{61}BM$ -enriched regions are colored *sky-blue* and *pink*, respectively, together with the $PC_{61}BM$ volume fraction profile (*solid curve*). The *dotted curve* near the surface depicts an additional $PC_{61}BM$-enriched layer accumulated below the surface P3HT layer (reprinted permission from [44]. Copyright © 2011 Royal Society of Chemistry)

local phase separation for PCBM and P3HT nanodomains observed using GISAXS/GIWAXS.

In general, the observed stratified film morphology comprises a surface layer of high porosity, a main layer of uniform composition (being close to the prescribed composition, when below the miscibility limit), and a PCBM-enriched (or P3HT-depleted) interface layer exhibiting a small fraction of porosity adjacent to the substrate. The porosity features of the surface and interface transition layers of the two-component system had been overlooked in many previous studies performed using microscopic techniques or scattering tools that lack contrast variation or adequate spatial resolution. The notion of high surface porosity, together with the absolute vertical volume fraction profiles, helped to reconcile several previously seemingly contradictory suggestions regarding the vertical phase separation behavior of P3HT and $PC_{61}BM$ in the blend. Also discussed in that report were the respective mechanistic origins of the 1-D vertical phase separation for the stratified morphology upon film drying and the subsequent local phase separation for formation and growth of three-dimensional (3-D) $PC_{61}BM$ nanograins and P3HT lamellae upon annealing, as revealed by GISAXS/GIWAXS. These results hint at further advances in device performance through minimization of porosity, thereby improving the interfacial contacts of the active layer with the electrodes of BHJ thin-film solar cells.

Using the contrast variation of XR/NR with high spatial resolution in the film in-depth direction and a three-phase model, we determined the vertical phase separation behavior of composite films of P3HT:$PC_{61}BM$. The stratified composition profiles obtained for the films feature, in general, a porous surface layer, a solid main layer, and a PCBM-enriched interfacial layer of small porosity; a PCBM-excess layer begins to form beneath the surface P3HT layer when the metastable miscibility limit of the two components is approached (weight ratio: ca. 1:1). Within the studied ranges of composition and annealing temperature, annealing was found to modestly influence the global vertical (1-D) phase separation of the film through diffusion of non-localized PCBM molecules and amorphous P3HT chains. In contrast, upon annealing, a substantial amount of demixed PCBM and P3HT formed intercalated—hence, localized—$PC_{61}BM$ and P3HT nanograins, as revealed using GISAXS/GIWAXS; such critical local phase separation significantly improved the device performance, but it contributed only marginally to the global changes in the vertical composition profile. The observed high surface porosity and the concentration-dependent vertical volume fractions of P3HT and $PC_{61}BM$ not only help to reconcile several previously seemingly contradictory conclusions regarding the surface compositions of BHJ thin-film solar cells but also provide hints about the mechanistic origins of the related phase separation behavior.

8.3 Electron Microscopy-Based Techniques

The phase separation of polymer and fullerene domains can affect the performance of photovoltaic cells because they critically affect exciton dissociation and charge transport. In organic semiconductors, high-efficiency charge separation occurs only at the boundary between the donor and acceptor. Understanding the phase separation process will assist researchers to optimize fabrication processes and, thereby, improve device performance.

8.3.1 Transmission Electron Microscopy (TEM)

Transmission electron microscopy (TEM) has been used widely to characterize the morphologies of the active layers in OPVs, as a result of its high spatial resolution (up to 1 nm) and rapid acquisition rate. Three main operation modes (imaging, diffraction, spectroscopy) can be equipped in TEM to provide information regarding the chemical and phase compositions of various materials. In the imaging mode, the transmitting electron beam interacts with an ultra-thin specimen. The image is magnified and focused onto an imaging device (e.g., a fluorescent screen) or a layer of photographic film, or it is detected using a charge-coupled device (CCD). When the electron beam is transmitted through the specimen, some electrons will undergo inelastic scattering, which means that they lose energy and have their paths deflected randomly. The amount of energy that is lost can be measured using an electron spectrometer, recorded as an energy profile. This spectroscopy mode is typically called electron energy loss spectroscopy (EELS). In diffraction mode, crystallite materials can induce a diffraction pattern after placing apertures in the back focal plane. The preparation of specimens for TEM can be a complex procedure because they are required to be at most hundreds of nanometers thick. For example, carving with a focused ion beam (FIB) can provide specimens suitable for cross-sectional TEM investigation. In the case of OPVs, the main concern is beam damage through heating and charging of the largely semi-crystalline organic materials. Accordingly, special precautions, such as imaging at cryogenic temperatures or varying the incident beam energy, are often required to alleviate beam damage.

P3HT:$PC_{61}BM$ BHJ Film

Figure 8.6a displays bright-field TEM images of pristine and thermally annealed (120 °C, 60 min) P3HT:$PC_{61}BM$ layer [46]. Here, the annealing process was performed on a complete device. For specimen preparation, the top metal contact of the OPV device was etched with HCl solution and then the bottom ITO layer was dissolved to allow the photoactive layer (P3HT:$PC_{61}BM$) to float to the water surface; the active layer was transferred to a TEM grid for further analysis. In the pristine film, fibril-shaped P3HT crystals having sizes in the nanometer range appeared bright relative to the background and exhibited a tendency to form a

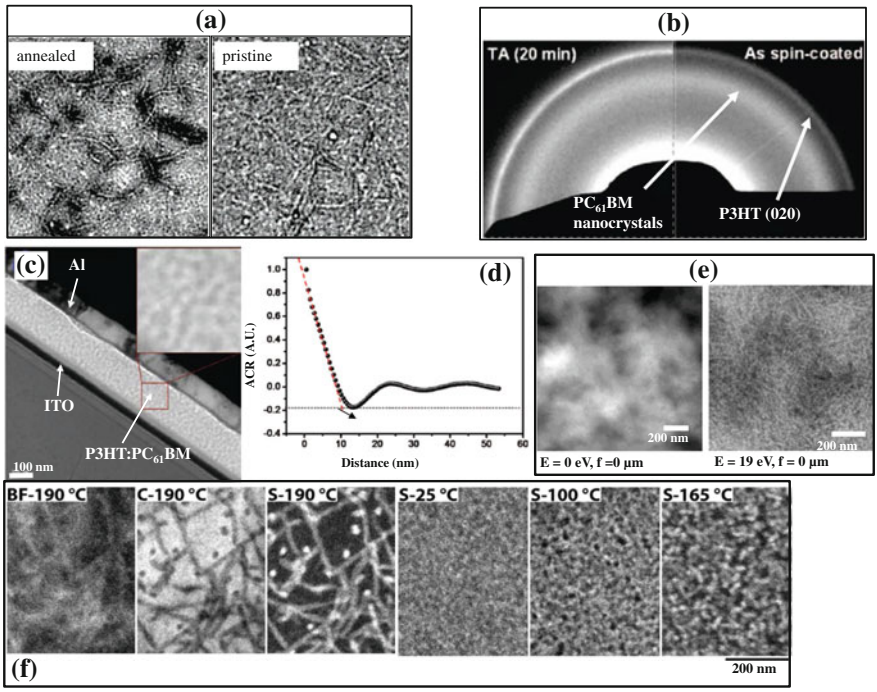

Fig. 8.6 **a** BF TEM images of pristine and thermally annealed P3HT:$PC_{61}BM$ films (reprinted permission from [46]. Copyright © 2005 American Chemical Society). **b** Diffraction patterns of the as-deposited (pristine) and thermally annealed P3HT:$PC_{61}BM$ films (reprinted permission from [10]. Copyright © 2009 American Chemical Society). **c** Cross-sectional TEM image of the P3HT:$PC_{61}BM$ film. *Inset* Magnified image (reprinted permission from the [23]. Copyright © 2009 American Chemical Society). **d** ACR obtained from the cross-sectional TEM image (reprinted permission from [23]. Copyright © 2009 American Chemical Society). **e** EFTEM images of zero energy-loss (E = 0 eV; f = 0 µm) and energy-loss (E = 19 eV; f = 0 µm) (reprinted permission from [49]. Copyright © 2010 American Chemical Society). **f** BF, S, and C maps for a P3HT:$PC_{61}BM$ film annealed for 30 min at 25, 100, 165, and 190 °C (reprinted permission from [13]. Copyright © 2011 American Chemical Society)

network. After thermal annealing, the most pronounced feature was the increased contrast of the fibrillar P3HT crystals throughout the entire film. The widths of these crystals remained almost constant relative to those in the pristine film, but their average length increased. In addition, various larger dark regions ($PC_{61}BM$-rich domains) appeared as evidence for increased demixing between P3HT and $PC_{61}BM$.

Figure 8.6b displays an outer ring corresponding to the (020) reflections of the P3HT fibrillar crystals randomly oriented within the film sample area, with a broader inner ring attributed to nanocrystalline $PC_{61}BM$ structures [10]. Prior to thermal annealing, few P3HT crystals were formed during spin-coating, with the films also featuring a large number of stacking defects. The crystallinity of P3HT

increased significantly after thermal annealing. The intensities of the $PC_{61}BM$ reflection rings in the diffraction patterns also increased slightly relative to that in the pristine film. Based on the TEM images and diffraction patterns, the thermal annealing process appeared to produce and stabilize a nanoscale interpenetrating network, with crystalline order for both P3HT and $PC_{61}BM$, thereby increasing the PCE [32]. Nevertheless, mesoscale phase separation features are usually difficult to distinguish through TEM because the small differences in chemical structure result in low contrast and superposition on the nanoscale. To overcome this obstacle, Heeger [47] and co-workers performed a spatial Fourier transform of the TEM image intensity to obtain the power spectral density (PSD), which could be used to quantitatively analyze the mesoscale phase separation. They found that nanoscale phase separation could be optimized rapidly (10 min required) to form a structure that remained stable for 2 h at high temperature. Both mesoscale and nanoscale phase separation occurred for P3HT and $PC_{61}BM$. The cross-sectional morphology [23] (see Fig. 8.6c) of the active layer after FIB provided information regarding the pathways for charge transport throughout the thickness of the film. The proposed autocorrelation function (ACR) provided important information about the semiperiodic structures and domain size. When a tangential straight line was drawn from the point ($x = 0$) of the ACR, the line intercepted the baseline at the minimum point, giving an average $PC_{61}BM$ domain size of 11 nm (see Fig. 8.6d) [48]. The PSD and ACR analyses both indicated that the morphologies of the RR-P3HT:$PC_{61}BM$ materials were nearly ideal for efficient charge separation and the resulting generation of mobile carriers.

In addition to the Fourier transform analysis, tomographic analysis [10, 22] is another powerful tool providing insight into the morphologies of P3HT:$PC_{61}BM$ photoactive layers. Using a mathematical procedure, a 3-D nanoscale organization can be reconstructed from a series of 2-D projections. A great deal of new structural information, which can never be obtained from conventional microscopy or various scattering methods, can be evaluated directly from the 3-D volume data provided by electron tomography—especially to quantify the amount and distribution of fibrillar P3HT nanocrystals throughout the volume of the active layer. It has been reported that the most efficient photovoltaic devices were obtained, after thermal annealing, when the $PC_{61}BM$ loading was 40 % by weight. The photoactive layer characterized by 3-D tomography presented an overall high degree of P3HT crystallinity (45 %). When the $PC_{61}BM$ loading ratio was increased to 60 %, the overall crystallinity of P3HT decreased to 27 %. In addition, the crystallinity distribution, concentrated in the upper part of the film (close to the electrode), had a detrimental effect on the device performance [22].

8.3.2 Energy-Filtered Transmission Electron Microscopy (EFTEM)

Even though electron tomography is a powerful tool for 3-D characterization, it is difficult to use this method to generate contrast from typical high-efficiency devices prepared from compositionally similar materials. Therefore, low-loss energy-filtered transmission electron microscopy (EFTEM) has been combined with tomography to generate spectroscopic contrast from P3HT and $PC_{61}BM$ domains. When a beam of high-energy electrons illuminates a thin sample, most electrons will pass through it without losing energy, but some electrons will lose energy through inelastic scattering from the sample. In EFTEM, the electron beam emerging from the sample is passed through a magnetic prism. The resulting flight path of the electrons will vary depending on their energy, forming an EELS spectrum. An adjustable slit can be placed to allow the passage of electrons having a certain range of energies; an image is then reformed on a detector. Herzing et al. [49] reported the use of EFTEM to generate spectroscopic contrast for a P3HT:$PC_{61}BM$ photoactive layer. The zero energy-loss TEM image of a BHJ film at Gaussian focus in Fig. 8.6e demonstrates the difficulty in generating distinguishable contrast between the polymer and fullerene phases, due to the intrinsically low amplitude contrast differentiating these compositionally similar phases. The contrast of the spectral image in Fig. 8.1e was improved significantly after performing EFTEM with the energy-selecting slit centered at 19 eV loss and Gaussian focus. As a result of electron–sample interactions in the electron microscope, EFTEM allows mapping of the local elemental analysis. Figure 8.6f displays bright-field (BF), carbon (C), and sulfur (S) maps of the nanoscale morphology after annealing at temperatures from 25 to 190 °C. For samples annealed at 190 °C, the contrast in the images of P3HT (fibers shape) in the C and S maps was higher than that in the BF image [13]. The image intensities in S or C maps were proportional to the concentrations of S or C atoms. In addition, the S maps revealed that increasing the annealing temperature transformed the amorphous P3HT into fibrillar P3HT nanocrystals in a $PC_{61}BM$-rich matrix. Another application of EELS was elemental analysis [14]. The penetration of aluminum into the photoactive layer could be detected in the devices prior to thermal annealing. To reliably identify the P3HT and $PC_{61}BM$ phases, EELS was combined with nonlinear multivariate statistical analysis to classify multispectral image data [25]. By capturing a sufficient number of imaging planes of the sample, visualization of the 3-D structure was possible, revealing the interfacial morphology of the donor and acceptor phases. This approach allows the nanoscale morphology determined through material contrast to be correlated with the measured solar cell efficiency.

8.4 Morphology of Low-Bandgap Conjugated Polymer: PCBM BHJ Films

In addition to P3HT:$PC_{61}BM$ systems, organic solar cells incorporating photoactive layers of other low-bandgap conjugated polymers and PCBM have also attracted much attention because of their high PCEs. Park et al. [2] reported certified high-efficiency solar cells (5.9 %) fabricated using poly[N-9″- heptadecanyl-2,7-carbazole-alt-5,5-(4,7′-di-2-thienyl-2′,1′,3′-benzothiadiazole)] (PCDTBT):$PC_{71}BM$ as the photoactive layer. Figure 8.7a presents TEM images of spin-cast PCDTBT:$PC_{71}BM$ films prepared at various blending ratios. Upon increasing the amount of $PC_{71}BM$ in the film, the fibrillar PCDTBT structure gradually emerged, appearing clearly in their TEM images, as a result of nanoscale phase separation; the implication is that increasing the amount of fullerene caused the PCDTBT network to form longer and better-connected pathways. Figure 8.7b displays TEM images of a blend film [5] comprising self-assembled poly(3-butylthiophene) nanowires (P3BT-NWs) and $PC_{71}BM$ at a weight ratio of 1:1. Two different processing conditions were applied—one involving a short drying time (3 min) and subsequent annealing at 175 °C and the other involving a long drying time (100 min) without high temperature annealing—to determine how the evolution of the structure affected the device performance. The sample obtained after short drying/high temperature annealing featured fewer random P3BT nanowires than did the sample obtained after merely a long drying time. Three strong electron diffraction rings [at (100), (200), and (010)] and a single weak one (inset) were associated with crystalline P3BT and nanocrystalline $PC_{71}BM$, respectively, similar to the diffraction pattern of P3HT:$PC_{61}BM$ (see Fig. 8.1b). A comparison of the performance of the devices obtained under these two sets of conditions revealed that the PCE obtained after high temperature annealing (2.27 %) was greater than that (1.18 %) for the sample processed without annealing. The PCE could be increased further upon increasing the drying time prior to high temperature annealing. The cartoon representation in Fig. 8.7b [5] depicts the structural evolution in P3BT-NW:$PC_{71}BM$ blends. A short or long drying time had very little effect on the density of P3BT-NWs. The device performance improved after the annealing process, which caused the fullerene phase to aggregate significantly in the interstices of the P3BT-NWs. Adding an additive decreased the grain sizes of the fullerene domains.

Su et al. [37] tested the effects of small amounts (0.5 vol.%) of additives—including 1,4-diiodobutane (DIB), 1,6-diiodohexane (DIH), and 1,8-diiodooctane (DIO)—in blended poly[bi(dodecyl)thiophene- thieno(3,4-c)pyrrole-4,6-dione] (PBTTPD):$PC_{71}BM$ systems; they found that the addition of DIH resulted in the highest PCE (7.3 %). The TEM morphological images in Fig. 8.7c feature bright and dark regions corresponding to PBTTPD-and $PC_{71}BM$-rich domains, respectively. Large $PC_{71}BM$ grains (dimensions: ca. 150 nm; mean spacing: ca. 340 nm) are evident in the image of the film processed without any additives; the average size of the $PC_{71}BM$ grains decreased to ca. 30 nm for the film prepared with DIH as the additive.

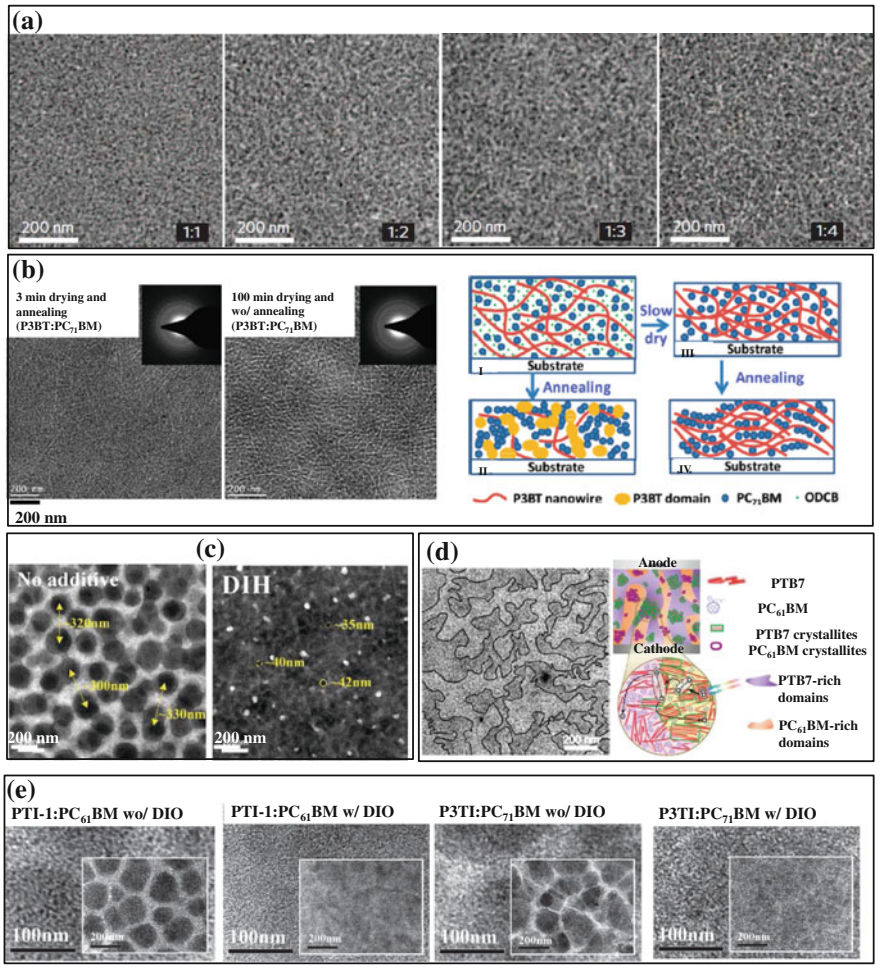

Fig. 8.7 **a** TEM images of PCDTBT:$PC_{71}BM$ films prepared at blend ratios of 1:1, 1:2, 1:3, and 1:4 (reprinted permission from [2]. Copyright © 2009 Nature Publishing Group). **b** BT-TEM images of P3B-NW:$PC_{71}BM$ films and a cartoon of the drying process (reprinted permission from [5]. Copyright © 2010 American Chemical Society). **c** TEM images of PBTTPD:$PC_{71}BM$ films prepared with and without DIH (reprinted permission from [37]. Copyright © 2011 Wiley-VCH Verlag GmbH & Co). **d** BF-TEM images of PTB7:$PC_{61}BM$ films prepared with DIO as the additive and a cartoon of the BHJ refined model (reprinted permission from [33]. Copyright © 2011 American Chemical Society). **e** TEM images of blends of PTI-1:$PC_{61}BM$ (2:3) and P3TI: PC71BM, both prepared with and without DIO as the additive. *Insets* Lower-magnification images (reprinted permission from [50]. Copyright © 2012 Wiley-VCH Verlag GmbH & Co)

Recently, a high PCE of 7.4 % [33] was obtained for a device incorporating a PTB7:$PC_{61}BM$ blend as the photoactive layer, prepared using dichlorobenzene as the solvent and DIO as the additive. The BF-TEM image in Fig. 8.7d reveals that

the PTB7- and $PC_{61}BM$-rich domains were differentiated by solid lines at the heterojunctions. The proposed refined model (Fig. 8.7d-cartoon) indicated that features of three length scales were present in this blend: nanocrystallites of several nanometers, polymer/fullerene nanocrystallite aggregates of tens of nanometers, and polymer/fullerene domains of hundreds of nanometers. Crystalline structures can minimize the charge transfer energy and lead to a larger separation distance in the charge transfer state, thereby facilitating exciton dissociation. The photocurrent was attributed primarily to the dissociated excitons photogenerated in the PTB7 nanocrystallite aggregates, rather than the amorphous intermixed PTB7/$PC_{61}BM$–rich domains. Vandewal et al. [50] compared the morphologies of PTI-1:$PC_{61}BM$ and P3TI:$PC_{71}BM$ blends prepared with and without DIO as the additive (see Fig. 8.7e). For both systems, clear phase separation occurred in the active layers processed without DIO. In contrast, the addition of DIO caused the big domains to disappear and form a much finer morphology.

References

1. G. Yu, J. Gao, J.C. Hummelen, F. Wudl, A.J. Heeger, Science **270**, 1789–1791 (1995)
2. S.H. Park, A. Roy, S. Beaupre, S. Cho, N. Coates, J.S. Moon, D. Moses, M. Leclerc, K. Lee, A.J. Heeger, Nat. Photonics. **3**, 297–303 (2009)
3. S. Barrau, V. Andersson, F.L. Zhang, S. Masich, J. Bijleveld, M.R. Andersson, O. Inganas, Macromolecules **42**, 4646–4650 (2009)
4. G. Li, Y. Yao, H. Yang, V. Shrotriya, G. Yang, Y. Yang, Adv. Funct. Mater. **17**, 1636–1644 (2007)
5. H. Xin, O.G. Reid, G.Q. Ren, F.S. Kim, D.S. Ginger, S.A. Jenekhe, ACS Nano **4**, 1861–1872 (2010)
6. M.Y. Chiu, U.S. Jeng, M.S. Su, K.H. Wei, Macromolecules **43**, 428–432 (2010)
7. Y. Yao, J.H. Hou, Z. Xu, G. Li, Y. Yang, Adv. Funct. Mater. **18**, 1783–1789 (2008)
8. F. Padinger, R.S. Rittberger, N.S. Sariciftci, Adv. Funct. Mater. **13**, 85–88 (2003)
9. D.M. Stevens, Y. Qin, M.A. Hillmyer, C.D. Frisbie, J. Phys. Chem. C **113**, 11408–11415 (2009)
10. S.S. van Bavel, E. Sourty, G. de With, J. Loos, Nano Lett. **9**, 507–513 (2009)
11. S. Honda, T. Nogami, H. Ohkita, H. Benten, S. Ito, Acs. Appl. Mater. Int. **1**, 804–810 (2009)
12. W.C. Tsoi, S.J. Spencer, L. Yang, A.M. Ballantyne, P.G. Nicholson, A. Turnbull, A.G. Shard, C.E. Murphy, D.D.C. Bradley, J. Nelson, J.S. Kim, Macromolecules **44**, 2944–2952 (2011)
13. D.R. Kozub, K. Vakhshouri, L.M. Orme, C. Wang, A. Hexemer, E.D. Gomez, Macromolecules **44**, 5722–5726 (2011)
14. D.A. Chen, A. Nakahara, D.G. Wei, D. Nordlund, T.P. Russell, Nano Lett. **11**, 561–567 (2011)
15. D. Chen, F. Liu, C. Wang, A. Nakahara, T.P. Russell, Nano Lett. **11**, 2071–2078 (2011)
16. G. Li, V. Shrotriya, J.S. Huang, Y. Yao, T. Moriarty, K. Emery, Y. Yang, Nat. Mater. **4**, 864–868 (2005)
17. T. Erb, U. Zhokhavets, G. Gobsch, S. Raleva, B. Stuhn, P. Schilinsky, C. Waldauf, C.J. Brabec, Adv. Funct. Mater. **15**, 1193–1196 (2005)
18. Y. Kim, S. Cook, S.M. Tuladhar, S.A. Choulis, J. Nelson, J.R. Durrant, D.D.C. Bradley, M. Giles, I. Mcculloch, C.S. Ha, M. Ree, Nat. Mater. **5**, 197–203 (2006)
19. C.H. Woo, B.C. Thompson, B.J. Kim, M.F. Toney, J.M.J. Fréchet, J. Am. Chem. Soc. **130**, 16324–16329 (2008)

20. C.W. Chu, H.C. Yang, W.J. Hou, J.S. Huang, G. Li, Y. Yang, Appl. Phys. Lett. **92,** 103306 (2008)
21. H.Y. Chen, H.C. Yang, G.W. Yang, S. Sista, R.B. Zadoyan, G. Li, Y. Yang, J. Phys. Chem. C **113**, 7946–7953 (2009)
22. S.S. van Bavel, M. Barenklau, G. de With, H. Hoppe, J. Loos, Adv. Funct. Mater. **20**, 1458–1463 (2010)
23. J.S. Moon, J.K. Lee, S.N. Cho, J.Y. Byun, A.J. Heeger, Nano Lett. **9**, 230–234 (2009)
24. J.S. Moon, C.J. Takacs, Y.M. Sun, A.J. Heeger, Nano Lett. **11**, 1036–1039 (2011)
25. M. Pfannmoller, H. Flugge, G. Benner, I. Wacker, C. Sommer, M. Hanselmann, S. Schmale, H. Schmidt, F.A. Hamprecht, T. Rabe, W. Kowalsky, R.R. Schroder, Nano Lett. **11**, 3099–3107 (2011)
26. M.Y. Chiu, U.S. Jeng, C.H. Su, K.S. Liang, K.H. Wei, Adv. Mater. **20,** 2573–2578 (2008)
27. W. Chen, M.P. Nikiforov, S.B. Darling, Energy Environ. Sci. **5**, 8045–8074 (2012)
28. H. Sirringhaus, P.J. Brown, R.H. Friend, M.M. Nielsen, K. Bechgaard, B.M.W. Langeveld-Voss, A.J.H. Spiering, R.A.J. Janssen, E.W. Meijer, P. Herwig, D.M. de Leeuw, Nature **401**, 685–688 (1999)
29. R.J. Kline, M.D. McGehee, E.N. Kadnikova, J.S. Liu, J.M.J. Frechet, M.F. Toney, Macromolecules **38**, 3312–3319 (2005)
30. B.A. Collins, J.E. Cochran, H. Yan, E. Gann, C. Hub, R. Fink, C. Wang, T. Schuettfort, C.R. McNeill, M.L. Chabinyc, H. Ade, Nat. Mater. **11**, 536–543 (2012)
31. M. Kobashi, H. Takeuchi, Macromolecules **31**, 7273–7278 (1998)
32. W.L. Ma, C.Y. Yang, X. Gong, K. Lee, A.J. Heeger, Adv. Funct. Mater. **15**, 1617–1622 (2005)
33. W. Chen, T. Xu, F. He, W. Wang, C. Wang, J. Strzalka, Y. Liu, J.G. Wen, D.J. Miller, J.H. Chen, K.L. Hong, L.P. Yu, S.B. Darling, Nano Lett. **11**, 3707–3713 (2011)
34. W. Yin, M. Dadmun, ACS Nano **5**, 4756–4768 (2011)
35. D. Chirvase, J. Parisi, J.C. Hummelen, V. Dyakonov, Nanotechnology **15**, 1317–1323 (2004)
36. W.R. Wu, U.S. Jeng, C.J. Su, K.H. Wei, M.S. Su, M.Y. Chiu, C.Y. Chen, W.B. Su, C.H. Su, A.C. Su, ACS Nano **5**, 6233–6243 (2011)
37. M.S. Su, C.Y. Kuo, M.C. Yuan, U.S. Jeng, C.J. Su, K.H. Wei, Adv. Mater. **23**, 3315–3319 (2011)
38. H.Y. Lu, B. Akgun, T.P. Russell, Adv. Energy Mater. **1**, 870–878 (2011)
39. L.M. Chen, Z. Xu, Z.R. Hong, Y. Yang, J. Mater. Chem. **20**, 2575–2598 (2010)
40. J.W. Kiel, B.J. Kirby, C.F. Majkrzak, B.B. Maranville, M.E. Mackay, Soft Matter **6**, 641–646 (2010)
41. A.J. Parnell, A.D.F. Dunbar, A.J. Pearson, P.A. Staniec, A.J.C. Dennison, H. Hamamatsu, M.W.A. Skoda, D.G. Lidzey, R.A.L. Jones, Adv. Mater. **22,** 2444–2447 (2010)
42. M. Campoy-Quiles, T. Ferenczi, T. Agostinelli, P.G. Etchegoin, Y. Kim, T.D. Anthopoulos, P.N. Stavrinou, D.D.C. Bradley, J. Nelson, Nat. Mater. **7**, 158–164 (2008)
43. Y. Vaynzof, D. Kabra, L.H. Zhao, L.L. Chua, U. Steiner, R.H. Friend, ACS Nano **5**, 329–336 (2011)
44. H.J. Liu, U.S. Jeng, N.L. Yamada, A.C. Su, W.R. Wu, C.J. Su, S.J. Lin, K.H. Wei, M.Y. Chiu, Soft Matter **7**, 9276–9282 (2011)
45. Y.S. Huang, U.S. Jeng, C.H. Hsu, N. Torikai, H.Y. Lee, K. Shin, M. Hino, Phys. B **385**, 667–669 (2006)
46. X.N. Yang, J. Loos, S.C. Veenstra, W.J.H. Verhees, M.M. Wienk, J.M. Kroon, M.A. J. Michels, R.A.J. Janssen, Nano Lett. **5**, 579–583 (2005)
47. W.L. Ma, C.Y. Yang, A.J. Heeger, Adv. Mater. **19,** 1387–1390 (2007)
48. G.R. Strobl, M. Schneider, J. Polym. Sci. Polym. Phys. **18**, 1343–1359 (1980)
49. A.A. Herzing, L.J. Richter, I.M. Anderson, J. Phys. Chem. C **114**, 17501–17508 (2010)
50. K. Vandewal, Z.F. Ma, J. Bergqvist, Z. Tang, E.G. Wang, P. Henriksson, K. Tvingstedt, M.R. Andersson, F.L. Zhang, O. Inganas, Adv. Funct. Mater. **22**, 3480–3490 (2012)

Chapter 9
Interfacial Materials for Efficient Solution Processable Organic Photovoltaic Devices

Chang-Zhi Li, Hin-Lap Yip and Alex K.-Y. Jen

Abstract The introduction of proper interfacial materials to optimize properties between organic/metal and organic/organic interfaces has become an important criterion to improve the performance and stability of polymer solar cells. This chapter presents an overview on the recent development of effective interfacial materials (including organic, inorganic and hybrid materials) used for both organic/metal and organic donor/acceptor interface engineering, and the integration of these materials in different device architectures to enhance efficiency and stability are also discussed.

9.1 Introduction

Aiming for solar energy harvest, photovoltaic technology exhibited its promise for meeting the urgent demand for clean and renewable energy, of which both inorganic and organic PVs attracted extensive research efforts. As the one of most abundant renewable energy source, solar energy is as high as 120,000 TW accounting for sunlight reaches to the earth surface per year (far beyond the global energy demand $\sim$15 TW/year) [1]. Photovoltaic research is therefore extremely motived to tackle energy problem by pursuing efficient conversion of solar energy into electricity. In the past two decades, organic photovoltaics (OPVs) processing their extra merits (to inorganic one) of mechanical flexibility, light-weight, and large scale processability, have experienced rapid development [2, 3]. One may be impressed by the significant progress on improving the performance of OPVs with power conversion efficiencies (PCE) from 1 % [4] to state-of-the-art 8–9 % [5, 6] and achieving in-depth understanding of the physics. Material development always drives the progress of OPV technology. Along with the research on the design and

C.-Z. Li · H.-L. Yip · A.K.-Y. Jen (✉)
Department of Materials Science and Engineering, University of Washington, Seattle, WA, USA
e-mail: ajen@u.washington.edu; ajen@uw.edu

Y. Yang and G. Li (eds.), *Progress in High-Efficient Solution Process Organic Photovoltaic Devices*, Topics in Applied Physics 130,
DOI 10.1007/978-3-662-45509-8_9

processing of active materials [7–12], tremendous efforts have been made on the creation and introduction of proper interfacial materials to optimize properties of interfaces in OPV, which have become important criterion to influence the performance and stability of devices. Recent successful examples demonstrated that engineering of interface is equally important to the efforts on optimizing active materials and processing to get device tuned to obtain maxim achievable performance.

From the device architecture point of view, OPVs usually sandwich a layer of donor and acceptor between a transparent electrode and metal electrode. Basing on electrode polarity of device, basic device architecture divided into conventional and inverted structures (Fig. 9.2). Critical interfaces involving organic/electrode and organic/organic junction were therefore created in device, the quality of which significantly influence (or determine) overall device performance. Electron (ESL) and hole (HSL) selective layer were required to optimize organic/electrode interface and to improve charge extraction efficiency and selectivity of electrode [13–18]. For instance, PEDOT:PSS is commonly used HSL and LiF/Al and Ca/Al used for top cathode to ensure effective charge extraction and maximizing achievable Voc. Another important interface is organic/organic interface created from the heterojunction of donor and acceptor in active layer. Different from the inorganic components, organic semiconductors are excitonic materials generate tightly bonded electron–hole pairs (excitons) upon photo excitation, since their inherent low dielectric constant (usually, $\varepsilon_r =$ 2–4), which require screening force to overcome the binding energy of excitons (for the Frenkel exciton in the range of 0.3–1 eV) to dissociate excitons into free charges. Organic donor/acceptor junction allow providing energy offset at their interface, where became most important interface involving charge separation and recombination, thus directly influence charge photogeneration and photovoltage of device.

In this chapter, we provide an overview of the recent progress on organic/electrode and donor/acceptor interface engineering, as well as the innovation of the related material. Some design criteria and the functions of interfacial layers for efficient OPVs are summarized. Regarding to organic/electrode interface, several classes of interfacial materials integrating high-performance OPVs are highlighted, which including metal oxides, cross linkable charge-transporting materials, conjugated semiconductor electrolytes, self-assembled functional molecules and graphene-based interface materials. It is worthy to note that fundamental understanding of the surface and interface science, and the device physics associated with the interfaces of OPVs is equally important and in-depth discussions on these areas can be found in several review articles [19–24]. Some recent studies involved donor/acceptor interface engineering through insertion of dipole layers for optimizing contact and examples for selective load of fullerene-thiophene hybrids into donor/acceptor interface are also summarized.

OPV device operation and performance evaluation can be briefly described as following: under illumination, excitons will be generated from light-absorbed semiconductors, which then diffused to donor–acceptor interface and dissociate with the assistance of energy offset between donor and acceptors. The separated

charges will then drift under the inherent electric field created by the work-function difference between the asymmetric electrodes, and ultimately, will be collected by the corresponding electrodes. The PCE of OPV is defined by the product of three parameters including short-circuit current density (J_{sc}), open-circuit voltage (V_{oc}), and fill factor (FF). J_{sc} is directly related to the efficiencies of light absorption, exciton generation and dissociation, charge transport and charge collection at the electrodes. V_{oc} is related to the difference between the highest occupied molecular orbital (HOMO) of the donor and the lowest unoccupied molecular orbital (LUMO) of the acceptor in the BHJ. More specifically, it is determined by the difference between the quasi-Fermi levels of holes ($E_{F,h}$) and electrons ($E_{F,e}$) under illumination provided that barrierless contacts to the electrodes are formed (Fig. 9.1) [21, 25]. FF is governed by both the parasitic series resistance (R_s) and shunt resistance (R_p) of the solar cell [26, 27]. R_s is determined by the bulk conductivity of the electrodes, active and interfacial layers, and the contact resistance between them. R_p is determined by the quality of the thin films and their interfaces. Small R_p originates from the loss of charge carriers through leakage paths including pinholes in the films and the recombination and trapping of the carriers during their transit through the cell that can lead to decreased device performance. The nature of electrical contact between the BHJ layer and the electrodes can significantly affect all three device-related parameters and modification of those interfaces by inserting appropriate interfacial layers can significantly alter the contact properties to improve the PCE of OPVs. The donor/acceptor interface affects exciton collection and dissociation, which determined charge photogeneration and photovoltage of device. Engineering of those interfaces through application of appropriate interfacial material can significantly alter the contact and photo physic processes of device leading to improve the performance and stability of OPVs.

9.1.1 Donor/Acceptor Interface

The heterojunction of donor and acceptor in active blend created large area of D/A interface, where excitons get collected and dissociated, thus influence overall device performance. In this section, some of the studies related to donor/acceptor interface engineering with proper interfacial material are introduced and the advance in design criteria is also discussed. As demonstrated by Durrant et al. schematic illustration of charge dissociation at the polymer:PCBM interface is shown in Fig. 9.2. The donor singlet exciton diffuses to the interface, and subsequently generate the charge-transfer (CT) state (Fig. 9.3) at donor/acceptor interface. Exciton itself processes limited lifetime and diffusion length ($\sim$10–20 nm). The one created far away from the interface would relax itself to the ground state without photocurrent contribution. At the CT state, initial electron-hole separation has a distance of the thermalization length (a). The probability of full dissociation into the free charge carriers (the CS state, Fig. 9.3) depends upon the ratio between distance (a) and the coulomb capture radius.

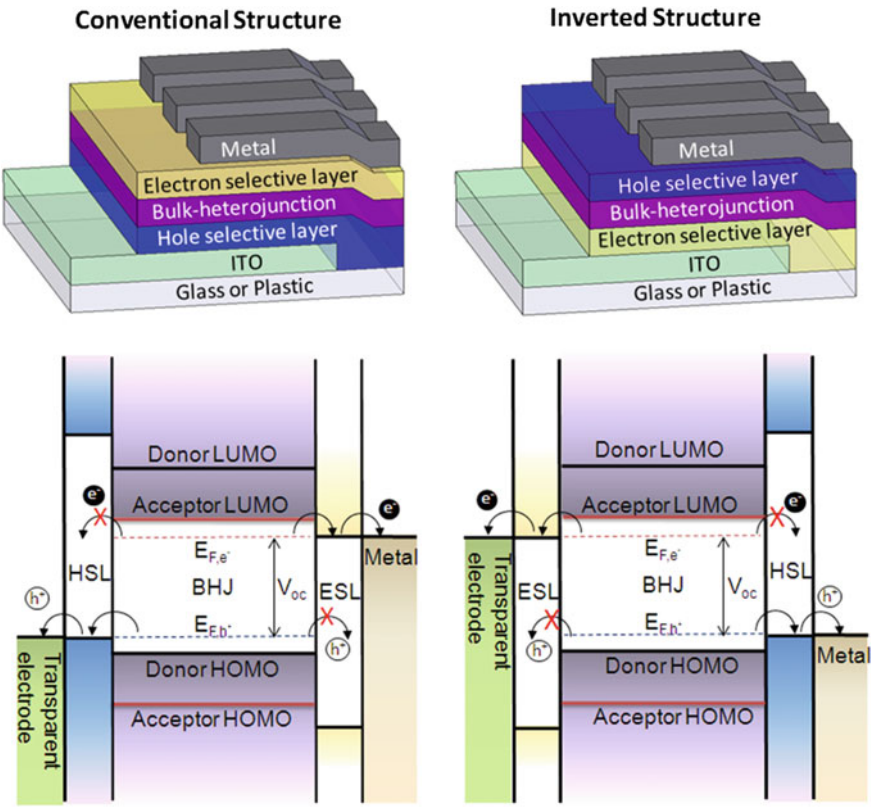

Fig. 9.1 Device architecture of conventional OPV (*upper left*) and inverted OPV (*upper right*). Schematic view of the energy level alignment in a conventional OPV (*bottom left*) and an inverted OPV (*bottom right*) with interfacial layers providing Ohmic contacts and charge selectivity at both electrodes

Charge photogeneration at donor/acceptor interface is one of the most important processes in OPV device. As shown in Fig. 9.4 [26, 28], the singlet exciton generated upon photo excitation of light-absorption semiconductor, which pumped an electron from grand state S_0 into S_1. The exciton then diffused to the interface, where hot charge transfer state, CT* can dissociate into a fully charge-separated (CS) state (K_{CS*}) and migrate away from the D/A interface. This process compete with the thermal relaxation of CT* to CT state (K_{therm}^{CT}). It worthy to note that conjugated materials usually present strong electron-vibration coupling, thus promote relaxing excited state down to the lowest energy level of excited state. At CT state, significant energy loss pathway involved. One is recombination ($K_{triplet}$) of the ^{3}CT (^{1}CT to ^{3}CT, K_{ISC}) to the triplet state of semiconductors, T_1. Another is decay of the ^{1}CT back to the ground state through geminate recombination. Dissociation of the thermally relaxed CT state into the CS state (K_{CS*}) is achieved with the assistance of interfacial energy offset. The diffusion-limited bimolecular process

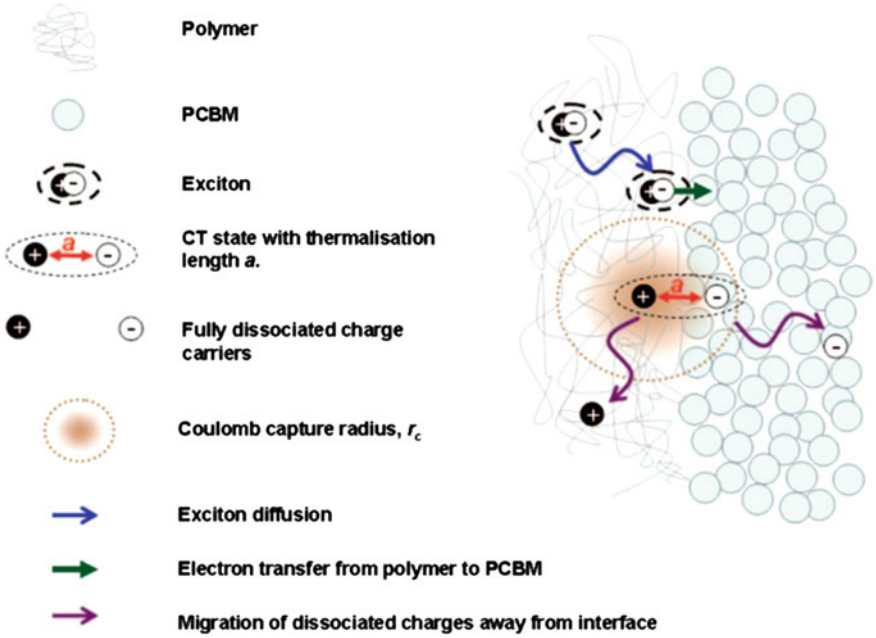

Fig. 9.2 Schematic of charge dissociation at the polymer:PCBM interface. Reproduced with permission from [28] Copyright 2010 American Chemical Society

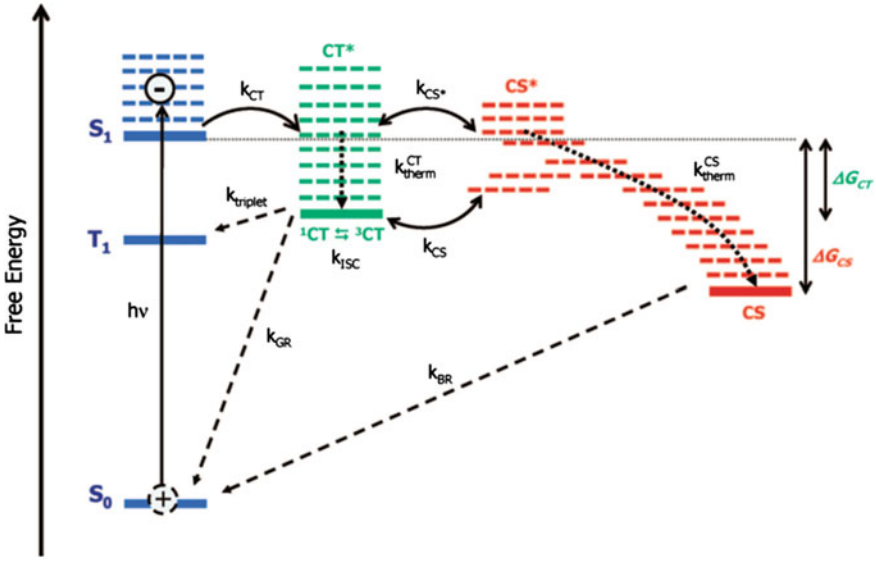

Fig. 9.3 Energy level diagram showing the charge photogeneration at donor/acceptor interface. Reproduced with permission from [28] Copyright 2010 American Chemical Society

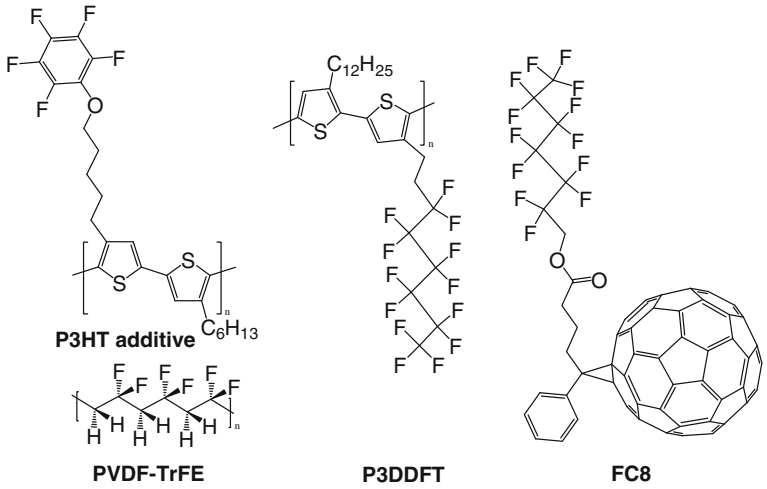

Fig. 9.4 Structure of dipole materials used as interfacial modifier at donor/acceptor junction

may result from bimolecular recombination (K_{BR}). The competition between charge separation and recombination is strongly influence the efficiency of charge photogeneration in organic solar cells [29]. Energy level offset and interfacial coupling at donor/acceptor interface are the important factors to influence charge photo generation. These electronic structures at interface depend on how the materials make contact, which in turn is governed by many factors such as interfacial dipole.

Recently, several studies demonstrated that proper treatment of polymer/fullerene interface in OPVs can influence their performance. Hashimoto et al. demonstrated a model of p–n junction PV build through connection of P3HT and PCBM layers by film-transfer method. Each semiconducting layer can be modified with a surface-segregated fluorinated PC8 (for PCBM) or P3DDFT (for P3HT) monolayer, which is reported to tune the strength and surface dipole direction. In their bilayer devices, introduction of interfacial dipole layer alter the device Voc with a wide range between 0.3 and 0.86 V. Authors attribute the effect to aligned dipole shift energy difference between the LUMO of the acceptor and the HOMO of the donor (ΔE_{HL} in Fig. 9.5). In case that FC8 on top of PCBM, interfacial dipole point from P3HT to PCBM, which downshift of ΔE_{HL}, to give a low Voc, 0.5 V. When planting P3DDFT on the top of P3HT, the interfacial dipole is reversed by pointing from PCBM to P3HT, thus enlarge ΔE_{HL} and Voc, 0.85 V [30].

Another approach to tune energy offset of the donor/acceptor junction is achieved with introduction of ferroelectric P(VDF-TrFE) layers. Recently, Huang et al. demonstrated that P3HT/PCBM bilayer devices with ultrathin P(VDF-TrFE) dipole layer at donor/acceptor interface to enlarge device Voc. As shown in Table 9.1. The Voc was increased from 0.55 to 0.67 V after poling the P(VDF-TrFE) layer with reverse bias on the device. Jsc and Voc showed increase. It is explained that dipole layer tune the relative energy level alignment at donor/acceptor junction. Both Jsc

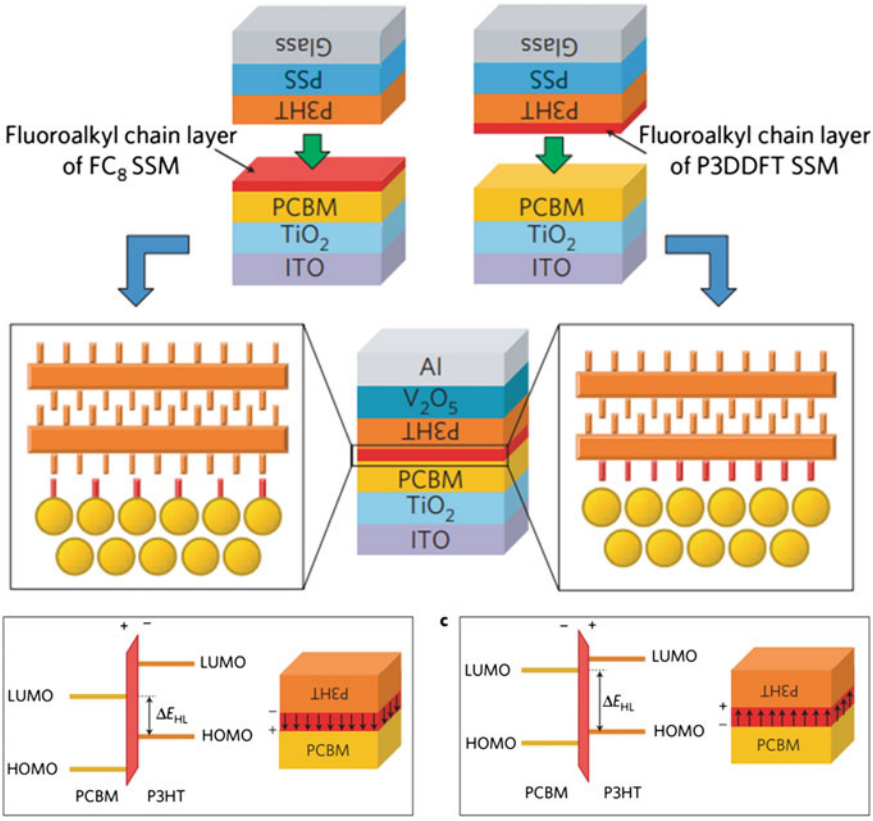

Fig. 9.5 Schematic representation and energy diagrams of the P3HT/PCBM bilayer devices with interfacial dipole layer of FC_8 and P3DDFT. Reproduced with permission from [30] Copyright 2010 Nature Publishing Group

and FF also increased due to the reduced recombination loss of charge-transfer excitons (CTEs) [31]. The dipoles of ferroelectric P(VDF-TrFE) can preserve their alignment after removing the polling field. The PCE is almost doubled with the polled dipole layer (P(VDF-TrFE). In the authors previous study, an ultrathin (1 nm) layer of P(VDF-TrFE) has been inserted between different BHJs and Al cathode to show significantly improved device characteristics [27].

It is interesting to see how the properties of organic/organic interfaces influence performance under conditions that more resemble those of an actual device. The ferroelectric PVDF-TrFE has been doped into bulk, which leads to better device performance from P3HT:PCBM BHJs [32]. The internal electric field enhancement estimate to be $\sim$150 and $\sim$300 V-m^{-1} for the devices with 5 and 10 % PVDF-TrFE concentration, which facilities singlet-exciton (SE) and charge-transfer-exciton (CTE) harvesting in BHJ, thus lead to IQE of BHJ devices approached 100 % for some wavelengths. Swager et al. reported that some fine-designed polymer

Table 9.1 Summary of device characteristics of representative polymer solar cells employing donor/acceptor interfacial engineering

Anode configuration	Active layer	Cathode configuration	V_{oc} (V)	J_{sc} (mA/cm^2)	FF	PCE (%)	References
ITO/TiO_2	$PC_{61}BM$/P3HT	V_2O_5/Al	0.50	1.51	0.53	0.40	[30]
ITO/TiO_2	$PC_{61}BM$/FC_8/P3HT	V_2O_5/Al	0.31	1.51	0.50	0.23	[30]
ITO/TiO_2	$PC_{61}BM$/P3DDFT/P3HT	V_2O_5/Al	0.86	0.70	0.38	0.23	[30]
ITO/PEDOT:PSS	P3HT/$PC_{61}BM$	Ca/Al	0.55	8.2	0.33	1.5	[31]
ITO/PEDOT:PSS	P3HT/PVDF-TrFE/$PC_{61}BM$	Ca/Al	0.67	9.0	0.55	3.3	[31]
ITO/PEDOT:PSS	P3HT:$PC_{61}BM$ (0 % PVDF-TrFE)	Al	0.55	9.6	0.48	2.5	[32]
ITO/PEDOT:PSS	P3HT:$PC_{61}BM$ (10 % PVDF-TrFE)	Al	0.57	11.3	0.60	3.9	[32]
ITO/PEDOT:PSS	P3HT:$PC_{61}BM$ (0.25 wt% additive)	Al	0.60	12.2	0.53	5.3	[33]

additives processing same polymer backbone with P3HT, while different polar side chain. The polymer additive (Fig. 9.4) was doped into P3HT/PCBM BHJ and proposed to be selectively localized at the donor/acceptor interface [33]. Authors suggested that polar aromatic moieties at side-chain termini at polymer/fullerene interface, decreasing the rate of bimolecular recombination and improves charge collection across the active layer. At low loadings of 0.25 % additive, the short circuit current and the series resistance have been optimized and yield ~30 % increase in PCE, which is up to 5.3 %.

Besides of aforementioned dipole (or polar) material modified donor/acceptor interface, strategies reported on selectively locating thiophene-fullerene dyads at the donor/acceptor interfaces were also interesting, since these approaches not only allow reducing the interfacial energy between immiscible components to stabilize the phase morphology, but also can serve as effective method to load materials at donor/acceptor interface. As shown in Fig. 9.6, Fréchet et al. demonstrated an amphiphilic di-block copolymer **1** could be used as an additive, also as a compatibilizer, to stabilize device structure against destructive thermal phase segregation

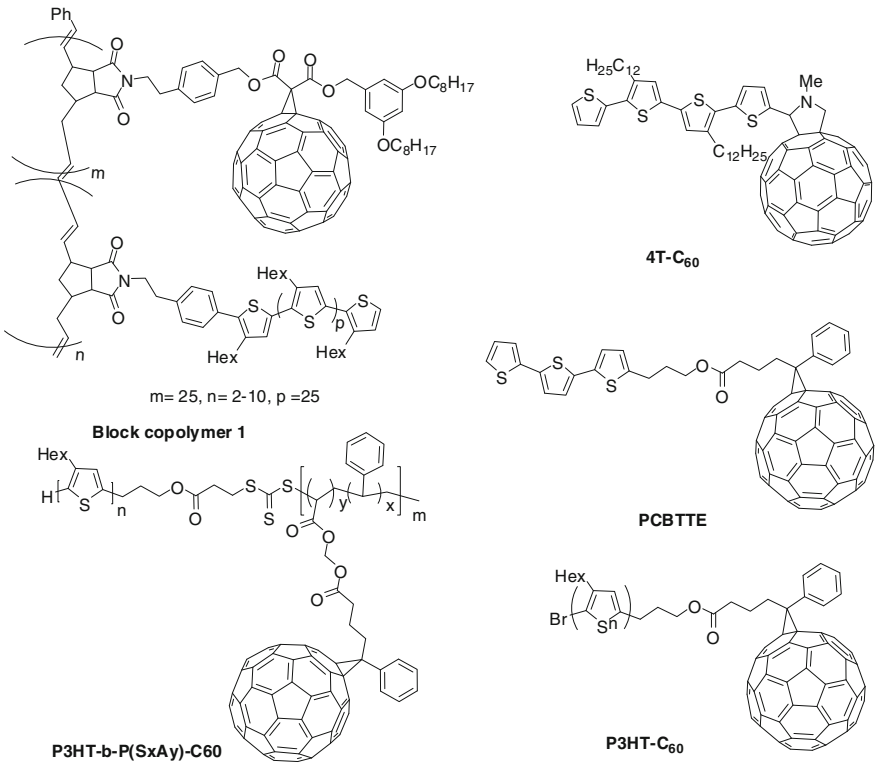

Fig. 9.6 Structure of thiophene-incorporated fullerene used as Morphology Stabilizer in BHJ

[34]. Another example was given using a well-defined rod–coil block copolymers (P3HT-b-P(SxAy)-C_{60}) [35]. Alternatively, A poly(3-hexylthiophene) end capped with fullerene (P3HT-C_{60}) [36] also exhibited effective control of BHJ morphology. In addition to block-copolymers, small thiophene-C_{60} derivatives [37, 38], such as 4T-C_{60} have been prepared by Loo et al. It showed a surface energy of 18.40 mN/m (4T-C_{60}), which is between that of P3HT (16.8 mN/m) and PCBM (30.1 mN/m). The addition of 4T-C_{60} reduces the interfacial energy between P3HT and PCBM, as evidenced by the constancy of the efficiency with thermal annealing at 170 for 3 h [39]. It effectively stabilized the blends (5 wt% to P3HT and PCBM) for PSC application.

9.1.2 Organic/Electrode Interface

In addition to the emerging studies on donor/acceptor interface engineering, most efforts related to interfacial engineering have been demonstrated on the improving organic/electrode contact. The introduction of proper interfacial materials have been proven to effectively optimize the electronic and electrical properties between the interfaces of active layer and electrode, which has become an important criterion to improve the performance of polymer solar cells. As reviewed by others [19–24] and ours [40–42], efficient interfacial materials for organic/electrode contact of OPV should generally fulfill several requirements, like (i) promote Ohmic contact formation between electrodes and the active layer; (ii) have appropriate energy levels to improve charge selectivity for corresponding electrodes; (iii) have large bandgap to confine excitons in the active layer; (iv) possess sufficient conductivity to reduce resistive losses, (v) have low absorption in the Vis-NIR wavelengths to minimize optical losses; (vi) have chemical and physical stability to prevent undesirable reactions at the active layer/electrode interface; (vii) have the ability to be processed from solution and at low temperatures; (viii) be mechanically robust to support multilayer solution processing; (ix) have good film forming properties and (x) be producible at low cost.

Several classes of materials and their hybrids had been introduced including conducting polymers, metal oxides, cross linkable materials, conjugated polymer electrolytes, self-assembled functional molecules and graphene-based materials. In this section, we mainly focus on discussing some of recent advancements on the design and application of interfacial materials in high-efficiency device. The chemical structures and energy diagram of some of the conjugated polymer donors and fullerene acceptors that will be discussed are shown in Figs. 9.7 and 9.8.

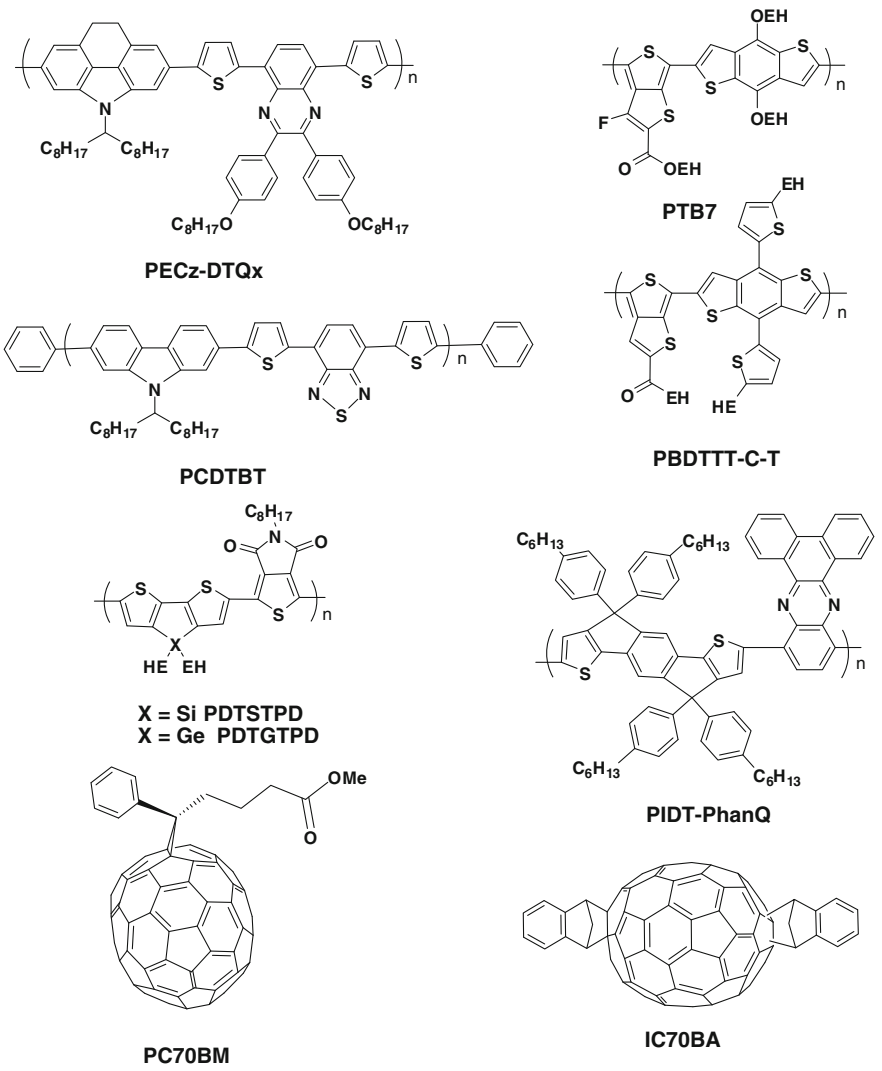

Fig. 9.7 Molecular structures of selected conjugated polymer donors and fullerene acceptors used as active materials in BHJs

9.2 Organic/Electrode Interfacial Materials for Conventional OPVs

The device characteristics of high-efficiency conventional OPVs employing newly developed interfacial layers are summarized in Table 9.2. PEDOT:PSS is the most commonly used solution-processible hole-transporting layer for anode modification

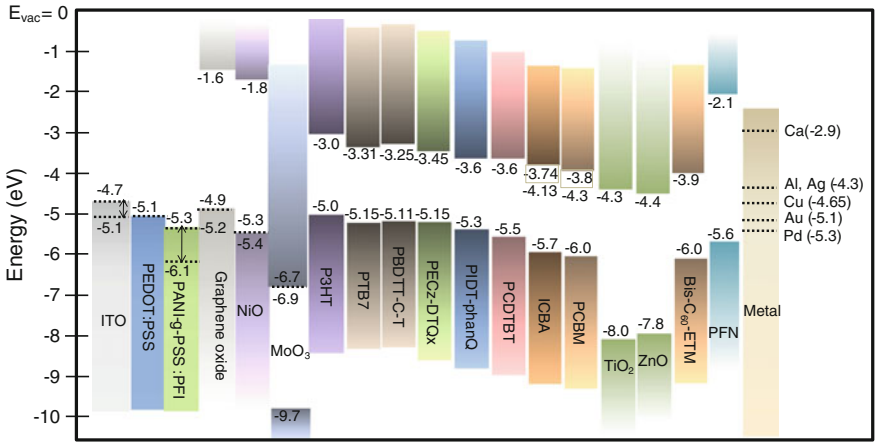

Fig. 9.8 Schematic view of the energy gaps and energy levels of some of the components of recent OPVs including transparent electrodes, hole selective materials, polymer donors, fullerene acceptors, electron selective materials and metal electrodes. The *dotted line* corresponds to the work functions of the materials. Adapted with permission from [42] Copyright 2012 Royal Society of Chemistry

in conventional solar cells. Some of the best reported OPV efficiencies are those using PEDOT:PSS as the hole-transporting layer [43, 44]. It has a wide range of electrical conductivities from 10^{-6} to 10^{3} S/cm (tuned by changing the compositional ratio between PEDOT+ and PSS− and processing with additives), work function ($\sim$5.1 eV) and optical transparency, which provide great flexibility in tuning the electrical property at the active layer/electrode interface. However, the deficiencies (strong acidity and hygroscopic nature) of PEDOT:PSS can induce chemical instability between the active layer and electrodes [45]. Some of the newly developed conducting polymers, PSSA-g-PANI [46] and sulfonated poly(diphenylamine) (SPDPA) [47] have been explored with tuned conductivity and acidity. Cross linkable materials were other classes of charge-transporting materials, and their crosslinked film improved solvent resistance for subsequent processing of the BHJ layer [48–51]. These new organic and polymeric hole-transporting materials exhibited the promise to replace PEDOT:PSS, but continuous improvement are still needed.

Besides of organic material, p-type inorganic transition metal oxides such as vanadium oxides (V_2O_5) [52] and nickel oxides (NiO) [53] have also been used as hole-selecting materials for OPVs, owning to their optical transparency and suitable energy level. Their conduction band is sufficiently higher than the LUMO of both organic donor and acceptor materials, for electron blocking. Work functions of p-type metal oxides (NiO $\sim$5.3 and V_2O_5 $\sim$5.3–5.4 eV) also can promote good Ohmic contact at the BHJ/anode interface with minimal contact resistance. As a result, good diode characteristics and fill factors of $\sim$70 % could be achieved in OPVs using optimized p-type NiO layers which outperform over PEDOT:PSS

Table 9.2 Summary of device characteristics of representative conventional polymer solar cells employing different interfacial layers

Anode configuration	Active layer	Cathode configuration	V_{oc} (V)	J_{sc} (mA/cm^2)	FF	PCE (%)	References
ITO/PEDOT:PSS	P3HT:$PC_{61}BM$	Ca/Al	0.61	10.6	0.67	4.4	[52]
ITO/NiO(sputtered)	P3HT:$PC_{61}BM$	LiF/Al	0.64	11.3	0.69	5.2	[53]
ITO/NiO_x (sol-gel)	PCDTBT:$PC_{71}BM$	Ca/Al	0.88	11.5	0.65	6.7	[54]
ITO/MoO_3(vac)	PCDTBT:$PC_{71}BM$	TiO_x(sol-gel)/Al	0.89	10.9	0.67	6.5	[63]
ITO/MoO_3(NPs)	P3HT:$PC_{61}BM$	Al	0.57	7.7	0.67	2.9	[67]
ITO/Graphene oxide	P3HT:$PC_{61}BM$	Al	0.57	11.4	0.54	3.5	[69]
ITO/PEDOT:PSS	P3HT:$PC_{61}BM$	TiO_x(sol-gel)Al	0.61	11.1	0.66	5.0	[75]
ITO/PEDOT:PSS	PCDTBT:$PC_{71}BM$	$TiO_{x(}$(sol-gel)/Al	0.88	10.6	0.66	6.1	[76]
ITO/PEDOT:PSS	P3HT:$PC_{61}BM$	TiO_2:Cs NPs/Al	0.58	10.8	0.67	4.2	[78]
ITO/PEDOT:PSS	P3HT:$PC_{61}BM$	ZnO NPs/SAM/Al (Ag, Au)	0.65	11.1	0.63	4.6	[80]
ITO/PEDOT:PSS	P3HT:$PC_{61}BM$	ZnO NPs-PEG/Al (Ag, Au)	0.60	10.7	0.69	4.4	[82]
ITO/PEDOT:PSS	P3HT:$PC_{61}BM$	P(VDF-TrFE)/Al	0.59	12.8	0.60	4.5	[27]
ITO/PEDOT:PSS	P3HT:$PC_{61}BM$	WPF-6-oxy-F/Al(Cu, Ag, Au)	0.64	10.1	0.60	3.9	[87]
ITO/PEDOT:PSS	PCDTBT:$PC_{71}BM$	PF2/6-*b*-P3TMAHT/Al	0.89	10.6	0.67	6.5	[84]
ITO/PEDOT:PSS	PECz-DTQx-$PC_{71}BM$	PFN/Al	0.81	11.4	0.66	6.1	[86]
ITO/PEDOT:PSS	PTB7:$PC_{71}BM$	PFN/Ca/Al	0.76	15.8	0.70	8.4	[88]
ITO/PEDOT:PSS	P3HT:$PC_{61}BM$	PEG-C_{60}/Al (Cu, Au)	0.66	10.5	0.65	4.4	[91]
ITO/PEDOT:PSS	PIDT-PhanQ:$PC_{71}BM$	C_{60}-surfactant/Ag (Al, Cu)	0.88	11.5	0.61	6.2	[93]

devices [53]. Recently, more promising approach form solution-processed NiO_x films is reported, which showed high PCE (6.7%) from PCDTBT:$PC_{71}BM$ BHJ and better stability than those PEDOT:PSS-based devices [54, 55]. A sol-gel derived VO_x film obtained by annealing at lower temperature (110 °C) also showed quite encouraging performance that is comparable to that of PEDOT:PSS-based devices but with better stability [56]. However, the optical absorption of VO_x in the visible range (400–500 nm) may limit its application as an efficient HSL.

Molybdenum oxides (MoO_3) and tungsten oxides (WO_3) have also been extensively investigated for anode modification in OPVs [52, 57, 58]. Its intrinsic n-type with deep-lying electronic states promote interfacial p-doping of various polymers [59], small molecules [60], and even fullerenes [61], since interfacial electron transfer from the organic semiconductor to MoO_3 is thermodynamically favorable. For example, the measured electron affinity, work function and ionization potentials for vacuum-deposited MoO_3 are −6.7, −6.86 and −9.68 eV [62]. The interfacial stability of OPVs based on evaporated MoO_3 film has been studied in different BHJ systems (P3HT:$PC_{61}BM$ and PCDTBT:$PC_{71}BM$) and the results showed that greatly enhanced lifetime could be achieved compared to the PEDOT:PSS-based devices [63, 64]. The recent demonstration of MoO_3 interfacial layers in OPV devices using either sol-gel processes [58, 65, 66] or nanoparticle suspensions [67, 68] further showed the promise of using metal oxides for anode modification.

Solution-processible Graphene Oxide (GO) is another promising HSL for OPVs [69]. Its HOMO and LUMO were measured to be −5.2 and −1.6 eV, which is good for hole transport and electron blocking, respectively. The work function of GO was between −4.9 and −5.1 eV, by scanning Kelvin probe microscopy [70]. Li et al. first explored the use of GO as HSL and reported that 2 nm GO nanosheets HSL in P3HT:PCBM OPV have comparable performance to that of PEDOT:PSS-based devices [69]. Further transient open-circuit voltage delay (TOCVD) measurements suggested that GO is more effective in suppressing leakage current and separating carriers via efficient hole-transporting to ITO and blocking of electrons. To further improve the anode contact, a hybrid bilayer structure based on GO and sol-gel processed NiO_x was developed [71], showing GO/NiO_x structure lead to major improvement of FF. These encouraging findings have opened the way for developing new interfacial materials for OPV.

Interface engineering for cathode is also very important for improving the performance of OPVs. In conventional OPVs, low work function cathode, such as Ca and Al are vulnerable to air and ambient condition. To improve the contact, vacuum-deposited materials such as BCP [72], PCBM [73], and C_{60}:LiF [74] have been introduced between the BHJ layer and the Al cathode. However, the development of solution processible ESLs is important for printable OPVs. The optimized ESLs should support the use of more stable and printable metals (such as colloidal Ag) as cathode for roll-to-roll manufacturing of OPV.

N-type metal oxides like TiO_2 and ZnO are the most widely studied ESL for OPVs. Using low temperature sol-gel processing, amorphous TiO_x films can be directly deposited on a BHJ layer to fabricate OPV devices [75]. The TiO_x films not only showed good electron selectivity, but also functioned as an optical spacer and

a good water and oxygen barrier, leading to significantly improved device efficiency and stability. The optical spacer effect of TiO_x has also been investigated in different BHJ systems. A PCE of 6.1 % has been reported when TiO_x interfacial layer was applied to a PCDTBT:$PC_{71}BM$ BHJ solar cell [76]. Furthermore, by replacing the anode PEDOT:PSS layer with MoO_3, the PCE of a PCDTBT:$PC_{71}BM$ device increased to 6.5 % and the stability of the device also improved significantly [63]. TiO_2 films prepared from solution processed crystalline nanoparticles (NPs) can also be used as an efficient ESL for OPVs [77]. By doping TiO_2 NP with Cs, it can further decrease the work function for more efficient electron extraction. As a result, the P3HT/PCBM based solar cells showed enhancements in PCE compared to those using a pure TiO_2 ESL [78]. ZnO is another efficient n-type metal oxide used for cathode modification in OPVs. Solution processed ZnO NP films has a high electron mobility (2.5 cm^2/Vs) [79], which can minimize Ohmic loss in the device. The electrical and electronic properties of ZnO can also be easily tuned by modifying the ZnO surface with a self-assembled molecular layer, to engineer the contact and surface dipoles between ZnO and metal, devices showed significant improvement in efficiency and it also enabled high work function metals such as Ag and Au to be used as cathode [80, 81]. Hybridization of ZnO NPs with poly(ethylene glycol) can also tune work function, morphology, refractive index and charge transporting properties of the ESL, which provides an efficient way to improve OPV performance [82]. The use of PVP as an organic capping molecule and polymeric matrix for ZnO modification produced electron-transporting nanocomposite films, which had excellent film-forming characteristics. Further UV-ozone treatment to remove PVP from the surface of the hybrid film consequently exposed the ZnO nanoclusters, which gave certificated PCE of 7.4 % from PDTG-TPD:PC71BM BHJ [83].

Organic-based interfacial materials that can be processed through orthogonal solvents of the BHJ layer were extensively studied ESL materials for OPVs. Their chemical structures are highlighted in Fig. 9.9. Conjugated polymers and polymer electrolytes that can be processed from alcoholic/water solvents attracted significant research attention in the past two years [84–86]. Polythiophene and polyfluorene with polar amines, amine salts, phosphates, and alkoxy side chains are the most commonly investigated systems. Oh et al. have demonstrated that an ESL based on a water soluble polyfluorene derivative (WPF-oxy-F) can effectively reduce the work functions of different metals including Al, Ag, Cu and Au, resulting in Ohmic contact between the P3HT:$PC_{61}BM$ BHJ and cathode to improve V_{oc} and PCE of the OPV [87]. Seo et al. demonstrated the effect of cationic polythiophene (P3TMAHT) and its polyfluorene block copolymer derivative (PF2/6-b-P3TMAHT) on PCDTBT:$PC_{71}BM$ based devices with improved PCE from 5 % to over 6.3 % [84].

Water/alcohol soluble polyfluorene derivative, PFN, which contains side chains terminated with neutral alkylamines has also been studied with BHJs composed of different polymer donors [88]. It was found that the improvements of PCE are relied heavily on the chemical structures of the polymer donors. Though the effect of PFN on P3HT and PPV-based OPVs was minimal, significant improvement of the PCE in a group of N-heterocycle-containing polymer donors was effectively

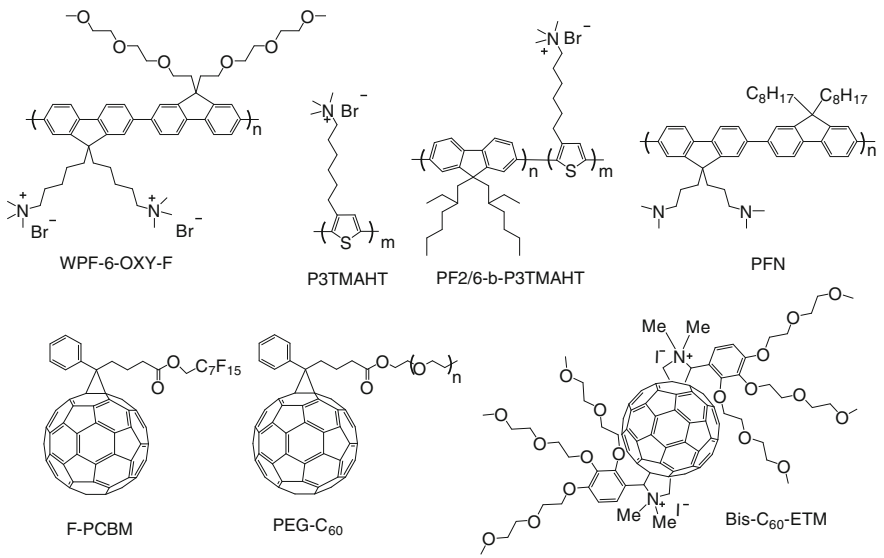

Fig. 9.9 Molecular structures of some electron selective materials used in conventional OPVs including conjugated polymer electrolytes and fullerene-based interfacial materials

demonstrated [89]. For example, OPVs based on PECz-DTQx:$PC_{71}BM$ showed PCE increases from 4.0 to 6.1 % when Al was used as cathode [85], while for the PCDTBT:$PC_{71}BM$ BHJ, the best device employed the PFN ESL in combination with a Ca/Al cathode, showing a PCE of 6.8 %. When high performance low bandgap polymer, PTB7 applied, a record OPV device performances with a PCE of 8.4 % were reported from PFN ESL modified Ca/Al cathode [86]. The authors suggested that the improved device performance could have multiple origins including enhanced built-in potential across the device, improved charge-transport, reduced space charge buildup, and minimized recombination losses due to increases in built-in field and charge carrier mobility.

Fullerene-based interfacial materials present another obvious option for ESL in BHJ OPVs since their energy levels, electron transport, and chemical compatibility to the BHJ fit the requirements of a good ESL. However, there are only limited reports of fullerene-based ESL, which is probably due to challenge in synthesizing proper fullerene materials with adequate solubility that can be used for solution processing. PCBM derivatives with fluorinated alkyl (F-PCBM) [90] and polymer (ethylene glycol) (PEG-C_{60}) [91, 92] are two interesting fullerene derivatives that have been explored as ESL. In both cases, small amounts of the fullerene derivatives were added into the P3HT:PCBM solution. During the film drying process, a thin layer of the fullerene derivative was found to segregate on the surface of the BHJ film, forming a self-organized interfacial layer. The OPV devices were then completed by evaporation of an Al cathode. In both cases, the fullerene surfactants were found to interact with the Al electrode, forming an appropriate interfacial

dipole that promoted better Ohmic contact and improved the device performance. Although the simplicity of self-organized ESLs is very attractive, it may not be generally applicable to different BHJ systems since the film drying kinetics may vary in different polymer:fullerene blends.

Fullerene ESLs that can be directly processed on top of different BHJ layers might represent a better option. This has been recently realized in a new fullerene derivative (bis-C_{60}-ETM) in which side chains composed of an amine salt and an alkoxy dendron were introduced to improve its solubility in alcohols [93, 94]. The bis-C_{60}-ETM could be directly spin-coated on top of the active layer to form a smooth ESL. To evaluate the general applicability of the fullerene ESL, devices based on different BHJs were tested and in all cases, the devices with bis-C_{60}-ETM showed significantly improved V_{oc}, J_{sc}, FF, and PCE. The effect of different metal cathodes (Al, Ag, and Cu) on the OPV efficiency and stability were further investigated based on the PIDT-phanQ:$PC_{71}BM$ BHJ system. The best PCE (6.6 %) was found when Ag was used as the cathode. Work function studies suggested that the bis-C_{60}-ETM film efficiently reduced the effective work functions of all three metals, which facilitated Ohmic contact at the BHJ/cathode interface to achieve a maximized V_{oc} independent of the choice of metal. However, devices with Cu and Ag cathodes showed much better ambient stability than the one with Al. These findings can be very important for developing efficient, stable, and roll-to-roll processible polymer solar cells.

9.3 Interfacial Materials for Inverted Structure OPVs

Since their initial application in 2006, inverted OPVs have attracted growing attention due to their improved stability and compatibility with roll-to-roll processes [95–97]. For inverted OPVs, the device polarity is reversed compared to that based on the conventional structure. The performance of the inverted OPV is critically dependent on the choice of the interfacial layers and their contact properties with the BHJ layer and the corresponding electrodes. The device characteristics of the representative inverted OPVs containing different interfacial layers and BHJ layers are summarized in Table 9.3.

Alkali metal salts can be used as an interfacial modifier to tune the work function of ITO for electron collection [98]. By spin-casting Cs_2CO_3 for ITO modification and V_2O_5 as the HSL underneath the Al top electrode, the PCE of inverted P3HT:PCBM BHJ OPVs could reach as high as 4.2 % [99]. It was found that upon annealing at 150 °C, Cs_2CO_3 will decompose to into doped cesium oxide (Cs_2O). This significantly improved electron collection by reducing the work function of ITO from 4.7 to 3.06 eV [100]. However, the insulating property of Cs_2O may limit its broader application for OPVs. TiO_2 and ZnO are the most widely studied electron selective materials for inverted OPVs. White et al. have demonstrated one of the earliest inverted P3HT:PCBM BHJ solar cells based on a sol-gel derived ZnO film on ITO as the ESL and an Ag anode as the top electrode [101].

Table 9.3 Summary of device characteristics of representative inverted polymer solar cells employing different interfacial layers

Cathode configuration	Active layer	Anode configuration	V_{oc} (V)	J_{sc} (mA/cm^2)	FF	PCE (%)	References
ITO/Cs_2CO_3	P3HT:$PC_{61}BM$	V_2O_5/Al	0.59	11.1	0.63	4.2	[99]
ITO/TiO_x(sol-gel)	P3HT:$PC_{61}BM$	PEODT:PSS/Au	0.56	9.0	0.62	3.1	[126]
ITO/TiO_x/FPQ-Br	P3HT:$PC_{61}BM$	MoO_3/Au	0.58	8.9	0.70	3.6	[127]
ITO/TIPD	PBDTTT-C-T:$PC_{71}BM$	MoO3/Ag	0.70	16.26	0.65	7.4	[114]
ITO/WPF-6-oxy-F	P3HT:$PC_{61}BM$	PEDOT:PSS/Ag	0.66	8.8	0.59	3.4	[128]
ITO/ZnO(sol-gel)	PDTGTPD:$PC_{71}BM$	MoO_3/Ag	0.85	12.6	0.68	7.3	[103]
ITO/ZnO(sol-gel)	PCDTBT:$PC_{71}BM$	MoO_3/Ag	0.88	10.4	0.69	6.3	[129]
ITO/ZnO(sol-gel)	aPTPTBT:$PC_{71}BM$	VO_x (sol-gel)/Ag	0.82	11.6	0.53	5.0	[104]
ITO/ZnO NPs	P3HT:$PC_{61}BM$	PEDOT:PSS/Ag	0.62	10.7	0.54	3.6	[107]
ITO/ZnO NPs/C_{60}-SAM	P3HT:$PC_{61}BM$	PEDOT:PSS/Ag	0.63	12.0	0.61	4.5	[107]
ITO/ZnO(sol-gel)/C-PCBSD	P3HT:$PC_{61}BM$	PEDOT:PSS/Ag	0.60	12.8	0.58	4.4	[109]
ITO/ZnO(sol-gel)/C-PCBSD	P3HT:ICBA	PEDOT:PSS/Ag	0.84	12.4	0.60	6.2	[110]
ITO/ZnO–PVP	PDTGTPD:$PC_{71}BM$	MoO_3/Ag	0.86	14.0	0.67	8.1	[83]
ITO/PEIE	P3HT:ICBA	MoO_3/Ag	0.81	11	0.66	5.9	[112]
ITO/BPCO	PCDTBT:PC71BM	MoO_3/Ag	0.89	9.5	0.62	6.2	[113]
ITO/n-doped P-PCBM-S	P3HT:$PC_{61}BM$	PEDOT:PSS/Ag	0.63	9.1	0.44	2.5	[115]
ITO/n-doped PNDI-1Th	P3HT:$PC_{61}BM$	PEDOT:PSS/Ag	0.59	10.0	0.58	3.4	[116]
ITO/ZnO NPs/C_{60}-SAM	P3HT:$PC_{61}BM$	GO/Ag (Au,Al)	0.62	10.3	0.62	3.9	[122]
ITO/ZnO NPs	PIDT-phanQ:$PC_{71}BM$	GO/Ag	0.86	10.9	0.62	5.9	[125]

The crystallinity of the ZnO films could be increased by thermal annealing at 300 °C to improve their electrical properties. By inserting a thermally evaporated HSL, such as V_2O_5 or MoO_3 between the BHJ layer and metal anode, it promotes better Ohmic contact at the anode, leading to further improved ZnO-based inverted OPVs [102]. Such a device platform has shown good compatibility with different BHJ layers. Recently, very high efficiency inverted OPVs were demonstrated based on PDTSTPD:$PC_{71}BM$ and PDTGTPD:$PC_{71}BM$ BHJ layers with PCEs of 6.6 and 7.3 %, respectively [103].

In addition to the n-type metal oxides as ESL, the development of solution processed p-type metal oxide as HSL for inverted cells is equally important. Chen et al. have demonstrated that a VO_x HSL could be prepared by spin-coating the sol-gel solution on the BHJ layer followed by low temperature annealing at 100 °C [104]. Inverted P3HT:$PC_{61}BM$ and PTPBT:$PC_{71}BM$ devices showed enhanced performance as a result of increased Jsc. The encapsulated inverted devices also showed very good thermal stability with no performance loss after annealing at 65 °C for 1,000 h. These results are very encouraging since low temperature process is more compatible with flexible plastic substrates.

The modification of metal oxide films with functional SAMs can efficiently alter the interfacial properties between the ESL and BHJ. Bulliard et al. [105] reported that the morphology of the BHJ film could be optimized by virtue of a ZnO surface with tailored surface energy leading to an improved PCE in inverted cells. This can be achieved by changing the surface compositions of the two different SAMs with either polar $–NH_2$ or non-polar $–CH_3$ end groups, resulting in a wide range of surface energies from 40 to 70 mN/m. Modification of metal oxides with fullerene-based SAMs have also been employed to improve the ESL/BHJ contact. It was found that good quality fullerene-SAM (C_{60}-SAM) with proper anchor groups could be obtained by simple spin-coating on ZnO [106]. The C_{60}-SAM serves multiple purposes, including enhancement of interfacial exciton-dissociation efficiency, passivation of inorganic-surface trap states, and optimization of upper organic layer morphology. As a result, a C_{60}-SAM modified P3HT:PCBM inverted cell showed improved PCE from 3.7 to 4.5 % [107]. This strategy has also been applied to other BHJ layer composed of new low bandgap polymers, which resulted in similar improvement in device efficiency [108]. The interfacial property between the metal oxide ESL and the BHJ can also be improved by inserting a thin layer of crosslinked fullerenes(C-PCBSD) (Fig. 9.10) [109, 110]. In situ cross-linking of the PCBSD film on ZnO could be achieved by annealing the film at 160 °C for 30 min to generate a robust, adhesive, and solvent-resistant film, showing an improvement of the performance of inverted P3HT:PCBM OPV from 3.5 to 4.4 %, and inverted P3HT:ICBA from 4.8 to 6.2 % [111].

Compared to their inorganic counterparts, organic materials as ESL is less explored in spite of their promise as interfacial materials for OPVs. Organic materials allow tailoring to have versatile functionalities. Their intrinsic mechanical robustness and flexibility are more suitable for flexible OPVs. Recent studies from Kippelen et al. demonstrated water soluble polymer surfactant, PEIE (Fig. 9.10) can strongly modified ITO electrodes and greatly shift its work function more than

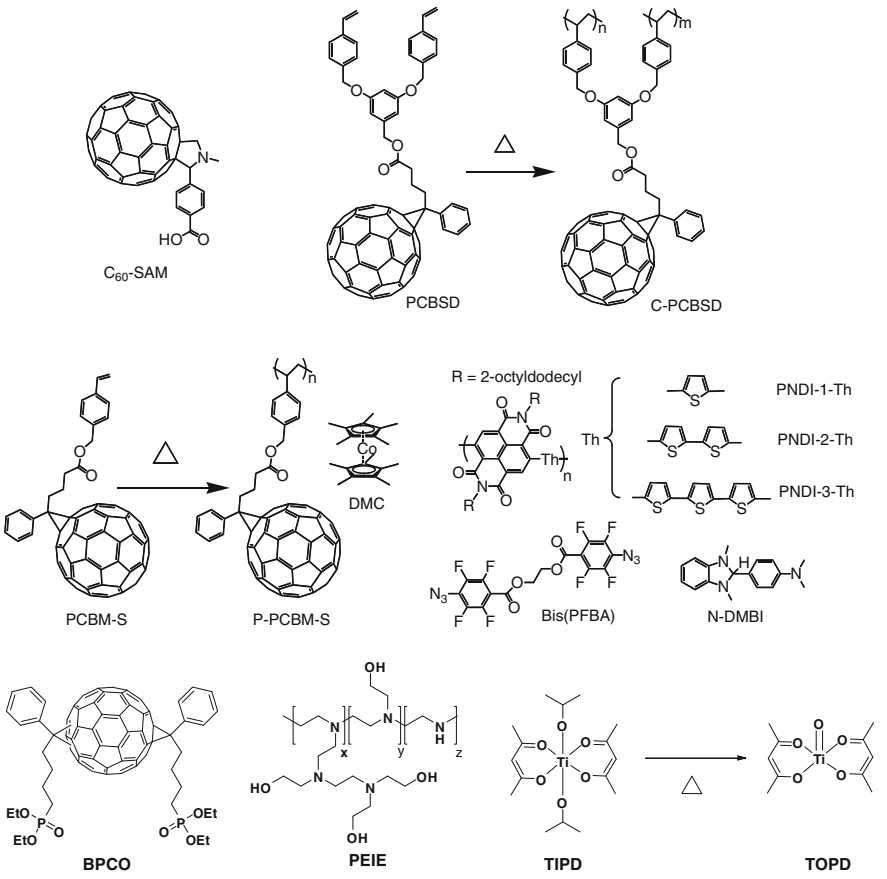

Fig. 9.10 Molecular structures of electron selective materials used in inverted OPV

1 eV. An ultrathin layer of insulating PEIE (<10 nm) on glass ITO can get PCE of 5.9 % from P3HT:ICBA BHJ, and all polymer based devices with a PEIE-coated PH1000 bottom electrode yielded high durability toward repeated bending [112]. A phosphate-containing bisadducts fullerene (B-PCPO) with alcohol solubility and good electron transporting ability also showed good application as ESL for inverted OPV, showed improvement of performance from 4.83 % (ITO) to 6.20 % (B-PCPO/ITO) [113]. Inverted PSCs based on PBDTTT-C/PC71BM with iso-propanol solution-processed TIPD as ESL on ITO was reported 7.4 % PCE, which was facilitated by thermal convert of TIPD to TOPD at 150 °C [114].

One of the major limitations of interfacial organic materials is their low inherent conductivities. To overcome this limitation, n-doping of organic-based ESL has been applied to improve the contact [115–117]. A n-doped polymerizable PCBM-S ESL provide not only good solvent resistance, but also improve conductivity from 1.7×10^{-7} S/m (undoped film) to 6.0×10^{-1} S/m (10 % decamethylcobaltocene

(DMC) doped film). N-doped ESL showed improved J-V characteristics and PCE [115]. Similar strategy was studied by using N-doped cross linkable ESL layer. An in situ n-doping and crosslinking of a series of naphthalene diimide and thiophene copolymers (NPDI-Th) has been studied with bis-PFPA crosslinker [118] and N-DMBI dopant [119] to generate conductive ESLs, resulted in significant increased electrical conductivity, as a result, the PCE of inverted P3HT:PCBM OPVs increased from 0.69 to 3.42 % [116].

For anode modification of inverted cells, besides the widely used PEDOT:PSS, n-type metal oxides such as WO_3 and MoO_3 are efficient materials that can promote Ohmic contact between the BHJ layer and metal anode due to their ability to p-dope the polymer donor [59, 120, 121]. GO as the HSL were also reported for anode modification of inverted OPVs [122–124]. Inverted P3HT:PCBM-based OPV devices modified with a 2–3 nm thick of GO HSL exhibited a remarkable improved PCE compared to devices without any interfacial layer and is even slightly better than that of PEDOT:PSS-based devices, indicating GO can effectively modify the anode to facilitate efficient hole collection [123]. It was found that protonic acid doping of the conjugated polymer at the BHJ/GO interface occurred due to the high proton density of GO, resulted in a highly conductive interface that facilitated Ohmic contact with the metal anode [122]. Another good example was recently demonstrated in inverted OPV based on PIDT-PhanQ:$PC_{71}BM$ BHJ, which showed a PCE of 5.9 % when GO was used as the HSL [125].

9.4 Conclusions

The introduction of proper interfacial materials to optimize properties between organic/metal and organic/organic interfaces has been turn out to be an equally important criterion as the design and process of new active materials, both of which pave the way to high performance and stability of organic photovoltaics. This chapter aimed to provide an overview on the recent development of effective interfacial materials, and the integration of these materials in different device architectures. Regarding to organic/electrode interface, tremendous progress have been achieved with developing several classes of organic, inorganic and hybrid interfacial materials, including conducting polymers, metal oxides, cross linkable materials, conjugated polymer electrolytes, self-assembled functional molecules and graphene-based materials. The electronic, electrical, optical, chemical and mechanical properties of interlayer materials are considered to be improved for maximizing PCE and device stability. For the emerging studies involved donor/acceptor interface engineering, it is critical to achieve in-depth understanding of physic at this organic/organic interface. The development of new strategies and materials to get control of the chemical and physical properties at these interfaces are very important for improving OPV technology.

Acknowledgments The authors thank the support from the National Science Foundation (DMR-0120967), the Department of Energy (DE-FC3608GO18024/A000), the Air Force Office of Scientific Research (FA9550-09-1-0426), the Asian Office of Aerospace R&D (FA2386-11-1-4072), Office of Naval Research (N00014-11-1-0300). A.K.-Y.J. thanks the Boeing Foundation for support.

References

1. http://www.eia.doe.gov/oiaf/ieo/index.html
2. C.J. Brabec, G. Dennler, M.C. Scharber, Adv. Mater. **21**, 1323 (2009)
3. F.C. Krebs, Sol. Energy Mater. Sol. Cells **93**, 394 (2009)
4. C.W. Tang, Appl. Phys. Lett. **48**, 183 (1986)
5. M.A. Green, K. Emery, Y. Hishikawa, W. Warta, E.D. Dunlop, Prog Photovoltaics **19**, 565 (2011)
6. R. F. Service, Science **332**, 293 (2011)
7. E. Bundgaard, F.C. Krebs, Sol. Energ. Mat. Sol. C **91**, 954 (2007)
8. Y.J. Cheng, S.H. Yang, C.S. Hsu, Chem. Rev. **109**, 5868 (2009)
9. Y. Liang, L. Yu, Acc. Chem. Res. **43**, 1227 (2010)
10. G. Li, V. Shrotriya, J. Huang, Y. Yao, T. Moriarty, K. Emery, Y. Yang, Nat. Mater. **4**, 864 (2005)
11. J. Peet, M.L. Senatore, A.J. Heeger, G.C. Bazan, Adv. Mater. **21**, 1521 (2009)
12. F.C. Krebs, Sol. Energ. Mat. Sol. C **93**, 394 (2009)
13. H. Ma, H.-L. Yip, F. Huang, A.K.Y. Jen, Adv. Funct. Mater. **20**, 1371 (2010)
14. L.-M. Chen, Z. Xu, Z. Hong, Y. Yang, J. Mater. Chem. **20**, 2575 (2010)
15. E.D. Gomez, Y.-L. Loo, J. Mater. Chem. **20**, 6604 (2010)
16. R. Steim, F.R. Kogler, C.J. Brabec, J. Mater. Chem. **20**, 2499 (2010)
17. J.H. Park, T.-W. Lee, B.-D. Chin, D.H. Wang, O.O. Park, Macromol. Rapid Comm. **31**, 2095 (2010)
18. R. Po, C. Carbonera, A. Bernardi, N. Camaioni, Energy Environ. Sci. **4**, 285 (2011)
19. S. Braun, W.R. Salaneck, M. Fahlman, Adv. Mater. **21**, 1450 (2009)
20. W.J. Potscavage Jr, A. Sharma, B. Kippelen, Acc. Chem. Res. **42**, 1758 (2009)
21. E.L. Ratcliff, B. Zacher, N.R. Armstrong, J. Phys. Chem. Lett. **2**, 1337 (2011)
22. C. Deibel, V. Dyakonov, Rep. Prog. Phys. **73**, 096401 (2010)
23. J. Hwang, A. Wan, A. Kahn, Mat. Sci. Eng. R **64**, 1 (2009)
24. P.W.M. Blom, V.D. Mihailetchi, L.J.A. Koster, D.E. Markov, Adv. Mater. **19**, 1551 (2007)
25. V.D. Mihailetchi, P.W.M. Blom, J.C. Hummelen, M.T. Rispens, J. Appl. Phys. **94**, 6849 (2003)
26. J.-L. Brédas, J.E. Norton, J. Cornil, V. Coropceanu, Acc. Chem. Res. **42**, 1691 (2009)
27. Y.B. Yuan, T.J. Reece, P. Sharma, S. Poddar, S. Ducharme, A. Gruverman, Y. Yang, J.S. Huang, Nat. Mater. **10**, 296 (2011)
28. T.M. Clarke, J.R. Durrant, Chem. Rev. **110**, 6736 (2010)
29. K. Tvingstedt, K. Vandewal, A. Gadisa, F. Zhang, J. Manca, O. Inganäs, J. Am. Chem. Soc. **131**, 11819 (2009)
30. A. Tada, Y. Geng, Q. Wei, K. Hashimoto, K. Tajima, Nat. Mater. **10**, 450 (2011)
31. B. Yang, Y. Yuan, P. Sharma, S. Poddar, R. Korlacki, S. Ducharme, A. Gruverman, R. Saraf, J. Huang, Adv. Mater. **24**, 1455 (2012)
32. K.S. Nalwa, J.A. Carr, R.C. Mahadevapuram, H.K. Kodali, S. Bose, Y. Chen, J.W. Petrich, B. Ganapathysubramanian, S. Chaudhary, Energ. Environ. Sci. **5**, 7042 (2012)
33. J.M. Lobez, T.L. Andrew, V. Bulović, T.M. Swager, ACS Nano **6**, 3044 (2012)
34. K. Sivula, Z.T. Ball, N. Watanabe, J.M.J. Fréchet, Adv. Mater. **18**, 206 (2006)
35. C. Yang, J.K. Lee, A.J. Heeger, F. Wudl, J. Mater. Chem. **19**, 5416 (2009)

36. M. Wang, A.J. Heeger, F. Wudl, Small **7**, 298 (2011)
37. T. Nishizawa, K. Tajima, K. Hashimoto, J. Mater. Chem. **17**, 2440 (2007)
38. J.L. Segura, N. Martin, D.M. Guldi, Chem. Soc. Rev. **34**, 31 (2005)
39. J.B. Kim, K. Allen, S.J. Oh, S. Lee, M.F. Toney, Y.S. Kim, C.R. Kagan, C. Nuckolls, Y.L. Loo, Chem. Mater. **22**, 5762 (2010)
40. H. Ma, H.-L. Yip, F. Huang, A.K.Y. Jen, Adv. Func. Mater. **20**, 1371 (2010)
41. C.-Z. Li, H.-L. Yip, A.K.Y. Jen, J. Mater. Chem. **22**, 4161 (2012)
42. H.-L. Yip, A.K.Y. Jen, Energy. Environ. Sci. **5**, 5994 (2012)
43. Y. Liang, Z. Xu, J. Xia, S.-T. Tsai, Y. Wu, G. Li, C. Ray, L. Yu, Adv. Mater. **22**, E135 (2010)
44. H.-Y. Chen, J. Hou, S. Zhang, Y. Liang, G. Yang, Y. Yang, L. Yu, Y. Wu, G. Li, Nat. Photonics **3**, 649 (2009)
45. K.W. Wong, H.L. Yip, Y. Luo, K.Y. Wong, W.M. Lau, K.H. Low, H.F. Chow, Z.Q. Gao, W.L. Yeung, C.C. Chang, Appl. Phys. Lett. **80**, 2788 (2002)
46. J.W. Jung, J.U. Lee, W.H. Jo, J. Phys. Chem. C **114**, 633 (2010)
47. C.-Y. Li, T.-C. Wen, T.-F. Guo, J. Mater. Chem. **18**, 4478 (2008)
48. A.W. Hains, T.J. Marks, Appl. Phys. Lett. **92**, 023504 (2008)
49. A.W. Hains, J. Liu, A.B.F. Martinson, M.D. Irwin, T.J. Marks, Adv. Funct. Mater. **20**, 595 (2010)
50. A.W. Hains, C. Ramanan, M.D. Irwin, J. Liu, M.R. Wasielewski, T.J. Marks, ACS Appl. Mater. Inter. **2**, 175 (2010)
51. Y. Sun, S.-C. Chien, H.-L. Yip, Y. Zhang, K.-S. Chen, D.F. Zeigler, F.-C. Chen, B. Lin, A. K.Y. Jen, Chem. Mater. **23**, 5006 (2011)
52. V. Shrotriya, G. Li, Y. Yao, C.W. Chu, Y. Yang, Appl. Phys. Lett. **88**, 073508 (2006)
53. M.D. Irwin, B. Buchholz, A.W. Hains, R.P.H. Chang, T.J. Marks, P. Natl. Acad. Sci. U.S.A. **105**, 2783 (2008)
54. K.X. Steirer, P.F. Ndione, N.E. Widjonarko, M.T. Lloyd, J. Meyer, E.L. Ratcliff, A. Kahn, N.R. Armstrong, C.J. Curtis, D.S. Ginley, J.J. Berry, D.C. Olson, Adv. Energy Mater. **1**, 813 (2011)
55. K.X. Steirer, J.P. Chesin, N.E. Widjonarko, J.J. Berry, A. Miedaner, D.S. Ginley, D.C. Olson, Org. Electron. **11**, 1414 (2010)
56. K. Zilberberg, S. Trost, H. Schmidt, T. Riedl, Adv. Energy Mater. **1**, 377 (2011)
57. S. Han, W.S. Shin, M. Seo, D. Gupta, S.-J. Moon, S. Yoo, Org. Electron. **10**, 791 (2009)
58. S. Murase, Y. Yang, Adv. Mater. **24**, 2459 (2012)
59. M.C. Gwinner, R. Di Pietro, Y. Vaynzof, K.J. Greenberg, P.K.H. Ho, R.H. Friend, H. Sirringhaus, Adv. Funct. Mater. **21**, 1432 (2011)
60. T. Matsushima, G.-H. Jin, Y. Kanai, T. Yokota, S. Kitada, T. Kishi, H. Murata, Org. Electron. **12**, 520 (2011)
61. M. Kubo, K. Iketaki, T. Kaji, M. Hiramoto, Appl. Phys. Lett. **98**, 073311 (2011)
62. M. Kroger, S. Hamwi, J. Meyer, T. Riedl, W. Kowalsky, A. Kahn, Appl. Phys. Lett. **95**, 123301 (2009)
63. Y. Sun, C.J. Takacs, S.R. Cowan, J.H. Seo, X. Gong, A. Roy, A.J. Heeger, Adv. Mater. **23**, 2226 (2011)
64. E. Voroshazi, B. Verreet, A. Buri, R. Mueller, D. Di Nuzzo, P. Heremans, Org. Electron. **12**, 736 (2011)
65. F. Liu, S. Shao, X. Guo, Y. Zhao, Z. Xie, Sol. Energ. Mat. Sol. C **94**, 842 (2010)
66. C. Girotto, E. Voroshazi, D. Cheyns, P. Heremans, B.P. Rand, ACS Appl. Mater. Inter. **3**, 3244 (2011)
67. T. Stubhan, T. Ameri, M. Salinas, J. Krantz, F. Machui, M. Halik, C.J. Brabec, Appl. Phys. Lett. **98**, 253308 (2011)
68. J. Meyer, R. Khalandovsky, P. Gorrn, A. Kahn, Adv. Mater. **23**, 70 (2011)
69. S.S. Li, K.H. Tu, C.C. Lin, C.W. Chen, M. Chhowalla, ACS Nano **4**, 3169 (2010)
70. K.-H. Tu, S.-S. Li, W.-C. Li, D.-Y. Wang, J.-R. Yang, C.-W. Chen, Energ. Environ. Sci. **4**, 3521 (2011)

71. M.S. Ryu, J. Jang, Sol. Energ. Mat. Sol. C **95**, 2893 (2011)
72. C.-C. Chang, C.-F. Lin, J.-M. Chiou, T.-H. Ho, Y. Tai, J.-H. Lee, Y.-F. Chen, J.-K. Wang, L.-C. Chen, K.-H. Chen, Appl. Phys. Lett. **96**, 263506 (2010)
73. A. Kumar, G. Li, Z. Hong, Y. Yang, Nanotechnology **20**, 165202 (2009)
74. D. Gao, M.G. Helander, Z.B. Wang, D.P. Puzzo, M.T. Greiner, Z.H. Lu, Adv. Mater. **22**, 5404 (2010)
75. J.Y. Kim, S.H. Kim, H.H. Lee, K. Lee, W.L. Ma, X. Gong, A.J. Heeger, Adv. Mater. **18**, 572 (2006)
76. S.H. Park, A. Roy, S. Beaupre, S. Cho, N. Coates, J.S. Moon, D. Moses, M. Leclerc, K. Lee, A.J. Heeger, Nat. Photonics **3**, 297 (2009)
77. T. Salim, Z. Yin, S. Sun, X. Huang, H. Zhang, Y.M. Lam, ACS Appl. Mater. Inter. **3**, 1063 (2011)
78. M.-H. Park, J.-H. Li, A. Kumar, G. Li, Y. Yang, Adv. Funct. Mater. **19**, 1241 (2009)
79. H. Faber, M. Burkhardt, A. Jedaa, D. Kaelblein, H. Klauk, M. Halik, Adv. Mater. **21**, 3099 (2009)
80. H.-L. Yip, S.K. Hau, N.S. Baek, A.K.Y. Jen, Appl. Phys. Lett. **92**, 193313 (2008)
81. H.-L. Yip, S.K. Hau, N.S. Baek, H. Ma, A.K.Y. Jen, Adv. Mater. **20**, 2376 (2008)
82. S.B. Jo, J.H. Lee, M. Sim, M. Kim, J.H. Park, Y.S. Choi, Y. Kim, S.-G. Ihn, K. Cho, Adv. Energy Mater. **1**, 690 (2011)
83. C.E. Small, S. Chen, J. Subbiah, C.M. Amb, S.-W. Tsang, T.-H. Lai, J.R. Reynolds, F. So, Nat. Photon **6**, 115 (2012)
84. J.H. Seo, A. Gutacker, Y. Sun, H. Wu, F. Huang, Y. Cao, U. Scherf, A.J. Heeger, G.C. Bazan, J. Am. Chem. Soc. **133**, 8416 (2011)
85. Z. He, C. Zhang, X. Xu, L. Zhang, L. Huang, J. Chen, H. Wu, Y. Cao, Adv. Mater. **23**, 3086 (2011)
86. Z. He, C. Zhong, X. Huang, W.-Y. Wong, H. Wu, L. Chen, S. Su, Y. Cao, Adv. Mater. **23**, 4636 (2011)
87. S.H. Oh, S.I. Na, J. Jo, B. Lim, D. Vak, D.Y. Kim, Adv. Funct. Mater. **2010**, 20 (1977)
88. C. He, C. Zhong, H. Wu, R. Yang, W. Yang, F. Huang, G.C. Bazan, Y. Cao, J. Mater. Chem. **20**, 2617 (2010)
89. L.J. Zhang, C. He, J.W. Chen, P. Yuan, L.A. Huang, C. Zhang, W.Z. Cai, Z.T. Liu, Y. Cao, Macromolecules **43**, 9771 (2010)
90. Q. Wei, T. Nishizawa, K. Tajima, K. Hashimoto, Adv. Mater. **20**, 2211 (2008)
91. J.W. Jung, J.W. Jo, W.H. Jo, Adv. Mater. **23**, 1782 (2011)
92. Q.D. Tai, J.H. Li, Z.K. Liu, Z.H. Sun, X.Z. Zhao, F. Yan, J. Mater. Chem. **21**, 6848 (2011)
93. K. O'Malley, C.-Z. Li, H.L. Yip, A.K. Y. Jen, under review
94. C.-Z. Li, C.-C. Chueh, H.-L. Yip, K.M. O'Malley, W.-C. Chen, A.K.Y. Jen, J. Mater. Chem. **22**, 8574 (2012)
95. L.-M. Chen, Z. Hong, G. Li, Y. Yang, Adv. Mater. **21**, 1434 (2009)
96. S.K. Hau, H.-L. Yip, A.K.Y. Jen, Polym. Rev. **50**, 474 (2010)
97. F. Zhang, X. Xu, W. Tang, J. Zhang, Z. Zhuo, J. Wang, J. Wang, Z. Xu, Y. Wang, Sol. Energ. Mat. Sol. C, **95**, 1785
98. M. Reinhard, J. Hanisch, Z. Zhang, E. Ahlswede, A. Colsmann, U. Lemmer, Appl. Phys. Lett. **98**, 053303 (2011)
99. H.H. Liao, L.M. Chen, Z. Xu, G. Li, Y. Yang, Appl. Phys. Lett. **92**, 173303 (2008)
100. J.S. Huang, G. Li, Y. Yang, Adv. Mater. **20**, 415 (2008)
101. M.S. White, D.C. Olson, S.E. Shaheen, N. Kopidakis, D.S. Ginley, Appl. Phys. Lett. **89**, 143517 (2006)
102. A.K.K. Kyaw, X.W. Sun, C.Y. Jiang, G.Q. Lo, D.W. Zhao, D.L. Kwong, Appl. Phys. Lett. **93**, 221107 (2008)
103. C.M. Amb, S. Chen, K.R. Graham, J. Subbiah, C.E. Small, F. So, J.R. Reynolds, J. Am. Chem. Soc. **133**, 10062 (2011)
104. C.-P. Chen, Y.-D. Chen, S.-C. Chuang, Adv. Mater. **23**, 3859 (2011)

105. X. Bulliard, S.-G. Ihn, S. Yun, Y. Kim, D. Choi, J.-Y. Choi, M. Kim, M. Sim, J.-H. Park, W. Choi, K. Cho, Adv. Funct. Mater. **20**, 4381 (2010)
106. S.K. Hau, Y.-J. Cheng, H.-L. Yip, Y. Zhang, H. Ma, A.K.Y. Jen, ACS Appl. Mater. Inter. **2010**, 2 (1892)
107. S.K. Hau, H.-L. Yip, H. Ma, A.K.Y. Jen, Appl. Phys. Lett. **93**, 233304 (2008)
108. Y. Zhang, S.K. Hau, H.-L. Yip, Y. Sun, O. Acton, A.K.Y. Jen, Chem. Mater. **22**, 2696 (2010)
109. C.-H. Hsieh, Y.-J. Cheng, P.-J. Li, C.-H. Chen, M. Dubosc, R.-M. Liang, C.-S. Hsu, J. Am. Chem. Soc. **132**, 4887 (2010)
110. Y.-J. Cheng, F.-Y. Cao, W.-C. Lin, C.-H. Chen, C.-H. Hsieh, Chem. Mater. **23**, 1512 (2011)
111. Y.-J. Cheng, C.-H. Hsieh, Y. He, C.-S. Hsu, Y. Li, J. Am. Chem. Soc. **132**, 17381 (2010)
112. Y. Zhou, C. Fuentes-Hernandez, J. Shim, J. Meyer, A.J. Giordano, H. Li, P. Winget, T. Papadopoulos, H. Cheun, J. Kim, M. Fenoll, A. Dindar, W. Haske, E. Najafabadi, T.M. Khan, H. Sojoudi, S. Barlow, S. Graham, J.-L. Brédas, S.R. Marder, A. Kahn, B. Kippelen, Science **336**, 327 (2012)
113. C. Duan, C. Zhong, C. Liu, F. Huang, Y. Cao, Chem. Mater. **24**, 1682 (2012)
114. Z. Tan, W. Zhang, Z. Zhang, D. Qian, Y. Huang, J. Hou, Y. Li, Adv. Mater. **24**, 1476 (2012)
115. N. Cho, H.-L. Yip, S.K. Hau, K.-S. Chen, T.-W. Kim, J.A. Davies, D.F. Zeigler, A.K.Y. Jen, J. Mater. Chem. **21**, 6956 (2011)
116. N. Cho, H.-L. Yip, J.A. Davies, P.D. Kazarinoff, D.F. Zeigler, M.M. Durban, Y. Segawa, K. M. O'Malley, C.K. Luscombe, A.K.Y. Jen, Adv. Ener. Mater. **1**, 1148 (2011)
117. C.S. Kim, S. Lee, L.L. Tinker, S. Bernhard, Y.-L. Loo, Chem. Mater. **21**, 4583 (2009)
118. R.-Q. Png, P.-J. Chia, J.-C. Tang, B. Liu, S. Sivaramakrishnan, M. Zhou, S.-H. Khong, H.S. O. Chan, J.H. Burroughes, L.-L. Chua, R.H. Friend, P.K.H. Ho, Nat. Mater. **9**, 152 (2010)
119. P. Wei, J.H. Oh, G. Dong, Z. Bao, J. Am. Chem. Soc. **132**, 8852 (2010)
120. C. Tao, S. Ruan, G. Xie, X. Kong, L. Shen, F. Meng, C. Liu, X. Zhang, W. Dong, W. Chen, Appl. Phys. Lett. **94**, 043311 (2009)
121. J. Meyer, S. Hamwi, S. Schmale, T. Winkler, H.-H. Johannes, T. Riedl, W. Kowalsky, J. Mater. Chem. **19**, 702 (2009)
122. Y. Gao, H.-L. Yip, K.-S. Chen, K.M. O'Malley, O. Acton, Y. Sun, G. Ting, H. Chen, A.K.Y. Jen, Adv. Mater. **2011**, 23 (1903)
123. Y. Gao, H.-L. Yip, S.K. Hau, K.M. O'Malley, N.C. Cho, H. Chen, A.K.Y. Jen, Appl. Phys. Lett. **97**, 203306 (2010)
124. Y.-Y. Lee, K.-H. Tu, C.-C. Yu, S.-S. Li, J.-Y. Hwang, C.-C. Lin, K.-H. Chen, L.-C. Chen, H.-L. Chen, C.-W. Chen, ACS Nano **5**, 6564 (2011)
125. J. Zou, H.-L. Yip, Y. Zhang, Y. Gao, S.-C. Chien, K. O'Malley, C.-C. Chueh, H. Chen, A. K. Y. Jen, Adv. Funct. Mater **22**, 2804 (2012)
126. C. Waldauf, M. Morana, P. Denk, P. Schilinsky, K. Coakley, S.A. Choulis, C.J. Brabec, Appl. Phys. Lett. **89**, 233517 (2006)
127. H. Choi, J.S. Park, E. Jeong, G.-H. Kim, B.R. Lee, S.O. Kim, M.H. Song, H.Y. Woo, J.Y. Kim, Adv. Mater. **23**, 2759 (2011)
128. S.-I. Na, T.-S. Kim, S.-H. Oh, J. Kim, S.-S. Kim, D.-Y. Kim, Appl. Phys. Lett. **97**, 213301 (2010)
129. Y. Sun, J.H. Seo, C.J. Takacs, J. Seifter, A.J. Heeger, Adv. Mater. **23**, 1679 (2011)

Chapter 10
Surface Plasmonic Effects of Nanostructures on the Performance of Polymer Solar Cells

Ming-Kai Chuang, Jyh-Lih Wu, Shang-Chieh Chien and Fang-Chung Chen

Abstract In this chapter, we review recent progress related to the incorporation of plasmonic nanostructures in organic photovoltaic devices (OPVs) as a means of enhancing power conversion efficiencies. We begin by describing the fundamental properties of surface plasmons (SPs). We then outline the two primary schemes that are commonly employed for excitation of the SPs: the use of noble metal particles to trigger the SPs and the creation of propagating surface plasmon polaritons (SPP) through approaches that can overcome the problem of momentum mismatch (e.g., periodic corrugation at the metal–dielectric interface). Next, we discuss some recent remarkable approaches toward increasing the light absorption efficiency of OPVs, highlighting three categories of plasmonic structures that enhance the performance of OPVs. Finally, we provide a brief outlook regarding the future use of SPs in high-efficiency OPVs.

10.1 Introduction

Organic photovoltaic devices (OPVs) are receiving increasing attention because of their many advantageous properties, including low cost, light weight, ease of processing, flexibility, and abundant availability [1–5]. At present, OPVs based on conjugated polymers as electron-donor materials blended with fullerene derivatives as electron-acceptor materials can exhibit power conversion efficiencies (PCE) as high as 8–9 % [6]. The working principle of an OPV involves six general processes: (i) photon absorption, (ii) exciton generation, (iii) exciton diffusion, (iv) exciton

M.-K. Chuang · J.-L. Wu · S.-C. Chien
Department of Photonics and Institute of Electro-optical Engineering,
National Chiao Tung University, Hsinchu 300, Taiwan

F.-C. Chen (✉)
Department of Photonics and Display Institute,
National Chiao Tung University, Hsinchu 300, Taiwan
e-mail: fcchen@mail.nctu.edu.tw

Y. Yang and G. Li (eds.), *Progress in High-Efficient Solution Process Organic Photovoltaic Devices*, Topics in Applied Physics 130,
DOI 10.1007/978-3-662-45509-8_10

dissociation, (v) charge transport, and (vi) charge collection. Based on these steps, the external quantum efficiency (EQE) (or photo-to-electron conversion efficiency, IPCE) can be determined using the following equation [7],

$$\mathrm{EQE}(\lambda) = \eta_{\mathrm{A}}(\lambda) \times \eta_{\mathrm{G}}(\lambda) \times \eta_{\mathrm{C}}(\mu) \tag{10.1}$$

where $\eta_{\mathrm{A}}(\lambda)$, $\eta_{\mathrm{G}}(\lambda)$, and $\eta_{\mathrm{C}}(\mu)$ are the absorption efficiency, carrier generation efficiency, and charge collection efficiency, respectively. In real devices, unfortunately, it is very difficult to decouple the relationships among these factors; indeed, simultaneous improvement of each of these efficiencies is challenging. For example, one common method toward increasing the absorption efficiency is the use of a thicker photoactive layer; because of low carrier motilities in organic materials, however, the possibility of charge recombination and device resistance will inevitably increase if the film is too thick, thereby decreasing the charge collection efficiency. For some conjugated polymers displaying higher hole mobilities [e.g., poly(3-hexylthiophene) (P3HT)], the thickness could reach up to approximately 200 nm. For most of the polymers used in OPVs, however, the optimal thickness is often less than 100 nm, leading to insufficient solar power absorption. Therefore, the challenge remains to achieve OPVs with high absorption efficiencies without degrading their charge collection efficiencies [8–14].

Many light trapping strategies have provided OPVs exhibiting promising behavior [8–14]. For example, the incorporation of optical spacers that can redistribute the optical electrical field in the device can enhance the absorption efficiency [9, 10]. Other techniques, including photonic crystals [11, 12] and folded device architectures [13, 14], have also been proposed to effectively improve the light harvesting efficiency in OPVs. Recently, the exploitation of surface plasmon resonance (SPR) effects has attracted much attention as a means of improving the efficiency of OPVs [15–20]. Surface plasmons (SP) are confined electromagnetic waves propagating along the surface of a conductor; they have many unique optical properties, including local field enhancement and strong light scattering, that might improve absorption processes in OPVs. Two primary schemes are commonly used for excitation of SPs. In one, surface plasmon polaritons (SPPs) propagating at the metal–dielectric interface can be excited by metal nanostructures (e.g., periodic arrays or gratings) [21–23]; in the other, SPs are triggered by metal nanoparticles (NPs; e.g., Cu, Ag, Pt, and Au NPs), resulting in localized surface plasmon resonance (LSPR) [21–24]. In this chapter, we first discuss the background of SPs and outline the potential plasmonic-enhanced structures for organic solar cells. We then review some recent progress in this area and discuss the potential of this approach for future OPV development. The main purpose of this Chapter is to introduce the basic concepts of plasmonic-enhanced OPVs, rather than completely reviewing all of the literature in this area. Therefore, we apologize if some outstanding studies are absent from this article.

10.2 Fundamental Properties of Surface Plasmons

10.2.1 Localized Surface Plasmons

Localized surface plasmons (LSPs) are the coherent collective oscillations of conduction electrons confined by noble metal NPs, as illustrated in Fig. 10.1a. Excitation of these particle plasmons can be achieved when the frequency of the incident light matches their resonance frequency, resulting in unique optical properties—selective light extinction and local enhancement of the electromagnetic field near the surface of the metal NPs. The resonance peaks of LSPs depend strongly on the size, shape, and dielectric environment of the metal NPs [25].

The extinction behavior—defined as the sum of light absorption and scattering—of localized SPs is strongly dependent on the size of the metal NPs. In the quasi-static approximation, the polarizability (P) of a spherical metal NP having a sub-wavelength diameter (a) can be expressed as [26]

$$P = 4\pi a^3 \frac{\varepsilon - \varepsilon_m}{\varepsilon + 2\varepsilon_m} \tag{10.2}$$

where ε is the dielectric constant of the surrounding medium and ε_m is the complex dielectric function of the metal NP. The value of P reaches its maximum when ε_m is equal to -2ε, giving rise to dipolar SPR.

As drawn in Fig. 10.1b, assuming that the particle size is much smaller than the incident wavelength ($a \ll \lambda$), the corresponding cross sections of light scattering (C_{sca}) and absorption (C_{abs}) can be expressed as [25, 27]

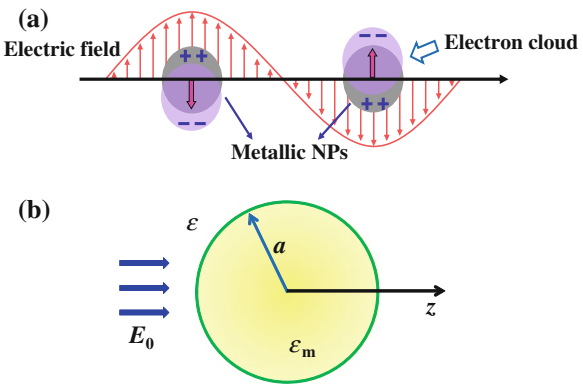

Fig. 10.1 **a** Schematic representation of the LSPs in metal NPs. **b** A spherical NP (radius: a) enforced by an external electric field (E_0). The complex dielectric functions for the metal NP and the surrounding medium are ε_m and ε, respectively

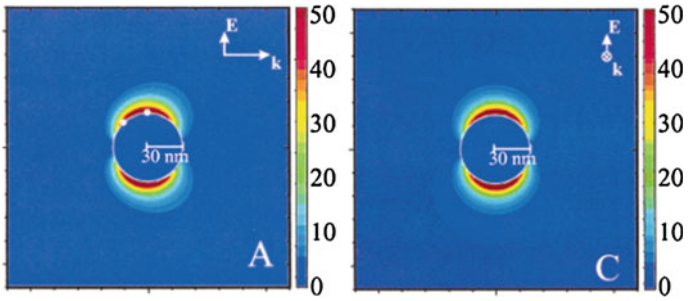

Fig. 10.2 In a vacuum, an Ag NP (radius: 30 nm) experiences an intense local field in the vicinity of its surface [25]

$$C_{abs} = k\,\mathrm{Im}[P] = 4\pi k a^3 \frac{\varepsilon - \varepsilon_m}{\varepsilon + 2\varepsilon_m}$$
$$C_{sca} = \frac{k^4}{6\pi}|P|^2 = \frac{8\pi}{3}k^4 a^6 \left|\frac{\varepsilon - \varepsilon_m}{\varepsilon + 2\varepsilon_m}\right|^2 \tag{10.3}$$

where k is the wavenumber of light. The total extinction cross section (C_{ext}) can be calculated as the sum of C_{sca} and C_{abs}. According to (10.3), the particle size apparently plays an important role in determining the extinction process—smaller NPs absorb light more efficiently, whereas scattering dominates the overall light extinction for larger NPs.

In addition to light extinction, another prominent feature of LSPs is local enhancement of the electromagnetic field in the vicinity of the metal NPs (Fig. 10.2). The resulting plasmonic field decays exponentially with respect to the distance from the surface of the metal NP; the decay length of the plasmonic field is typically on the order of the particle size of the metal NP [28]. Light concentration can result in an enhancement factor of up to 100 [21, 29]. This interesting phenomenon has been exploited extensively in the field of SP-enhanced spectroscopy; for example, the optical signal can be amplified significantly to allow the sensing of biological analytes [30].

10.2.2 Surface Plasmon Polaritons

One excited mode induced by incident photons on a metal surface is an SPP, a surface wave travelling at the interface between the metal and the dielectric material. Figure 10.3a presents a schematic representation of the SPP mode at the metal–dielectric interface [31, 32]. The SPs are strongly confined at the surface and have both electromagnetic wave and surface charge characteristics. The electric field perpendicular to the surface is significantly enhanced, decaying exponentially

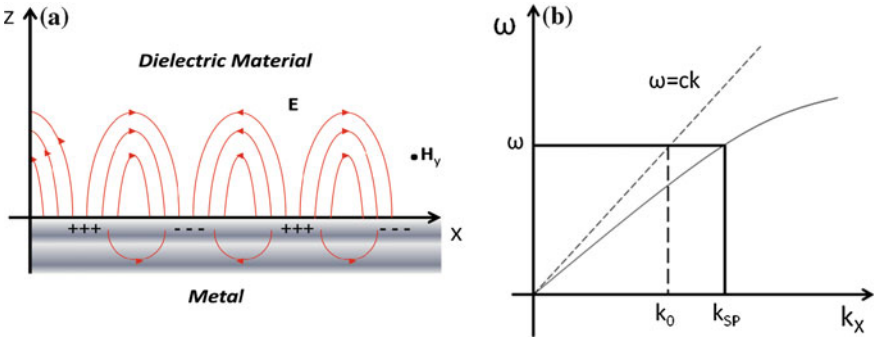

Fig. 10.3 **a** Schematic representation of the SPP mode generated at the metal–dielectric interface; **b** dispersion curve for an SP mode. A momentum mismatch could be found between the light and SP mode [31]

into both surrounding media. Notably, the decay length of the field is longer in the dielectric material than it is inside the metal film, where it is determined by the skin depth of the metallic material. Figure 10.3b displays the dispersion relationship for an SP mode; it can be derived from Maxwell's equations under the appropriate boundary conditions for a plane interface [27, 33],

$$k_{SP} = k_0 \sqrt{\frac{\varepsilon_d \varepsilon_m}{\varepsilon_d + \varepsilon_m}} \tag{10.4}$$

where k_{sp} is the wavevector of the SP mode, ω is the angular frequency, and ε_d and ε_m are the relatively permittivities of the dielectric and metal materials, respectively. The vacuum wave vector (k_0) is equal to ω/c, where ω and c are the angular frequency and the speed of light, respectively. Apparently, the SP vector is always larger than the in-plane wave vector of light. Therefore, no direct coupling between SPs and photons is allowed in the case of a planar interface. As a result, the problem of momentum mismatch must be overcome to couple SP modes and light.

Three primary approaches have been developed toward solving the problem of momentum mismatch [31]: (i) using prism coupling to increase the momentum of the incident photons; (ii) employing scattering centers (e.g., sub-wavelength defects) to trigger SPs; and (iii) fabricating periodic corrugated structures at the interface. The latter is the most common approach for OPVs. The next section provides several examples of periodic structures.

10.2.3 Designs of Plasmonic-Enhanced OPVs

As indicated in Fig. 10.4, plasmonic structures for the enhanced performance of OPVs can be generally divided into three categories [23]. In the first, metal NPs are

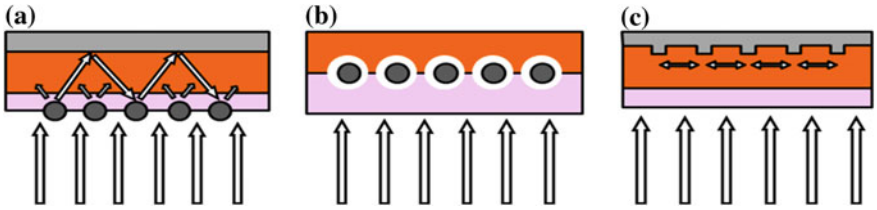

Fig. 10.4 Geometric structures using SP technology to increase the efficiency of thin-film solar cells. **a** Metal NPs at the thin film surface cause incident light to scatter mostly into the material having the higher dielectric constant, thereby confining the photons in the solar cell. **b** Metal NPs embedded in the semiconductor material enhance the near-field in the cell. **c** A periodic structure at the back metal electrode induces SPPs, which can turn the incident solar flux by 90° [23]

incorporated as scattering centers on the surface of the active thin film in the solar cell (Fig. 10.4a). In contrast to light scattering in a homogeneous medium, light will preferentially scatter into the material having the larger permittivity when the NPs are located at the interface between two different kinds of media. Through multiple and high-angle scattering, the overall optical path length will effectively increase, thereby trapping the photons in the device. In the second case, the NPs are embedded directly into the organic semiconducting layer (Fig. 10.4b). Theoretically, the enhanced near-field induced by the SPs can increase the absorption efficiency because the absorption is proportional to the intensity of the electromagnetic field [27]. In reality, however, the construction of such a device is quite difficult because the metal NPs tend to undergo phase separation from the organic materials. Furthermore, the inclusion of NPs might affect the device's electrical properties and decrease the carrier collection efficiency. Therefore, device designs adopting this concept remain rare. In the final case, a periodic corrugated structure is fabricated at the interface between a metal electrode and the semiconducting layer to sustain propagating SPPs (Fig. 10.4c). The evanescent electromagnetic fields induced by the SPPs are confined near the interface, guiding the light effectively into the semiconductor layer. Theoretically, because photons are absorbed along the lateral direction and because the optical length is several orders of magnitude longer than the thickness of the semiconductor absorber layer, the absorption efficiency should increase dramatically in such a structure.

10.3 Experimental Results of Plasmonic-Enhanced OPVs

In this section, we discuss some recent remarkable approaches that have led to increases in the light absorption efficiency of OPVs. Firstly, the most common strategy for triggering SPs is to incorporate metal NPs, which can produce an LSPR, into the device. For example, in 2008, Morfa et al. deposited Ag NPs through thermal evaporation onto indium tin oxide (ITO)–coated glass substrates (Fig. 10.5a) [34]. A layer of poly(3,4-ethylenedioxythiophene): polystyrenesulfonate (PEDOT:

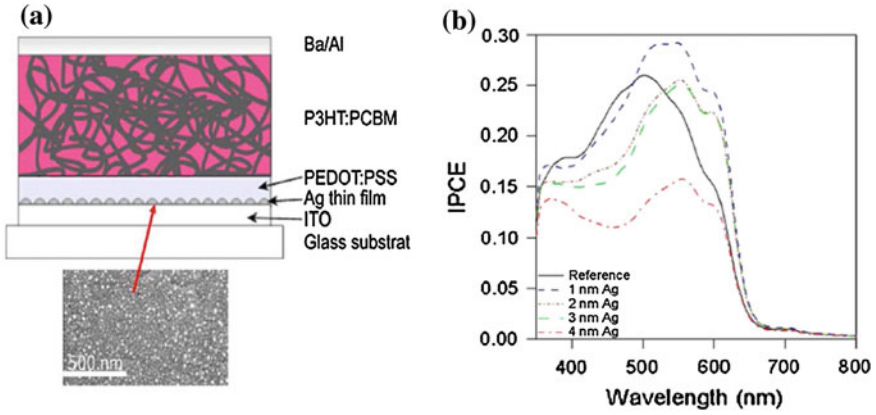

Fig. 10.5 **a** Schematic representation of the device structure of an Ag NP–mediated plasmonic-enhanced OPV. *Inset* Field-emission scanning electron microscopy image of 2 nm-thick Ag NPs deposited on ITO. **b** IPCE spectra of devices containing Ag NPs of various thicknesses [34]

PSS) was then spin-coated onto the nanostructure. The photoactive layer, a solution of P3HT and [6, 6] -phenyl-C_{61}-butyric acid methyl ester (PCBM), was deposited on top of the PEDOT:PSS. A bilayer cathode was formed upon sequential deposition of Ba and Al through thermal evaporation. Figure 10.5a presents the device structure. The PCE of the device formed without Ag NPs was 1.3 ± 0.2 %. The efficiency improved to 2.2 ± 0.1 % when the height of the Ag NPs was 1 nm. The PCE decreased slightly upon increasing the thickness of the Ag NPs. Figure 10.5b displays the corresponding IPCE spectra; a strong increase in EQE at longer wavelengths occurred for each modified device.

Similarly, Kim et al. [35] in the same year, fabricated Ag NPs through pulse-current (PC) electrodeposition onto ITO substrates. The advantage of their approach is the ability to control the size, density, and morphology of the NP films. With this method, they fabricated relatively uniform Ag NPs having an average particle size of approximately 13 nm. Figure 10.6 displays the device structure and the

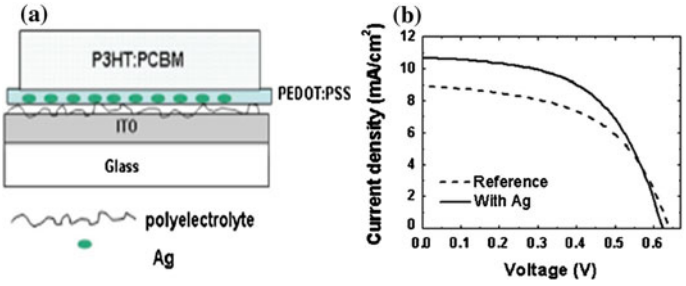

Fig. 10.6 **a** Device structure featuring Ag NPs. **b** *J–V* curve of devices prepared with and without Ag NPs [35]

photocurrent–voltage (*J–V)* curves of these devices under illumination. The photocurrent increased after incorporating these Ag NPs; the PCE improved from 3.05 to 3.69 %. The authors attributed the increased photocurrent to the SPR effect of the NPs.

Gold (Au), another noble metal, is also a promising candidate for producing LSPR phenomena. In 2009, Lee et al. [36] reported the enhanced performance of OPVs prepared with wet-deposited interfacial Au nanostructures. More interestingly, they prepared Au nanorods through layer-by-layer electrostatic assembly; the particle density could be controlled by varying the number of deposition cycles. As displayed in Fig. 10.7a, different particle densities are clearly evident in the two- and five-layer structures. Figure 10.7b presents the *J–V* curves of the various devices. The reference device prepared without Au NPs exhibited a PCE of 3.04 %; the PCE of a device containing a low density of Au nanodots increased to 3.65 %, suggesting the positive effect of the incorporation of these NPs.

Recently, our group reported a simple approach for incorporating surface-plasmonic NPs into OPVs [37, 38]. Because these Au NPs were prepared in water, they could be blended directly with the PEDOT:PSS solution. A nanocomposite layer

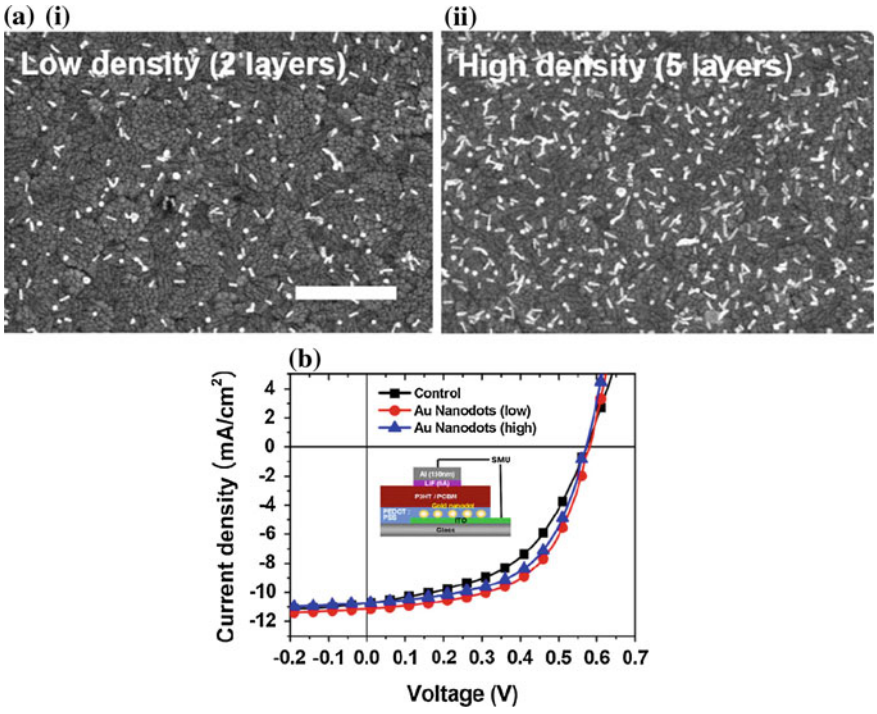

Fig. 10.7 **a** SEM images of Au nanorods in (i) low-density (*two layers*) and (ii) high-density (*five layers*) configurations. *Scale bar* 500 nm. **b** *J–V* curves of OPVs prepared with and without Au *nanodots*, recorded under AM1.5 simulated light (100 mW/cm^2). *Inset* Device structure [36]

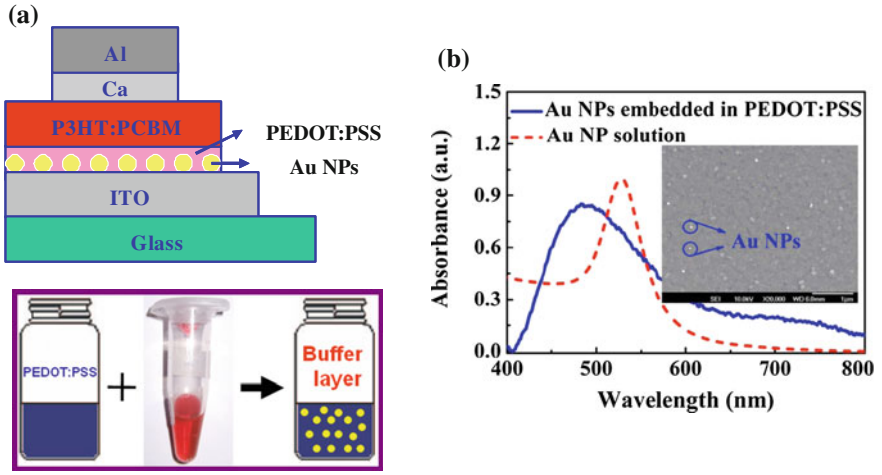

Fig. 10.8 **a** Structure of a device featuring Ag NPs and method of preparation of the buffer solution containing Au NPs. **b** Absorption spectra of a Au NP solution and of Au NPs embedded in PEDOT:PSS. *Inset* SEM image of a PEDOT:PSS film prepared with Au NP blended in the matrix [37]

was formed after spin-coating such a mixture. Figure 10.8a displays the simple device structure. The resonance peak, determined using UV–Vis spectroscopy, of the Au NPs in solution appeared near 550 nm. The average particle size, estimated from a scanning electron microscopy (SEM) image (inset to Fig. 10.8b), was approximately 30–40 nm. This image also reveals that the distribution of the Au NPs (white dots) in the PEDOT:PSS layer was uniform, with no apparent aggregation of the Au NPs. With this architecture, the PCE increased from 3.47 to 4.29 % [37].

As stated above, many reports have indicated that the incorporation of metal NPs in the vicinity of the photoactive layer can increase the device efficiency. Nevertheless, studies that provide a comprehensive understanding of the SP effect in OPVs have been rare. Because our fabrication approach is simple and highly repeatable, and the device's electrical properties are barely affected [38], it became a suitable platform for conducting a systematic study of such SP effects.

The enhanced light absorption efficiency of our OPVs might have resulted from two possible factors [38]. First, similar to the case illustrated in Fig. 10.4a, forward scattering might have increased the optical path in the active layer, thereby enhancing the degree of light absorption. Second, excitation of the LSPR might have resulted in local enhancement of the electromagnetic field in the vicinity of the Au NPs; the resulting high local field might have increased the total number of excitons in the active layer (Fig. 10.4b). As stated above, the particle size determines the extinction behavior. According to (10.3), the cross sections of light scattering are usually lower than the cross sections of light absorption for NPs having particle sizes of less than 100 nm. Because the particle size of the Au NPs

used in our study was less than 50 nm, light scattering would not have been the major mechanism responsible for the enhancement in device performance. On the other hand, time-resolved photoluminescence (TRPL) spectroscopy revealed that the exciton lifetime ($\tau_{exciton}$) of P3HT in the blend varied dramatically after Au NPs had been incorporated into the device.

To further investigate the SP effect, we performed exciton lifetime mapping of the photoactive film in the OPVs by combining the time-resolved PL measurement system with confocal laser scanning microscopy [38]. This technique enabled us to obtain the vertical evolution of $\tau_{exciton}$ in the P3HT/PCBM films at various z-axial positions (close to or away from the PEDOT:PSS layer, in which the Au NPs were blended) [39]. The histograms in Fig. 10.9 summarize the vertical evolution of $\tau_{exciton}$ in the P3HT/PCBM films. For the standard sample, the average value of $\tau_{exciton}$ decreased from 0.48 ns close to the PEDOT:PSS layer (Fig. 10.9c) to 0.35 ns away from the PEDOT:PSS layer (Fig. 10.9a). The difference between the lifetimes resulted from the inhomogeneous distribution of PCBM molecules in the P3HT matrix. On the other hand, for the plasmonic sample, we observed a complete reversal of the trend in the evolution of $\tau_{exciton}$. Because the plasmonic field decays exponentially away from the surface of metal NPs, the value of $\tau_{exciton}$ reached as short as 0.23 ns, due to strong coupling between the plasmons and excitons.

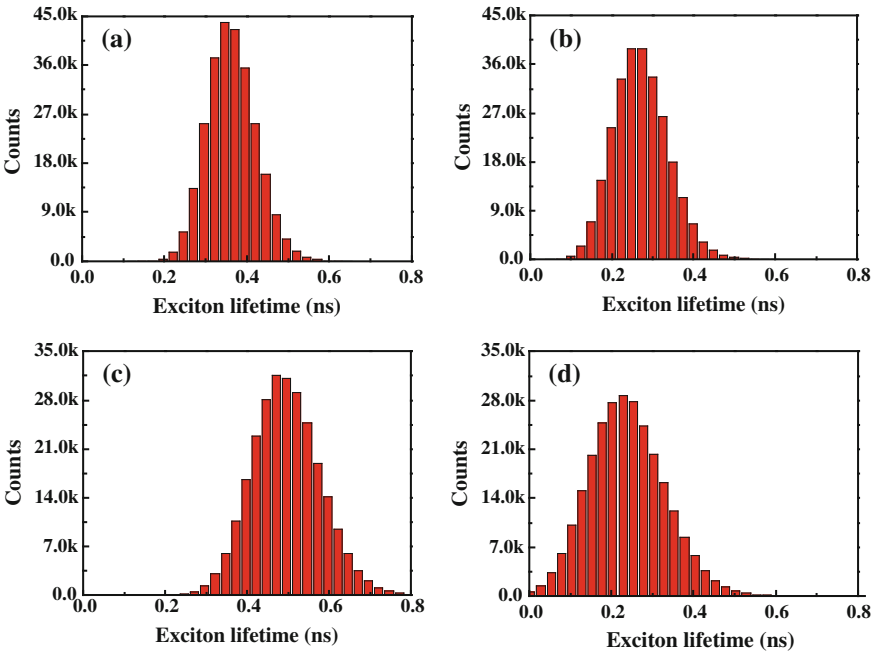

Fig. 10.9 Histograms corresponding to the exciton lifetime images for the reference (**a**, **c**) and plasmonic (**b**, **d**) samples. (**a**, **b**) Positions away from the PEDOT:PSS layer; (**c**, **d**) positions close to the PEDOT:PSS layer. Average values of $\tau_{exciton}$: **a** 0.35, **b** 0.27, **c** 0.48, and **d** 0.23 ns [38]

We would not expect the scattering scheme to influence the exciton lifetime significantly; therefore, the dynamic PL measurements indicated that the field enhancement mechanism plays an important role in improving the absorption efficiency [38].

In 2004, Ag and Au NPs were doped into the photoactive layer of bulk heterojunction OPVs. Although Kim and Carroll improved the device efficiency, they indicated that the dominant mechanism behind the enhanced efficiency was the improved electrical conductivity [40]. Similarly, in 2010, Xue et al. blended Ag NPs directly into the P3HT:PCBM layer, but did not observe significant device enhancement (Fig. 10.10a) [41]; they did, however, find that the mobility in the active layer had increased, but the total extracted carrier numbers had decreased. A study of the surface morphology suggested (Fig. 10.10b) that the Ag NPs tended to phase-segregate from the organic materials. These surface images also reveal the formation of a Ag NP sub-network, which can explain the increase in mobility. Xue et al. [41] concluded that charge trapping in the sub-network enhanced recombination, thereby decreasing the degree of charge extraction.

Recently, Sha et al. [42] developed a rigorous electrodynamic approach to study optical absorption in OPVs. They found remarkable differences between systems in which the metal NPs had been placed within the interlayer (spacer; i.e., between the active layer and the anode) and those embedded directly within the photoactive layer. The enhancement factors for the latter were generally higher than those of the former (Table 10.1), indicating that direct contact of metal NPs could increase the absorption process effectively in thin-film organic solar cells.

In 2007, Tvingstedt et al. [43] fabricated periodic nanostructures to excite SPPs at a metal–dielectric interface. Figure 10.11a presents the device structure; the Al

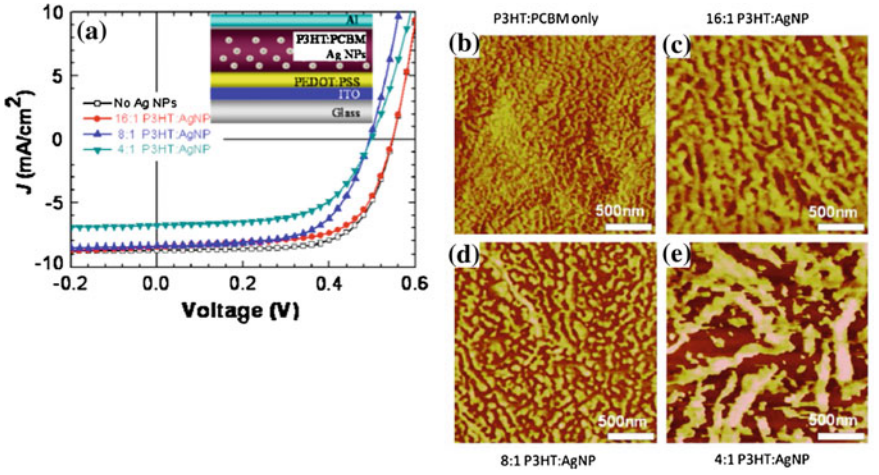

Fig. 10.10 **a** *J–V* curves of P3HT:PCBM solar cells incorporating Ag NPs at various concentrations. *Inset* Device structure. (**b–e**) Surface morphologies of active layers containing P3HT:AgNP ratios of **b** 1:0, **c** 16:1, **d** 8:1, and **e** 4:1 [41]

Table 10.1 Enhancement factors for metal NPs embedded within either the spacer or the active layer [42]

Spacer layer	Vertical incidence	Oblique incidence
Separated small	0.992	1.078
Close-packed small	0.989	1.174
Separated large	0.927	0.935
Close-packed large	0.725	0.589
Active layer	Vertical incidence	Oblique incidence
Separated small	1.366	1.374
Close-packed small	1.985	1.821
Separated large	1.118	1.216
Close-packed large	1.342	1.589

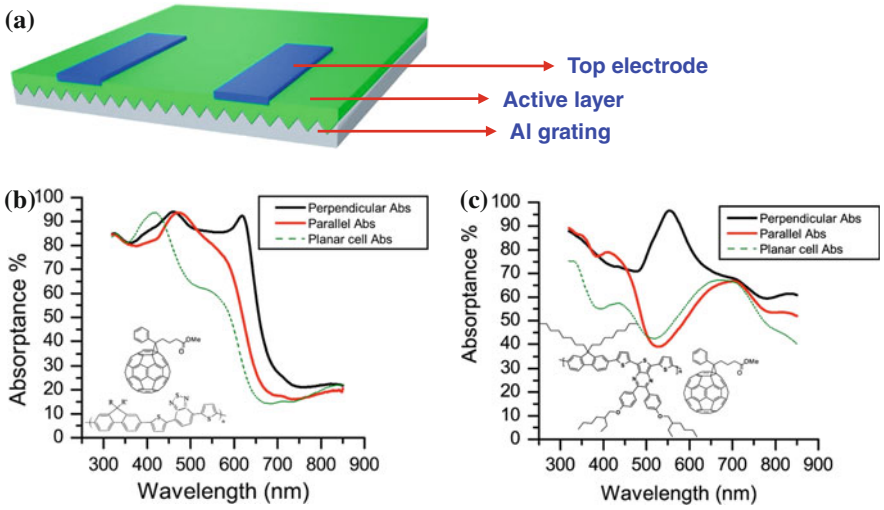

Fig. 10.11 **a** Periodic grating structure for propagating SPs. (**b**, **c**) Absorption spectra of the polymer blends **b** APFO3/PCBM and **c** APFO Green5/PCBM on the grating structures, obtained through illumination at different polarization directions [43]

grating was used as the bottom cathode and a PEDOT:PSS layer served as the top anode; the grating period and height were 277 and 50 nm, respectively. They used two different polymer blends as the active layer. Figure 10.11b, c display the corresponding measured absorption spectra. Relative to the planar sample, the absorption profiles for both of the material systems were changed by the SPPs

triggered on the nanostructures. Different spectra could be obtained when the samples were illuminated with different polarized directions. Tvingstedt et al. suggested that the TE polarization electromagnetic wave could not excite the SPs. IPCE measurements revealed a clear influence of the polarization directions on the spectrum, suggesting that the propagating SPs could enhance the photocurrent.

More recently, Sefunc et al. [44] designed and simulated plasmonic back-contact gratings for P3HT:PCBM cells; they found that absorption of light in the thin active film could be increased by a maximum factor of approximately 21 % in all polarization directions. Although no real device has been fabricated yet, their study suggests that the use of periodic gratings might be the correct approach toward enhancing absorption efficiency in OPVs.

10.4 Conclusion and Outlook

The field of plasmonic-enhanced OPVs is still expanding. A recent study has indicated that the internal quantum efficiency of OPVs has the ability to approach 100 % [45]; therefore, light absorption of the solar irradiation remains one of the major limitations toward even higher PCEs. The light trapping/concentration ability of SPs appears to be a promising approach toward solving this problem. In this Chapter, we introduced the fundamental features of SPs and reviewed recent literature relating to approaches employed to improve the efficiency of OPVs. We divided these methods into three main categories; the most common is the positioning of metal NPs at the interface between the photoactive layer and the electrodes. So far, this approach has led to the photocurrent usually increasing by 20–30 %. Because the optical field of SPs decays exponentially, the near-field nature of NPs probably limits their functions in OPVs. Theoretically, the direct introduction of nanostructures into the active layer should be the best approach toward enhancing the absorption efficiency [42]. Nevertheless, this method still encounters many problems, mainly arising from serious phase separation between the nanostructures and the organic materials. Therefore, new structures and materials that can increase the absorption efficiency without sacrificing the device electrical properties should be designed. For plasmonic-enhanced OPVs incorporating periodic nanostructures, pronounced enhancement remains rarely observed. Furthermore, the 1-D grating structures often exhibit high polarization-dependence; simultaneous optimization of both polarization modes is quite difficult. More recently, 2-D structures possessing higher-order symmetries, which might overcome the polarization dependence, have been proposed [45]. In the near future, we foresee the fabrication of many more periodic nanostructures that will improve the device efficiency effectively. Finally, in addition to conventional single-junction devices, plasmonic nanostructures have also been applied in other types of device structures. For example, Yang et al. [46] demonstrated plasmonic effects in tandem polymer solar cells after blending Au NPs into the intermediate layer connecting the two subcells. Experimentally, they observed a 20 % enhancement in efficiency,

suggesting great potential for the plasmonic effect. In conclusion, with a clear need for technologies that can lead to high photon absorption, plasmonics has revealed its potential in the initial stage. We believe that OPVs will continue to benefit from these new developments, eventually delivering low-cost, high-efficiency cells.

Acknowledgments We thank the National Science Council of Taiwan and the Ministry of Education of Taiwan (through the ATU program) for financial support.

References

1. R.F. Service, Science **332**, 293 (2011)
2. B. Kippelen, J.-L. Bredas, Energy Environ. Sci. **2**, 251 (2009)
3. J.-L. Bredas, J.E. Norton, J. Cornil, V. Coropceanu, Acc. Chem. Res. **42**, 1691 (2009)
4. S. Sista, Z. Hong, L.-M. Chen, Y. Yang, Energy Environ. Sci. **4**, 1606 (2011)
5. G. Li, R. Zhu, Y. Yang, Nat. Photonics **6**, 153 (2012)
6. L. Dou, J. You, J. Yang, C.C. Chen, Y. He, S. Murase, T. Moriarty, K. Emery, G. Li, Y. Yang, Nat. Photonics **6**, 180 (2012)
7. A. Moliton, J.M. Nunzi, Polym. Int. **55**, 583 (2006)
8. D.H. Ko, J.R. Tumbleston, A. Gadisa, M. Aryal, Y. Liu, R. Lopez, E.T. Samulski, J. Mater. Chem. **21**, 16293 (2011)
9. J.Y. Kim, S.H. Kim, H.H. Lee, K. Lee, W.L. Ma, X. Gong, A.J. Heeger, Adv. Mater. **18**, 572 (2006)
10. J. Gilot, I. Barbu, M.M. Wienk, R.A.J. Janssen, Appl. Phys. Lett. **91**, 113520 (2007)
11. J.R. Tumbleston, D.H. Ko, E.T. Samulski, R. Lopez, Opt. Express **17**, 7670 (2009)
12. D.H. Ko, J.R. Tumbleston, L. Zhang, S. Williams, J.M. DeSimone, R. Lopez, E.T. Samulski, Nano Lett. **9**, 2742 (2009)
13. K. Tvingstedt, V. Andersson, F. Zhang, O. Inganas, Appl. Phys. Lett. **91**, 123514 (2007)
14. Y.H. Zhou, F.L. Zhang, K. Tvingstedt, W.J. Tian, O. Inganas, Appl. Phys. Lett. **93**, 033302 (2008)
15. M.G. Kang, T. Xu, H.J. Park, X.G. Luo, L.J. Guo, Adv. Mater. **22**, 4378 (2010)
16. N.C. Lindquist, W.A. Luhman, S.H. Oh, R.J. Holmes, Appl. Phys. Lett. **93**, 123308 (2008)
17. I. Diukman, L. Tzabari, N. Berkovitch, N. Tessler, M. Orenstein, Opt. Express **19**, A64 (2011)
18. A.P. Kulkarni, K.M. Noone, K. Munechika, S.R. Guyer, D.S. Ginger, Nano Lett. **10**, 1501 (2010)
19. W. Ren, G. Zhang, Y. Wu, H. Ding, Q. Shen, K. Zhang, J. Li, N. Pan, X. Wang, Opt. Express **19**, 26536 (2011)
20. A.E. Ostfeld, D. Pacifici, Appl. Phys. Lett. **98**, 113112 (2011)
21. S.A. Maier, H.A. Atwater, J. Appl. Phys. **98**, 011101 (2005)
22. W.A. Murray, W.L. Barnes, Adv. Mat. **19**, 3771 (2007)
23. H.A. Atwater, A. Polman, Nat. Mat. **9**, 205 (2010)
24. E. Hutter, J.H. Fendler, Adv. Mat. **16**, 1685 (2004)
25. K.L. Kelly, E. Coronado, L.L. Zhao, G.C. Schatz, J. Phys. Chem. B **107**, 668 (2003)
26. S. Lal, S. Link, N.J. Halas, Nat. Photonics **1**, 641 (2007)
27. V.E. Ferry, J.N. Munday, H.A. Atwater, Adv. Mater. **22**, 4794 (2010)
28. M.E. Stewart, C.R. Anderton, L.B. Thompson, J. Maria, S.K. Gray, J.A. Rogers, R.G. Nuzzo, Chem. Rev. **108**, 494 (2008)
29. B.P. Rand, P. Peumans, S.R. Forrest, J. Appl. Phys. **96**, 7519 (2004)
30. J.N. Anker, W.P. Hall, O. Lyandres, N.C. Shan, J. Zhao, R.P.V. Duyne, Nat. Mater. **7**, 442 (2008)
31. W.L. Barnes, A. Dereux, T.W. Ebbesen, Nature **424**, 824 (2003)

32. K. Okamoto, Y. Kawakami, IEEE J. Sel. Top. Quantum Electron. **15**, 1199 (2009)
33. L. Novotny, B. Hecht, *Principles of Nano-Optics* (Cambridge University Press, Cambridge, 2007)
34. A.J. Morfa, K.L. Rowlen, T.H. Reilly, M.J. Romero, J. van de Lagemaat, Appl. Phys. Lett. **92**, 013504 (2008)
35. S.S. Kim, S.I. Na, J. Jo, D.Y. Kim, Y.C. Nah, Appl. Phys. Lett. **93**, 073307 (2008)
36. J.H. Lee, J.H. Park, J.S. Kim, D.Y. Lee, K. Cho, Org. Electron. **10**, 416 (2009)
37. F.C. Chen, J.L. Wu, C.L. Lee, Y. Hong, C.H. Kuo, M.H. Huang, Appl. Phys. Lett. **95**, 013305 (2009)
38. J.L. Wu, F.C. Chen, Y.S. Hsiao, F.C. Chien, P. Chen, C.H. Kuo, M.H. Huang, C.S. Hsu, ACS Nano **5**, 959 (2011)
39. J.H. Huang, F.C. Chien, P.L. Chen, K.C. Ho, C.W. Chu, Anal. Chem. **82**, 1669 (2010)
40. K. Kim, D.L. Carroll, Appl. Phys. Lett. **87**, 203113 (2005)
41. M. Xue, L. Li, B.J. Tremolet de Villers, H. Shen, J. Zhu, Z. Yu, A.Z. Stieg, Q. Pei, B. J. Schwartz, K.L. Wang, Appl. Phys. Lett. **98**, 253302 (2011)
42. W.E.I. Sha, W.C.H. Choy, Y.G. Liu, W.C. Chew, Appl. Phys. Lett. **99**, 113304 (2011)
43. K. Tvingstedt, N.K. Persson, O. Inganas, A. Rahachou, I.V. Zozoulenko, Appl. Phys. Lett. **91**, 113514 (2007)
44. M.A. Sefunc, A.K. Okyay, H.V. Demir, Opt. Express **19**, 14200 (2011)
45. S.H. Park, A. Roy, S. Beaupre, S. Cho, N. Coates, J.S. Moon, D. Moses, M. Leclerc, K. Lee, A.J. Heeger, Nat. Photonics **3**, 297 (2009)
46. J. Yang, J. You, C.C. Chen, W.C. Hsu, H.R. Tan, X.W. Zhang, Z. Hong, Y. Yang, ACS Nano **5**, 6210 (2011)

Chapter 11
Tandem Solar Cell—Concept and Practice in Organic Solar Cells

Ziruo Hong, Letian Dou, Gang Li and Yang Yang

Abstract In the past decade, organic solar cell (OPV) technology has been intensively studied and improved significantly due to its attractive properties in manufacturability, flexibility, light weight etc. The power conversion efficiency (PCE) has been enhanced dramatically from ~2–3 to ~12 % through materials, interface and device architecture innovations such as tandem. This chapter focuses on multi-junction or tandem solar cell which is the architecture for highest solar cell efficiency. First, the principle of solar photovoltaic process and the theoretical limits of solar cell in single and multiple junction cells were presented. After the brief description of the realization of tandem cell concept in inorganic solar cells, we provided an overview of the development of organic tandem solar cells. This includes two very distinct technologies—vacuum deposited small molecule tandem solar cells, and solution processed polymer tandem solar cells. The progress in active materials with different bandgap, interconnection layer, and tandem device structure are presented.

11.1 Introduction

Energy has been identified as the largest problem the world is facing in the new century. The sun is the ultimate energy source for human being. The solar energy is abundant—an hour of solar energy from sunlight is almost the same as the world energy consumption in 1 year (~16 TW). Unlike the dominate fossil fuel energy

Z. Hong · L. Dou · G. Li (✉) · Y. Yang (✉)
Department of Materials Science and Engineering,
University of California Los Angeles, Los Angeles, CA 90095, USA
e-mail: gangl@ucla.edu

Y. Yang
e-mail: yangy@ucla.edu

Y. Yang and G. Li (eds.), *Progress in High-Efficient Solution Process Organic Photovoltaic Devices*, Topics in Applied Physics 130,
DOI 10.1007/978-3-662-45509-8_11

source, the solar energy is clean. However solar energy so far is still only a small fraction of our energy source (~0.1 % in US), [1] which is due mainly to the high cost of solar energy.

Solar photovoltaic (PV) is dominated by inorganic solar technologies, where Silicon PV has ~90 % of market today. The pursuit of low cost solar cell technology has always been keen to the scientific community. In recent years, there has been growing interest in organic solar cells (OPV) technology, due to its attractive features such as synthetic variability, low-temperature processing, and the possibility of producing lightweight, flexible, roll-to-roll compatible manufacturing, and inexpensive solar cells [2–5]. The OPV technology, however, has its weakness in efficiency and lifetime. As a late comer in solar cell technology, OPV continuously learns from inorganic solar cell society. In the history of pursuing high efficiency in inorganic solar cells, one significant event is the introduction and realization of tandem/multi-junction concept. The tandem crystalline inorganic solar cells require very high quality crystal growth and strict lattice matching, thus the cost is high which prohibits its wide use. The organic tandem solar cell is not limited by these restrictions due to van de Waals bonding. It therefore has the chance to achieve both higher efficiency and low cost.

In this chapter, we intend to provide the readers a brief yet self-sustain view of tandem solar cell—from the tandem cell concept, to the realization in inorganic solar cell since 1980, and finally the organic tandem solar cell works in the past decade.

11.2 Tandem Solar Cell—Concept

Photovoltaic is a process that converts photons directly to electrons, i.e. light to electricity. Semiconductors are the suitable materials for this purpose. Followed by the invention of first modern solar cell in Bell lab in 1954 [6], there have been intensive efforts to investigate how efficient, in ideal operational condition, a photovoltaic cell could be to convert solar light into electricity. In a landmark paper in 1961, Shockley and Queisser proposed reliable approach to calculate power conversion efficiency (PCE) from p-n junction solar cells under the illumination of solar spectra [7]. Interestingly the efficiency limit was proved to have nothing to do with a p-n junction, but related to the system in which light absorption generates electron-hole pairs. Their prediction is valid under the condition of four commonly accepted assumptions. These assumptions hold in both single- and multi- junction photovoltaic cells:

1. One incident photon generates one electron-hole pair;
2. Photons with energy larger than the bandgap of photoactive materials are completely absorbed, while those with lower energy than the bandgap do not contribute to photogeneration of charge carriers;

3. Photovoltaic device is free of charge recombination loss via non-radiative decay;
4. The incident light is neither concentrated nor anisotropic.

It is noted that there are exceptional cases in which these assumptions are no valid, under which it simply suggests the ways to surpass the efficiency limit. For example, multiple photon generation occurs in a single junction is a possible way [8]. In this case, the first assumption can be removed. Another example is the inter-band concept, which was also proposed that makes the second assumption invalid. Using focal lens or mirrors to concentrate incident light would also induce further separation of quasi-Fermi levels in photovoltaic system, in which the 4th assumption does not hold [9]. These concepts have been either demonstrated in real photovoltaic cells [10] or proposed in designing new material systems [11]. With these, there would be a more optimistic upper limit for photovoltaic efficiency, which is beyond the scope of discussion in this book chapter.

To understand the solar cell efficiency limit, there are two major issues to address. One is solar spectrum, and other is the operational principle of photovoltaic devices.

The sun has a surface temperature of ~6,000 K, and thus its emission spectrum can be approximately expressed by black body irradiation at the same temperature as shown in Fig. 11.1. To describe the energy distribution of the radiation, a numerical expression of 5,250 K blackbody is given here. This would be the starting point to detail the efficiency limit.

$$n(E,T,\mu,\Omega) = \frac{2\Omega}{c^2h^3}\frac{E^2}{e^{\left(\frac{E-\mu}{kT}\right)}-1} \tag{11.1}$$

where T is the temperature of the emitting body, c is the speed of light, h is Planck's constant and k is Boltzmann's constant. In the case of thermal emission, such as solar radiation, μ = 0 [12].

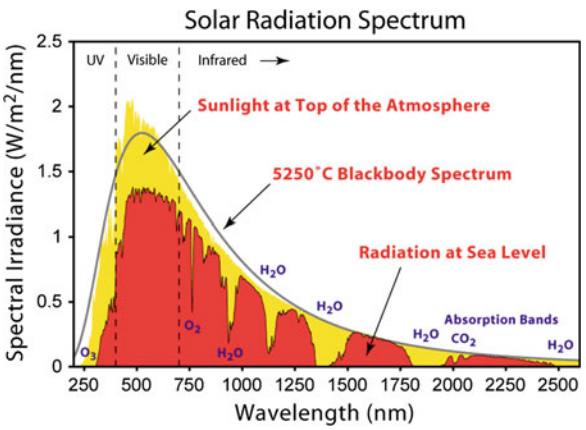

Fig. 11.1 Solar spectra outside of atmosphere (*yellow* area, AM0) and on the ground (*red* area, AM1.0); and the radiation from 5,250 °C blackbody (*black line*)

The solar spectrum is very close to the black body emission outside the atmosphere, namely Air Mass 0 (AM0). When the sun light passes through the atmosphere (more Air Mass), part of solar energy were absorbed by different molecules in the atmosphere. Thus the process changes the shape of solar spectrum. The spectrum on the earth surface also varies with incident angle, which corresponds to AM 1.0 (solar zenith angle of Z = 0°) and AM1.5 (solar zenith angle of Z = 48.2°). Such a spectrum shows how solar irradiation is distributed with respect to energy, and more importantly should be taken into account for device design and material selection of solar cells. AM1.5 Global (including both direct and diffused light) with light density of 1,000 W/m^2 is regarded as a standard for solar PV calibration on earth. We now briefly discuss several important mechanisms of energy loss from light to electricity in photovoltaics.

11.2.1 Thermodynamics Consideration

All energy-conversion devices that convert a certain type of energy into another have clear limitation on their conversion efficiencies due to the law of thermodynamics. Eventually, the second law of thermodynamics concerning entropy of the system consisting of both energy source and the converter sets the ultimate limitation for device efficiencies, including that of photovoltaic cells. It dictates the maximal work that a photovoltaic system can do by absorbing radiation from a black body at certain temperature. That means the temperature of photovoltaic cells should be as high as the radiation source to maximize the conversion efficiency, i.e. so-called Carnot efficiency. On the other hand, the cell temperature should be lowered as much as possible to minimize the radiation and the entropy increase within, i.e. so-call Landsberg efficiency. As the result of the two efficiency definitions, the upper limit efficiency according to thermodynamics, is approximately 85.4 % at a temperature of ~2,400 K. With further losses, the efficiency upper limit is approximately 31 % for single junction photovoltaic cells [7].

Recently Hirst and Ekins-Daukes reported detail analysis of photovoltaic process [13]. In additional to efficiency limit of devices, energy loss was specifically divided into several loss mechanisms as shown in Fig. 11.2, including optical loss for photons with energy below bandgap, thermolization energy from photons to bandgap, radiative recombination etc.

11.2.2 Breakdown of the Loss Mechanisms

(a) Photon energy versus the bandgap (or below Eg loss)

Under the first assumption, only the photons with energy ≥ band gap of semiconductors can be absorbed, and absorption efficiency is 100 %. Figure 11.2b (top

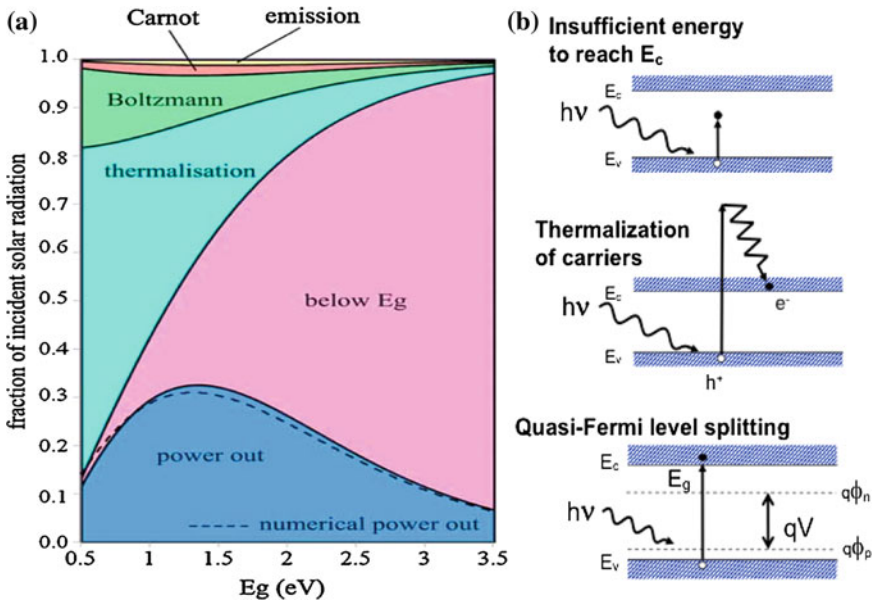

Fig. 11.2 **a** Intrinsic loss processes and hence, maximal power conversion efficiency are shown to be dependent on Eg. All incident radiation is accounted for, illustrating why intrinsic loss mechanisms lead to fundamental limiting efficiency. **b** First order loss mechanisms in photovoltaic cells (reprinted permission from the [13]. Copyright © 2011 John Wiley & Sons Inc.)

panel) shows that the energy of photons exceeding the band gap is dissipated as thermal energy, while photons below the band gap just pass through with no absorption.

(b) Carnot Loss:

The origin of the energy flow from the sun to the solar cell is determined by the temperature difference in between, and the solar cell is considered as a heat engine that absorbs thermal energy from the sun and does work (generating electricity). Such an energy conversion process is always accompanied with a loss in V_{oc} [14].

(c) Boltzmann loss

The absorption and emission angles are different, which results in an entropy generation process because of the expansion of photon modes (Boltzmann loss). This optical mismatch introduces irreversibility, which limits the conversion efficiency. The irreversible entropy generation is also counted as a loss associated with $T\Delta S$.

(d) Intrinsic loss in semiconductors—Emission/Radiative recombination loss

Assuming ideal condition when all the possible loss mechanisms in experimental condition can be excluded, the energy loss during this photovoltaic process would

be only dominated by two factors. One is illumination spectrum of the light source, and the other is the bandgap of the semiconductors. Since the standard solar spectrum does not change, the maximal efficiency is solely a function of bandgap.

Upon the light incidence, electron-hole pairs are generated and charge carriers may travel to electrodes to generate photocurrent. On the other hand, the recombination also occurs. Non-radiative decay is a process subject to the coupling of charges and matrix, which can be neglected in perfect crystals at 0 K, or be minimized in high quality crystalline structures. However, photoluminescence is an inevitable process, competing with charge extraction. A radiative limit of V_{oc} from single junction photovoltaic cells is described by:

$$V_{oc} = \frac{kT}{q}\ln\left(\frac{J_{ph}}{qn_i^2 wB}\right) = \frac{kT}{q}\left(\ln\left(\frac{J_{ph}}{qw}\right) - \ln\left(n_i^2\right) - \ln(B)\right) \tag{11.2}$$

11.2.3 *Efficiency Limit of Single Junction (Monolithic) Photovoltaic Cells*

In late 1950s, Price reported the estimation of maximal power conversion efficiency of photovoltaic cells according to some empirical rules [15]. In 1961, Shockley and Quisser [7] presented the very first example on analyzing the photovoltaic efficiency in a systematic way by incorporating the major parameters including solar spectrum, bandap of photovoltaic cells and thermal dynamics etc.

As Shockley and Quisser pointed out, the optimal bandgap of $\sim$1.4 eV was predicted for single-junction photovoltaic cells under illumination of AM1.5G. This prediction includes optimizing bandgap to maximize the product of photocurrent and electrical potential. With wide bandgap, the absorption covering shorter wavelength range, one can certainly gain in electrical potential from the semiconductor. However, this also loses photocurrent due to less photon flux harvested. Larger bandgap should reduce light harvesting, and smaller bandgap results in low open circuit voltage (V_{oc}). Theoretically, the maximum efficiency is $\sim$31 % under 1 sun illumination, when the optimal product of photocurrent and photovoltage can be reached.

It should be noted that Shockley-Quisser prediction is, as the authors emphasized, a general way to derive the efficiency limit, rather than accurate calculation. Therefore the solar spectrum used in their study is taken from blackbody radiation. Later on, complementary works adopted AM1.5G standard spectrum as a reference, and generated efficiency limit that make more sense with respect to practical photovoltaic applications. It should be noted that curves (c) and (d) in Fig. 11.3 are calculated using real solar spectrum, and thus not as smooth as curves (a) and (b), due to the deviation of incident spectra from the blackbody irradiation.

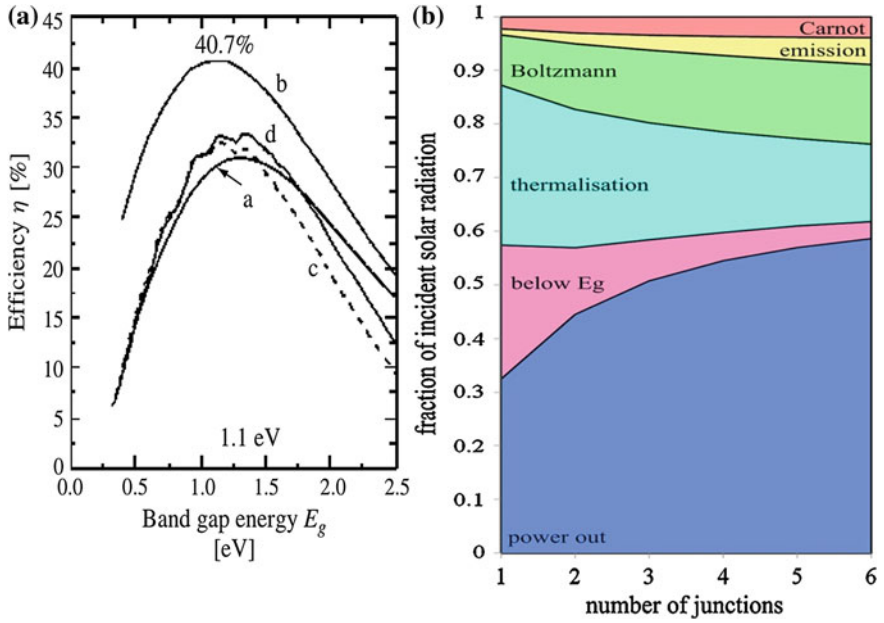

Fig. 11.3 **a** Shockley-Quisser efficiency limit [7] for an ideal solar cell versus band gap energy for unconcentrated black body illumination, for full concentrated illumination and for illumination under the terrestrial sun spectrum: **a** unconcentrated 6,000 K black body radiation (1,595.9 W/m^2), **b** full concentrated 6,000 K black body radiation (7,349.0 × 10^4 W/m^2), **c** unconcentrated AM1.5D (767.2 W/m^2), and **d** AM1.5G (962.5 W/m^2); **b** loss processes and power out in an unconstrained, multijunction device under one sun illumination (reprinted with the permission from [7] and [13]. Copyright © 1961 American Institute pf Physics, and ©2011 John Wiley & Sons Inc.)

11.2.4 Beyond Shockley-Quisser Limit

In order to understand how to overcome Shockley-Queisser efficiency limit, we first address the major loss mechanisms, which dominate in Shockley-Queisser estimation.

Providing sufficient absorption and efficient charge collection, the major loss in photovoltaic conversion is not due to the quantum efficiency, but the potential loss. When photons are absorbed by the photoactive layers, the excited electrons would relax down to a low energy state, corresponding to the bottom of conduction band (the 1st excited states in organic materials). This part of loss is determined by the access energy of the photon with respective to the material bandgap. Since the relaxation occurs much faster than charge transporting process, such a loss is inevitable.

Next, upon generation of free carriers, it is required to have sufficient chemical potential difference to pull out the charge carriers. Eventually the V_{oc} is always smaller than bandgap. Furthermore, the photovoltage at maximum power output is smaller than open circuit voltage, and electrical potential of several kT is further consumed.

Two major losses were identified in Fig. 11.2b. One is the optical loss which corresponds to the low energy photons beyond the band edge of photoactive films. The other is the so-called cooling energy, the excess energy of photon above the bandgap. The peak efficiency in S-Q limit is achieved at a compromise point in between. Therefore, in order to minimize the potential loss in these two steps, ideally it is possible to harvest high-energy photons in a material with large-bandgap, and then to collect the penetrating light by stacking a low-bandgap material behind, i.e. tandem structure.

In stacking structure with sub-unit number of N, we may divide the solar spectrum into N parts with equal amount of photon flux. Each individual cell covers its share according to its bandgap edge, and all the unit cells are jointed in serial connection. The assumption for Shockley-Queisser efficiency still holds for the sub-cells. All the photons with energy above the bandgap should be absorbed to generate charge carriers, and that rest will pass to the next sub-cell, and so on.

Figure 11.3b shows the loss processes and power output in an unconstrained, multi-junction device under one sun illumination. We can see that thermalization loss is tremendously reduced. On the other hand, consumed energy subjected to Carnot engine, radiative recombination and Boltzmann loss increases in multiple junctions, since such a prediction is also based on optimal condition in individual junctions which compose the multiple junction cells. Power conversion efficiency increases with the number of junctions. Two junctions lift efficiency limit to ~43 %, and three junctions enable approximately 50 % limit, in contrast to 31 % from single junctions. An infinite multi-junction cell of optimal design may reach a maximal efficiency, where the losses due to (1) below Eg, (2) thermolization, and (3) Boltzmann will be completely neglected.

$$\eta = \frac{1}{\sigma_{SB} T_S^4} \int_0^\infty i(\varepsilon, V) V_{\max} d\varepsilon \tag{11.3}$$

This way the efficiency is ascribed by the above and it yields 86.8 % peak value for Ts = 6,000 K and Tc = 300 K.

11.3 Realization of Inorganic Multi-junction Solar Cells

The tandem or multi-junction concept is straightforward but the realization of the concept is not easy. The tandem approach typically requires the incident light photons with different energy be mainly absorbed in correct subcell. Using optically

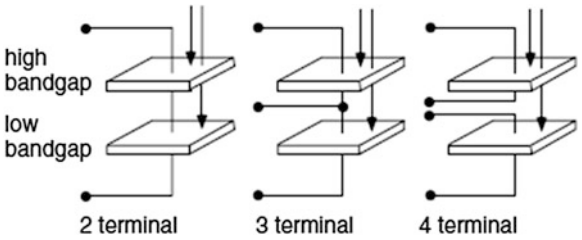

Fig. 11.4 Two, three, and four terminal configurations of two-junction solar cells (reprinted permission from the [16]. Copyright © 2011 John Wiley & Sons Inc.)

dispersive elements such as prism can spatially divide photons with different energies to different locations, so appropriate cells can be placed to collect them. This concept is simple, but in reality the scheme is complex due to mechanical and optical complicity. This also will require large area to place cells, and the cell efficiency is not necessarily high. The preferred (and most widely used) configuration is the stacked approach, as illustrated in Fig. 11.4 [16]. The incident light first strikes the high bandgap cell, then the low bandgap cell(s). Thus the cells act as low-pass photon energy filters, and this arrangement eliminate separate optical elements (e.g. prism) to distribute the spectrum. The stack configuration can have different ways of connection. The 2-terminal case has physically separated subcells, and the tandem cell is a mechanically stacked unit. The two subcells can be connected either in series or in parallel, depends on the electrical connection scheme. In the 3-terminal case, the two subcells share one common terminal, therefore the two cells are in parallel connection, and do not need to have same photocurrent. The third and the most attractive scheme is the two-terminal (series-connected) configuration. This scheme requires current matching of subcells as they are connected in series. This requirement puts constriction on subcells' bandgap, thickness etc. The two-terminal configuration has a clear advantages that it only needs two conductive electrodes (thus reduces processing steps and cost), and it can be integrated into modules in the same monolithic manner as if it's a single-junction solar cell. This makes the engineering integration a much easier task than the four and three terminal configurations. In fact, the first commercially viable multijunction solar cell proposed by Olson et al. in 1985 is a two terminal GaInP/GaAs double junction solar cell [17].

11.3.1 The Practical Challenge—Lattice and Bandgap Matching

The real challenge of inorganic multi-junction photovoltaic cells lies on deposition processes, which requires good material compatibility between the sequential films. High quality crystalline structures are the prerequisite of high efficiency

photovoltaic cells, which needs high-quality film growth. Lattice match is one more critical point limiting materials selection for the multi-junction cells. For example, the GaInP/GaInAs/Ge based triple junction has optimal bandgaps of 1.9, 1.5 and 0.7 eV to reach maximized light harvesting and optical balance. Lattice mismatch has to be eliminated at the heterojunction interfaces to ensure the feasibility of the multi-layer deposition.

To manufacture high quality multi-junction photovoltaic cells, sophisticated deposition techniques are needed to grow multiple photoactive and charge collection layers in sequence. It makes the state-of-the-art multijunction PV cells extremely expensive.

11.3.2 Interconnection Between Subcells

In an inorganic multijunction cell, the interconnection is a tunneling-junction or tunneling diode to provide low resistance connection between the subcells. A tunneling junction is simply a $p^{++}n^{++}$ junction where "$^{++}$" represent degenerate/heavy doping. The direction of the $p^{++}n^{++}$ diode is opposite to that of the two subcells, otherwise it would produce a photovoltage negative to the photovoltage generated by the subcells. The space charge region for a $p^{++}n^{++}$ junction is very narrow $\sim$10 nm in inorganic multijunction cells. Under small forward bias or any reversed bias, the tunneling diode behaves like a resister when the current tunneling through the narrow space charge region. When the forward bias is large enough so the current becomes bigger than a threshold tunneling current, the tunneling diode becomes thermoionic emission dominated. The threshold tunneling current needs to be bigger than the photocurrent of tandem cell. In reality, many multijunction cells worked under concentrated condition for lowering the system cost. A typical photocurrent number for 1,000× concentrated cell is $\sim$14 A/cm^2, which gives a feeling of the tunneling current requirement of the tunneling diode.

11.4 Organic Tandem Solar Cells

The efficiency upper limit of organic photovoltaic cells is significantly reduced due to two facts:

1. Strong exciton binding energy usually on the order of 0.3–1.0 eV; [18, 19] this is the necessary price to pay in order for free carrier to be generated in organic heterojunctions. It is a huge amount comparing to their inorganic counterparts. Such a loss is inevitable for organic materials, due to the fact that the strong coupling of excitons and molecules requires sufficient chemical potential difference to split the electron-hole pair at the interfaces between electron donor and acceptor. Other than this, it is almost the same way to predict the efficiency limit for organic/polymer solar cells.

2. Limited charge transport in organic films; the optimal fill factor in inorganic crystalline based photovoltaic cells reaches, in theory, ~89 %. Experimental values are very close to this level, approaching the level over 85 %. However in contrast, organic photovoltaic cells show much lower FF, typically below 75 %, suggesting much entropy production in the photovoltaic processes.

As a result, the maximal efficiency one can expect from single junction photovoltaic cells are strongly depending on the binding energy according to reports from various groups. Photo-induced electron-hole pairs in organic materials have strong coupling with molecular orbital, and thus large binding energy, preventing the excitons from delocalization. To release the carriers from the strong binding states, a concept of using donor and acceptor with large difference in chemical potentials has been introduced. The organic photoactive layers are sandwiched between selective contacts, i.e. ideally ohmic contacts, for efficient extracting electrons and holes.

In organic heterojunctions, open circuit voltage (V_{oc}) is dominated by energy offset of donor's HOMO and acceptor's LUMO, which is contrast to inorganic photovoltaic cells. The relatively low efficiency obviously makes the tandem concept attractive for organic solar cells. On the other hand, organic semiconductors are dominated by van de Waals interaction, rather than covalent bonding in inorganic crystalline semiconductors. This removes the strict lattice matching requirement in inorganic tandem solar cell. Therefore, organic tandem solar cell has promising chance of achieving high efficiency and low cost processing.

11.4.1 Efficiency Limit of Organic/Polymer Tandem Photovoltaic Cells

In 2006, Scharber et al. [20] discussed OPV efficiency based on progress in OPV field up to 2005. The efficiency estimation in this work is relatively realistic. First, organic donor and acceptor system is considered, instead of traditional p-n junction, and a fullerene derivative with fix lowest unoccupied molecular orbital (LUMO) level is used to simplify the case. Second, quantum efficiency and FF are 65 %, which are quite conservative. By varying bandgap of donor materials, the maximal efficiency of ~11 % can be reached when the donor material has bandgap of 1.5 eV in single junction OPV device (Fig. 11.5a). Similar method can be generalized to two-junction tandem cells, yielding a peak efficiency of ~15 % as shown in Fig. 11.5b [21]. With less spectral competition, such efficiency enhancement shall be even higher than 40 %, and thus the tandem architecture becomes a promising way.

The assumed key device parameters in the two paper—FF 65 %, EQE 65 % etc., were later found to be too conservative. Detail studies reveal that the efficiency limit can be much higher, if only the exciton binding energy is deducted from S-Q efficiency estimation [22]. Obviously efficiency limit for tandem cells should also roar up under same condition, and thus efficiency well above 20 % can be expected in real world.

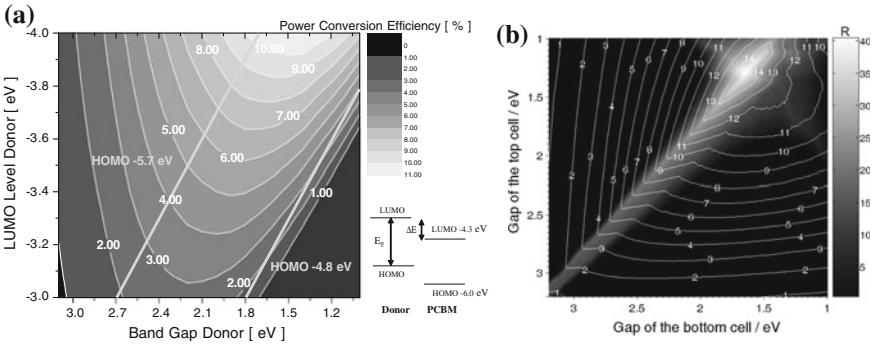

Fig. 11.5 **a** Efficiency of a donor–acceptor organic solar cell versus the band gap energy of the donor, and the LUMO offset between the two materials, **b** efficiency of a donor–acceptor tandem organic solar cell made of two sub-cells stacked in series versus the band gap energy of the *top* and *bottom* donors; both *top* and *bottom* donor–acceptor couples are assumed to have a LUMO offset of 0.3 eV (reprinted permission from the [20] and [21]. Copyright © 2006 and 2008 John Wiley & Sons Inc.)

Organic tandem solar cells have been achieved either via vacuum deposition or solution process, or a combination. In the following, we will first review the progress in vacuum deposited organic tandem solar cells, followed by the solution processed polymer solar cells in the last decade.

11.4.2 Vacuum Deposited Organic Tandem Cells

Various approaches have been taken to build organic tandem cells based on the processing technique or device configuration. Most commonly employed device structure is two-terminal monolithic structure in which two sub-cells are connected in series. Owing to the easy control over multilayer deposition via thermal evaporation, small molecule tandem cells have been explored. From fabrication point of view, lab scale multi-layer vacuum deposited organic tandem cells do not require complicated techniques, and the only requirement is that the materials can be sublimed in vacuum. Therefore many organic compounds with relatively low molecular weight and weak intermolecular interaction fall into this category, i.e. so-called small molecule materials. From spectral consideration, there are many choices for absorbers in wide spectral range. Two sub-units are almost enough to cover the visible and near infrared (NIR) range. Also vacuum deposition has the advantage that any number of cells can be stacked easily using dry coating process [23, 24]. Solution process sometimes is a complimentary method in combination with thermal deposition for fabricating the multi-layer structures. It provides more options for material selection, for example polymer [25].

Because of the absorption efficiency of small molecule solar cells more photons in the same wavelength range can be harvested by stacking two single cells [26]. The first report on two-terminal organic tandem solar cell was by Hiramoto et al. Two identical sub-cells were connected by a very thin and incomplete Au layer between the acceptor of the front cell and the donor of the rear cell [27], the efficiency improvement is minor or even negative in most of the cases due to the competing absorption. Using more efficient unit cells, the tandem architecture has resulted in increase in efficiency even though identical component cells were used [28].

With exploration of photoactive materials with various bandgaps, nowadays the small molecule based tandem cells have made significant advance in efficiency, which represents one of the promising strategies to bring OPV into real applications. Here we briefly discuss the major technical routes, except for evolution of materials.

11.4.2.1 Small Molecule Materials for Tandem OPVs

(a) Wide-bandgap small molecule OPV materials

In small molecule photovoltaic cells, there are various n-type materials proposed, however, in view point of satisfied photovoltaic performance, fullerene C60 and C70 are still commonly used acceptor materials so far. Due to the limited optional acceptors, material development is rather focused on p-type donors with deep HOMO levels.

To match the spectral requirements in tandem cells, one sub-cell should have relatively large bandgap, covering spectral range in visible, while the other extend the absorption into infrared. Many organic donors deliver relatively high V_{oc} of $\sim$0.9 V. Figure 11.6a, b shows two typical wide bandgap small molecule OPV materials. Thiophene oligomers (DCV-6T) have been proved to be very promising, offering V_{oc} approaching 1 V. Subphthalocyanine chloride (SubPc) with exceptional high $V_{oc} > 1$ V was also explored [29]. However due to its limited photocurrent from planar heterojunctions, the efficiency of tandem cells is limited to $\sim$5 %. Introducing donor: fullerene blend increases photocurrent significantly, however, the serious recombination occurs because of low carrier mobilities.

(b) Low-bandgap small molecule OPV materials

Since the solar spectrum has much energy in near infrared range, the limited option of low bandgap materials are so far critical to achieve high efficiency from tandem cells. Figure 11.6c–e shows two typical low bandgap small molecule OPV materials

Phthalocyanines have been considered as absorbers for infrared light. Zinc- and copper- phthalocyanines (ZnPC and CuPc) were the first ones used in OPV [26, 30]. The shallow highest occupied molecular orbital (HOMO) level and crystallinity in solid films lead to V_{oc} below 0.6 V, which is far less than the bandgap of 1.6 eV. HOMO level of phthalocyanines can be deepened by attaching electron-withdrawing groups to the molecules, and it has been demonstrated that

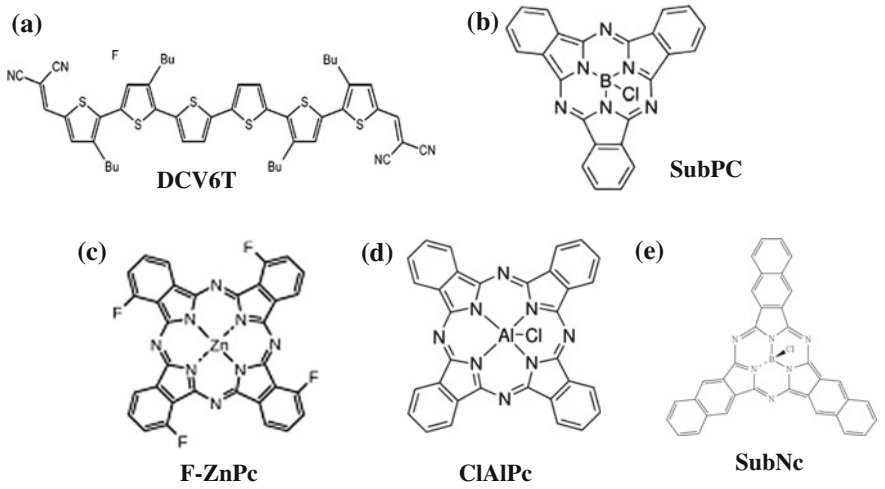

Fig. 11.6 Molecular structure of representative small molecules for OPV—Wide bandgap **a** DCV6T, **b** SubPC, and low bandgap **c** F4-ZnPC, and **d** ClAlPC, and **e** SubNc

fluorinated zinc phthalocyanine (F4-ZnPC) enhanced V_{oc} and thus efficiency by 30 % in comparison to zinc phthalocyanine in bulk heterojunctions [31]. Other phthalocyanine metal complexes have bandgap similar or even small than that of CuPc, while HOMO level is deeper. For example, chloroaluminum phthalocyanine (ClAlPc) has been explored for application of tandem cells [32].

Another effective strategy is to narrow down the bandgaps of some existing materials via extending π-conjugation. As mentioned above, SubPc has a bandgap of 2.0 eV and HOMO of 5.6 eV. Its analog, chloroboron (III) subnaphthalocyanine (SubNc), shows smaller bandgap of 1.7 eV, while HOMO level upshift reduces V_{oc} to ∼0.8 V [33].

11.4.2.2 Electrical Connection Between Two Small Molecule Sub Cells

Between two sub-cells, electrons and holes from the two units come into the interlayers where they cancel each other, i.e. recombination with zero or little potential loss. A good interlayer should be a good conductor forming ohmic contact with photoactive layers, and extracting charge carriers selectively. It is able to wire the charge carriers out of individual sub-cells, and unify their potential via quarsi-Fermi level alignment. Additional to this, such absorption of layers should be minimized.

(a) Heavy metal particles as recombination layer

In early works by Hiramoto [27] and Yakimov and Forrest [23] several angstrom of Ag or Au to connect the two sub-cells was deposited as a simple recombination

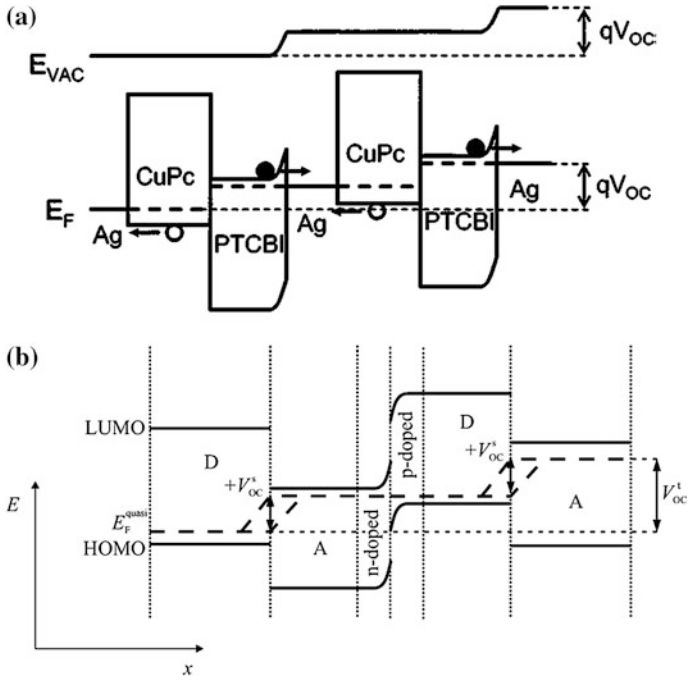

Fig. 11.7 **a** Energy diagram of a simple tandem cell with thin Ag as recombination layer under flat band condition, **b** energy level diagram at open circuit of a double heterojunction solar cell with highly doped layers as recombination contact *D* denotes the donor material and *A* the acceptor material (reprinted permission from the [23] and [30]. Copyright © 2002 and 2005 American Institute of Physics)

layer shown in Fig. 11.7 [34]. It is called metal particle layer because such a thin film is not continuous. It is obviously that the acceptor layer in the front cell and donor in the rear cell forms the reverse junction working against the two sub-cells, if there is no such a layer of heavy metal. Inserting a metal layer, HOMO level of CuPc donor is lifted up to match LUMO of PTCBI layer, such that this third junction does not generate photocurrent or photovoltage, and becomes no longer photoactive. Therefore the recombination of electrons from the front cell and holes from the rear takes place, enabling open circuit voltage add-up of the two sub-cells.

However charge recombination sites for photogenerated carriers also induce significant exciton quenching, which should be avoided to get high photocurrent. It is desirable to keep the recombination away from the photoactive layers. The metal layer is thus too simple to accomplish the mission.

(b) Multi-layer structures for electrical connection

The main idea is to isolate photoactive layers and recombination zone, such that individual sub-cells work without any influence of connection layers.

Forrest et al. reported 3,4,9,10 perylenetetracarboxylic bisbenzimidazole (PTCBI) (5 nm)/Ag (0.5 nm)/F4-TCNQ:m-MTDATA (5 nm) as interconnection layer in a tandem cell. PTCBI, an n-type semiconductor, collected electrons from C60 layer in the front cell, and p-doped 4,4′,4″-Tris[phenyl(m-tolyl)amino]triphenylamine (m-MTDATA) extracted holes from the rear cell [23]. The recombination is supposed to happen close or within Ag particles, while the thickness of both charge transport layers was very small, approximately 5 nm, mainly limited by the poor conductivity.

Similarly, thin connection layers were demonstrated by others. N-type materials, such as lithium fluoride (LiF), PTCBI and Bathocuproine (BCP), were widely used, and typical P-type materials are MoO_3, p-doped m-MTDATA, 1,4,5,8,9,11-hexaazatriphenylene hexacarbonitrile (HAT-CN) [35] etc. Materials used in between of n- and p-type materials can be ultra-thin silver or gold nano-particle layer. Such a combination serves as charge collection and recombination layers efficiently. Yet these connection layers have limited thickness, in order to maintain sufficient conductivity.

Alternatively the doping concept has been realized to be effective in organic semiconductors [36]. Such an approach may elevate conductivity of organic thin films up to 10^{-3} S/cm, which is sufficient to wire charge carriers into and out of active layers. In addition to hole transport nature in a p-type organic layer, certain amount of acceptor with deep LUMO close to the HOMO of the host induces high concentration free charge carriers therein. Such p-doping turns the hole transport layer from semiconductive into metallic. In the same way, n-doping layers can be obtained for electron transporting and injection. When the p- and n- layers are combined, it forms ohmic contact for electric current, and good charge recombination sites in tandem cells.

More importantly, the doping layers consist of large bandgap host and small amount of dopant. So these films can be made as thick as a few hundred of nanometer without causing any optical loss. This offers a unique tool to tune the optical field distribution in the multi-stacking devices, and record high efficiency has been reported from Heliatek using this method. Figure 11.7b illustrates the contact behavior of two heavy doped layers in conjunction of two sub-cells in tandem architecture. The alignment of quarsi-Fermi levels results in adding up of V_{oc} from individual sub-cells, and therefore high efficiency can be expected [37, 38].

11.4.2.3 Optical Balance

In small molecule based photovoltaic cells, thickness of active layer is normally on the order of several tens of nanometer. There is a significant variation of light distribution within the thin film structures with respect to the distance to the reflective electrode. Through optimization of optical field distribution the photocurrent from tandem cell was maximized.

Manipulation of optical field can be more effective when the thickness of charge transporting and recombination layers can be tuned in large range. Using similar photoactive materials, Leo's group demonstrated tuning of absorption in individual photoactive layers, such that photocurrent matching between the sub-cells can be obtained at maximal overall absorption [39].

Unlike inorganic tandem cells in which bandgaps of materials are arranged in cascade, layer sequence is another concern due to the strong interference effects. An example given by Chenys et al. showed light harvesting is more efficient when a small bandgap material is in front of the large bandgap one [40].

11.4.3 Solution Process Tandem Organic Polymer Solar Cells

While small molecule solar cell typically uses vacuum evaporation process, polymer solar cell has strong advantage of low cost manufacturability, due to its solution process capability compatible with coating and printing techniques. In addition, historically, polymer solar cell has long been the leader in power conversion efficiency race. The solution process, on the other hand, makes the realization of tandem devices harder due to the more complex multilayer structure.

It is interesting that the development of polymer tandem solar cell is quite similar to the beginning of inorganic multijunction cell. Figure 11.8 shows the structure of first two terminal GaInP/GaAs double junction solar cell. The high bandgap unit is GaInP, with a bandgap of 1.85 eV. This is very close to the long time workhorse material for polymer solar cell—poly (3-hexylthiophene) P3HT (bandgap 1.9 eV), on which many effective approaches have been implemented to improve efficiency and processability. The second subcell—GaAs has a bandgap of 1.42 eV. This represents significant challenge in the OPV society to develop high quality low bandgap (LBG) polymers for both single-junction and tandem solar cells. In this section, we will start from the development of challenging LBG polymer materials.

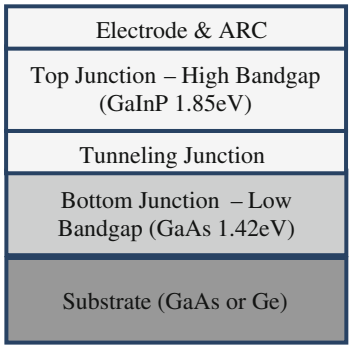

Fig. 11.8 Device structure of the first two terminal inorganic GaInP/GaAs double junction tandem solar cell

It will be followed by the typical high/wide bandgap materials, and the device architecture renovation. Overall we hope to provide a clear picture of tandem polymer solar cell development if the past decades.

11.4.3.1 Active Polymer Materials in Tandem OPVs

(a) Low bandgap polymer

In 2006, a promising LBG polymer **P1** (X = C, E_g = 1.4 eV, PCPDTBT, Fig. 11.9) was reported by Brabec et al. with an encouraging PCE of 3.2 % [41]. P1 is based on alternating strong electron rich cyclopentadithiophene (CPDT) and strong electron deficient benzothiadiazole (BT) units, and soon realized that the morphology of system has significant room to improve. A year later, Bazan and Heeger et al. optimized the performances of solar cell by introducing solvent additives (i.e., 1,8-diiodooctane, DIO) approach to improve the morphology [42]. The optimized morphology led to significantly higher J_{sc} (16 mA/cm^2) and a PCE of 5.5 %. The polymer blend covers from 350 nm all the way to nearly 900 nm with average EQE value of ~45 %, with 0.62 V V_{OC} and 55 % FF achieved. Due to this advantage, Heeger et al. selected **P1** as LBG cell in an all-solution processed tandem polymer solar cell, in which titanium oxide (TiO_x) layer and PEDOT:PSS

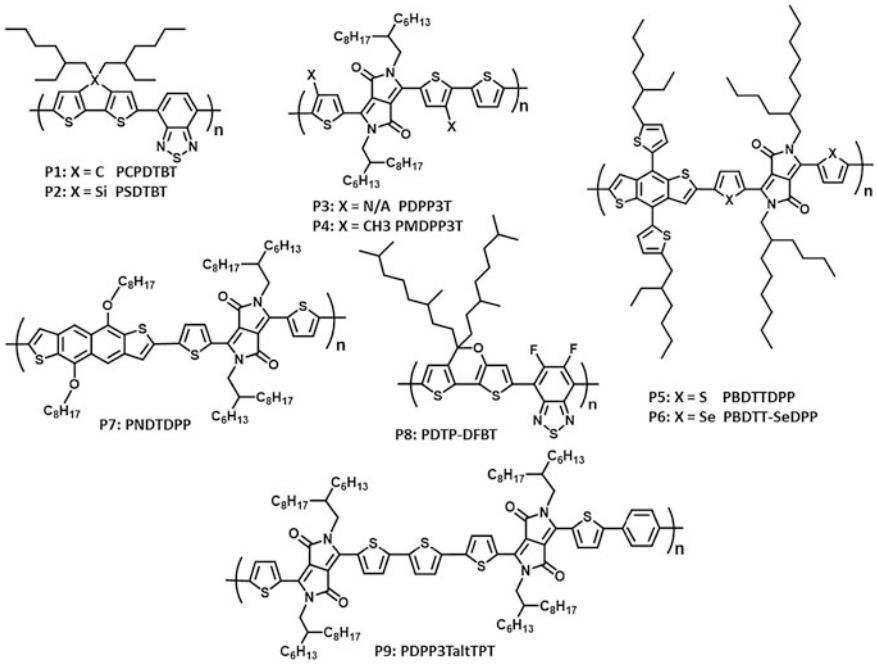

Fig. 11.9 Molecular structures of nine high performance low bandgap polymers that are promising for tandem organic solar cells

were used as interconnecting layer to connects the front cell and the rear cell [43]. The maximum efficiency of 6.5 % (J_{SC} = 7.8 mA/cm^2, V_{OC} = 1.24 V, FF = 0.67) was achieved in this study under an illumination of 100 mW/cm^2. Yang et al. reported a new LBG polymer (**P2**, **PSDTBT**) replacing a Carbon atom with a Silicon atom as the bridging atom to the two thiophenes [44]. The optical bandgap (1.45 eV) is very close to that of **P1**. It was found that the hole mobility of this polymer is 3×10^{-3} cm^2 V^{-1}s^{-1}, which is approximately three times higher than the mobility of **P1**. The V_{OC} of **P2** was slightly higher at 0.68 V but the J_{SC} was lower at 12.7 mA/cm^2 and that leads to a PCE of 5.1 %. The C–Si bond is longer than C–C bond in the fluorine core. Consequently, there is less steric hindrance created in the dibenzosilole core, leading to a better π-π stacking [45]. The crystallinity was further increased using thermal annealing, and the efficiency was enhanced to 5.4 %. Yang et al. later used **P2** (**PSDTBT**):$PC_{71}BM$ cell as the rear cell and the front cell based on P3HT:PCBM to construct tandem cell.

Another type of LBG polymer is based on diketopyrrolopyrrole (DPP) unit, which was developed in the last 3–4 decades as high-performance pigments [46]. It is highly absorbing in the visible region and strongly electron withdrawing. When polymerized with other electron donating monomers, the resulting polymers typically show energy bandgaps smaller than 1.5 eV. Another attractive property is its good charge-carrier mobility for both holes and electrons. The first highly performing polymer based on DPP unit was reported by Janssen et al. in 2008, which contains a backbone of alternating thienyl-substituted DPP and bithiophene units and has a small bandgap of 1.4 eV. Later, the same group reported that by co-polymerizing with a simple thiophene unit, a new LBG polymers **P3** (PDPP3T) was successfully synthesized [47]. **P3** shows a very high molecular weight (54 kDa) and a very low bandgap of 1.3 eV. High hole mobility of 1×10^{-2} cm^2 V^{-1} s^{-1} was achieved by field-effect transistors (FET). This low bandgap polymer showed a photo-response up to 900 nm when combined with $PC_{71}BM$, and EQE can reach around 35 % in this region. High photovoltaic performance of 4.7 % with V_{OC} = 0.65 V, J_{SC} = 11.7 mA/cm^2, and FF = 0.60 was achieved. The polymer actually has more potential, envisioned by the fact that by increasing the molecular weight and improving the thin film morphology, PCEs over 6 % have been achieved recently [48]. Fine-tuning the energy level and bandgap by adding two additional methyl groups on the thiophene units led to a new polymer **P4**, which gave a reduced bandgap of 1.29 eV and enhanced efficiency of 7.0 % [49]. Using this polymer in the rear cell for tandem solar cells, an efficiency of 8.9 % was obtained. The power conversion efficiency was further improved to 9.64 % when a triple junction structure was employed to harvest as much light as possible.

Yang et al. successfully merged the high planar BDT unit with DPP to form high performing LBG polymer **P5** (PBDTT-DPP, Eg = 1.46 eV) [50]. By replacing the oxygen atoms attached to the traditional BDT unit with thiophene moieties to form the thienylbenzodithiophene (BDTT) unit, the HOMO and LUMO levels of **P5** are simultaneously shifted deeper (−5.30/−3.63 eV vs. −5.16/−3.51 eV) to increase V_{OC}. Bulkier 2-ethylhexyl side chains on BDTT and 2-butyloctyl side chains on DPP are used to increase the solubility of the resulting polymers and thus obtain

much higher molecular weights (40.7 kDa vs. 8.5 kDa). High power conversion efficiencies around 6.5 % were achieved in single-cell devices with both a regular and an inverted structure (V_{OC} = 0.74 V, J_{SC} = 13.7 mA/cm^2, FF = 64 %). The EQE of the **P5** based device from 650 to 850 nm has peak value around 50 %.

Further lowering the bandgap to harvest more photons in the NIR part of the solar radiation, as well as increasing the charge carrier mobility of the LBG polymers is desired to reach higher efficiency. It is found that the reduction of the bandgap and the enhancement of the charge transport properties of **P5** can be accomplished simultaneously by substituting the sulfur atoms on the DPP unit with selenium atoms [51]. The new polymer **P6** (**Se-PDBTTDPP**, Eg $\sim$1.38 eV) gave excellent photovoltaic performance in single junction devices with PCEs of 7.2 % (V_{OC} = 0.69 V, J_{SC} = 16.8 mA/cm^2, FF = 0.62). Higher EQE of 53 % and broader photo-response (up to 900 nm) of the **P6** based device can be attributed to the high J_{SC}. This result is an excellent example of the selenium-substitution approach to improve the photovoltaic performance of LBG polymers.

Another interesting approach is to extend the conjugation by replacing the benzodithiophene unit a naphthodithiophene (NDT) unit suggested by Peng et al. [52]. The NDT-DPP based polymer, **P7** (PNDTDPP) showed similar bandgap but deeper HOMO/LUMO levels compared to the BDT-DPP polymer. Due to the enhanced π-π interaction, higher hole mobility was observed for the NDT-DPP based polymer (9.7×10^{-4} vs. 4.4×10^{-4} cm^2 V^{-1} s^{-1}). A **P7** based conventional device exhibits a promising PCE of 5.4 % with V_{OC} = 0.77 V, J_{SC} = 11.9 mA/cm^2, and FF = 0.59. By using an inverted device configuration, the PCE can be further increase to 6.9 %. The EQE from 600 to 900 nm is about 45 % in average. Later, the same group used this polymer and another highly performing wide bandgap polymer to fabricate a tandem solar cell. Efficiency as high as 9.4 % was achieved using an inverted device structure [53].

Recently, Yang et al. reported a new family of low bandgap polymers using an asymmetric electron rich dithieno[3,2-b:2′,3′-d]pyran (DTP) unit [54]. The electron-donating property of the DTP unit was found to be the strongest among the most frequently used donor units, such as BDT, DTS or CPDT. When the DTP unit was polymerized with the strongly electron-deficient DFBT unit, a regiorandom polymer (P**8**, PDTP-DFBT, bandgap = 1.38 eV) was obtained. It was found that the DTP based polymer **P8** shows significantly improved solubility and processability compared to the BDT or CPDT based polymers with same alkyl side chains. Consequently, very high molecular weight and soluble **P8** can be obtained with less bulky side chains. P8 shows excellent performance in bulk-heterojunction solar cells with power conversion efficiencies reaching 8.0 % (V_{OC} = 0.69 V, J_{SC} = 18.0 mA/cm^2, FF = 0.64), with EQE over 60 % in the NIR region [55].

Very recently, Janssen et al. reported a new materials design to use three different monomers to construct the polymer backbone. Surprisingly, The terpolymer, **P9** (PDPP3TaltTPT) based on DPP, thiophene, and benzene units, showed enhanced photovoltage performance over the conventional copolymers based on DPP with either thiophene or benzene units [56]. The terpolymer provides an optimized energy levels and optical band gap positioned in between those of the

parent copolymers, providing PCEs up to 8.0 % in a single-junction solar cell. More highly efficient polymers and high performance tandem devices are anticipated using the terpolymers.

(a) High bandgap polymers in tandem polymer OPV devices

The tandem polymer solar concept is actually started with using only high bandgap polymers, as there is a lack of efficient low bandgap polymers. Polymers based on poly-phenylene vinylene (PPV) backbone, such as soluable poly[2-methoxy-5-(2′-ethylhexyloxy)-*p*-phenylene vinylene] (**MEH-PPV**) developed by Wudl et al. [57] are among the earliest workhorse in OPV research. **MEH-PPV** has high bandgap of 2.2 eV, which limits the light absorption. The low carrier mobility together limited OPV efficiency at 2–3 % range. High regioregularity (RR) poly(3-hexylthiophene) (**P3HT**), invented in 1992 by McCullough and Lowe [58] and Rieke [59] independently, has a bandgap of 1.9 eV—very close to that of GaAs in inorganic tandem devices. The high hole mobility [60] and broader spectrum coverage, made it the most studied electron donor polymer material in polymer OPV devices in the last decade. RR-P3HT based solar cells were shown to be highly sensitive to the film morphology. Thermal annealing [61–64], solvent annealing [65, 66] as well as solvent additive approaches are the most effective methods for morphology control in this classical OPV system. While 4–5 % PCE was limited to RR-P3HT system, it worth to mention that the progress in acceptor has enabled significant efficiency improvement through V_{oc} enhancement, and 6–7 % PCE has been reported [67, 68].

Significant efforts on polymers with similar bandgap as P3HT, but with deeper HOMO level have also been reported to realize higher V_{oc} and thus PCE. Although the efforts were purely for single junction solar cell efficiency enhancement, due to lack of tandem experience, the materials are definitely valuable for tandem polymer solar cell. Leclerc's group reported a carbazole and benzothiadiazole (BT) based polymer (**PCDTBT**), which has bandgap of 1.88 eV with a low-lying HOMO energy level of −5.50 eV. The photovoltaic devices was first reported with a high V_{OC} of 0.89 V, a J_{SC} of 6.92 mA/cm^2, a FF of 63 %, and a PCE value of 3.6 %, which was later pushed to 6 % via interface engineering in a collaboration with Heeger et al. In 2010, four different groups [69–72] independently published polymers based on BDT and strong electron acceptor unit thieno[3,4-*c*]pyrrole-4,6-dione (TPD) moieties. These polymers showed a bandgap of ∼1.8 eV and very deep HOMO level of ∼−5.6 eV. The performance was varied from 4.1 to 6.8 %, and thus quite encouraging for both single junction and tandem OPV devices.

Other representative polymers with lower bandgap including Tao's **PDTS-TPD** (bandgap 1.73 eV, PCE of 7.3 %),and Reynold's **PDTG-TPD** (bandgap 1.69 eV, HOMO of −5.65 eV and 7.3 % PCE) et al. It worths mentioning that You et al. used a strong electron deficient unit, difluorobenzothiadiazole (DFBT) to copolymerize with BDT moiety, and the new polymer, **PBDT-DTffBT** (bandgap of 1.7 eV, HOMO of −5.54 eV) enabled a high V_{oc} of 0.91 V, and 7.2 % PCE. The improved solar cell efficiency using these slightly lower bandgap polymers were achieved mainly due to a higher J_{SC} compared to the PBDT-TPD, and P3HT based devices.

Comparing to single junction application, solution processed OPV has additional requirement for the bottom cell—it needs to be physically tough to avoid electrical short during fort formation of multiple layers on top. This is also one reason that RR-P3HT is still very valuable in tandem polymer solar cell, as thick P3HT:PCBM device still keep high quality.

11.4.3.2 Tandem Polymer OPV Device Development

(a) Tandem polymer solar cells with identical subcell polymers—HOMO tandem cells

The tandem polymer solar cells started from devices with identical polymer layers in the subcells in mid-2000s. This is not surprising as there were very limited choice of good polymer materials for solar cell application.

Yang et al. worked on semitransparent polymer cell in 2006 using MEH-PPV: PCBM as active layer, and 1 nm LiF/2 nm Al/12 nm Au as transparent electrode, which gives 2.6 mA/cm^2 J_{sc}, 0.86 V V_{oc}, and 45 % FF. A stacking scheme was used to build tandem stacking solar cell with the semi-transparent cell and a common non-transparent MEH-PPV:PCBM solar cell [73]. This four-terminal stacking configuration allows both parallel and series connection. In fact both connection methods gave 2.4 % tandem cell efficiency. This approach, however, suffers from loss in non-ideal transparent electrode. In two-terminal tandem polymer cell, Kawano and Sakai et al. were among the first to report a tandem cell using two MDMO-PPV:PCBM subcells. The structure is: ITO/PEDOT/MDMO-PPV:PCBM/ITO/PEDOT/MDMO-PPV:PCBM/Al. A single layer of ITO is used as interconnection layer, covered by PEDOT:PSS. As ITO has high workfunction, it is not a good cathode material. The ITO/PEDOT:PSS/MDMO-PPV:PCBM/ITO cell has V_{oc} of only 0.48 V, much lower than the typical cell with Al as cathode (0.73 V V_{oc}), or with Ca/Al as cathode ($\sim$0.86 V V_{oc}). Therefore the stacked cell reached average V_{oc} of only 1.31 V [74].

Other efforts on polymer tandem solar cells by sub-cells with identical wide bandgap polymer-fullerene system include P3HT:$PC_{61}BM$, [75, 76] PCDTBT: $PC_{61}BM$, [77] and poly[9,9-didecanefluorene-alt-(bis-thienylene) benzothiadiazole] (PF10TBT): $PC_{61}BM$ [78] etc. The performance of the HOMO type of tandem cell is hardly higher than the optimal single junction cell, thus diminish the application of this concept.

However, it is only recently realized that the real beauty of the HOMO tandem concept is to overcome the low carrier mobility difficulty of the state-of-the art polymer tandem solar cells. In accordance with materials and interconnecting layer progress, Li and Yang recently showed that high performance low bandgap polymer, such as PDTP-DFBT (Single junction polymer solar cell PCE $\sim$8.0 %, optimal thickness $\sim$100 nm), can benefit from the HOMO tandem structure. A homo (generous) tandem structure, which contains two identical PDTP-DFBT:$PC_{71}BM$ sub-cells[235] [79] was successfully constructed. Assisted by optical simulation, they optimized the HOMO tandem cell structure, and successfully improved the PCE

from 8 % in single junction cell to 10.2 % in HOMO tandem cell—a 25 % PCE enhancement. In principle, the homogeneous tandem cell works differently than hetero-tandem cell, as it is not to reduce the thermal loss by stacking active layer with complementary absorption. It however enhances the optical absorption via stacking two or more thin active material layers while maintaining the charge transport and collection. The PCE of the identical sub-cell-based tandem cells is still limited by the Shockley-Queisser theory. Yet, considering the fact of low carrier mobility in majority of polymer-fullerene blend films, the homogeneous tandem cell architecture has a higher chance to enhance the effective EQE of the cells. Figure 11.10 shows the absorption of single and tandem polymer solar cells (a), and calculated total quantum efficiency of the homogeneous tandem solar cells (b). As can be seen from (c) that even when the combined thickness in the two cells being 180 and 200 nm total, the HOMO tandem cell still can achieve excellent fill factor of 65 and 63 % respectively. The same thickness in single junction solar cell will lead to significantly reduced fill factor and efficiency.

(b) Tandem cells with subcells covering different solar spectrum ranges—Hetero tandem cells

HOMO tandem cell cannot overcome S-Q limit, a threshold multijunciton cell is designed for. Although we are not there yet in OPV, the intensive research efforts in the last decade have provided a rich pool of low bandgap polymers, and enabled high efficiency tandem polymer solar cells, particularly in the last 3–5 years. We will elaborate the exciting progress from the angle of device structure—regular sequence (ITO substrate as anode) versus inverted sequence (ITO as cathode).

(i) Hetero tandem polymer solar cell based on regular OPV structure

Low bandgap polymer development is the enabling force of polymer tandem solar cell consisting of two sub-cells with different materials. In 2006, de Boer and Janssen et al. demonstrated tandem polymer cell using poly((2,7-(9,9-dioctyl)-fluorene)-alt-5,5-(4′,7′-di-2-thienyl-2′,1′,3′-benzothiadiazole) (PFDTBT) as wide-bandgap

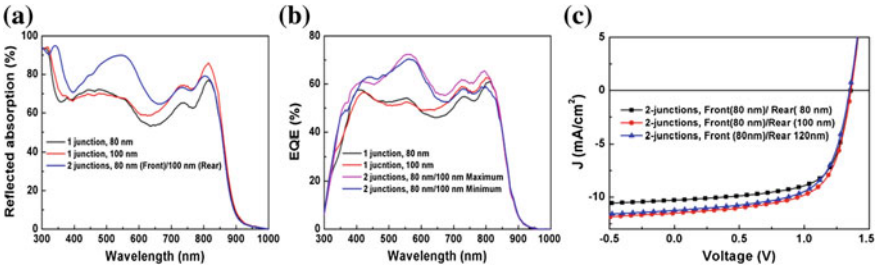

Fig. 11.10 **a** Absorption of single and tandem polymer solar cells, **b** calculated total quantum efficiency of the homogeneous tandem solar cells (based on total absorption and sub-cells internal quantum efficiency and the external quantum efficiency of single junction solar cells), and **c** J-V *curves* of 2-junction HOMO tandem solar cells with different subcell thickness combinations

polymer (absorption peak at 550 nm), and poly{5,7-di-2-thienyl-2,3-bis(3,5-di(2-ethylhexyloxy) phenyl)-thieno[3,4-b]pyrazine} (PTBEHT) as the low-bandgap polymer (absorption peak at 850 nm) [80]. The tandem device structure and absorption spectra are shown in Fig. 11.11a, b. The interconnection layer (ICL) structure is a combination of vacuum process and solution process in the first Hetero-tandem polymer solar cell work. The n-type section is LiF (0.5 nm)/Al (0.5 nm), followed by 15 nm Au and 60 nm PEDOT:PSS as p-type portion of the ICL. The tandem solar cell efficiency is 0.57 %, which was higher than that of each sub-cell.

Progress in solution processed electron transport layer (ETL) soon became a key component in polymer solar cell development. *N*-type inorganic metal oxides such as sol-gel based titanium oxide (TiO_x [81]) and zinc oxide (ZnO_x) [82] have been shown to be good candidates for organic electronics. Low temperature (150 °C) hydrolysis sol-gel process amorphous TiO_x was demonstrated to be effective in OLED and PSC [83]. TiO_x also functions as a hole blocking layer and optical spacer (to modulate the optical field inside thin device to enhance absorption). The device with a TiO_x optical spacer showed ~40 % enhancement in photocurrent and

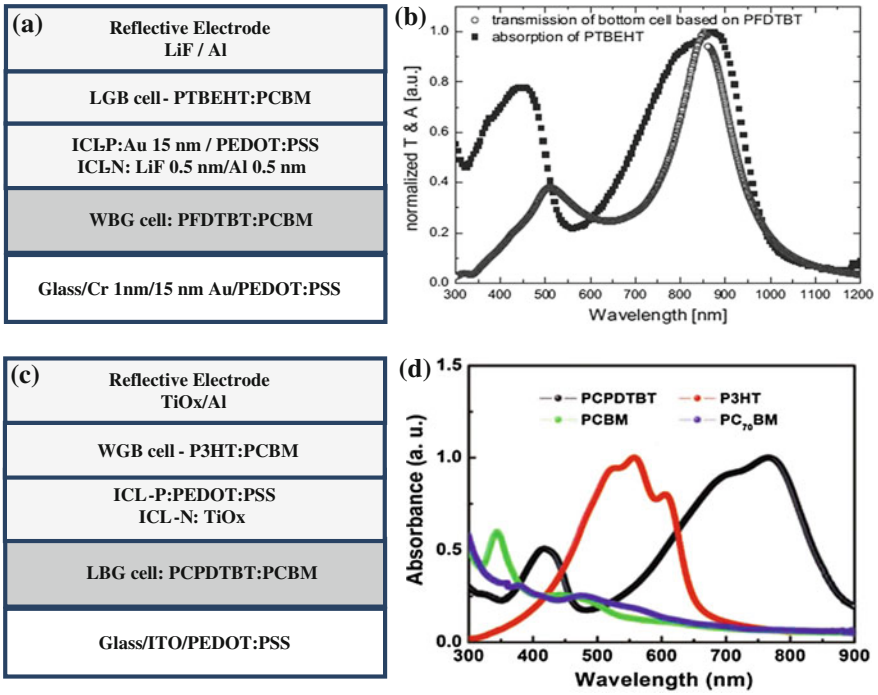

Fig. 11.11 **a** Device structure, and **b** absorption and transmission of two subcells of Janssen et al's hetero-tandem polymer solar cell, **c** device structure, and **d** absorption of active polymers in Heeger et al.'s hetero-tandem polymer solar cell (reprinted permission from the [80] and [85]. Copyright © 2006 John Wiley & Sons Inc. and 2007 AAAS)

EQE in P3HT:PCBM system [81] and nearly 100 % internal quantum efficiency in PCDTBT:PCBM devices. Crystalline TiO_x nanoparticles from non-hydrolysis sol-gel process are also shown to work well [84]. By incorporating Cs_2CO_3 into nanocrystalline TiO_x, Park et al. observed the Cs-doping effect on TiO_x, which lowers the TiO_x work function and improves PLED and PSC performance.

These ETLs brought possibility of combining solution processed ETL with solution processed HTL (e.g. PEDOT:PSS) to function as interconnecting layer in tandem structure. Heeger et al. demonstrated the solution processed ICL with TiO_x(n-type)/PEDOT:PSS(p-type) to bridge two sub-cells in tandem structure [85]. The device structure is also opposite to the conventional inorganic tandem cell, as the light first shines through the lower bandgap cell—PCPDTBT (absorption up to 900 nm) and $PC_{61}BM$ blend, and then to the rear cell of P3HT and $PC_{71}BM$. A 6.5 % efficiency of tandem solar cell was achieved, which is significantly higher than the individual front (3.0 %) and rear cell (4.7 %). In this important work, the major limiting factor is the lower quantum efficiency in the low band gap polymer PCPDTBT cell, which inhibits the higher current. The lower PCPDTBT cell FF than the P3HT: $PC_{61}BM$ cell also limits the FF in the tandem cell.

It is noticed the contact between n-type and p-type layer in ICL is critical. In one of the earliest all solution process tandem polymer solar cell work, Janssen et al. used ZnO nanoparticle as the n-type layer, and modified PEDOT dispersion at neutral pH as p-type layer [86]. They noticed the MDMO-PPV:PCBM and P3HT: PCBM tandem cell does not show a V_{oc} as high as the sum of two single junction cells' V_{oc}, which was attributed to non-Ohmic contact between the two layers. Insertion of thin metal layer and UV excitation to dope ZnO layer are shown to improve the contact [86].

Yang et al. achieved improved low bandgap polymer by substituting bridging C-atom in PCPDTBT with larger Si atom. The new polymer, **PSBTBT**, has a higher crystallinity and improved hole mobility due to the large atom induced effect. The larger planar structure also improves transport by enhancing molecule packing and thus photocurrent. With the new LBG polymer, Yang's team developed 0.5 nm Al/ naocrystalline TiO_2 / PEDOT:PSS ICL structure for tandem polymer solar cell—the structure is: ITO/PEDOT:PSS/P3HT:$PC_{71}BM$/0.5 nm Al /TiO_2 /PEDOT:PSS/ PSBTBT: $PC_{71}BM$/TiO_2:Cs /Al. The ultrathin Al (UT-Al) layer, improving both the wettability and electrical contact of the TiO_2 film on the bottom WBG P3HT blend film. While the WBG P3HT subcelll gives 3.77 % PCE, and LBG PSBTBT subcell gives 3.94 % PCE, the tandem PCE has reached 5.84 % [87]. The V_{oc} is only 0.02 V less than the sum of subcells' V_{oc}s, indicating the high quality of ICL structure. The tandem cell FF is also high at 63.2 %, again a good indication of the successful tandem structure. Adopting the same tandem cell strategy, a 7 % tandem polymer solar cell was achieved by introducing P3HT:ICBA as WBG subcell. The enhancement is mainly due to the higher V_{oc} from the new WBG subcell [88].

The ZnO(n-type)/pH-neutral PEDOT (p-type) ICL structure is also further progressed by Janssen's group. The development of the low bandgap polymers (PDPP3T and its derivatives) enabled the team to achieve about 9 % PCE tandem polymer solar cells [49].

(ii) Hetero tandem cells with inverted structure

The inverted polymer solar structure using n-type function interface layer(s) was reported by UCLA group [89] and NREL group [90] in 2006. The p-type transition metal oxides (V_2O_5, MoO_3, WO_3 etc.), and n-type ZnO interfacial layers introduced by UCLA and NREL group, respectively, were soon become most widely used in inverted solar cell. The removal of reactive metal gives a significant boost in polymer solar cell stability. The structure is also more compatible with roll-to-roll manufacturing process. Some recent high impact work on inverted polymer solar cells include: (a) So et al.'s report of >8 % PCE inverted cell using germole-based polymer, and PVP modified ZnO as n-type buffer; [91] and (b) Wu and Cao et al.'s work using a thin layer of polyelectrolyte (PFN) as a n-type buffer and MoO_3 as p-type buffer, the PCE was dramatically enhanced from 7.4 to 9.2 % based on PTB7:PC_{71}BM system [92].

Krebs et al. [93] reported inverted tandem polymer solar cell using novel concept thermocleave polymer to enhance processability, and Jen et al. [94] reported inverted tandem polymer solar cell using a fullerene self-assembled (C_{60}-SAM) to modify the interface between the ZnO and the P3HT:PC_{61}BM and a PEDOT:PSS/ZnO recombination contact between two P3HT:PC_{61}BM photoactive layers. These two early reports has novel concept, although both also suffer from low performance, in fact lower than single junction solar cell.

Yang et al. reported a 5.1 % power conversion efficiency inverted polymer tandem cell using P3HT:PCBM and PSBTBT:PCBM subcells, and using a thin Al layer (to reduce the resistance) inserted between two metal oxide interconnecting layer—p-type MoO_3 and n-type ZnO [95]. Although over 5 % PCE is exciting, this specific interconnecting layer was not robust enough and inhibited it from active layers using common (and high performance) organic solvent with high boiling point such as ODCB and CB. This is the motivation for Yang et al. to develop a robust, higher conductivity, and thick PEDOT:PSS layer to replace the typical thin PEDOT:PSS or MoO_3. The enhanced conductivity of PEOT:PSS also improved its contact with n-type buffer layer initially TiO_2:Cs and then ZnO NPs in the tandem solar cell. In 2011, another breakthrough on low bandgap polymer was demonstrated by Yang et al. The PBDTT-DPP polymer (**P5**) has narrow absorption and has complementary absorption with wide band gap polymers, such as P3HT. Both regular and inverted structure single junction devices showed 6.5 % PCE with fill factor close to 70 %. Tandem polymer solar cells were built with **P5**:PCBM and P3HT:ICBA sub-cells, and the improved PEDOT:PSS/ZnO ICL. As a result, an 8.62 % PCE [48] was certified by NREL in 2011. The achieved tandem J_{sc} of 8.2 mA/cm^2 is ok for P3HT:ICBA cell, but clearly see a trade-off for tandem cell to work.

Bandgap of polymer was further lowered by introducing Se to replacing S by larger Se atom. The new low bandgap polymer **P6** (PBDTT-SeDPP) enabled 9.5 % power conversion efficiency tandem solar cells using the same P3HT:ICBA subcell. This clearly shows the potential of the tandem structure [51].

Once robust functional ICL structure was developed, it provides large freedom to incorporate different materials systems to improve the tandem polymer solar cell performance. For example, polymer **P8** (PDTP-DFBT) with a band gap of 1.38 eV was designed by Sumitomo Chemical and UCLA. The EQE of single junction PDTP-DFBT:fullerene photovoltaic cells reached over 60 % in the near infrared region, and is especially precious for tandem structure to provide complimentary spectrum response. The tandem architecture with a PDTP-DFBT:$PC_{61}BM$ rear sub-cell and P3HT:ICBA front sub-cell showed very well spectrum matching—the PDTP-DFBT cell responsible for the near-infrared light in the 650–900 nm, and P3HT cell covers from ~350 to 650 nm. Careful acceptor and device tuning successfully lead to a certificated power conversion efficiency of 10.6 %, tested by NREL. Figure 11.12a shows the typical inverted tandem polymer solar cell structure; Fig. 11.12b shows the absorption of low and wide bandgap polymers for front (P3HT) and rear (PDTP-DFBT) cells. The quantum efficiency of the subcells is shown in Fig. 11.12c and the NREL certified I–V curve of the 10.6 % PCE tandem cell [53] in Fig. 11.12d. This breakthrough progress sets a new record efficiency in the OPV field.

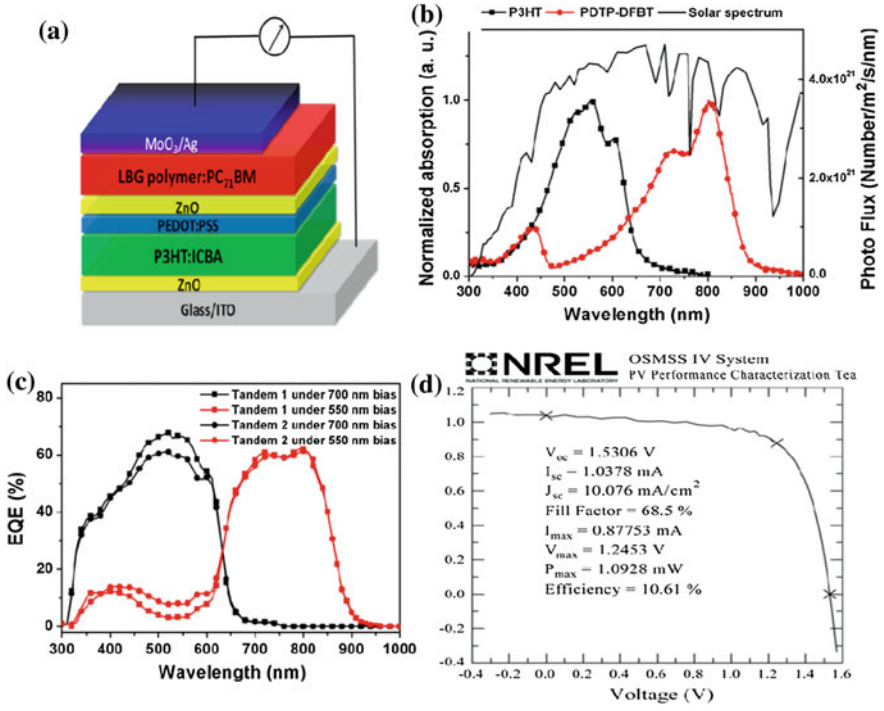

Fig. 11.12 **a** Device structure, and **b** polymers' absorption curves versus AM1.5G solar spectrum in Li and Yang et al's hetero-tandem polymer solar cell, **c** EQE curves of front and rear cells in two types of hetero-tandem polymer solar cells, and **d** NREL certification of UCLA hetero-tandem polymer solar cell

Before closing the discussion, there have been new progresses worth mentioning. Brabec et al. used aluminum-doped ZnO (AZO) and low-conductivity PEDOT:PSS as the interconnecting layer. The work shows the thicknesses of the interconnecting layer could range from ~50 to >60 nm, which fits the optical interference maximum in tandem cells, and probably more importantly the structure is friendly to large-scale production [228] [96]. A non-conjugated polyelectrolyte, ethoxylated polyethylenimine (PEIE), has attracted significant attention as a new and effective electron transporting material in polymer solar cell. Kipperlen et al. further applied PEIE in the interconnecting layer to build tandem polymer cell. The device structure is: ITO/PEIE/P3HT:ICBA/PEDOT:PSS PH1000/PEIE/PBDTT-C:PCBM/MoO_3/Ag. High conductivity PH1000 and PEIE formed ICL layer. Actually higher FF of the tandem cell compared to both of the single junction sub-cells was obtained and PCEs reached 8.2 % using inverted device structure [97]. Consider the two polymers actually only covered up to 800 nm, the result is very interesting.

Very recently, Janssen et al. has also developed a homogeneous tandem solar cell and applied it into a triple junction device. Specifically, the first junction is a wide band polymer and the other two junctions consist of two identical low bandgap PMDPP3T:$PC_{71}BM$ based sub-cells. Interestingly, they achieved 9.64 % efficiency in the triple junction solar cells [49].

11.5 Outlook and Summary

It has taken the society a long way to get to the current state-of-the art tandem OPV efficiency ~11–12 %. Although exciting, it's still far from what the technology can offer. We here will use two-junction tandem structure as an example to show where to improve for higher efficiency. Please note there have been excellent discussions on the potential of organic solar cells using the similar approaches and assumptions in S-Q limit [98, 99]. The discussion here is aiming to be more in real world.

In the widely cited and simple Scharber model, the authors adopted the state-of-the art FF and EQE from P3HT:PCBM cell around year 2006- both 65 %. After almost half decade, both parameters have been shown can be much higher. EQE peak value of over 80 % has been reported, [92, 100] and the FF is also close to 80 % in cell [101]. This brings hope that OPV could further improve the EQE to the level close to other technology—for example dye-sensitize solar cell, in which 90 % peak PCE has been demonstrated [102].

A significant loss even in today's champion OPV cells is the photovoltage loss. The bandgap-V_{oc} offset ($W_{oc} = Eg/e - V_{oc}$) concept is widely adopted in inorganic PV technology. W_{oc} is typically around 0.4–0.5 V in various crystalline inorganic semiconductor based solar cells [103] [290]. The lowest W_{oc} value so far is 0.3 V, from almost epitaxial grown GaAs solar cell, which is close S-Q limit efficiency. In OPV, the excitonic nature of organic semiconductor leads to larger W_{oc}. Various experimental results showed the limit of W_{oc} in OPV is 0.6–0.7 V. In the several recent low bandgap polymers with relatively high EQE such as PBDTT-DPP,

Table 11.1 Power conversion efficiency of 2-junction tandem cells with various EQE, W_{oc} and FF conditions

Polymer 1 BG:1.9 eV Polymer 2 BG:1.4 eV	J_{sc}	FF (%)	V_{oc}	PCE (%)
Current status	10.1	70	1.53	10.6
$EQE_{max} \sim 80$ %	13.3	70	1.53	14.3
$EQE_{max} \sim 90$ %	15	70	1.53	16
W_{oc} = 0.7 V/$EQE_{max} \sim 90$ %	15	70	1.9	20
W_{oc} = 0.6 V/$EQE_{max} \sim 90$ %/FF = 80 %	15	80	2.1	25

PBDTT-SeDPP, PDTP-DFBT, the W_{oc} is now ~0.7 V. On the other hand, the solar cell based on wideband gap polymers—P3HT, PCDTBT etc., although appeared earlier, still suffer from much larger W_{oc} loss. For example, P3HT (1.9 eV):ICBA has V_{oc} of ~0.85 V, which indicates the W_{oc} is over 1 V. This is also one of the reasons that tandem solar cell based on PDTP-DFBT and P3HT (excellent complementary spectrum) is not too much better than PDTP-DFBT homo tandem device, as the wide bandgap P3HT cell does not provide enough V_{oc} benefit.

Table 11.1 shows the achievable PCEs (under several assumptions) of a two-junction tandem polymer solar cell (keeping the bandgaps of the two polymers in the recent 10.6 % cell—1.9 and 1.38 eV, respectively). Assuming the same EQE shape but EQE peak value increases to 90 %, and the W_{oc} of both subcells can be 0.7 V, a cell with 70 % FF will reach 20 % efficiency. W_{oc} of 0.6 V, 90 % peak EQE and 80 % FF will enable 25 % PCE in the two-junction tandem cell.

Beyond two-junction, triple junction approach like in inorganic case is also a possible way to further advance the polymer solar cell efficiency. This will need significant organic semiconductor innovation, as not only much lower bandgap polymer (<1 eV) with high NIR spectral response is needed, the W_{oc} has be to lowered to inorganic solar cell level to realize this goal.

In summary, the concept of multiple junction tandem solar cells has lead to significant efficiency improvement in inorganic solar cell, and gone beyond S-Q limit. In the last decades, the concept has also been implemented in Organic solar cells. The implementation is a result of comprehensive efforts in organic semiconductor material chemistry, inter face engineering, device structure innovation and engineering. While the close to 12 % efficiency is encouraging progress, the understanding of physics and the identification of the key problems in the state-of-the-art material and device systems are more important, as they will pave the way for the field to achieve 20–25 % PCE in the near future. The future progress will truly help to make OPV a commercially viable disruptive solar technology.

Acknowledgments This work was financially supported by the Air Force Office of Scientific Research (AFOSR, Grant No. FA9550-12-1-0074, Program Manager: Dr. Charles Lee), Office of Naval Research (ONR, Grant No. N00014-04-1-0434, Program Manager: Dr. Paul Armistead), and National Science Foundation (NSF, Grant No. ECCS-1202231, Program Manager P. Werbos).

References

1. U.S. Energy Information Administration, Monthly Energy Review, http://www.eia.gov/totalenergy/data/monthly/
2. S. Gunes, H. Neugebauer, N.S. Sariciftci, Chem. Rev. **107**, 1324 (2007)
3. L.-M. Chen, Z. Hong, G. Li, Y. Yang, Adv. Mater. **21**, 1434 (2009)
4. B.C. Thompson, J.M.J. Frechet, Angew. Chem. Int. Ed. **47**, 58 (2008)
5. G. Li, R. Zhu, Y. Yang, Nat. Photon. **6**, 153 (2012)
6. D.M. Chapin, C.S. Fuller, G.L. Pearson, J. Appl. Phys. **25**, 676 (1954)
7. W. Shockley, H.J. Queisser, J. Appl. Phys. **30**, 510 (1961)
8. V. Sukhovatkin, S. Hinds, L. Brzozowski, E.H. Sargent, Science **324**, 1542 (2009)
9. H. Cotal, C. Fetzer, J. Boisvert, G. Kinsey, R. King, P. Hebert, H. Yoon, N. Karam, Energy Environ. Sci. **2**, 174 (2009)
10. O.E. Semonin, J.M. Luther, S. Choi, H.-Y. Chen, J. Gao, A.J. Nozik, M.C. Beard, Science **334**, 1530 (2011)
11. A. Luque, A. Marti, Phys. Rev. Lett. **78**, 5014 (1997)
12. C.H. Henry, J. Appl. Phys. **51**(8), 4494 (1980)
13. L.C. Hirst, N.J. Ekins-Daukes, Prog. Photovolt: Res. Appl. **19**, 286 (2011)
14. P.T. Landsberg, T. Markvart, The Carnot factor in solar-cell theory. Solid-State Electron. **42** (4), 657 (1998). doi:10.1016/S0038-1101(97)00253-0
15. M.B. Prince, J. Appl. Phys. **26**, 534 (1955)
16. D.J. Friedman, J.M. Olson, S. Kurtz, High-efficiency III-V multijunction solar cells, in *Handbook Photovoltaic Science and Engineering*, 2nd edn. ed. by A. Luque, S. Hegedus (Wiley, New York, 2011). ISBN:978-0-470-72169-8
17. J.M. Olson, T. Gessert, M.M. Al-Jassim, in 18th IEEE Photovoltaic Specialists Conference (1985), p. 552
18. S.R. Forrest, Nature **428**, 199 (2004)
19. Y.F. Li, Account Chem. Res. **45**, 723 (2012)
20. M.C. Scharber, D. Mühlbacher, M. Koppe, P. Denk, C. Waldauf, A.J. Heeger, C.J. Brabec, Adv. Mater. **18**, 789 (2006)
21. G. Dennler, M.C. Scharber, T. Ameri, P. Denk, K. Forberich, C. Waldauf, C.J. Brabec, Adv. Mater. **20**, 579 (2008)
22. N.C. Giebink, G.P. Wiederrecht, M.R. Wasielewski, S.R. Forrest, Phys. Rev. B **83**, 195326 (2011)
23. A. Yakimov, S.R. Forrest, Appl. Phys. Lett. **80**, 1667 (2002)
24. J. Drechsel, B. Mannig, F. Kozlowski, M. Pfeiffer, K. Leo, H. Hoppe, Appl. Phys. Lett. **86**, 244102 (2005)
25. G. Dennler, H.J. Prall, R. Koeppe, M. Egginger, R. Autengruber, N.S. Sariciftci, Appl. Phys. Lett. **89**, 073502 (2006)
26. J.G. Xue, S. Uchida, B.P. Rand, S.R. Forrest, Appl. Phys. Lett. **85**, 5757 (2004)
27. M. Hiramoto, Chem. Lett. **327** (1990)
28. V. Steinmann, N.M. Kronenberg, M.R. Lenze, S.M. Graf, D. Hertel, H. Bürckstümmer, F. Würthner, K. Meerholz, Appl. Phys. Lett. **99**, 193306 (2011)
29. M.D. Perez, C. Borek, S.R. Forrest, M.E. Thompson, J. Am. Chem. Soc. **131**, 9281–9286 (2009)
30. J. Drechsel, B. Männig, F. Kozlowski, M. Pfeiffer, K. Leo, H. Hoppe, Appl. Phys. Lett. **86**, 244102 (2005)
31. J. Meiss, A. Merten, M. Hein, C. Schuenemann, S. Schäfer, M. Tietze, Adv. Funct. Mater. **22**, 405 (2012)
32. R.F. Bailey-Salzman, B.P. Rand, S.R. Forrest, Appl. Phys. Lett. **91**, 013508 (2007)
33. B. Verreet, S. Schols, D. Cheyns, B.P. Rand, H. Gommans, T. Aernouts, P. Heremans, J. Genoe, J. Mater. Chem. **19**, 5295 (2009)
34. P. Peumans, A. Yakimov, S.R. Forrest, J. Appl. Phys. **93**, 3693 (2003)

35. M.L. Zhang, H. Wang, C.W. Tang, Org. Electron. **13**, 249 (2012)
36. K. Walzer, B. Maennig, M. Pfeiffer, K. Leo, Chem. Rev. **107**, 1233 (2007)
37. R. Timmreck, S. Olthof, K. Leo, M.K. Riede, J. Appl. Phys. **108**, 033108 (2010)
38. J.X. Tang, M.K. Fung, C.S. Lee, S.T. Lee, J. Mater. Chem. **20**, 2539 (2010)
39. R. Schueppel, R. Timmreck, N. Allinger, T. Mueller, M. Furno, C. Uhrich, K. Leo, M. Riede, J. Appl. Phys. **107**, 044503 (2010)
40. D. Cheyns, B.P. Rand, P. Heremans, Appl. Phys. Lett. **97**, 033301 (2010)
41. Z. Zhu, D. Waller, R. Gaudiana, M. Morana, D. Muhlbacher, M. Scharber, C. Brabec, Macromolecules **2007**, 40 (1981)
42. J. Peet, J.Y. Kim, N.E. Coates, W.L. Ma, D. Moses, A.J. Heeger, G.C. Bazan, Nat. Mater. **6**, 497 (2007)
43. J.Y. Kim, K. Lee, N.E. Coates, D. Moses, T.Q. Nguyen, M. Dante, A.J. Heeger, Science **317**, 222 (2007)
44. J.H. Hou, H.Y. Chen, S.Q. Zhang, G. Li, Y. Yang, J. Am. Chem. Soc. **130**, 16144 (2008)
45. H.-Y. Chen, J. Hou, A.E. Hayden, H. Yang, K.N. Houk, Y. Yang, Adv. Mater. **22**, 371 (2010)
46. M.M. Wienk, M. Turbiez, J. Gilot, R.A.J. Janssen, Adv. Mater. **20**, 2556 (2008)
47. J.C. Bijleveld, A. Zoombelt, S.G.J. Mathijssen, M.M. Wienk, M. Turbiez, D.M. de Leeuw, R.A.J. Janssen, J. Am. Chem. Soc. **131**, 16616 (2009)
48. W.W. Li, K.H. Hendriks, W.S.C. Roelofs, Y. Kim, M.M. Wienk, R.A.J. Janssen, Adv. Mater. **25**, 3182 (2013)
49. W.W. Li, A. Furlan, K.H. Hendriks, M.M. Wienk, R.A.J. Janssen, J. Am. Chem. Soc. **135**, 5529 (2013)
50. L.T. Dou, J.B. You, J. Yang, C.-C. Chen, Y.J. He, S. Murase, T. Moriarty, K. Emery, G. Li, Y. Yang, Nat. Photon. **6**, 180 (2012)
51. L.T. Dou, W.-H. Chang, J. Gao, C.-C. Chen, J.B. You, Y. Yang, Adv. Mater. **25**, 825 (2013)
52. K. Li, Z. Li, K. Feng, X. Xiaopeng, L. Wang, Q. Peng, J. Am. Chem. Soc. **135**, 13549 (2013)
53. Q. Peng, Q. Huang, X. Hou, P. Chang, J. Xu, S. Deng, Chem. Commun. **48**, 11452 (2012)
54. L. Dou, C.-C. Chen, K. Yoshimura, K. Ohya, W.-H. Chang, J. Gao, Y. Liu, E. Richard, Y. Yang, Macromolecules **46**, 3384 (2013)
55. J.B. You, L.T. Dou, K. Yoshimura, T. Kato, K. Ohya, T. Moriarty, K. Emery, C.-C. Chen, J. Gao, G. Li, Y. Yang, Nat. Commun. **4**, 1446 (2013)
56. K.H. Hendriks, G.H.L. Heintges, V.S. Gevaerts, M.M. Wienk, R.A.J. Janssen, Angew. Chem. Int. Ed. **52**, 8341 (2013)
57. F. Wudl, G. Srdanov, Conducting polymer formed of poly(2-methoxy-5-(2′-ethylhexyloxy)-P-phenylene vinylene). U.S. Patent 5,189,136 (1993)
58. R.D. McCullough, R.D.J. Lowe, Chem. Commun. **70** (1992)
59. T.-A. Chen, R.D. Rieke, J. Am. Chem. Soc. **114**, 10087 (1992)
60. H. Sirringhaus, P.J. Brown, R.H. Friend, M.M. Nielsen, K. Bechgaard, B.M.W. Langeveld-Voss, A.J.H. Spiering, R.A.J. Janssen, E.W. Meijer, P. Herwig, D.M. de Leeuw, Nature **401**, 685 (1999)
61. F. Padinger, R.S. Rittberger, N.S. Sariciftci, Adv. Funct. Mater. **13**, 85 (2003)
62. W.L. Ma, C.Y. Yang, X. Gong, K. Lee, A.J. Heeger, Adv. Funct. Mater. **15**, 1617 (2005)
63. Y. Kim, S.A. Choulis, J. Nelson, D.D.C. Bradley, S. Cook, J.R. Durrant, Appl. Phys. Lett. **80**, 3885 (2005)
64. G. Li, V. Shrotriya, Y. Yao, Y. Yang, J. Appl. Phys. **98**, 043704 (2005)
65. G. Li, V. Shrotriya, J. Huang, Y. Yao, T. Moriarty, K. Emery, Y. Yang, Nature Mater. **4**, 864 (2005)
66. G. Li, Y. Yao, H. Yang, V. Shrotriya, G. Yang, Y. Yang, Adv. Funct. Mater. **17**, 1636 (2007)
67. D.W. Laird et al., Organic photovoltaic devices comprising fullerenes and derivatives thereof. U.S. Patent 20080319207A1 (2008)
68. G.J. Zhao, Y.J. He, Y.F. Li, Adv. Mater. **22**, 4355 (2010)
69. C. Piliego, T.W. Holcombe, J.D. Douglas, C.H. Woo, P.M. Beaujuge, J.M.J. Frechet. J. Am. Chem. Soc. **132**, 7595 (2010)

70. Y. Zhang, S.K. Hau, H.-L. Yip, Y. Sun, O. Acton, A.K.-Y. Jen. Chem. Mater. **22**, 2696 (2010)
71. G.B. Zhang, Y.Y. Fu, Q. Zhang, Z.Y. Xie, Chem. Commun. **46**, 4997 (2010)
72. Y.P. Zou, A. Najari, P. Berrouard, S. Beaupre, B.R. Aich, Y. Tao, M. Leclercl. J. Am. Chem. Soc. **132**, 5330 (2010)
73. V. Shorotriya, E.H.-E. Wu, G. Li, Y. Yao, Y. Yang, Appl. Phys. Lett. **88**, 064104 (2006)
74. K. Kawano, N. Ito, T. Nishimori, J. Sakai, Appl. Phys. Lett. **88**, 073514 (2006)
75. V.C. Tung, J. Kim, L.J. Cote, J.X. Huang, J. Am. Chem. Soc. **133**, 9262 (2011)
76. X.W. Sun, D.W. Zhao, L. Ke, A.K.K. Kyaw, G.Q. Lo, D.L. Kwong, Appl. Phys. Lett. **97**, 053303 (2010)
77. A. Puetz, F. Steiner, J. Mescher, M. Reinhard, N. Christ, D. Kutsarov, H. Kalt, U. Lemmer, A. Colsmann, Org. Electron. **13**, 2696 (2012)
78. D.J.D. Moet, P. de Bruyn, J.D. Kotlarski, P.W.M. Blom, Org. Electron. **2010**, 11 (1821)
79. J.B. You, C.C. Chen, Z.R. Hong, K. Yoshimura, K. Ohya, R. Xu, S.L. Ye, J. Gao, G. Li, Y. Yang, Adv. Mater. **25**, 3973 (2013). doi:10.1002/adma.201300964
80. A. Hadipour, B. de Boer, J. Wildeman, F. Kooistra, J.C. Hummelen, M.G.R. Turbiez, M.M. Wienk, R.A.J. Janssen, P.W.M. Blom, Adv. Funct. Mater. **2006**, 16 (1897)
81. J.Y. Kim, S.H. Kim, H.-H. Lee, K. Lee, W. Ma, X. Gong, A.J. Heeger. Adv. Mater. **18**, 572 (2006)
82. J. Gilot, I. Barbu, M.M. Wienk, R.A.J. Janssen, Appl. Phys. Lett. **91**, 113520 (2007)
83. K. Lee, J.Y. Kim, S.H. Park, S.H. Kim, S. Cho, A.J. Heeger, Adv. Mater. **19**, 2445 (2007)
84. M.H. Park, J.H. Li, A. Kumar, G. Li, Y. Yang, Y. Adv. Funct. Mater. **19**, 1241 (2009)
85. J.Y. Kim, K. Lee, N. Coates, D. Moses, T.-Q. Nguyen, M. Dante, A.J. Heeger. Science **317**, 222 (2007)
86. J. Gilot, M.M. Wienk, R.A.J. Janssen, Appl. Phys. Lett. **90**, 143512 (2007)
87. S. Sista, M.H. Park, Z.R. Hong, Y. Wu, J.H. Hou, W.L. Kwan, G. Li, Y. Yang, Adv. Mater. **22**, 380 (2010)
88. J. Yang, R. Zhu, Z. Hong, Y. He, A. Kumar, Y. Li, Y. Yang, Adv. Mater. **23**, 3465 (2011)
89. G. Li, C.W. Chu, V. Shrotriya, J. Huang, Y. Yang, Appl. Phys. Lett. **88**, 253503 (2006)
90. M.S. White, D.C. Olson, S.E. Shaheen, N. Kopidakis, D.S. Ginley, Appl. Phys. Lett. **89**, 143517 (2006)
91. C.E. Small, S. Chen, J. Subbiah, C.M. Amb, S.-W. Tsang, T.-H. Lai, J.R. Reynolds, F. So, Nat. Photon. **6**, 115 (2012)
92. Z.C. He, C.M. Zhong, S.J. Su, M. Xu, H.B. Wu, Y. Cao, Nat. Photon. **6**, 591 (2012)
93. O. Hagemann, M. Bjerring, N.C. Nielsen, F.C. Krebs, Solar Energy Mater. Solar Cells **92**, 1327 (2008)
94. S.K. Hau, H.-L. Yip, K.-S. Chen, J. Zou, A.K.-Y. Jen, Appl. Phys. Lett. **97**, 253307 (2010)
95. C.H. Chou, W.L. Kwan, Z. Hong, L.-M. Chen, Y. Yang, Adv. Mater. **23**, 1282 (2011)
96. N. Li, T. Stubhan, D. Baran, J. Min, H. Wang, T. Ameri, C.J. Brabec, Adv. Energy Mater. **3**, 301 (2013)
97. Y. Zhou, C.F. Hernandez, J.W. Shim, T.M. Khan, B. Kippelen, Energy Environ. Sci. **5**, 9827 (2012)
98. N.C. Giebink, G.P. Wiederrecht, M.R. Wasielewski, S.R. Forrest, Phys. Rev. B **83**, 195326 (2011)
99. R.A. Janssen, J. Nelson, Adv. Mater. **2013**, 25 (1847)
100. M.D. Irwin, B. Buchholz, A.W. Hains, R.P.H. Chang, T.J. Marks, Proc. Natl. Acad. Sci. USA **105**, 2783 (2008)
101. M. Hirade, C. Adachi, Appl. Phys. Lett. **99**, 153302 (2011)
102. A. Yella, H.-W. Lee, H.N. Tsao, C. Yi, A.K. Chandiran, M.K. Nazeeruddin, E.W.-G. Diau, C.-Y. Yeh, S.M. Zakeeruddin, M. Grätzel, Science **334**, 629 (2011)
103. R. King, D. Bhusari, A. Boca, D. Larrabee, X.-Q. Liu, W. Hong, C.M. Fetzer, D.C. Law, N.H. Karam, Prog. Photovoltaics Res. Appl. **19**, 797 (2011)

Part IV
Fabrication and Application

Chapter 12
Advanced Manufacturing Technology of Polymer Photovoltaic Cells

Hui Joon Park and L. Jay Guo

Abstract Bulk heterojunction (BHJ) polymer PV cells have shown strong potential for low cost, easy processable and flexible solar cells with acceptable efficiencies. Manufacturability is viewed as a key advantage of this new technology, but not yet fully realized. This chapter will first introduce a novel processing technology, which allows evaporation of solvent through surface encapsulation and with induced alignment (ESSENCIAL) of polymer chains by applied pressure, which leads to optimized morphology, more uniform distribution and crystallinity of the components favorable for charge generation and transportation. The second part of this chapter will discuss the optimization of BHJ blends with hundreds of nanometers thick photoactive layers, which are thick enough to fully absorb the light and also roll-to-roll fabrication friendly. In the third part of this chapter, a new type of heterojunction structure that has almost 100 % internal quantum efficiency (IQE) even in over 300 nm thick photoactive layer, consequently providing superior photocurrent and fill factor compared with optimized BHJ PV cells, will be introduced. In the last section of this chapter, we will discuss our recent work on nanoimprint lithography (NIL)-based transparent metal electrode (TME) technology as a promising alternative for the ITO electrode that can pave the way toward large area flexible organic PV (OPV) cells.

H.J. Park
Division of Energy Systems Research, Ajou University, Suwon 443-749, Korea
e-mail: huijoon@ajou.ac.kr

L. Jay Guo (✉)
Macromolecular Science and Engineering, University of Michigan, Ann Arbor, Michigan 48109, USA
e-mail: guo@umich.edu

L. Jay Guo
Electrical Engineering and Computer Science, University of Michigan, Ann Arbor, Michigan 48109, USA

Y. Yang and G. Li (eds.), *Progress in High-Efficient Solution Process Organic Photovoltaic Devices*, Topics in Applied Physics 130,
DOI 10.1007/978-3-662-45509-8_12

12.1 Introduction

Photovoltaic (PV) cells have attracted our attentions as a promising solution to the energy crisis and environmental pollution [1]. Among various types of PV technologies, bulk heterojunction (BHJ) polymer PV cells have shown strong potential for low cost, easy processable and flexible solar cells with acceptable efficiencies [2–7]. Because polymer BHJ structures are composed of interpenetrating nanoscale networks of electron-donor and electron-acceptor with domain sizes on the order of exciton diffusion length and with large interfacial areas between the domains, such network can facilitate efficient dissociation of photo-induced excitons at the domain interface. This advantage has made this approach a strong candidate for high efficiency polymer PV cells. However, randomly distributed blend morphologies in BHJ structures inevitably require external treatment to form effective pathway for the photo-generated charges to reach each electrode. Accordingly, advanced processing technologies to optimize random blend morphology is needed to achieve high efficiency BHJ polymer PV cells.

For this purpose, a number of works, based on poly(3-hexylthiophene) (P3HT): [6,6]-phenyl C_{61} butyric acid methyl ester (PCBM) as a model system, have been reported, and thermal annealing (TA) and solvent-assisted annealing (SAA) after spin-casting the blend film are general and commonly used approach to control the blend morphology, because well-organized interpenetrating networks composed of highly crystallized components can be achieved [5, 6, 8]. However, recent works that investigated phase separation of components in the vertical direction revealed that the BHJ structures fabricated by these methods have a non-uniform vertical distribution having P3HT phase dominant near the top cathode and PCBM phase dominant near the bottom anode [9–12]. Such non-uniform distribution is opposite to the ideal solar cell structure that requires a donor rich phase near the anode and an acceptor rich phase near the cathode, therefore unfavorable to charge transport to the electrodes. In addition, both annealing processes require relatively long processing time, at least tens of minutes, and spin-casting deposition can only be applied to small and rigid substrate, making these approaches not suitable to practical large area and mass production of polymer PV cells. Even though high-speed fabrication processes on flexible substrates have been reported, their device performances still cannot compare to those of spin-casting based polymer solar cells, followed by further post-treatments [13–15]. This is because the traditional high speed roll-to-roll coating method may not provide sufficient annealing time for crystallization and hence result in lower device efficiency [13–15].

As a solution to these problems, in the first part of this chapter, we will introduce a novel processing technology, which allows evaporation of solvent through surface encapsulation and with induced alignment (ESSENCIAL) of polymer chains by applied pressure [16]. The process leads to optimized morphology, more uniform distribution and crystallinity of the components favorable for charge generation and transportation that cannot be achieved by conventional TA and SAA methods. Moreover, this process is applicable to high-speed dynamic process, ultimately

demonstrated in a roll-to-roll process while preserving high device performances. All the PV cells explained in this part have about 200 nm thick photoactive layers. Meanwhile, the positive effects of the ESSENCIAL process on blend morphology is still valid to the BHJ PV cells having hundreds of nanometers thick photoactive layer, which usually suffers from low fill factor due to restricted charge transport and extraction [17]. Taking advantage of its effectiveness, in the second part of this chapter, we will discuss the optimization of BHJ blends with hundreds of nanometers thick photoactive layers, which are thick enough to fully absorb the light. Especially, the factors affecting the device performance, which become prominent as the film thickness is increased, are investigated [17]. In the third part of this chapter, a new type of heterojunction structure that has almost 100 % internal quantum efficiency (IQE) even in over 300 nm thick photoactive layer, consequently providing superior photocurrent and fill factor compared with optimized BHJ PV cells, will be introduced [18]. Additionally, we will introduce nanoimprint lithography (NIL)-based transparent metal electrode (TME) technology [19, 20] as a promising alternative for the ITO electrode that can pave the way toward large area flexible organic PV (OPV) cells in the last part of this chapter.

12.2 ESSENCIAL Process Applicable to Roll-to-Roll Process Without Sacrificing High Device Performances

The essence of the ESSENCIAL process is to utilize a gas-permeable cover layer for solvent evaporation that simultaneously protects the otherwise free surface and induces shear flow of the blend solution by an applied pressure (Fig. 12.1). The thickness of the active layer can be controlled by adjusting the solution concentration and the applied pressure, and the evaporation and solidification time can be reduced to a few seconds by controlling the applied pressure. Furthermore, poly(3,4-ethylenedioxythiophene):poly(styrenesulfonate) (PEDOT:PSS) layer, widely used on top of transparent anode in organic PVs, is not indispensable to this processing, and will be further explained later with roll-to-roll application. The advantages of ESSENCIAL process are shown in various aspects. Firstly, the effects of different processing methods on the crystallinity of the conjugate polymer are investigated by absorbance spectroscopy. The chain ordering of the conjugate polymer in a BHJ structure is one of the essentials to achieve improved crystallinity for high efficiency PV cell, because the improved organization of polymer chains facilitates hole transport and the long conjugation length enhances the absorption of light resulting in efficient exciton generation [21]. Thus, the conjugate polymer with high crystallinity such as P3HT is advantageous. The absorption spectrum of the blend film fabricated by ESSENCIAL method is compared with that made by the spin-casting method in Fig. 12.2a. To further evaluate the efficiency of the ESSENCIAL method, the samples treated by TA and SAA after spin-casting, which are generally used to

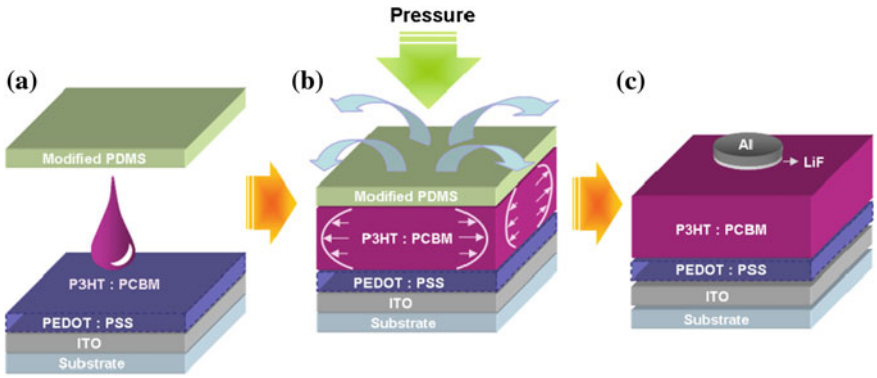

Fig. 12.1 Schematic of the ESSENCIAL process for fabricating polymer PV cells: **a** applying blend solution; **b** active layer formation during solvent evaporation under pressure; **c** isolated island-type electrode deposition on top of polymer blend film after removing the PDMS stamp. Note that PEDOT:PSS layer is not indispensable to this processing as described in the text. Copyright Wiley-VCH Verlag GmbH & Co. KGaA. Reproduced with permission from [16]

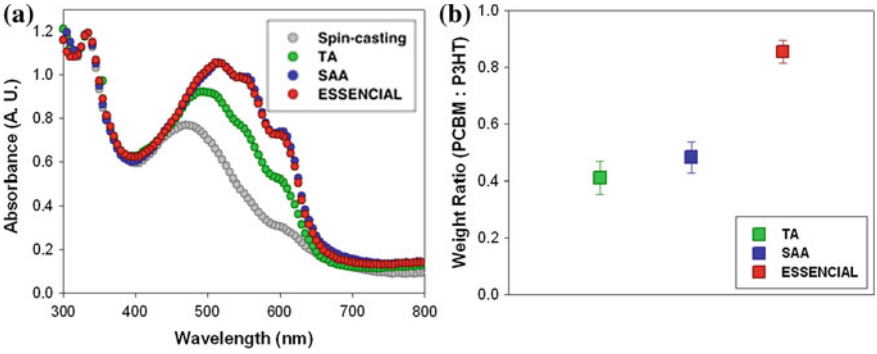

Fig. 12.2 Characteristics of bulk heterojunction structures obtained by different processing methods. **a** Absorption spectra of the blend films. The spectra have been normalized to the PCBM peak around 325 nm. **b** Weight ratio of PCBM to P3HT calculated by X-ray photoelectron spectroscopy results for different processing methods. The *error bars* represent standard deviation. Copyright Wiley-VCH Verlag GmbH & Co. KGaA. Reproduced with permission from [16]

improve the crystallinity of the P3HT, are also examined. A shear stress applied to polymer solution, which causes the organization of polymer, across entire depth between two plates is much more effective than that between a plate and air surface (e.g. spin-casting), which is continuously decreased from the plate and subsequently zero at air interface [22]. Therefore, as expected, enhanced vibronic peaks in the absorbance spectra as well as significant red-shift, which indicate a higher degree of ordering of P3HT chains, [23] are observed in the ESSENCIAL sample. Additionally this processing can be completed in just a few seconds, but the enhancement found in this sample is much higher than that in sample thermally annealed for

20 min and is even comparable to that of the solvent-assisted annealed sample in which P3HT crystals are slowly grown for 2 h. Such property permits this method to be applied to high speed roll-to-roll process and can produce well-ordered P3HT domains.

In addition to improved polymer crystallinity, the nanodomains of each blend component should be well-connected in order for holes from charge-separated excitons to be effectively transported to anode, and the electrons to cathode through continuous pathways. However, the non-uniform distribution of the donor and acceptor components found in spin-casted sample, even after TA or SAA, is not helpful to the effective charge transport to the electrodes [9–12]. This non-uniform distribution of components in vertical direction is a consequence of the surface energy difference between P3HT (26.9 mN m^{-2}) and PCBM (37.8 mN m^{-2}), which pushes P3HT to the low surface energy air surface to minimize the overall free energy [10–12]. In contrast, much uniform vertical distribution is expected for films prepared by the ESSENCIAL process, because the gas-permeable silicone film effectively provides a higher surface energy than that of air surface. XPS results shown in Fig. 12.2b clearly illustrate these trends. Though the weight ratio of PCBM to P3HT in the blend solution is 1:1, the weight ratio of PCBM to P3HT of thermal and solvent-assisted annealed samples measured at the top surface are 0.411 and 0.488, respectively, which indicates a large accumulation of P3HT at the top. But the ESSENCIAL sample produces much more balanced value (0.855), which implies more uniform distribution of components in the vertical direction.

In order to confirm that the uniformly distributed components in ESSENCIAL-treated sample are truly beneficial to effective charge transport by providing more continuous pathways through the film, hole- and electron-only devices are constructed in order to evaluate the charge transport properties in the phase-separated blend film [24, 25]. The hole-only device is fabricated by replacing LiF with high work-function molybdenum oxide (MoO_3) to block the injection of electrons from the Al cathode, and electron-only device by using low work function cesium carbonate (Cs_2CO_3) to replace PEDOT:PSS to block the hole injection from the ITO anode [25]. Both hole- and electron-mobility are calculated using space-charge-limited-current (SCLC) model at low voltage, which is represented by $J = 9\varepsilon_o\varepsilon_r\mu V^2/8L^3$, where $\varepsilon_o\varepsilon_r$ is the permittivity of the component, μ is the carrier mobility, and L is the thickness [26]. Table 12.1 shows the calculated hole and

Table 12.1 The calculated carrier mobilities depending on the different processing methods. Copyright Wiley-VCH Verlag GmbH & Co. KGaA. Reproduced with permission from [16]

Method	Carrier mobility (10^{-4} cm^2 V^{-1} S^{-1})		Ratio (μ_e/μ_h)
	Electron (μ_e)	Hole (μ_h)	
TA	–	1.57	–
SAA	4.95	3.29	1.5
ESSENCIAL[a]	14.6	12.6	1.16

[a] ESSENCIAL sample was further treated by heat for 1 min

electron mobilities depending on the processing methods. The most optimized transport pathways for both charge carriers are achieved in the post heat-treated ESSENCIAL sample, and well-balanced mobilities ($\mu_e/\mu_h \sim 1.2$) are obtained. Even though the electron-mobility of thermally annealed device is not well-matched with SCLC model, the significantly lower expected values (10^{-8}–10^{-7} cm^2 V^{-1} s^{-1}) do not affect any conclusions here.

As a last aspect, the domain size in the BHJ structures and their effects on the exciton quenching are investigated using atomic force microscope (AFM) and photoluminescence (PL) shown in Fig. 12.3. Compared with the non-uniform mixture where one phase is dominant at one surface, more uniformly mixed donor and acceptor phases throughout the film are expected to have finer interpenetrating nanodomains that are advantageous to efficient dissociation of photo-generated excitons, and hence result in suppressed PL from the donor polymer. It has been reported that the PL of annealed sample is enhanced as compared with just spin-casted film, because the higher crystallinity induced by annealing gives relatively poor exciton dissociation due to the reduction of interfacial area between the donor and acceptor domains [27]. However, the improved charge transport of the annealed samples due to increased crystallinity can offset the poor exciton dissociation effect,

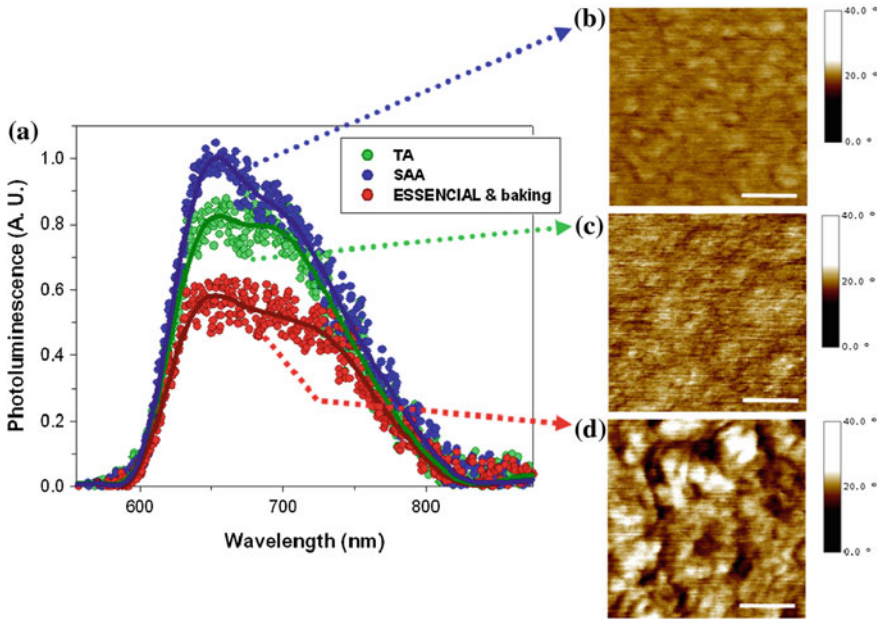

Fig. 12.3 **a** Photoluminescence spectra of blend films. ESSENCIAL sample was further treated by heat: *filled symbols* and *lines* represent experimental data and their polynomial regressions, respectively. **b–d** Atomic force microscope phase images. The images in (**b**)–(**d**) correspond to solvent-assisted annealed sample, thermal annealed sample and heat-treated ESSENCIAL sample, respectively. The *white scale bars* represent 50 nm. Copyright Wiley-VCH Verlag GmbH & Co. KGaA. Reproduced with permission from [16]

still producing high efficiency PV cells [28]. Therefore, the solvent assisted-annealed sample having higher crystallinity than the thermal annealed sample shows well-defined domains in AFM phase images, and this improved crystallinity induces the enhancement of PL in Fig. 12.3a. As for the heat-treated ESSENCIAL sample, finer interpenetrating networks than the solvent-assisted annealed sample is expected due to the more uniform distribution of the blend, and well-defined nanodomains are much more discernable in AFM phase images. These uniformly distributed and fine interpenetrating nanodomains not only permit good charge pathways, but also facilitate the efficient exciton dissociation therefore suppressing the PL from the donor, and consequently give the lowest PL in Fig. 12.3a.

The device performances including power conversion efficiency (PCE) and *J–V* curves measured under AM 1.5 G simulated sunlight (at 100 mW cm^{-2} intensity) are summarized in Fig. 12.4. The devices fabricated by the ESSENCIAL method followed by baking show the highest PCE due to the optimized domain morphologies and charge pathways that resulted in both increased short circuit current and fill factor (Fig. 12.4c, d). The favorable morphology also leads to the lowest series resistance ($\sim$1.2 Ω cm^2) as expected. The improvement of PCE is confirmed by improved external quantum efficiency (EQE) in the range from 350 to 650 nm. The detailed measured values are shown in Fig. 12.4b.

Before advancing toward the roll-to-roll fabrication, another remarkable merit of the ESSENCIAL-based device is addressed. PEDOT:PSS is the most widely used buffer layer between ITO anode and the active organic semiconductor to improve the performances of polymer PV cells. One of the important roles of this PEDOT:PSS layer is to provide efficient electron blocking [29] to prevent electron leakage from the BHJ acceptors [30]. If PEDOT:PSS is not used, the thermally annealed spin-casted device shows the significant drop of fill factor (e.g. from 65.1 to 54.8 %) that results in much reduction in PCE. However, the ESSENCIAL-based device shows only small drop of fill factor (e.g. from 69.1 to 67.3 %) that results in negligible effect on PCE. This effect is consistent to the improved morphology in ESSENCIAL devices discussed above. In the devices with spin-casted film, large amount of PCBM are non-uniformly assembled near the ITO anode, thereby inducing electron leakage. However, the uniform distribution of components in ESSENCIAL-based devices drastically reduces these electron leakage pathways. Therefore, this observation alone can be an important evidence for the uniform distribution of components in the blend film fabricated by ESSENCIAL. Moreover, avoiding the use of PEDOT:PSS can significantly reduce the processing time as it eliminates the PEDOT:PSS coating and the baking step to remove residual H_2O molecules from PEDOT:PSS used in conventional fabrications, which is especially attractive for high-speed roll-to-roll processing. The advantages of ESSENCIAL method to induce superior BHJ morphology in short processing time pave the way to scalable high efficiency polymer PV cells fabrication. Here, we demonstrate fabrication of polymer PV cells using a roll-to-roll apparatus composed of dual rollers and tensioned belt covered with gas-permeable silicone film, which enables coating of polymer blend with uniform thickness and fast solvent evaporation in a continuous fashion (Fig. 12.5). According to the dynamic elastic contact model

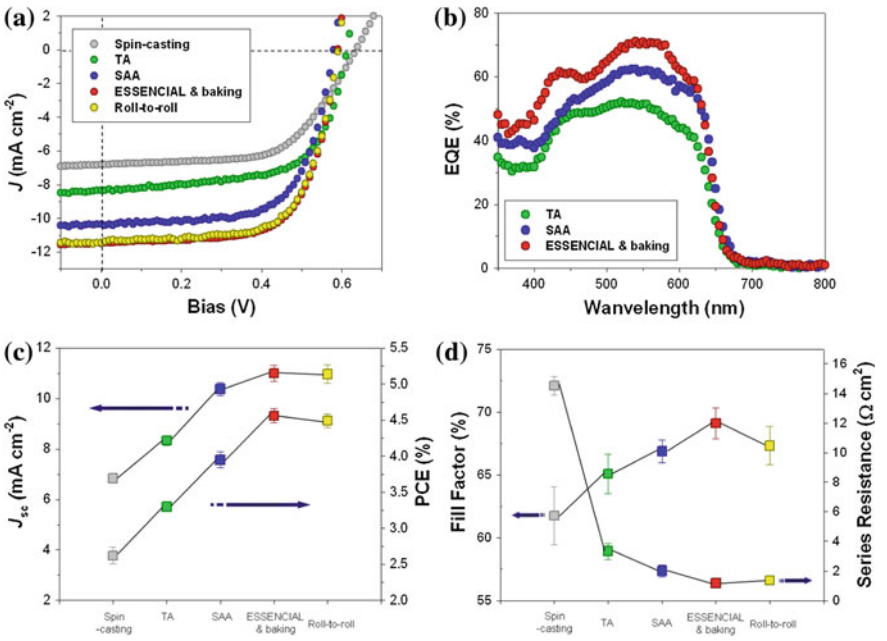

Fig. 12.4 Device performances depending on different processing methods. All data were measured at AM 1.5 G/100 mW cm^{-2}. **a** *J–V* plots. **b** External quantum efficiency. **c** Power conversion efficiency (*PCE*) and short circuit current density (J_{sc}). The error bars represent standard deviation. **d** Fill factor (*FF*) and series resistance (R_s). Average PV cell characteristics are summarized as follows: spin-casting (J_{sc} = 6.67 mA cm^{-2}, V_{oc} = 0.65 V, *FF* = 61.7 %, R_s = 14.5 Ω cm^2, PCE = 2.50 %); thermal annealing (J_{sc} = 8.14 mA cm^{-2}, V_{oc} = 0.61 V, *FF* = 65.1 %, R_s = 3.3 Ω cm^2, PCE = 3.23 %); solvent-assisted annealing (J_{sc} = 10.11 mA cm^{-2}, V_{oc} = 0.58 V, *FF* = 66.9 %, R_s = 2.0 Ω cm^2, PCE = 3.84 %); heat treated ESSENCIAL (J_{sc} = 10.68 mA cm^{-2}, V_{oc} = 0.60 V, *FF* = 69.1 %, R_s = 1.2 Ω cm^2, PCE = 4.46 %); roll-to-roll (J_{sc} = 10.59 mA cm^{-2}, V_{oc} = 0.60 V, *FF* = 67.3 %, R_s = 1.4 Ω cm^2, PCE = 4.40 %). The PV cells fabricated by roll-to-roll processing were prepared without PEDOT:PSS layer. Copyright Wiley-VCH Verlag GmbH & Co. KGaA. Reproduced with permission from [16]

developed for the roll-to-roll nanoimprinting [31] (Fig. 12.5b), the thickness of coated active layer can be controlled by the solution concentration and roller pressure, which is the same condition as the small scale ESSENCIAL experiment discussed earlier, and the film uniformity can be preserved by the belt tension during the solvent evaporation process. Figure 12.5c and inset image show 3 in. wide uniform BHJ active layer film made of P3HT:PCBM blend on ITO coated PET substrate for flexible PV cells using the continuous roll-to-roll process. After 1 min baking, LiF and Al cathode are deposited, and a PCE (∼4.5 %) comparable with the small scale ESSENCIAL experiment is achieved using the roll-to-roll process as shown in Fig. 12.4.

Consequently, the novel ESSENCIAL-based technique shows the most optimum BHJ morphology compared with conventional methods and permits us to realize high efficiency polymer PV cell using high seed roll-to-roll process. More

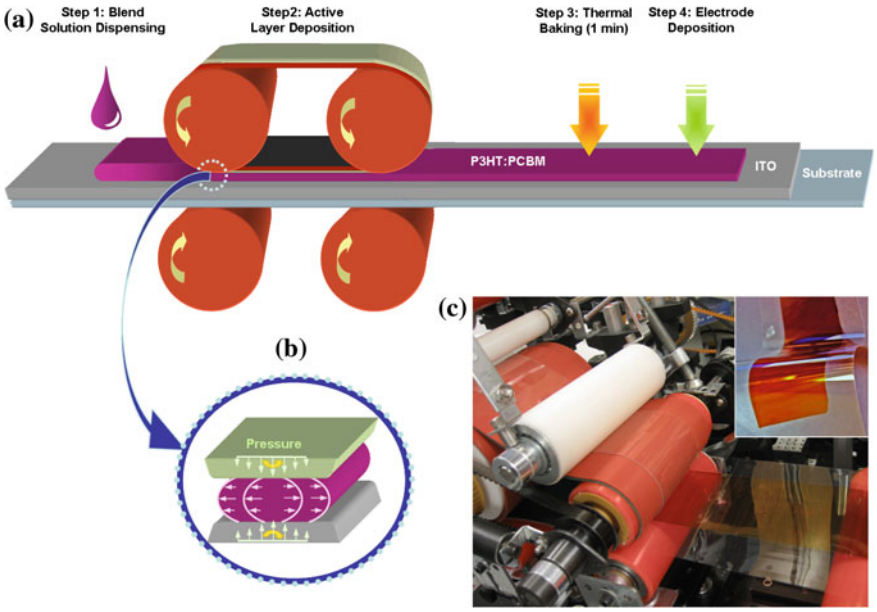

Fig. 12.5 Roll-to-roll processing for polymer PV cells: **a** schematic of roll-to-roll process for polymer PV cell fabrication, **b** a schematic to depict the squeezed flow behavior of solution during dynamic roll-to-roll process. The thickness of liquid coating is affected by concentration of solution, roller pressure and rolling speed according to the dynamic elastic contact model, **c** a photograph of the roll-to-roll apparatus and process. The *inset image* is the resultant flexible polymer PV cell before electrode deposition. Copyright Wiley-VCH Verlag GmbH & Co. KGaA. Reproduced with permission from [16]

importantly, it is expected that this new process is equally applicable to BHJ structures using other materials (e.g. the low band gap polymer semiconductors that demonstrated higher PCE [7]), making it a potential manufacturing technique for mass production of low cost high efficiency polymer PV cells.

12.3 Optimization of BHJ PV Cells with Hundreds of Nanometer Thick Blend Film

One of the primary requisites to achieve high PCE from the BHJ PV cells is to maximize their light absorption for efficient exciton generation. At given absorption coefficient, the absorption of a conventional film can be simply improved by increasing its thickness [32, 33]. Moreover, the increased film thickness is beneficial to minimize the additional absorption loss in multilayer structure, induced by optical interference effect [33, 34]. However, the difficult is that the random nature of the nanodomains in a BHJ structure makes the optimization process challenging

as the thickness of the photoactive layer is increased. Furthermore, this difficulty comes with the aforementioned vertical non-uniformity issue of blend components having electron-donor phase dominant at the top cathode especially in the most commonly used P3HT:PCBM blend system, [9–12] which becomes more prominent in the thicker layer. As a result, the improvement of performances of BHJ PV cells is not always guaranteed by simply increasing the thickness of photoactive layer merely for the sake of improved light absorption and exciton generation. In this section, we will firstly explain the effectiveness of ESSENCIAL process depending on the thickness of BHJ photoactive layer. Based on these results, we will discuss the optimization of hundreds of nanometers thick BHJ photoactive layers, which usually suffers from low fill factor due to restricted charge transport and extraction in a thicker cell. For this purpose, the charge transport properties, closely related with blend morphologies, are investigated using single carrier devices. In addition, their surface morphologies, affecting the interfacial properties between the blend layer and electrode, are further studied by calculating their contact resistances and their diode characteristics such as series resistance, shunt resistance and diode ideality factor.

Figure 12.6 shows the short circuit current, fill factor, PCE and *J*–*V* characteristics of a series of BHJ PV cells with increasing thickness of the photoactive layer. The performance characteristics of devices fabricated using both conventional thermal annealing process after spin-casting and ESSENCIAL are presented for comparison. Also included are the data showing the impact of adding a thin C_{60} layer at the top of device before depositing the cathode, which is applied to improve their surface morphology. This effect will be discussed later in this section. As shown in Fig. 12.6c, most noticeable for the thermally annealed devices is that the PCEs begin to decrease as the thickness of photoactive layer is increased over 300 nm, and this is mainly due to the decreased fill factors (Fig. 12.6b), which represents that this approach is no longer adequate to optimize the BHJ photoactive layer for thicker photoactive films. As discussed above, we believe that the opposite to the ideal PV cell distribution of donor and acceptor components in the vertical direction [9–12], which is inevitably induced during the spin-casting processes, is one of the important factors giving this limitation. Therefore, we can expect that the ESSENCIAL process, which is shown to impart much more uniform vertical distribution of the blend components, [16] can be a possible solution to this issue. Furthermore, merits from the ESSENCIAL process are not only limited to forming favorable vertical distribution of components, but also providing advantageous morphological properties such as large interfacial area for improved exciton dissociation and continuous domain pathways for efficient charge transportation, as explained former section [16]. Thus, all the performance metrics of PV cells fabricated by the ESSENCIAL process shown in Fig. 12.6 supersede those of thermal annealed devices. Meanwhile, the vertical uniformity from ESSENCIAL process is generated by using the gas-permeable film that provides a higher surface energy than air, which prevents the P3HT component having lower surface energy from migrating to the top air intersurface. Since these effects mostly originate from the change of components at the surface of photoactive layer, it is expected that they

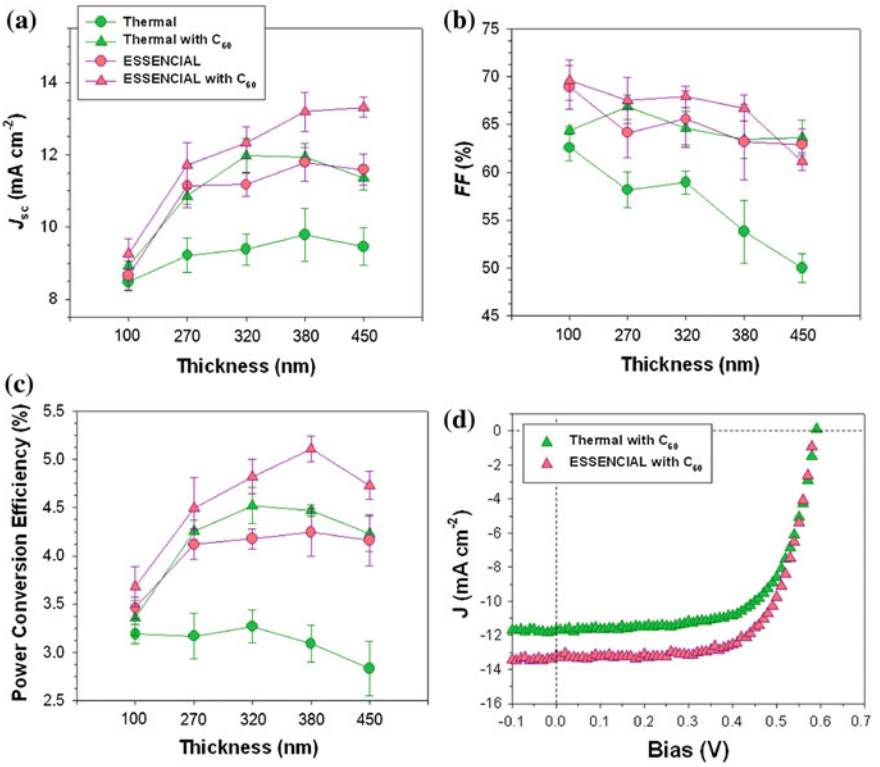

Fig. 12.6 Performances of P3HT:PCBM BHJ PV cells according to the photoactive layer thickness with/without C_{60} layer: **a** short-circuit current densities, **b** fill factors, **c** power conversion efficiencies and **d** *J–V* curves of polymer PV cells: thermally annealed device (320 nm active layer with C_{60}, J_{sc} = 11.97 mA cm^{-2}, V_{oc} = 0.58 V, *FF* = 64.6 %, PCE = 4.52 %) and ESSENCIAL device (380 nm active layer with C_{60}, J_{sc} = 13.19 mA cm^{-2}, V_{oc} = 0.58 V, *FF* = 66.7 %, PCE = 5.11 %): *green circle*, *green triangle*, *pink circle* and *pink triangle* represent thermal anneal without C_{60}, thermal anneal with C_{60}, ESSENCIAL without C_{60} and ESSENCIAL with C_{60}. All data were measured at AM 1.5 G (100 mW cm^{-2} intensity) Copyright Royal Society of Chemistry. Reproduced with permission from [17]

become less effective as the thickness of active layer is increased. This is the reason why the overall PCEs cannot be continuously improved by simply increasing thickness (Fig. 12.6c). Nonetheless, over 60 % high fill factor value preserved even in 450 nm thick ESSENCIAL devices is truly noteworthy (Fig. 12.6b). Therefore, we can speculate that it is possible to further improve the stagnant PCEs by solving the hidden issues of the blend morphology in these thicker photoactive layers.

Table 12.2 shows the carrier mobilities of polymer PV cell having hundreds of nanometer thick photoactive layer, calculated by SCLC model using single carrier devices [26]. The calculated electron mobility in the thermal annealed devices is about a third of the hole mobility, which means the collection of photoelectrons at the cathode is not efficient. Even in ESSENCIAL device, the electron mobility is

Table 12.2 The carrier mobilities calculated by SCLC model depending on the different processing methods Copyright Royal Society of Chemistry. Reproduced with permission from [17]

Method	Carrier mobility (10^{-4} cm^2 V^{-1} S^{-1})			
	Hole (μ_e)		Electron (μ_h)	
	Without C_{60}	With C_{60}	Without C_{60}	With C_{60}
ESSENCIAL	11.5	10.9	5.25	13.6
Thermal	3.27	3.35	1.23	5.84

The thickness conditions that show the highest devices performances (380 and 320 nm for ESSENCIAL and thermal annealing, respectively) are selected for measurement. All of the carrier mobilities measured from the devices are effective mobilities, as explained in the text

about a half of the hole mobility. From the unbalanced mobilities obtained from the devices with hundreds of nanometer scale thick BHJ layer, we can conjecture that fairly large amount of donors are still accumulated at top surface, hampering the transport of photoelectron at the cathode; and this trend is more discernible in the thermally annealed BHJ layer. As a possible solution to this congestion problem, an additional thin acceptor layer (C_{60} ~ 5 nm) is inserted between the photoactive layer and the cathode, and its effect is investigated by evaluating their contact resistances at the cathode interface. For this purpose, organic thin film transistor (OTFT)-like devices are prepared for the measurement of resistance. The measured resistances between electrodes are composed of contact resistances, bulk resistance and sheet resistance. At the fixed width of electrode, the measured resistances are plotted by the distance between the electrodes, and the intercept at the y-axis gives the contact resistance combined with negligibly small bulk resistance component, which is represented by $V/I = R \approx 2R_c + R_sL/W$, where V is bias, I is current, R is the total resistance, R_c is contact resistance, and R_s is sheet resistance. L is the distance between LiF/Al electrodes and W is their constant width. The calculated contact resistances in both ESSENCIAL and thermal annealed devices with and without C_{60} layer are summarized in Table 12.3. In both cases, the contact resistances are significantly reduced after introducing additional thin C_{60} layer, which suggests more efficient charge carrier transport through the cathode interface (Fig. 12.7). Another remarkable feature from these results is that the contact resistances in the ESSENCIAL devices (150–1,000 kΩ) are over two orders of magnitude smaller

Table 12.3 Summary of the calculated contact resistances Copyright Royal Society of Chemistry. Reproduced with permission from [17]

Method	Contact resistance	
	Without C_{60}	With C_{60}
ESSENCIAL (kΩ)	1,000	150
Thermal (MΩ)	220	30
PCBM single layer (kΩ)	15	
P3HT single layer (MΩ)	380	

Area of electrode: 0.08 cm^2
The thickness conditions of BHJ layers are the same with Table 12.2

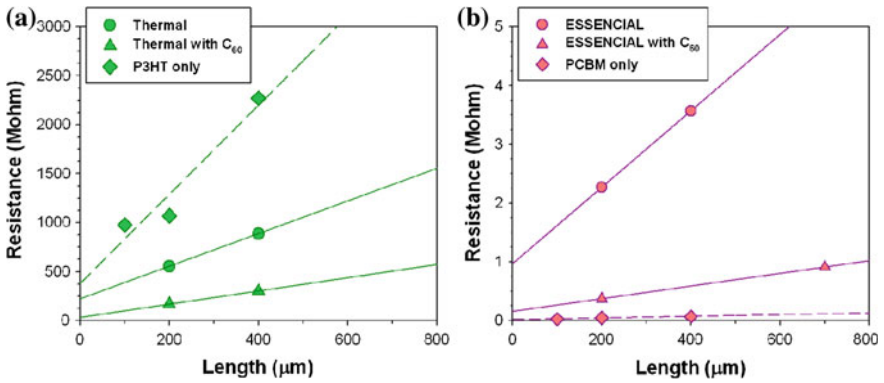

Fig. 12.7 Measured resistances according to the distance between LiF/Al electrodes on **a** thermally annealed BHJ films and P3HT single layer, and **b** BHJ films formed by ESSENCIAL process and PCBM single layer. The intercepts in y-axis are the contact resistances, R_c and the slopes are sheet resistances, R_s: The thickness conditions of BHJ layers are the same with Table 12.2 Copyright Royal Society of Chemistry. Reproduced with permission from [17]

than those in thermally annealed devices (30–220 MΩ). In order to clarify the reason, the contact resistance of PCBM (i.e. C_{60}-derivative) single layer and P3HT single layer with LiF/Al electrode are measured, respectively. As shown in Fig. 12.7, the resistances between PCBM and cathode showed the similar range of values (e.g. kΩ scale) with those in ESSENCIAL devices and they were much smaller than those between P3HT and cathode, which show the similar range of values (e.g. MΩ scale) with those in thermally annealed devices. Therefore, we can confirm that much larger quantity of P3HT domain are assembled at the top surface of the thermally annealed photoactive layer, and they induce much worse electron transport at cathode interface resulting in lower PCE. In contrast, the relatively larger amount of PCBM at the surface of ESSENCIAL devices, which comes from better vertical uniformity, forms better contact between the photoactive layer and electrode, providing better electron transportation to electrode. This also means we need to re-consider the mobility values discussed before, as the carrier mobility is an intrinsic property of the material, which can be affected by the donor–acceptor morphology in the bulk PV film, but not by the contact interface. However in the experiment, the voltage drop at the contact would affect the obtained mobility values. For this reason, we will call the mobility calculated from the devices here as effective mobility, which is affected by the contact interface. It can be used to compare the relative effectiveness of carrier extraction at the electrode contact with buffer layer such as C_{60} in this section.

The role of C_{60} layer can be further evaluated by comparing the improvement of carrier mobility of PV cells. The decreased contact resistances originated from the additional C_{60} layer spontaneously improve the electron transport at the cathode interface and consequently increase electron mobility; however, the hole mobility, which is not directly related with the cathode interface, remains almost the same even after inserting the C_{60} layer (Table 12.2). This is another proof that the

positive effect of C_{60} layer is from the improved carrier transportation property at the interface not from the strong potential change affecting the internal electric field. Meanwhile, overall the mobilities of both holes and electrons in ESSENCIAL devices are higher than those in thermal annealed devices, indicating that much favorable morphology can be achieved by ESSENCIAL process.

The effect of the additional C_{60} layer is further analyzed from diode point of view. The diode characteristics of BHJ polymer PV cells have been often described by the generalized Shockley equation (12.1) [35, 36].

$$J = \frac{R_{sh}}{R_s + R_{sh}} \left[J_s \left\{ \exp\left(\frac{q(V - JR_s)}{nkT} \right) - 1 \right\} + \frac{V}{R_{sh}} \right] - J_{ph}(V) \tag{12.1}$$

In this equation, R_{sh} is the shunt resistance, R_s is the series resistance, J_s is the dark saturation current density, n is the diode ideality factor, and $J_{ph}(V)$ is the voltage-dependent photo-generated current density. All these parameters can be obtained by fitting the *J–V* curves with (12.1), and the results are summarized in Table 12.4. Among various parameters, the major change that comes with added C_{60} layer is the increases of shunt resistances in both ESSENCIAL (from 4.28×10^3 to 1.65×10^4 Ω cm^2) and thermal annealed (from 4.20×10^2 to 1.64×10^3 Ω cm^2) devices, which means that the C_{60} layer works as a hole-blocking layer thereby suppressing the hole leakage current at the cathode. The reason is that the C_{60} layer, whose highest occupied molecular orbital (HOMO) energy level lower than that of donor, effectively presents a barrier to holes and therefore when added before depositing the cathode prevents donor domains that are phase-segregated to the top interface from directly contacting the cathode. Meanwhile, the diode ideality factors, which reflect the properties of the interface between donor and acceptor, [37, 38] are almost unchanged with the addition of C_{60}. This effect is expected, as the additional thin C_{60} layer should not give any effects on internal BHJ morphology.

All the device performances are summarized in Fig. 12.6. The optimized PV cells based on ESSENCIAL process and the additional C_{60} layer show both high photocurrent (13.19 mA cm^{-2}) and fill factor (66.7 %), giving high PCE (5.11 %) in 380 nm thickness BHJ blend film.

Normally, thick BHJ devices show low fill factors and decreased PCE, and we have explained the factors having negative effects on those device performances, which become prominent as the film thickness is increased. Through this study we

Table 12.4 The effect of the additional C_{60} layer on the diode characteristics of BHJ PV cells fabricated by ESSENCIAL and thermal annealing processes Copyright Royal Society of Chemistry. Reproduced with permission from [17]

Parameters	ESSENCIAL		Thermal	
	No C_{60}	With C_{60}	No C_{60}	With C_{60}
Shunt resistance (Ω cm^2)	4.28×10^3	1.65×10^4	4.20×10^2	1.64×10^3
Series resistance (Ω cm^2)	7.3	5.3	10.5	6.4
Diode ideality factor	1.87	1.8	1.94	1.95

The thickness conditions of BHJ layers are the same with Table 12.2

identified the ways to solve those problems. The blend morphology can be controlled by ESSENCIAL process and the interface between blend and cathode electrode modified with thin C_{60} layer leads to more balanced charge transportation. The additional C_{60} layer not only significantly decreases the contact resistance, but also improves the hole blocking property at the cathode.

12.4 Advanced Heterojunction Structure and Fabrication Process

As already explained, significant efforts have been made to optimize and understand the BHJ structures. However, the random nature of such interpenetrating network, based on the simple blending of two components, limits further optimization of the structures as well as thorough understandings of their physical properties. Especially, these become more challenging with the increased film thickness to improve its absorption property, as discussed in former section. In this section, as a fundamental solution to these difficulties, we will explain a new type of polymer PV cell architecture, bilayer-based heterojunction structures. The bilayer structure of electron-donor and acceptor is a simple structure that can help easy optimization of devices and better understanding about their properties. However, it has been well known as inefficient architecture for organic PV cells, because it cannot efficiently produce photo-carriers due to the limited interfacial areas between domains responsible for charge separation. Therefore their device performances are not compatible to BHJ-based PV cells. Even though several works have been recently reported that this type of structure could mimic the BHJ structure by increasing the intermixing of donor and acceptor layer using solution casting, they just could utilize tens of nanometers scale thin donor layer to fully diffuse the acceptor, giving inefficient absorption of light. So, their polymer PV cell performances are limited to those of conventional BHJ-based devices [39, 40].

In contrast, the bilayer-based PV cells explained here show the optimized heterojunction morphology between donor and acceptor having internal quantum efficiency (IQE) approaching almost 100 % around 600 nm at even over 300 nm thick photoactive layer, ultimately providing high photocurrent that cannot be achieved by BHJ-based PV cells. For the practical application, P3HT and PCBM pair, which is most widely used materials, is demonstrated as a model system. Overall processing is composed of two consecutive ESSENCIAL processes for each donor and acceptor material. Firstly, P3HT layer as electron-donor is formed on the PEDOT:PSS-casted anode using the first ESSENCIAL process. The crystallinity of pristine P3HT domain is undoubtedly higher than that in BHJ blend, because PCBM molecules in the blend prevent them from being efficiently crystallized. More importantly, the induced shear flow during the ESSENCIAL process helps the alignment of the polymer chains, and this effect is much more efficient in chain ordering than spin-casting method. Those well-organized P3HT nanodomains are shown in SEM and AFM images (Fig. 12.8).

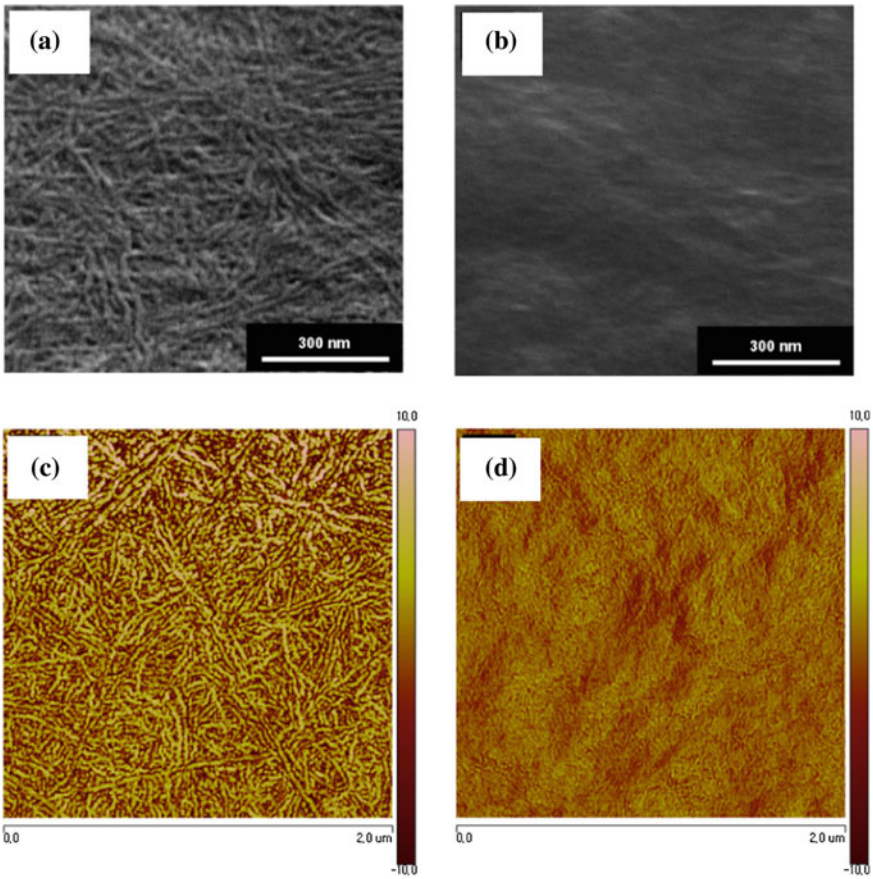

Fig. 12.8 Characterization of P3HT nanodomains fabricated by ESSENCIAL (**a**, **c**) and spin-casting followed by thermal annealing (**b**, **d**): (**a**), (**b**) SEM images; (**c**), (**d**) AFM phase image Copyright Wiley-VCH Verlag GmbH & Co. KGaA. Reproduced with permission from [18]

On top of P3HT nanodomains, PCBM acceptor is casted using another ESSENCIAL process to maximize the interdiffusion of PCBM into P3HT donor layer. The sequential casting of bilayer-type of structure is possible using the solvent having the orthogonality between donor and acceptor such as dichloromethane. The amount of PCBM penetrated into P3HT domains through the photoactive layer is characterized by dynamic secondary ion mass spectroscopy (DSIMS). As shown in Fig. 12.9, the amount of PCBM penetrated into P3HT layer during ESSENCIAL process, due to longer solvent dwelling time, is about three times higher than that during spin-casting even without any post annealing process. Recently, it has been reported that PCBM molecules diffuse through the amorphous phase of P3HT polymers during annealing process without disturbing any crystal domains of P3HT [40, 41]. Therefore, large amount of PCBM molecules can diffuse through the amorphous region of P3HT among tens of nanometer scale crystallized

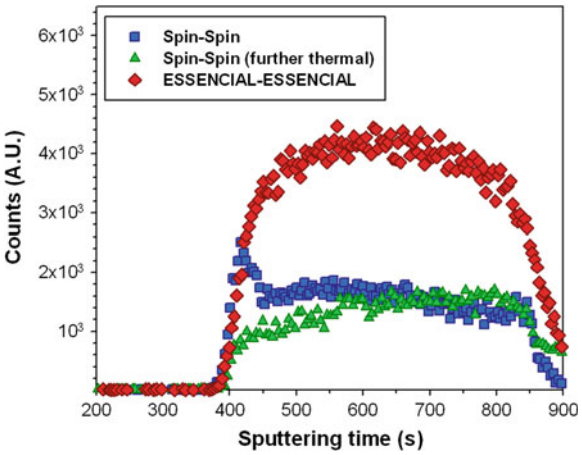

Fig. 12.9 ^{2}H DSIMS results of photoactive layers composed of P3HT and deuterated PCBM. *Square*, *triangle* and *diamond* represent the blend films made by Spin-Spin, Spin-Spin followed by thermal annealing, and ESSENCIAL-ESSEICIAL Copyright Wiley-VCH Verlag GmbH & Co. KGaA. Reproduced with permission from [18]

P3HT nanowire domains during second ESSENCIAL process, which is beneficial to form tens of nanometer scale heterojunction between donor and acceptor for efficient exciton dissociation. Furthermore, those PCBM molecules spontaneously form continuous pathways during their diffusion into P3HT domains. Consequently, in our bilayer-based heterojuntion structures, the continuous donor phase with maximum crystallinity is firstly formed using first ESSENCIAL process, and the continuous acceptor phase can be further formed through the donor phase using second ESSENCIAL process, providing efficient bicontinuous phases heterojunction structure without any isolated island nanodomains. On the contrary, in BHJ blends, the crystallinity of each phase cannot be maximized due to the other phases and the isolated nanodomains are inevitably present due to the random nature of the blend, which is particularly evident with the increased blend thickness.

The carrier mobilities are characterized by photo-charge extraction by linearly increasing voltage (photo-CELIV) method. The photo-CELIV is an efficient method permitting us to calculate the mobility of carrier and recombination in low conductivity materials at the same time [42, 43]. As summarized in Table 12.5, the devices fabricated by two step consecutive ESSENCIAL processes (denoted as ESS-ESS) show the highest mobility value, and the devices composed of spin-casted

Table 12.5 The calculated carrier mobilities using photo-CELIV Copyright Wiley-VCH Verlag GmbH & Co. KGaA. Reproduced with permission from [18]

Method	Carrier mobility (10^{-4} cm^2 V^{-1} S^{-1})
BHJ (thermal annealed)	0.35
Spin-ESS	0.61
ESS-ESS	1.58

P3HT and PCBM layer formed by following ESSENCIAL process (denoted as Spin-ESS) also show about two times higher mobility than thermally annealed BHJ devices. Using photo-CELIV measurements, the bimolecular recombination of charge carrier in photoactive layer can be also studied. The bimolecular recombination rate has following equation (12.2) [43, 44].

$$\frac{dn}{dt} = \frac{dp}{dt} = -\beta(t)np \tag{12.2}$$

where n, p are the concentration of electron and holes, respectively, and β is the bimolecular recombination coefficient. By integrating the photo-CELIV transients, the concentration of extracted charge carriers can be calculated at specific delay time between light pulse and extraction [43]. The bimolecular recombination constant of ESS-ESS device shows the lowest value, which means that the bimolecular recombination is significantly suppressed in ESS-ESS devices compared with conventional BHJ structures [18]. We attribute the reduction in bimolecular recombination to the formation of effective bicontinuous phases that facilitate the charge transport and the improved charge mobility in the structure. The thermally annealed BHJ devices used for the comparison with ESS-ESS devices in this section have 320 nm thickness photoactive layer that show the best performances as explained in the former section.

The optimized heterojunction morphology in ESS-ESS devices is verified by evaluating the internal quantum efficiency (IQE). Recently, Mcgehee et al. reported the method to precisely calculate the IQE by considering parasitic absorption from the reflection spectrum of the organic PV cell devices [45]. The parasitic absorption in polymer PV structure was calculated by transfer matrix method and it was eliminated from the experimentally measured reflection spectrum of PV cells. Following the relation (EQE = absorption in active layer × IQE), IQE signals are calculated (Fig. 12.10). As expected, ESS-ESS devices having optimized

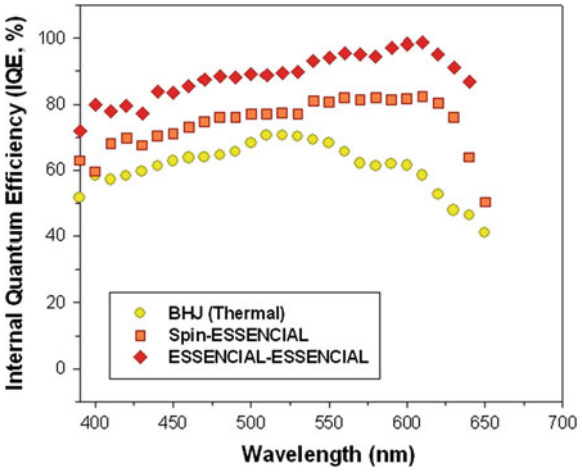

Fig. 12.10 Calculated internal quantum efficiency. *Circle*, *square* and *diamond* represent BHJ blend, Spin-ESSENCIAL and ESSENCIAL-ESSEICIAL cases, respectively Copyright Wiley-VCH Verlag GmbH & Co. KGaA. Reproduced with permission from [18]

morphology show the highest IQE value and this value is approaching 100 % around 620 nm, which means the most of the generated exciton are fully dissociated and transported to electrode without recombination.

The device performances and *J–V* curves are summarized in Table 12.6, and their *J–V* curves are displayed in Fig. 12.11. The performances of the thermally annealed BHJ PV cells are around 3.27 % with 9.38 mA cm^{-2} short circuit current (J_{sc}) and 59.0 % fill factor (*FF*). Compared with these PV cells, ESS-ESS devices having optimized morphology show extremely high J_{sc} (13.83 mA cm^{-2}) and *FF* (67.0 %), and spin-ESS device also showed high J_{sc} (11.84 mA cm^{-2}).

The bilayer-based efficient heterojunction structure, of which intermixing of donor and acceptor phases are maximized by interdiffusion, is introduced. The optimized morphology has maximized crystallinity, high carrier transport, and low recombination coefficient, resulting in high IQE approaching almost 100 %.

Table 12.6 Summary of device performances according to the different processing Copyright Wiley-VCH Verlag GmbH & Co. KGaA. Reproduced with permission from [18]

Method	J_{sc} (mA cm^{-2})	V_{oc} (V)	FF (%)	PCE (%)
BHJ (thermal annealed)	9.38 ± 0.44	0.59 ± 0.00	58.96 ± 1.20	3.27 ± 0.17
Spin-ESSENCIAL	11.84 ± 0.70	0.54 ± 0.03	60.98 ± 3.89	3.91 ± 0.30
ESSENCIAL-ESSENCIAL	13.83 ± 0.52	0.51 ± 0.01	66.98 ± 5.05	4.71 ± 0.36

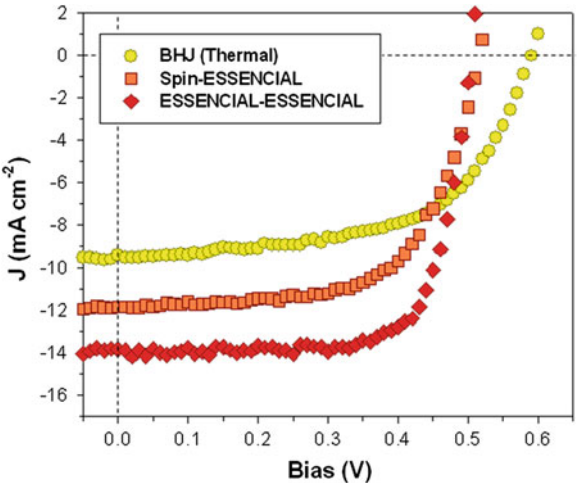

Fig. 12.11 *J–V* plots of PV cells according to the different fabrication process. PV cell characteristics are summarized as follows: BHJ (thermal) (J_{sc} = 9.38 mA cm^{-2}, V_{oc} = 0.59 V, *FF* = 59.0 %, PCE = 3.27 %); Spin-ESS (J_{sc} = 11.84 mA cm^{-2}, V_{oc} = 0.54 V, *FF* = 61.0 %, PCE = 3.91 %); ESS-ESS (J_{sc} = 13.83 mA cm^{-2}, V_{oc} = 0.51 V, *FF* = 67.0 %, PCE = 4.71 %); The symbols are the same with Fig. 12.10 Copyright Wiley-VCH Verlag GmbH & Co. KGaA. Reproduced with permission from [18]

Consequently, the devices based on this structure show significantly high photocurrent (about 50 % higher than that in thermally annealed BHJ PV cells). This new type of structure introduced in this part can help us further understand the charge transport properties in donor-acceptor heterostructures and improve the performance of polymer PV cells.

12.5 Transparent Metal Electrode for High Performance Flexible OPV

Most of OPVs have been made on indium tin oxide (ITO) substrate because ITO offers transparency in the visible range of the electromagnetic spectrum as well as electrical conductivity. However, ITO may not be the best choice for low-cost and high-performance flexible OPV applications, because the high quality ITO, especially high conductivity, requires high temperature annealing, which is incompatible with plastic-based flexible substrates. For example, the poor conductivity of the ITO film on flexible substrates reduces the fill-factor (FF) of the device resulting in low PCE of large area OPVs [46]. The rather brittle ITO film is also not sufficient for flexible applications. In fact, the poor mechanical stability of ITO can cause device failure when the ITO-coated flexible substrate is bent [47, 48]. Our previous study has shown that the conductivity of ITO coated flexible PET substrates drops drastically when bent beyond a 3 cm radius of curvature [49]. It has also been reported that the migration of indium from ITO into organic layer can reduce the device performance [50, 51]. Moreover, the price of ITO drastically increases due to the limited supply of the indium element and the increasing demand from the rapidly expanding display market.

We developed a new approach to address the aforementioned challenges in realizing large area flexible, scalable alternative to ITO transparent conductors. We have been investigating a type of transparent and conductive electrode based on metallic nanostructures. Such transparent metal electrode (TME) [19, 20] is in the form of a periodic nanoscale metal wire grid fabricated by nano imprint lithography (NIL) technology [52] and has high optical transparency and, good electrical conductivity. Moreover, unlike ITO, those properties are adjusted independently by changing the metal line width and thickness in the metal grid structure. The TME also exhibits greatly improved mechanical flexibility and durability. In addition, we have also exploited a kind of roll-to-roll process as an initial effort toward scalable manufacturing. Not only do metal electrodes provide excellent optical transmittance and electrical conductivity, but also the nanoscale metallic nanowire structures exhibit unique optical properties due to the excitation of surface plasmon resonance (SPR), which can be exploited in specially designed OPV structures to enhance the efficiency [53].

High transparency and conductivity The transparent metal electrodes (Fig. 12.12a) are fabricated using nanoimprint technique and based on two design considerations: (1) the line-width of the metal mesh is designed to be sub-wavelength to provide

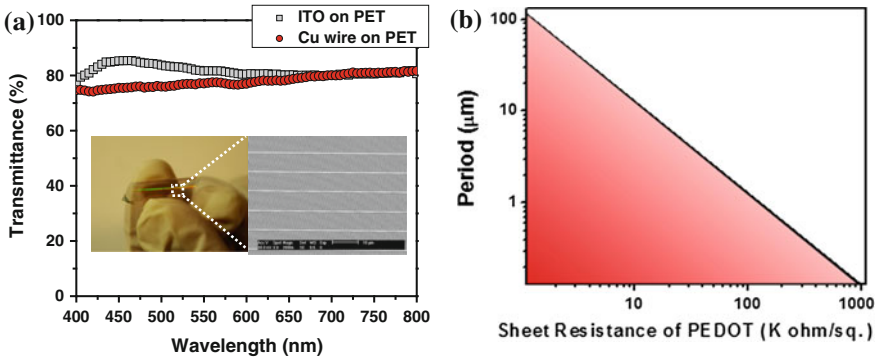

Fig. 12.12 **a** Transmission spectra of ITO electrode and Cu mesh electrode on PET substrate. *Inset* a Photograph and SEM image of the high transparency Cu mesh electrode, linewidth 70 nm, period 700 nm. **b** Calculated optimum period of the nanopatterned metal grating in transparent metal electrode as a function of the sheet resistance of the PEDOT:PSS layer. Choosing the metal grating period and the PEDOT sheet resistance within the *red* region will lead to negligible loss of photocurrent. Copyright Wiley-VCH Verlag GmbH & Co. KGaA. Reproduced with permission from [20]

sufficient transparency and to minimize light scattering and reflection; (2) the period of the mesh is chosen to be submicron to ensure the uniformity of the current collection from the organic semiconductors. As shown in Fig. 12.12b, the optimum period of the transparent metal electrode can be found in the red area for OPVs made with conductive PEDOT:PSS transporting layer [20]. The more close to the lower left corner, the better the OPV performance will be. Outside the red area the transparent metal electrode will still be able to collect generated photocurrent but with reduced efficiency.

Nanoscale patterned metal film provides high transparency conductive electrode whose transmittance is comparable to the commercially available standard ITO electrode as shown in Fig. 12.13a. High transparency metal electrodes using Au, Cu and Ag are shown, but any other metals can be used for this purpose as well. Figure 12.13b shows the typical behavior of the average transmittance of the metal electrode in the visible range as a function of different sheet resistance. Transparent metal electrodes with a line-width of 120 nm were considered in this case. As shown in Fig. 12.13b, the sheet resistance of the metal electrode can be decreased to less than a few ohms per square with only a small decrease of the average transmittance. This characteristic is another advantage over an ITO electrode, in which the sheet resistance has to be compromised in order to achieve high transmittance.

Excellent Flexibility and durability The fabricated Cu electrode was found to be much more flexible than the ITO by simple bending test and the results are shown in Fig. 12.14. In the case of the transparent Cu electrode, it can be bent to about 3 mm radius of curvature with no degradation of the conductance. On the other hand, the ITO exhibits a reduction of the conductance even at a radius of $\sim$30 mm, which can reach close to zero due to the micro-cracking in ITO film on the order of 20 μm after the bending.

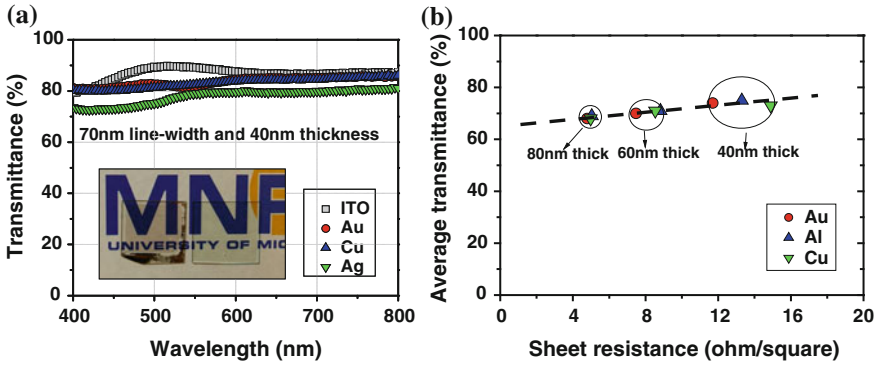

Fig. 12.13 **a** Optical transmittance of the ITO and transparent metal electrodes with a period of 700 nm and line-width of 70 nm. **b** Average transmittance versus sheet resistance of transparent metal electrodes with a line-width of 120 nm. Copyright Wiley-VCH Verlag GmbH & Co. KGaA. Reproduced with permission from [19]

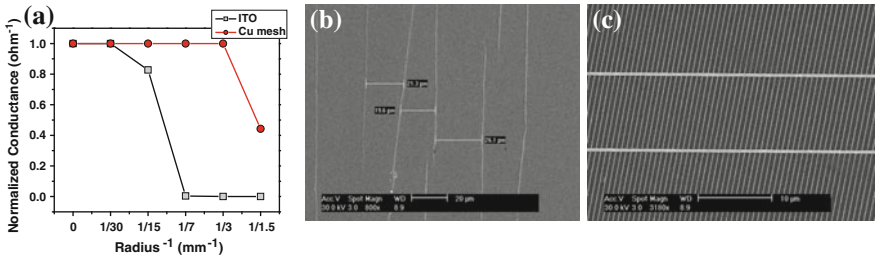

Fig. 12.14 **a** Normalized conductance versus inverse of the radius of curvature of the Cu wire mesh *filled circle* and the ITO electrode *filled square*. The Cu mesh electrode on PEDOT coated PET substrate showed a superior flexibility and can be bent to ~3 mm curvature with no degradation of conductance. SEM images of the ITO (**b**) and Cu mesh electrode (**c**) after the bending test, respectively. In contrast to Cu mesh structure, the ITO severely cracked from the bending. Copyright Elsevier. Reproduced with permission from [49]

Extendable to roll-to-roll fabrication The fabrication of the nanopatterned metal electrode using the metal transfer printing technique can be extended to cost effective and large area fabrication such as roll-to-roll nanoimprint lithography (R2RNIL) [54, 55] with the use of flexible molds. As a proof of principle, we fabricated nanoscale metal (e.g. Au) gratings on large area PET substrates using a roll-to-roll transfer printing process [49]. Recently we developed a near-field optical nanolithography method by using a roll-type phase-shift mask [56]. Sub-wavelength resolution is achieved using near-field exposure of photoresist through a cylindrical phase-mask, allowing a dynamic and high throughput continuous patterning. The large area capability and the diversity of the substrates that can be used in the process make it attractive for large area device applications. We adopted this technique to

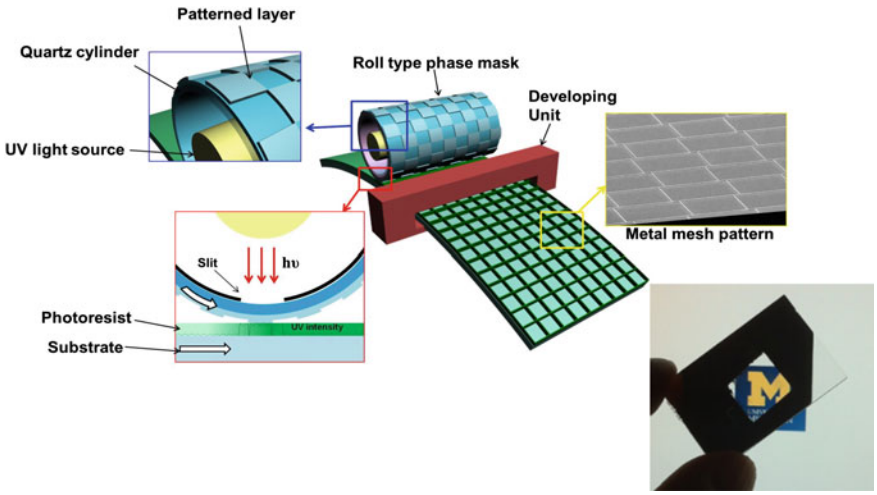

Fig. 12.15 Schematic of roll-to-roll phase-shift lithography and a SEM and photograph of the fabricated metallic wire grid that is transparent to light. Copyright Institute of Physics. Reproduced with permission from [56]

produce large metal mesh patterns as transparent electrode. To fabricate mesh type metal pattern, a specific phase-shift mask was designed and critical experimental parameters were studied.

Figure 12.15 shows the schematic of the process and an example of the fabricated wire grid transparent electrode. Transparency and sheet resistance can be controlled by adjusting the geometry of the wire grid patterns. When combined with a conducting layer such as PEDOT:PSS, such structures are attractive as ITO-alternatives for large area OPVs. The mass production method of metal transparent electrode, which is a promising alternative for the ITO electrode, has scientific and industrial significance. The new process can allow large area and cost effective fabrication of metal mesh electrodes and flexible OPVs.

References

1. O. Morton, Nature **443**, 19 (2006)
2. N.S. Sariciftci, L. Smilowitz, A.J. Heeger, F. Wudl, Science **258**, 1474 (1992)
3. G. Yu, J. Gao, J.C. Hummelen, F. Wudl, A.J. Heeger, Science **270**, 1789 (1995)
4. J.J.M. Halls, C.A. Walsh, N.C. Greenham, E.A. Marseglia, R.H. Friend, S.C. Moratti, A.B. Holmes, Nature **376**, 498 (1995)
5. W. Ma, C. Yang, X. Gong, K. Lee, A.J. Heeger, Adv. Funct. Mater. **16**, 1617 (2005)
6. G. Li, V. Shrotriya, J. Huang, Y. Yao, T. Moriarty, K. Emery, Y. Yang, Nature Mater. **4**, 864 (2005)
7. H.-Y. Chen, J. Hou, S. Zhang, Y. Liang, G. Yang, Y. Yang, L. Yu, Y. Wu, G. Li, Nature Photon **3**, 649 (2009)

8. SSv Bavel, E. Sourty, G.D. With, J. Loos, Nano Lett. **9**, 507 (2009)
9. M. Campoy-Quiles, T. Ferenczi, T. Agostinelli, P.G. Etchegoin, Y. Kim, T.D. Anthopoulos, P.N. Stavrinou, D.D.C. Bradley, J. Nelson, Nature Mater. **7**, 158 (2008)
10. Y. Yao, J. Hou, Z. Xu, G. Li, Y. Yang, Adv. Funct. Mater. **18**, 1783 (2008)
11. Z. Xu, L.-M. Chen, G. Yang, C.-H. Huang, J. Hou, Y. Wu, G. Li, C.-S. Hsu, Y. Yang, Adv. Funct. Mater. **19**, 1227 (2009)
12. D.S. Germack, C.K. Chan, B.H. Hamadani, L.J. Richter, D.A. Fischer, D.J. Gundlach, D.M. DeLongchamp, Appl. Phys. Lett. **94**, 233303 (2009)
13. F.C. Krebs, S.A. Gevorgyan, J. Alstrup, J. Mater. Chem. **19**, 5442 (2009)
14. F.C. Krebs, Org. Electron. **10**, 761 (2009)
15. L. Blankenburg, K. Schultheis, H. Schache, S. Sensfuss, M. Schrödner, Sol. Energy Mater. Sol. Cells **93**, 476 (2009)
16. H.J. Park, M.-G. Kang, S.H. Ahn, L.J. Guo, Adv. Mater. **22**, E247 (2010)
17. H.J. Park, H.S. Kim, J.Y. Lee, T. Lee, L.J. Guo, Energy Environ. Sci. **6**, 2203 (2013)
18. H.J. Park, J.Y. Lee, T. Lee, L.J. Guo, Adv. Energy Mater. **3**, 1135 (2013)
19. M.-G. Kang, L.J. Guo, Adv. Mater. **19**, 1391 (2007)
20. M.-G. Kang, M.-S. Kim, J. Kim, L.J. Guo, Adv. Mater. **20**, 4408 (2008)
21. K.M. Coakley, M.D. McGehee, Chem. Mater. **16**, 4533 (2004)
22. S.-S. Kim, S.-I. Na, J. Jo, G. Tae, D.-Y. Kim, Adv. Mater. **19**, 4410 (2007)
23. M. Sunderberg, O. Inganas, S. Stafstrom, G. Gustafsson, B. Sjogren, Solid State Commun. **71**, 435 (1989)
24. V.D. Mihailetchi, L.J.A. Koster, P.W.M. Blom, C. Melzer, Bd Boer, J.K.J. Duren, R.A. J. Janssen, Adv. Funct. Mater. **15**, 795 (2005)
25. V. Shrotriya, Y. Yao, G. Li, Y. Yang, Appl. Phys. Lett. **89**, 063505 (2006)
26. M.A. Lampert, P. Mark, *Current Injection in Solids* (Academic, New York, 1970)
27. Y. Kim, S. Cook, S.M. Tuladhar, S.A. Choulis, J. Nelson, J.R. Durrant, D.D.C. Bradley, M. Giles, I. Mcculloch, C.-S. Ha, M. Ree, Nature Mater. **5**, 197 (2006)
28. G. Li, V. Shrotriya, Y. Yao, J. Huang, Y. Yang, J. Mater. Chem. **17**, 3126 (2007)
29. N. Koch, A. Elschner, R.L. Johnson, J. Appl. Phys. **100**, 024512 (2006)
30. M.D. Irwin, D.B. Buchholz, A.W. Hains, R.P.H. Chang, T.J. Marks, PNAS **105**, 2783 (2008)
31. S.H. Ahn, L.J. Guo, ACS Nano **3**, 2304 (2009)
32. H. Hoppe, N.S. Sariciftci, J. Mater. Res. **2004**, 19 (1924)
33. A. Pivrikas, H. Neugebauer, N.S. Sariciftci, IEEE J. Sel. Top. Quantum Electron. **16**, 1746 (2010)
34. H. Hoppe, N. Arnold, N.S. Sariciftci, D. Meissner, Sol. Energy Mater. Sol. Cells **80**, 105 (2003)
35. A.L. Fahrenbruch, J. Aranovich, *Solar Energy Conversions Solid-State Physics Aspects*, vol. 31 (Springer, Berlin, 1979)
36. A.L. Fahrenbruch, H.R. Bube, *Fundamentals of Solar Cells* (Academic, New York, 1981), p. 163
37. C. Waldauf, M.C. Scharber, P. Schilinsky, J.A. Hauch, C.J. Brabec, J. Appl. Phys. **99**, 104503 (2006)
38. J.H. Lee, S. Cho, A. Roy, H.-T. Jung, A.J. Heeger, Appl. Phys. Lett. **96**, 163303 (2010)
39. K.H. Lee, P.E. Schwenn, A.R.G. Smith, H. Cavaye, P.E. Shaw, M. James, K.B. Krueger, I.R. Gentle, P. Meredith, P.L. Burn, Adv. Mater. **23**, 766 (2011)
40. D. Chen, F. Liu, C. Wang, A. Nakahara, T.P. Russell, Nano Lett. **11**, 2071 (2011)
41. N.D. Treat, M.A. Brady, G. Smith, M.F. Toney, E.J. Kramer, C.J. Hawker, M.L. Chabinyc, Adv. Energy Mater. **1**, 82 (2011)
42. G. Juška, K. Arlauskas, M. Viliunas, Phys. Rev. Lett. **84**, 4946 (2000)
43. A.J. Mozer, G. Dennler, N.S. Sariciftci, M. Westerling, A. Pivrikas, R. Österbacka, G. Juška, Phys. Rev. B **72**, 035217 (2005)
44. G. Sliauzys, G. Juška, K. Arlauskas, A. Pivrikas, R. Österbacka, M. Scharber, A. Mozer, N.S. Sariciftci, Thin Solid Films **511**, 244 (2006)
45. G.F. Burkhard, E.T. Hoke, M.D. McGehee, Adv. Mater. **22**, 3293 (2010)

46. B. Maennig, J. Drechsel, D. Gebeyehu, P. Simon, F. Kozlowski, A. Werner, F. Li, S. Grundmann, S. Sonntag, M. Koch, K. Leo, M. Pfeiffer, H. Hoppe, D. Meissner, N.S. Sariciftci, I. Riedel, V. Dyakonov, J. Parisi, Appl. Phys. A **79**, 1 (2004)
47. Z. Chen, B. Cotterell, W. Wang, E. Guenther, S.-J. Chua, Thin Solid Films **394**, 202 (2001)
48. M.W. Rowell, M.A. Topinka, M.D. McGehee, H.-J. Prall, G. Dennler, N.S. Sariciftci, L. Hu, G. Gruner, Appl. Phys. Lett. **88**, 233506 (2006)
49. M.-G. Kang, H.J. Park, S.-H. Ahn, L.J. Guo, Sol. Energy Mater. Sol. Cells **94**, 1179 (2010)
50. J.R. Sheats, D.B. Roitman, Synth. Met. **95**, 79 (1998)
51. M.P. De Jong, D.P.L. Simons, M.A. Reijme, L.J. van Ijzendoorn, A.W. Denier van der Gon, M.J.A. de Voigt, H.H. Brongersma, R.W. Gymer, Synth. Met. **110**, 1 (2000)
52. L.J. Guo, Adv. Mater. **19**, 495 (2007)
53. M.G. Kang, T. Xu, H.J. Park, X.G. Luo, L.J. Guo, Adv. Mater. **22**, 4378 (2010)
54. H. Ahn, L.J. Guo, Adv. Mater. **20**, 2044 (2008)
55. S.H. Ahn, L.J. Guo, ACS Nano **3**, 2304 (2009)
56. M.K. Kwak, J.G. Ok, J.Y. Lee, L.J. Guo, Nanotechnology **23**, 344008 (2012)

Chapter 13
Semitransparent Organic Solar Cells

Fu Rong Zhu

Abstract The organic solar cell technology has attracted great interests due to its potential of low cost solution process capability. Bulk heterojunction organic solar cells offer a potentially much cheaper alternative way to harness solar energy, and can be made flexible and large area. They can also be made translucent and in different colors. A broad range of distinct device technologies based on organic and organic/inorganic hybrid materials are being developed very rapidly, including polymer/fullerene blends, small molecule thin films and hybrid polymer/nanocrystal photovoltaic cells. As a result, the inexpensive fabrication process such as solution-process techniques, mechanical flexibility, light weight and visible-light transmissivity features make organic solar technology attractive for application in new markets such as smart sensors, power generating window panes, building architecture, greenhouses and outdoor lifestyle etc. The development of high performance semitransparent organic solar cells constitutes the next major step in this exciting and fast growing organic photovoltaic field.

13.1 Introduction

Compared to current silicon-based solar cells that are rigid, organic solar cells (OSCs) are simpler and less expensive to manufacture. A broad range of distinct device technologies based on organic and organic/inorganic hybrid materials are being developed very rapidly, including polymer/fullerene blends, small molecule thin films and hybrid polymer/nanocrystal solar cells. A power conversion efficiency (PCE) of >9.0 % single junction solar cell bas been demonstrated based on conjugated polymers. The progresses made in tandem device having two or multiple cells vertically stacked in series have also led to the double increase in open circuit voltage (Voc) of OSCs. OSCs can be made flexible, semitransparent and are

F.R. Zhu (✉)
Department of Physics, Hong Kong Baptist University, Hong Kong, China
e-mail: frzhu@hkbu.edu.hk

Y. Yang and G. Li (eds.), *Progress in High-Efficient Solution Process Organic Photovoltaic Devices*, Topics in Applied Physics 130,
DOI 10.1007/978-3-662-45509-8_13

light weight. Its unique flexibility, visible-light transparency and color tunable feature also adds a decorative and aesthetic dimension to the solar cells so that it can be used on curved and irregular surfaces—something that cannot be realized using traditional inorganic rigid silicon solar cells.

OSCs based on the blends of different polymers with fullerene [1, 2] are already demonstrated with PCE of ~9 % [3]. Theoretical prediction suggests that >10 % PCE in single junction, and 15 % in tandem OSCs can be achievable through band-gap tuning of electron donating material (donor) and introducing tandem structure [4]. The certified tandem OSC has achieved 10.6 % PCE [3]. The most commonly used blend materials for the fabrication of bulk heterojunction (BHJ) are poly(3-hexylthiophene) (P3HT) donor and electron accepting material (acceptor) [6,6]-phenyl C_{61}-butyric acid methyl ester (PCBM) [5]. However, P3HT only absorbs a part of the visible light, which limits the utility of sunlight. Therefore, recent attention has been paid on low band gap polymers to improve coverage of the solar spectrum and hence to boost the PCE of OSCs by extending the absorption to longer wavelengths. Low band gap conjugated organic polymers are emerging as promising materials for the development of OSCs because of the improved absorption [6–8].

Much effort has been devoted to developing new organic donor materials, and establishing what their properties should have to afford efficient OSCs by blending with PCBM. One attractive alternative is the development of OSCs that are based on the exploitation of strongly absorbing metallopolymers as the electron donors in bulk heterojunction devices. On the other hand, the role of singlet and triplet excitons in conjugated polymers is still the focus of many researchers [9, 10]. It is expected that triplet excitations are important in optical and electrical processes within conjugated organic polymers with direct implications for application in OSCs. While it is crucial to chemically tune the singlet-triplet energy gap, a vast body of new photoactive materials has been extensively employed to explore the triplet excited states in conjugated polymers directly, e.g., the presence of heavy metals in the conjugated polymers is shown to increase the spin-orbit coupling, thus enabling the spin-forbidden phosphorescence partially allowed [11]. A detailed consideration of the triplet photophysics and the associated bandgap in the polymer as well as their trade-off problem are all necessary for designing highly efficient and photovoltaically-active materials.

In parallel to the synthesis of novel photoactive materials, significant improvements on the PCE of OSCs have been achieved using the BHJ between an electron donating conjugated polymer and an electron accepting fullerene derivative. Tandem or stacked OSCs have been also explored with an aim to utilize the solar energy effectively. In tandem or stacked OSCs, two or more sub-cells, with ideally non-overlapping spectral response, are stacked in order to cover the broader solar spectrum compared to the single junction cells. These sub-cells are connected with suitable transparent electrode which allows light transmission into the subsequent photoactive layers [12–14]. It is very important to develop high quality upper transparent or inter electrode by identifying a suitable electrode material and design in order to obtain the photocurrent match in the tandem solar cells. In addition,

OSCs with transparent bottom and upper electrodes have a see-through feature which makes them suitable for new application in architectural structures, greenhouse and power-generating window panes.

A conventional OSC consists of a front transparent anode, a stack of photoactive organic layers or blends material that absorbs photons and converts them into electrons and holes, and a reflective cathode. In this chapter, we will discuss the design and realization of high performance semitransparent OSCs based on polymeric and organic photoactive materials thorough understanding and effective engineering of interfacial properties at organic/transparent electrode interface. Realization of high quality upper transparent electrode on functional organic layer and simultaneous optimization of the performance of OSCs over the two competing parameters of absorption enhancement and visible-light transparency will be described. An optical admittance analysis which takes into account the interference effects in multilayer thin film OSCs will be introduced. The choice of organic photoactive materials, design and fabricate high efficiency semitransparent OSCs through improved transparent electrodes, organic/electrode interfacial analysis, new device design and device optimization will be also reviewed in the following discussion.

13.2 Optical Admittance Analysis

In this section we introduce the optical admittance method [15, 16] and discuss possible designs to improve the conversion efficiency of OSCs of the type: glass/transparent conducting oxide (TCO)/blend of donor and acceptor photoactive materials/opaque metal cathode, and glass/TCO/blend of donor and acceptor photoactive materials/upper transparent cathode. The effect of upper TCO-based transparent cathode on the performance of semitransparent OSCs will be analyzed.

An OSC with a thin film configuration can be considered generally as a multilayer thin film system composed of materials with different optoelectronic properties. For example, Fig. 13.1a shows a schematic representation of a thin film solar cell with a stack of functional layers on a substrate, while Fig. 13.1b illustrates a cross sectional view of a typical solution-processed BHJ OSC of the type: glass/indium tin oxide (ITO)/P3HT:PCBM/metal cathode and the corresponding energy diagram of the functional materials used in the device. Let's assume an organic solar cells has m layers, the effective optical admittance, $y_{eff,}$ of this multilayer system can be defined as $y_{eff} = C/B$, where B and C can be determined by solving the following characteristic matrix equation [17, 18]:

$$\begin{pmatrix} B \\ C \end{pmatrix} = \left[\prod_{j=1}^{m} \begin{pmatrix} \cos\delta_j & (i\sin\delta_j)/y_j \\ iy_j \sin\delta_j & \cos\delta_j \end{pmatrix} \right] \begin{pmatrix} I \\ y_{m+1} \end{pmatrix}. \tag{13.1}$$

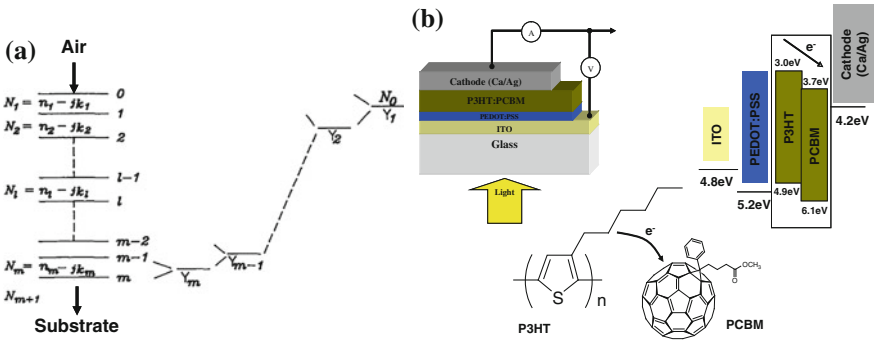

Fig. 13. 1 **a** Schematic representation of a thin film organic solar cell, and **b** a cross sectional view of a representative OSC made with a photoactive blend of P3HT:PCBM

where y_j and y_{m+1} are the optical admittance of the jth layer and substrate respectively. I is the unit matrix, δ_j is the angular phase given by:

$$\delta_j = \frac{2\pi N_j d_j \cos\theta}{\lambda}, \tag{13.2}$$

where d_j is the actual thickness of the jth layer in this m layered structure, and N_j is the corresponding complex refractive index given by $N_j = n_j(\lambda) - ik_j(\lambda)$. Where $n_j(\lambda)$ and $k_j(\lambda)$ are real and imaginary parts of N_j, respectively. The characteristic matrix (13.1) takes into account the effect of the multiple reflections in a multi-layer structure. Using the value y_{eff} calculated from an m layered thin film system, the total reflectance as a function of wavelength, $R(\lambda)$, can be expressed as [17, 18]:

$$R(\lambda) = \left|\frac{N_0 - y_{eff}}{N_0 + y_{eff}}\right|^2, \tag{13.3}$$

where N_0 is the refractive index of air. The reflectance thus obtained depends on the wavelength of the incident radiation. Assuming normal incidence, the total transmittance as a function of wavelength, $T(\lambda)$, can be expressed as [17, 18]:

$$T(\lambda) = [1 - R(\lambda)]\prod_{j=1}^{m}\psi_j \tag{13.4}$$

where ψ_j is the ratio of the time averaged numerical magnitude of the Poynting's vector at the jth and $(j-1)$th boundaries, and is given by [17, 18]:

$$\psi_j = \frac{\mathrm{Re}(Y_{j+1})}{\mathrm{Re}(Y_j)\left|\cos\delta_j + \frac{Y_{j+1}\sin\delta_j}{N_j}\right|^2}, \tag{13.5}$$

where $\mathrm{Re}(Y_{j+1})$ and $\mathrm{Re}(Y_j)$ represent the real parts of the effective admittance for the $(j+1)$th, $Y_{j+1,}$ and jth, Y_j, layers respectively. The total absorbance as a function of wavelength, $A(\lambda)$, in this m layer system can be calculated from the following expression [17, 18]:

$$A(\lambda) = 1 - T(\lambda) - R(\lambda). \tag{13.6}$$

Similarly, the net absorbance of the ith layer, $A_i(\lambda)$, in an m layer organic solar cell can be determined by [18]:

$$A_i(\lambda) = [1 - R(\lambda)][1 - \psi_i(\lambda)] \prod_{j=1}^{i-1} \psi_j(\lambda), \tag{13.7}$$

Using the flux of the incident solar radiation $F(\lambda)$, measured in $\mathrm{Wm}^{-2}\ \mu\mathrm{m}^{-1}$, for example AM1.5G spectrum, the integrated absorbance of any individual layer, $\overline{A_i}$, and the total absorbance of an m-layered system, e.g., an OSC, $\overline{A}$ can be calculated as [17, 18]:

$$\overline{A_i} = \frac{\int A_i(\lambda) F(\lambda) d\lambda}{\int F(\lambda) d\lambda}. \tag{13.8}$$

$$\overline{A} = \frac{\int A(\lambda) F(\lambda) d\lambda}{\int F(\lambda) d\lambda}. \tag{13.9}$$

Similarly, the total reflectance, $\overline{R}$, and total transmittance, $\overline{T}$, of an OSC under AM1.5G spectrum can be expressed and calculated as:

$$\bar{R} = \frac{\int R(\lambda) F(\lambda) d\lambda}{\int F(\lambda) d\lambda}. \tag{13.10}$$

$$\overline{T} = \frac{\int T(\lambda) F(\lambda) d\lambda}{\int F(\lambda) d\lambda}. \tag{13.11}$$

Thus it is possible to calculate absorbance, transmittance and reflectance of an entire device and also an active region in an OSC. The optical performance of organic solar cells can then be analyzed and optimized based on the above principles discussed. Optical admittance analysis can be employed to investigate light distribution and absorption enhancement in OSCs, realizing simultaneous optimization of cell performance and visible-light transmissivity.

The aim of the overall device design for organic solar cells is to maximize light absorption and hence to achieve high power conversion efficiency. This approach becomes easy and effective to design a variety of OSCs with multi-layer single BHJ junction, a stack of sub-cells and semitransparent device structures. The tandem OSC allows each sub-cell to respond actively to different parts of the incident solar

radiation. Thus the distribution of the incident light distribution can be optimized in the active region of the organic solar cells for efficient photo current generation and current matching. The thickness of the photoactive layer in the tandem OSCs can be optimized through maximizing the integrated absorbance in each sub-cell. $\overline{A_i}$ and $\overline{A}$ calculated from (13.8) and (13.9) provide a way to optimize the thickness of the cell through maximizing the integrated absorbance in opaque and semitransparent OSCs. An optimal structure of a thin film solar cell thus designed will be useful in fabrication of such cells with stacked configuration.

13.3 Development of NIR Absorbs

To date, much effort has been devoted to developing new low bandgap light absorbing materials for efficient OSCs. BHJ is the dominant device architecture used in different OSCs, in which the blended donor and acceptor materials are used as the active light harvesting layer to form a bi-continuous network structure. In such a structure, it requires: (1) the donor material to absorb as much light as possible to maximize light absorption efficiency; (2) both donor and acceptor materials with comparable high mobility of the two types of charge carriers to achieve high photocurrent density and high fill factor (FF); (3) the energy level difference between the highest occupied molecular orbital (HOMO) of the donor material and the lowest unoccupied molecular orbital (LUMO) of the acceptor material is optimized for open circuit voltage (Voc).

Researchers and scientists have many interests to develop a semitransparent OSCs. Unlike conventional solar cells that absorb visible and infrared light to generate power, this cell allows visible light to pass through it while absorbs UV and NIR radiation and converts it into electricity. In the near future, a low-cost, semitransparent OSC technology will be eventually proven viable that can be integrated onto window panes in homes, offices, and even automobiles, enhancing the functionality of already utilized transparent surfaces. Presently, window glass used in automobiles and in architectural installations is typically 70–80 % and 55–90 % transmissive, respectively, to visible light [19], with the reduction in light transmission introduced in the form of absorptive or reflective tinted windows. The additive semitransparent OSC technology can similarly modify the glass transparency, but the non-transmitted light would be utilized for power generation.

In order to realize high absorption in semitransparent OSCs with reasonable visible-transparency, novel photoactive polymers with enhanced absorption at UV region (e.g., λ = 350–500 nm) and NIR (e.g., λ = 700–900 nm) are desired. Such an absorption profile can be achieved by incorporating a wide bandgap segment into a low bandgap polymer backbone either in the side chains or as blocks in the backbone. A NIR absorbing OSC utilizing a molecular organic donor with peak-absorption in UV and NIR (λ = 650–850 nm) with visible-transparency of >55 % was reported recently via thermal evaporation [20]. This architecture suggests one possible strategy for high-efficiency power-generating windows and highlights an

application uniquely benefiting from excitonic electronics. However materials with absorption selectively in UV and NIR regions are required for semitransparent OSCs for making sun shading and solar power window applications possible [21].

For application in semitransparent OSCs, NIR absorbers are desired. The photoactive materials should ideally possess two strong absorption bands at UV-blue region (e.g., absorption peak located between 300 and 500 nm) and also NIR region (e.g., the absorption peak located between 700 and 900 nm). Such an absorption profile can be achieved by incorporation of a wide bandgap segment into a low bandgap polymer backbone either in the side chains or as blocks in the backbone, for example, using fused aromatic ring compounds, oligomers. This may be achieved by combing low bandgap and wide bandgap components into one structure through side chain or main chain approach. In order to achieve light absorption in the active layer and high transmission simultaneously for semitransparent OSCs, the development of novel NIR absorbing photoactive materials are required. The advantages of using NIR absorbing materials enable to use a relatively thick active layer with relatively high transmission in the visible wavelength region for application in semitransparent OSCs. In practical application, a thick photoactive layer, e.g., >250 nm, is preferred and is desirable for fabrication of large area OSCs using roll-to-roll printing process. Increasing the film thickness can largely enhance the reliability and reproducibility for large area OSC fabrication. For semitransparent OSCs with NIR absorbing type of photoactive materials, it is expected that $\sim$50 % of the transparency in the visible wavelength region can be expected while OSCs have relatively high absorption in the NIR region.

Various donor-acceptor type polymers with the optical bandgap in the range of 1.4–1.9 eV have been developed to improve light-harvesting efficiency of the solar light. However, the NIR absorbing conjugated semiconducting polymer with bandgap of 1.0–1.3 eV are rather rare. In addition to the optical bandgap, the choice of the electron-rich moieties provide a means to proper control of the position of the HOMO level of a donor material which is indispensable to achieve a large V_{OC} of an OSC and also directly related to the photostability of the semiconducting materials. Among various classes of NIR absorbers, the donor-acceptor (D–A) type of compounds with alternating electron-rich donor and electron-deficient acceptor units are particularly attractive as potential NIR chromophores because their bandgap, energy levels and other properties can be readily tuned through a systematic variation of the D and A units. A range of electron-deficient moieties will be chosen to afford D-A chromophores with electron-rich thiophene or triarylamine rings. Among these, naphtho[2,3-c] [1,2,5] thiadiazole, benzo[1,2-c; 4,5-c′]bis [1, 2, 5] thiadiazole and diketopyrrolopyrrole were shown to be excellent electron-deficient components for the production of low-bandgap conjugated polymers (1.4–1.6 eV) [22]. The squaraine dyes are also of attractive materials for various electronic and photonic applications including photoconductivity [23], OSCs [24], photodynamic therapy [25] and lasers [26] because of their remarkable oxygen and moisture stability, facile synthetic access and wide structural variations. The polysquaraines have theoretically and experimentally shown to be useful candidates for low-bandgap semiconducting polymers with a high conductivity

[27], they may have potential for application in semitransparent OSCs harvesting NIR emission. The use of the intramolecular charge transfer from an electron-rich unit to an electron-deficient unit has become a promising approach to obtain low bandgap polymers.

13.4 Upper Transparent Electrode and Device Optimization

13.4.1 Transparent Conducting Interlayer

Although the absorption coefficients for organic semiconductors are very high ($>10^5$ cm^{-1}), however, the absorption depth is usually greater than the diffusion range of the photo-generated excitons. Thus only a fraction of the excitons is able to diffuse to the donor-acceptor heterojunction interface at which exciton dissociation can take place. The low efficiency of OSCs comes from the nature of charge transportation and charge photogeneration within the organic materials. Poorer utilization of photo-generated excitons and exciton dissociation by rapid and efficient charge transfer usually cause the lower photocurrent. It has been recognized that the most efficient exciton dissociation in organic materials can occur at a D-A interface. Depending on the alignment of energy levels of the donor and acceptor, the dissociation of bound exciton can become energically favorable at the interface. The time scale for such a dissociation is of a few hundred femtoseconds, which is much shorter than any other competing process, thus the exciton dissociation (or charge transfer from the donor to the acceptor) efficiency could also be about 100 %. Therefore, the device efficiency will be mainly determined by the remaining two factors: exciton diffusion to a D-A interface and free charge transport to the opposite electrode. The possible approach to improve the exciton dissociation efficiency can be realized in OSCs through use of a thin blend layer of the donor and acceptor materials to form a BHJ junction.

The limited absorption of the sun spectrum and a relatively low open circuit voltage are the two main factors limiting the efficiency of single junction OSCs. In addition to search for new low band gap organic semiconducting materials for photovoltaic application, high performance stacked or tandem OSCs is highly desired. The basic idea for tandem OSCs is that each single sub-cell can be made very thin (20–40 nm), which has advantages for charge transport. The open circuit voltage will be added up. This aside, tandem OSCs can fully utilize the solar spectrum by stacking 2 or more different sub-cells which response to different parts in the solar spectrum. The quality of transparent inter electrode that integrates the two sub-cells plays an important role in determining the performance of the OSCs with stacked structure, with the absorption of the materials being complementary to each other, for example, with the top cell efficiently absorbing high energy light, and the lower absorbing in the low energy part of the spectrum. The transparent

inter electrode serves as a transparent cathode for one sub-cell and also functions simultaneously as an anode for the adjacent sub-cell. The top cells should be transparent so that any light not absorbed by the top cell can pass through it and captured by the lower one to broaden the utilization of the incident solar spectrum.

A variety of transparent cathodes such as conducting polymer [28], thin metallic layers [29], e.g., Sm (3 nm)/Au (12 nm) contact was used as the translucent cathode for semitransparent OSCs [30]. Recently transparent electrodes include rare-earth alloys (e.g., Yb:Ag, Sm:Ag etc.) for use in transparent organic light-emitting diodes (OLEDs) [31–33], and layers of graphene or graphene oxides for OSCs [34–36], have been reported. However, ultrathin metal as semitransparent electrode has some limitations for application in semitransparent OSCs as a high reflection at metal/air interface reduces the effective light absorption in the device. This aside, thin metal cathode is also not stable in air. Although graphene-based transparent electrode can be solution-processed and is suitable for large area process, its surface morphology and relatively poor conductivity as compared to the TCO are the technical challenges for application in semitransparent OSCs. A transparent cathode based on transparent conducting oxide (TCO) [37, 38] has been applied for semitransparent OSCs, which requires a transparent buffer layer on the polymer before sputtering of TCO. Apparently, development of high performance semitransparent OSCs with NIR organic active materials and improved transparent electrodes are desired.

13.4.2 Issues of Upper Transparent Electrode on Functional Organic Layers

In most OSCs, a thin metal upper transparent cathode, e.g., Al cathode, is often used. The use of metal oxide-based upper transparent electrode for application in semitransparent OSCs was also reported. Metal oxide-based cathode has much higher work function than Al. Using a high work function oxide upper electrode results in a change in the energy level alignment at the donor/acceptor junction and thus the device performance. The high work function would also reduce the built-in potential between the two electrodes. An appropriate selection of optimized semitransparent cathode is designed for application in semitransparent OSCs.

In addition to the use of ultra-thin metal and metal/ITO-based semitransparent cathode [34, 35], semitransparent cathodes, such as rare-earth based alloys of Yb:Ag, Sm:Ag etc. cathodes in transparent OLEDs [31–33] were also reported. More recently, graphene, metal oxides (e.g., NiO), metal/oxide multilayer and metal/oxide/TCO were also explored as possible transparent anode candidates for application in OLEDs and OSCs. It is expected that several issues would have to be addressed before they can be applied for use as transparent cathode for application in semitransparent OSCs. For example, in most OSCs, Al cathode is used. During the deposition of Al cathode, defects states would be generated in the exciton-blocking layer (EBL). It is considered that such defect states are essential for

electrode transportation through the EBL [39]. Replacing the Al cathode would suggest that there might be a problem in electron injection via the EBL. Some possible solutions are (i) deposition of an ultra thin layer of Al to create suitable defect states in the EBL before fabricating transparent cathode, (ii) application of special EBLs (e.g., Yb doped BPhen) which do not require the Al induced defect states. On the other hand, it has to be pointed out that most metal oxides has much higher work function than Al. Using such high work function oxides would change the energy level alignment at the donor/acceptor junction and thus the device characteristic. The high work function would also reduce the built-in potential between the two electrodes. These issues can be studied by photoelectron spectroscopy to determine the effects of oxide cathodes on the donor/acceptor energy level alignment. Based on these results, optimized semitransparent cathode can then be designed and optimized for application in semitransparent OSCs.

13.4.3 ITO-Based Upper Transparent Electrode

Thin films of ITO have been widely used as a transparent electrode in optoelectronic devices such as organic light-emitting diode (OLED) displays and solar cells because of the unique characteristics of high electrical conductivity and optical transparency over the visible light wavelength region. Generally, ITO thin films are deposited on the rigid glass substrates over a processing temperature range of 150–250 °C [40–46]. The present OSC technologies are focused on rigid substrates, such as glass, but flexible devices are getting more attention nowadays due to their lightweight, low cost, and flexibility. The success of the flexible OSC will open the possibility of fabricating devices by roll to roll processing, thus providing the basis for very-low-cost mass production. However, organic photoactive components set the limit of the ITO processing temperature below 150 °C [40]. ITO thin films formed at a processing temperature below 200 °C usually have relatively higher resistivity and poorer optical transparency than the films prepared at a higher substrate temperature. When ITO thin film is deposited on the functional organic layer, e.g., organic photoactive materials, the high temperature deposition process is not compatible with OSC process. Therefore the development of high quality ITO films with smooth surfaces, low resistivity and high transmission over the visible spectrum and at a low processing temperature, is of practical importance. There remains a need for high quality ITO-based cathode that can be fabricated at a low processing temperature for application in OSCs.

The requirement of transparent conducting recombination zone in tandem OSCs creates a need for the development of a high performance transparent conducting cathode. Many of the needs and requirements of transparent electrode extend beyond the conventional TCO, for example, ITO, characteristics of transparency and conductivity. Low process temperatures and increased process flexibility including high-rate, high conductivity and low cost are crucial for OSCs and other

organic electronic devices. For application in organic solar cells, the requirement of TCO-based transparent electrode must be formed on the photoactive layer or organic blend stack without damage to the functionality of the underlying organic materials. The deposition of TCO-based transparent electrode is also preferred to be formed without involving the postal annealing treatment or with a post-deposition process that is compactable with the solar cell process conditions. Amongst several TCO-based transparent upper electrodes thus reported, a low processing temperature ITO deposition technology has been successfully applied for application in semitransparent OSCs [34]. The low processing temperature ITO has the following advantages for semitransparent OSCs:

1. The upper ITO electrode can be prepared at low process temperatures without damage to the underlying functional polymer/organic layers.
2. The transparent cathode thus developed has high stability in air and can be fabricated at a relatively high deposition-rate using convention magnetron sputtering processes.
3. An upper ITO electrode deposition process must be scalable for mass production at a low-cost.

Thin film of ITO prepared at a processing temperature of over 200 °C is not suitable for application in semitransparent OSCs. The low processing temperature ITO technology developed using magnetron sputtering process was developed for fabricating an upper transparent electrode in semitransparent OSCs (the concept and the related technology can also be extended to include other TCO materials). A hydrogen-argon gas mixture was used for ITO deposition. The hydrogen partial pressure can be varied to modulate and optimize the properties of the ITO films. This technique enables fabricating an ITO-based electrode with smooth surface, high electric conductivity and optical transparency at process temperatures of less than 60 °C. The sheet resistance and resistivity of ITO films on a glass substrate as a function of hydrogen partial pressure are plotted in Fig. 13.2. Both the sheet resistance and resistivity decreased dramatically after introducing hydrogen into the

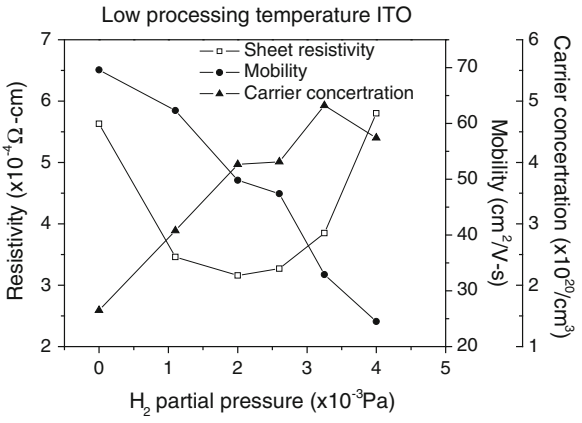

Fig. 13.2 Resistivity, carrier mobility and carrier concentration of low processing temperature ITO films as a function of hydrogen partial pressure in gas mixture

sputtering gas mixture. The use of a hydrogen-argon gas mixture allowed a broader process window for preparation of the ITO film with a high conductivity.

An ITO film of this type with a thickness of 130 nm exhibits a sheet resistance of 25 ± 5 Ω/sq and an average transmittance of above 85 %. With this technology, a high performance ITO-based upper cathode can be fabricated for application in organic electronics including OLEDs and OSCs. ITO-based upper electrode has a dual functions serving as a transparent electrode and an optical coupling layer tuning the optical properties in semitransparent OSCs, which enables to optimize the performance of semitransparent OSCs over the two competing performance indices: power conversion efficiency and transmittance, for stacking up or transparency.

The optical properties of ITO films prepared on glass substrates at different hydrogen partial pressures were also measured. The optical transmittance of the film was measured by a double beam spectrophotometer over the wavelength range from 200 to 1,000 nm. A blank glass substrate was used as a reference to subtract the baseline absorption from the glass substrate. Measured film transmittance over the visible wavelength range was also used to estimate the optical energy band gap of the films. Figure 13.3 shows the transmittance of a set of 210 nm thick ITO films as a function of hydrogen partial pressure. ITO films with average transmittance of 86, 89, 90 and 89 % over the visible wavelength of 400–800 nm were obtained at the hydrogen partial pressures of 0, 1.1×10^{-3}, 2.0×10^{-3} and 2.6×10^{-3} Pa, respectively. The hydrogen partial pressure that produced the most transparent ITO film was almost the same as that which gave the most conductive film as shown in Fig. 13.2. In this work, the ITO sputtering condition (hydrogen partial pressure: 2.6×10^{-3} Pa) which exhibited the best electrical and optical film properties was used for the fabrication of semitransparent OSCs.

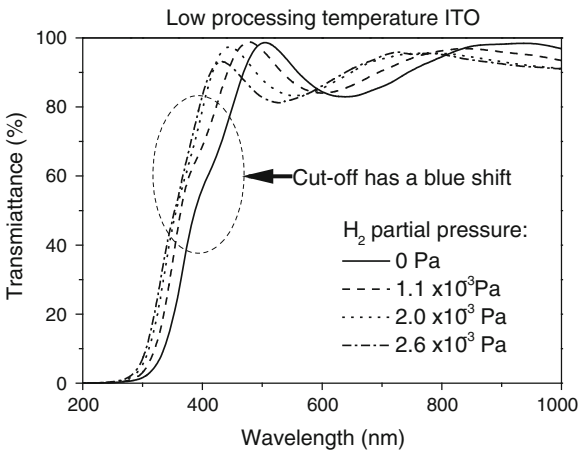

Fig. 13.3 Measured wavelength dependent transmittance of ITO thin films as a function of hydrogen partial pressure

13.4.4 Optical and Optimal Design of Semitransparent OSCs

From an optical point of view, a semitransparent OSC can be considered as a multilayer thin film system that is composed of absorbing and non-absorbing material layers. In order to improve the performance of semitransparent OSCs, it is essential to understand the effect of the active layer thickness on the transmission and absorption of light. For such a purpose, the structure of semitransparent OSCs, based on transfer matrix approach and optical admittance method, can be optimised using (13.10) and (13.11). Figure 13.4 shows a schematic cross-sectional view of a semitransparent OSC, where the NIR absorbing layer forms the cavity. NIR reflecting mirror, e.g., a dielectric distributed Bragg reflector (DBR) consisting of a stack of alternating low refractive index material, e.g., SiO_2 (n = 1.5), and high refractive index material, e.g., TiO_2 (n $\sim$ 2–2.6), can be used to achieve light trapping in semitransparent OSCs.

NIR reflecting mirror enables simultaneous optimization of the semitransparent OSC performance and transparency. By tuning the thickness of NIR mirror (it can be an asymmetric DBR), cavity length, it is possible to selectively trap photons of interest by the NIR absorbs, thereby to enhance the absorption in the semitransparent OSC cavity. The optical constants of the dielectric layers, transparent electrode and the NIR photoactive materials can be used for optical and optimal design of the device structure. The optimized thickness of each layer can be calculated for effectively trapping photons in a specific region and for the best solar cell performance.

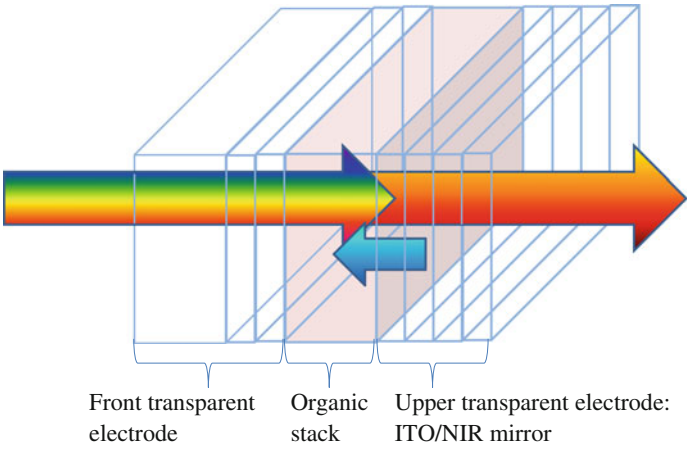

Fig. 13.4 A cross-sectional view of a semitransparent OSC using a front transparent electrode and a rear NIR mirror. NIR reflecting mirror enables simultaneous optimization of the semitransparent OSC performance and visible-light transparency

Based on the knowledge gained on optical and optimal design, emerging design concepts, e.g., inverted semitransparent OSCs, semitransparent OSCs with an upper NIR mirror and a bottom NIR mirror (or both) can be fabricated. The photovoltaic performance of anode- and cathode-illuminated semitransparent OSCs, that would not otherwise be possible in conventional opaque OSCs, can be studied. This approach also provides an effective, more in-depth understanding of exciton generation profile and charge transport properties in OSCs. The mechanisms of charge trapping and interfacial recombination can be studied in details by combining interfacial and charge transport results. Semitransparent OSCs with NIR absorbing materials are also of particular interest for application in window panes.

13.5 Semitransparent Solution-Processed Polymer OSCs

13.5.1 Basic Consideration of Semitransparent OSCs Having an Upper ITO Electrode

In order to achieve high photocurrent density in OSCs, different light harvesting approaches are used to improve light absorption in OSCs. In this section, we discuss simultaneous optimization of the cell performance and the visible-light transparency of solution-processed semitransparent OSCs, with a device configuration of glass/ITO/poly(styrene sulfonate)-doped poly(3,4-ethylene dioxythiophene) (PEDOT:PSS)/P3HT:PCBM blend/interlayer/upper-ITO- cathode. The upper cathode in semitransparent OSCs is much more demanding, serving as a charge collecting contact and a transparent conducting capping electrode to overcome the lateral current limitation. In this type of semitransparent OSCs, an electron collecting favorable interlayer is often used to improve the charge collection efficiency at the organic/cathode interface. The thickness of upper ITO electrode, prepared by radio frequency (RF) magnetron sputtering, can be optimized to enhance the visible-light transparency of semitransparent OSCs.

The implementation of low process temperature ITO as a cathode in semitransparent OSCs has advantages to increase light transmittance T(λ) of the device, but ITO deposition may also induce a possible damage to the underlying organic photoactive materials. Therefore, introducing a buffer layer at the polymer/upper-ITO-cathode interface is preferred, e.g., using an interlayer of metal oxide, an ultrathin metal or polymer layer. The interlayer has to be electrically favored to the device operation, and also serves a buffer to prevent possible damage to the underlying organic photoactive materials during ITO sputtering process. An amorphous carbon nitride (a-C:N) was reported serving as a buffer at organic/ITO interface in a semitransparent organic photodetectors [47]. A semitransparent OSC using bilayer compound cathode of Ag/ITO was reported [48]. It was observed that light transmission properties of the entire device can be varied by adjusting the thickness of the Ag interlayer. The average light transmission of 26 % with a PCE of 0.62 % was

obtained for a 10 nm thick Ag interlayer whereas light transmission of 60 % with a PCE 0.28 % was achieved without the Ag interlayer. The low power conversion efficiency without the Ag layer was attributed to the relatively low light absorption in the active layer of the semitransparent OSCs. However, the effect of the thickness of upper ITO electrode on the performance of the semitransparent OSCs was not discussed.

The integrated absorptance, A(λ) and the T(λ) of the semitransparent OSCs with the structure of glass/ITO/PEDOT:PSS/P3HT:PCBM/interlayer/upper-ITO cathode can be analyzed and optimized prior to the device fabrication. The optimal device structure can be obtained by maximizing light absorption of the active layer, in this case a P3HT:PCBM-based photoactive blend, and the transmission of the semitransparent OSCs. This simulation uses the dispersive refractive index and extinction coefficient of the materials that measured from the ellipsometry. In this work, an ultrathin Ca/Ag interlayer was used. It is observed that the semitransparent OSC with an upper cathode combination of Ca(10 nm)/Ag(10 nm)/ITO is superior to a thin transparent metal cathode. A semitransparent OSC with only a bilayer metal cathode, e.g., Ca(10 nm)/Ag(10–15 nm), causes a large internal reflection at the metal/air interface due to its high refractive index. The upper ITO cathode serves as a transparent conducting index matching layer to enhance the total light transmission in semitransparent OSCs. In addition, the upper ITO contact also acts as a passivation layer to protect the underlying functional organic layers in semitransparent OSCs from any possible moisture attack from the environment.

A blend of P3HT (from Sigma Aldrich) and PCBM (from American Dye Source) was used as light harvesting active layer in our P3HT:PCBM-based OSCs. P3HT and PCBM were dissolved in dichlorobenzene at a concentration of 15 mg P3HT and 12 mg PCBM per ml (ratio 1:0.8). 160 nm thick ITO coated glass substrates (from Merck Display Technologies), with a sheet resistance of $\sim 10\ \Omega$/sq, were used for the device fabrication. The wet-cleaned ITO substrates were pre-annealed at 100 °C in an ozone cleaner prior to spin coating a 40 nm thick PEDOT:PSS hole transporting layer. P3HT:PCBM blend layer with different layer thicknesses were then spin-coated in a glove box under nitrogen atmosphere. The cathode layer was evaporated through a shadow mask at 8×10^{-5} Pa pressure to form OSCs with an active area of 9.0 mm^2. A high electric conductivity and optical transparent ITO layer was sputtered right after the Ca and Ag evaporation using an argon-hydrogen gas mixture at a room processing temperature. The upper transparent cathode deposition is conducted in a vacuum condition. The thickness of the upper ITO layer can be controlled by the deposition time and is optimized in order to enhance simultaneously light harvesting and the transmission in semitransparent OSCs.

Device characterization was carried out in a glove box under nitrogen atmosphere with water and oxygen levels less than 1 ppm. The current density–voltage (J–V) characteristics of the OSCs were measured using a simulated AM1.5 solar simulator with a calibrated power density (100 mW/cm^2) and recorded using a Keithley 2,400 source measure meter. The OSCs were illuminated from the glass side.

13.5.2 Simultaneous Optimization of Cell Performance and Visible-Light Transmissivity

The optical properties of a conventional opaque OSC (control cell), with the type of glass/ITO/PEDOT:PSS/P3HT:PCBM(25–300 nm)/Ca(10 nm)/Ag(100 nm), were calculated using the optical admittance analysis for comparison studies. An ultra-thin interlayer of calcium in OSCs serves as a work function matching contact for improving the electron collection property. The correlation between the integrated absorbance in the P3HT:PCBM blend layer and its thickness range from 25 to 300 nm for an opaque control OSC is shown in Fig. 13.5. The results show clearly that the absorbance in the P3HT:PCBM blend layer has an oscillation behavior in relation to its layer thickness. The relative maximum absorption peaks are located at the P3HT:PCBM layer thickness of 75 and 200 nm respectively. The calculation agrees with the reported results in showing that a 200 nm thick active layer is suitable for P3HT:PCBM based OSCs [48].

The integrated absorbance and the total transmittance as a function of P3HT:PCBM layer thickness for semitransparent OSCs of the type: glass/ITO/P3HT:PCBM(25–300 nm)/Ca(10 nm)/Ag(10 nm)/upper-ITO-electrode, were also calculated. The integrated transmittance and absorptance of the semitransparent OSCs as a function of the P3HT:PCBM active layer thickness are shown in Fig. 13.6. The oscillating behavior in the integrated absorbance relating to the P3HT:PCBM blend layer thickness in a semitransparent OSC is weaker compared to a control OSC, as shown in Fig. 13.5, due to the poor internal reflection at P3HT:PCBM/upper-ITO electrode interface. In order to performance a realistic simulation, a 10 nm thick Ag layer in the calculation of the optical properties for semitransparent OSCs is also considered. In the device application, a thin silver layer is used to improve the lateral electrode conductivity and also prevents the possible damage to the underlying calcium and polymer blend during the ITO deposition. It shows that the

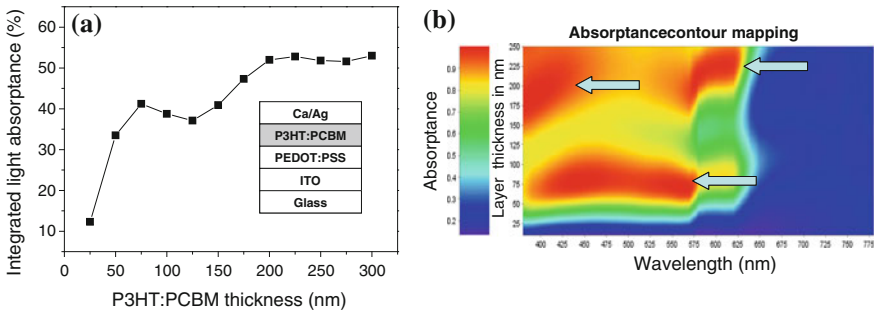

Fig. 13.5 Calculated integrated absorptance as a function of the P3HT:PCBM layer thickness for a control OSC of the type: glass/ITO/PEDOT:PSS(40 nm)/P3HT:PCBM(25–300 nm)/Ca(10 nm)/Ag(100 nm). The corresponding contour map of light absorbance calculated for the control OSC is also shown

transmittance of a semitransparent OSC decreases from about 50 to 25 % when the thickness of the P3HT:PCBM layer increases from 25 to 300 nm. According to the simulation results shown in Figs. 13.5 and 13.6a, a 75 nm thick active layer of P3HT:PCBM for a semitransparent OSC is chosen. This is because a thinner OSC, e.g., a relative maximum light absorption occurred at a 75 nm P3HT:PCBM layer, enables to achieve good charge transport properties and also possesses a reasonable visible-light transparency. For example, a semitransparent OSC having an integrated absorptance of 34 % in the P3HT:PCBM layer possesses a visible-light transparency of 42 %, as shown in Fig. 13.6a. A photo picture taken for a semitransparent OSC having an optimized device structure of glass/ITO/PEDOT:PSS (40 nm)/P3HT:PCBM(75 nm)/Ca(10 nm)/Ag(10 nm)/ITO(60 nm) is shown in Fig. 13.6b.

In practical application, a semitransparent OSC with an optimized Ca(10 nm)/Ag (10 nm)/ITO cathode can be more preferred than a layer of a thin transparent metal cathode. A semitransparent OSC finished with a thin metal cathode, e.g., Ca (10 nm)/Ag(10–15 nm), causes a large internal reflection at the metal/air interface due to its high refractive index. When an upper cathode of Ca(10 nm)/Ag(10 nm)/ ITO is used, the unique electric and optical properties of ITO capping layer enable it functions as a transparent conducting index matching layer to enhance the total light transmission. This aside, ITO layer also acts as an upper passivation layer to protect the OSCs.

The effect of upper ITO electrode thickness on the total transmittance and integrated absorbance of P3HT:PCBM layer in the semitransparent OSCs is analyzed. The calculated results are plotted in Fig. 13.7. For a semitransparent OSC with a configuration of glass/ITO/PEDOT:PSS(40 nm)/P3HT:PCBM(75 nm)/Ca (10 nm)/Ag(10 nm)/upper-ITO, the results indicate that a maximum transmittance

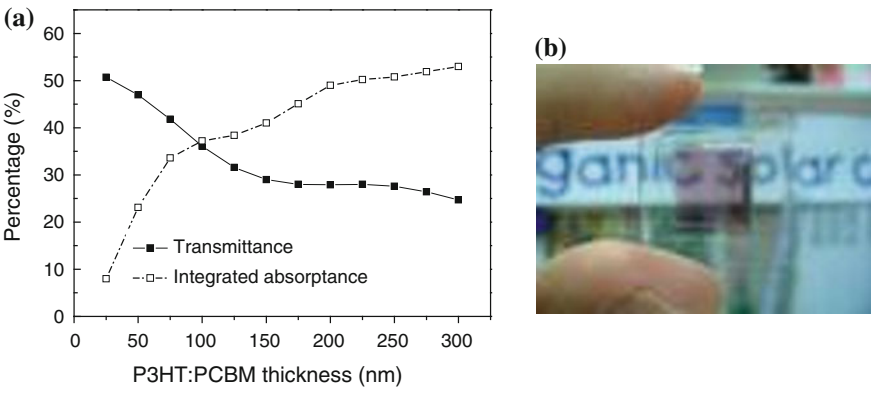

Fig. 13.6 **a** Calculated transmittance and integrated absorptance as a function of the P3HT:PCBM active layer thickness for semitransparent OSCs of the type: glass/ITO/PEDOT: PSS(40 nm)/ P3HT:PCBM(25–300 nm)/Ca(10 nm)/Ag(10 nm)/ITO(60 nm). **b** A photo picture showing a semitransparent OSC having an optimized cell structure of glass/ITO/PEDOT:PSS(40 nm)/P3HT: PCBM(75 nm)/Ca(10 nm)/Ag(10 nm)/ITO(60 nm)

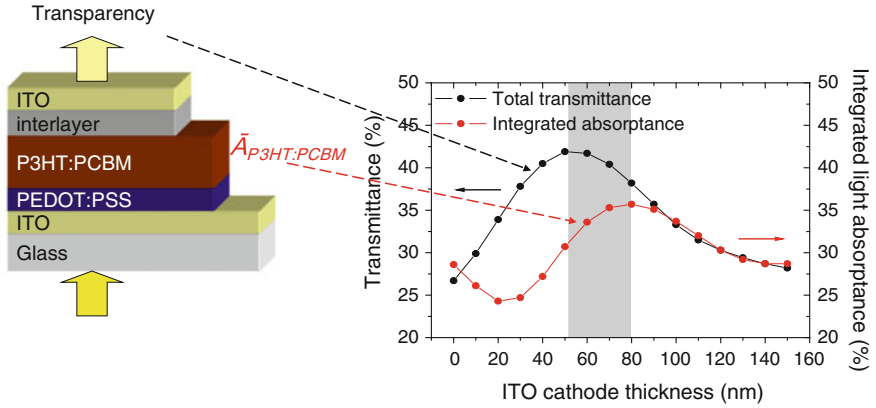

Fig. 13.7 Calculated results showing the effect of the upper ITO layer thickness on the integrated absorbance of P3HT:PCBM layer and the transmittance of a semitransparent OSC of the type: glass/ITO/PEDOT:PSS(40 nm)/P3HT:PCBM(75 nm)/Ca(10 nm)/Ag(10 nm)/ITO(0–160 nm)

of the semitransparent OSCs can be achieved at an upper ITO cathode thickness of 50 nm, whereas the maximum light absorption is occurred in P3HT:PCBM (75 nm) at an upper ITO cathode thickness of 80 nm. In order to illustrate the point clearly, a gray region is depicted in Fig. 13.7, which corresponds to an ITO layer thickness chosen in the region that could result in an OSC achieving possible maximum light absorption and transmission simultaneously. As a result, a 60 nm thick upper ITO is selected for OSCs with a configuration of glass/ITO/PEDOT:PSS(40 nm)/P3HT:PCBM(75 nm)/Ca(10 nm)/Ag (10 nm)/ITO (60 nm). This leads to a total transmittance 42 % and an integrated absorbance of 34 % for the resulting semitransparent OSCs.

The wavelength dependent transmittance, T(λ), of the semitransparent OSCs with two different cathode structures of Ca(10 nm)/Ag(10 nm) and Ca(10 nm)/Ag (10 nm)/ITO(60 nm) was also calculated. The simulated and measured T(λ) of semitransparent OSCs made with two different cathode structures of Ca(10 nm)/Ag (10 nm) and Ca(10 nm)/Ag(10 nm)/ITO(60 nm) are shown in Fig. 13.8a. It can be seen clearly that semitransparent OSCs with an upper transparent cathode of Ca (10 nm)/Ag(10 nm)/ITO(60 nm) possess a higher T(λ) throughout the whole visible light wavelength region as compared to a structurally identical semitransparent OSC having a thin layer Ca(10 nm)/Ag(10 nm) cathode. The Ca(10 nm)/Ag(10 nm) cathode in semitransparent OSC causes a large amount of internal reflection at the metal/air interface, leading to a low T(λ). The visible-light transparency of the semitransparent OSCs with an upper ITO capping layer, e.g., simulated (solid black line) and measured (solid red line) in Fig. 13.8a, is higher than that of the semitransparent OSC having an upper Ca(10 nm)/Ag(10 nm) cathode, e.g., simulated T (λ) in Fig. 13.8a. The measured T(λ) of the semitransparent OSCs having ITO capping layer does not overlap exactly as compared to that of the simulated T(λ) obtained for the same device, the deviation in the T(λ) between the experimental

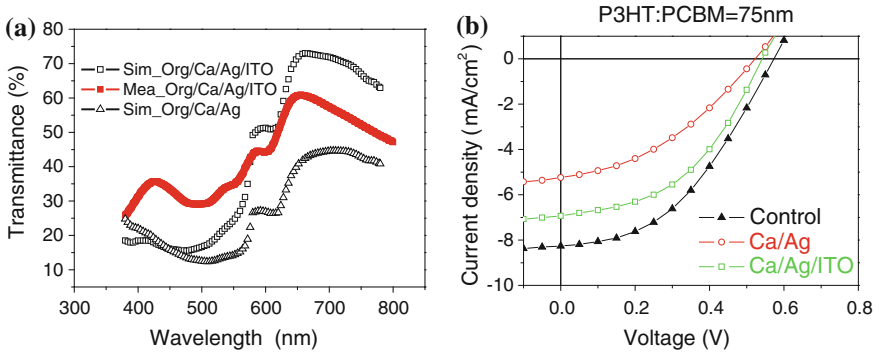

Fig. 13.8 **a** Transmission spectra calculated for two structurally identical semitransparent OSCs with Ca(10 nm)/Ag(10 nm) and Ca(10 nm)/Ag(10 nm)/ITO(60 nm) upper cathodes, respectively. The *solid square symbols* represented the transmission spectral measured for semitransparent OSCs made with a Ca(10 nm)/Ag(10 nm)/ITO(60 nm). **b** A comparison of J–V characteristics measured for a control OSC, semitransparent OSCs with upper cathodes of Ca(10 nm)/Ag(10 nm) and Ca(10 nm)/Ag(10 nm)/ITO(60 nm)

and calculated transparency in the semitransparent OSCs may be attributed to the assumption of a perfect film smoothness, while the non-homogeneity of the organic thin films may be possible in the actual OSCs. From the above discussion, it is clear that the structure and the process optimization of ITO-based cathode are very important for the design and fabrication of high performance semitransparent OSCs. Simultaneous optimization of cell performance and visible-light transparency for a semitransparent OSC can be realized.

Based on the knowledge gained on the improved upper transparent cathode and emerging cell design concepts, semitransparent OSCs with different upper cathode contacts were fabricated and characterized. The performance of a control OSC with the configuration of glass/ITO/PEDOT:PSS(40 nm)/P3HT:PCBM(75 nm)/Ca (10 nm)/Ag(100 nm) was also analyzed for comparison studies. The J–V characteristics measured for a control OSC and two structurally identical semitransparent OSCs with different upper transparent cathodes of Ca(10 nm)/Ag(10 nm) and Ca (10 nm)/Ag(10 nm)/ITO(60 nm) were measured using a calibrated AM1.5 solar simulator in the nitrogen glove box. The results are plotted in Fig. 13.8b.

According to the J–V characteristics, as shown in Fig. 13.8b, the control OSC yielded a higher current density of 8.22 mA/cm^2 in comparison with that of the semitransparent OSCs with Ca(10 nm)/Ag(10 nm) cathode (Jsc = 5.20 mA/cm^2) and Ca(10 nm)/Ag(10 nm)/ITO(60 nm) (Jsc = 6.89 mA/cm^2). It is shown that the fill factor of a semitransparent OSC with a cathode of Ca(10 nm)/Ag(10 nm) is lower than that of a semitransparent OSC having an upper Ca(10 nm)/Ag(10 nm)/ITO(60 nm) transparent cathode and a control OSCs, which limits the power conversion efficiency. The increase in the photocurrent density of the semitransparent OSC with a cathode of Ca(10 nm)/Ag(10 nm) in the forward bias region is slightly lower than that measured for semitransparent OSC with a Ca(10 nm)/Ag

(10 nm)/ITO(60 nm) cathode and the control OSC. This implies that the semitransparent OSC with only a thin metal cathode has a higher series resistance than the one having a Ca(10 nm)/Ag(10 nm)/ITO(60 nm) upper cathode. It is clear that semitransparent OSCs with a Ca(10 nm)/Ag(10 nm)/ITO(60 nm) cathode also possesses a high Voc as compared to the semitransparent OSC with a thin metal cathode. The decrease in Voc observed in semitransparent OSCs without upper ITO capping layer could be attributed to the poor contact at organic/Ca/Ag interface, as a total 20 nm thick Ca/Ag stack formed on the polymer blend is likely discontinuous. A summary of the device performance measured for a control cell, and the semitransparent OSCs with different upper cathodes is summarized in Table 13.1.

In additional to the study of optical properties of semitransparent OSC structure for optimizing the transparency and the performance, the interfacial properties at the cathode/organic interface in semitransparent OSCs also play an important role in determining the overall cell performance. For example, the relatively poor fill factor in the semitransparent OSCs as compared to the control cell, as shown in Fig. 13.8b, could be related to the deterioration of the contact quality at organic/upper-transparent-cathode interface. It is possible that a thin layer of poor conducting CaO may be formed at the organic/Ca/Ag interface, leading to an increase in series resistance in semitransparent OSCs. The possible formation of a CaO interlayer occurred at organic/cathode in the semitransparent OSCs was analyzed using time-of-flight secondary ion mass spectroscopy (TOF-SIMS) technique. The TOF-SIMS measurements were performed using Ar^+ at 3 keV and analyzed using Ga^+ at 25 keV over a detecting area of 200 × 200 μm^2 on a control and semitransparent OSCs with different cathode contacts. In particular, the changes in calcium ions at cathode/organic interface in control and semitransparent OSCs were recorded. TOF-SIMS depth profiles measured for a control cell and semitransparent OSCs with two different cathodes of Ca(10 nm)/Ag(10 nm) and Ca(10 nm)/Ag (10 nm)/ITO(60 nm) are given in Fig. 13.9a, b.

As shown in Fig. 13.9a, the intensity of the metallic calcium detected at the organic/Ca(10 nm)/Ag(100 nm) interfacial region in a control OSC is much higher than the ion counts contributed from CaO species. The predominant portion of metallic calcium as compared to the calcium ions from its oxide reveals clearly that the metallic calcium interlayer was dominated at the cathode/organic interface in a control OSC. This implies that the calcium contact in the control cell was well protected by overlaying a 100 nm thick Ag layer, resulting in a good ohmic contact.

Table 13.1 A summary of device characteristics measured for a control OSC and semitransparent OSCs with and without the upper ITO capping layer

Device #	Voc (V)	Jsc (mA/cm^2)	FF (%)	PCE (%)
Control OSC	0.57	8.22	43	2.02
Semitransparent OSC without upper ITO layer	0.52	5.20	38	1.04
Semitransparent OSC with upper ITO layer	0.54	6.89	46	1.70

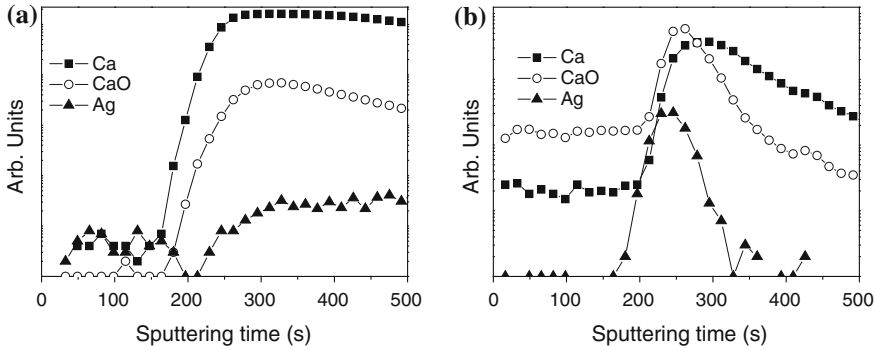

Fig. 13.9 TOF-SIMS depth profiles measured for **a** a control OSC having a conventional opaque Ca(10 nm)/Ag(100 nm) cathode, and **b** a semitransparent OSC having an upper Ca(10 nm)/Ag (10 nm)/ITO(60 nm) cathode

This analysis agrees with the J–V characteristic measured for control OSC as discussed above.

Figure 13.9b shows the TOF-SIMS depth profile measured for a semitransparent OSC finished with an upper Ca(10nm)/Ag(10nm)/ITO(60 nm) cathode. As compared to results given in Fig. 13.9a, it can be seen clearly that there is a reduction in the ratio of the metallic calcium ion intensity to the calcium species derived from the calcium oxide. The relative increase in the calcium oxide suggests that an oxidized calcium interlayer could have formed, which might by induced by the ITO deposition. By analyzing the location of the calcium oxide species in the TOF-SIMS depth profile, a poor conductivity calcium oxide layer could be formed within this semitransparent cathode, resulting in light increase in the series resistance in semitransparent OSC. Although a 10 nm thick Ag interlayer was covered on Ca contact a thin oxidized calcium interlayer may be formed, which was induced by the ITO deposition. This work reveals that a careful control of an ITO deposition is required in order to form a good cathode contact in semitransparent OSCs. With the results we have obtained so far, it shows that the structure semitransparent OSCs and the deposition of high quality ITO based upper cathode are very important for simultaneous optimization of cell performance and transparency.

13.6 Semitransparent Small Molecule Solar Cells

13.6.1 Semitransparent OSCs with an Upper DC-Sputtered ITO Electrode

In previous section, realization of high performance solution-processed semitransparent OSCs using an upper RF-sputtered ITO electrode is discussed. The device concept and optimization approach can also be applied for the design of high

performance small molecule-based semitransparent OSCs. Although RF magnetron sputtered-ITO was demonstrated for making small sized semitransparent OSCs, a scalable ITO cathode that can be fabricated with direct current (DC) magnetron sputtering has a great impact for potential mass production at a low-cost, a thin film deposition process that is widely adopted by ITO coating industry. This section describes the design, fabrication and characterization of efficient semitransparent BHJ OSCs based on zinc phthalocyanine (ZnPc): fullerene (C_{60}) system using an upper DC sputtered-ITO upper transparent cathode. The upper transparent cathode consists of an ultrathin Ag/LiF interlayer and an upper ITO capping layer. It has been found that a transparent cathode of Ag(20 nm)/LiF(5 nm)/DC-sputtered-ITO is a suitable top transparent cathode for semitransparent OSCs. It is shown that a combined Ag(20 nm)/LiF(5 nm) interlayer helps to produce a good interfacial property at organic/cathode interface favorable for application in semitransparent OSCs. The interlayer is to improve the charge collection efficiency at organic/upper-cathode interface, while the upper DC-sputtered ITO serves as an index matching layer to enhance light in-coupling efficiency in semitransparent small molecule OSCs, and also improves lateral current spreading due to its superior optical transparency and high electric conductivity. The upper DC-sputtered ITO electrode was formed without the post annealing to avoid possible deterioration of the underlying functional organic layers. The simultaneous optimization of cell performance and visible-light transparency in the ZnPc:C_{60}-based semitransparent OSCs is also realized using an optical admittance analysis.

An oxidized target (6 in. in diameter) with In_2O_3 and SnO_2 in a weight ratio of 9:1 was employed for the deposition of the top ITO electrode. The top ITO electrode was prepared by DC magnetron sputtering with a power of 10 W, the deposition rate was estimated to be about 2 nm/min. The base pressure in the sputtering system was approximately 2.0×10^{-4} Pa. During the film deposition, an argon-hydrogen gas mixture was employed. The argon partial pressure was set at $\sim 2.9 \times 10^{-1}$ Pa, the hydrogen partial pressure was varied from 1.1×10^{-3} Pa to 4.0×10^{-3} Pa to modulate and optimize the properties of ITO films. The thickness of the upper ITO electrode was controlled by varying the deposition time.

BHJ ZnPc:C_{60}-based OSCs with a structure of ITO/ZnPc:C_{60}(35 nm)/C_{60}(25 nm)/BPhen (7 nm)/Ag(20 nm)/LiF(5 nm)/upper-ITO-electrode were fabricated on commercial ITO-coated (thickness $\sim$150 nm, sheet resistance $\sim 10\ \Omega$/sq) glass substrates. The ITO substrates were cleaned using acetone, isopropanol and de-ionized water in an ultra-sonicator. This was followed by oxygen plasma treatment. A 35-nm-thick photoactive blend layer of ZnPc (donor):C_{60} (acceptor) in a volume ratio of 1:1 was deposited via co-evaporation on the ITO substrate. Next, a 25-nm-thick C_{60} acceptor layer was deposited on the ZnPc:C_{60} blend followed with a 7-nm-thick (BPhen) exciton-blocking layer. The fabrication of semitransparent OSCs was then completed by overlaying an upper cathode Ag(20 nm)/LiF (5 nm)/ITO, on the stack of organic layers. A control OSC with an identical organic layer structure but finished with a 100 nm thick Ag cathode was also made for comparison studies. The ZnPc, C_{60}, BPhen, LiF and metal layers were thermally evaporated in a vacuum chamber with a base pressure of $\sim 10^{-5}$ Pa. Both

semitransparent and control OSCs had the same active area of 3 mm × 3 mm. J–V characteristics of the OSCs were measured under AM1.5G illumination at 100 mW/cm^2. The possible designs to improve the performance of semitransparent OSCs over the two competing indexes of power conversion efficiency and transmittance are discussed.

13.6.2 Performance of Semitransparent OSCs Based on ZnPc:C_{60} Photoactive Layer

The upper ITO electrode in semitransparent OSCs must meet the requirements of high conductivity, good stability in film conductivity, good contact with and no damage to the underlying organic/inorganic layer. The dispersive refractive index and extinction coefficient of the materials are used to calculate the optical absorbance and transmittance of the semitransparent OSCs. The wavelength dependent refractive index, n(λ), and extinction coefficient, k(λ), of thin films of ITO, ZnPc, C_{60}, BPhen and ZnPc:C_{60} mixture were measured using variable angle spectroscopic ellipsometry, n(λ) and k(λ) as a function of the wavelength measured for the photoactive layer of ZnPc:C_{60} are plotted in Fig. 13.10a. The dispersive complex refractive index of Ag and LiF used for the simulation of the optical properties of devices were taken from the reference [49]. Figure 13.10b illustrates the calculated results of light distribution at a wavelength of 630 nm in a semitransparent ZnPc:C_{60}-based OSC. The thicknesses of ZnPc:C_{60} active layer and upper ITO electrode are optimized simultaneously for achieving absorption enhancement and visible-light transparency for semitransparent OSCs. For the given material system, maximum light absorption occurs at the 35 nm-thick ZnPc:C_{60} active region.

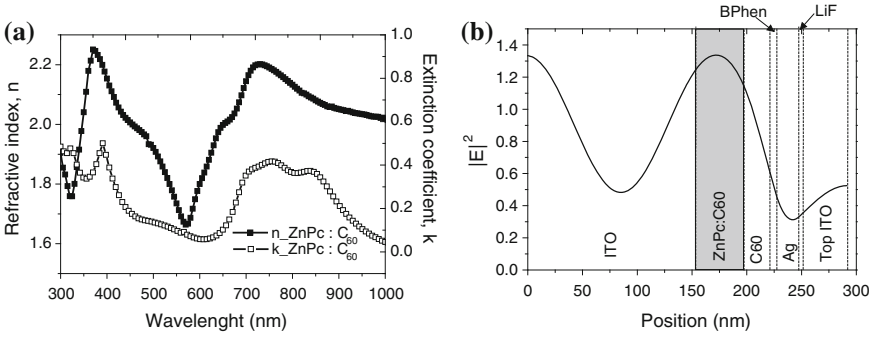

Fig. 13.10 **a** Plots of dispersive refractive index and extension coefficient of ZnPc:C_{60} blend layer as a function of wavelength, measured by the variable angle spectroscopic ellipsometry. **b** Calculated square of electromagnetic field distribution (at λ = 630 nm) in a semitransparent OSCs of the type: glass/ITO/ZnPc:C_{60}(35 nm)/C_{60}(25 nm)/BPhen(7 nm)/Ag(20 nm/LiF(5 nm)/ITO(40 nm)

The optical properties of a control OSCs with a structure of glass/ITO/ZnPc:C_{60}/C_{60}/BPhen/Ag(100 nm) is also analyzed for comparison studies.

The upper ITO electrode is optimized to enhance light harvesting in the active layer as well as the transmission of the semitransparent OSCs. The calculated total transmittance and integrated absorptance in a 35 nm thick ZnPc:C_{60} as a function of top ITO electrode thickness for semitransparent OSCs of glass/ITO/ZnPc:C_{60}(35 nm)/C_{60}(25 nm)/BPhen (7 nm)/Ag(20 nm)/LiF(5 nm)/ITO(0–100 nm) are shown in Fig. 13.11. The shaded area in Fig. 13.11 indicates a region where high transparency OSCs with reasonable light absorption can be expected if the upper ITO layer is chosen within this film thickness range. The results indicate that high transparency semitransparent OSCs can be achieved at an ITO layer thickness of 40 nm, whereas relative maximum light absorption in active layer occurs at an ITO thickness of 140 nm. In order to achieve higher visible-light transparency, a combination of Ag(20 nm)/LiF (5 nm)/ITO(40 nm) cathode was selected for application in the semitransparent OSCs, resulting in a total transmittance of 42 % and an integrated absorptance of 26 %.

Light transmission of a semitransparent OSC of glass/ITO/ZnPc:C_{60}(35 nm)/C_{60}(25 nm)/BPhen (7 nm)/Ag(20 nm)/LiF(5 nm)/ITO(40 nm) was also measured. As shown in Fig. 13.12, the measured transmission agrees well with the one calculated using the optical admittance method. An insert picture in Fig. 13.12 is a photo taken for an actual semitransparent OSC of glass/ITO/ZnPc:C_{60}(35 nm)/C_{60}(25 nm)/BPhen (7 nm)/Ag(20 nm)/LiF(5 nm)/ITO(40 nm) thus designed, showing its green tint, transparency, and possibility for dual-sided illumination. Semitransparent small molecule OSCs, as illustrated in Fig. 13.12, also block most ultraviolet (UV) and infrared (IR) irradiation from sunlight. This is because the transmission of UV (<380 nm) and IR light (>800 nm) in this type of

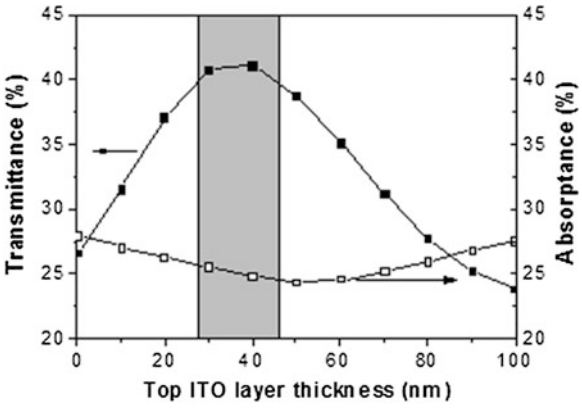

Fig. 13.11 Calculated results showing the effect of the upper ITO electrode thickness on the integrated absorptance of the ZnPc:C_{60} layer and the overall transmittance of semitransparent OSCs of the type: glass/ITO/ZnPc:C_{60}(35 nm)/C_{60}(25 nm)/BPhen(7 nm)/Ag(20 nm)/LiF(5 nm)/ITO(0–100 nm)

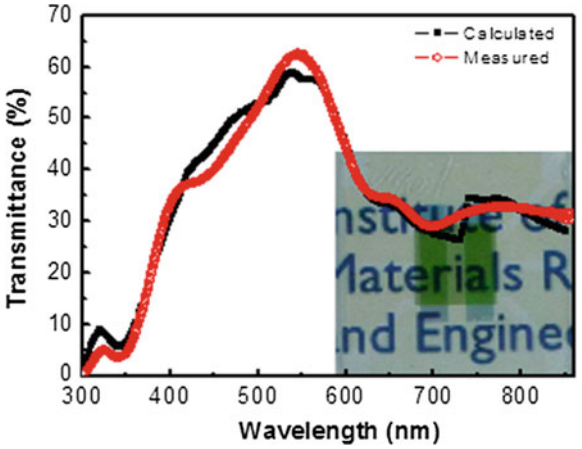

Fig. 13.12 Comparison of calculated and measured transmission spectra of a semitransparent OSC of glass/ITO/ZnPc:C_{60}(35 nm)/C_{60}(25 nm)/BPhen(7 nm)/Ag(20 nm)/LiF(5 nm)/ITO(40 nm). An *inset* picture is a photo taken for a semitransparent OSC fabricated according to the cell structure thus optimized, showing its transparency and possibility for dual-sided illumination

semitransparent OSCs is less than 20 and 30 % respectively. The color, semitransparency, shielding from UV and IR irradiation also add a decorative, aesthetic and practical dimension to these solar cells.

The J–V characteristics measured in the dark and under simulated AM1.5G illumination of 100 mW/cm^2 for a semitransparent OSC of glass/ITO/ZnPc:C_{60}(35 nm)/C_{60} (25 nm)/BPhen(7 nm)/Ag(20 nm)/LiF(5 nm)/ITO(40 nm) and a control OSC of glass/ITO/ZnPc:C_{60}(35 nm)/C_{60} (25 nm)/BPhen(7 nm)/Ag(100 nm) are plotted in Fig. 13.13. The control OSC had a J_{SC} of 11.8 ± 0.3 mA/cm^2, a FF of 60 ± 1 %, a V_{OC} of 0.56 V and a PCE of 4.0 ± 0.2 %. The errors correspond to the standard deviation calculated from 5 sets of OSCs fabricated under identical conditions. In comparison, the semitransparent OSCs had a J_{SC} of 9.6 ± 0.2 mA/cm^2, a FF of 57 ± 1 %, a V_{OC} of 0.55 V and a PCE of 3.0 ± 0.1 %. As both semitransparent and control OSCs had an identical organic layer structure and were made in the same system using the same sets of the process conditions, the same V_{OC} value obtained for both semitransparent and control OSCs suggests that the contact property at the organic/cathode interface for charge collection in semitransparent OSCs and control cells is very similar. There was no observable reduction in Voc for semitransparent OSCs. However a ~20 % decrease in J_{SC} measured for semitransparent OSCs can be observed as compared to the control device. Such a reduction in photocurrent is expected due to the use of an upper transparent electrode, as there is more than 35 % of the incident light being transmitted through the semitransparent OSCs (see Fig. 13.12).

A summary of photovoltaic characteristics measured for structurally identical OSCs with cathodes of Ag(20 nm)/LiF(5 nm)/ITO(40 nm) and Ag(100 nm) is listed in Table 13.2. The results of this work have yielded an optical transparency

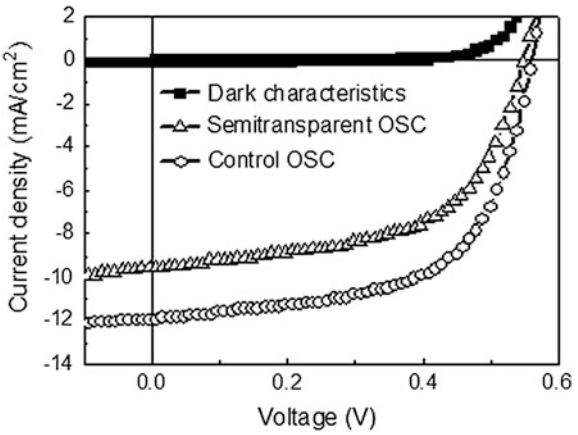

Fig. 13.13 J–V characteristics of a semitransparent OSC of glass/ITO/ZnPc:C_{60}(35 nm)/C_{60}(25 nm)/Bphen(7 nm)/Ag(20 nm)/LiF(5 nm)/ITO(40 nm) and a control OSC of glass/ITO/ZnPc: C_{60}(35 nm)/C_{60}(25 nm)/BPhen(7 nm)/Ag(100 nm) measured in the dark and under the simulated AM1.5G illumination of 100 mW/cm^2

Table 13.2 A summary of photovoltaic characteristics measured for a semitransparent OSC of glass/ITO/ZnPc:C_{60}(35 nm)/C_{60}(25 nm)/Bphen(7 nm)/Ag(20 nm)/LiF(5 nm)/ITO(40 nm) and a control OSC of glass/ITO/ZnPc:C_{60}(35 nm)/C_{60}(25 nm)/BPhen(7 nm)/Ag(100 nm) measured in the dark and under the simulated AM1.5G illumination of 100 mW/cm^2

Device #	Voc (V)	Jsc (mA/cm^2)	FF (%)	PCE (%)
Control OSC	0.56	11.8 ± 0.3	60 ± 1	4.0 ± 0.2
Semitransparent OSC	0.55	9.6 ± 0.2	57 ± 1	3.0 ± 0.1

of >40 % and a power conversion efficiency of ~3 % for a semitransparent OSCs using a ZnPc:C_{60}-based photoactive layer and a compound Ag(20 nm)/LiF(5 nm)/ITO(40 nm)-based upper cathode. It is envisaged that the quality of an upper ITO electrode thus developed for semitransparent OSCs can also be used for application in inverted or tandem OSCs, semitransparent white OLED lighting and organic sensors etc.

13.6.3 Monolithic Integration of a Semitransparent OSC with an OLED

OLEDs and OSCs can be made translucent when both transparent anode and cathode are used. The accomplishment of semitransparent OSCs and semitransparent OLEDs offers potentially great freedom for integration of semitransparent OSC and OLED units for new applications. The integration of an OLED with other

functional organic electronic device components has also attracted great interests due to its process flexibility and enhanced performance for new device concept [50]. In a conventional OLED, the metal electrode acts collectively like a mirror leading to a high ambient light reflection. This causes the OLED-based emissive displays to exhibit a poor legibility. The integration of OLED with an OSC in a stacked geometry results in high visual contrast in OLED [51, 52]. The rear OSC component in the stacked OLED/OSC device architecture serves as light absorber to eliminate the reflection from ambient light and to improve the visual contrast of the emissive source.

The similar idea of stacked OLED/OSC devices has also been explored for possible application in optical sensor and energy-circle optoelectronic components using ambient illumination, though such integration still faces some challenges [53–56]. One of them is to achieve an optical matching between the spectral responsivity of the OSC and the EL emission spectrum of the OLED in the integrated device. In other applications, when the OSC in an OLED/OSC structure is operated based on the absorption of light emitted from the OLED component for application in optical sensors, it is then desired that the spectral responsivity of the photovoltaic component matches with the EL emission spectrum of the OLED [55]. The sensor platform technology, based on an integration of organic light transmissible devices, such as an OSC and an OLED with polymer waveguides [56], provides significant cost benefit as well as the functional superiority for application in low cost bioassay device, sign monitoring, and compact information systems.

The performance of an organic optoelectronic device based on the monolithic integration of a front semitransparent OSC [57, 58] with a bottom OLED will discuss in this section. In an integrated functional semitransparent OSC/OLED system, the photoactive materials used in the front semitransparent OSC are chosen in such a way that the OSC component has a very low absorption in the wavelength region of light emitted by the integrated OLED unit. The front OSC is transparent to the EL emission of the underneath OLED. For example, an 8-tris-hydroxyquinoline (Alq_3):10-(2-benzothiazolyl)-1,1,7,7-tetramethyl-2,3,6,7- tetrahydro-1H,5H, 11H (13.1) benzopyrano(6,7,8-ij)-quinolizin-11-one (C545)-based OLED and a ZnPc:C_{60}-based semitransparent OSC were used for fabrication of the integrated OSC/OLED device. Alq_3:C545-based OLED has a peak EL emission at ~530 nm, while the spectral response of ZnPc:C_{60}-based OSC has a very low photoresponse at the same wavelength, but relatively high absorption over the visible light wavelength range. Hence, the combination of a ZnPc:C_{60}-based semitransparent OSC and an Alq_3:C545-based OLED in an integrated OSC/OLED structure allows light emitted from the OLED unit to pass through the front semitransparent OSC without a significant loss.

The integrated device was fabricated on an ITO-coated glass substrate with a sheet resistance of ~10 Ω/sq. The organic and electrode materials were thermally evaporated in a vacuum system having a base pressure $<10^{-6}$ mbar. The ITO substrates were subjected to an O_2 plasma treatment at 100 W for 10 min. In this integrated organic light transmissible device, the semitransparent OSC component consists of a co-evaporated ZnPc:C_{60} layer (35 nm), a C_{60} acceptor layer (25 nm), a

BPhen exciton-blocking layer (7 nm) and a 30 nm thick Ag semitransparent cathode, which also acts as a front electrode to the upper OLED unit. The Ag contact was then modified with plasma, forming a plasma-polymerized fluorocarbon film (CF_X) ($\sim$1 nm). The surface of the CF_X-modified Ag serves as an anode contact for the OLED [59]. The OLEDs consist of a N,N′-bis(l-naphthyl)-N,N′-diphenyl-1,l′-biphentl-4,4′-diamine (NPB) layer (55 nm), an emitting layer of Alq_3 doped with C545 (0.8 %), and an electron-transporting layer of undoped Alq_3. Finally, a 150 nm thick of Al electrode was deposited on the organic layers through a shadow mask that defines an active area of 3 mm × 3 mm. The J–V characteristics of the OSCs were measured using an AM1.5G solar simulator, calibrated by a KG-5 filtered photodiode.

In order to achieve an efficient light output, a microcavity OLED (MOLED) was used in the integrated device in order to achieve a narrow emission spectrum [60, 61] to maximize light output through the front semitransparent OSC. An optimization of the structure of semitransparent-OSC/MOLED thin film system was investigated. From optical point view, an integrated OSC/MOLED device can be also considered as a multi-layer thin film system composed of absorbing and non-absorbing materials. The photovoltaic performance and the transparency of the front semitransparent OSC, as well as the electroluminescence efficiency of the underneath OLED component can be optimized using the theoretical simulation approach discussed in the previous sections. Therefore the optical properties and optimal structure of an integrated semitransparent-OSC/MOLED device can be calculated using (13.4) and (13.7). An structure of the integrated semitransparent OSC/OLED device, e.g., glass/ITO/ZnPc:C_{60} (35 nm)/C_{60} (25 nm)/Bphen(7 nm)/Ag (30 nm)/CF_X /NPB (55 nm)/Alq_3: C545(25 nm)/Alq_3 (25 nm)/LiF (0.7 nm)/Al (150 nm), is thus optimized to enhance the absorption in the front semitransparent OSC component and high output of the emitted light by the MOLED unit at 530 nm.

In addition to the device design and the materials selection, an optical transparent and electrical conductive inter electrode that functions simultaneously as a cathode for the front semitransparent OSC and an anode for the MOLED unit plays a critical role in determining the device performance. An ultra-thin CF_X-modified silver interlayer (Ag/CF_X) was used to vertically connect the front OSC and the rear MOLED unit. An Ag/CF_X bi-layer has been applied for making high performance top-emission OLEDs [59] and can be made easily without causing damage to the underlying organic layers. An optical admittance analysis was used to study the optical properties and optimize the structure of the semitransparent-OSC/MOLED prior to the device fabrication. The performance of the OLED and OSC components in the stacked devices was shown to have a luminous efficiency of 11.5 cd/A operated at 4.5 V and a PCE of 3.30 %, achieving as high as 88 % of the performance measured for the discrete control OSC. A cross sectional view of the structure of the integrated device is shown in Fig. 13.14.

The incident photon to current conversion efficiency (IPCE) measured for the semitransparent OSCs and the EL spectra measured for the MOLEDs in the integrated device are plotted in Fig. 13.15a. ZnPc:C_{60}-based semitransparent OSCs thus fabricated have an optical transparency of >70 % at 530 nm, allowing the emitted

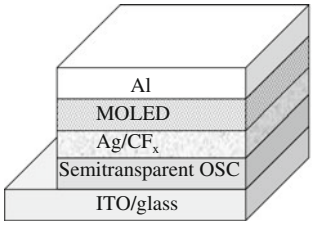

Fig. 13.14 Schematic diagram of an integrated OSC/MOLED device, with a layer configuration of glass/ITO/ZnPc:C_{60} (35 nm)/C_{60} (25 nm)/Bphen (7 nm)/Ag (30 nm)/CF_X/NPB (55 nm)/Alq_3: C545 (25 nm)/Alq_3 (25 nm)/LiF (0.7 nm)/Al (150 nm)

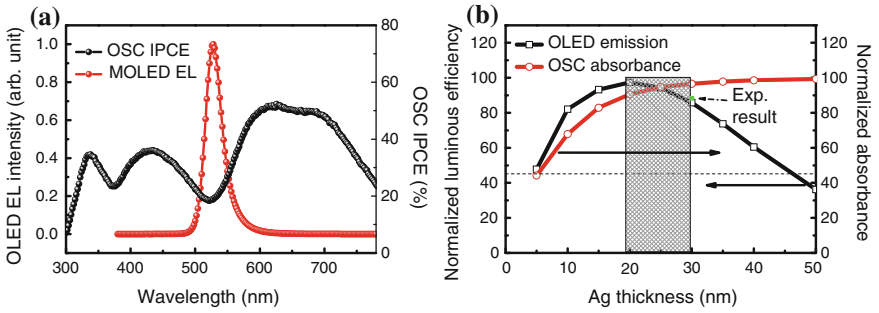

Fig. 13.15 Spectral response and electroluminescence characteristics of the integrated semitransparent-OSC/MOLED device, **a** IPCE and EL emission spectra measured for the front semitransparent OSC and the rear MOLED in the integrated device. **b** Calculated results showing the effect of Ag interlayer thickness on absorbance and emission of the integrated device (normalization is taken with reference to a discrete MOLED and a semitransparent OSC having identical structures used in the integrated device). The *dash line* refers to the normalized luminous efficiency measured for a normal OLED, which is equivalent to 45 % of an MOLED

light from the bottom MOLED with a peak EL wavelength of 530 nm to pass through with a very low absorption lost. As shown in Fig. 13.15a, the emission peak from the MOLED complementarily falls within the valley of the IPCE spectrum of the front semitransparent OSC. Such a result is achieved through an optical and optimal design of the device structure.

The results of the effect of the semitransparent Ag inter-electrode thickness on the normalized absorbance of the front semitransparent OSC component and luminous efficiency of underneath MOLED unit in the integrated device, with the normalization taken reference with a control OSC and a control MOLED, are presented in Fig. 13.15. The luminous efficiency of an OLED without microcavity structure is about 45 %, as depicted by the dash line in Fig. 13.15b. The calculation results indicate that the maximum luminous efficiency of the MOLED in the integrated devices can be achieved at an Ag interlayer thickness of 20 nm. On the other hand, the maximum light absorption by the front semitransparent OSC occurs when the thickness of the Ag layer is over 60 nm. A shaded region as depicted in

Fig. 13.15b corresponds to the required Ag interlayer thickness to achieve high light absorption by the front semitransparent OSC and the high luminous efficiency of the rear MOLED in the integrated device. Based on the simulation results, an Ag interlayer thickness of 30 nm was selected as an optimal solution, corresponding to light absorbance in the front OSC equivalent to 97 % of a control OSC and, a luminous efficiency of a rear MOLED equivalent to 86 % of a control MOLED, respectively.

The results of simulated and measured EL spectra obtained for a normal OLED, a discrete MOLED and an MOLED in the integrated devices are shown in Fig. 13.16a, b. The wavelength of peak emission by the MOLED in the integrated device is located at 521 nm, which is hypsochromically shifted from 526 and 531 nm, the emission wavelengths for the single MOLED and the OLED, respectively. The full width at half maximum (FWHM) of the emission band is 33 nm, which is the same as that for the control MOLED and smaller than 58 nm for a conventional OLED.

J–V characteristics of the OSC in the integrated device as well as that for a control OSC, measured under AM1.5G irradiation of 100 mW/cm^2, are shown in Fig. 13.17a. The control cell, with a configuration of glass/ITO/ZnPc: C_{60}(35 nm)/C_{60}(25 nm)/Bphen(7 nm)/Ag(100 nm), was fabricated for comparison studies. The control device shows a PCE of 3.76 %, a FF of 58.9 % and a J_{SC} of 11.4 mA/cm^2. The corresponding values for a front semitransparent OSC in the integrated semitransparent-OSC/MOLED device are 3.30, 57.2 % and 10.5 mA/cm^2. V_{OC} measured for the front OSC in the integrated device is the same as the control device. It is interesting to note that the PCE obtained for the integrated device is as high as 88 % of that for the reference OSC, labeled as "Experimental result" in Fig. 13.15b. The results of the luminous efficiency measured for a discrete MOLED and an MOLED in the integrated device are given in Fig. 13.17b. The luminous efficiency

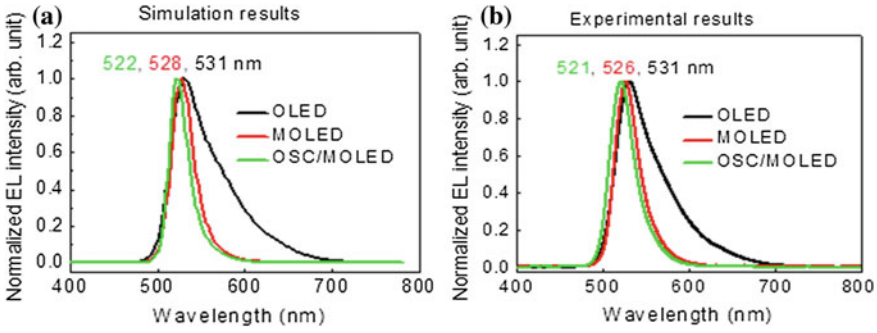

Fig. 13.16 Electroluminescence of OLEDs. **a** Simulated EL spectra obtained for a set of structurally identical light emitting diodes of a normal OLED, a discrete MOLED and an MOLED in an integrated device. **b**, EL spectra measured for a normal OLED, a discrete MOLED and an MOLED in an integrated device

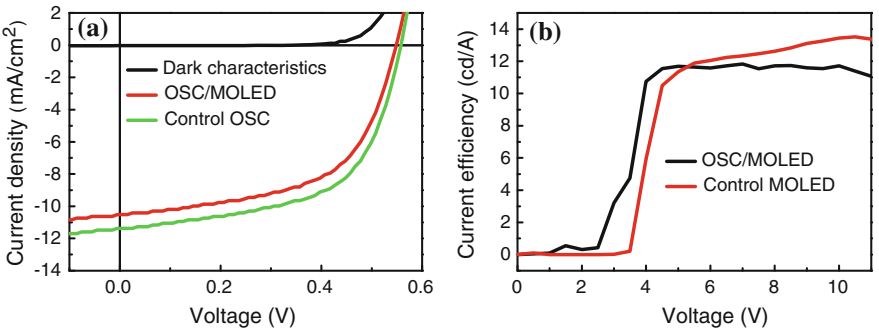

Fig. 13.17 **a** J–V characteristics measured for a control OSC and a semitransparent OSC in the integrated device under AM1.5G. **b** Luminous efficiency measured for a control MOLED and an MOLED unit in the integrated semitransparent-OSC/MOLED device

of the rear MOLED unit in the integrated device achieves 11.5 cd/A as compared to that of 10.5 cd/A for a control MOLED at 4.5 V, as shown in Fig. 13.17b.

OSCs and OLEDs as the key components in the organic electronics have the potential advantages in terms of cost effectiveness, chemical tenability and flexibility. A functional organic optoelectronic device that integrates a front semitransparent OSC and a rear OLED connected with an ultrathin Ag/CF_X interlayer was demonstrated. Table 13.3 lists a summary of luminous efficiency measured for a control MOLED and an MOLED unit in the integrated OSC/MOLED device, as well as the photovoltaic characteristics measured for a control OSC and a front semitransparent OSC unit in the integrated OSC/MOLED device. Through proper selection of the active materials, and optimal design, the integrated device can be capable of providing the power by absorption of the ambient illumination by the front semitransparent OSC component and also emitting light by the underneath OLED, for example, a PCE of 3.30 % measured under AM1.5G irradiation and a

Table 13.3 A summary of luminous efficiency measured for a control MOLED and an MOLED unit in the integrated OSC/MOLED device at 4.5 V, and photovoltaic characteristics measured for a control OSC and a front semitransparent OSC component in the integrated OSC/MOLED device under AM1.5G irradiation

OLED characteristics	EL peak position (nm)	FWHM (nm)	Luminous efficiency (cd/A)	
Control MOLED	526	32	10.5 (@ 4.5 V)	
OSC/MOLED	521	33	11.5 (@ 4.5 V)	
OSC characteristics	V_{OC} (V)	FF (%)	J_{SC} (mA/cm^2)	PCE (%)
Control OSC	0.56	58.9	11.4	3.76
OSC/MOLED	0.55	57.2	10.5	3.30

high luminous efficiency of 11.5 cd/A operated at 4.5 V. The technology based on the monolithic integration of OLEDs and OSCs has a potential to create an organic sensor platform technology for application in organic electronics including organic optical switches, sensors, image-retaining displays, automatic brightness control, and other organic photonic logic circuits.

13.7 Summary

Organic solar cells offer an attractive option for achieving low-cost and clean energy sources. They have efficiencies comparable to conventional inorganic amorphous silicon-based solar cells. Organic semiconductors as the active components in photovoltaic devices have advantages especially in terms of large area, cost effectiveness, chemical tenability, color variation, visible-light transparency and flexibility. The semitransparent OSC technology can be advanced through continuous development of novel organic photoactive materials with enhanced absorption in NIR region, high performance upper transparent electrodes and new device design. The simultaneous optimization of performance and visible-light transparency for semitransparent OSCs reviewed in this chapter may serve an introduction to provide ideas and process know-how to the fast growing field of OSCs. The high performance semitransparent OSCs would offer potentially more opportunities for application in new markets such as mobile electronics, smart sensors, automotive, power generating window panes, greenhouses and outdoor lifestyle etc.

References

1. S. Günes, H. Neugebauer, N.S. Sariciftci, Chem. Rev. **107**, 1324 (2007)
2. A.C. Arias, N. Corcoran, M. Banach, R.H. Friend, J.D. MacKenzie, W.T.S. Huck, Appl. Phys. Lett. **80**, 1695 (2002)
3. M.A. Green, K. Emery, Y. Hishikawa, W. Warta, Prog. Photovolt: Res. Appl. **20**, 606 (2012)
4. G. Dennler, M.C. Scharber, C.J. Brabec, Adv. Mater. **21**, 1323 (2009)
5. G. Li, V. Shrotriya, Y. Yao, Y. Yang, J. Appl. Phys. **98**, 043704 (2005)
6. G. Li, R. Zhu, Y. Yang, Nat. Photon. **6**, 153 (2012)
7. Y.-J. Cheng, S.-H. Yang, C.S. Hsu, Chem. Rev. **109**, 5868 (2009)
8. B.C. Thompson, J.M. Frechet, Angew. Chem. Int. Ed. **47**, 58 (2008)
9. J.S. Wilson, A.S. Dhoot, A.J.A.B. Seeley, M.S. Khan, A. Köhler, R.H. Friend, Nature **413**, 828 (2001)
10. W.Y. Wong, Dalton Trans. 4495 (2007)
11. W.Y. Wong, C.L. Ho, Coord. Chem. Rev. **250**, 2627 (2006)
12. A. Yakimov, S.R. Forrest, Appl. Phys. Lett. **80**, 1667 (2002)
13. J. Xue, S. Uchida, B.P. Rand, S.R. Forrest, Appl. Phys. Lett. **85**, 5757 (2004)
14. G. Dennler, H.J. Prall, R. Koeppe, M. Eggiger, R. Autengruber, N.S. Sariciftci, Appl. Phys. Lett. **89**, 073502 (2006)
15. F.R. Zhu, J. Singh, J. Non-Cryst. Solids **163**, 65 (1993)

16. F.R. Zhu, J. Singh, Sol. Energy Mater. Sol. Cells **31**, 119 (1993)
17. F.R. Zhu, T. Fuyuki, H. Matsunami, J. Singh, Sol. Energy Mater. Sol. Cells **39**, 1 (1995)
18. F.R. Zhu, P. Jennings, J. Cornish, G. Hefter, K. Luczak, Sol. Energy Mater. Sol. Cells **49**, 163 (1997)
19. C. Tuchinda, S. Srivannaboon, H.W. Lim, J. Am. Acad. Dermatol. **54**, 845 (2006)
20. R.R. Lunt, V. Bulovic, Appl. Phys. Lett. **98**, 113305 (2011)
21. J. Meiss, K. Leo, M.K. Riede, C. Uhrich, W.-M. Gnehr, S. Sonntag, M. Pfeiffer, Appl. Phys. Lett. **95**, 213306 (2009)
22. G. Qian, Z.Y. Wang, Chem. Asian J. **5**, 1006 (2010)
23. K.Y. Lam, Chem. Rev. **93**, 449 (1993)
24. F. Silvestri, M.D. Irwin, L. Beverina, A. Facchetti, G.A. Pagani, T.J. Mark, J. Am. Chem. Soc. **130**, 17640 (2008)
25. P.F. Santos, L.V. Reis, P. Almeida, J.P. Serrano, A.S. Oliveira, L.F. Vieira Ferreira, J. Photochem. Photobiol., A **163**, 267 (2004)
26. B.P. Rand, J.G. Xue, F. Yang, S.R. Forrest, Appl. Phys. Lett. **87**, 233508 (2005)
27. A. Ajayaghosh, Chem. Soc. Rev. **32**, 181 (2003)
28. A. Gadisa, K. Tvingstedt, S. Admassie, L. Lindell, X. Crispin, M.R. Andersson, W.R. Salaneck, O. Inganäs, Synth. Met. **156**, 1102 (2006)
29. V. Shrotriya, E.H.E. Wu, G. Li, Y. Yao, Y. Yang, Appl. Phys. Lett. **88**, 064104 (2006)
30. A. Hadipour, B. de Boer, P.W.M. Blom, J. Appl. Phys. **102**, 074506 (2007)
31. S.L. Lai, M.Y. Chan, M.K. Fung, C.S. Lee, L.S. Hung, S.T. Lee, Chem. Phys. Lett. **366**, 128 (2002)
32. M.Y. Chan, S.L. Lai, M.K. Fung, S.W. Tong, C.S. Lee, S.T. Lee, Appl. Phys. Lett. **82**, 1784 (2003)
33. K.C. Lau, W.F. Xie, H.Y. Sun, C.S. Lee, S.T. Lee, Appl. Phys. Lett. **88**, 083507 (2006)
34. S.S. Li, K.H Tu, C.C. Lin, C.W. Chen. M, Chhowalla, ACS Nano, 4, 3169 (2010)
35. Y.Y. Lee, K.H. Tu, C.C. Yu, S.S. Li, .Y. Hwang, C.C. LinK.H. Chen, L.C Chen, H.L. Chen and C.W. Chen, ACS Nano, 5, 6564 (2011)
36. Z.K. Liu, J.H. Li, Z.H. Sun, G.A. Li, S.P. Lau, F. Yan, ACS Nano **6**, 810 (2012)
37. G.M. Ng, E.L. Kietzke, T. Kietzke, L.W. Tan, P.K. Liew, F.R. Zhu, Appl. Phys. Lett. **90**, 103505 (2007)
38. X.Z. Wang, G.M. Ng, J.W. Ho, H.L. Tam, F.R. Zhu, IEEE J. Sel. Top. Quantum Electron. **16**, 1685 (2010)
39. P. Peumans, A. Yakimov, S.R. Forrest, J. Appl. Phys. **93**, 3693 (2003)
40. P.F. Carcia, R.S. Mclean, M.H. Reilly, Z.G. Li, L.J. Pillione, R. F. Messier. J. Vac. Sci. Technol. A: Vac. Surf. Films, 21 745 (2003)
41. Y.R. Cui, X.H. Xu, Thin Solid Films **115**, 195 (1984)
42. C. Coutal, A. Azema, J.C. Roustan, Thin Solid Films **288**, 248 (1996)
43. H.J. Krokoszinski, R. Oesterlein, Thin Solid Films **187**, 179 (1990)
44. F.R. Zhu, C.H.A. Huan, K. Zhang, A.T.S. Wee, Thin Solid Films **359**, 244 (2000)
45. H. Morikawa, M. Fujita, Thin Solid Films **359**, 61 (2000)
46. D. Y. Lee, S. J. Lee, K. M. Song, H. K. Baik, J. Vac. Sci. Technol. A: Vac., Surf. Films, **21**, 1069 (2003)
47. T. Morimune, H. Kajii, Y. Ohmori, Jpn. J. Appl. Phys. **44**, 2815 (2005)
48. A.J. Moulé, J.B. Bonekamp, K. Meerholz, J. Appl. Phys. **100**, 094503 (2006)
49. E. D. Palik, Handbook of Optical Constants of Solids, vol. I (1998), pp. 355–356, 688–690
50. P. Peumans, S.R. Forrest, Appl. Phys. Lett. **76**, 3855 (2000)
51. C.J. Yang, T.Y. Cho, C.L. Lin, C.C. Wu, Appl. Phys. Lett. **90**, 173507 (2007)
52. C.J. Yang, T.Y. Cho, Y.Y. Chen, C.J. Yang, C.Y. Meng, C.H. Yang, P.C. Yang, H.Y. Chang, C.Y. Hsueh, C.C. Wu, S.C. Lee, Appl. Phys. Lett. **90**, 233512 (2007)
53. J. Park, J. Lee, D. Shin, J. Display Technol. **6**, 247 (2010)
54. J.G. Xue, S.R. Forrest, Appl. Phys. Lett. **82**, 136 (2003)
55. Y. Ohmori, H. Kajii, M. Kaneko, K. Yoshino, M. Ozaki, A. Fujii, M. Hikita, H. Takenaka, T. Taneda, IEEE J. Select. Top. Quan. Electron. **10**, 70 (2004)

56. C. J. Yang, T. Y. Cho, C. L. Lin, C. C. Wu J. SID 16 691 (2008)
57. J.Y. Lee, S.T. Connor, Y. Cui, P. Peumans, Nano let. **10**, 1276 (2010)
58. X.Z. Wang, H.L. Tam, K.S. Yong, Z.K. Chen, F.R. Zhu, Org. Electron. **12**, 1429 (2011)
59. Y.Q. Li, L.W. Tan, X.T. Hao, K.S. Ong, F.R. Zhu, L.S. Hung, Appl. Phys. Lett. **86**, 153508 (2005)
60. T. Nakayama, Y. Itoh, A. Kakuta, Appl. Phys. Lett. **63**, 594 (1993)
61. N. Takada, T. Tsutsui, S. Saito, Appl. Phys. Lett. **639**, 2032 (1993)

Index

Y. Yang and G. Li (eds.), *Progress in High-Efficient Solution Process Organic Photovoltaic Devices*, Topics in Applied Physics 130,
DOI 10.1007/978-3-662-45509-8